THÈSE DE DOCTORAT DE L'ÉTABLISSEMENT UNIVERSITÉ DE BOURGOGNE FRANCHE-COMTÉ

PRÉPARÉE À L'UNIVERSITÉ DE BOURGOGNE
Laboratoire Interdisciplinaire Carnot de Bourgogne

Ecole doctorale n°553

Carnot-Pasteur

Doctorat de physique

Par

M. RAJA KUMAR Manoj

Study of the vapor plume formed during the dissimilar laser welding: the application in the case of titanium/aluminum couple

Soutenue le 21 décembre 2023, à Le Creusot, France

Composition du Jury :

M. SCHNEIDER Matthieu	MCF-HDR, Arts et Métiers, PIMM	Rapporteur
M. PELLERIN Stéphane	Pr, GREMI, Université d'Orléans	Rapporteur
M. MERIAUDEAU Fabrice	Pr, ICMUB, Université de Bourgogne	Président du jury
M. SEMMAR Nadjib	Pr, GREMI, Université d'Orléans	Examinateur
M. COURTOIS Mickaël	MCF-HDR, IRDL, Université Bretagne Sud	Examinateur
M. JOUVARD Jean-Marie	Pr, ICB, Université de Bourgogne	Directeur de thèse
Mme. TOMASHCHUK Iryna	MCF-HDR, ICB, Université de Bourgogne	Co-directrice de thèse

Titre : Étude de la plume de vapeur lors du soudage laser des matériaux dissemblables : application au cas de l'assemblage titane/aluminium

Mots clés : soudage laser, plume de vapeur, matériaux dissemblables, imagerie rapide

Résumé : La soudure au laser de métaux dissemblables, tels que le titane et l'aluminium, suscite un vif intérêt au sein de l'industrie manufacturière. Toutefois, l'incompatibilité entre ces matériaux constitue un défi considérable en raison des disparités dans leurs propriétés physiques et thermophysiques. Comprendre les mécanismes physiques en cours au sein de le capillaire revêt une importance cruciale en vue de l'optimisation et de l'assurance de la qualité des soudures. Le comportement de la plume de vapeur émergeant du capillaire est intimement lié aux phénomènes survenant à l'intérieur de cette dernière. De ce fait, l'objectif de cette thèse consiste à appréhender et caractériser la plume de vapeur dissemblable au moyen de techniques d'imagerie rapide, conjointement à la spectroscopie d'émission. Nous avons établi une corrélation entre la plume de vapeur et le comportement du capillaire par le biais d'une investigation in-situ de la zone fondue/de la capillaire au moyen de l'imagerie rapide.

En outre, nous avons réalisé une analyse post-mortem en utilisant SEM-EDX des zones fondues. L'influence de divers décalages du faisceau laser de la ligne de jonction a été étudiée concernant le comportement du capillaire et la plume de vapeur de soudage dissimilaire en configuration bout à bout. L'observation de la plume de vapeur à différentes longueurs d'onde, notamment dans les régimes infrarouge et ultraviolet, conjuguée à des techniques de traitement d'image et de caractérisation, a été fait pour le panache dissimilaire. La spectroscopie d'émission a été mise en œuvre afin d'étudier les émissions thermiques et atomiques de la plume de vapeur, ce qui a permis d'estimer sa température et d'identifier sa composition chimique. Enfin, la plume de vapeur et le comportement du capillaire ont fait l'objet d'une étude, en utilisant les mêmes techniques in-situ et post mortem, dans le contexte du soudage par transparence. Cette démarche visait à observer et à appréhender les divergences par rapport au soudage en configuration bout à bout.

Title : Study of the vapor plume formed during the dissimilar laser welding: the application in the case of titanium/aluminum couple

Keywords : laser welding, vapor plume, dissimilar materials, high-speed imaging

Abstract : Laser welding of dissimilar metals such as titanium and aluminum is highly sought-after in manufacturing. However, incompatibility between these materials is challenging due to the differences in their physical and thermophysical properties. Understanding the physical processes in the keyhole could lead to better optimization and quality control of the welded joints. The behavior of the vapor plume exiting the keyhole is closely related to the processes occurring within the keyhole. Therefore, the aim of this thesis is to understand and characterize the dissimilar vapor plume using in-situ techniques such as high speed imaging and emission spectroscopy. Correlation of the vapor plume with the keyhole behavior was done through in-situ investigation of the keyhole-melted zone using high-speed imaging and also post-mortem SEM-EDX analysis of the melted zones.

The influence of different laser beam offsets from the joint line on the keyhole and vapor plume behavior were studied for the dissimilar welding experiments in butt-configuration. Observation of the vapor plume at different wavelengths in the infrared and ultraviolet regimes, along with image processing and characterization techniques were done for the dissimilar plume. Emission spectroscopy, conducted to study the continuous thermal and atomic emissions from the vapor plume allowed temperature estimation and identification of the chemical composition of the vapor plume. Finally, the vapor plume and keyhole behavior were studied using the same in situ and post-mortem techniques for overlap welding to observe and understand the differences from welding in butt-configuration.

எல்லா விளக்கும் விளக்கல்ல சான்றோர்க்குப்
பொய்யா விளக்கே விளக்கு.

<div align="right">- திருக்குறள் 299</div>

Ellaa Vilakkum Vilakkalla Saandrorkkup
Poiyaa Vilakke Vilakku
(Transliteration)

Not all lights cause illumination; For the wise,
Only the light of truth is illuminant.

<div align="right">- Thirukkural 299</div>

Acknowledgements

Table of contents

Nomenclature

Symbol	Meaning
a	Thermal diffusivity
$A(T)$	Temperature dependent absorptivity
A	Total absorptivity of the keyhole
A_{A5754}, A_{Ti}	Areas of A5754 and Ti melted zones
A_0	Absorptivity of the flat surface
A_R	Aspect ratio of the keyhole
A_s	Einstein's spontaneous emission coefficient
c	Speed of light
c_i	Molar concentration of the species
C_p	Thermal capacity at constant pressure
C_0, C_1	Classes of pixels with gray level values between $[0,1,2, \ldots, T_h]$ and $[T_h + 1,\ T_h + 2, T_h + 3, \ldots, L]$
d_{Ti}	Global dilution of Ti in melted zones
D_i	Stokes-Einstein diffusion coefficient
D_s	Spatter droplet diameter
E_n	Energy of the quantum level n
E_{min}	Minimum energy for vaporization
$E_{j,\infty}^{(z)}$	Ionization energy
E_{ej}	Spatter ejection energy
g_n	Degeneracy of the quantum level n
$g_{j,u}^{(z)}$	Statistical weight for element j
$g_j^{(z+1)}, g_j^z$	Statistical Weights for states $z + 1, z$
g_e	Statistical weights for electron number
$\vec{g}$	Acceleration due to gravity
h	Planck's constant
I	Relative intensity of atomic emission
$I_{measured}$	Measured intensity of thermal radiation
i	Gray level value, complex number
J	Quantum number related to angular momentum

J_i	Quantum number for state i
K	Thermal conductivity
k_c	Complex part of refractive index (attenuation coefficient/extinction coefficient)
k_B	Boltzmann's constant
L	Bit depth / Number of gray levels
$L_\lambda^B(\lambda, T)$	Spectral radiance of a blackbody
$L_{394\,nm}(T)$	Luminance in the region of the 394 nm optical bandpass filter
$L_{810\,nm}(T)$	Luminance in the region of the 810 nm optical bandpass filter
L_v	Latent heat of vaporization
L_0	Lorenz number
m	Atomic mass
Ma	Local Mach number
m_e	Mass of electron
m_a	Emitter mass
$\dot{m}$	Vaporization mass flux
M_a	Molar mass
n	Real part of refractive index (phase velocity)
N	Total number of pixels
n_i	Number of pixels with gray level value i
$\underline{n}$	Refractive index (complex)
N_n	Population at quantum level n
$N_j^{(z+1)}, N_j^{(z)}$	Number densities of states $z+1, z$
$N_j^{(z)}$	Number density of element j at degree of ionisation z
N_e^W	McWhirter criterion/Minimum electron number density
N_e	Electron number density
p	Slope of Boltzmann plot
p_r	Recoil pressure
p_i	Probability of occurrence of gray level value i
P_{i-1}, P_i	Keyhole penetration depths in successive frames

P_{jl}	Melted zone depth at joint line
P_{max}	Maximum keyhole/melted zone penetration depth
P_n	Relative probability of a specific quantum state n
P_{sat}	Saturated pressure
P_{atm}, p_0	Atmospheric pressure
$P_0(T_h), P_1(T_h)$	Cumulative probabilities corresponding to C_0, C_1
q''	2D Heat flux
$Q(t)$	Total heat rate
Q	3D Heat flux
Q_0	Maximum volumetric heat flux density
R	Ideal gas constant
r_e, r_i	Upper and lower 3D cone radii
r_s	Solute radius
R_0	Beam radius
T	Temperature
t_1	Pulse duration
T_v	Vaporization temperature
T_s	Surface temperature
T_m	Melting point
T_{ion}	Ionic temperature
T_{ex}	Excitation temperature
T_e	Electronic temperature
T_a	Maxwellian distribution of temperature
T_{KN}	Temperature of the Knudsen layer
T_h	Threshold of gray value
T_0	Temperature at a point
u_w	Welding speed
u_D	Spatter droplet velocity
$\vec{u}, \vec{u_r}$	Velocity field
$U_j^{(z)}$	Partition function of element j
v_x	Emitter velocity

V_i	Instantaneous keyhole drilling velocity
$\bar{V}$	Average keyhole drilling velocity
Z	Partition function
z_e, z_i	3D cone length parameters
α	Incident angle
β	Thermal expansion coefficient
β_r	Recombination coefficient
$\delta(T)$	Electrical resistivity
Δt	Uncertainty of time intervals during measurement
ΔE	Uncertainty of energy of atomic system
$\Delta\lambda_{1/2}^G$	Halfwidth of a Gaussian line shape function
ΔH_v	Phase transition enthalpy
ΔE_{nm}	Largest energy gap between adjacent levels
ε	Thickness of the interface
$\varepsilon_{u,l}$	Spectral radiance
ε_r	Real part of relative permittivity
$\underline{\varepsilon}_r$	Complex relative permittivity
$\tilde{\varepsilon}_r$	Complex part of relative permittivity
γ	Mobility of the interface
λ	Wavelength of light
λ_s	Spontaneous emission wavelength
λ_{pq}	Doppler shift of wavelength
λ_{me}	Mixing energy
μ	Overall mean gray value
$\mu_0(T_h), \mu_1(T_h)$	Mean gray levels corresponding to C_0, C_1
ν	Frequency of light
ϕ	Phase field function
ρ	Mass density
ρ_{ref}	Reflectance
ρ_m	Melt density
σ	Surface tension

σ_e	Electrical conductivity
σ_I	Standard deviation in intensity during profile fitting
σ_{ln}	Logarithm of standard deviation
σ_m	Surface tension at the melting point
σ_p	Standard deviation obtained during liner regression
σ_T	Standard deviation in estimation of atomic temperature
$\sigma_b^2(T_h)$	Between-class variance
$\sigma_0^2(T_h), \sigma_1^2(T_h)$	Variances corresponding to C_0, C_1
$\sigma_w^2(T_h)$	Within-class variance
χ	Mobility turning parameter
ω_{pq}	Doppler shift of angular frequency
Ω	Laser spot position relative to the joint line

Context

The team "Laser et Traitements des Matériaux" situated in Le Creusot, France, a part of "Procédés Métallurgiques, Durabilité, Matériaux" department of "Laboratoire Interdisciplinaire Carnot de Bourgogne" has been involved in the research about assembly of metallic materials by high energy processes such as laser, electric arcs, and thermal spraying. The issue of assembly of metallic materials is tackled from different angles by studying processes happening during and after the assembly.

The improvisation of the durability or mechanical performance of laser brazing by optimization of the operational conditions was done for steel/aluminum [1]. The thermogram of the surface, temperature profile during this process, and the thermal field in the structure was measured by an infrared camera [2]. The evolution of the observed temperatures was studied along with the geometry of the keyhole for laser and hybrid (laser + MIG) welding, which led to a conclusion stating that mathematical modelling or simulation require more than just a formulation of a power supply but rather the internal temperature data [3]. Simultaneously, the interaction of the laser and the material was being uncovered by identification of the relationship between theory and experiment in the absorption coefficient values of metals like aluminum and magnesium when welded by Nd:YAG laser [4]. The relationship between the surface conditions (roughness), material removal rate and the operational conditions was construed for metals like stainless steel, titanium alloy, aluminum alloy [5]. In addition, methods such as the effects of powder on selective laser melting and inserts in dissimilar laser welding have also been studied on separate occasions [6], [7].

Similar surface treatment studies were also conducted for surface characterization with a Q-switched Nd:YAG nanosecond laser for titanium substrates [8]. Following up on the characterization of the laser material interaction and the changes in the metallurgical properties in the treatment with a nanosecond laser, several studies were conducted which involved the study of the laser plasma plume structure, nano-particles formed in the plasma plume (experimental: X-ray scattering, numerical: hydrodynamic code coupled with nucleation model), influence on the surface through oxygen, nitrogen insertion in the surface of the metals, etc. [9]–[15].

Several numerical simulation studies were done to complement the experimental work. To start, the morphology of the dissimilar copper-steel electron beam welds were done using level-set method to study the shape, fluid flow and mixing patterns [16], which led to a multiphysical model that included diffusion in dissimilar welding [17]. And then a different method called 'phase field method' was used to create the models since it allowed intense mixing while convection of immiscible liquids was fairly limited with the previous 'level-set' method [18]. And then the models were built for hybrid laser/MIG welding using an equivalent heat source [19]. 3-D multiphysical models were built to study the transport phenomenon coupled with diffusion for laser welding of steel which allowed the observation of the Marangoni effect which leads to the hourglass shaped welds [20], [21]. Mechanical properties such as residual stresses were also studied for laser welding of dissimilar materials [22]. Limitations in the previous models which led to mismatch with the experimental results were studied and corrected through multiple modifications in the model [23]. Progress was achieved in building the keyhole model for continuous welding as well [24].

Similarly, validation of the simulations was also done by experimental work. For example, the thermal and surface strain fields were studied using thermocouples and IR imaging in order to validate the thermo-mechanical simulations of hybrid welding [25]. Another imaging method using polarimetric parameters was also developed to observe the thermal radiations by the melt

pool for arc welding [26]. Vision based algorithms were developed with the objective to compute wire extension in gas metal arc (MAG)/laser hybrid welding while simultaneously detecting the path of the melt pool [27] which is one of the first step taken towards the journey to reach laser welding process control in this team. Laser/electron beam welding between dissimilar metals have been a topic of interest [28] for quite some time now due to the problems in the control and weld zone quality. The differences in the melting and vaporization temperatures between the two materials can produce highly asymmetric welds and several defects in the melted zone. Similarly, differences in thermal diffusivity and laser absorptivity can also lead to defects due to asynchronous melting and vaporization. A strong gradient of physical properties across the melted zone and the presence of undesired brittle intermetallic phases can lead to poor weld quality and cracking. Thus, the compatibility/incompatibility between the different metals (Figure 1) not only makes dissimilar welding difficult in some cases but also as an interesting subject to be studied and understood. And so, instead of using only statistical optimization techniques to make advancements in the process control, it becomes necessary to better comprehend first, the phenomenology of the complex processes in laser welding of dissimilar materials, as those details can let us understand the observations made, while providing complementary information to optimization techniques from a physical point of view.

Introduction

Laser welding has been a topic of interest in the applied physics community for more than half a century, ever since the invention of the laser. There is large interest in studying the application of laser in the process of joining metals due to several advantages:

- Good control of the process, excellent reproducibility, and increased quality enables new part designs.
- Precision of assembly, narrow beam that allows, for example, welding at the bottom of the groove or in inaccessible areas by conventional techniques.
- reduced energy input and low component heating, for example, for the manufacture of hollow bodies or for the manufacture of compact electronics.
- small deformations allow the use of light clamping tools.
- thorough or little post-weld recovery or straightening to build finished parts.
- One-pass welding, eliminating lengthy preparation and partial turning operations.
- Overlap welding without contact and with access from only one side.
- Reduction of consumables: no welding filler, no electrode wear.
- Short cycle time due to high welding speed.
- overcomes the problems from magnetic effects.
- optical fiber for the YAG laser suitable for the assembly of large parts or for multi-station work
- possibility of assembling dissimilar materials.
- possibility of welding and cutting with the same source, for example, cutting of the worn part and welding of a new part.

Research in this area is usually driven by the applications of the materials which need to be welded. And by this context, the weldability of metals such as titanium and aluminum hold high interest in this field. These metals have enormous potential in terms of applications due to their properties, availability, and cost.

The properties of titanium which allow for its numerous applications also play a crucial role in its weldability with aluminum. The relationship between these properties and the physics behind the phenomenology, for this combination of dissimilar laser welding is one of the

significant aspects of this thesis. The importance of understanding this dissimilar laser welding phenomena is not only application oriented but also concerned with the scientific progress in terms of understanding the underlying physics principles in this complicated process.

Over the years, a large number of useful applications have been developed from these materials, and the need to weld them together has been a primary interest in many of these industries. However, laser welding, which is a very complicated process, becomes even more difficult to understand when welding dissimilar materials due to incompatibilities in their physical and chemical properties. This is the reason why many articles describing the phenomenological process of laser welding of standalone materials from different points of view have been published, while such phenomenological descriptions for dissimilar welding are meagre in comparison. The materials which were studied for dissimilar laser welding in the context of this thesis were T40 commercially pure titanium and the A5754 aluminum alloy. T40 has higher absorptivity (40%) compared to A5754 (10%-30%), higher melting (T40 – 1941 K, A5754 – 883-902 K) and boiling (T40 – 3560 K, A5754 – 2792 K) points, but lower thermal diffusivity (T40 – 9.4 x 10^{-6} m^2/s, A5754 – 98.8 x 10^{-6} m^2/s). These physical properties render them to be only fairly compatible (Figure 1) by nature if we try to weld them using a laser. However, a wide community of researchers in both academic and industrial domains over the course of time have developed a wide variety of methods to study, understand and improvise the laser welding of titanium and aluminum by a laser [29]–[35]. The A5754 aluminum alloy was chosen to be studied instead of pure aluminum due to the presence of elements such as magnesium and manganese in the alloy, which may yield some insights from the perspective of spectroscopy. The dissimilar combination of A5754 and T40 were chosen because this combination has already been well studied from a metallurgical point of view and so, the remaining work shall be dedicated to understanding the physics of the interactions. Hence such a dissimilar combination with such mismatch in the thermal and spectral properties can yield notable results.

	W	Ta	Mo	Cr	Co	Ti	Be	Fe	Pt	Ni	Pd	Cu	Au	Ag	Mg	Al	Zn	Cd	Pb
Ta	E																		
Mo	E	E																	
Cr	E	P	E																
Co	F	P	F	G															
Ti	F	E	E	G	F														
Be	P	P	P	P	F	P													
Fe	F	F	G	E	E	F	F												
Pt	G	F	G	G	E	G	P	G											
Ni	F	G	F	G	E	F	F	G	E										
Pd	F	G	G	G	E	F	F	G	E	E									
Cu	P	P	P	P	F	F	F	F	E	E	E								
Au	*	*	P	F	P	F	F	F	E	E	E	E							
Ag	P	P	P	P	P	F	P	P	F	P	E	F	E						
Mg	P	*	P	P	P	P	P	P	P	P	P	F	F	F					
Al	P	P	P	P	F	F	P	F	P	F	P	F	F	F	F				
Zn	P	*	P	P	F	P	P	F	P	F	F	G	F	G	P	F			
Cd	*	*	*	P	P	P	*	P	F	F	F	P	F	G	E	P	P		
Pb	P	*	P	P	P	P	*	P	P	P	P	P	P	P	P	P	P	P	
Sn	P	P	P	P	P	P	P	P	F	P	F	P	F	F	P	P	P	P	F

*Figure 1. Laser weldability of binary metal combinations. (E = excellent, G = good, F = fair, P = poor, * = no data available) [28]*

Thesis objectives

Since laser welding research in this laboratory has been done mainly over the metallurgical aspects of the materials, and most of the studies in the laser welding research community has been dedicated to the welding of standalone materials, this thesis approaches laser welding of dissimilar metals from a phenomenological point of view. Previous studies on the dissimilar welding of titanium alloy and niobium showed that the weld was asymmetrical [36]. And this asymmetricity depends on the operation conditions and does not necessarily follow the position of the laser spot. And since the behavior of this keyhole largely influences almost all the complex processes (velocity fields in the melt pool, melt pool dilutions, extent of the heat affected zone, penetration depth, vapor plume behavior, etc.) involved in laser welding, understanding it has been the primary concern. The primary aspect of this asymmetric keyhole is the tendency of its root (bottom-most point) to shift towards one of the materials. While some authors observe that this root tends to shift towards the material with more laser absorptance,

others find that the root tends to shift towards the material with the lower vaporization temperature [37], [38]. In-situ characterization of the capillary (1.2.4) thus becomes essential to observe and understand the mechanisms which lead to the formation of this asymmetry.

Besides the keyhole behavior, another interesting feature being explored in the recent times, is the vapor plume behavior [39]–[52]. While the research on the dissimilar vapor plume is just beginning, it is clear that the vapor plume and the distribution of the elements in the melted zone are strongly linked [53]. Unlike the common ground where researchers are well set on the methodology and parameters for the observation of the keyhole, the in-situ observation methods and analyses of the vapor plume are yet to be defined. And so, before establishing a convention, it becomes even more necessary to relate every step of the method to the observation and findings and only then the dissimilar vapor plume's phenomenology can be studied in a relatable manner. A part of this thesis attempts at providing a more detailed explanation and resolution to this problem. Another important subject in the laser welding community is the spectroscopic characteristics of the melt pool and the vapor plume. Once again, this subject matter of research is concentrated on one side towards the laser treatment of materials using nano-second pulses in Laser Induced Breakdown Spectroscopy (LIBS) [54], and less about either lasers with longer pulses or continuous lasers due to physical limitations. Similarly, the numerical modelling of the laser welding has been repeatedly done to simulate the keyhole and the melt pool due to well understood underlying physics [55], while such works for the vapor plume are almost non-existent. However, in-situ observation and spectroscopy are necessary to obtain data such as temperature, shape/asymmetry of the keyhole, nature of the vaporized species, which can be used to build and validate numerical models. This thesis is oriented towards filling these gaps in knowledge by studying the case of the dissimilar laser welding of titanium and aluminum.

The chapter 1 will focus on the subjects like laser/matter interaction, the keyhole and melted zone phenomenology, vapor plume and plasma behaviors, experimental techniques such as High-Speed Imaging (HSI), spectroscopy and finally, numerical models concerning this process which describe the keyhole, the melted zone and the vapor plume. This chapter will be concluded with the research gap that remains in the field of dissimilar welding, novel techniques which could be used to fill this gap and the work that has been done during this thesis.

In the chapter 2 the experimental techniques employed during this thesis to understand the dissimilar laser welding are described. The properties of the materials studied, laser welding installation, the schematics of different setups for the different experiment campaigns conducted during this thesis, data volume and treatment methods are presented. Noteworthy information in HSI and spectroscopy such as the image processing techniques, details on apparatus capabilities and limitations will be discussed. And then, the processes involved in post-mortem analysis such as sample preparation, microscopy, etc., will be explained in detail.

Continuous laser welding is discussed in chapter 3 from the perspective of HSI, spectroscopy and post-mortem analysis. The experimental setup is reintroduced along with supplementary details which were not mentioned in chapter 2. The chapter 3 consists of three sections: Two sections are dedicated to the vapor plume analysis with HSI and spectroscopy, and the third section described the melted zone studies from post-mortem observations.

Chapter 4 is dedicated to pulsed laser welding in butt-configuration, which will provide insights on the keyhole properties and the vapor plume behavior under several sections. After a brief introduction in the first section of this chapter, the second section discusses the preliminary pulsed welding studies on the HSI observations of vapor plume and post-mortem examination of the corresponding melted zones. The third section, after a brief discussion about the post-

mortem observations of the melted zone, is dedicated to a deep analysis of the vapor plume in pulsed welding with multiple sub-sections dedicated to image processing and data treatment. The third section ends with a discussion and results about the vapor plume. The fourth section of this chapter is dedicated to keyhole and melted zone studies done with HSI and post-mortem analysis. The fifth section is dedicated to emission spectroscopy of the vapor plume in pulsed dissimilar welding in the butt-configuration. The chapter ends with a comprehensive summary of the results and conclusions from HSI and spectroscopy about the vapor plume and the correlations between the keyhole/melted zone and the vapor plume.

Overlap welding with laser pulses is discussed in chapter 5. The introduction and experimental details are given in the first and second sections respectively. The second, third and fourth sections are dedicated to post-mortem observations, HSI results and emission spectroscopy in pulsed overlap welding. The fifth section briefly discusses the summary of the results from the three techniques before the conclusion of this chapter.

The final chapter 6 briefly recalls how the thesis was structured along with the most notable observations, hypotheses, and conclusions. The methodology in image processing and analysis developed for high speed imaging of the vapor plume during the period of this thesis is briefly recalled. A global perspective on the vapor plume is provided by correlating with the most significant conclusions from emission spectroscopy. Along with brief details on the relationship between the vapor plume and the keyhole behavior for both butt- and overlap-welding, perspectives on next steps which could be taken to confirm the findings from this thesis and to further the understanding of laser welding phenomena are briefly enunciated.

In the annex, a published work in the context of numerical of modelling of the keyhole and the vapor with COMSOL Multiphysics has been provided. In addition, the work in numerical modelling of the keyhole which was done alongside the overlap welding experiments in Chapter 5 is also provided.

Chapter 1. Bibliography

1.1. Laser Welding

1.1.1. Laser matter interaction - Context

Applications foreseen focus most of the research in this field to understand the influence of the different process parameters on the weld quality, because the weld quality determines the robustness and applicability of welded joints [56]. Although the capital cost of laser welding is higher than other conventional methods, the superior weld quality compensates for this additional investment [57], because high welding speed leads to high production rates [58].

In practice the quality control is usually done post-mortem, but the research community is more focused on developing methods to perform quality analysis in situ. X-ray tomography has been used in addition to high-speed imaging (HSI) for 3D reconstruction of the melt pool geometry [59]. Real-time in-situ observation of weld penetration for TIG welding was done using ultrasonic transducers performed with sample temperature limiting the observations [60]. By inspecting the disruption of eddy currents when an alternating current is introduced into the sample by magnetic induction, cracks in the material were detected [61]. But this technique is limited by several factors such as material composition, heat treatment, etc., and its inability to detect defects parallel to the surface eddy current flow [62].

It is imperative to first understand the laser matter interaction which happens in the laser welding process to comprehend the above-mentioned complex techniques of quality analysis. Laser welding is basically using a coherent beam of monochromatic light to heat an object to temperatures high enough to produce fusion through melting [28]. Laser welding can be performed in three modes: penetration or keyhole, conduction, and transition mode [58].

After the Helium-Neon lasers, the CO_2 lasers were developed to deliver high power (3 – 10 kW) for welding and machining research [63]. While the CO_2 laser was used earlier for laser welding, disk lasers with higher power, efficiency and optical quality are preferred in the recent times [64]. Nd:YAG laser is preferred for laser welding of thin materials due to several advantages such as lower heat input and higher flexibility with the laser parameters such as peak power, pulse time, spot size, welding speed, etc. [58]. However, certain materials like aluminum are better absorbers of CO_2 laser than the YAG lasers [65]. Therefore, the compatibility of the materials to the wavelength of the laser (Figure 2) used in welding plays a major role in choosing the appropriate laser source in dissimilar welding.

visible spectrum 400 nm-800 nm

Dye-Laser

Argon-Ionic Laser
488, 514 nm

He-Ne-Laser
632 nm

Eximer-Laser
e.g. 193, 248, 308 nm

Diode-Laser

Nd:YAG-Laser
1064 nm

CO$_2$-Laser
10,6 µm

Er:YAG-Laser
2,9 µm

200   300   400   500   600   700   800   900   1000   nm   10^4

wavelength λ ⟶

frequency doubled
Nd:YAG-Laser
532 nm

frequency trebled
Nd:YAG-Laser
355 nm
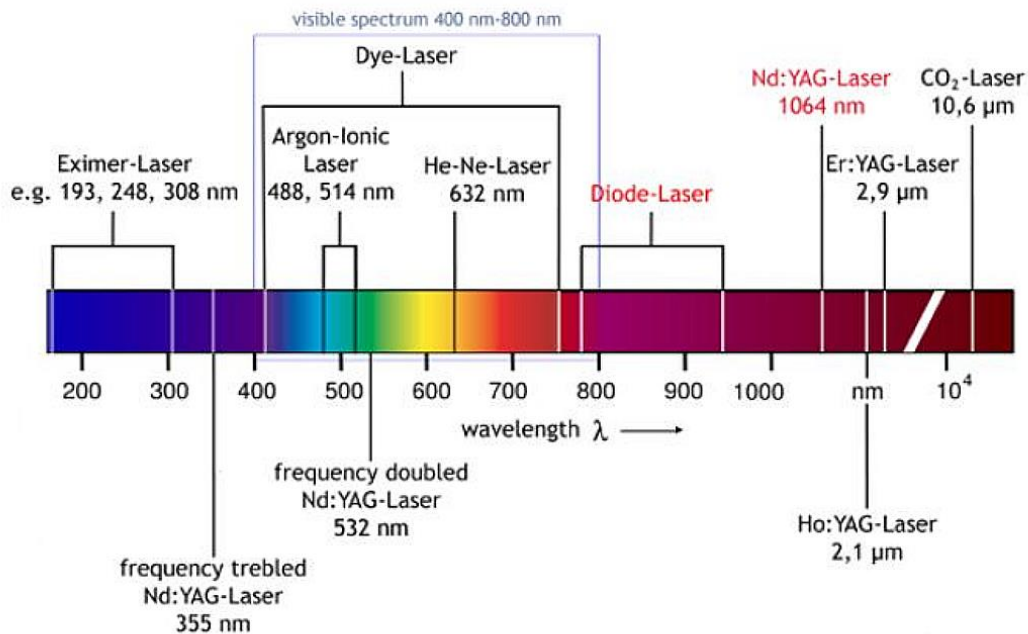
Ho:YAG-Laser
2,1 µm

Figure 2. Wavelengths of some of the lasers [66].

The YAG lasers are capable of emissions in the infrared spectral regime around 1 µm range (Nd:YAG – 1060 nm, Yb:YAG – 1030 nm) in either pulsed or continuous mode. When such a powerful laser beam is focused on a metal surface, under the right conditions, the metal surface undergoes melting and then vaporization. This melting (which creates a melt pool) and vaporization that happens in and around a hole (capillary or keyhole) (Figure 3), is controlled by an interplay of different operational parameters.

In pulsed welding, the incident beam is generally stationary during the pulse time. Whereas in continuous welding, the beam moves relative to the metal piece on the joint line with a specified velocity in either a straight line or in different oscillatory patterns.

The process of formation of the keyhole and the melt pool depend on a multitude of parameters constituted by; 1) the parameters of the laser such as power, pulse time, intensity profile, etc.; 2) the welding condition such as the welding speed, oscillating pattern, incident beam angle, shielding gas, filler material, configuration of the metal plates, etc. and; 3) the material properties such as melting and boiling point, absorptivity at the laser's wavelength, thermal conductivity, viscosity, etc. which are interdependent on each other as most of them vary with respect to change in temperature.

And so, the case of dissimilar welding of two metal pieces together with different properties complicates the welding process even further due to mismatch in the material properties, giving rise to the asymmetrical nature of the keyhole, incompatibility between the materials in the joint (due to formation of intermetallic compounds) to name a few.
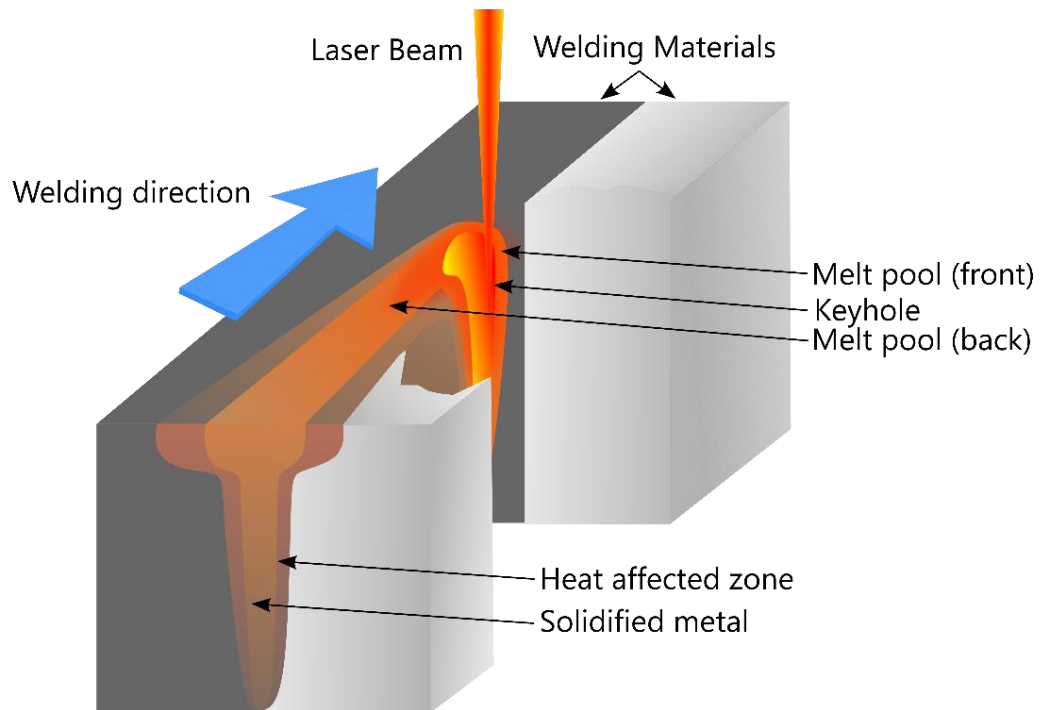
Figure 3. Schematic for continuous laser welding.

To obtain the highest quality in the heat affected zone and therefore in turn, the solidified metal, several post-mortem investigations have been done. However, researchers have been eager to understand the processes occurring in the keyhole and the melted zone. In recent times, vapor plume studies which describe the behavior of the vaporized metals emitted from the keyhole have been trending, to analyze in situ, understand, predict, and quantify and compare the welding process to the vapor plume behavior.

1.1.2. Types of laser welding.

In continuous laser welding, the incident laser beam on the material is uninterrupted. And so, the weld joint formed from this uninterrupted laser irradiation is also continuous instead of being just a series of spots as in pulsed laser welding. Continuous laser welding of 5083 aluminum alloy with the Yb:YAG laser was studied to understand the relationship between the laser parameters such as power and beam profile with the interaction time and the weld properties [67]. Continuous laser welding is usually plagued due to the formation of porosities from the unescaped gas and the intermixing of the metals [68]. Several techniques have been developed to reduce this drawback of continuous laser welding. To enhance the coupling of laser energy with the material, parallel water flow has been used to perform underwater wet welding without too much scattering and loss of radiation in the water [69]. Lowering the ambient pressure which leads to lower evaporation temperature of the material, consequently produced higher laser-matter interaction which deepened the keyhole of aluminum alloy [70]. The dissimilar welding of pure copper and aluminum alloy was performed with a wobbling laser head that introduces spatial beam oscillation, which led to a higher degree of control over the aspect ratio of the weld seam with higher quality in terms of hardness and electrical contact resistance [71]. Several different modes of beam oscillation (Figure 4) have been studied along with their effects on the melt flow, joint quality etc. for the welding of β-21S titanium alloy [72].
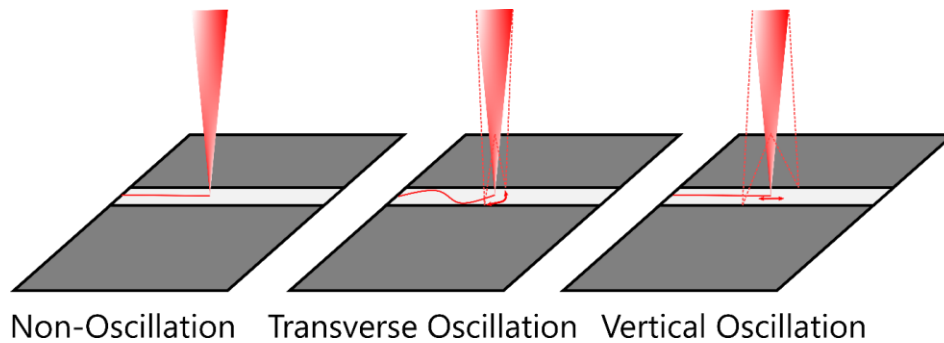
Figure 4. Types of beam oscillation modes [72].

Pulsed welding offers more process control and a better seam while producing deeper penetration than continuous welding. Because continuous welding with fewer control parameters (welding speed, laser power, focal distance) than pulsed welding (power, duration, repetition rate, peak power, etc.) is not able to provide the advantages of pulsed welding such as lower heat input, shorter welding cycle, spatial input precision, ability to weld small components etc. [73]. Pulse repetitions can be performed while the metals are moved with a welding velocity where the pulse overlaps. Since this method offers better control over the heating rate, cooling rate, thermal cycle repetitions in the material, the properties of the welded joint are better controlled. The overlapping factor is calculated using various equations which consider the pulse energy, duration, repetition rate, travel speed etc. [74]. This overlapping factor's effect on the microstructure and mechanical properties of Ti6Al4V weld joints have been investigated [75]. In dissimilar welding, the intermixing of materials is undesirable and leads to poor quality joints. The modification of the beam profile from rectangular to ramp-down, for pulsed welding of commercially pure titanium with stainless steel has shown to reduce the formation of intermetallics [76]. Due to increased demands in production quantity and quality over the last few decades and the advancements made in the field of laser technology and robotics, many of these novel methods have been invented and implemented in the industries, while the research community still lags in catching up to understand these processes completely. To say it even more plainly, we still lack the complete picture in basic dissimilar laser welding without using any of the fancy processes like beam oscillation, beam profile modifications, etc.

1.1.3. Laser matter interaction - Absorptivity

In the laser welding of a standalone material, its properties such as laser absorptivity, thermal diffusivity, melting point, boiling point, density, viscosity, etc., guide the process since most of these properties behave as a function of temperature. However, among these properties, only absorptivity is dependent on the laser wavelength (Figure 5) and thus consequently affects the surface temperature.
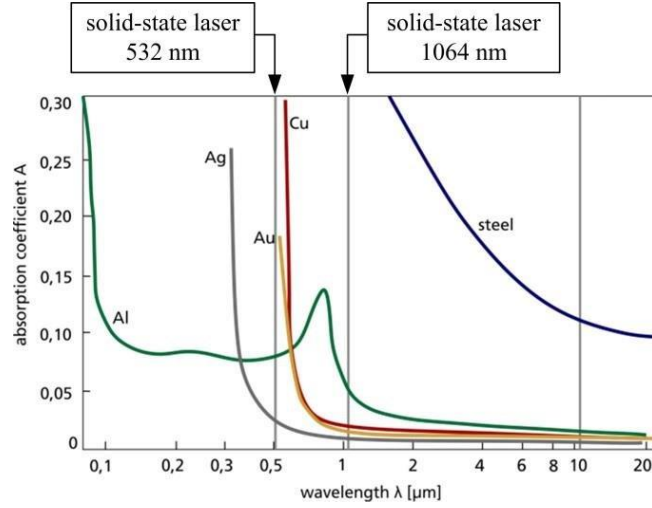
Figure 5. Wavelength dependence of the absorptivity for different metals [77].

In the process of dissimilar welding, the compatibility/incompatibility of the materials influences the nature of the welding process and the quality of the weld joint to a much greater extent. However, the very first factor that decides the direction of the process is the difference in the laser-matter interaction which is exhibited between the two materials. In other words, the absorption coefficient of the materials at the wavelength of the welding laser plays a major role in determining their compatibility. The absorption coefficient of a metal, also known as the extinction coefficient or attenuation coefficient (k), is defined by the amount of light that is attenuated by the material. This attenuation coefficient is calculated from quantities such as the refractive index or the relative permittivity from experiments such as ellipsometry and reflectometry. the complex refractive index of the material ($\underline{n}$) is,

[78]
$$\underline{n}^2 = (n + ik_c)^2$$
1

And since the complex relative permittivity of a material ($\underline{\varepsilon}$) is given by

[79]
$$\underline{\varepsilon}_r = \varepsilon_r + i\tilde{\varepsilon}_r = n^2$$
2

The attenuation coefficient is,

[79]
$$k_c = \sqrt{\frac{|\underline{\varepsilon}_r| - \varepsilon_r}{2}}$$
3

Due to differences in the refractive indices of the two materials in dissimilar welding, coupled with other phenomena like multiple reflections from beam-solid coupling, temperature dependent reflectance, plasma shielding effects of the vapor plume, self-focusing in the vapor plume, light-scattering due to microscopic surface imperfections, incident angle dependence on subsequently produced macroscopic surface imperfections, etc., the laser-matter interaction process defined by the absorption coefficient alone in dissimilar welding becomes quite complicated.

Two types of absorption mechanisms are identified with laser welding: Fresnel absorption and Inverse Bremsstrahlung absorption. By the continuous welding of glass using CO_2 laser, the Fresnel absorption and reflections in the keyhole were identified to be different between the

front and rear keyhole walls due to the keyhole shape [80]. This Fresnel absorption contributes the maximum amount of energy transfer from the laser to the material. This absorptivity is composed of both the intrinsic property of the material and supplementary absorptivity from surface phenomena such as roughness, defects and impurities, adsorbed substances etc. [81] and a discussion in detail could lead to several chapters. However, to state it in simple terms, absorbance depends on the angle of incidence by,

[82] $\qquad$ spectral absorbance = 1- (reflectance + transmittance) $\qquad$ 4

And reflectance ρ_{ref} is dependent on the incident angle α by [83]

[83] $$\rho_{ref} = \frac{1}{2}\left[\frac{(n - cos\alpha)^2 + k_c^2}{(n + cos\alpha)^2 + k_c^2} + \frac{\left(n - (\frac{1}{cos\alpha})\right)^2 + k_c^2}{\left(n + (\frac{1}{cos\alpha})\right)^2 + k_c^2}\right] \qquad 5$$

To maximize this absorption process and reduce the formation of defects simultaneously, techniques for surface treatment such as sandblasting [84] or cleaning using pulsed laser [85] are developed for high quality applications. Absorptivity has been measured for laser processing of metals with CO_2 and Nd:YAG laser using integrating sphere radiometry [86]. Higher absorption has been observed using integrating sphere radiometry for dissimilar welding of aluminum and steel compared to welding the standalone materials [87]. Since the laser absorption changes by the incidence angle (Figure 6), Fresnel absorption is not only different between the front and the rear keyhole walls, but also it is distributed along the keyhole wall itself due to temperature dependent reflections. The absorptivity of the keyhole depends on the distribution of the laser energy on the keyhole walls [70]. And so, with the offset in the absorption coefficient between different materials in dissimilar welding, the laser absorption in the keyhole where each wall exhibits differences in absorption, temperature, and reflectivity, augmented by the energy transport through conduction and convection processes, the phenomenon of dissimilar laser welding becomes very convoluted. And this increase in absorptivity in relation to the depth of the capillary in laser cutting has been well noted in literature [88], [89] and a similar phenomenon occurs in the laser welding keyhole as well [90]. Especially, with the changing shape of the surface (aspect ratio of the keyhole), the absorption of the laser in the keyhole could be very different at each moment than just the absorption on a flat surface with an incident angle [91].

[91] $$A = \frac{A_0}{A_0(2 + 4A_R) + 1 - A_0}\left(2 + 4A_R - \frac{1}{2A_R}(1 - A_0)\right) \qquad 6$$

where A is the total absorptivity of the keyhole, A_0 is the absorptivity of the flat surface, and A_R is the aspect ratio of the keyhole.

Fresnel absorptivity usually is around 30 to 40 % for liquid metals at 1060 nm laser wavelength [81]. The relation between thermal conductivity and the temperature dependent laser (infrared regime) absorptivity (for a polished metallic surface) is explained through the Hagen-Rubens model by relating to the temperature dependent electrical resistivity,

[92] $$A(T) = 0.365 \sqrt{\frac{\delta(T)}{\lambda}} \qquad 7$$

where $A(T)$ is the temperature dependent absorptivity, λ is the wavelength of the laser and $\delta(T)$ is the electrical resistivity, while the Wiedemann-Franz law connects the thermal

conductivity (K) to electrical conductivity (σ_e) by the Lorenz number ($L_0 = 2.44$ x 10^{-8} V^2K^{-2}) and temperature (T)

$$[93] \qquad\qquad \frac{K}{\sigma_e} = L_0 T \qquad\qquad 8$$

A)   B)
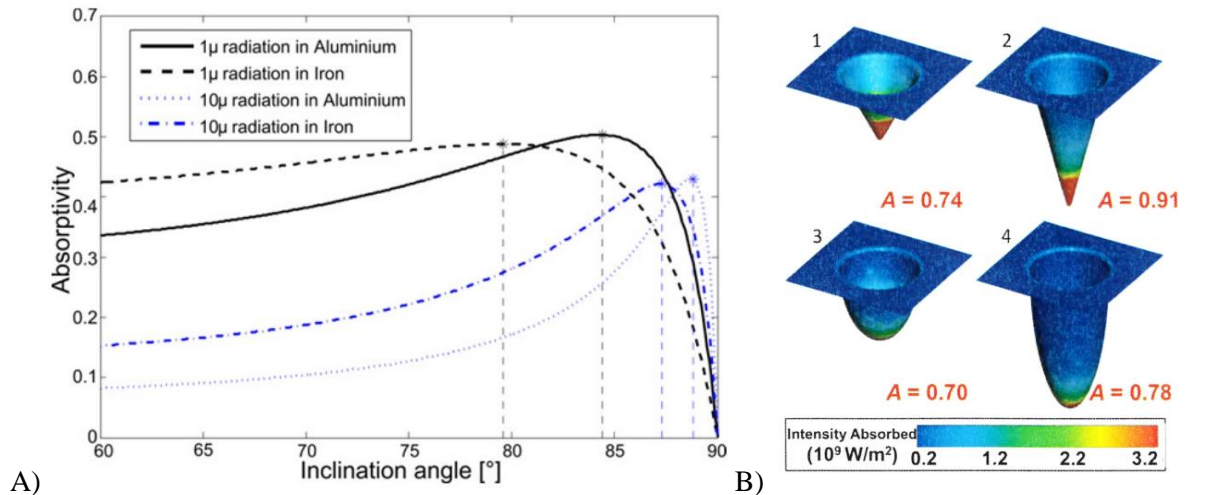
Figure 6. A) Absorptivity as a function of incidence angle [94] (direct diode lasers) and B) Calculated absorbed laser power distribution for keyhole depths 238 µm (1,3) and 476 µm (2,4)[90].

Understanding the laser-matter interaction is the first step to understand the entire laser welding phenomenology. Because, by understanding the type of laser interaction (pulsed or continuous), and the consequent relationship between the laser parameters (wavelength, power, pulse duration, etc.), the material properties (absorptance in solid, liquid, gaseous state, self-focusing plume, surface roughness, etc.) and the process conditions (angle of incidence, temperature, keyhole depth, etc.), the first steps in understanding the key relationships between the different processes in laser welding are taken.

1.2.   Keyhole Phenomenology and Observation Methods

1.2.1.   Melt pool and Recoil Pressure

After the laser-matter interaction, the physical phenomena occurring in the keyhole and melt pool form the second part of the story. Once the laser starts to heat the surface of the metal, it transitions into a liquid after the melting point threshold is crossed, followed by the liquid to vapor transition at the threshold of the vaporization temperature. While these phenomena exist, during the liquid to vapor transition, the recoil pressure exerted by the vapor on this liquid layer pushes the liquid to the sides leading to the development of a capillary or the keyhole (Figure 7). In deep penetration laser welding, this keyhole is surrounded by the melted zone in both pulsed laser welding [58] and continuous laser welding [68].
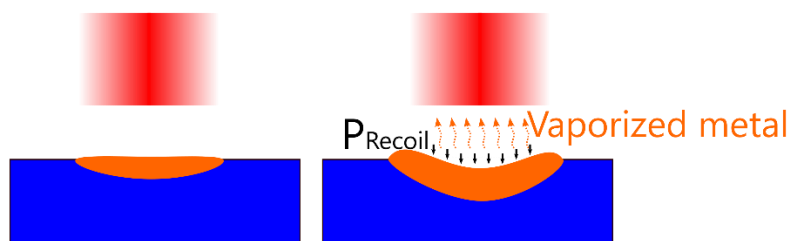
Figure 7. Effect of recoil pressure.

The liquid layer surrounding this capillary forms the melt pool, which in continuous welding exhibits several types of behavior depending on the welding parameters. According to Fabbro et al. [95], five different regimes (Figure 8) were observed for the Nd:YAG continuous laser welding of stainless steel at different welding speeds with the laser power and spot diameter kept constant : 1) The Rosenthal regime, 2) The Single Wave regime, 3) The Elongated Keyhole regime, 4) The Pre-Humping regime and 5) The Humping regime. The differences in the characteristics of these regimes such as the shape, size and stability of the keyhole, the position of the melt pool, the convection phenomena in the melt pool, the temperature distribution, the direction of spatters, etc., arise with the welding velocity as its origin. In other words, the effect of the welding velocity which defines the amount of energy imparted on the material per unit length, is multiplied several times by accompanying coupled processes in the keyhole such as the keyhole depth, keyhole opening diameter, multiple reflections, recoil pressure, the fluid flow in the melt pool etc. The inclination of the front keyhole wall is small for the Rosenthal regime and is significant for the Single Wave regime and the Elongated regime. The inclination does not vary by much in the Pre-Humping and the Humping regime. This shows that, for optimizing welding speeds, the change in the inclination of the front keyhole wall is very important. While there are different processes contributing to these regimes such as heat conduction, conventional heat convection, Marangoni convection, etc., the importance of recoil pressure in creating these phenomena and maintaining the stability of the keyhole cannot be exaggerated enough. Because even if the welding velocities, beam oscillations, etc. can influence the keyhole and the melt pool, the recoil pressure remains the heart of the whole welding situation, having an influence on every phenomenon, especially the melt pool. For example, in the welding Al-6Mg alloy using beam oscillation, the flow of the melt pool was influenced only by the recoil pressure in the non-oscillating beam mode, and in the oscillation mode, the flow was influenced by both the recoil pressure and the beam oscillation [96]. The recoil pressure is often expressed as

[97]
$$p_r = \frac{(1 + \beta_r)}{2} P_{sat}$$
9

Where, β_r is the recombination coefficient (value between 0.18 to 1) which takes into account the mechanical forces of recondensation and the Mach number dependent vapor phase change dynamics through the Knudsen layer [97]. P_{sat} is the surface temperature dependent saturated pressure that is described by the Clausius-Clapeyron equation.

[97]
$$P_{sat} = P_{atm} \, exp\left(\frac{M_a L_v}{R}\left(\frac{1}{T_v} - \frac{1}{T_s}\right)\right)$$
10

Where, P_{atm} is the atmospheric pressure, M_a is the molar mass, L_v is the latent heat of vaporization, R is the ideal gas constant, T_v is the vaporization temperature and T_s is the surface temperature. Experimental measurements of the momentum exerted from the recoil pressure were in the order of a few MW.cm^{-2} [98]. This pressure value has been measured to be about 1.5 bar for Nd:YAG laser welding of steel [99].
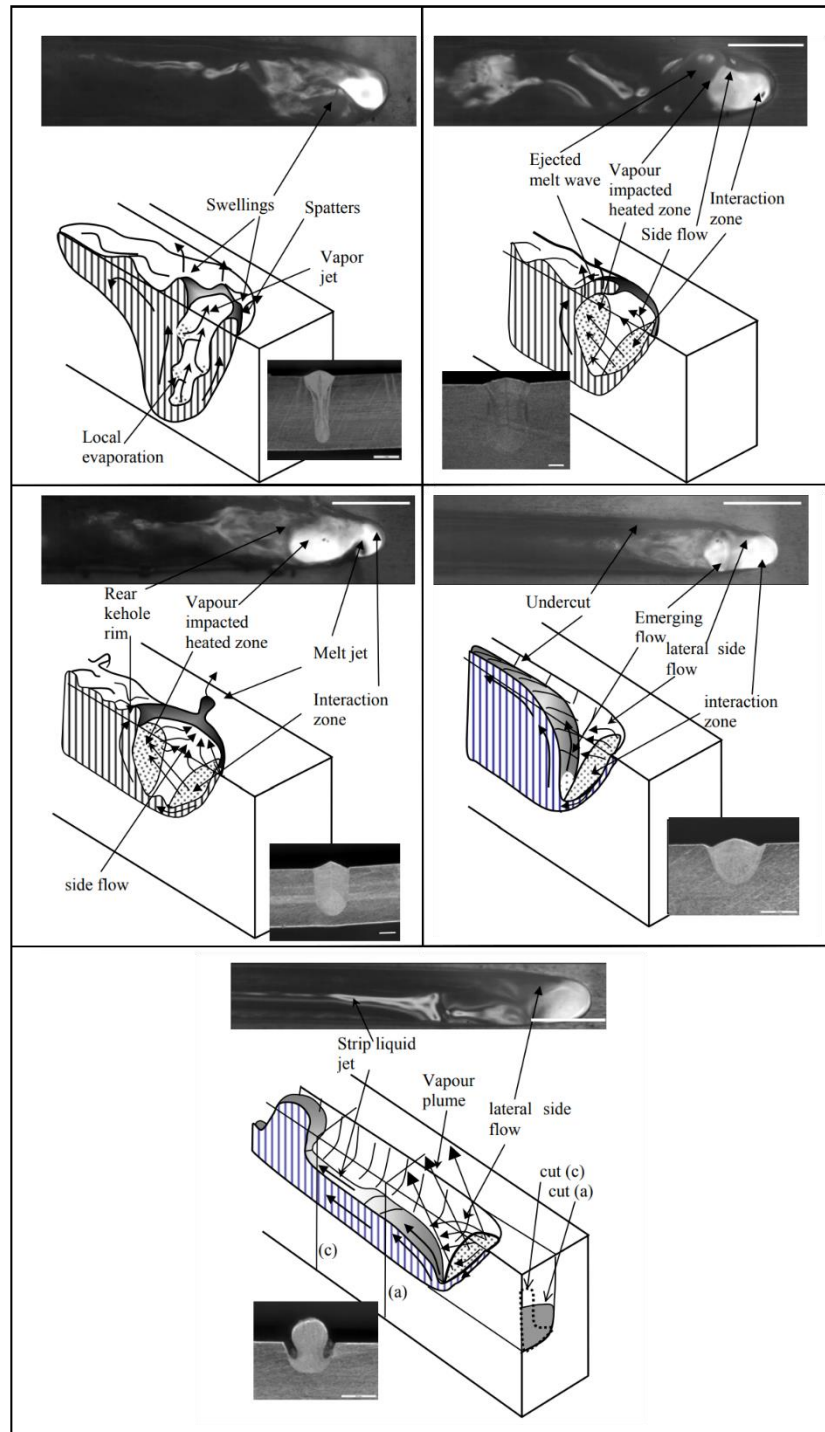
Figure 8. Laser welding keyhole regimes of the melt pool [95].

1.2.2. Knudsen layer

As much as the welding process characteristics depend on the parameters, their relationship cannot be construed directly with the recoil pressure phenomenon. Because, the recoil pressure which is exerted by the metallic vapor is not exactly on the surface of the liquid, but rather on a very thin intermediate film where the liquid vapor transitions happen, called the Knudsen layer [100]. The Knudsen layer is fundamentally a correction, acting as a solution to the boundary layers between the liquid (incompressible Navier-Stokes flow) and the gas (compressible Navier-Stokes flow) in order to maintain continuity of the macroscopic variables

such as temperature, velocity, mass flux, density, etc. in the direction normal to the boundary [101].

The thickness of this Knudsen layer (usually in the order of mean free path of the gas molecules) has been theoretically estimated to be below 10 µm by [102]. And so, the properties of this layer are difficult to be identified by experimental methods such as atomic emission spectroscopy. The microscopic processes occurring within this layer by the thermodynamics between the liquid edge and the vapor edge, and the balance between vaporization and condensation affect the macroscopic processes such as recoil pressure, saturated pressure and the temperature gradients within the keyhole and the hottest layers of the melt pool. Three different interlinked regimes such as the Knudsen layer, the condensation regime on the vaporization edge and the hydrodynamic regime on the melt pool edge have been theoretically analyzed to understand the mass, momentum, and energy balance. The temperature boundary between the liquid surface and the vapor in the keyhole is considered to be in the layer (Figure 9) just outside the Knudsen layer, where the vapor reaches a new thermodynamic equilibrium after undergoing collisions in the Knudsen layer [103] .
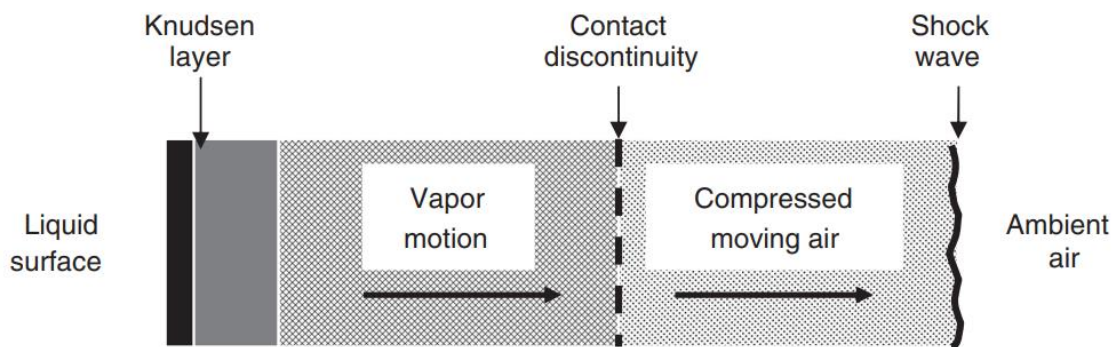
Figure 9. Schematic diagram of the gas dynamic and air away from a liquid surface at an elevated temperature [103].

1.2.3. Surface tension

Even though the recoil pressure plays the main role in the formation of the keyhole in laser welding, surface tension (one among the several forces in the melt pool such as Marangoni force, arc drag force, Lorentz electromagnetic force, buoyancy force) of the liquid metal (with the tendency to minimize the surface area) acts as an opposing force with a tendency to close the keyhole [103]. One of the consequences of this surface tension is the undesired spatter formation. The mechanisms of spatter formation have been studied in varying levels of detail by several researchers. In a simplistic manner, Kägeler and Schmidt state that the spatters in continuous laser welding are formed when the vapor pressure (ablation pressure, gas stream pressure) exceeds the surface tension (hydrostatic, hydrodynamic pressure) of the keyhole [104]. Li et al. have studied the effects of laser power and the position of the focal spot (above or inside the metal) on the formation of spatters [105]. Robertson et al. provide a heuristic spatter formation mechanism while describing four different types of material ejection events: protuberance, scalloping, melt migration and spattering [106]. These hydrodynamic phenomena driven by the conduction and convection of heat in the melt pool [107] can be estimated in the energy in ejection (E_{ej}) of a single droplet of melt using its diameter D, surface tension (σ), melt density (ρ_m) and droplet velocity (u_D).

[107]
$$E_{ej} \geq \rho_m \frac{D_s^3 \pi}{12} u_D^2 + \sigma D_s^2 \pi$$
11

The temperature dependent surface tension of the liquid influences the inner liquid layers by shear viscosity thereby influencing the convection. This gradient in the surface tension over the varying temperature produces the thermocapillary Marangoni convection.

$$\sigma(T) = \sigma_m + \frac{\partial \sigma}{\partial T}(T - T_m) \qquad 12$$

Where, $\sigma(T)$ is the temperature dependent surface tension, σ_m is the surface tension at the melting point and T_m is the melting point of the liquid metal. $\frac{\partial \sigma}{\partial T}$ is the surface tension gradient over temperature which drives the mixing of the liquid layers enacting heat transfer, giving rise to intermixing of different molten materials. The sign of this coefficient of surface tension gradient determines the direction of convection in the melt pool. Other than the thermocapillary Marangoni convection, natural convection is also present (forces in lower orders of magnitude).
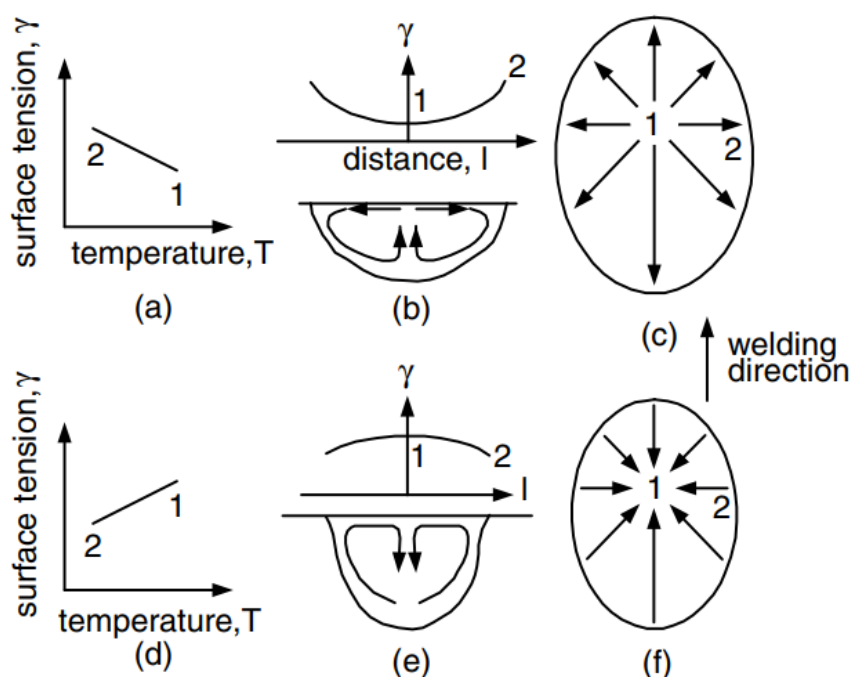
Figure 10. Heiple's model for Marangoni convection in a weld pool: (a, b, c) low- sulfur steel; (d, e, f) high -sulfur steel [109].

1.2.4. Keyhole observation, visualization, and characterization

While many post-mortem studies exist to describe the characteristics of the capillary, very few techniques exist to perform in-situ analysis of the capillary/keyhole behavior. X-ray flash radiography or X-ray imaging has been used to observe the evolution of the geometry of the keyhole in terms of its width and depth for the Nd:YAG pulsed laser welding of standalone tantalum and standalone titanium alloy Ti-6Al-4V [110]. The keyhole evolution was described to be linear after taking into account the contrast and resolution. This type of non-destructive testing method employs a pulsing type X-ray generator and a panel-detector high-speed imaging system setup In another study using an ultra-high-speed synchrotron X-ray imaging in continuous welding of Ti-6Al-4V, five regimes of behavior: (i) melting, (ii) vapor depression formation and growth, (iii) vapor depression instability, (iv) keyhole formation and growth, and (v) melt pool shape change were observed [111]. In another similar study, the relationship between the keyhole behavior and the process parameters were examined for the continuous

welding of stainless steel with a Yb:YAG laser using X-ray radiography [112]. Pore formation and related melt ejections arising due to keyhole instabilities have also been observed using X-ray imaging for the Yb:YAG continuous welding of copper. It is clear from the images of the keyhole produced from this technique that while X-ray radiography allows in-situ observation of the keyhole, the grainy texture of the images accompanied with low sharpness can lead to low accuracy in the calculations about the keyhole characteristics. In a more recent work, the use of synchrotron to enhance the temporal and spatial resolution of X-ray imaging has shown to produce higher quality images of the keyhole, which can lead to keyhole behavior studies with a reliable degree of accuracy, while presenting some challenges [113].
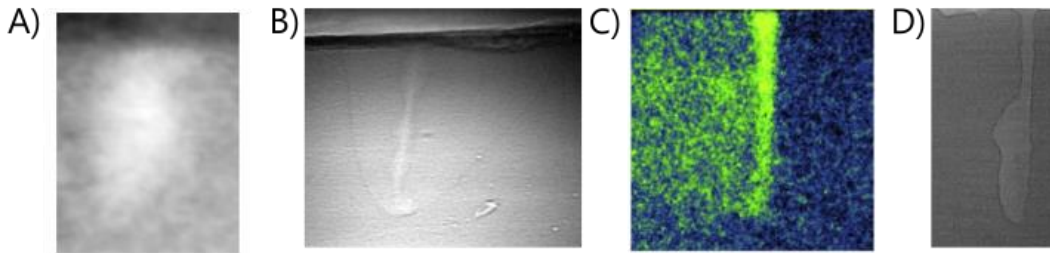
Figure 11. X-ray image of keyhole A) [110], B)[114] C) [112], and D) [113]

Another emerging method that allows in-situ observation of the keyhole depth with a much higher precision is Optical Coherence Tomography (OCT). The basic principle in this method is the utilization of interferometry, where a beam of light from an illuminating source is split into two and is made to interfere with itself after reflection from the keyhole (Figure 12). This technique while offering high resolution in the depth calculations with precision in the micrometer scale, it is limited by the several factors such as the relative positioning of the light source to the laser spot, the sudden changes in keyhole depth leading to false values, bubble formations, noise, etc. (Figure 13). In this image, mismatch between the inline coherent imaging values and the microscope images are noticeable in the regions for large laser power changes around 0.025 s and 0.1 s [115]. Due to the large number of points and the variations from the actual weld depth, algorithms need to be developed for the statistical treatment of the OCT signal to obtain the weld depth [116]. The OCT measurements' relation to the laser beam incidence angle, and the stability of the data for different welding processes have been researched [117]. In laser spot welding, OCT has been used to observe the differences in the depth measurements with and without the presence of argon shielding gas [118].
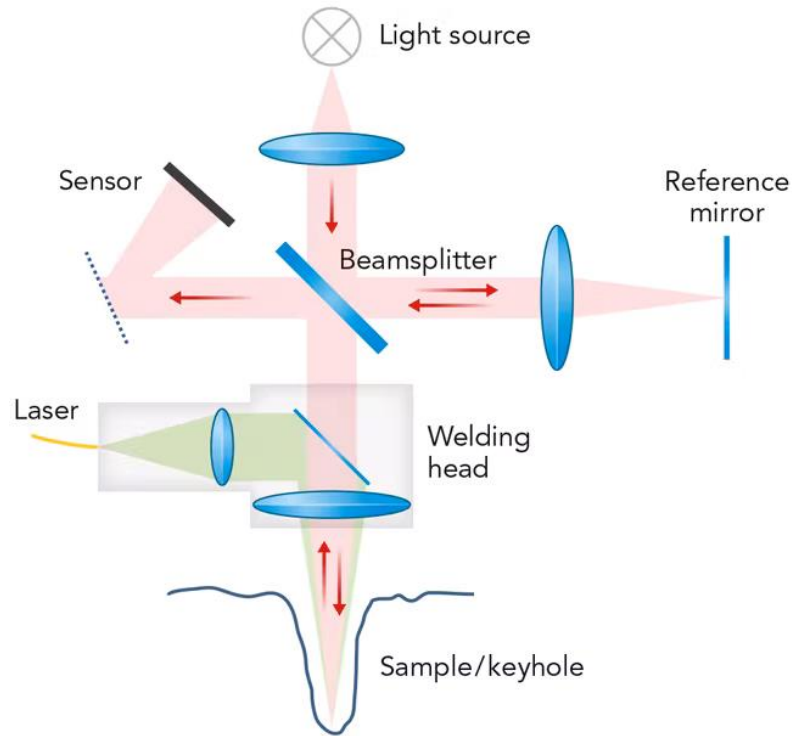
Figure 12. Schematic of experimental setup for OCT [119].
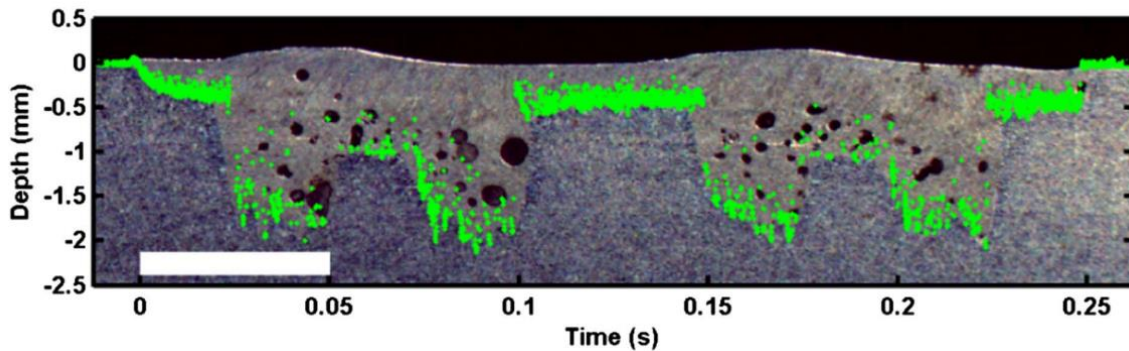
Figure 13. Measured depths (green dots) overlaid on microscopy images of longitudinal cross section [115].

In another trend, without using interferometry, automated systems are being developed using optical methods such as the triangulation principle in high-speed imaging to track the seam during laser welding to improve beam quality [120]. Other non-optical methods exist to characterize the keyhole. Pyrometry is used to directly determine the temperatures in the vicinity of the capillary [100]. However, the utilization of pyrometry is not preferred since thermal measurement with pyrometers are related with emissivity and the estimation of emissivity in laser welding processes is a particularly complicated task [121]. The study of Acoustic Emission (AE) signals (usually in the ultrasonic regime) is also a part of research in the laser welding community where the AE signal generating mechanisms have been linked to the welding defects, however require the use of complex data processing algorithms and artificial neural networks to handle the massive amounts of data points for measurement stability [122], [123]. A combination of the acoustic and optical monitoring methods albeit a challenging task and also while mostly depending on the mechanisms in the vapor plume/plasma, has been shown to produce data about the penetration depth and weld quality for different welding conditions [124], [125]. And in recent times, the use of multiple sensors combined with deep learning models are becoming prevalent in keyhole monitoring [126]–

[129]. For example, HSI at 500 Hz combined with spectrometer signals at 100 Hz were used as input for a convolutional neural network to predict penetration depths by OCT for the dissimilar welding of aluminum and copper alloys in the overlap configuration[130].

However, to observe the geometry of the keyhole, HSI has also been used as it offers higher accuracy. But the keyhole can only be observed from above at an angle (Figure 14) due to experimental spatial constraints [131]. Such observations combined with dynamic radial basis function neural networks have been used to estimate the penetration depth and inclination angle by establishing a relationship among the welding parameters, measurements and keyhole dynamics [132].
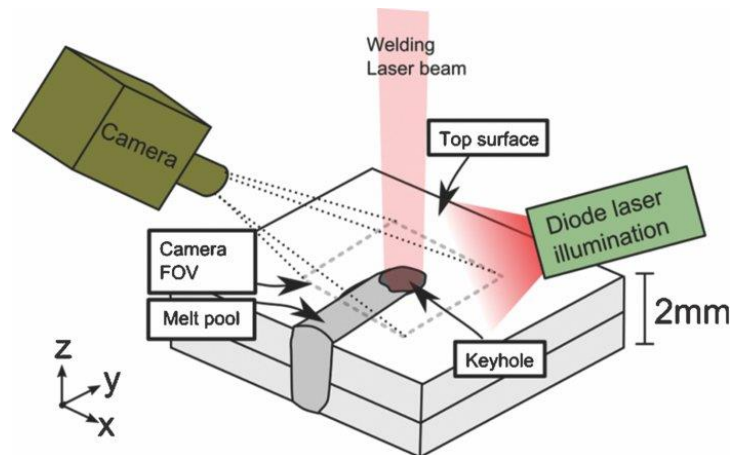
Figure 14. Schematic for HSI of laser welding (top view) [131].

In order to avoid this limitation, researchers use quartz or borosilicate in a viable configuration to directly observe the keyhole in a lateral view (Figure 15). In such an experiment, the laser spot is usually shared between the metal and the transparent material [133]. Using this technique, the migration of the keyhole (Figure 15) in the pulsed dissimilar laser welding of magnesium AZ31 and aluminum A5754 alloys, was observed [134]. Just like OCT, this technique using a transparent material to observe the keyhole is precise enough to provide a feedback loop control in continuous dissimilar welding in an overlap configuration [135]. But when it comes to HSI, an understanding of the spectral data of the emissions from the keyhole and the vapor plume become necessary. Soda lime glass has been used adjacent to film the keyhole in continuous welding by electron beam or laser due to its high thermal diffusivity [136]. In another similar experiment with GG17 glass on both sides, a thin film of aluminum (thickness = 0.02 mm) was welded with CO_2 laser to perform HSI on one side, while spectrometry was performed on the other [137]. In the methods using a transparent material, care should be taken to choose a material with: 1) a low thermal expansion coefficient, 2) sharp solid-liquid and liquid-gas interfaces with significant differences between the melting and boiling points, 3) equal permeability for light at different wavelengths, 4) high ionization energy compared to the metals being welded [137].
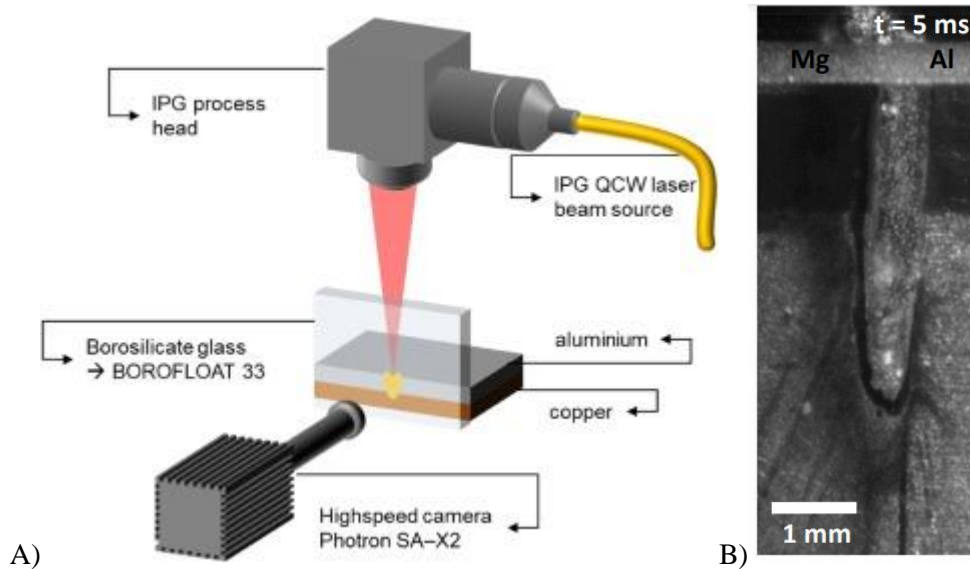
Figure 15. A) Schematic of front view HSI of capillary [135] and B) Dissimilar capillary observed between Mg and Al [134]

1.2.5. Dissimilar welding

In dissimilar welding, the compatibility of materials can either facilitate the welding process or make it challenging. This compatibility between the different metals have already been presented in Figure 1 [28]. Based on whether these materials can form continuous solid solutions (Cu-Ni, Ag-Au, etc.) or limited inter-solubility without the formation of intermetallic phases (Cu-Fe, Cu-Co, etc.) or fragile intermetallic phases (Al-Fe, Ti-Fe, Ag-Ti, etc.), they have been assigned 100%, close to 100% and zero, or close to zero, joint coefficients respectively. The formation of intermetallic phases has been problematic in obtaining good quality welds as they lead to fragility and cold cracking issues.

Nevertheless, while the metallurgical aspects of dissimilar metallic welding are not the focus of this thesis work, the causes and effects of the several phenomena contributing to these compatibility issues have to be understood.

Disparities in the physical properties like fusion and vaporization temperatures between different materials have been noted to yield undesirable results in the melted zone in terms of composition and shape which end up affecting the weld quality and strength. In some works, it has been noted that the dissimilar laser welding of metals results in an asymmetrical keyhole shape caused by the melted zone root shifting gradually away from the joint line during the process. In literature, the displacement of the root of the melted zone away towards the metal with lower vaporization temperature have been observed for the welding of titanium/tantalum [37], Ti-6Al-4V titanium alloy/niobium [138] (Figure 16.b), AZ31magnesium alloy/A5754 aluminum alloy [134]. In instances where the disparity in vaporization temperatures was not significant but the dissimilar metals exhibited disparate reflectivity towards the welding laser, the melted zone root shifted away from the metal with higher reflectivity such as copper/steel [139] (Figure 16.a) and copper/nickel [38]. Thus, it can be inferred that mismatch in the vaporization temperature and reflectivity can contribute to the keyhole asymmetry.
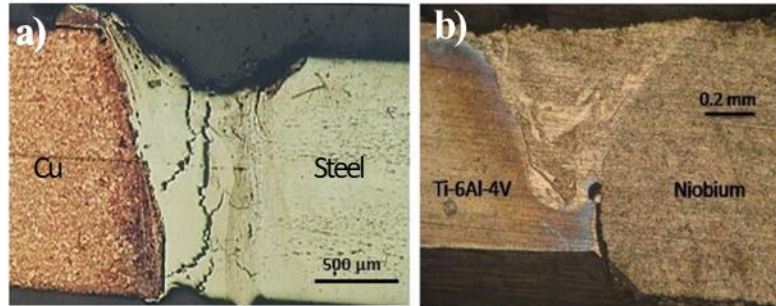
Figure 16. Post-mortem images of the melted zone development in a) Cu/Steel [139] and b)Ti-6Al-4V/Niobium [138].

Not only was the shift in the position of the keyhole an effect in dissimilar welding, but changes in the keyhole shape have also been observed in dissimilar welding while associating with other properties such as laser spot position relative to the joint line, welding speed, etc.
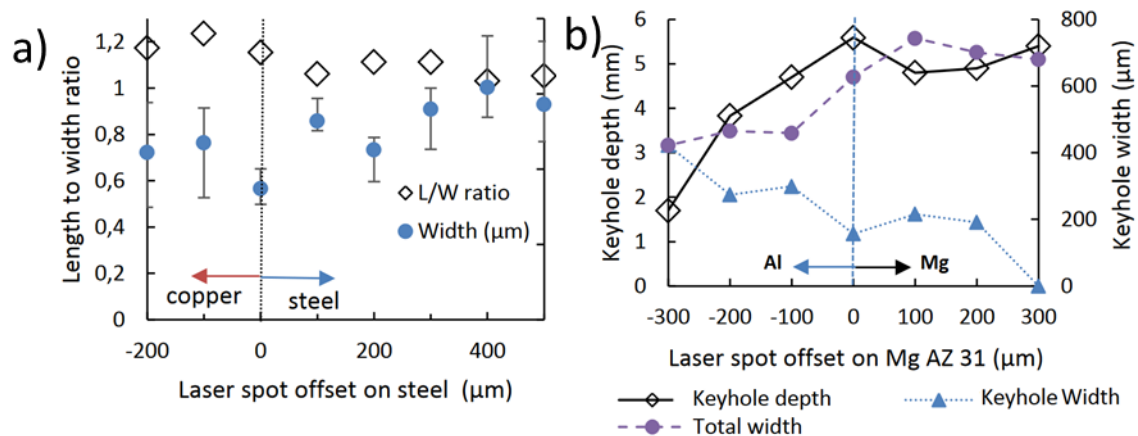
Figure 17. Changes in aspect ratio of the keyhole in relation to the laser spot offset from the joint line in dissimilar laser welding of a) copper/steel and b) aluminum/magnesium [134].

A numerical study [140] was undertaken to understand further the association between the melted zone root, the keyhole area and the mismatch in properties such as vaporization temperature and absorptivity, which concurred with the results from the previously mentioned experimental studies.

While most of these experimental works rely on the post-mortem analysis of the melted zone, to understand the dissimilar keyhole development, in-situ observations of the dissimilar keyhole are being done using the methods mentioned in the previous section 1.2.4, with each technique posing its own set of advantages and challenges. However, for now it has become quite obvious that, in dissimilar laser welding, the intricacies in the dynamics of the keyhole behavior have to be understood to understand the evolution of the melted zone and henceforth, the quality of the welded joint.

1.2.6. Conclusions

During laser welding, the laser beam heats the surface of the metal until it melts and subsequently the keyhole is formed when the vapor pressure produced during the transition from liquid to vapor pushes the liquid to the sides, creating a capillary shape. The liquid surrounding the keyhole forms the melt pool, which exhibits different behaviors depending on the welding speed, named as the Rosenthal regime, Single Wave regime, Elongated Keyhole regime, Pre-Humping regime, and Humping regime. The recoil pressure, which is a result of the vapor phase change dynamics and mechanical forces of recondensation, plays a significant

role in the stability and characteristics of the keyhole and melt pool, and can be expressed using the recombination coefficient and the Clausius-Clapeyron equation. Experimental measurements of the momentum from the recoil pressure have been found to be in the order of a few MW/cm^2, with the values of the recoil pressure around 1.5 bar for Nd:YAG laser welding of steel.

The recoil pressure that is exerted on the material during laser welding is not exactly on the surface of the liquid, but rather on a thin intermediate film called the Knudsen layer, where the liquid-vapor transition occurs. The properties of this layer, which is usually less than 10 µm thick, are difficult to identify experimentally. The microscopic processes within the Knudsen layer affect the macroscopic processes such as recoil pressure, saturated pressure, and temperature gradients within the keyhole and the melt pool. Three different regimes, including the Knudsen layer, the condensation regime on the vaporization edge, and the hydrodynamic regime on the melt pool edge, have been analyzed to understand the mass, momentum, and energy balance during laser welding. The temperature boundary between the liquid surface and the vapor in the keyhole is considered to be in a layer just outside the Knudsen layer. While recoil pressure plays a major role in the formation of the keyhole in laser welding, surface tension also has an opposing force that can lead to the closure of the keyhole. This can result in the formation of spatters. The temperature-dependent surface tension of the liquid metal can influence the inner layers through shear viscosity and cause thermocapillary Marangoni convection. Natural convection is also present, but with a much slower velocity field.

There are several techniques available for studying the keyhole behavior during laser welding in situ, such as X-ray flash radiography or imaging, synchrotron X-ray imaging, optical coherence tomography (OCT), and high-speed imaging using the triangulation principle. X-ray radiography allows for the observation of the keyhole, but the images produced have low sharpness and can lead to low accuracy in keyhole measurements. OCT offers high resolution and precision in depth calculations at the micrometer scale but can be limited by various factors such as the positioning of the light source, sudden changes in keyhole depth, bubble formation, and noise. High-speed imaging using the triangulation principle can track the seam during laser welding to improve beam quality. Non-optical methods for characterizing the keyhole include pyrometry and the study of acoustic emission signals, but these methods also have their limitations. Laser-induced fluorescence and scattered light techniques can provide information about the keyhole temperature and the vapor pressure, respectively.

1.3. Vapor Plume and High-Speed Imaging

Another novelty in laser welding research is the understanding of the keyhole behavior from the characteristics of the vapor plume. Although the idea of the formation of the vapor plume emitted after vaporization when the atoms of the metal leave the Knudsen layer seems like a relatively easy process to understand, the story of the vapor plume itself gets much deeper and more complicated. To start, the underlying physics which are used to explain the laser welding process for the metal in the solid and melted states are no longer the same for metallic vapors. For example, the fluid flow is no longer incompressible for the vapor state, temperature is no longer equilibrated and electronic temperature is used, data on some of the physical properties of the metals such as conductivity, viscosity, etc. have not yet been measured at the temperature exceeding the vaporization temperatures thereby rendering theories of understanding of gas systems partly useless, interaction of the laser with the vapors is different, the state of the surroundings (vacuum, water, air, shielding gas) can also affect the properties of the vapor. In addition, if two dissimilar metals with differing properties are being vaporized, then these ideas become even more complicated.

The vapor plume created from the rapid heating and vaporization of the metals contain atoms which exhibit translational [141], rotational [142] and vibrational [143] motion accompanied by the thermal motion of electrons [144] in the gas if ionization occurs. These motions lead to the continuous thermal emissions from the vapor plume. While the continuous thermal emission occurs due to the random motions of these particles, atomic or ionic emissions [42], [145]–[149] which are a rather discrete set of emissions may occur depending on the energy input into the processes. These emissions happen at particular wavelengths which correspond to the energy difference between the excited state and the ground state. Researchers try to determine the composition and the temperature of the vapor plume by using spectroscopy (discussed in section 1.4), the size, shape, velocity and flow patterns of the vapor plume from HSI and numerical modelling (section 1.5).

1.3.1. Imaging parameters

Different types of High-Speed Imaging remain a popular tool in this research domain such as high-speed photography and using stroboscopic sources. With the development of electronic imaging technology, HSI has evolved rapidly with capabilities of imaging from 50 – 60 fps with Charge-Coupled Device (CCD) sensors to several thousand frames per second (fps) with the advent of Complementary-Metal-Oxide-Semiconductor (CMOS) sensors [150], [151]. But still, HSI has its own limitations, especially in the case of dissimilar laser welding. While state of the art HSI cameras use sensors of similar sizes as conventional cameras, their pixel sizes are much larger. As an example, two cameras have been compared to identify the differences in their characteristics in Table 1. The conventional mirrorless camera from Sony [152] and the HSI Phantom camera [153] have a Full Frame (36 mm x 24 mm) sensor. But the pixel size of the Phantom camera is almost 5 times larger than the Sony. This relative increased pixel size found in HSI cameras is not uncommon [154]. While the increased pixel sizes allow more photons to be captured, it comes at the cost of a decreased maximum resolution. While the maximum resolution of a camera is an interesting feature, increasing the frame rates always diminishes the resolution in both conventional and HSI cameras due to cropping of the sensor. The delicate balance between the frame rate and the resolution in HSI cameras should be considered while determining the parameters of HSI in the field of laser welding. Because, with a constant focal length, the resolution becomes the determining factor for the size of the field of view (FOV).

Table 1. Comparison of features between a conventional camera and a high-speed camera.

Type	Conventional camera	High speed camera
Model name	Sony Alpha 7 III	Phantom v2012
Year	2018	2016
Photo		
Sensor size	35.6 mm × 23.8mm	35.8 mm x 22.4 mm
Pixel size	5.93 µm	28 µm
Maximum Resolution	6000 x 4000 (6K)	1280 x 800 (HD)
FPS at Max Resolution	30 fps (4K)	22,600 fps (HD)
Max FPS	120 fps (HD)	1,000,000 fps (128 x 32)

While researchers consider the FOV from the size of their region of interest (ROI) and adjust the focal length accordingly, HSI at high frame rates and a low resolution come with the drawbacks of low light due to increased focal length and low sharpness due to low resolution. When the interest in the rate of capture supersedes the clarity of the vapor plume, researchers opt to this method of using low resolution with high frame rates. In 2002, the vapor plume was captured with a frame rate of 9000 frames per second and no information on the resolution was provided [155]. In 2006, the frame rate of 4000 fps was used to capture the vapor plume images with a bandpass filter at 602 nm wavelength [156]. In 2010, while the researchers boast a frame rate of 40,000 fps at 1064 nm, the resolution was still not being discussed [157]. However, in the more recent works, the information on the resolution have been provided. Wang et al. [158] captured their vapor plume at 2000 fps with 512 x 512 resolution. Zheng et al. [159] did it at 20,000 fps with 106 x 762 pixels and Mihai et al. [160] at 20,000 – 30,000 fps with 384 x 384 pixels. While it is notable how the higher frame rates demand a lower resolution due to RAM memory and data write speed constraints, it is unfair to compare the state of the art only based on frame rate without accounting for resolution, especially when comparing works produced by different HSI systems.

Another critical factor that researchers must consider while opting for high frame rates is the exposure time period. The maximum exposure possible is the multiplicative inverse for a given frame rate. Once again, it can be noted that authors have started to mention the HSI exposure only in the last decade. For example, Kawahito et al., [161] while mentioning the exposure time for the spectroscopy of the vapor plume, do not provide any information on the exposure time for HSI. However, this trend had changed, and researchers have started to seriously consider the impact of choosing the right amount of exposure which usually ranges between 1 µs to 500 µs depending on the interest. Lower exposure times such as $1 - 5$ µs are used to reduce the motion blur created from fast moving objects within the FOV, be they the plume or the spatters or even the melt pool [162], [163]. Higher exposure times are usually used in situations where the objects of interest have low emissivity with no additional illumination [163], [164].

Other imaging parameters controlling the lens system such as the aperture, the focal distance, depth of field, the reproduction ratio, etc. also have a significant impact on certain qualities of the image. For example, the need for higher exposure in low emitting objects of interest can be

compensated by increasing the aperture of the lens system. But it could lead to lower values for the depth of field (especially in long distance macro-objectives) thereby reducing applicability to 2-dimensional objects or objects with very low thickness. Among these parameters controllable externally from the camera, the most important parameter is the wavelength of acquisition or in other words, the optical filter used along with the lens system. While the importance of the wavelength of emission is discussed in detail in the section 1.4 (p.44), it can be briefly mentioned that some researchers mention using different types of optical filters over various wavelength regimes to observe the vapor plume [49], [156], [165], and some others don't. But most of the researchers base their HSI studies on the thermal emissions [137], [166]–[170]. And most of the authors do not discuss the impact of the chosen wavelength regime on the observations and acquired data on the vapor plume.

1.3.2. Image processing and the vapor plume

1.3.2.1. General overview

To observe the oscillations in the keyhole indirectly, the frequency of change in the inclination angle of the vapor plume accompanied by stabilization using a gas jet have been performed using HSI [171]. This angle of the vapor plume has always been considered significant for understanding the inclination of the keyhole walls [156]. But the definition of the angle of the vapor plume is not usually explicitly defined. For example, sometimes no explanation is provided on the methodology for the determination of the inclination angle other than just a picture and its description [46]. However, in the more recent times, some authors mention that they calculate the angle of the plume from the horizontal and the line connecting the center of the bottom to the centroid [167]. But this poses the question about the position of the centroid. What determines the border of the vapor plume and how is the relative position of this centroid calculated with respect to the plume border? It is not uncommon to find that most of the authors doing laser welding plume research do not provide detailed explanations on their image processing methods. Hence a discussion of the image processing methodology becomes significant in order to validate the correctness of the resulting data. A very common practice in the image processing of vapor plume images is binarization segmentation.

A   B   C   D   E   F
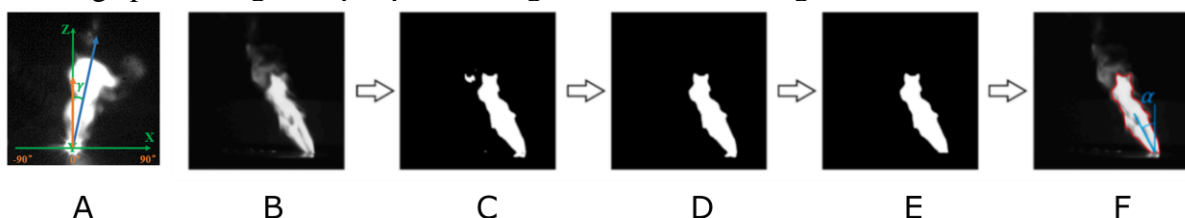
Figure 18. A) Depiction of inclination angle of the vapor plume [46]. B) Original image, C) Otsu binarization, D) Filling holes, E) Cropping, F) Data extraction [167].

While it is essential to discuss the image processing methods, it is crucial to identify the different areas in the vapor plume which is generally composed of several parts [172]: the oscillating part just above the keyhole opening and the slender plume which is much taller than the oscillating part accompanied with smoke rising from the oscillating part (Figure 19). In the earlier research works, such distinctions between the different parts of the plume were rarely made, and even when identified, they were much different, and less studied due to limitations in the imaging technology [173]. The physical characteristics of these two parts of the vapor plume are different from each other [49] and so the image traits will also be different and therefore must be taken into account during image capture and processing. For example, the values of the FOV, frame rate, exposure time etc. have to be set according to the part of the plume to be studied and subsequently, during image processing, the parameters of the image capture and other details on instruments (Example: sensitivity of the camera sensor, objective) have to be included. Besides these two significant parts of the vapor plume, there are other

parts which usually hold less interest since their appearance depend too much on the acquisition parameters such as the diffuse smoke around the vapor plume and the spatters which are visible in Figure 19.A, but not so much in Figure 19.B.
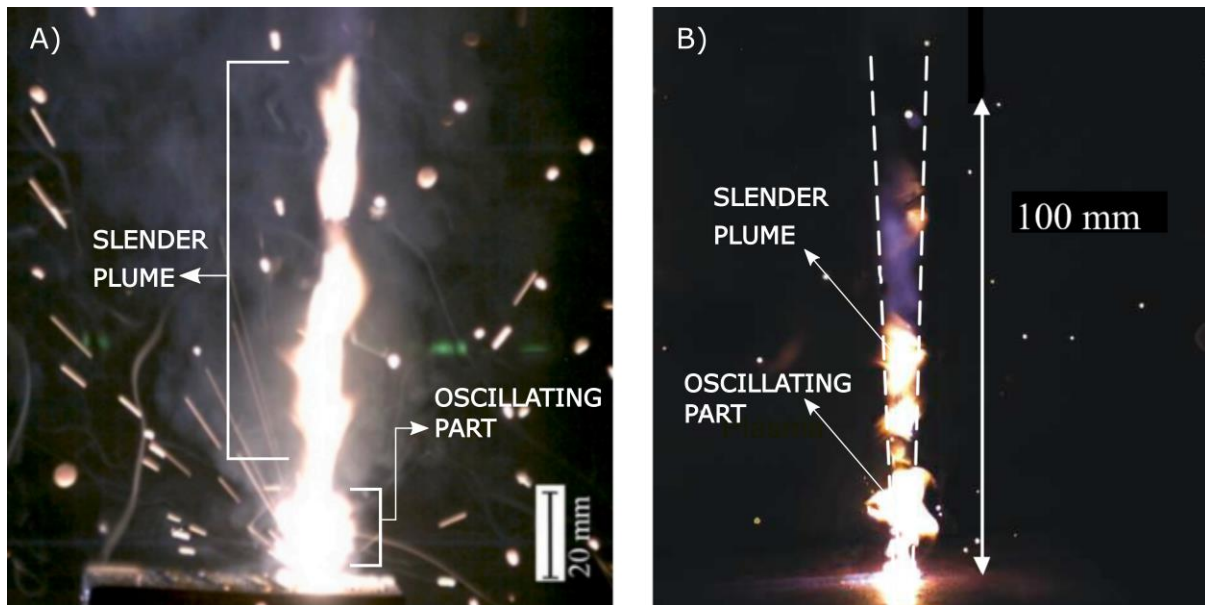
Figure 19. Different parts of a vapor plume A)[172] B)[49].

Hence this brings into question what constitutes a welding vapor plume? Is it only the oscillating part or does it include the slender plume as well? Why is the surrounding smoke neglected in vapor plume studies? Depending upon the subject of interest, a researcher chooses to study a particular part or several parts of the vapor plume. To find the overall characteristics of the vapor plume, or to find the different phenomena involved in the interaction of the plume with its surrounding environment or to compare the vapor plume with a model, a researcher may choose to study the oscillating part along with the slender plume. To study the spectral characteristics of the plasma which may form in the plume, or to find the immediate effects of the keyhole behavior on the vapor plume, a researcher may choose to study only the lower oscillating part of the vapor plume. For online monitoring and providing process control through a feedback loop, imaging of the spatters can be essential. In the future, may be even the smoke would be included in the research of the vapor plume. However, once the researcher knows the subject of interest, the part of the plume to be studied, and makes the acquisition with the parameters set accordingly, next arrives the question, what constitutes the edge of a diffuse cloud-like object. The reasoning behind the definition for the edge of a welding vapor cloud that has rapid, dynamic interactions with its environment can be explained using a simpler analogy.

1.3.2.2.   Thresholding

When researchers asked what is at the edge of a water vapor cloud we see in the sky, they flew a plane at the edges of those clouds to study the distribution of the cloud particles (super cooled water droplets in a submillimeter scale) using a Holographic Detector for Clouds (HOLODEC) equipped with a Nd:YLF laser and a CCD camera [174]. Similar to how an edge of a cloud in the sky that extends over several kilometers is defined by tiny water droplets and their interactions in a submillimeter scale, the edges of the welding vapor cloud that extends over a few or several millimeters can be identified from processes leading to optical emission phenomena happening at a sub-nanometric scale. Upon capturing these optical emissions by a HSI camera, automatically the region of interest becomes a bright region on a dark background. However, once such an image is captured, it is essential to separate the ROI from the rest of

the image since the background is never perfectly black and is always polluted by electronic noise, bleeding or blooming effects from pixel saturation, pixel illumination from the vapor smoke, spatters, etc. Several edge detection techniques are available in image processing such as Laplacian Edge Detection, Sobel-Prewitt, Marr-Hildreth, Canny Edge Detection, Gaussian Gabor filter to name a few [175]. However, any researcher who uses any of these edge detection methods should be able to reason out the purpose and utility of the used algorithm in this context. And since most of the researchers in the laser welding community are not experts in image processing methods, the simplest form of edge detection mostly used is image processing done through binarization of the image by the application of a global threshold. A single value threshold was applied on an image or a stack of images which would then be binarized. In other words, the pixel intensities are compared to a single global value and will be subsequently darkened or brightened based on whether they were lower or higher than the threshold value. Local thresholding is where the thresholding function depends on not only the pixel intensities, but also some other local property. An example of the difference between a global threshold and local threshold is shown in Figure 20, where the local threshold is applied using a gaussian filter of the original image [166]. While the local thresholding seems to be more advantageous in this example, image binarization is still a destructive method of image processing.

Figure 20. Comparison between local and global thresholding operations [166].

Whether one uses global thresholding or local thresholding, the method used to calculate the threshold value is also another subject of significance since there are several thresholding algorithms available. Some of the thresholding algorithms in the ImageJ software [176] are Huang, Huang2, Intermode, IsoData, Li, MaxEntropy, Mean, MinError, Minimum, Moments, Otsu, Percentile, RenyiEntropy, Shanbhag, Triangle and Yen. A brief analysis of all these algorithms in the context of biological image treatment has been provided by Nichele et al. [177]. However, researchers in the laser welding community prefer using the Otsu thresholding algorithm over the others and this can be seen in many articles [167]–[170], [178]–[181]. The reason behind this choice is because the Otsu method is easy to use since it is an automatic thresholding method. And, since it uses the statistical information of the image to compute the threshold value which separates the object (such as the melt pool or the vapor plume) from the background while taking into account the diversity in the background (such as the luminescence from the smoke and the spatters accompanied by image artifacts), this process appears less complicated from a very general point of view. To be a little more specific, this technique separates the histogram (and henceforth, the image) into two regions (classes) and calculates the variances between and within each class to determine the threshold value (usually tends to be towards the class with the higher variance) to separate the object and the background

[182]. This is accomplished by finding a gray level value that separates the image histogram into two groups in such a way that the maximum between-class variance equates to the minimum within-class variance, where between-class variance is the total variation between mean of each class and the overall mean, while the within-class variance is the total variation of the individual values within a class and the class mean [183].

Depending on the bit depth of an image, if there are L gray levels in each pixel from 0 to L, let n_i denote the number of pixels at level i and N, the total number of pixels. Then,

$$N = \sum_{i=0}^{L} n_i \qquad\qquad 13$$

And the probability of occurrence of level i is given by,

$$p_i = {n_i}/{N} \qquad\qquad 14$$

If the image should be divided into two classes C_0 and C_1 by a threshold T_h, as such C_0 and C_1 consist of pixels with $[0,1,2,\dots,T_h]$ and $[T_h + 1,\ T_h + 2, T_h + 3, \dots, L]$ gray values respectively, with $P_0(T_h)$ and $P_1(T_h)$ as cumulative probabilities, $\mu_0(T_h)$ and $\mu_1(T_h)$ as mean gray levels and $\sigma_0^2(T_h)$ and $\sigma_1^2(T_h)$ as variances of the respective classes, they can be expressed by,

$$P_0(T_h) = \sum_{i=0}^{T_h} p_i \qquad\qquad 15$$

$$P_1(T_h) = \sum_{i=T_h+1}^{L} p_i = 1 - P_0(T_h) \qquad\qquad 16$$

$$\mu_0(T_h) = \sum_{i=0}^{T_h} i\,\frac{p_i}{P_0(T_h)} = \frac{1}{P_0(T_h)} \sum_{i=0}^{T_h} i p_i \qquad\qquad 17$$

$$\mu_1(T_h) = \sum_{i=T_h+1}^{L} i\,\frac{p_i}{P_1(T_h)} = \frac{1}{P_1(T_h)} \sum_{i=T_h+1}^{L} i p_i \qquad\qquad 18$$

$$\sigma_0^2(T_h) = \sum_{i=0}^{T_h} (i - \mu_0(T_h))^2 \frac{p_i}{P_0(T_h)} \qquad\qquad 19$$

$$\sigma_1^2(T_h) = \sum_{i=T_h+1}^{L} (i - \mu_1(T_h))^2 \frac{p_i}{P_1(T_h)} \qquad\qquad 20$$

If μ is the overall mean gray value of the image, $\sigma_b^2(T_h)$ is the variation of the mean of the individual classes from the mean gray value of the image (between-class variance) and $\sigma_w^2(T_h)$ is the variation of the individual pixel gray values within the class from the class mean (within-class variance), they can be represented by,

$$\mu = \sum_{i=0}^{L} iP_i = P_0(T_h)\mu_0(T_h) + P_1(T_h)\mu_1(T_h) \qquad 21$$

$$\sigma_b^2(T_h) = P_0(T_h)(\mu_0(T_h) - \mu)^2 + P_1(T_h)(\mu_1(T_h) - \mu)^2 \qquad 22$$

$$\sigma_w^2(T_h) = P_0(T_h)\sigma_0^2(T_h) + P_1(T_h)\sigma_1^2(T_h) \qquad 23$$

The Otsu threshold is chosen in such a way that provides the maximum ratio of the between-class variance and within-class variance in such a way that can be represented by,

$$T^* = arg\max_{0 \le T_h \le L}\{\sigma_b^2(T_h)\} = arg\min_{0 \le T_h \le L}\{\sigma_w^2(T_h)\} \qquad 24$$

However, due to certain limitations of this method, image analysis experts continuously keep developing extensions or modified Otsu methods to improve its efficiency such as the "recursive Otsu method" , "two-dimensional" Otsu method, "multi-level thresholding two stage" Otsu method, etc. [184]–[186]. While many such advanced thresholding techniques are being developed, there is no easy one fix for all solution and every researcher must choose carefully what technique to use for the treatment of their image based on several factors such as the raw image quality, processing time and power, result oriented applicability, etc., especially in the laser welding image treatments since large variations within and between different experiments are quite a common occurrence.

1.3.2.3.   Fitting and Measurement

Once the edges of the vapor plume or melted zone can be determined using an appropriate thresholding technique, it is essential to find a good method to characterize the figure (whether the image is binarized or not). Characterizing the size and the shape and assigning values to the vapor plume is not an easy issue to deal with due to two reasons:

1. The vapor plume has a rapidly changing irregular shape and orientation with certain common traits like brightening and tapering towards the keyhole.

2. The vapor plume exhibits differences in properties depending on the materials being welded, acquisition parameters, thresholding techniques used, etc.

The most fundamental way to describe any image is by its aspect ratio. But a detailed study of an irregular shape requires the use of shape descriptors. 1D shape descriptors such as height [46] and width, or 2D shape descriptors such as perimeter [187], area, and even 3D shape descriptors such as sphericity and volume [155] may be used.

While certain parameters such as the area or perimeter of an irregular shape can be measured relatively easily if a sufficiently high enough resolution is used during image capture, properties like the height of the plume can be difficult to measure. However, since the aspect ratio of an image does not take orientation into account, the use of certain algorithms to measure the shape is inevitable. Several such algorithms such as the fit ellipse, convex hull, ferret diameter, etc. can be used to measure the size of an irregular object [188]–[190].

With automatization for image analysis over thousands of images, such algorithms become a necessity and the measurements cannot be done manually. But a blind use of such algorithms can yield undesirable data and therefore an understanding of these algorithms are a prerequisite in image analysis.

1.3.3. Data Analysis and Conclusion

After image processing and analysis, thousands of lines of data can be produced while working with either a large number of videos, or a few videos with very high frame rates, or both. This data is usually classified, treated, analyzed and the results can be produced using any data handling software. To produce understandable results, most of this data is compiled based on existing knowledge about the relationships between the different parameters and phenomena. While the classification of the data is usually based on the welding and acquisition parameters, compilation of the data and results are usually done by setting a constant value to all the parameters with only two or three variables. Most of the time a comparison of the plume behavior is done for different welding parameters such as laser power, spot width, pulse duration, etc., while the acquisition parameters are fixed. For example, comparison of plume areas between two materials should not be done if the plumes of those materials weren't captured with the same exposure time.

And therefore, almost all the articles cited in this bibliography mention the use of a constant acquisition parameters such as frame rate, exposure time, etc. for their experiments for the ease of data handling, while changing the experimental parameters such as welding materials, laser power, etc. For example, most of the authors cited in this bibliography have either used a narrow band optical filter in the infrared regime or a broadband filter which covers a wide range from ultraviolet to infrared. The relationship between what is observed through these filters and the wavelength of observation is very rarely discussed. Comparative studies between the behaviors of the vapor plume observed at different wavelength regimes has not yet been done. Similarly, the reasons behind the choice of acquisition parameters are not usually mentioned and still require further research and explanations. Since there isn't an established convention because every camera and optical components vary slightly from each other, researchers cannot test or reproduce the observations exactly especially when details about the acquisition parameters are obscured or poorly understood. And so, with the recent technological advancements in the HSI cameras, the latest trends in low-cost high-performance CPUs, and the latest software which can handle large datasets, this research area is still young and rapidly expanding both technically and in community-size. Once enough researchers are involved in the HSI of the vapor plume, conventions and calibration methods will be established. The number of research publications (Figure 21) for the search with keywords: "laser welding" and "vapor plume" and "high speed imaging", show that in the last ten years there is an increasing interest in this research domain. But all the experimental parameters relate to the optimally selected acquisition parameters majorly through one specific property of the vapor plume - its luminosity. And so, to study the phenomena existing behind this property, optical emission spectrometry can prove to be a powerful tool.
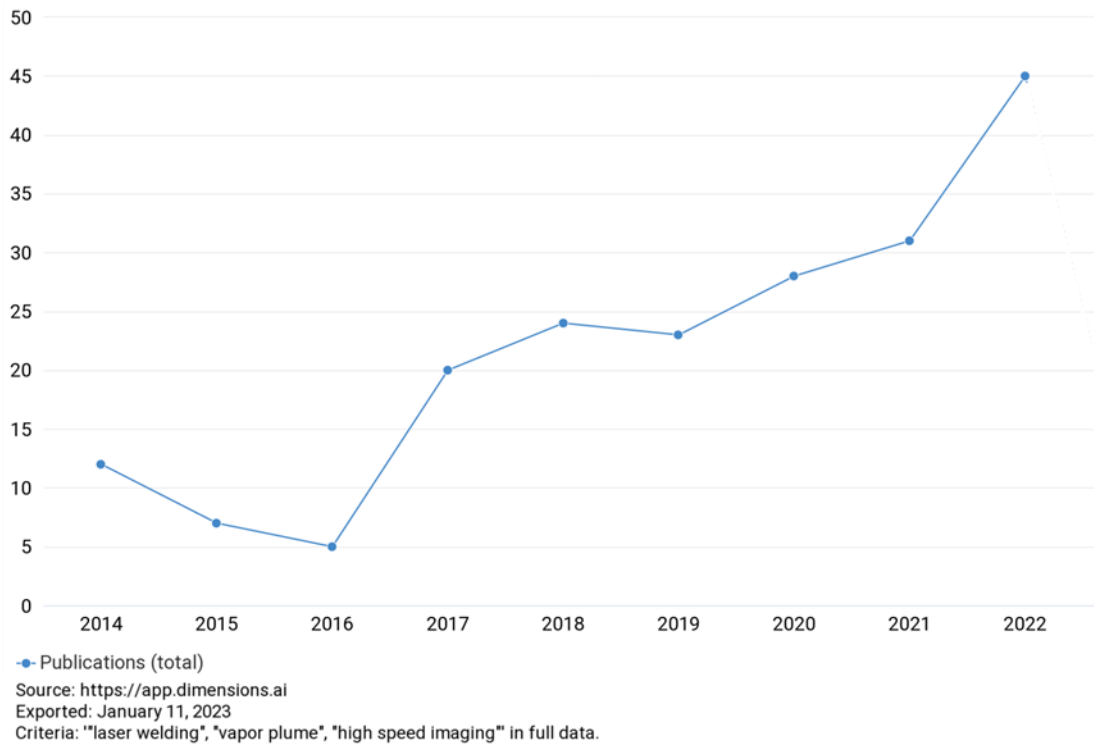
Figure 21. Publications per year with keywords 'laser welding', 'vapor plume' and 'high speed imaging'.

1.4. Spectroscopic studies of the vapor plume

Laser-Induced Breakdown Spectroscopy (LIBS) has been established as a prominent subject in research over the past twenty years. LIBS usually means spectroscopic plasma characterization from short laser pulses (ns) and the vapor plume from laser welding is not usually considered to be a part of this domain. But spectroscopic characterization of the welding vapor plume uses almost the same techniques as LIBS. Moreover, the vapor plume does undergo weak ionization to produce a plasma plume under combination of certain conditions such as high power (10-15 kW), high repetition rate, low wavelength, high absorption coefficient, using an electrically charged probe, etc. [145], [146], [161]. So, optical emission spectroscopy can be applied to estimate the plume characteristics and to comprehend the processes in laser and arc welding [42]. Spectral analysis of the plasma plume led to the idea that condensation of the metallic vapors can have an important role in fiber laser welding of steel [146]. Because the plume in pulsed laser welding has been considered to have low temperature and high density metallic vapor [147], [148], this temperature (electron temperature) is mostly calculated from the ratio of multiple atomic/ionic emission lines using the Boltzmann diagram method [149]. However, the particulate matter and condensates in the plume also influence the laser radiation when directly in the laser beam path [50], [191]. While the emissions from the particulate matter and even the liquid metal can be studied, the vapors play the main role in spectroscopic studies. And while vaporization depends on multiple parameters such as the laser duration, wavelength, power, absorbance of the material, etc., one of the fundamental requirements is that the amount of energy (E_{min}) deposited on the surface of the material should be greater than the latent heat of vaporization (L_v) of the material to overcome the heat lost into the material through conduction.

[192]
$$E_{min} = \rho L_v a^{1/2} t_1^{-1/2}$$
25

where ρ is the mass density, a is the thermal diffusivity and t_1 is the pulse duration. And this vaporized material can produce optical emissions. However, the process of atomic/ionic emission from the interaction of a metal with a laser is much more complicated.

The absorption of photons with sufficient energy from the laser source by the metals liberate the conduction electrons. This releases energy into the crystal lattice by electron-electron and electron-nucleus collisions. The relaxation period for these collisions is much smaller ($<10^{-13}$ s) than the laser pulse (10^{-3} s ~ 10^{-6} s), which makes it seem like the heat source is continuous. The Drude model explains the absorption of laser photons by the free electrons for temperatures below the vaporization temperature [193]. While this forms the basis for emissions happening from the liquids and solids, this thesis is oriented towards the emissions of the vapor plume. Because the spectroscopic analysis of the vapor plume allows us to determine the temperature, electron densities and the elemental composition.

1.4.1. Local Thermodynamic Equilibrium

Any radiation field as a consequence of temperature is defined by Planck's law. In the case of plasma, it depends on the ratio of population densities (ion, atom, or molecule) in the upper and lower states which is given the Boltzmann distribution (Eqn. 28).

When a plasma is in complete thermodynamic equilibrium, it can be described by a single temperature where, $Tradiation = Telectronic = Tionic = Texcitation$.

Planck's law determines the equilibrium between the different processes of emission and absorption for this plasma that is considered to be optically thick like a blackbody. The ability

of a given path length of gas to attenuate radiation of a given wavelength is called optical thickness [194]. The spectral radiance of a blackbody ($L_\lambda^B(\lambda, T)$) is given by,

$$[195] \qquad L_\lambda^B(\lambda, T) = \frac{2hc^2}{\lambda^5} \frac{1}{e^{h\nu/k_B T} - 1} \qquad\qquad 26$$

where h is the Planck's constant, c is the speed of light, k_B is the Boltzmann's constant, T is the temperature of the blackbody, λ and ν are the wavelength and frequency of the emitted light respectively.

However, complete thermodynamic equilibrium doesn't exist in laboratory plasmas because the radiation escapes from the plasma while not being completely reabsorbed. This leads to radiation fields inside the plasma reducing below the Planckian radiant energy density. However, this plasma which obey the Boltzmann (Eqn. 28) and Saha equations (Eqn. 27) (defined by electronic temperature) is said to be in local thermodynamic equilibrium. When a plasma is in complete thermodynamic equilibrium, its temperature is defined by, $T electronic = T excitation.$

$$[196] \qquad \frac{N_j^{(z+1)} N_e}{N_j^{(z)}} = \frac{g_j^{(z+1)} g_e}{g_j^z} \frac{(2\pi m_e k_B T_{ion})^{3/2}}{h^3} e^{\left(-\frac{E_{j,\infty}^{(z)}}{k_B T_{ion}}\right)} \qquad 27$$

with, $N_j^{(z+1)}$, $N_j^{(z)}$, and N_e being the number densities at the states $z + 1$ and z, and the electron number density respectively, $g_j^{(z+1)}$, g_j^z, g_e being the statistical weights for the previously mentioned quantities, T_{ion} being the ionic temperature, and $E_{j,\infty}^{(z)}$ and m_e being the ionization energy and mass of the electron.

In other words, the temperatures defining the motion of the electrons and the heavier particles (atoms, ions or molecules) are decoupled. This requires spatial and temporal variations within the plasma to be negligible. In this concept of local thermodynamic equilibrium, the electron collisions which are much faster than the ion collisions lead to an equilibrium between the states. For this system, the Atomic State Distribution Function (relative population of excited levels in an atom/ion) is given by the Boltzmann distribution:

$$[196] \qquad N_n = N \frac{g_n e^{\frac{-E_n}{k_B T}}}{Z(T)} \qquad\qquad 28$$

where, N_n is the population, E_n is the energy and g_n is the degeneracy of the quantum level n. N is the number density of the species, k_B is the Boltzmann constant, T is the temperature an Z is a partition function of the atomic level system at that temperature. The minimal electron number density required for local thermodynamic equilibrium is called the McWhirter criterion expressed by

$$[197] \qquad N_e(m^{-3}) > N_e^W = 2.55 \times 10^{17} \frac{T_e^{1/2} \Delta E_{nm}^3}{\langle \bar{g} \rangle} \qquad 29$$

where $\langle \bar{g} \rangle$ is the Gaunt factor averaged over electron energy distribution function, T_e and ΔE_{nm} are the electronic temperature (K) and the largest energy gap (eV) between adjacent levels.

1.4.2. Line Broadening

Spectral lines usually are not infinitely thin because the energy levels of excited states are not infinitely thin and so there are several phenomena which could lead to their broadening. Some of the broadening mechanisms are natural broadening (Lorentzian), collisional broadening/pressure broadening (Lorentzian), Doppler broadening (Gaussian).

Natural broadening is a consequence of the Heisenberg's uncertainty principle which connects the uncertainty of energy (ΔE) of any atomic system with the uncertainty of the time intervals (Δt) during which the measurements of the energy are made.

$$\Delta E \Delta t \geq h/4\pi \qquad\qquad 30$$

However, this equation can be reduced [198] to find the relative broadening ($\Delta \lambda$)

[199] $$\Delta \lambda = \frac{\lambda_s^2 A_s}{2\pi c} \qquad\qquad 31$$

with λ_0 being the wavelength of emissions and A_s being the Einstein's spontaneous emission coefficient.

Doppler broadening is a consequence of the motion of the emitters with non-relativistic velocities leading a Doppler shift of the angular frequency (ω_{pq}),

[195] $$\frac{\omega - \omega_{pq}}{\omega_{pq}} = \frac{v_x}{c} \qquad\qquad 32$$

where v_x is the velocity component in the direction of emission and c is the speed of light. In local thermodynamic equilibrium, the prerequisite of Maxwellian distribution of temperature (T_a) makes the line shape function a Gaussian with a halfwidth ($\Delta\lambda_{1/2}^G$)

[195] $$\frac{\Delta\lambda_{1/2}^G}{\lambda_{pq}} = 7.715 \times 10^{-5} \sqrt{\frac{k_B T_a/eV}{m_a/u}} \qquad\qquad 33$$

where (eV is electron Volts and u is the atomic mass unit)

Collisional broadening/pressure broadening happens due to collisions between the emitter and another particle. Collision with neutral atoms in the ground-state leads to Van der Waals broadening. Collision with another neutral emitter leading to exchanging energy between different levels causes resonance broadening. And collision with charged particles such as ions or electrons lead to Stark broadening. Pressure broadening usually leads to a Lorentzian profile with a negligible shift. Even though metal vapors generated from solid state laser usually do not form any plasma, it would be prudent to assume that the emission lines are broadened by these mechanisms (except Stark broadening when ions are absent). And so, a convolution of the Gaussian and Lorentz profiles of equal half widths, being a Voigt profile (Figure 22) would form the right fit for the emission lines for metal vapors from interaction with an Nd:YAG laser.
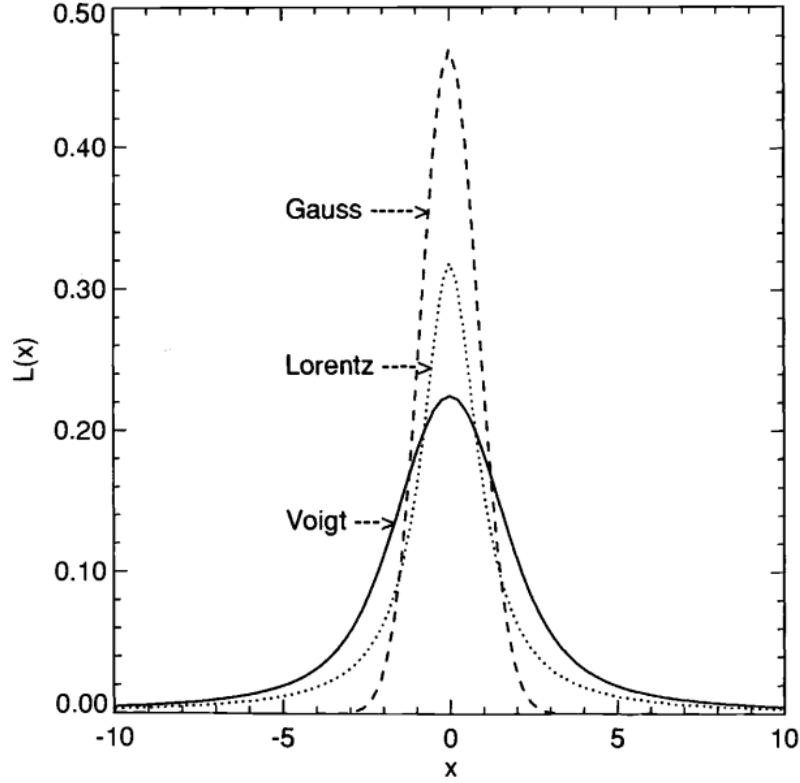
Figure 22. Normalized Gauss (Doppler) and Lorentz (impact) profiles of equal half widths (FWHM width = 2 in x-units). Also shown is the Voigt profile resulting from the convolution of these two profiles [198].

1.4.3. Temperature

1.4.3.1. Boltzmann temperature

If a Boltzmann distribution (partial local thermodynamic equilibrium) is assumed for upper levels, rotational and vibrational temperatures are estimated by fitting a Boltzmann distribution to the population densities of rotational and vibrational levels of the electronically excited states. And so, excitation temperature (equals electron temperature in local thermodynamic equilibrium) can be calculated by fitting Boltzmann distribution to the population densities. Substituting emissivity for population of the upper level in Boltzmann's law,

[199]
$$\varepsilon_{u,l} = N_j^{(z)} \frac{g_{j,u}^{(z)} A_s}{U_j^{(z)}} \frac{hc}{4\pi\lambda_s} e^{\left(-\frac{E_{j,u}^{(z)}}{k_B T_{ex}}\right)}$$
34

where $N_j^{(z)}$(cm^{-3}) is the number density of element j at a given z degree of ionization, $U_j^{(z)}$ is the partition function, and $g_{j,u}^{(z)}$ is a statistical weight. Applying logarithm, Eqn. 34 becomes

$$\ln\left(\frac{\varepsilon_{u,l}\lambda_s}{g_{j,u}^{(z)} A_s}\right) = \ln\left(\frac{N_j^{(z)} hc}{4\pi U_j^{(z)}}\right) - \frac{E_{j,u}^{(z)}}{k_B T_{ex}}$$
35

which can be used to make the Boltzmann plot (Figure 23). With the emission intensities at different wavelengths known, along with the other constants obtained from the NIST database

[200], the slope of the straight line $\left(-\dfrac{1}{k_B T_{ex}}\right)$ leads to temperature estimation. Continuous fiber laser welding of 304 austenitic stainless steel with laser power 10kW produced an emission spectrum of the vapor plume which in turn led to an average vapor plume temperature estimate of ~6000K [161].
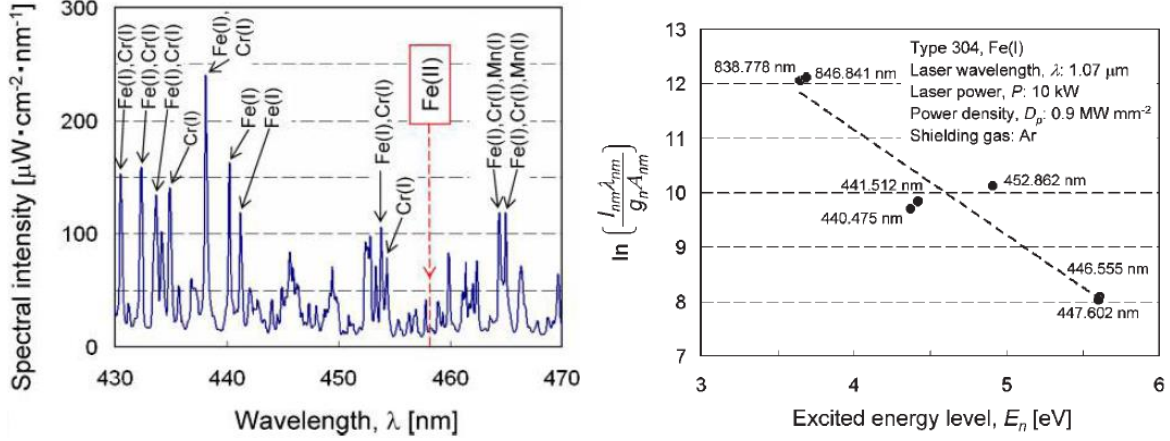
Figure 23. Emission spectra of the vapor plume for 10kW fiber laser welding of 304 stainless steel within 430-470 nm and the corresponding Boltzmann plots [161].

1.4.3.2. Continuous emission

Compared to solids, gases have a less continuous spectrum due to different types of transitions. However, superposition of various emissions from photodissociations, photoionizations, free electron-atom-photon interactions lead to a continuous part in the emissions. Thus, a continuous part is ever-present in both emission and absorption spectra as much as the emission lines as shown in Figure 24. The Stefan-Boltzmann law [201] obtained by integrating Planck's law over all frequencies for a blackbody radiator at temperature T is

$$B(T) \equiv \int_0^\infty B_\nu(T) = \frac{\sigma_{SB} T^4}{\pi} \qquad 36$$

where σ_{SB} is called the Stefan-Boltzmann constant

$$\sigma_{SB} = \frac{2\pi^5 k_B^4}{15 c^2 h^3} \qquad 37$$

A)   B)
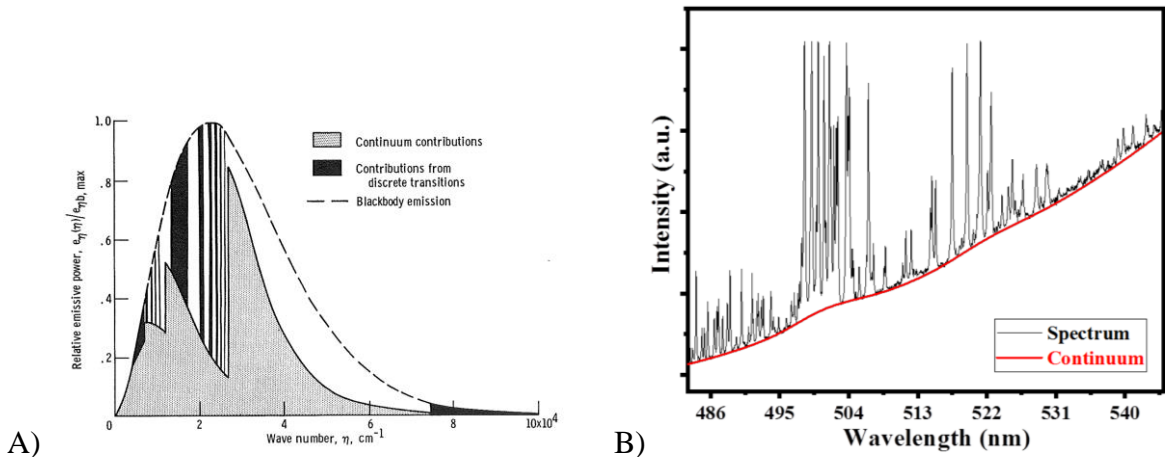
Figure 24. A) Normalized emission spectrum of hydrogen at 11300 K, 40 atm, and for a path length of 50 cm [194], [202] and B) Continuous emission spectrum and the atomic emission lines of the laser welding of Ti-6Al-4V [203].

1.4.4. Auto-absorption

Differences in temperature between the center of a plasma plume and its outer edges can cause emissions from the center to be reabsorbed by the cooler atoms or ions at the edges (Figure 25). This can lead to a decrease in the emission intensity and a change in the shape of the profile. Auto-absorption leads to profiles having a depression in the place of a peak [204]. The resulting line profile and broadening from auto-absorption depends on several factors such as temperature, electron density, homogeneity of the plasma, etc. Auto-absorption originating due to the cooler outer edges with low electron density lead to peak reversal but auto-absorption in a homogeneous plasma can only distort the profile shape slightly [205].
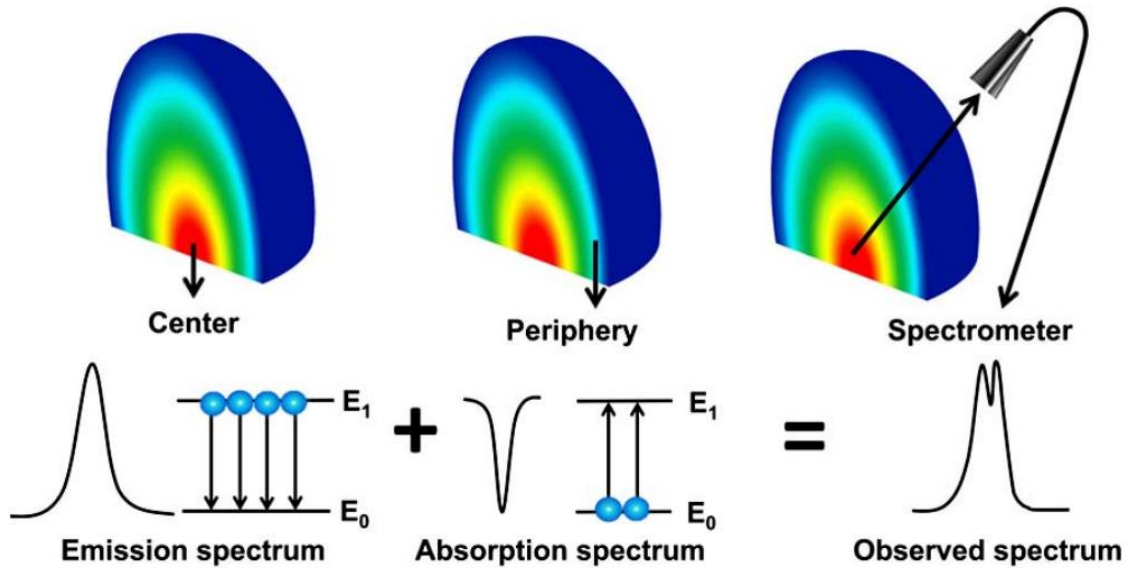
Figure 25. Schematic for auto-absorption [206].

1.4.5. Objectives and conclusion

While the techniques of characterization of an ionized plasma from LIBS can be borrowed for the analysis and characterization of the YAG laser welding vapor plume, such as establishing LTE, calculating the electronic temperature, assuming Voigt profiles on the broadened lines, this optically thin low temperature vapor plume poses certain limitations such as low emission intensities (at the level of the background noise), insufficient energy for certain elements to reach the excited levels, high uncertainties in the calculation of the Boltzmann temperature, etc. [207] But still, the spectroscopic analysis of the welding vapor plume (especially in the case of dissimilar welding) serves to be very useful in complementing the HSI vapor plume studies done over different wavelength regimes. And so, with the objective of characterizing the vapor plume for its temperature and composition, the principles discussed in the bibliography section can be applied to study the aluminum and titanium combination (very different spectroscopic properties) in the welding by a YAG fiber laser.

1.5. Numerical modelling

The use of numerical models is crucial for gaining insight into the processes involved in laser welding. Advancements in technology have led to significant progress in this field in recent years, with better numerical methods, more robust solvers, and greater access to high-performance computing. However, since welding involves a complex interplay of various physical processes, which can occur rapidly and result in large variations in physical properties, it can be challenging to strike a balance between model complexity and computation time. Depending on the specific research or practical goal of the modeling, several assumptions may be used. In numerical modeling of welding, the objective is to describe the processes that affect the development of the melt pool and, potentially, the final weld bead. This involves modeling:

- Heat transfer, taking into account various types of heat sources such as surface and volumetric sources, and sources with fixed or evolving geometries.
- Convective phenomena, in the liquid zone and in the gaseous phase, and any potential effects on the free surface or volumetric defects
- Transport of matter, the movement of elements within the melt pool and the evaporation of elements into the gaseous phase
- Metallurgical changes, solidification, changes in the microstructure and the heat-affected zone
- Thermomechanical processes, the evolution of stress and deformation during heating and cooling, and the prediction of cracking risks.

Due to the highly complex nature of the welding phenomenon, every physical phenomenon cannot be easily quantified experimentally. Therefore, numerical modelling becomes an essential tool to quantify the different phenomena and elucidate their synergetic effect. Mathematical modelling of the welding phenomena started in 1940 by Rosenthal [109] and numerical models has been built over the past few decades [208]. However the scope of understanding the welding phenomena using modelling software is severely limited till the present due to several difficulties [209] such as:

- The dataset for materials' physical properties at elevated temperatures which is a requirement for simulation, is still incomplete.
- Modelling in complex configurations pose difficulties.
- When incorporating multiphysics and unstable phenomena, computation times increase multi-fold.

The first focus in modelling of welding is usually on the thermal processes. However, modelling of the fluid flow is prioritized when geometrical changes to the weld pool need to be understood [208]. As discussed earlier, the several multiphysical phenomena are modelled using equation for the heat source (section 1.1 p.18), recoil pressure (section 1.2 p.24)[210], Marangoni convection (section 1.2.3 p.27), vapor induced shear stress and heat transfer, multiple reflections on the keyhole wall, etc. [210]–[216]. Finite Element Method FEM or Computation Fluid Dynamics CFD (using Finite Volume Method or Finite Difference method) sometimes combined with ray-tracing methods are mostly used to solve the partial differential equations representing the previously mentioned phenomena [55], [217]–[221]. However, several problems exist in the models constructed till now [222] and are currently being resolved such as the following:

- Simplifications like neglecting temperature dependence on some of the physical properties of the materials in the liquid and vapor state.
- Simplified representation of heat sources.
- Considering the fluid flow to be incompressible and laminar.

1.5.1. Software in welding simulation

There are software which have been used in the numerical modelling of the welding phenomenon like COMSOL Multiphysics®, ABAQUS®, ANSYS® Fluent, FLOW-3D®, etc. [223]–[226] While each of these software are used by many researchers across the world for welding simulation, they have their own advantages and disadvantages. While ABAQUS® and COMSOL Multiphysics® are FEM software, ABAQUS has more learning resources and is more application oriented (allowing for complex geometry), but it is mostly concentrated on non-linear problems in solid mechanics. COMSOL Multiphysics on the other hand, while allowing access to the different types of physics and its equations, does not facilitate drawing complex geometry. While ANSYS® Fluent, FLOW-3D® are CFD based software which use Volume of Fluid (VOF) method, Fluent facilitates creation of turbulence models which accurately simulate complex flow and heat transfer phenomena, offers integration with other ANSYS® software, is CAD (Computer Aided Design) friendly, while on the other hand FLOW-3D is well suited for free surface tracking and is computationally much lighter, but is not as sophisticated as the others.

1.5.2. Type of the FEA model

Most of the numerical models solved by finite element analysis can be broadly classified into two types: stationery and time dependent. In a stationary model, the problem to be resolved is a static or steady state problem where there is a single (linear or non-linear) set of partial differential equations with variables such as the material properties, boundary conditions, etc. being constrained with respect to the solution. A time-dependent model solves a set of coupled or independent ordinary differential system of equations which are constrained by another system of time dependent differential algebraic equations.

Similarly, the type of geometry applied to the model can be classified into 2D, 2D-axisymmetric and 3D models. Depending on the objectives, the type of geometry is chosen. For example, a 2D-axisymmetric model (2D model rotated 360° around an axis) does not offer any advantage for simulating dissimilar laser welding in the butt configuration. Another example, the inclination of the front keyhole and back keyhole wall cannot be simulated with 2D models for the dissimilar laser welding in the butt-configuration. While 3D models offer versatility to simulate many of the processes, computationally they are much heavier.

1.5.3. Modelling the keyhole

Many keyhole models have been constructed and they have been usually done with some simplification of the processes. The first models were developed to represent the heat source (cylindrical, point source) of the laser [227], [228]. With the identification of the isotherms at the melting point, the fluid flow equations (Navier-Stokes) were introduced to study the motion of the liquid metal [229]. Meanwhile, the incorporation of multiple reflections with a deepening keyhole was also studied [230]. More recently, the multi-solute diffusion in the laser welding of 304 stainless steel and pure nickel substrate has been modelled [231].

1.5.3.1. Heat transfer

In any of the welding simulations, the very first necessity is to model the thermal processes starting from the heat gained by a source to the heat lost at the boundaries. Depending on the type of model (section 1.5.2) the equations may vary slightly. A 2D-time dependent model may have a Gaussian heat source defined by

[232]
$$q''(x, y, t) = \frac{Q(t)}{\pi R_0^2} e^{-3\frac{((x - u_w t)^2 + y^2)}{r^2}}$$
38

where q'' is the heat flux, $Q(t)$ is the total heat rate, R_0 is the weld radius and u_w is the welding speed. And a 3D conical model with a Gaussian distribution (currently the most used) is represented by,

[233]
$$Q(x, y, z) = Q_0 e^{\left(-\frac{x^2+y^2}{r_0^2(z)}\right)}$$
39

[233]
$$r_0 = r_e + \frac{r_i - r_e}{z_i - z_e}(z - z_e)$$
40

with Q_0 being the maximum volumetric heat flux density, r_e, r_i are the upper and lower 3D cone radii, z_e, z_i are the 3D cone length parameters as shown in
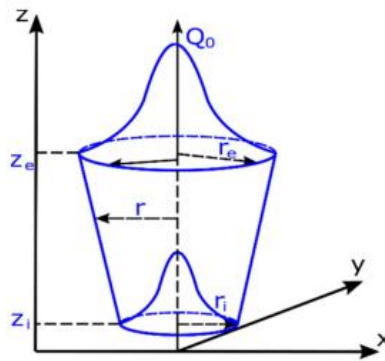
Figure 26. Three-dimensional conical heat source model [233].

Similarly, the equations for the other phenomena are also adapted to suit the dimensionality of the model while taking care not to change the underlying physics. For example, the heat transfer equation at the beginning for the heating of the material by conduction is,

$$\rho C_p \frac{\partial T}{\partial t} + \vec{\nabla}(-KT) = 0$$
41

where T is the temperature, ρ is the density of the material, C_p is the thermal capacity at constant pressure, and K is the thermal conductivity. But once the metal melts, the equation should be altered to account for the heat transfer through convection. And so, the equation becomes,

$$\rho \left(C_p \frac{\partial T}{\partial t} + C_p \vec{u} . \vec{\nabla}T \right) + \vec{\nabla}(-K\vec{\nabla}T) = 0$$
42

where $\vec{u}$ is the velocity field calculated from the Navier-Stokes equation for incompressible equation.

1.5.3.2. Fluid Flow

Once the temperature reaches the melting point, the movement of the incompressible liquid metal between the keyhole and the solid metal causes the transfer of energy by convection. This movement is calculated from the Navier-Stokes equation for incompressible fluids using the Boussinesq approximation,

$$\rho \frac{\partial \vec{u}}{\partial T} + \rho(\vec{u}.\nabla)\vec{u} = -\nabla p + \mu\nabla^2\vec{u} + \rho.\beta.\vec{g}.(T - T_m)$$
43

$$\nabla \cdot \vec{u} = 0 \qquad\qquad 44$$

where p is the fluid pressure, μ is the viscosity, β is the coefficient of thermal expansion, T_m is the melting point, and $\vec{g}$ is the acceleration due to gravity.

Another important idea, the recoil pressure (also known as recoil momentum) which was proposed in 1968 has been used till now for the modelling of the movement of the free surface of the liquid layer [234]. The recoil pressure is proportional to the saturated vapor pressure which is dependent on the surface temperature [235]. In recent works, the entire surface evaporation process has been linked to the ambient pressure as well [47].

[236]
$$p_r(T_s) = \frac{1 + \beta_r}{2} p_0 e^{\left(\frac{\Delta H_v}{k_B T_v} \left(1 - \frac{T_v}{T_s} \right) \right)} \qquad\qquad 45$$

[236]
$$\Delta H_v = m L_v \qquad\qquad 46$$

where T_v is the vaporization temperature at atmospheric pressure p_0, T_s is the surface temperature, β_r is the recombination coefficient, and ΔH_v is the phase transition enthalpy with m as the atomic mass and L_v, the latent heat of vaporization. In the study of fluid flow, the effects of temperature dependent surface tension and Marangoni convection have been accurately modeled using Eqn.12. [108]

1.5.3.3. Dissimilar joining

Modeling a dissimilar keyhole in laser welding is a complex process due to the increased complexity caused by the miscibility of the materials and the differences in thermophysical properties. To understand the effect of the differences in the thermophysical properties on the capillary's symmetry and other characteristics such as depth, melted zone width, etc., multiphysics models have been developed. To account for the changing properties of both the molten materials such as the thermal conductivity, density, absorptivity, viscosity, etc., smoothed Heaviside functions have been used [140]. To accurately represent the boundary between the liquid and solid in the model, Darcy damping forces were utilized to reduce the velocity to zero when the temperature drops below the melting temperature [237]. The equivalent enthalpy approach, which considers the specific latent heat of fusion of both materials involved, has been utilized in the calculation of the latent heat of fusion in the melted zone [238]. To understand the mixing process, various mathematical representations can be used, such as conservative phase field equations, Fick's laws of diffusion, level set methods, and transport equations for mass, momentum, and energy. These mathematical models can be used to simulate the movement of different liquid phases and their interface, the diffusion of elements within a liquid and their interactions, the dynamics of the liquid-gas interface, tracking the volume fraction of the different fluids in a given control volume, and modeling the heat and mass transport in the welding process and their interaction with the interface. The choice of the method will be based on the specific application and the level of complexity that is required in the model. The Fick's diffusion equation has been used to model the transport of species in a weld pool.

$$\vec{\nabla} \cdot (-D_i \cdot \vec{\nabla} c_i + \nabla \cdot \vec{u}) = 0 \qquad\qquad 47$$

where c_i is the molar concentration of the species, D_i is the Stokes-Einstein Diffusion Coefficient,

$$D_i(T) = \frac{k_B T}{6\pi r_s}$$

$$48$$

with r_s being the solute radius.

This mixing of the liquid domains are studied with significance with 3D simulations to understand the influence of the fluid flow on the heat transport which consequently determines the characteristics of the fusion zone [239], [240]. Therefore, several simulation studies since then have been dedicated to the research on the influence of the heat transfer coupled with fluid flow on the properties of the melted zone such as shape, microstructure, alloy composition, residual stresses. etc. [20], [24], [140], [241]–[258].

1.5.4. Modelling the vapor plume

To develop a universal model of laser welding, the vapor plume simulation should also be incorporated in the model. The vapor plume during the continuous welding of stainless steel has been modelled with considerations such as: the surrounding medium is incompressible and the flow velocity is below half the speed of sound [259]. Models with similar considerations while neglecting the possible friction effect were built to relate the different penetration regimes with the vapor plume dynamics [40]. It has been identified that the velocity and the temperature of the shielding gas can perturb the plasma plume dynamics for the CO_2 welding [260]. The absorption coefficient α of such plasma can be calculated by

[261]
$$\alpha = 1.63 \times 10^{-42} \frac{N_e^2}{T_e^{1/2}} \times \left[1 - e^{\left(\frac{-1.36\times 10^3}{T_e}\right)}\right] \; (\text{m}^{-1})$$

$$49$$

where the electron number density N_e and the electronic temperature T_e are obtained from experimental spectroscopic studies. And calculation of the inverse Bremsstrahlung absorption which is present in these ionized plasmas have been studied in detail [262]. And similarly, vapor plume models built for the case of Nd:YAG laser have been mostly dedicated to nanosecond or picosecond pulse regimes. However, a general approximate model of the surface vaporization has been made for different pressures [263]. More recently, the vapor plume that is not an ionized plasma has been modeled [264] in a 2D-axisymmetric geometry using the local temperature dependent vaporization mass flux ($\dot{m}$) while neglecting radiation and external convection Figure 27.

[265]
$$\dot{m} = (1 - \beta_r)\sqrt{\frac{M_a}{2\pi RT}} P_{sat}(T)$$

$$50$$

However, it has been stated that the vaporization mass flux depends not only on the local melt temperature, but also on the function of the local Mach number.

[263]
$$\dot{m} = \sqrt{\frac{M_a}{2\pi RT}}\left[P_{sat}(T) + \beta_r\sqrt{\frac{T}{T_{KN}}} P_{sat}(T_{KN}) f(Ma)\right]$$

$$51$$

with T_{KN} being the temperature just outside the Knudsen layer and Ma being the local Mach number.
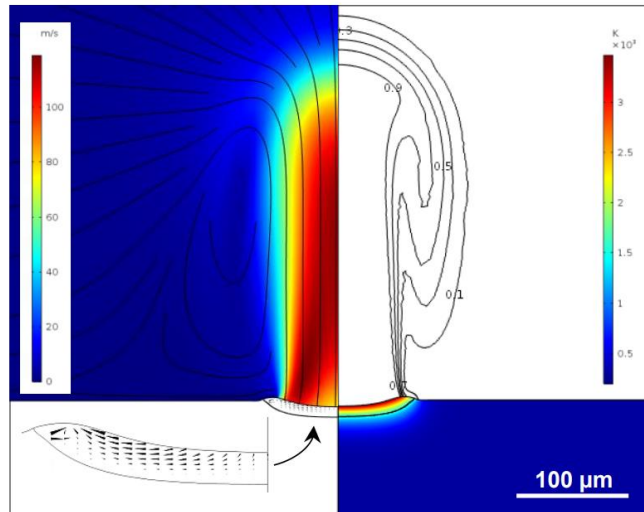
Figure 27. Shape, velocity field and streamlines of the melt pool and vapor plume [264].

As mentioned before, very few models exist for simulation of vapor plume, and they have been done only for standalone materials due to the problems yet to be resolved in simulating the vapor plume such as the high velocities (sub-sonic to supersonic), inexistent data at high temperatures, etc. Therefore, the vapor plume simulation for dissimilar welding without over-simplifying the assumptions on the temperature dependent physical properties is not yet successfully done in the research community.

1.5.5. Conclusions

Modeling the complex processes of laser welding using numerical methods is crucial for understanding the phenomena, but it can be difficult to balance the level of detail in the model with the computational cost. There are also limitations in current models, such as incomplete data on material properties, difficulties modeling in complex configurations, and discrepancies between model predictions and experimental results. Numerical models in welding can be divided into two types: stationery and time dependent. The geometry used in the model can also be 2D, 2D-axisymmetric, or 3D. The choice of type of model and geometry depends on the specific goals of the simulation. Models of keyhole in laser welding have been developed with simplifications. But some recent models have incorporated more advanced features like multi-solute diffusion. Modeling a dissimilar keyhole in laser welding requires various mathematical models, such as conservative phase field equations, Fick's laws of diffusion and interface capturing methods, to simulate the movement of liquid phases, interface diffusion, and heat and mass transport. Simulation studies have focused on the effects of fluid flow on heat transfer, which in turn can affect the shape, microstructure, and alloy composition of the melted zone. Models have been developed for the vapor plume simulation, but the vapor plume simulation for dissimilar welding materials is yet to be resolved due to problems such as inexistent data at high temperatures.

1.6.   Bibliography Conclusions

Comprehending the processes occurring in the keyhole and the melted zone of laser welding is necessary to improve quality control. Techniques such as beam oscillation and pulsed welding have been used to improve weld quality, but further research is needed to understand basic dissimilar laser welding without additional techniques. The most important factor in laser welding is the absorption coefficient of the materials at the wavelength of the laser, which affects the surface temperature and compatibility of different materials which subsequently influence the shape of the keyhole and henceforth the total energy deposited into the keyhole from multiple reflections. Researchers are using X-ray flash radiography or imaging and

Optical Coherence Tomography (OCT) to observe keyhole behavior. However, there is still much to be understood about the laser-matter interaction, the role of recoil pressure, and the influence of other forces such as surface tension and natural convection on the melt pool. Researchers are developing automated systems with deep learning models to improve the accuracy of monitoring the laser welding keyhole.

High-speed imaging has been used to study the vapor plume in laser welding to produce massive amounts of data. The data is usually compiled based on existing knowledge about the relationships between different parameters and phenomena, but further research is needed to fully understand the relationship between the vapor plume and the wavelength of observation, as well as the reasons behind the choice of acquisition parameters. With recent advancements in technology, this research area is expanding, but conventions and calibration methods have not yet been established. There is a lack of research on the optimally selected acquisition parameters and their relation to the vapor plume's luminosity, and optical emission spectrometry can be a powerful tool to study the phenomena behind this property. Overall, the research on laser welding and vapor plume using high-speed imaging is growing and there is still much more room for exploration in this field. While techniques from LIBS can be used to analyze and characterize the YAG laser welding vapor plume, there are limitations such as low emission intensities and high uncertainties in the calculation of temperature. Spectroscopic analysis of the welding vapor plume can be useful in complementing HSI studies, but research is needed to apply these principles to dissimilar welding materials such as aluminum and titanium. Further research is needed to effectively determine the temperature and composition of the vapor plume.

Chapter 2. Experimental work

2.1. Introduction

The focus of the experimental work in this thesis is centered around two parts: the vapor plume's behavior for dissimilar welding in the butt and overlap configuration and the keyhole's behavior for dissimilar welding in the butt configuration using laser pulses. The various experimental methods, their advantages and disadvantages have been already discussed in detail in the previous chapter.

This chapter is introduced with the description of the welding material and the laser used in the study. The sub-chapter following the introduction titled "Experimental campaigns", is divided into several sections, starting with a discussion of continuous welding in the butt configuration, followed by an examination of pulsed welding in the butt configuration, which includes experimental work done for the vapor plume and the keyhole investigation. This sub-chapter concludes with a section on overlap pulsed welding. The final sub-chapter is a discussion of the characterization methods employed, that explains high-speed imaging, spectrometry of the vapor plume and post-mortem characterization of the melted zone.

2.1.1. Materials

The metallic materials which were studied during this thesis work were titanium T40 and A5754 aluminum alloy. The physical properties of these materials are provided in Table 2 [266]. These two materials were chosen due to the significant differences in their thermophysical (T_m, T_v, a, …) and spectral ($A(T)$, $\lambda_{u,l}$, ΔE_{nm}, …) properties. Titanium has a higher melting point, boiling point, specific heat capacity, density, and absorptivity (at $\lambda \approx 1$ µm) than aluminum, while aluminum has higher thermal conductivity and coefficient of thermal expansion than titanium. The metal sheets used for welding were cut and rectified (to avoid shears). Oxide layers formed during the grinding process were removed by polishing using fine grit emery paper. Traces of grease were finally removed with ethanol.

Table 2: Material physical properties.

Materials	A5754 aluminum alloy	Ti T40
Elemental composition (wt.%)	2.6 Mg, 0.5 Mn, 0.4 Si, 0.4 Fe, 0.3 Cr, 0.15 Ti, 0.2 Zn, 0.1 Cu	99.9 Ti
Absorptivity at 1030 nm	10 ~ 30 %	40 %
Melting point (K)	883-902	1941
Boiling point (K)	2792	3560
Thermal diffusivity (10^{-6} m²/s)	98.8	9.4
UTS (MPa)	220	345

UTS: ultimate tensile strength

2.1.2. Laser

The laser used for the experiments was the TruDisk 6001 by TRUMPF Yb:YAG laser with 1030 nm wavelength. The TruDisk 6001 is a solid-state disk continuous welding laser with a power output in the range 120 W to 6 kW and capable of using fibers 100 µm, 200 µm and 600 µm (with corresponding spot diameters). The laser head consisted of a system of lenses that focused the output from the fiber at 300 mm. This disk laser which has a near-gaussian spatial intensity profile [267], was used for both continuous welding and pulsed welding. And for all the experiments, the laser head was tilted ~3º to avoid back reflection of the laser into the laser head.

2.2. Experimental Methods

2.2.1. Continuous welding in butt configuration

The metal plates used in the continuous welding in butt-configuration experiments were of dimensions 150 mm × 50 mm × 3 mm. A 200 µm fiber with a 200 µm laser spot size was used, along with a 3 kW laser power. Argon shielding gas was employed at a flow rate of 20 L/min above and 10 L/min below, and the welding speed was set at 3 and 8 m/min. The HSI camera Phantom v9.1 (attached with an 810 nm optical bandpass filter) and the spectrometer were used to capture the front and side views of the vapor plume (Figure 28).
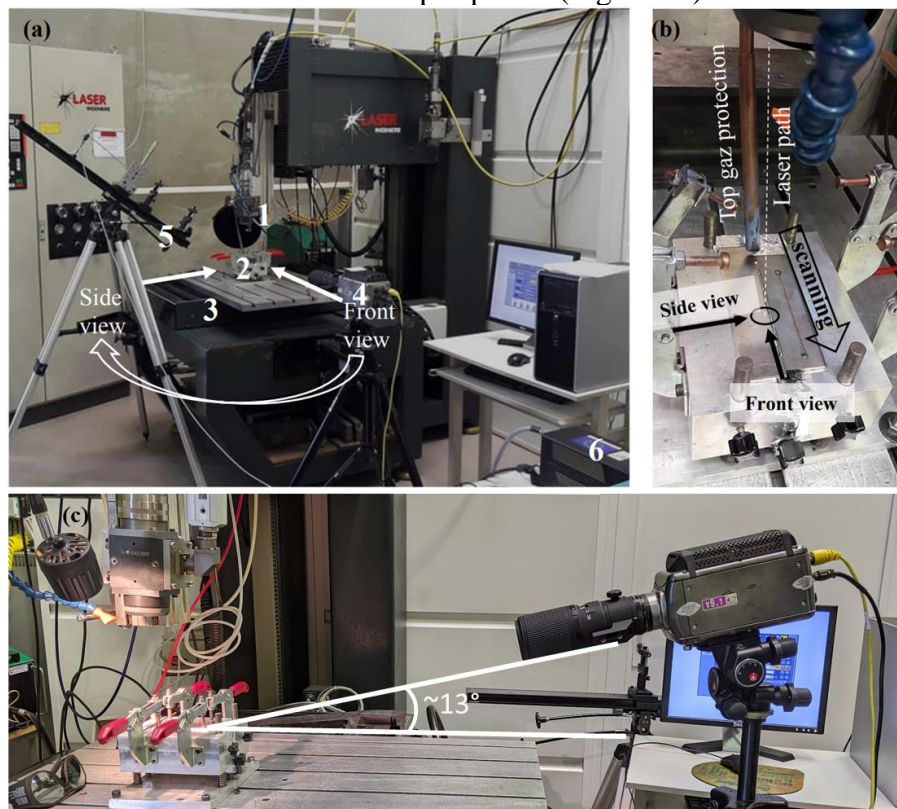
Figure 28. (a) Experimental setup: (1) welding heat, (2) sample, (3) welding table, (4) HSI camera, (5) spectra acquisition lens setup, (6) spectrometer CCD and (b) Sample position.

The experiments were first done on standalone materials of T40 and A5754. When the dissimilar experiments were done in the butt configuration, the laser spot was focused on 5 different positions with respect to the joint line (Ω) with the 200 µm spot diameter as represented in the Figure 29. To study the vapor plume on both sides of the aluminum and titanium plates, their positions were interchanged multiple times during the experiments. Although the figure below shows aluminum to be on the left and titanium on the right, it is important to note that their positions were alternated throughout the continuous welding study.
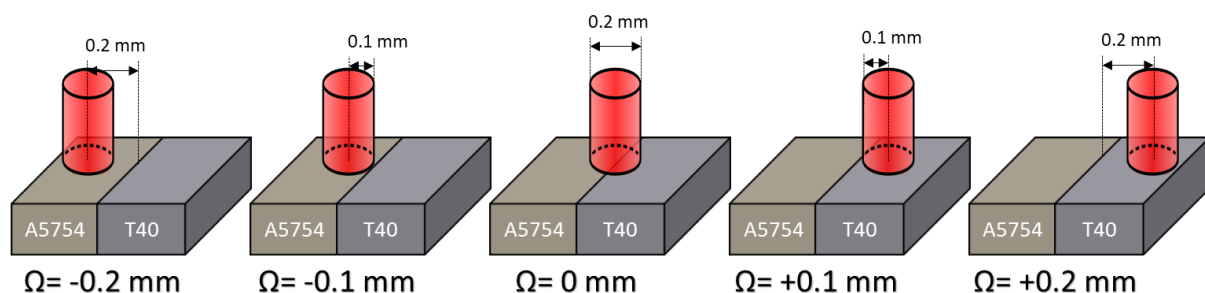
Figure 29. A schematic representation of the different Laser Spot Positions (Ω) on the joint line for continuous welding in butt-configuration.

2.2.2. Pulsed welding in butt configuration

After analysis of the results from the continuous welding experiments, it was noted that the entire process was highly energetic and very unstable and that it was necessary to minimize the process parameters in order to simplify the tasks at hand to facilitate clarification. Therefore, it was necessary to first understand in detail the dynamics of the vapor plume and the behavior of T40 and A5754 in a sub-millisecond level by welding experiments done using millisecond laser pulses (in the range of 1-15 ms).

2.2.2.1. *Plume investigation in butt configuration*

For pulsed laser welding experiments, the camera always had the front view, and the spectrometer was always on the side as represented in the schematic due to two reasons: 1) the focus of HSI was on the plume behavior in the front view, 2) since the welding table does not move during the pulse, there is no interruption of the optical signal for the spectrometer by the plate holders. Initially the pulsed welding experiments were done with the camera axis slightly inclined (<13º) and then were later done with a horizontal axis since the joint line visualization was found to be no longer absolutely necessary to obtain focus.

All the HSI acquisitions were done to observe the vapor plume. HSI was usually done with a working distance of ~ 65 cm in the front view and while the distance between the vapor plume and the collimating lens of the spectral acquisition setup remained to be ~ 40 cm. In addition, for all the pulsed welding experiments, A5754 was placed to the left and T40 to the right in the front view perspective for conformity as represented in Figure 30.

A 600 µm fiber with a 600 µm laser spot size was used for all the pulsed welding experiments. Two sets of experiments were conducted for the vapor plume studies, where HSI was used to observe the spatial and temporal behavior of the vapor plume while spectrometry was used to identify and quantify the evaporating materials in the plume by analysis of the fundamental emission lines of Al, Mg and Ti
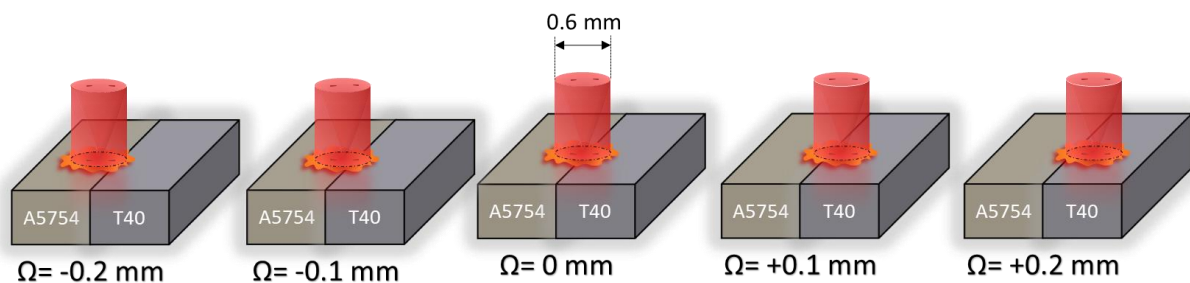
Figure 30. A schematic representation of the different Laser Spot Positions (Ω) on the joint line for pulsed welding experiments.

The first set of experiments was done with a power range of 1,1.2, … 3 kW and a pulse time of 2 ms for treating standalone A5754. A power range of 0.4, 0.6, ... 2 kW with a pulse time of 2 ms was used for standalone Ti, and a power range of 1.5, 2, 3 kW with pulse times of 1, 2, 3, 4, 6 was employed for the dissimilar combination. HSI was done for this set of experiments with the 810 nm optical filter to observe the temporal evolution of the vapor plume.

The second set of experiments was done with a constant power of 2 kW and a pulse time of 6 ms and it was conducted at each spot position and repeated five times to increase the accuracy and reliability of the results by averaging out any variations or measurement errors that may occur during a single trial, and also to determine the reproducibility of the results. HSI was done with two filters (394 nm and 810 nm) to study the relationship between the wavelength of the plume emissions and the shape of the vapor plume.

The Direct Observation of the Drilled hOle (DODO) experiment proposed by M.Schneider et al. [268], as the name implies was conducted to study the keyhole's spatial and temporal characteristics and to correlate the observations with the vapor plume behavior. For the DODO experiments, the metal plates in the butt configuration were positioned vertically and the quartz was placed in front for observation of the capillary by HSI as shown in the schematic (Figure 31.a). The laser spot was equally shared between the metals and the quartz. The quartz plates were clamped firmly to the metal plates to avoid any gaps. The thickness of both the metal plates used in the DODO experiments in the butt configuration and the quartz was 3 mm. However, the placement of A5754 to the left and T40 for conformity could not be maintained and the plates had to be cut into smaller pieces and placed alternately as can be seen in (Figure 31.b) to avoid cutting the expensive quartz plates. The 600 µm fiber with a 600 µm laser spot size was used, along with power 2 kW and pulse time 6 ms. EDS analysis for the melted zones and the plume deposits on the quartz were done for X-mapping the elements Al, Mg and Ti. The working distance of the camera for these experiments was ~ 40 cm.
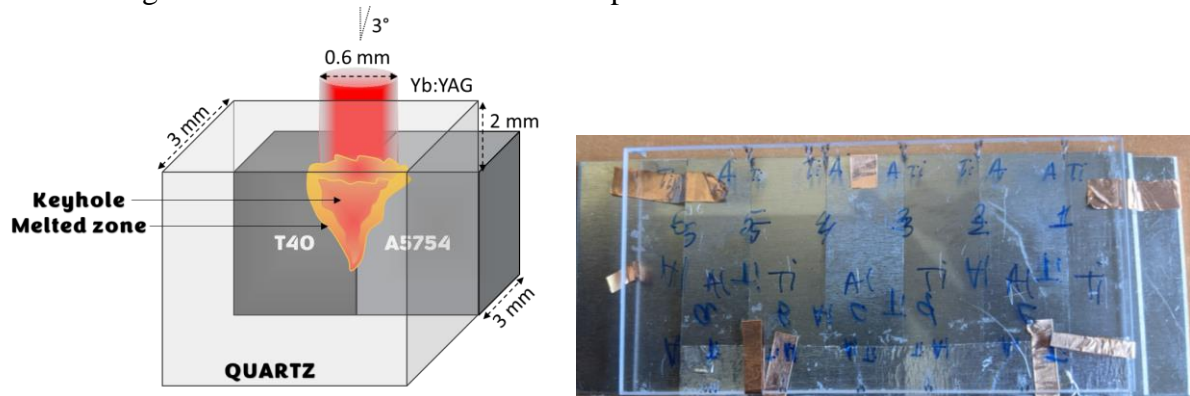
Figure 31. a) Schematic of the DODO experiments and b) photograph of the actual plates with the quartz post laser treatment.

The composition and physical properties of the electrically fused EN08 quartz glass are given in Table 3. The transmission curve of the used glass indicates that the quartz is almost transparent at the Yb:YAG laser wavelength of 1030 nm.

Table 3. Physical properties of fused quartz.

Elemental composition (%.ppm)	8.18 Al, 0.55 Li, 0.47 K, 1.24 Na, 0.5 Ca, 0.21 Fe, 3.51 Ti, 0.12 Mg, 0.01 Cu, 0.03 Cr, 0.06 Ni, 0.01 Mn, 0.04 Co, 99.995 SiO_2
Molar mass (g.mol^{-1})	60.08
Mass density (kg.m^{-3})	2230
Thermal conductivity (W.m^{-1}.K^{-1})	3.34
Heat capacity (J.kg^{-1}.K^{-1})	1048
Melting point (K)	1650
Boiling point (K)	2230
Refraction index	1.459
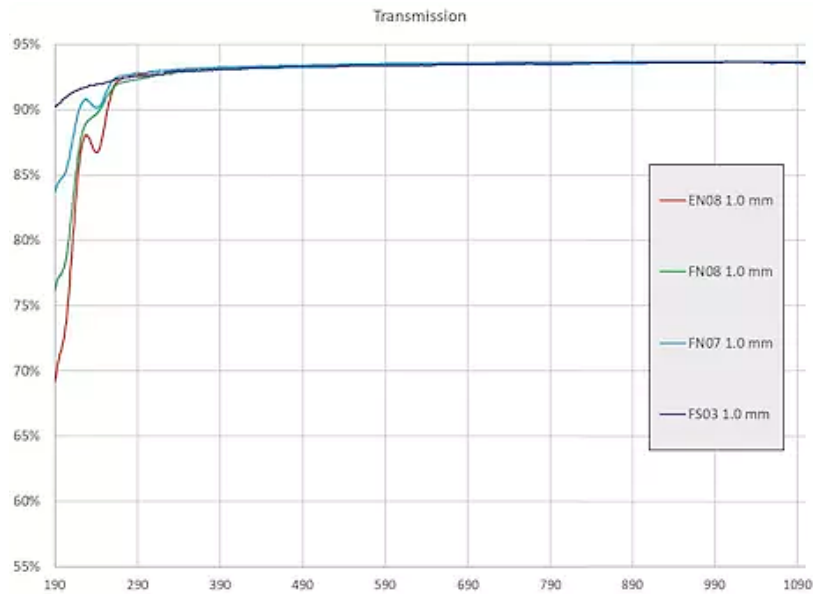
Figure 32. Transmission vs wavelength characteristics for different cases of 1mm thick quartz plates [269].

2.2.3. Overlap pulsed welding

In overlap welding experiments the vapor plume was observed to determine when the keyhole traverses the interface between the two materials. The objective of these experiments was to investigate the feasibility of employing HSI and spectrometry techniques to determine the moment when the laser pulse reaches the bottom plate and to assess the impact of the second material on the keyhole processes. Unlike the arrangement of the metal plates next to each other in previously discussed butt configuration experiments, for the overlap welding experiments the dissimilar metal plates were placed one above the other (Figure 33). A pulse time from 1 to15 ms was used with a 600 µm fiber and 600 µm spot size, with a power of 4.5 kW for 1 mm A5754 on 2 mm T40 and 2 kW for 1mm T40 on 2 mm A5754.
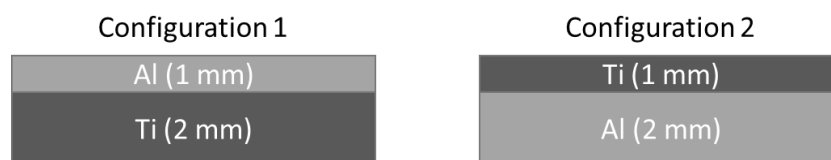
Figure 33. Schematic for the arrangements of plates for the overlap experiments.

2.3. Characterization methods

2.3.1. Spectrometry

2.3.1.1.   The spectrometer setup

The spectrometer used in this study consisted of a Monochromator and an Intensified CCD camera. The Monochromator was a McPherson Model 209 with a 1.33-meter focal length and f/9.4 aperture, featuring an adjustable entrance slit with adjustable height and width (Figure 34). The light entering the spectrometer was first collimated by a curved mirror (focal length = 1.33 m) before being dispersed by a rotatable reflective grating (120 mm x 140 mm). Two gratings with 300 lines/mm and 2400 lines/mm were utilized in this study, allowing for wavelength observation in the range of 185 nm to 5.2 µm (300 lines/mm grating) or 150 nm to 650 nm (2400 lines/mm grating) with respective resolutions of approximately 2.5 nm and 0.3 nm. The dispersed light was then refocused by another curved mirror and transmitted to the CCD sensor. The grating position was controlled by the McPherson 789A-3 Stepper Drive

Scan Controller [270], enabling the selection of a specific wavelength regime with a resolution of approximately 3 ~ 4 nm when using the high resolution grating.
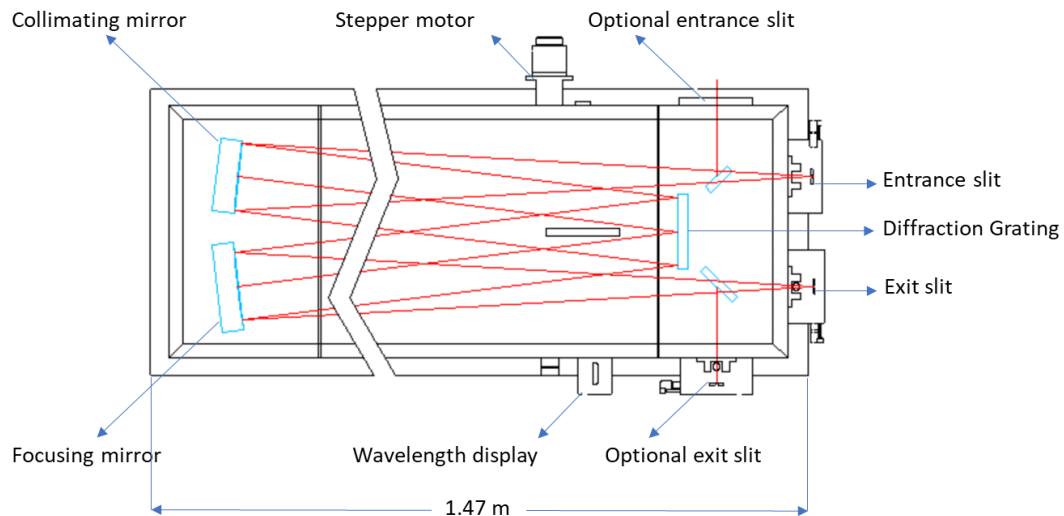
Figure 34. Cross sectional top view of the McPherson model 209 spectrometer [271].

The light emitted from the vapor plume was collected by a set of 2 lenses (Figure 35) 50 cm apart (with focal lengths 40 cm – collimating lens and 10 cm - focusing lens) to be focused into a 3 m long optical fiber (diameter 230 µm). The magnification from this combination of lenses is 4. Therefore, the light from a circular area (diameter ~1 mm) on the vapor plume was collected into the optical fiber. These lenses and a holder for the fiber were mounted on an optical bench which could be adjusted through translation and rotation to be able to collect light from different points above the keyhole opening. Once the fiber was well positioned exactly on the optical axis 10 cm behind the focusing lens, the other end of the fiber was connected to a milliwatt laser pointer to allow focusing of the collection point. The collection point was identified by placing a millimeter graduated block of metal on the point of impact of a trial laser pulse from the YAG laser on the surface of the metal plates. Every single change of the plates or the unnecessary physical displacement due to accidentally touching this optical system necessitated repeating this manual refocusing method to avoid differences in the position of the collection point from the keyhole openings between the different experiments and due to changes in thickness of the plates.
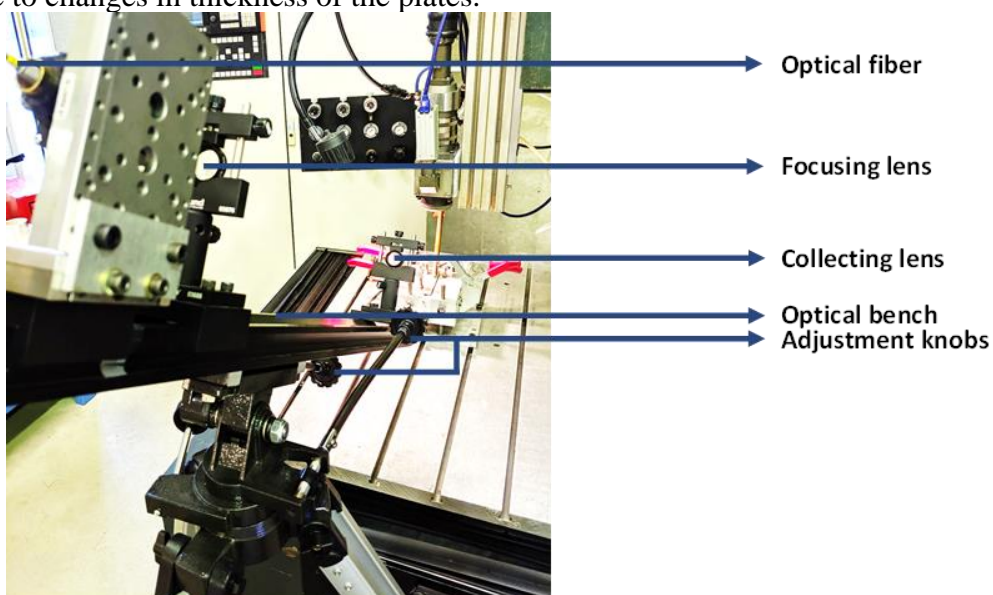
Figure 35. Vapor plume/keyhole light emission collection setup for spectrometry.

A Princeton Instruments PI-MAX 1K® Intensified-CCD camera [272] along with a Princeton Instruments camera controller model ST-133 [273] was used to measure the wavelength and intensity of the refocused light. The PI-MAX 1K® houses a Marconi CCD47-10© sensor [274] with an 18 mm intensifier. The sensor had an imaging area of 13.3 mm x 13.3 mm in which 1056 (H) x 1027(V) were active square pixels with a pixel size of 13 µm x 13 µm. The usable pixels for our experiments were arranged in 1024 rows and 1024 columns, providing a detection area of 177 mm². The spectral range of the detector is between 195 and 920 nm. The light signal is amplified by an intensifier. The minimum acquisition time on the intensifier is 2 ns. The signal received by the camera was visualized using WinSpec software, which provided the recorded spectra, representing the intensity of the received light for each column of pixels. The acquired spectrum corresponds to the summation of the light intensities from the pixels in a column.
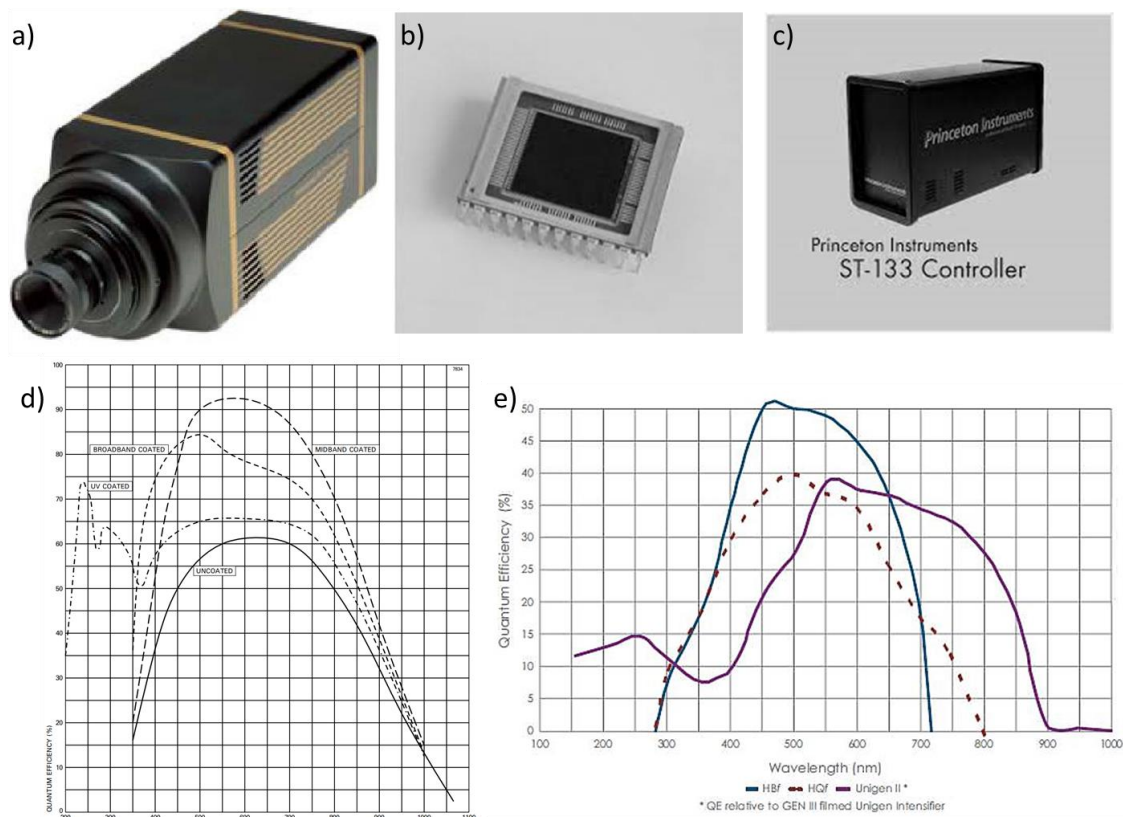
Figure 36. a) Princeton Instruments PI-MAX 1K® ICCD camera [272], b) Marconi CCD47-10© sensor [274], c) Princeton instruments ST-133 camera controller [273], d) Spectral response of the sensor at -20°, and e) Spectral response of different types of intensifiers used in the PI-MAX 1K®.

Even though the intensifier could function with a minimum Gate width of < 2 ns, the repetition rate was severely limited by the sensor due to its maximum readout frequency (5 Mpx/sec). The Programmable Timing Generator (PTG) module in the ST-133 was used to execute pulsed measurements with the camera without the need for an external trigger. The signal from the camera was intensified and transmitted to the ST-133 controller for digitization. The digitized signal was then transferred to a Windows XP computer, specifically a Dell Optiplex 780 with a Core 2 Duo CPU E7500 2.93 GHz processor and 3.25 GB of RAM, via USB 2.0 for display and storage. The spectroscopy software programs which were used to observe the image and the spectra were WinView and WinSpec by Teledyne Princeton Instruments [275]. These were not software development kits but rather offered some control over the camera and PTG for data acquisition and analysis. These software programs are no longer supported due to compatibility issues with the newer operating systems [275].

Like HSI, several sets of experiments were done with spectroscopy for various welding configurations and spectral acquisition parameters. The spectra in this study were acquired using WinSpec software and saved in either .spe or .tif format. As the software is no longer available for download and the spectrometer's computer is not connected to the internet, it was not possible to install new programs on the machine. To extract metadata from the .spe files, a macro written in JavaScript was used with the bio-formats importer [276] in FIJI. The resulting metadata was saved in .csv format and imported into Excel for curation and summary using VBA scripts. This allowed for the compilation and summarization of the entire body of spectrometry work.

More than 2500 .spe files were made during the duration of this thesis. Overall, a total of 90 acquisition parameters were extracted from each file. 918 files among these were made to capture the Hg (515), Deuterium (178) and Tungsten-Halogen (225) spectra for wavelength and intensity calibration of the spectrometer. 174 files were used to capture the noise levels. 789 files were made while capturing the spectra during dissimilar welding. In this study, images of spectra from laser welding were captured using 16-bit resolution (i.e., 65536 levels), while 32-bit resolution (i.e., 4294967296 levels) was used for calibration. A total of 140 wavelength regimes were analyzed, and the time period of acquisition per spectrum was done, with a range of options from 1 ms to 1 s. The number of spectra accumulated in a single .spe file also varied between 1 and 100. In total, 124344 spectra were acquired in 2417 files. In cases where the signal intensities were low, a higher number of accumulations were utilized. The intensifier was also varied, with 16 different gains employed (ranging from 1 to 255).

2.3.1.2. Wavelength calibration

The changing spectral response of this sensor over temperature, coupled with the spectral response of the intensifier necessitated wavelength and intensity calibration for each set of experiments. For the wavelength calibration of the spectra, an Ar-Hg calibration lamp (model HG1 - Ocean Optics) was employed. Spectra of mercury were acquired by adjusting the position of the spectrometer grating, thus capturing the spectral lines at various locations on the detector. This process enabled the establishment of a correspondence between the pixel number and the corresponding wavelength for each grating position. Subsequently, a Matlab program utilizing interpolation techniques was utilized to determine the precise spectral range under investigation for a given grating position. The collected data, stored in a file, facilitated accurate wavelength calibration for the recorded spectra.

2.3.1.3. Intensity calibration

The optical system's response, including signal collection and acquisition components such as lenses, optical fibers, grating diffraction, and detector characteristics, depended on the wavelength. To enable meaningful comparisons of spectra obtained across different wavelength ranges, an intensity calibration was performed.

For the intensity calibration, a Halogen-Deuterium calibration lamp (DH 2000 - Ocean Optics model) with a tungsten filament was used. This lamp had been calibrated in terms of spectral irradiance (mW/cm²/nm), denoted as $E_{Calib}(\lambda)$, throughout its entire operational spectrum.

The Deuterium lamp was suitable for ultraviolet (UV) wavelengths within the range of [220-400] nm. It was observed that its emission decreased as the wavelength increased, with discernible Deuterium lines being observed from 365 nm onwards. On the other hand, the Halogen lamp exhibited an increasing emission trend with longer wavelengths, covering the specified range of [300-1050] nm. However, it should be noted that the emission intensity at 300 nm was relatively low (Figure 37). For this study, the Halogen lamp was utilized to examine spectral lines within the range of [380-600] nm.
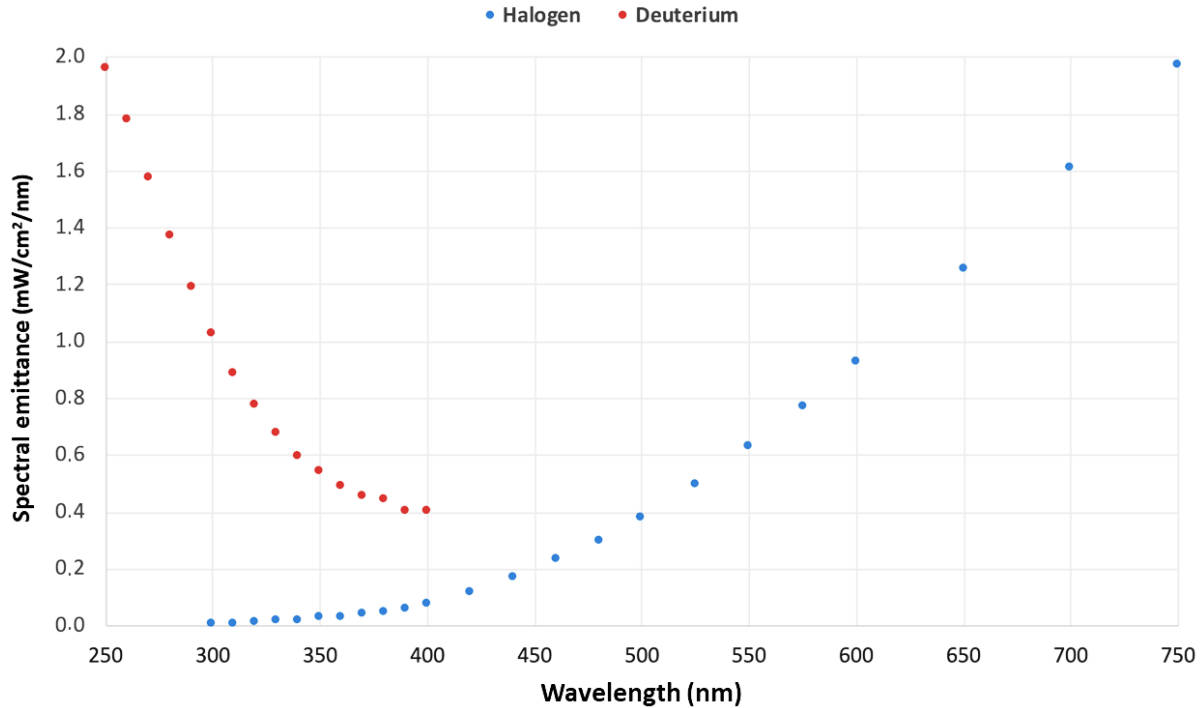
Figure 37. Spectral emittance of the calibration lamp.

Thus, the aim of spectral calibration was to facilitate the comparison of line intensities recorded in different spectral regions. However, it should be noted that during spectrum acquisition, with signal integration times varying between 1 ms and 1 second, it was crucial to reduce the noise (i.e., any part of the signal not originating from the vapor plume radiation).

The acquisition procedure involved:

- Recording the spectrum of the vapor plume $RawSpectrum(\lambda)$, along with the noise $Noise(\lambda)$ (the acquired signal before or after emission, using the same detector integration time).
- Obtaining the spectrum of the calibration lamp, $Cal(\lambda)$, along with the corresponding noise $NoiseCal(\lambda)$ (using the same detector integration time).

The calibrated spectral emission was derived using the following relationship:

$$Emission\ (\lambda) = \frac{RawSpectrum(\lambda) - Noise(\lambda)}{Cal(\lambda) - NoiseCal(\lambda)} \times E_{Calib}(\lambda) \qquad 52$$

This calibration was used to compare spectra acquired in different spectral regions, where the spectrometer could exhibit varying sensitivity based on the wavelength (detector sensitivity, diffraction grating, and optical fiber sensitivity). However, it should be noted that the signal acquisition chain (BK7 lenses used for imaging the plume onto the fiber optic input) was not taken into account.

The obtained signal does not correspond to a metrological measurement. For instance, the solid angle of the optical sampling systems was not considered. Additionally, the acquired spectrum depended on operational parameters such as detector integration time, photomultiplier gain, optical sampling system adjustments, spectrometer slit aperture, and so on. Therefore, the calibrated spectrum is expressed in arbitrary units.

Furthermore, it is important to acknowledge that different results could be obtained depending on the lamp used, considering factors such as lamp wear and the low emission of the Halogen

lamp in the 300-400 nm range (resulting in greater uncertainty). Consequently, in this study, only spectra calibrated with the same calibration lamp were compared.

A simplified representation of the spectrometric work done is given in Table 4 for ease of understanding.

Table 4. Spectra processing procedure

<table>
<tr><td colspan="1">SIGNAL ACQUISITION PROCEDURE</td></tr>
<tr><td>

- Adjustment of the sampling system to target the desired area.
- Signal acquisition using WinSpec software.
  - ◊ Configuration of acquisition parameters: monochromator slit width, integration time, gain, spectral range.
  - ◊ Acquisition of plume spectra and noise.
  - ◊ Acquisition of Hg spectra for wavelength calibration.
  - ◊ Acquisition of calibration lamp spectra and noise.
- Conversion of obtained files into text files for processing in MATLAB (one file per spectrum).
</td></tr>
<tr><td>SPECTRUM CALIBRATION PROCEDURE</td></tr>
<tr><td>

- MATLAB Processing
  - ◊ Wavelength calibration
  - ◊ Reading calibration files and noise
  - ◊ Reading the reference file: Ref(l) calibration
  - ◊ Reading spectra and noise
  - ◊ Calculation of calibrated spectra
</td></tr>
<tr><td>EXTRACTION OF SPECTROSCOPIC PARAMETERS</td></tr>
<tr><td>

From the calibrated spectra, the PeakFit software is used to fit the line profile and extract the primary parameters of the lines (wavelength, intensity, full-width at half-maximum), as well as the background level.
  - ◊ Line selection
  - ◊ Extraction: wavelength, intensity, FWHM
  - ◊ Background level
</td></tr>
</table>

2.3.1.4.   Extraction of the spectral characteristics

The wavelength calibration and intensity calibration are automated through a MATLAB program. The next step in the analysis is to extract the characteristics of each selected peak, including the central wavelength, intensity, and full-width at half-maximum (FWHM). For this purpose, a commercial software called PeakFit [277] was utilized. The PeakFit software provides "detected peaks," but it is crucial to verify the validity of these peaks in relation to background noise fluctuations or to correct for any issues such as unresolved peaks or auto-absorption. To ensure accuracy, a file containing the "observable peaks" has been prepared.

2.3.1.4.1.   Selection of observable rays : databases

Two databases were used:

The NIST database: Provides a list of observed or theoretical spectral lines. For observed lines, it provides a "relative intensity" derived from the spectrum acquisition conditions, which may have various experimental origins. However, with this information assessment of the

significance of the lines can be done. For calculating theoretical intensities or estimating temperature using the Boltzmann method, the Einstein's coefficients (transition strength) i.e., transition probabilities (A_s) may not always be available in this database.

The Kurucz database: Provides a list of analyzed spectral lines found in the literature. By comparing theoretical models with experimental data, the analysis allows for the determination of spectral information for the different listed transitions. Therefore, the database includes various details for each studied line that can be used for predictions, such as energy levels, electron configurations of lower and upper levels, and transition probabilities (A_s).

From studying the observable lines from these databases and considering the detected lines by PeakFit, a file of observable lines is generated which are modified based on the data from NIST and Kurucz. During this analysis, the following issues are also addressed:

- The problem of self-absorbed lines.
- Low intensity lines: determining whether they are due to background noise fluctuations or actually low intensity lines.

2.3.1.4.2. Calculation of theoretical intensities

For a given temperature (T), the theoretical intensity (I) of a spectral line (in arbitrary units) is proportional to:

$$I \ = \frac{hc}{\lambda} \ \times (2.J_s + 1) \times A_s \times e^{-E_s/k_B.T} \qquad\qquad 53$$

Where, A_s is the coefficient of Einstein for spontaneous emission (s^{-1}), E_s is the energy of the excited state, $(2.J_s + 1)$ is the degeneracy of the excited state, $h = 6.62607015 \times 10^{-34}$ J.s, $k_B = 1.380649 \times 10^{-23}$J.K^{-1}, 1 cm^{-1} = 1.98$\times 10^{-23}$ J.

Indeed, it is possible to predict the relative intensity of existing transitions within a spectral range for a given atomic element. The comparison of intensities among possible lines could be done by identifying the lines with the highest relative intensities in the detectable range, the presence of non-deconvolved lines (indicating the relative importance of each transition), or the possibility of self-absorbed lines.

However, this intensity calculation does not take into account the density of atoms present. It is not possible to directly compare the intensities of different atomic elements. For example, there may be aluminum or magnesium lines with very high theoretical intensities (but present in smaller proportions), resulting in smaller peaks compared to titanium lines with lower theoretical intensities. The relative intensities of lines should be considered in the context of the specific atomic element being analyzed.

2.3.1.4.3. Line assignment to observable peaks

Based on the data collected from the databases, an Excel file was prepared for each studied spectral range, containing relevant information for the assignment of observed peaks.

This file included, the theoretical wavelength (in air), Emission line parameters (energy, angular momentum J, electron configuration for the lower and upper levels), Einstein's spontaneous emission coefficient A_s, and the calculation of the theoretical intensity of the transition for temperatures of 3000 K and 5000 K (following the detailed procedure described in the previous section).

2.3.1.4.4. Optical peak detection and background subtraction of spectral analysis

The preprocessed spectra were analyzed using PeakFit to detect the peaks obtained and subtract the background continuum. The "detected peaks" suggested by the software and the file of

"observable peaks" were used to define the peaks to be processed by the software. The fitting of the preprocessed spectrum was performed using nonlinear least squares method between the experimental spectrum and the calculated spectrum.

2.3.2.   High Speed Imaging (HSI)

2.3.2.1. Cameras, basic image processing and experimental data sets.

During all the experiments with HSI, before and after each set of experiments, the physical dimensions of the field of view were measured by taking an image of a ruler (Figure 40) and by matching the resolution to the number of pixels to measure the objects of interest. Most of the HSI done during this thesis was done by the discontinued Phantom v9.1 high speed camera [278]. The spectral response curve for the Phantom v9.1 and v2012 has been provided (Figure 38, Figure 39).
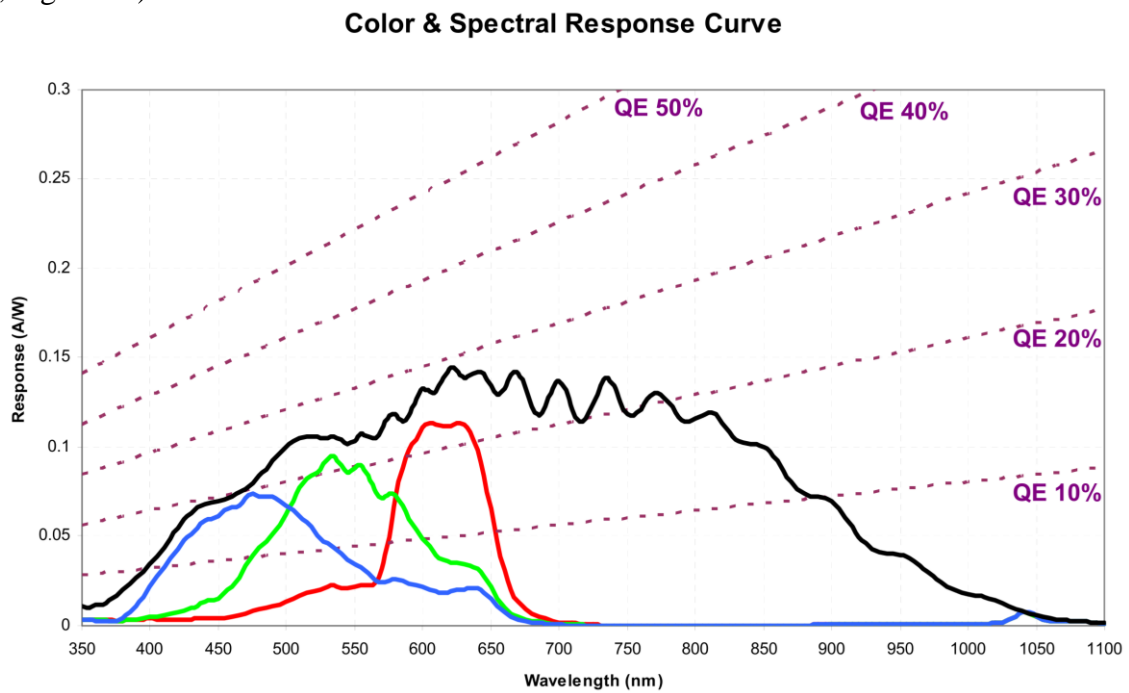

Figure 38. Phantom v9.1 spectral response curve [279]. (QE – Quantum Efficiency)
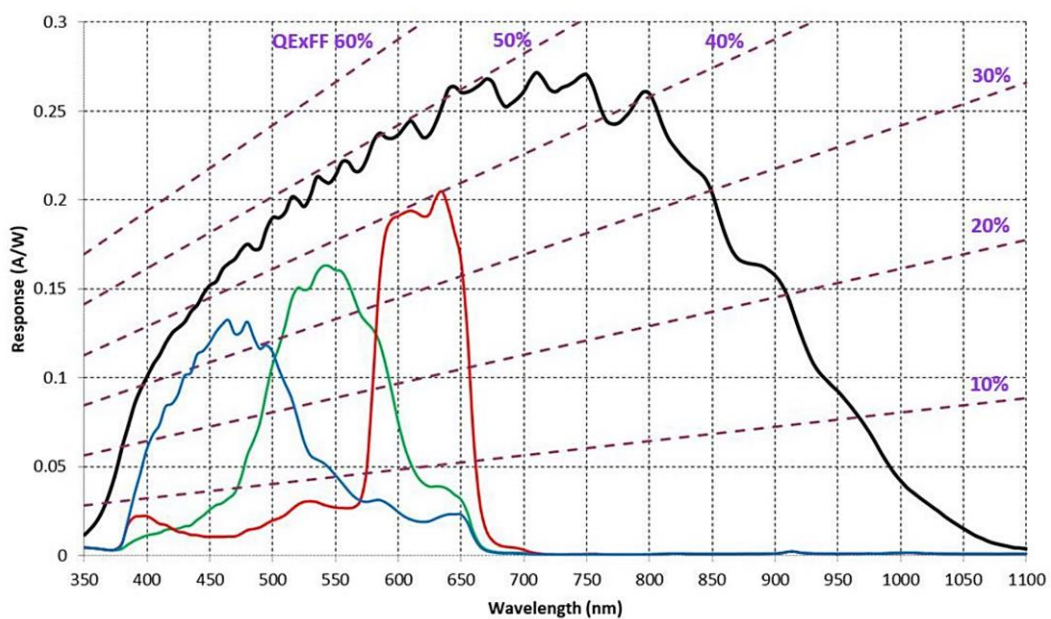
Figure 39. Phantom v2012 spectral response curve [280]. (QE – Quantum Efficiency)

Only the experiments in the overlap configuration were done using the newer Phantom v2012 high speed camera [153]. All the videos captured by the Phantom v9.1 were 8-bit in depth and the videos captured by the Phantom v2012 had 12-bit images. In an 8-bit image, each pixel was represented by an 8-bit number, which allowed for a total of 2^8, or 256, different values.

These values were typically used to represent different levels of gray, with 0 representing black and 255 representing white. In between, there were 254 shades of gray, ranging from nearly black to nearly white. The use of 8 bits per pixel allowed for a wide range of gray levels, making it possible to represent a wide range of contrasts and details in the image. This was often sufficient for many types of images, such as photographs and other images with a moderate range of tones. However, in some cases, such as when dealing with very high-contrast images or images with a very wide dynamic range, it was necessary to use a higher bit depth, such as 12 bits per pixel (4096 gray levels), to fully capture all of the detail in the image. Initially, the .cine video files were imported into an open source image processing software called ImageJ [176] using the Cine File Importer plugin [281].

The "File" menu was accessed, and the "Import" option was selected. The .cine file was located, and a dialog box was presented asking to choose the series to open. The correct series was chosen, after which the video was opened, and the frames were able to be viewed in the ImageJ window. The "Play" button in the ImageJ window was used, or the "Plugins > Animation > Animation Options" were used to adjust the playing speed, loop, and other options. The "File > Save As" option was used to save the video in a desired format, such as .tiff format. After the initial period during the thesis, multiple .cine videos were directly batch converted to .tiff using the Phantom Camera Control software [282] to save time.

A scale calibration procedure was performed utilizing ImageJ software to accurately align the dimensions of the observed field of view with the corresponding digital image representation. Because with varying working distances, resolution, and angle of tilt of the camera between the experiments, it was essential to note the physical dimensions of the field of view. This was done by capturing a photo of a ruler (Figure 40) in the plane of focus (before and after every set of experiments) and matching the number of pixels for every resolution to the number of millimeters marked on the ruler.
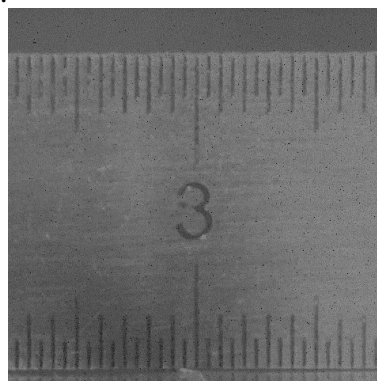
Figure 40. Capture of a steel ruler taken with 480x480 resolution using the Phantom v9.1 during one of the pulsed welding experiments

The Phantom v9.1 camera was used to capture a total of 452 videos over a period of three years. Some of the videos were not usable due to quality issues and were used as a reference to optimize the acquisition parameters. It would be difficult to present all the experimental details in a single table because of the wide range of parameters that were used, such as frame rates, exposure times, and sensitivity.

Instead of listing all the parameters in a table, the videos taken by the Phantom v9.1 can be grouped into categories based on the wavelength of the optical bandpass filter used, the welding mode, and the type of material being welded. Additionally, a few HSI acquisition parameters will be listed for each category.

This information is presented in a chart, which is represented by three concentric circles in a schematic (Figure 41). In summary, a simplified way of understanding the range of parameters used in the video acquisition has been provided. The innermost circle represents the wavelength of the optical bandpass filter used, the mid-concentric circle represents the welding mode, and the outermost represents the material type. The additional parameters used for the videos taken with the Phantom v2012 will be provided along with the discussion of results in the chapter 5. During every set of experiments done throughout the duration of this thesis, the image processing methodology was updated, the details of which will be provided in their respective chapters.
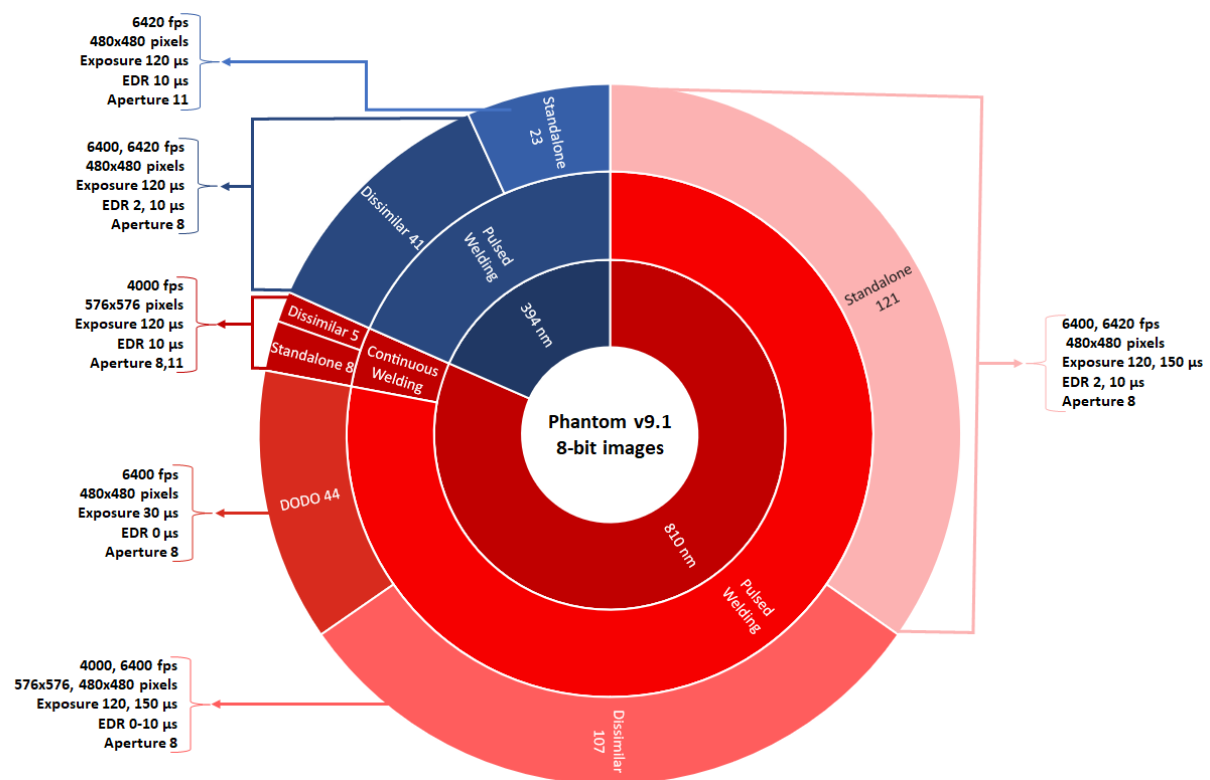
Figure 41. Sunburst chart representing the number of videos of acceptable quality made with the Phantom v9.1 under different welding and acquisition conditions (numbers on the outermost arcs represent the number of videos).

2.3.2.2. The Optical band-pass filters

During the experiments, different optical bandpass filters were utilized, with wavelengths of 810 ± 3 nm and 394 ± 2 nm, and full width at half maximum of 10 ± 2 nm. The transmission curves of these two optical filters are given in Figure 42. To state in simple terms, the two filters were chosen to observe the infrared emissions and the atomic emissions from the vapor plume. 394 nm filter was chosen because it was the only wavelength regime which had fundamental atomic emissions from both titanium and aluminum.
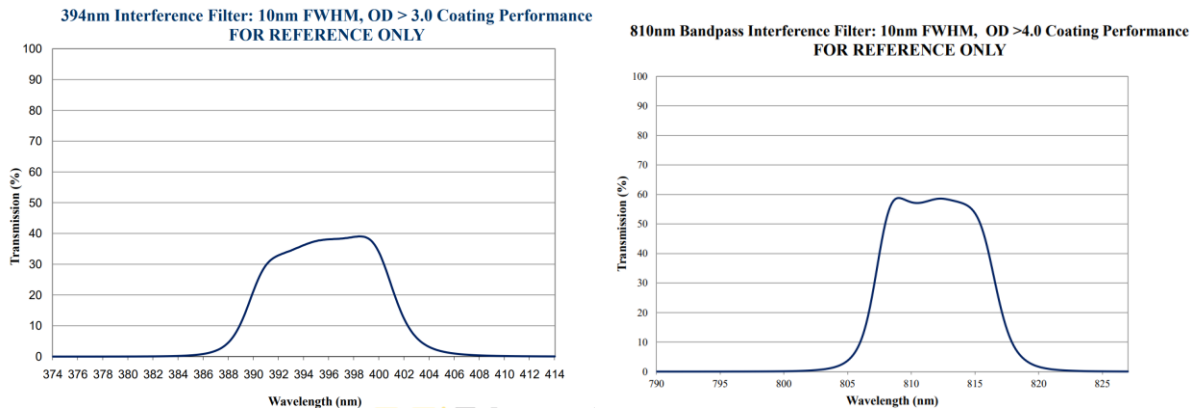
Figure 42. Transmission curves of the optical filters used with the HSI camera [283].

However, the choice behind the use of these two filters was not a simple one. Previous research conducted in this field, which encompassed the work of former interns [284]–[286], made significant contributions to understanding the spectral emissions of the laser welding vapor plume. These studies constituted observations of spectral emission lines superposed over a continuous underlying signal. The continuous background corresponded to thermal radiation. This led to two different hypotheses.

The first hypothesis was that the thermal radiation originated from the melted surface, as the light for the spectrometer was acquired at an angle of 20-30° relative to the horizontal surface. It was possible that the thermal radiation emitted by the melted zone behind the vapor plume was being visualized (with melting points (T_m) 900 K for aluminum and 1940 K for titanium).

The second hypothesis was that the thermal emission could be coming from the dense vapor exiting the capillary (boiling points (T_v) 2792 K for aluminum and 3560 K for titanium). And so, the optical setup was adjusted to make the spectral acquisitions almost horizontally with a very low angle at about 1 to 2 mm above the plate (Figure 43). By doing this, any interference to signal by the molten materials bulging up were avoided. Further justification for optimizing the height of the acquisition point will be later seen in the HSI studies of the vapor plume (section 4.3, p.113).
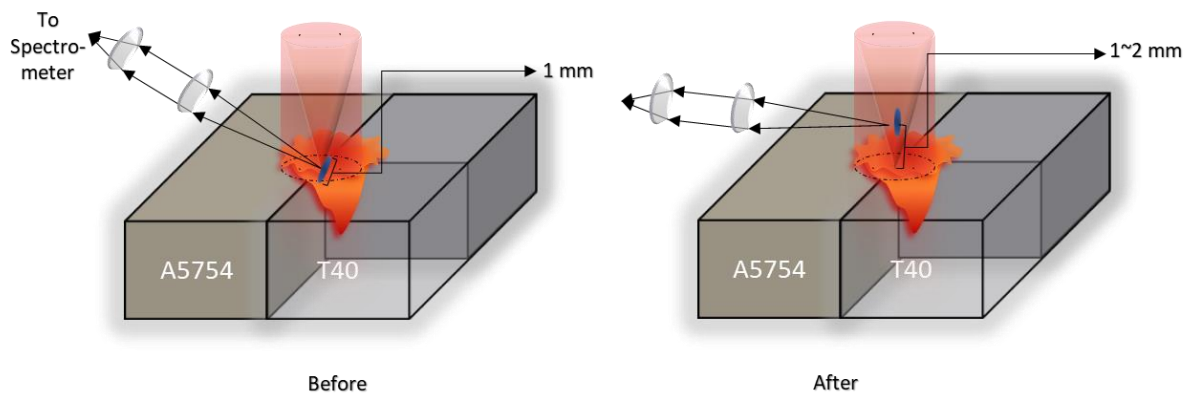
Figure 43. Schematic to show position of the collection point for spectral acquisitions before and after thermal radiation analysis.

And so, during this thesis, it was assumed that the radiation produced by the vapor plume was due to the combination of thermal radiation emitted by an opaque and dense vapor plume core and the emissions of atoms from the region with lower density where the vapor expands into the surrounding air. HSI's goal was to observe these different zones and their temporal evolution. So, the initial idea was to define different spectral filters that would allow the detection of the various components of the plume. And to make confirmations on these

71

hypotheses from spectrometry, two types of filters had to be chosen: 1) to observe and study the thermal radiation and 2) to observe and study only the atomic emissions from both aluminum and titanium separately.

From the experiments, it was understood that observing aluminum lines was difficult. However, it was noted that it was possible to detect emission lines from magnesium or manganese, which were present in small quantities in the A5754 aluminum alloy. The search for these emission lines are described in detail in section 4.5 (p.156). Nevertheless, the presence of aluminum vapor generates a fundamental line, due to the transition of atoms between the first excited level (with energy of 25347 cm^{-1}) and the ground state (has 2 sub-levels). The fundamental lines of aluminum which correspond to the two transitions from these levels are at 394.4 nm and 396.1 nm.

Titanium provides a very rich spectrum. The first excited level is at 6556 cm^{-1}, which is much lower compared to aluminum (first excited level at 25347 cm^{-1}). About 60 energy levels are observed to be lower than 25000 cm^{-1}. It is thus easy to excite titanium, and there are numerous lines in the observable domain. But after spectrometric analyses, it was observed that titanium emission lines were present in all regions where lines of aluminum or magnesium were searched. The initial objective was to identify characteristic regions of aluminum and other characteristic regions of titanium, but soon it was understood aluminum emission lines could not be isolated in dissimilar welding.

Therefore, the region of the two fundamental lines at [393-400] nm was chosen for the observation of aluminum. The spectra of aluminum and titanium are compared after welding them separately. Figure 44.A shows the two fundamental emission lines of aluminum at wavelengths of 394.4006 nm and 396.15201 nm. These lines correspond to emission between the first excited level of aluminum (with an energy of 25,347.756 cm^{-1}) and its ground state sublevels (with energies of 0 and 112.061 cm^{-1}). Figure 44.B was obtained from commercially pure titanium (T40). It shows a multitude of lines, including a prominent titanium peak consisting of two observable lines at 394.78 and 394.86 nm.

To study the simultaneous presence of titanium and aluminum, the spectrum of TA6V (titanium base alloy with 6% aluminum and 4% vanadium) was studied. The spectral analysis showed that the aluminum line at 394.40 nm was distinguishable and clearly separated from the nearby titanium line by a distance of 0.38 nm. However, the aluminum line at 396.15 nm was more difficult to deconvolve from the titanium lines.
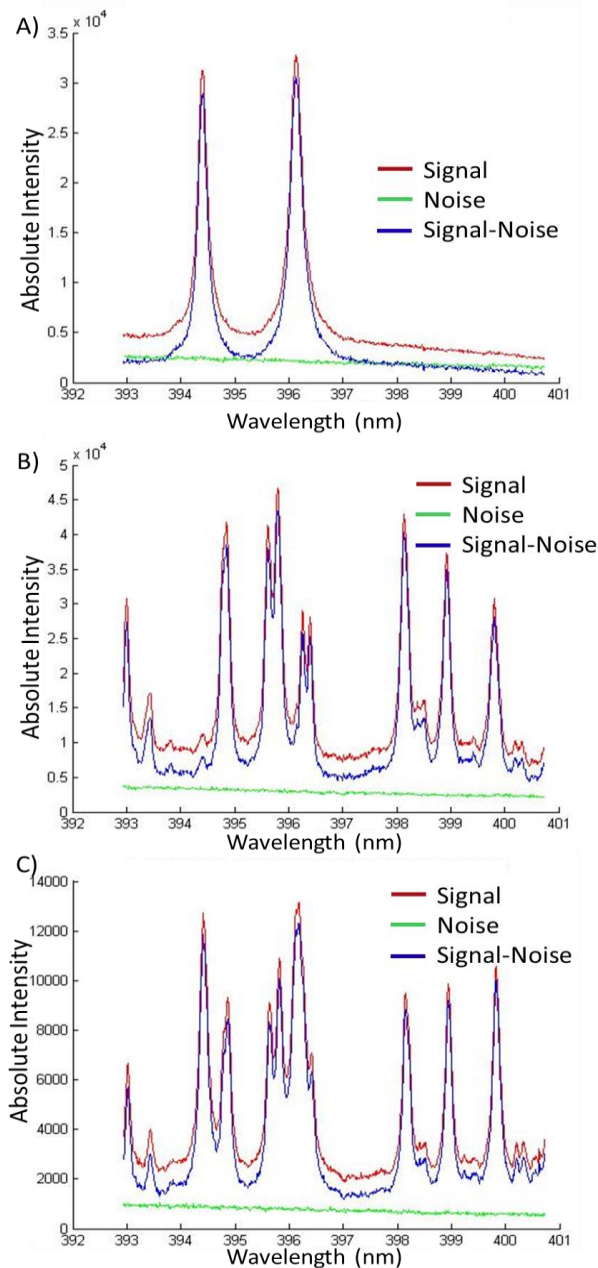
Figure 44. Comparison of spectra of A) Al, B) T40 and C) TiAl6V

Filter selection for thermal radiation observation: 810 nm

For HSI analysis, the 10 nm bandwidth bandpass interference filter centered at 810 nm was used. Nevertheless, the question remained as to whether the observed phenomenon was due to thermal radiation or to the emission lines of the vapor.

Typically, the spectra obtained from vapor plumes of T40 and A5754 (Al base, 2.6-3.6% Mg, 0.5% Mn) materials were acquired using a 2400 lines/mm grating. However, the use of this grating limited the studied wavelengths to below 650 nm (section 2.3.1). And so, for this study, the 300 lines/mm grating was used, which was optimized for the region of interest as it was blazed at 750 nm. It was also noted that by the laws of diffraction/interference by a grating, from 550 nm, second-order lines may be observed .

The results obtained from welding the A5754 aluminum alloy are presented in Figure 45. Figure 45.A represents A5754 spectrum calibrated with the halogen lamp. The spectra in

Figure 45.B and C are the result of a simulation of the spectra of aluminum and manganese obtained at the second order of the diffraction grating. The two peaks observed at 789 nm and 792 nm are the second order lines which correspond to the fundamental lines of aluminum (394.40 and 396.15 nm), and the broad peak at 806-807 nm corresponds similarly to the emission lines of manganese at 403.07, 403.30, and 403.44 nm.
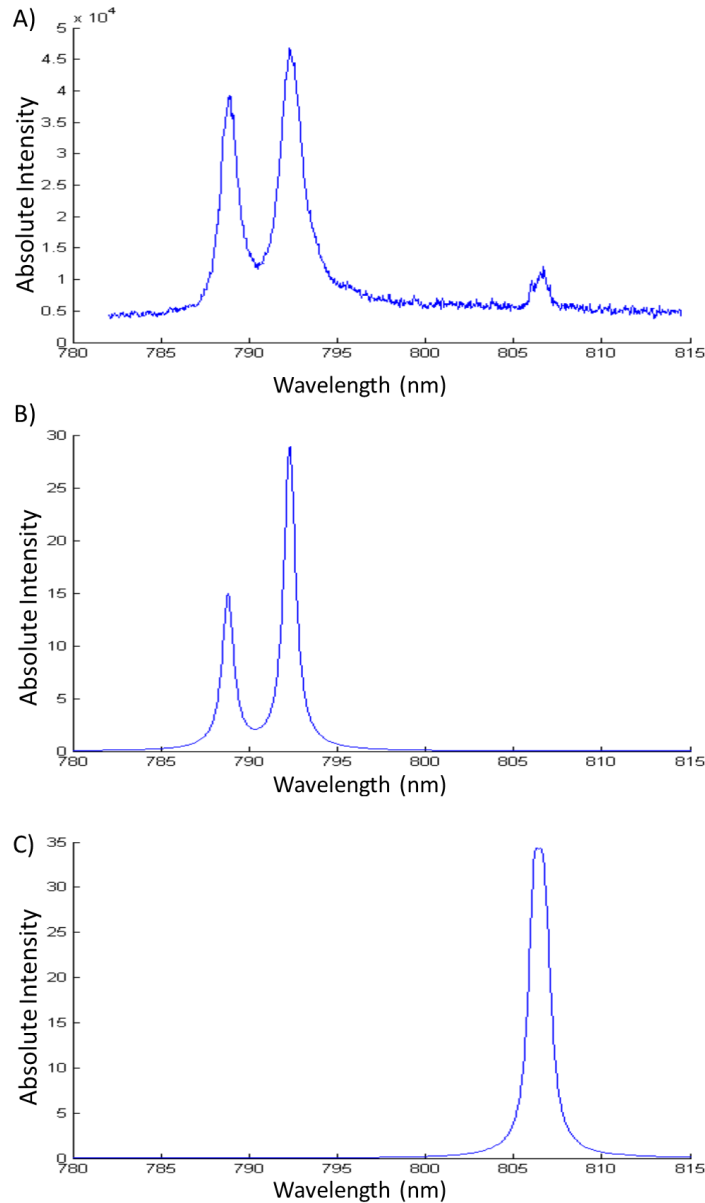
Figure 45. Spectra obtained in 810 nm region for A) A5754 with 300 lines/mm grating, and B) Simulated 2nd order lines of Al (I) and C) Mn (I).

In Figure 46, spectra obtained laser pulses on titanium are presented. Despite the presence of many peaks, all the lines were identified as a second-order spectrum of titanium. Therefore, it was concluded that there is no atomic emission in the 810 nm region transmitted through the filter. This led to the conclusion that the images observed in HSI with the 810 nm bandpass filter correspond to thermal radiation rather than the atomic emission of a particular element.
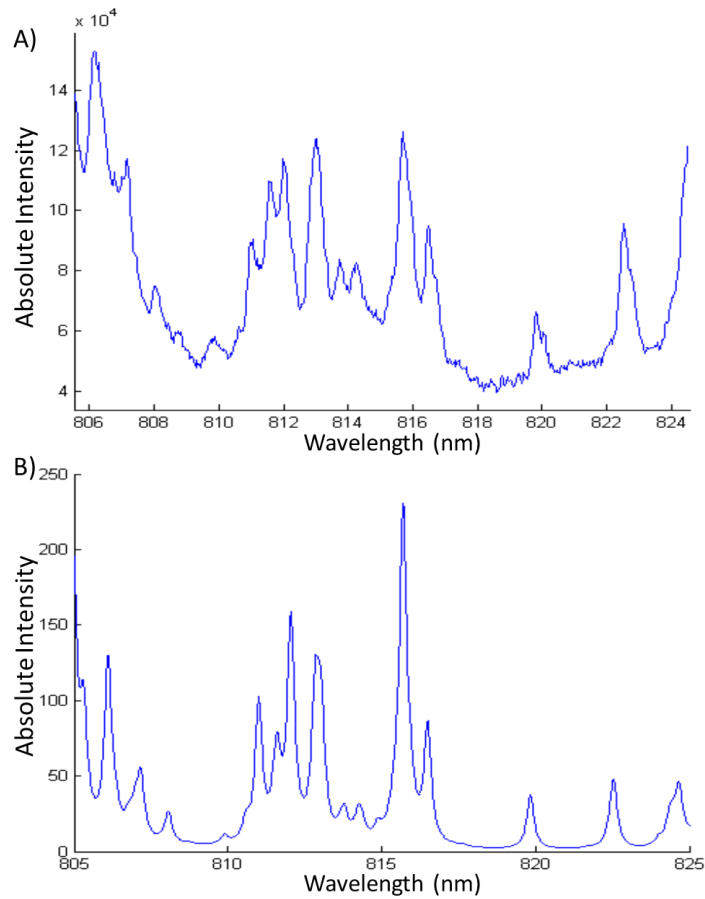
Figure 46. A) T40 spectra obtained in the 810 nm region and B) the simulated 2nd order lines of Ti.

To further verify this conclusion, a spectrum was recorded with a high-pass filter at 500 nm. It was observed that these lines disappeared from the spectrum, leaving only a continuous background.

The influence of the spectral region on thermal radiation

The purpose of this theoretical study was to compare the thermal radiation emitted by the vapor in the two transmission regions of the filters. Planck's law (Eqn.26, p.45) describes the spectral radiance of a blackbody.

To compare the radiation received by the filters, the luminance was calculated over an interval corresponding to the full width at half maximum (FWHM = 10 nm) of the filters

$$L_{394nm}(T) = \int_{389\ nm}^{399\ nm} L_{(\mu,T)}\ d\lambda \qquad\qquad 54$$

$$L_{810nm}(T) = \int_{805\ nm}^{815\ nm} L_{(\mu,T)}\ d\lambda \qquad\qquad 55$$

In Figure 47, the variation of the two quantities with respect to the vapor temperature is presented. The green curve displays the ratio of the calculated luminance at 810 nm to 394 nm. It was be observed that thermal radiation is more pronounced in the 810 nm region. Considering the vaporization temperature of aluminum to be 2792 K, the ratio of radiation flux between the two filter regions is by a factor of 20. For titanium with a vaporization temperature of 3560 K, the ratio of radiation flux between the two filter regions is by a factor of 5.
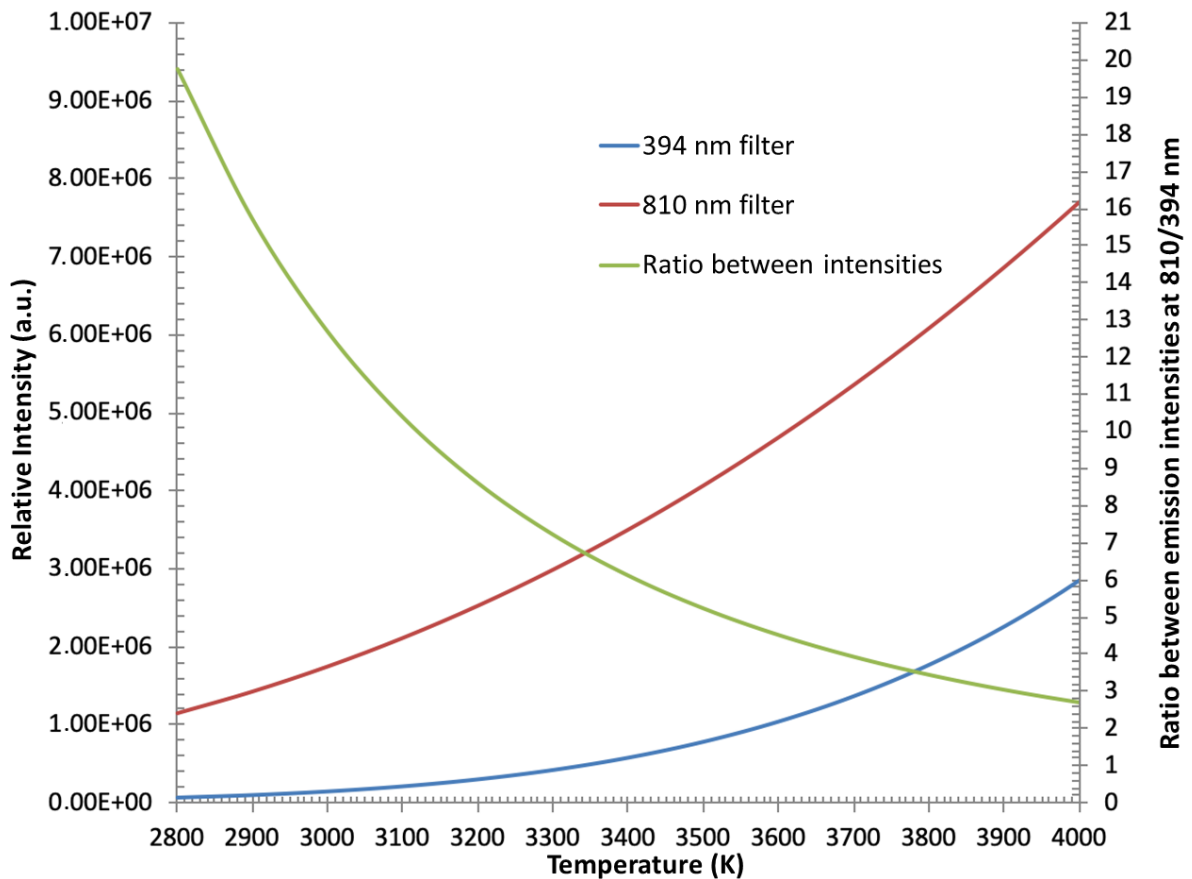
Figure 47. Comparison of thermal radiation emitted in the 394 nm and 810 nm regions.

2.3.3. Post-mortem characterization

After continuous welding, the samples were cut into pieces of approximately 1 cm in length and width using the "Presi Mechatome T210" microcutting machine with the cutting disc rotating at 3200 rpm over the samples at a speed of 0.5 mm/s (low speed to avoid uneven edges). These pieces with keyhole cross sections were embedded in polymerized resin charged in carbon, suitable for scanning electron microscopy. The polymerization was done using the "Buehler Simplimet 2000" automatic mounting press, which enables polymerization through the application of alternating compression, heating, and rapid cooling. After preparing the polymerized resins, the samples were polished using the "Buehler PowerPro 5000 variable speed grinder-polisher". The polishing process consisted of three stages for Ti. The components and parameters used in polishing the samples are given in Table 5.

Table 5. Polishing program

Stage	Disc	Abrasive	RPM	Pressure (N)	Time (s)
1	P240, P300	SiC	300	30	300
2	TOP	Diamond 9 µm polycrystalline suspension	150	30	240
3	SUPRA	SPM 0.03 µm non-crystalline suspension	150	25	60

Then, the samples were chemically etched using Keller's reagent (190 mL H_2O, 5 mL HNO_3, 3 mL HCl, 2 mL HF) before being observed through the optical microscope. The Leica Microscope M420 was used to measure the dimensions of the melted zones. The magnification of the Leica microscope was limited to 325, with the magnification of the camera included. It featured coaxial and lateral lighting by Schott KL 1500 LCD halogen lamp.

After pulsed welding, the samples were usually broken along the joint line for observation by the optical microscope and SEM-EDS analysis. Furthermore, for the dodo experiments, the quartz plates were also analyzed using SEM-EDS to investigate the vapor plume deposits on the surface resulting from condensation.

Global observations of the cross-cuts and broken dissimilar melted zones were made using the scanning electron microscope JSM-6610LA (Jeol) equipped with an EDS (Energy-Dispersive Spectroscopy) analyzer. EDS was often used to provide detailed information about the elemental composition of a sample. The distribution of the elements was evaluated using X-mapping.

The description of the post-mortem characterization above for the different welding experiments is condensed into the following table for ease of understanding.

Table 6. Post-mortem characterization details.

Experiment and configuration		Polished cross-section examination	Top view examination	Broken sample examination
Continuous welding		Yes, Optical microscopy, SEM-EDS	Yes, SEM-EDS	No
Pulsed welding	Butt	No	Yes, SEM-EDS	Yes, SEM (No EDS)
	Overlap	No	Yes, SEM-EDS	Yes, Optical microscopy
	DODO	No	No	Yes, SEM-EDS

Further details about the experimental techniques and evaluation methods are discussed in the following chapters.

Chapter 3. Evaluation and Findings in continuous welding

The initial focus of the thesis was on investigating the vapor plume and keyhole behavior in the dissimilar laser welding of A5754/T40 in the butt-configuration. Continuous welding was chosen as the starting point to establish a foundation and preliminary understanding of the process. It allowed for optimization of welding parameters and provided a basis for comparative analysis. Additionally, practical considerations such as ease of implementation and control played a role in the decision-making process. In this chapter dedicated to continuous dissimilar welding, the experimental setup, a more detailed methodology of study (HSI, spectrometry), the results (from HSI, spectrometry, and post-mortem analysis), and finally a discussion on the most notable results and their implications and how to advance in this research are presented.

3.1.   Experimental setup

The experimental setup included a Yb:YAG laser, welding table, high-speed camera, and spectrometer for observing and analyzing the vapor plume during welding (Figure 48). A laser power of 3 kW was used with a 200 µm diameter spot focused on the top surface of the materials being welded. Argon flow protected the top (20 l/min) and bottom (10 l/min) surfaces. Experiments were conducted using different positions of the laser spot relative to the joint line (Figure 49). Videos were captured using an 810 nm filter with no additional lighting. Welding speeds of 3 m/min and 8 m/min were tested because they corresponded to Rosenthal regime and Single wave regime for standalone pure titanium [287], and thus allowed exploring different keyhole dynamics. The welding time for each welding speed was adjusted to have a corresponding weld length of 12 cm.
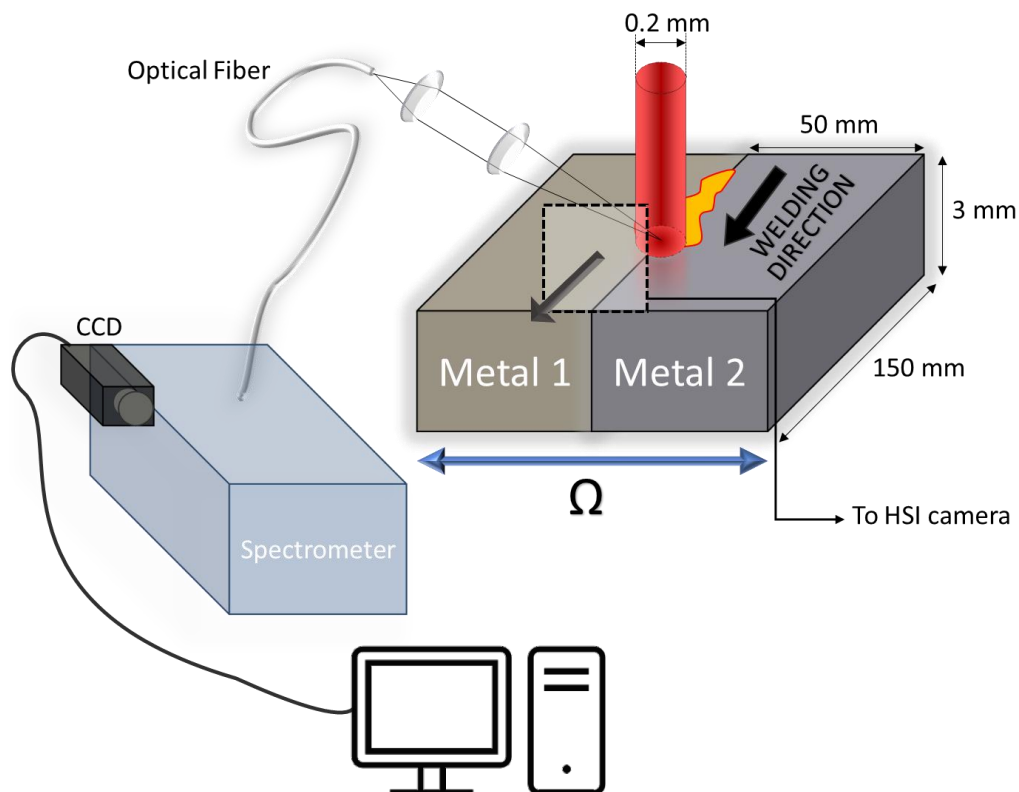
Figure 48. Schematic for continuous welding in butt configuration (not to scale).

Ω= -0.2 mm   Ω= -0.1 mm   Ω= 0 mm   Ω= +0.1 mm   Ω= +0.2 mm

Ti   Al
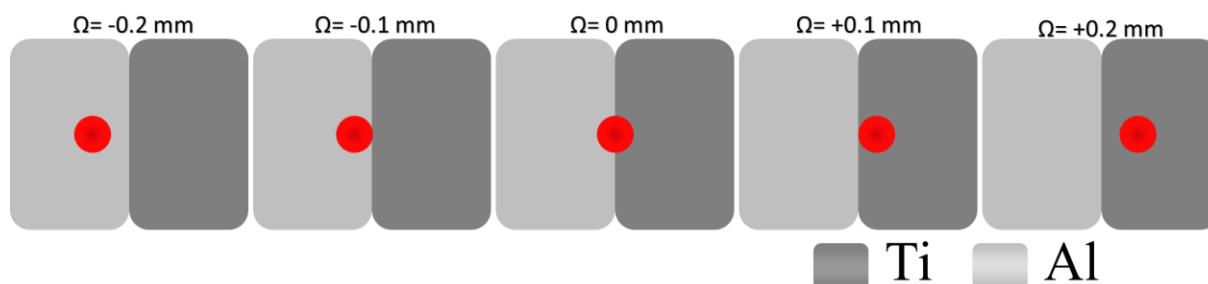
Figure 49. Positions of the laser spot relative to the joint line.

The camera and spectrometer were positioned in a way to capture both front and side views of the plume. If the camera was placed to capture the front view, the signals for the spectrometer would be collected from the side, and vice-versa. Imaging the vapor plume from both the side and front was done to observe and compare the similarities or dissimilarities in the shape and size of the plume. Similarly, spectrometry was done from the front and the side to analyze the relationship between spatial distribution of the chemical composition of the vapor plume. Both the locations offered significant advantages and disadvantages. Having the camera on the side and the spectrometer collecting light from the front, allowed observation of the effects of the inclination of the front keyhole wall on the vapor plume while providing an uninterrupted view for the spectrometer. And having the camera parallel to the joint line allowed observation of the effects of the keyhole side walls on the vapor plume. Whichever device was placed on the side, the optical signal to it from the vapor plume was periodically interrupted twice by the holders which held the metal plates firmly attached to the welding table. The camera was slightly elevated than the surface of the metal plates and the acquisition was done at an angle (~13º) in order to be able to have a view of the joint line which in turn was useful to focus correctly. However, it was not possible to place the camera or the spectrometer to film with a rear view or right-side view due to the spatial and logistical constraints (Figure 28.a, p.58) The in-situ observation of the vapor plume done by the high-speed camera was in the infrared wavelength regime using an 810 nm bandpass filter to observe the thermal radiation (Section 2.3.2.2, p.70).

3.2. Vapor Plume studies – High Speed imaging

In this study, the behavior of laser-induced vapor plumes was initially investigated with HSI for standalone Ti and A5754 at 4000 fps. Results showed that Ti produced a stable and luminous plume even at low exposure times of 10 µs. In contrast, A5754 resulted in a diffuse vapor plume of low luminosity accompanied by a high amount of chaotically emitted spatters, which were hardly distinguishable even at an exposure time of 520 µs. When welding dissimilar materials, such as Ti and A5754, with the laser beam centered on the joint line, a plume of intermediate luminosity, associated with intense emission of spatters was produced. Based on these findings, the optimal exposure time for dissimilar welds was chosen to be 120 µs. The untreated images of A5754 and Ti vapor plumes with an exposure time of 520 µs and 10 µs respectively are presented (Figure 50) to demonstrate the differences in luminosity between the two plumes of these standalone materials.
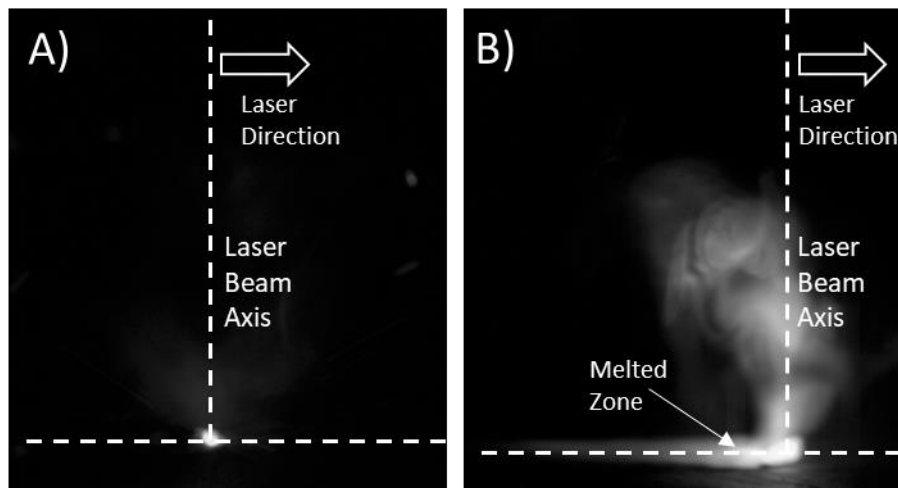
Figure 50. Vapor plumes (side view) of A) A5754 captured with 520 μs exposure time and B) Ti captured with 10 μs exposure time (Laser power:3 kW, Welding speed: 3 m/s).

3.1.1. Image processing - Standard deviation images

The standard deviation projections generated from a series of plume images in ImageJ can provide valuable insights into the spatial distribution and variability of pixel intensities within the plume. By analyzing the standard deviation image, the regions of high intensity fluctuations, indicating areas of significant changes or activity of the vapor cloud could be identified. Since each video consisted of thousands of images containing a very diffuse cloud-like object (plume) that varies irregularly in shape, size and position, the method that was used to initially study the vapor plume characteristics was by finding the areas of high variability in pixel intensity levels. A standard deviation image was made from the stack of images in ImageJ. Then, the "Z Project" function was applied to the stack, selecting the "Standard Deviation" option. This function was used to calculate the standard deviation of the pixel intensities for each position in the stack. The Auto Threshold function was utilized to binarize the standard deviation images, resulting in well-defined edges of the vapor plume which allowed for accurate estimation of its dimensions.

The Z Project function in ImageJ allows users to create a single image from a stack of images. The Standard Deviation option offers an improved representation of the stack, as it calculates the average for each pixel in the stack, subtracts the average from each value, and allows the user to specify a range of values to be considered in the computation. This range can be defined as the number of standard deviations from the average, thus eliminating outliers from the calculation. The standard deviation projection (Figure 51) takes the standard deviation of the pixel intensities through the stack, with positions with large differences in the pixel intensities through the stack appearing brighter in the image [288]. This technique provides a more accurate representation of the stack and can be used to improve the quality of analysis of datasets.
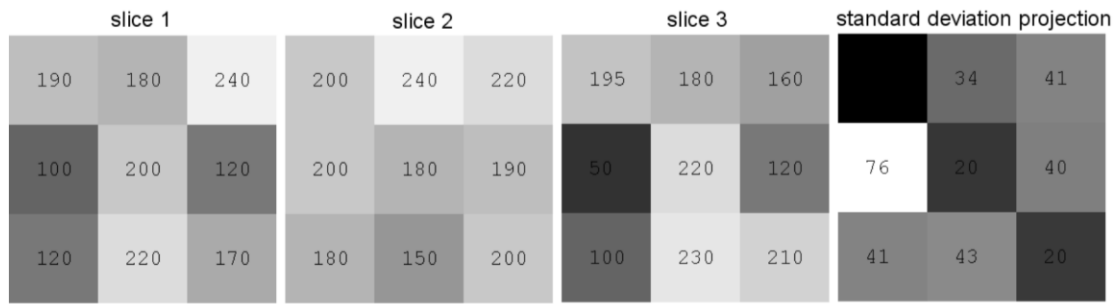
Figure 51. Schematic representation of standard deviation image with the numbers representing the gray values of each pixel [288].

3.1.2. Results – Vapor plume side view

The standard deviation projections indicated that the plume created by welding on titanium plates (Figure 52. a) was significantly larger than that of welding on A5754 plates (Figure 52. b), with the plume formed in dissimilar welding having intermediate dimensions (Figure 52. c, d). The majority of spatter was present on the A5754 side (which can be observed when the plates are inversed (Figure 52. c, d)), while the titanium side remained mostly spatter-free.

The luminosity difference between aluminum and titanium produced by Yb:YAG laser, results from their respective absorptivity to the laser radiation. Aluminum has a lower absorptivity (Table 2 p.57). As a result of the lower absorptivity of aluminum ($A \approx$ 10-30%) compared to titanium ($A \approx$ 40%), there is lower energy input into the process. In addition, the higher vaporization temperature of titanium ($T_v = 3560$ K) compared to that of aluminum ($T_v = 2792$ K), indicates that the titanium vapor plume at a higher temperature produces a more intense continuous thermal emission than the aluminum vapor. These plume dimensions correspond with studies that have found plume temperatures near the boiling point of aluminum for an energy density of 1 MW/cm² [289], and titanium with much higher temperatures of around 8000K when welded with CO_2 laser [51] and 6000K when deposited with 1070 nm fiber lasers [203].
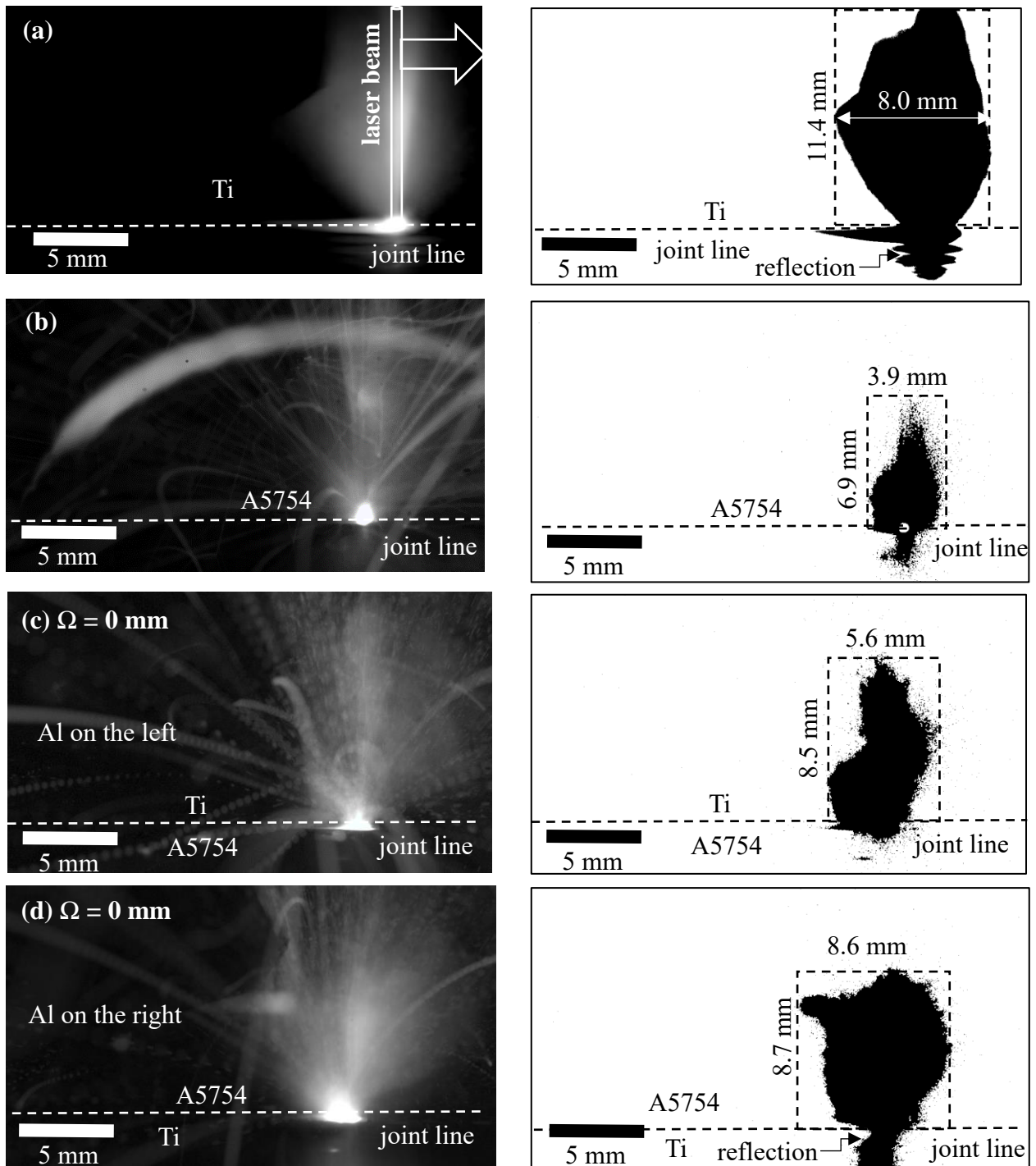
Figure 52. Standard deviation projection (on the left) and binary images (on the right) of the side view on the vapor plume during the laser welding of (a) standalone Ti, (b) A5754 and (c-d) Ti/A5754 joint with zero laser displacement from the joint line with laser power of 3 kW , welding speed of 3 m/min.

While the standard deviation images were not the most efficient to understand the temporal behavior of the vapor plume, they provided an accurate representation of the luminosity in general and an overview of the shape of the plume, in other words, where the plume is being emitted. And so, varying the laser beam offset on the joint line produced changes in the plume luminosity and shape (Figure 53).

Moving the laser spot 0.2 mm towards the aluminum side from the joint line (Ω = - 0.2 mm) produced a very small and dull vapor plume similar to the plume from the welding of standalone A5754. While the laser spot position (Ω = - 0.1 mm) produced a similar weak and

dull plume which was only slightly bigger, brighter and a little more continuous. However, moving the spot towards the titanium side ($\Omega = + 0.1$ mm) produced a very luminous vapor plume that was associated with an increase in spattering towards the A5754 side. And the laser displacement ($\Omega = + 0.2$ mm) produced a very stable, highly luminous, spatter-free plume similar to plume from the welding of standalone titanium.
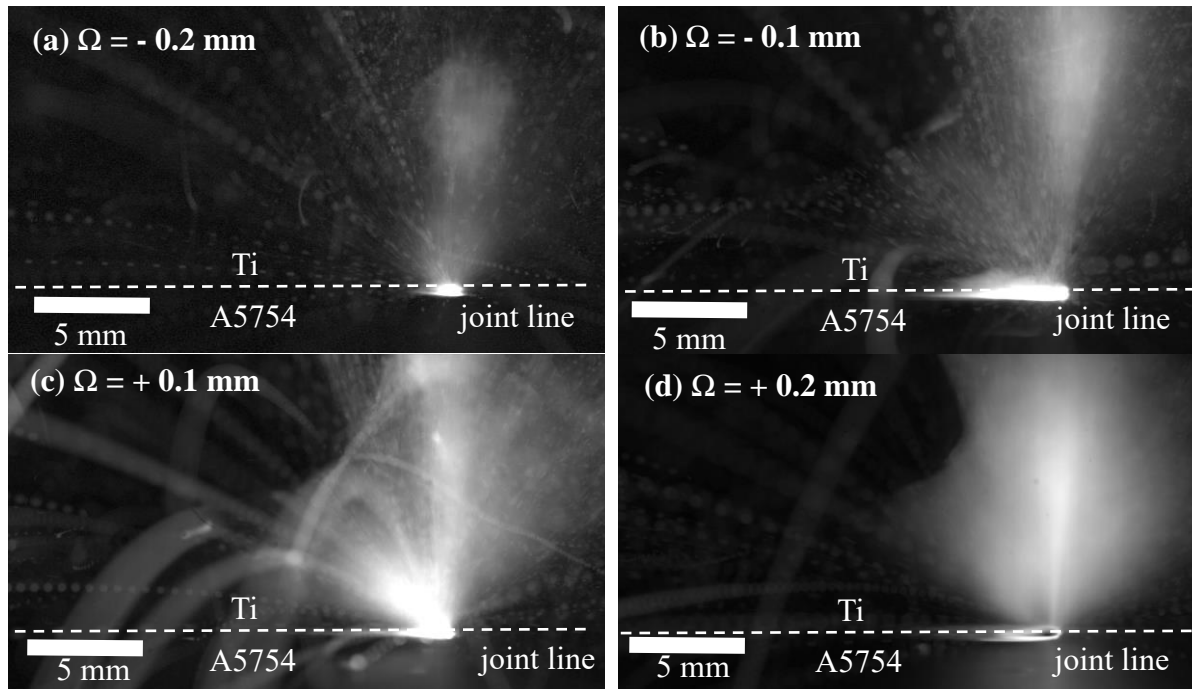
Figure 53. Lateral view on the plume between Ti and A5754 plates welded with different laser beam offsets from the joint line, 3 kW and 3 m/min (exposure time of 120 µs, STD images).

3.1.3. Results – Vapor plume front view

Similar to the side-view standard deviation images, the standard deviation images of the frontal view of the vapor plume provide information on the general position and the shape of the vapor plume. The standalone materials T40 and A5754 showed similar behavior as previously observed in the side view with the titanium plume being bright and the aluminum plume dull and hardly visible (Figure 54).
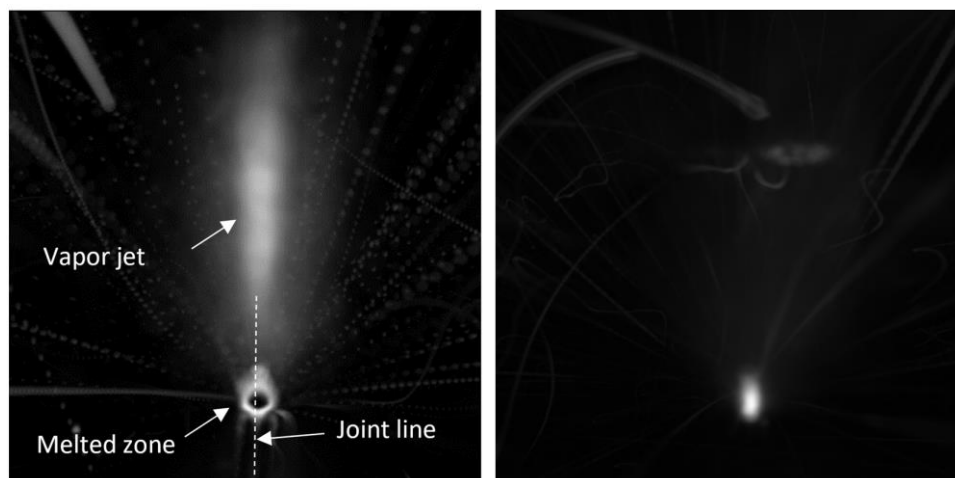
Figure 54. Standard deviation images for the frontal view of the vapor plume for: a)T40 (exposure 30) and b) A5754 (exposure 240) for the welding speed of 8 m/min.).

The STD images (brightness enhanced: + 25 %) from both the experimented welding speeds 3 m/min and 8 m/min indicated the presence of two jets of vapor : (1) a vertical jet and (2) an inclined jet towards the aluminum side that coincides with the direction of the spatters emission that can be seen in Figure 53.C. The inclination of the vapor jet seemed to be around 43° ~ 45° (Figure 56 (a)). The vertical jet was 7.28 mm in height and 1.82 mm in width while the inclined jet was 5.07 mm in height and 4.39 mm in width for the welding speed of 3 m/min.

Although the presence of these two jets were indicated by the STD images, temporal analysis was performed to study the periodicity in the occurrence of the inclined vapor jet. This was done by studying specific areas (boxes marked for the vertical and inclined jet in Figure 56 (a). These two jets could be attributed to the instability of the keyhole wall within the aluminum-rich liquid, as illustrated in Figure 56 (b). The inclination of the vapor plume mirrors the tilt of the associated keyhole wall and typically occurs towards the rear of the continuous weld, as documented by Fabbro et al [156].

When analyzing the standard deviation images, the inclined part of the vapor plume characteristically present only in dissimilar welding appeared to vary depending on the laser spot position relative to the joint line.
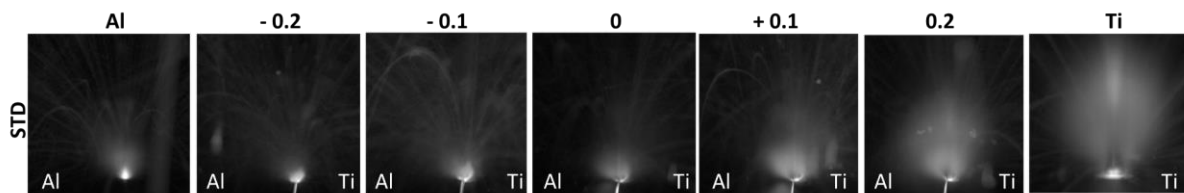
Figure 55. STD images for standalone, dissimilar welding plumes in front view with 3 kW at 3 m/min.

On pure titanium alone, welding at a speed of 3 m/min conforms to the Rosenthal regime, characterized by a nearly vertical keyhole front wall. Conversely, at 8 m/min, it falls into the single wave regime, featuring an inclined keyhole front and a liquid wave at the rear of the keyhole which had been previously observed [287]. However, when adjacent to the aluminum alloy, noticeable periodic fluctuations in the weld occur. In this scenario, the rapidly solidified molten material retains the shape of the keyhole opening (Figure 56 (d)), with the resulting defects spaced 2 mm apart.
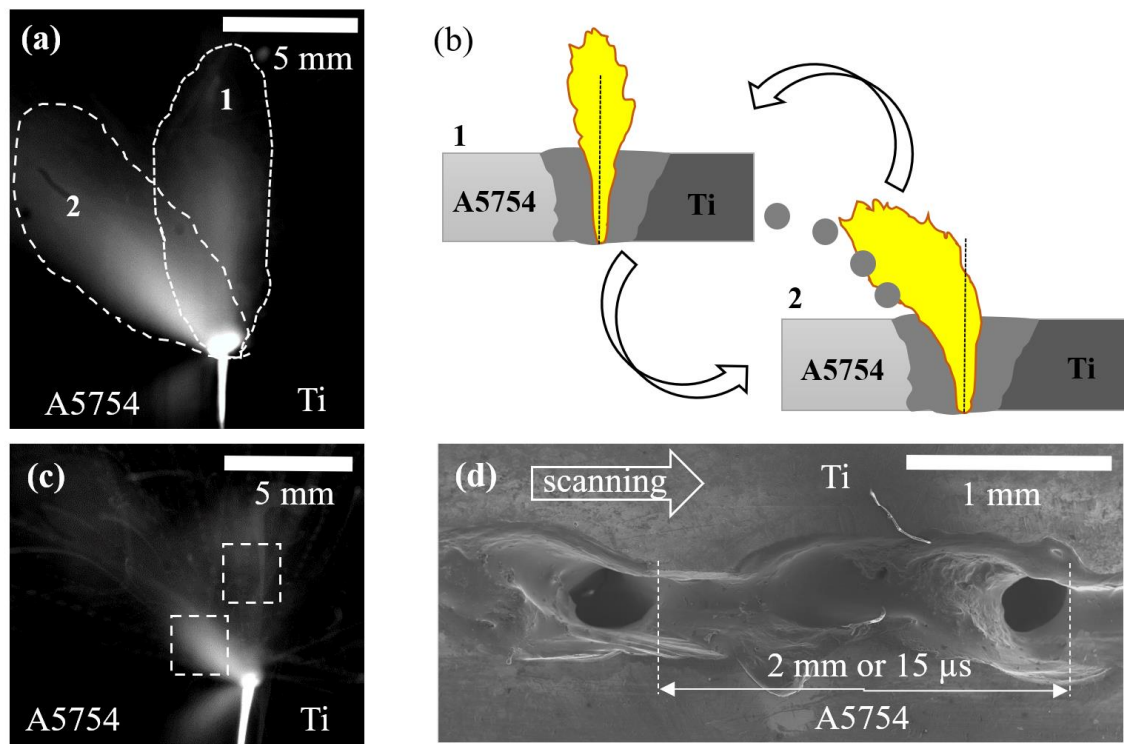
Figure 56. Dissimilar vapor plume front view (Ω = 0 mm) for (a) welding speed 3 m/min; (b) the scheme of keyhole fluctuation with straight (1) and inclined (2) plume situations; (c) welding speed 8 m/min and (d) corresponding SEM image of the top view of the weld.

The presence of vapor plume in the mentioned specific areas was done by calculating the average gray values for every image in the video. This was done for each of these boxes separately in ImageJ through the following steps. The "Set measurements" option was used to set the "Mean gray value" to be measured. And then the region of interest (the box mentioned earlier) was selected using "Rectangle" tool. And then "Image>>Stacks>>Measure Stack" was used to perform the measurement on the region of interest for every image in the video. This measurement calculated the average or mean of all pixel gray values within the region of interest for each image and displayed them as a table. These mean gray values were found to be in the range of 0 to 200. The tables for the different jets were later exported to Microsoft Excel for charting (Figure 57). These charts were used to understand the occurrence of the vertical and inclined jets temporally. Only fragments of these charts are represented here since the durations of the entire welds span 0.12~1.2 seconds depending on the welding speed.

And from these results, it was noted that for the welding speed of 8 m/min (Figure 57 (a)), the vapor plume (with gray values between 0 and 120) exhibited periodical behavior of (15.5~16 ms) corresponds to the repetitive pattern visible from the top view of the melted zone. It was also notable that the intensity of the vertical jet increased when the inclined jet disappeared or decreased in intensity. This indicated a periodical reorientation of the vapor plume (Figure 56 (c). This periodical reorientation of the vapor plume led to the hypothesis that there was periodical destabilization of the keyhole wall on the aluminum side. The inclined jets have a lifetime of 9.3 ms corresponding to a welding distance of 1.24 mm while the vertical jets have a lifespan of 6.7 ms. So, it was inferred that the inclined jet corresponds to the thinner, defect-free segment of the weld where the liquid appears to flow out from the melted zone onto solid A5754. The instances when the vertical jet prevailed similarly correspond to the visible keyhole opening and the solidified liquid wave expulsion. The keyhole opening's inclination on the keyhole's front wall and the presence of the solidified material expulsions along the rear wall indicate the occurrence of the single wave regime.

But for the welding speed at 3 m/min (Figure 57 (b)), not much periodicity or correlation between the occurrences of inclined and vertical jets (gray values between 0 and 210) were observed. However, the maximum average gray value reached up to 200 which is significantly higher than what was observed for the welding speed of 8 m/min. It was supposed that this increase in the intensity of the plume arose from the higher lineic energy deposited on the material at a lower welding speed.

The duration of the inclined jet was governed by the following sequence: as the aluminum-rich liquid reached its boiling point, causing evaporation-induced material loss and the subsequent inclination of the keyhole wall on the aluminum side, the titanium-rich liquid entered from the opposite side of the keyhole, not yet having reached its boiling point. When the wall temperature eventually attained the boiling point of titanium, an increase in keyhole pressure, driven by the contribution of titanium vapor, led to the expulsion of the vertical jet, accompanied by a substantial wave of liquid passing the keyhole. At 8 m/min, this process was observed periodically due to the extended duration required for heating the titanium-rich liquid to its boiling point. In contrast, at 3 m/min, the higher linear energy ensured continuous heating. Nonetheless, the dominant aluminum evaporation resulted in a robust inclined jet, while a less intense vertical jet was generated by titanium evaporation.
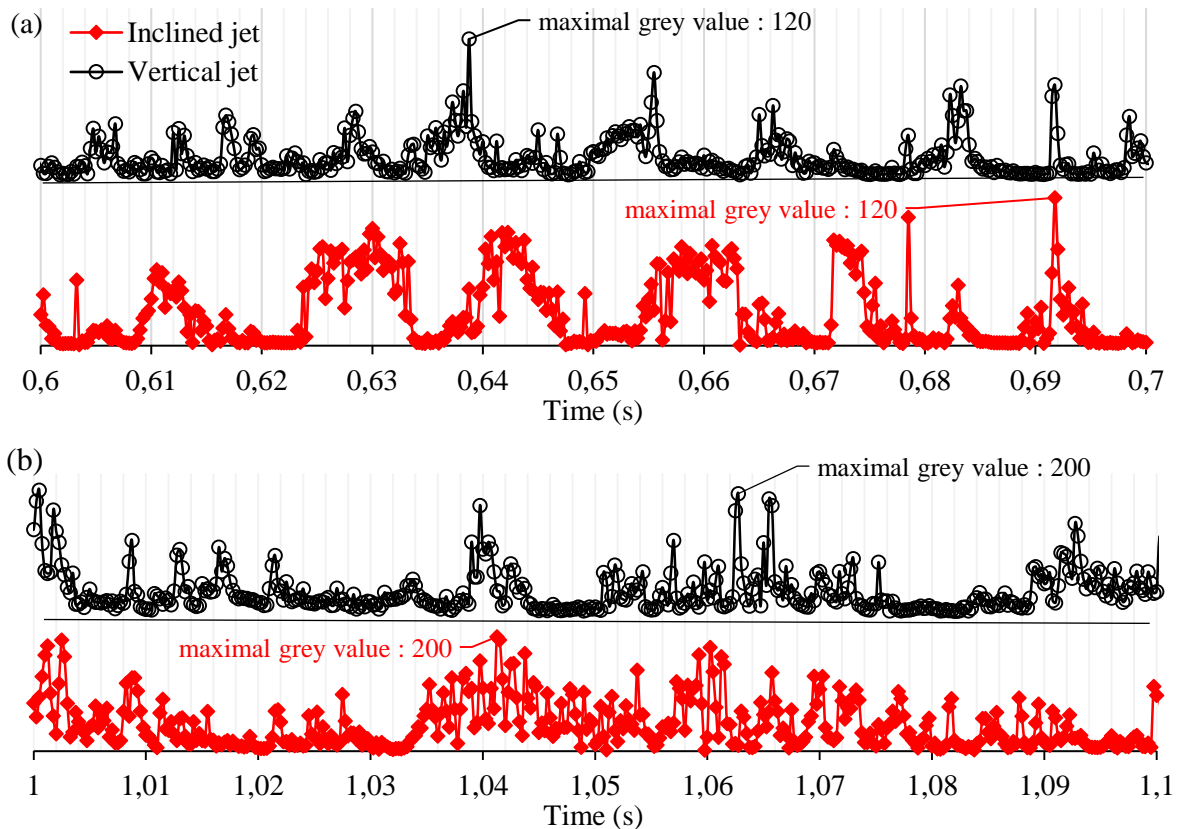
Figure 57. Fragments of temporal variation of mean gray value in the zones situated in vertical and inclined vapor jets formed during T40/A5754 welding with centered laser beam at (a) 8 m/min, (b) 3 m/min.

During the welding of standalone materials at a speed of 3 m/min, no periodic fluctuations were observed in the vapor plume, consistent with the appearance of regular weld surfaces (Figure 58). Notably, the intensity of the plume was significantly lower for A5754 (with a gray value of ≤ 100) compared to titanium (≤ 210). Additionally, sporadic, powerful explosive-like bursts accompanied by a high emission of spatters were observed in the A5754 weld.
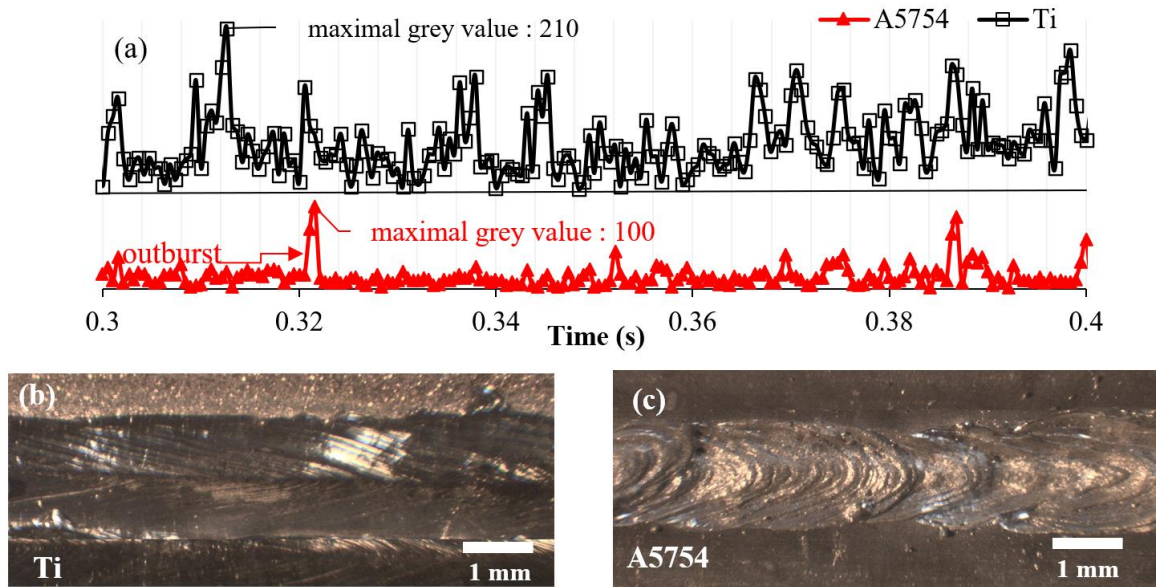
Figure 58. (a) Temporal variation of the mean gray value between 0.3 s - 0.4 s in vertical vapor jets of standalone materials formed during welding at 3 m/min, (b) top view of Ti weld and (c) A5754 weld.

When the welding speed was increased to 8 m/min, a consistent and smooth weld appearance was maintained by titanium, while noticeable irregularities were displayed in the A5754 weld, appearing as prominent bumps separated by distances of 6-8 mm (Figure 59). The maximum mean gray value decreased to 40, which can be attributed to the lower plume temperature compared to the 3 m/min case.
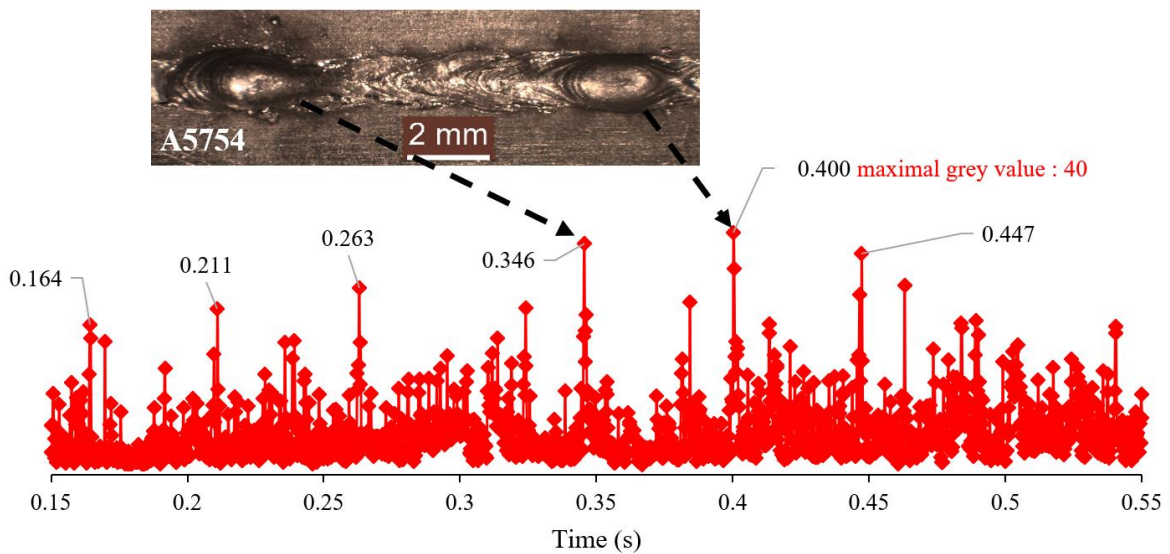
Figure 59. Temporal variation of the mean gray value (between 0.15 s – 0.55 s) in the vertical vapor jet in welding of A5754 at 8 m/min with the corresponding top view of the weld.

The fluctuations in the mean gray value above the keyhole revealed distinct and forceful bursts separated by approximately 45 - 50 ms, corresponding to the frequency of observed patterns. These bursts could be associated with the periodic ejection of a substantial amount of liquid material past the keyhole. An explanation for the occurrence of these significant bursts or spikes during aluminum welding was provided by Paleocrassas and Tu [207]: the presence of a sufficient liquid layer in front of the keyhole promotes the evaporation of aluminum from the illuminated liquid phase, resulting in a relatively calm vapor cloud. However, continuous

heating eventually leads to boiling, accompanied by violent evaporation, creating a more intense plume. Once a sufficient quantity of liquid is lost, the process returns to a calmer state until the next overheating event. In contrast, for the titanium alloy, more stable behavior of the keyhole is exhibited, regardless of whether the welding speed is low or high [287].

Although several features were observed about the shape and orientation of the vapor plume corresponding to the features of the melted zone, spectroscopy was deemed necessary to understand the composition of the vapor plume.

3.3. Vapor plume studies – Spectrometry

To understand the composition of the vapor plume, emission spectroscopy was performed to complement HSI and provide correlation to the post-mortem observations of the melted zone. Based on previous data which constituted the examination of T40 and A5754 vapors in 14 spectral zones between 210 nm – 600 nm using an echelle grating (300 lines/mm – width of spectral region = 30 nm), 12 spectral regions (Table 7) were chosen for inspection to study the emission lines of Ti, Al and Mn in continuous welding. The emission lines in these zones were studied using another echelle grating (2400 lines/mm – width of spectral region = 4 nm) with higher resolution (refer 2.3.1 p.61). Similar to HSI, the spectra of Ti and A5754 were first acquired separately and then, the spectra of dissimilar welding with different laser displacements from joint line were acquired.

Table 7. Spectral regions observed.

263.9 nm – 266.8 nm	393.6 nm – 396.5 nm
278.0 nm – 280.9 nm	400.1 nm – 403.0 nm
292.1 nm – 295.0 nm	464.2 nm – 467.1 nm
324.3 nm – 327.2 nm	487.9 nm – 490.8 nm
333.3 nm – 336.2 nm	516.4 nm – 519.3 nm
356.6 nm – 359.5 nm	554.5 nm – 557.4 nm

3.2.1. Emission spectra of Ti in continuous welding

Among the 12 spectral regions observed, no signal was present for wavelengths less than 300 nm. From 320 nm, there was a part of the continuous thermal emission, which increased initially and became constant after 550 nm. Only the lines of Ti (I) were observed essentially (with the possibility of Ti (II) lines existing in the magnitude of the background noise) (Figure 60).
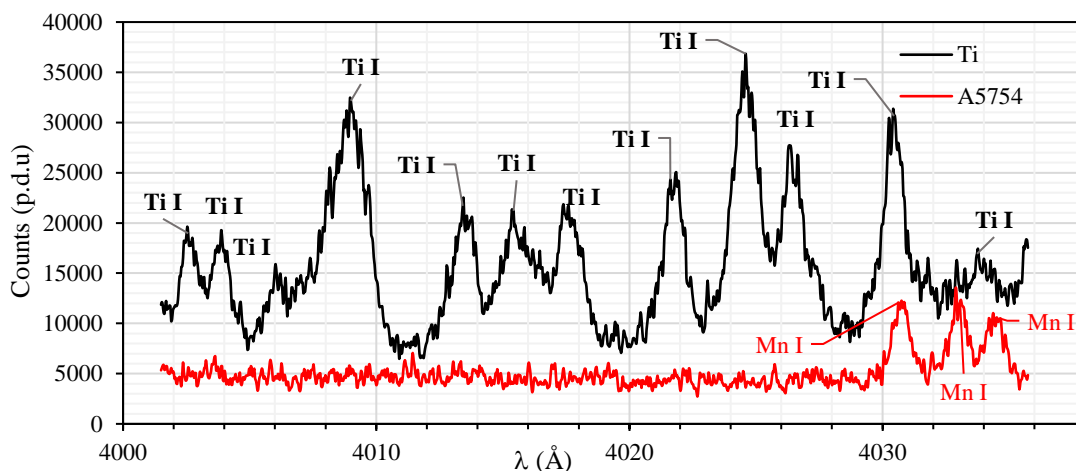
Figure 60. Emission spectrum of standalone materials during continuous laser welding (3 kW, 3 m/min) in 402 nm spectral region.

In order to make an estimation of the temperature using the Boltzmann's method (Eqn. 35, p.47), certain transitions that satisfy the following conditions were selected such as: isolated lines, sufficiently high signal-noise ratio, no saturation of CCD and no self-absorption. These lines are indicated along with their characteristic data from NIST [200] and Kurucz [290] databases in Table 8.

Table 8. Transitions used in Boltzmann's method for standalone Ti welding with continuous Yb:YAG laser. ($A_{u \to l}$ – Einstein's coefficient, E_i ,E_s– energy of lower and upper levels, J_i , J_s – degeneracies of lower and upper levels, D_{int} – Standard deviation of intensities).

Element	λ_s theoretical (nm)	A_s (s^{-1})	E_i (cm^{-1})	Conf.	J_i	E_s (cm^{-1})	Conf.	J_s	Intensity	σ_I
Ti I	401.537	5.721E+07	16817.16	(3F)sp z5F	1	41714.41	s4F)4d e5G	2	8.03E+09	1.44E+09
Ti I	402.182	4.795E+07	16961.44	(3F)sp z5F	3	41818.81	s4F)4d e5G	4	7.41E+09	1.03E+09
Ti I	402.457	6.142E+06	386.87	s2 a3F	4	25227.22	(3F)sp y3F	3	1.77E+10	1.28E+09
Ti I	402.654	3.570E+07	17075.26	(3F)sp z5F	4	41903.48	s4F)4d e5G	5	1.21E+10	1.60E+09
Ti I	403.051	4.889E+08	17215.39	(3F)sp z5F	5	42019.13	s4F)4d e5G	6	1.11E+10	2.70E+09
Ti I	464.518	8.568E+07	13981.77	(4P)4s a5P	1	35503.40	(4P)4p w5D	0	7.29E+09	2.27E+08
Ti I	465.000	2.642E+07	14028.44	(4P)4s a5P	2	35527.75	(4P)4p w5D	1	5.18E+09	1.98E+08
Ti I	465.646	1.985E+06	0.00	s2 a3F	2	21469.49	(3F)sp z3G	3	2.75E+10	3.30E+08
Ti I	466.757	2.175E+06	170.13	s2 a3F	3	21588.50	(3F)sp z3G	4	3.11E+10	3.54E+08
Ti I	517.374	3.796E+06	0.00	s2 a3F	2	19322.98	(3F)sp z3F	2	1.28E+10	1.94E+08
Ti I	519.295	3.483E+07	170.13	s2 a3F	3	19421.58	(3F)sp z3F	3	1.67E+10	2.13E+08
Ti I	556.545	1.408E+07	18037.21	(2H)4s a3H	4	36000.15	(1G)sp y1G	4	4.91E+09	1.52E+08

The slope of the Boltzmann line (Figure 61) was estimated in a MATLAB program using linear least squares scaled standard deviation of intensities (σ_I). The slope that corresponds here to the temperature of Ti atoms was estimated to $T_p = 8697$ K. The associated uncertainty 1900 K only takes account of the quality of the lines (non-aligned experimental points).
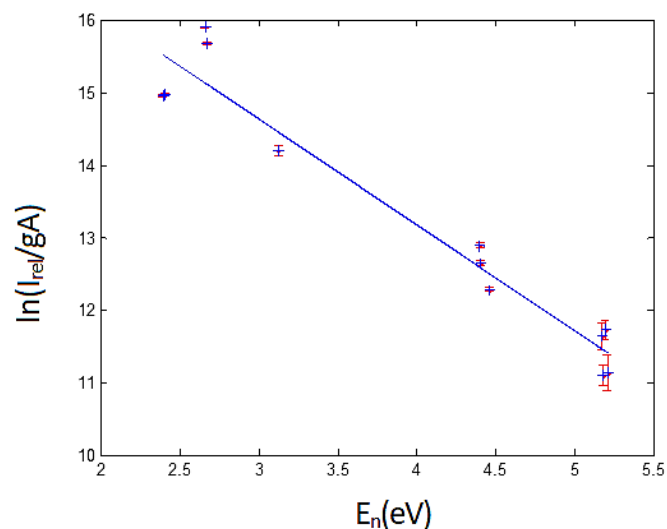
Figure 61. Boltzmann plot (weighted) for standalone Ti welding.

3.2.2. Emission spectra in continuous welding of A5754

Among the 12 spectral regions studied, only three regions contained observable transitions from Al (I) and Mn (I). The expected (from the NIST and Kurucz databases) and observed transitions from these regions are listed in Table 9. In the spectral regions of low wavelengths

(257 nm – 266 nm), the emission lines of Al (I) were not observed even in the cases where resonance could occur. In addition, the continuous thermal radiation was not observable either.

Table 9. The expected and observed (in bold) transitions for standalone A5754 during continuous Yb:YAG welding.

Element	λ_s theoretical (nm)	A_s (s^{-1})	E_i (cm^{-1})	Conf.	J_i	E_s(cm^{-1})	Conf.	J_s	Intensity
Al I	256.7984	2.20E+07	0.00	3p 2P	1/2	38929.41	4d 2D	3/2	2567.984
Mn I	257.276	2.44E+08	18531.64	(6S)sp z8P	7/2	57388.90	d5 4p2 e8P	9/2	2572.76
Al I	257.5094	2.66E+07	112.06	3p 2P	3/2	38933.97	4d 2D	5/2	2575.094
Al I	257.5393	4.37E+07	112.06	3p 2P	3/2	38929.41	4d 2D	3/2	2575.393
Mn I	257.551	3.06E+08	18531.64	(6S)sp z8P	5/2	57218.15	d5 4p2 e8P	7/2	2575.51
Mn I	258.431	3.79E+08	18705.37	(6S)sp z8P	9/2	57388.90	d5 4p2 e8P	9/2	2584.31
Mn I	259.294	3.96E+08	18531.64	(6S)sp z8P	7/2	57086.33	d5 4p2 e8P	5/2	2592.94
Al I	265.2484	1.34E+07	0.00	3p 2P	1/2	37689.41	5s 2S	1/2	2652.484
Al I	266.0393	2.65E+07	112.06	3p 2P	3/2	37689.41	5s 2S	1/2	2660.393
Al I	394.40058	5.10E+07	0.00	3p 2P	1/2	25347.76	4s 2S	1/2	3944.0058
Al I	396.152	1.01E+08	112.06	3p 2P	3/2	25347.76	4s 2S	1/2	3961.52
Mn I	**401.81**	**2.03E+08**	**17052.29**	**(5D)4s a6D**	**9/2**	**41932.64**	**(5D)4p z6D**	**7/2**	**4018.1**
Mn I	**403.076**	**1.36E+08**	**0.00**	**d5 4s2 a6S**	**5/2**	**24802.25**	**(6S)sp z6P**	**7/2**	**4030.76**
Mn I	**403.307**	**1.32E+08**	**0.00**	**d5 4s2 a6S**	**5/2**	**24788.05**	**(6S)sp z6P**	**7/2**	**4033.07**
Mn I	**403.449**	**6.32E+07**	**0.00**	**d5 4s2 a6S**	**5/2**	**24779.32**	**(6S)sp z6P**	**7/2**	**4034.49**
Mn I	**403.573**	**2.64E+08**	**17282.00**	**(5D)4s a6D**	**7/2**	**42053.73**	**(5D)4p z6D**	**5/2**	**4035.73**
Al II	466.680		125869.02	5p 1P	1	147290.98	11s 1S	0	4666.80

With increasing wavelength, continuous thermal radiation appeared and continuously increased. In the spectral region of 395 nm, two lines of Al were observed. These lines were resonance transition, leading to auto-absorption.

In the 467 nm spectral region, Mn (I) line is observed. Only in the 400.1 nm – 403.0 nm spectral region three Mn (I) lines of sufficient intensity were observed (Figure 62), and so this region was chosen as a region of interest for dissimilar welding study, because Ti (I) lines were also present in this wavelength range.
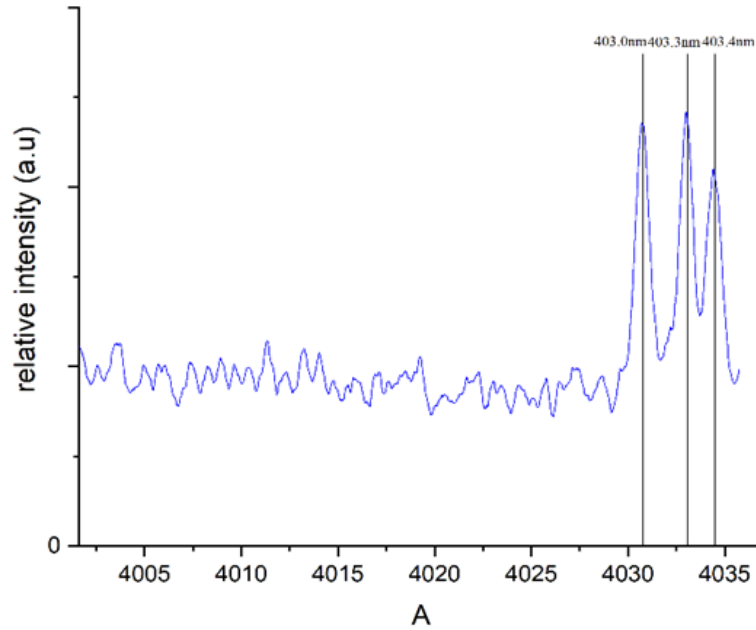
Figure 62. Emission spectrum of pure A5754 during continuous laser welding (3 kW, 3 m/min) in 402 nm spectral region.

3.2.3. Emission spectra of T40/A5754 continuous dissimilar welding plume

As mentioned before, only the 400.2 nm – 403.0 nm range was considered to be of interest for the dissimilar welding study since it contained Mn (I) lines of sufficient intensity and multiple Ti (I) lines. Because the observation of this spectral region presented information about the evaporation of T40 and A5754 simultaneously, 12 spectra with an acquisition time of 20 ms and 4 accumulations were acquired during the welding process to observe eventual fluctuations. The spectra acquired for dissimilar welds (Figure 63 (a)) with different laser displacements from joint line are given. For each case, the sum of 12 spectra per condition is given with noise removed and intensity calibrated.
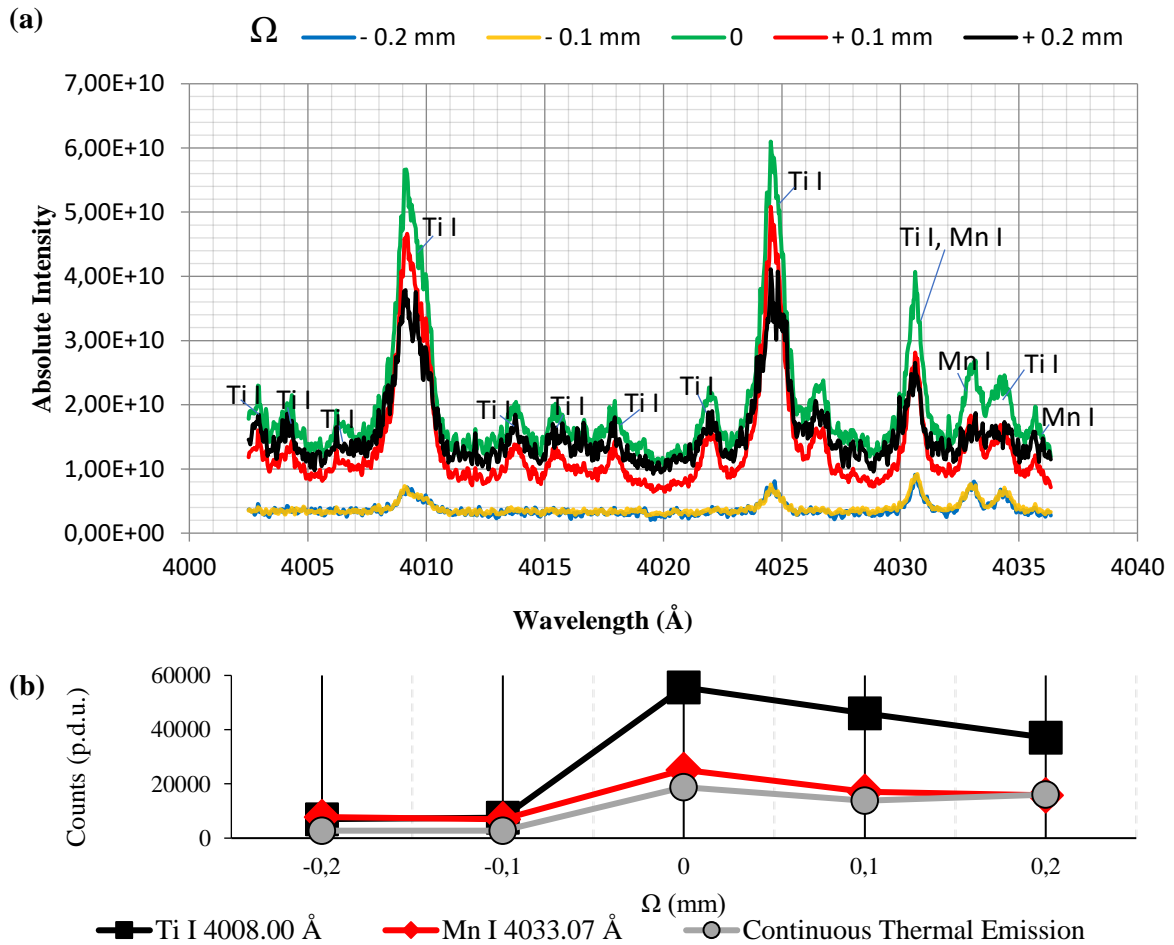
Figure 63. The plume spectra of (a) dissimilar welds with a different beam offset from the joint line acquired in a spectral region of 402 nm; (b) analysis of the intensity variation with a beam offset.

The presence of both the Mn (I) lines and Ti (I) lines in all the dissimilar welding experiments indicated the simultaneous vaporization of T40 and A5754. The Mn (I) lines (marked in bold in Table 10) are the emission lines produced from resonance. Since the higher energy levels of these Mn (I) lines have very close values, the estimation of temperature from these lines was not possible. For the offsets on A5754, the signal observed was weak. The continuous thermal emission of the plume was low, and the observed lines corresponded to Mn (I) and resonance transition of Ti (I). However, it was interesting that even with maximum laser displacement on A5754, Ti (I) lines could still be observed. This presence of Ti (I) lines for the maximum beam offset on aluminum corresponded to the post-mortem observation of minor quantities of Ti in the melted zone (Table 11).

This intensity of the lines was maximum when the beam was centered on the joint line which indicated that there was simultaneous evaporation of Ti and Al alloy (Figure 63 (a)) which could be due to the higher absorption coefficient of titanium along with the easier excitations of the Ti atoms compared to Al. For the beam offsets on T40, the spectra observed had slightly less intense Ti I emission lines because higher energy was needed for keyhole development without the joint gap initially participating in the keyhole formation. While the intensity of the Mn (I) lines decreased with the increase in the offset of T40, they were still present even for maximum beam offsets on T40 due to the transport of the A5754 alloying elements into the Ti-rich melt.

When comparing the spectra of $\Omega \leq 0$ with the spectra from standalone titanium (Figure 60), a difference in the ratio between the Ti (I) resonance lines ($E_s = 25{,}000$ cm^{-1}) and the most energetic lines ($E_s = 42{,}000$ cm^{-1}) could be noted. This disparity indicates that the vapor plume had a significantly lower temperature during the dissimilar welding compared to the standalone titanium. To estimate the temperature of the plume accurately, three reliable Ti (I) transitions (Table 10) were selected. The peak at 400.8 nm was not considered to contain two lines due to difficulties in deconvolution. With suboptimal quality of the spectra and a limited number of available transitions, only a primitive approximation of the plume temperature was feasible using the Boltzmann plot method. For $\Omega = + 0.2$ mm, the CCD frequently reached saturation, leading to the saturation of spectral lines. Consequently, the temperature calculation was conducted solely with the remaining unsaturated spectra, resulting in a less robust outcome compared to $\Omega = 0$, $+ 0.1$ mm.

The obtained results from the Boltzmann plot method were as follows: T = 5967 K for $\Omega = 0$, $T_e = 5072$ K for $\Omega = + 0.1$ mm, and T = 6157 K for $\Omega = + 0.2$ mm. Despite the preliminary nature of these estimations, it was apparent that the vapor temperature in the dissimilar welding process (ranging from 5000 to 6000 K) was considerably lower than the temperature observed during standalone titanium welding (9795 $\pm$ 394 K). This observation suggested that the presence of aluminum, which exhibits a lower absorption coefficient to Yb:YAG radiation, higher thermal diffusivity, and higher excitation energy values compared to titanium, leads to a less efficient laser-material interaction, resulting in a significantly weaker vapor plume which directly correlated to the HSI observations.

From Figure 63 (b) the intensity variations of Ti I 400.800 nm, Mn I 403.307 nm lines, and average thermal emission for different beam offsets can be compared. Drastic attenuation occurs from $\Omega = - 0.1$ mm, indicating keyhole formation in Al-rich liquid. This correlates with reduced vapor plume luminosity. For $\Omega \geq 0$, high absorption and low thermal diffusivity of Ti suggest that the keyhole is situated mainly in liquid titanium.

Table 10. The observable transitions for dissimilar T40/A5754 welding with continuous Yb:YAG laser (Blue : Emission lines used for temperature estimation with Boltzmann's method in case of dissimilar welding)

Element	λ_s theoretical (nm)	A_s (s^{-1})	E_i (cm^{-1})	Conf.	J_i	E_s (cm^{-1})	Conf.	J_s
Ti I	400.805	2.96E+07	17075.26	(3F)sp z5F	4	42017.98	s(4F)4d e5H	5
Ti I	400.892	7.03E+06	170.13	s2 a3F	3	25107.41	(3F)sp y3F	2
Ti I	401.358	2.20E+07	17215.39	(3F)sp z5F	5	42123.74	s(4F)4d e5H	6
Ti I	401.537	5.72E+07	16817.16	(3F)sp z5F	1	41714.41	s(4F)4d e5G	2
Ti I	401.776	4.48E+07	16875.12	(3F)sp z5F	2	41757.53	s(4F)4d e5G	3
Mn I	401.810	2.53E+07	17052.29	(5D)4s a6D	9/2	41932.64	(5D)4p z6D	7/2
Ti I	402.181	4.80E+07	16961.44	(3F)sp z5F	3	41818.81	s(4F)4d e5G	4
Ti I	402.457	6.14E+06	386.87	s2 a3F	4	25227.22	(3F)sp y3F	3
Ti I	402.653	3.57E+07	17075.26	(3F)sp z5F	4	41903.48	s(4F)4d e5G	5
Ti I	403.051	4.89E+07	17215.39	(3F)sp z5F	5	42019.13	s(4F)4d e5G	6
Mn I	403.076	1.73E+07	0.00	4s2 a6S	5/2	24802.25	(6S)sp z6P	7/2
Mn I	403.307	1.64E+07	0.00	4s2 a6S	5/2	24788.05	(6S)sp z6P	7/2
Mn I	403.449	1.58E+07	0.00	4s2 a6S	5/2	24779.32	(6S)sp z6P	3/2

3.4. Keyhole and melted zone studies: Post-mortem observations

When the dissimilar welds were examined from a top-down view, significant changes were observed in the melted zone features with varying beam offset from the joint line. Pure Ti welds exhibited a regular and symmetric joint line (Figure 64.b), whereas aluminum alloy resulted in more fluctuating melted zones with larger spatters, resembling the behavior of standalone A5754 (Figure 64.d). Notably, when the laser spot was shifted to the A5754 side, the weld features and color changed, indicating the dominance of liquid aluminum and the keyhole's location in the Al-rich liquid (Figure 64.g,h).
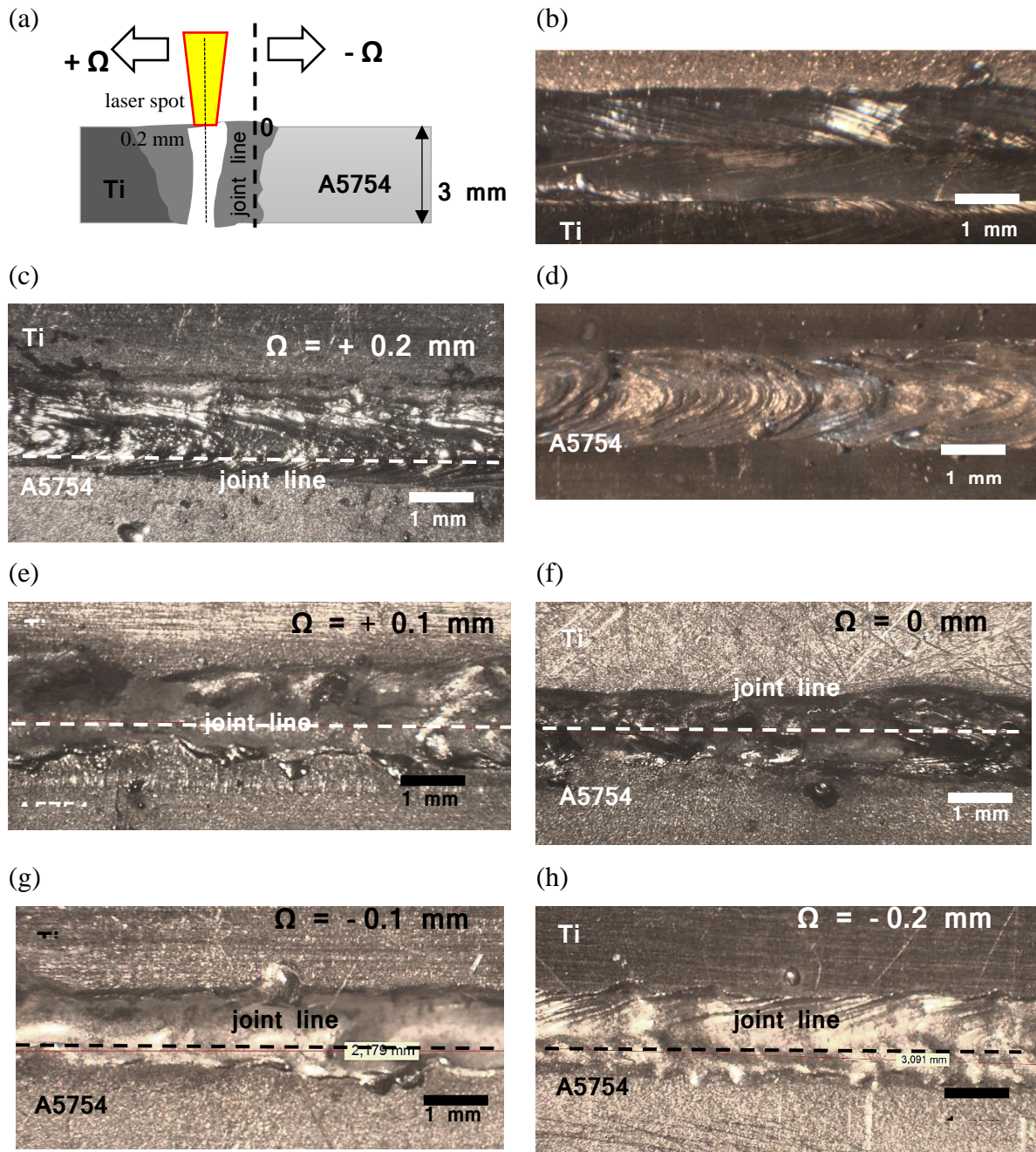
Figure 64. (a) Beam offset sketch and top view of the welds made with a laser power of 3 kW and welding speed of 3 m/min in (b) standalone Ti, (c) Ω = + 0.2 mm, (d) standalone A5754, (e) Ω = + 0.1 mm, (f) Ti/A5754 joint, (g) Ω = - 0.1 mm and (h) Ω = – 0.2 mm.

In the weld cross-sections (Figure 65), distinct Ti-rich and Al-rich domains were observed within the melted zone. This was attributed to the substantial difference in melting points

between liquid Ti and liquid Al. The early solidification of liquid Ti limited the mixing time between the two phases while the efficiency of mixing was directly influenced by the convection currents near the joint line.

It was possible to calculate the global dilution of Ti (d_{Ti}) using Eqn.56 from the areas of Ti-rich (A_{Ti}) and Al-rich (A_{A5754}) zones.

$$d_{Ti} = \frac{A_{Ti}}{A_{Ti} + A_{A5754}} \cdot 100 \qquad\qquad 56$$

As the laser beam position gradually shifted from Ti to Al, a consistent decrease in Ti dilution was observed, ranging from 67 at.% to nearly 0 at.% (Table 11). The centered beam position resulted in a mere 38.6% dilution of Ti, which can be attributed to its higher melting point compared to the aluminum alloy. This stepwise shifting of the laser spot not only reduced the Ti-rich areas of the melted zone but also influenced the mixing patterns between the Al and Ti liquids. When the welds were offset on the Ti side, a nearly straight interface between the Al and Ti-rich zones was observed, with mixing primarily occurring within a thin diffusive interface accompanied by localized fragmentation from convection. This restrained mixing was attributed to the formation of a stable keyhole entirely situated in the Ti-rich liquid which was previously observed by Casalino et al. [29]. On the other hand, for the laser spot positions $\Omega = 0$ and $\Omega = -0.1$ mm, the mixing had been more intense, indicating the mutual involvement of Ti and Al-rich liquids in the convection movements along the walls of the highly fluctuating keyhole. Interestingly, the maximum beam offset on the Al side ($\Omega = -0.2$ mm) resulted in minimal Ti melting and consequently no mixing occurred.
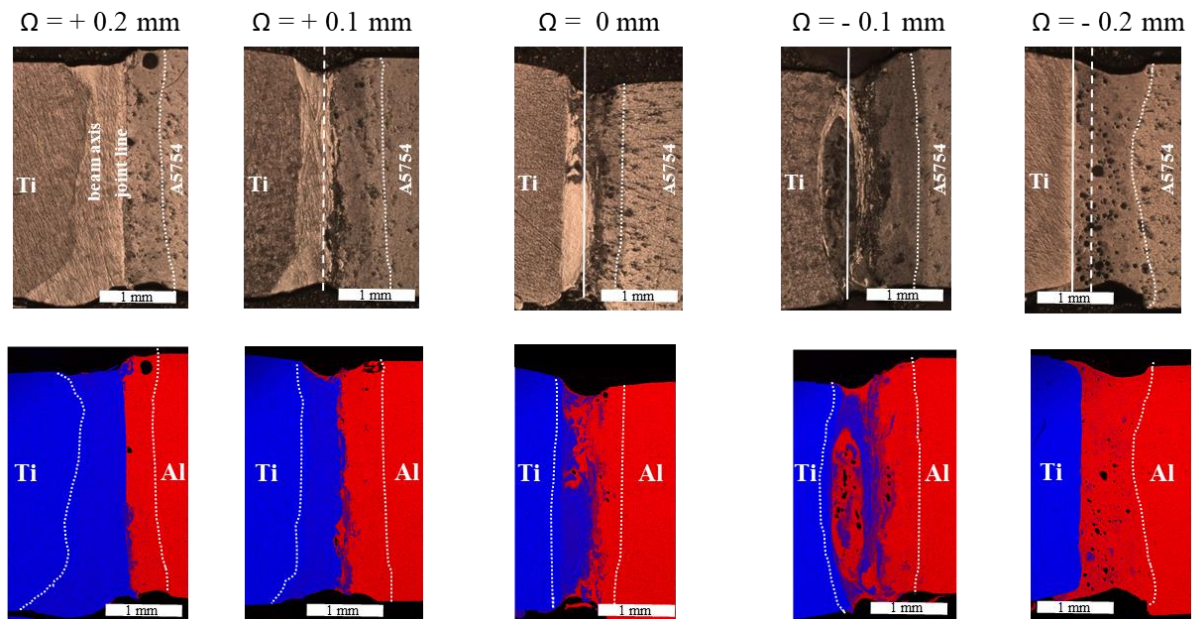
Figure 65. Optical microscopy and combined X-map view of weld crosscuts corresponding to the different beam offsets (laser power 3 kW, welding speed 3 m/min).

The welds with significant mixing ($\Omega = 0$ and $+0.1$ mm) exhibited the lowest ultimate tensile strength (UTS) among the samples, while those with a diffusive interface showed improved UTS (Table 11). Notably, the welds achieved their highest UTS value of 144 MPa when the beam offset on titanium was maximized, indicating the formation of a stable keyhole in the titanium material.

Table 11. Data from optical microscope and SEM-EDX.

Ω (mm)	d_{Ti} %	Average chemical composition (at.%)										UTS (MPa)
		Ti – rich zones					Al – rich zones					
		Ti	Al	Mg	Mn	Main phases	Ti	Al	Mg	Mn	Main phases	
+0.2	56.7	93.92	6.00	0.08	0.00	α-Ti	1.00	94.91	3.96	0.13	Al	131
+0.1	47.8	90.01	9.94	0.05	0.00	α-Ti +Ti$_3$Al	0.54	95.44	3.93	0.09	Al	44
0	38.6	77.77	22.00	0.23	0.00	Ti$_3$Al	0.27	95.65	3.99	0.09	Al	114
-0.1	9.4	67.60	32.00	0.40	0.00	Ti$_3$Al+ TiAl	11.00	85.63	3.37	0.00	Al+Al$_3$Ti	131
							1.16	94.62	4.00	0.10	Al	
-0.2	0	-	-	-	-	-	3.50	92.40	4.10	0.10	Al+Al$_3$Ti	144

For beam offsets of $\Omega \geq 0$, the melted zones exhibited Al-rich compositions similar to the A5754 alloy, with very low titanium content due to the limited solubility of titanium in aluminum. However, at a beam offset of $\Omega = 0.1$ mm, the intensified mixing process resulted in the formation of noticeable amounts of brittle Al$_3$Ti phase, as indicated in Table 11. In contrast, due to the favorable solubility of aluminum in α-Ti, the titanium-rich zones contained significant amounts of aluminum in the form of a solid solution and Ti$_3$Al phase. As the beam offset shifted from titanium to the joint line ($\Omega = + 0.2$ mm to 0 mm), the dissolved aluminum content progressively increased, ranging from 6 at.% (in the α-titanium solid solution) to 22 at.% (in the homogeneous Ti$_3$Al phase). Notably, at a beam offset of $\Omega = - 0.1$ mm, the intense mixing nearly dissolved the entire titanium-rich liquid, leading to the important formation of a high quantity of Ti$_3$Al and TiAl intermetallic phases. Lastly, a maximum beam offset of $\Omega = - 0.2$ mm resulted in the absence of a titanium-rich zone.

The examination of minor elements, namely Mn and Mg, offers further insights into the behavior of the melt, as indicated in Table 5. When the laser was offset on Ti, the Al-rich zones of the melt experienced a noticeable reduction in Mg and Mn compared to the initial amounts found in A5754 (4.00 ± 0.10 at.% Mg and 0.14 ± 0.15 at.% Mn). In contrast, the Ti-rich zones contained only negligible quantities of Mg and no Mn. A similar pattern was observed when the laser was centered, but the Mg content in the Ti-rich zone became more prominent, potentially due to the smaller volume of molten Ti.

When the keyhole was completely moved in the Ti-rich liquid, the Ti-rich melt reached its maximum temperature and lifetime, facilitating the diffusion of Mg and Mn atoms from the Al-rich zone into the Ti-rich zone, followed by evaporation from the keyhole. The presence of Mn I lines in the plume, even with an offset of $\Omega = 0.2$ mm, when the keyhole is distant from the A5754 alloy correlated with this observation (Section 3.2.3).

In a unique case ($\Omega = - 0.1$ mm) Al-rich area is observed to be encased within a fragmented flow of Titanium (Ti). This isolated Al-rich area lacked Mn and had only a minimal Mg content of 3.37 at.%, signifying substantial elemental loss due to evaporation. Adjacent to this, the Ti-rich flow held 0.40 at.% Mg and was devoid of Mn. However, the outer part of the Al-rich area, on the other hand, had an Mg content near to that of the base material while there was a reduction in Mn, down to 0.01 at.%.

This pattern suggested that the keyhole was present in a region of intense mixing which allowed a loss of the elements of the alloy through vaporization. However, the resulting colder plume did not provide sufficient energy for the effective excitation of Mn atoms. This led to weaker emission lines, as depicted in Figure 63 (b).

Lastly, the maximum shift of the keyhole on A5754 ($\Omega = - 0.2$ mm) led to a uniform decrease in Mn content to 0.01 at.% without significant alteration in Mg quantity, indicating a lower

temperature of the keyhole and less intense evaporation process. This aligned with the formation of a less luminous plume (Figure 53 (a)) and emission lines with lower intensity (Figure 63 (b), (c)).

3.5. Continuous welding: conclusions and perspectives

The vapor plume from the dissimilar welding of T40 and A5754 was critically studied simultaneously using spectroscopic characterization and high speed imaging techniques in situ. The vapor plume morphology, brightness, and estimations of temperature were studied for different welding conditions. The vapor plume characteristics inferred from the obtained results were associated with the post-mortem analysis of the welded joints.

A stable and intensely luminous vertical plume was observed for standalone titanium. The plume's temperature, estimated from the emission spectra comprising only Ti I, was determined to be 9795 ± 394 K. The resulting welds displayed a remarkably regular profile, indicative of the formation of a stable keyhole.

During the continuous welding of standalone A5754 alloy, a much less luminous and highly diffuse plume was observed, which was associated with intense spattering. Due to its low temperature, several expected lines of Al I could not be detected, while the detection of Mn I lines was possible due to the lower energy level of the first excited state for Mn. The estimation of the plume temperature using the Boltzmann plot method was not possible. However, it can be inferred that the plume temperature must be close to the boiling point of the alloy. The plume presented itself in the form of vertical outbursts, which were random for a low welding speed and periodic at higher speed, reflecting the unstable behavior of the keyhole. Consequently, the produced welds exhibited significant surface roughness at low speed and periodic bumps at high speed. It was noted that further investigation of other spectral regions was necessary to identify more observable lines of Al.

In dissimilar welding with the beam centered on the joint line, the simultaneous formation of an inclined vapor jet reflecting the instability of the keyhole wall on the liquid aluminum side, and a vertical vapor jet representing the contribution of Ti evaporation, was observed. At a low welding speed, these jets were present simultaneously, and their intensity fluctuations remained correlated. At a higher speed, the plume underwent periodic inclination, where the vertical position of the jet coincided with the intense expulsion of matter due to the boiling of Ti, which was associated with the formation of a hole-like defect.

The plume temperature in dissimilar welding was found to be lower than that of standalone Ti welding, estimated to be 5967 K. This estimation supported the hypothesis of the keyhole being shared between liquid titanium and aluminum.

The plume was found to exhibit increased luminosity and stability, with temperatures ranging between 5000 and 6000 K, when the beam was offset on the titanium side. This offset resulted in reduced spattering and minimized mixing between the melted materials, consequently having maximum joint Ultimate Tensile Strength (UTS). Notably, Mn I lines were still observed in the plume, originating from the evaporation of Mn atoms that had diffused from the Al-rich portion of the melt.

Conversely, when the beam was offset on the A5754 alloy, the plume experienced attenuation while spattering intensified. The intensities of both Mn I lines, and continuous thermal emission decreased, suggesting a complete shift of the keyhole within the liquid Al, starting from the tangent position of the laser spot to the joint line.

For all tested operational conditions in dissimilar welding, the evaporation process involved both the molten materials, since all spectra had Ti (I) and Mn (I) lines, however this did not

signify that the actual keyhole was shared between Ti-rich and Al-rich liquids at all times. And while Mn (I) lines were observable in the 467 nm spectral region the line of Al (II) is not observed in this region, which signified that there was no ionization of Al.

The keyhole was found to be completely in Ti-rich liquid for the maximum laser displacement on Ti (+ 0.2 mm), and this resulted in a highly luminous and stable plume with negligible spattering. Moreover, the absence of mixing between Ti-rich and Al-rich liquids facilitated the formation of a stationary, undisturbed keyhole. A tangential beam offset on Ti (+ 0.1 mm) also led to the formation of the keyhole primarily in the Ti-rich liquid due to the lack of intense mixing between Ti and Al. Notably, the layer of liquid Al likely had to have been melted by conduction.

Centered beam position apparently involved both materials, because of intense convective mixing in the melted zone, associated with formation of fluctuating plume with periodical inclination towards Al side, which signify the instability of keyhole wall formed from Al side.

The displacement of the beam on A5754 was associated with progressive increase of spattering in the rear and lateral (towards A5754) directions. Attenuation of the plume luminosity was observed from beam offset of (- 0.1 mm) on A5754 while associated with important dissolution process between molten materials. This indicated the preferential formation of the keyhole in Al-rich liquid. Complete (- 0.2 mm) beam offset on A5754 leads to very low melting of Ti and the keyhole entirely situated in Al alloy.

The vapor plume observations constituted the most interesting part in this study. We observed the process of excitation of atoms due to thermal radiation. The vapor jet exiting the keyhole was very dense and behaved similar to a blackbody, which explains its nature of emitted thermal radiation. Yet, the plume was transparent to the Yb:YAG laser radiation. May be the periphery of the vapor plume has lower density, and this was why atomic emission was observable. In this way, it can be hypothesized that the atoms were excited only from thermal radiation i.e., the population of the energy levels follows Boltzmann distribution. Moreover, since the thermal radiation varies according to Planck's law, it was understandable that there is a correlation between the emission curve of the black body and the excitation of the atomic levels. In the same way, the absence of thermal radiation and atomic emission in shorter wavelengths (lower than threshold wavelength) regions can be justified.

Especially in dissimilar welding, the peak at 401.8 nm which contained both Ti (I) and Mn (I) lines demonstrated the variations in the plume behavior with the variation of laser displacement from joint line. The resulted intensity was determined by Ti (I) and then by Mn (I) contribution. However, the same could not be done for peak at 400.8 nm which contained two lines that were difficult to deconvolve due to the fluctuations of the spectra. Ti (I) emissions still present in the plume for the maximum beam offset on A5754 correlated with the fact that the melted zone also contained some quantity of Ti. To progress further, it would be necessary to take into account the rapid fluctuations of the spectra, which are significant, since the plume evolves temporally in continuous welding. Similarly, from HSI the relationship between the welding speed and the observed periodicity in the inclination of the vapor plume is not clear. This necessitates the observation of the vapor plume with spectroscopy and HSI in lower time frames in the range of a few milliseconds to verify if these conclusions are valid.

Chapter 4. Phenomenology of pulsed welding

4.1. Introduction

Following continuous welding experiments, it was concluded that examining the front view of the vapor plume in lower time frames (several milliseconds) was necessary to gain a better understanding of the inclined vapor jet phenomenon and its spatial and temporal characteristics. One of the challenges encountered during the experimental process was determining the appropriate laser power and pulse duration, as well as the parameters for HSI and spectral acquisitions to have observable plume formation in each material separately and also in their dissimilar combination. This posed a significant obstacle, as these variables can significantly affect the quality and repeatability of the results. The selection of the laser fiber was also deemed to be important. The 600 µm fiber was chosen for the laser based on the reasoning that a wider laser spot diameter would lead to a broader keyhole opening and thus, a bigger plume. And the previous tested 5 laser spot positions in continuous welding were also applied for pulsed welding. However, the change in the laser spot diameter from 200 µm to 600 µm led to the sharing of the laser energy on both the materials for all laser spot positions. This was an important consideration because the keyhole opening plays a crucial role in laser welding, and any changes to the keyhole could significantly impact the vapor plume behavior.
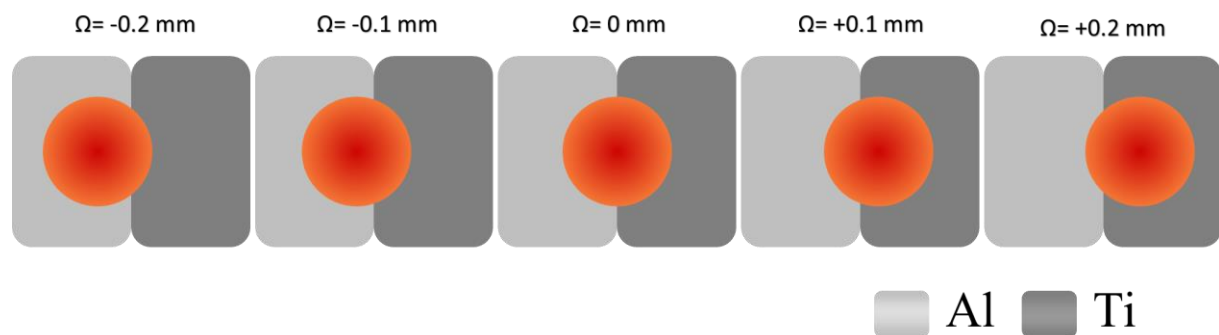
Figure 66. Schematic for the 5 different laser spot positions in pulsed laser welding of dissimilar materials.

So, in order to observe/study the phenomenology of dissimilar plume above the butt-joint, the HSI camera was always placed in the front and the spectrometer acquisitions were made from the A5754 side. Another added advantage of this setup was that since the welding table does not move during the laser pulse duration, there was no interruption of the optical signal for the spectrometer by the plate holders.
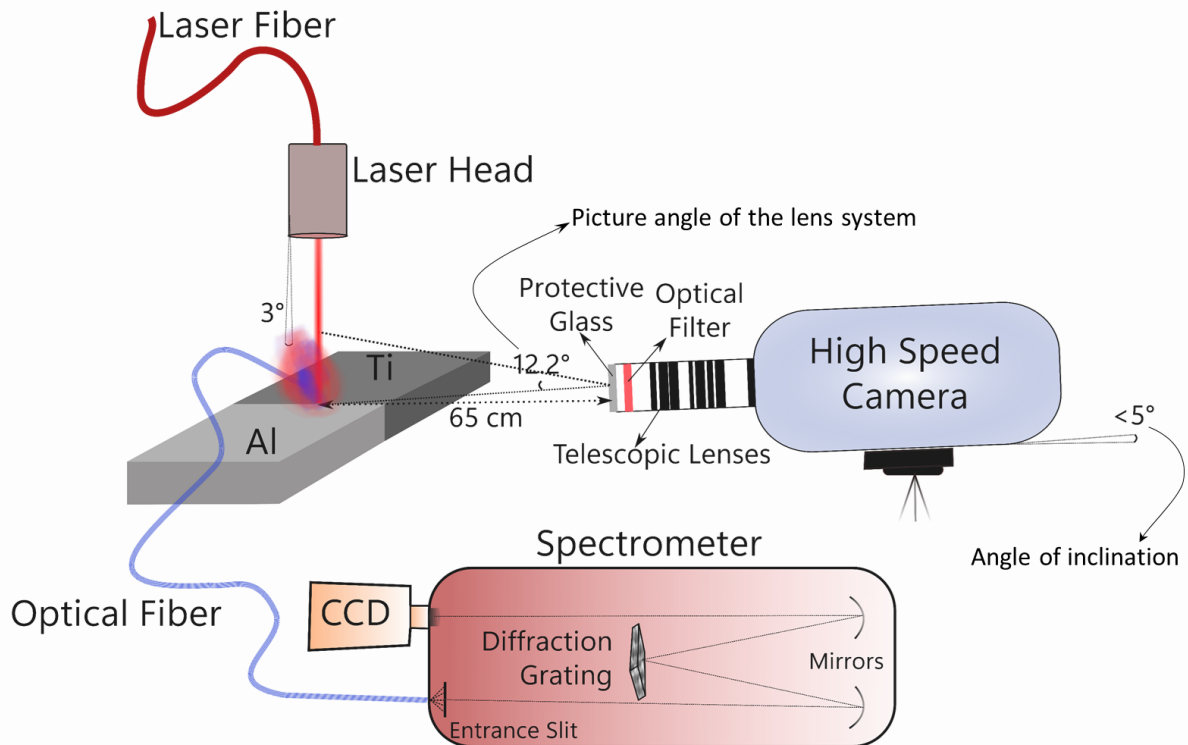
Figure 67. Schematic for pulsed welding experiments in butt-configuration.

The primary objective of the initial experimental campaign was to observe the plume behavior during the initiation of the keyhole at the beginning of the pulse. In addition, it was also useful to establish the welding parameters required for pulsed welding in the butt-configuration, especially the optimal laser power and pulse duration for studying the vapor plume and keyhole behavior. Additionally, it was necessary to formulate a better image processing methodology than what was done for continuous welding.

4.2. Preliminary studies

4.2.1. HSI acquisitions using 810 nm bandpass filter

4.2.1.1. Laser and HSI Parametrization

The initial set of experiments was done with laser powers from 400 W to 3 kW and pulse times 1 ms to 6 ms with the HSI in the front view and the spectral acquisition from the A5754 side as shown in the schematic (Figure 67). HSI videos were captured for these welding parameters with the Phantom v9.1 camera attached with an 810 nm optical bandpass filter. The HSI camera was at an angle (~ 13°) with respect to the horizontal plane. At the wavelength of 810 nm, the continuous thermal emission of the vapor plume is observed.

Based on the continuous welding experiments (section 3.2, p.79), and the visual observation of the plume characteristics during pulsed welding, it was identified that the titanium plume (clearly visible even at 10 μs) was too bright, leading to sensor saturation and subsequent image distortion, particularly under high exposure conditions. Conversely, the aluminum plume (poorly visible even at 520 μs) was found to be very dull, especially when lower powers, durations, and exposures were used. Therefore, 120 μs was chosen as the optimum intermediate value for the pulsed welding experiments. The different plumes when observed with an exposure of 120 μs for different laser powers are represented in Figure 68. It could be observed

that for the titanium plume, image bleeding from over-saturation could be observed from 800 W. Because titanium has a high absorption coefficient (Table 2, p.57) leading to a bright plume/keyhole formation even for the laser power of 800 W. And aluminum with low absorption needs much more power (at least 2.6 kW) to form a similar plume. The faintest of plume appearance only starts at 2 kW for Al. Therefore, a compromise was necessary in the choice of the welding power in order to have the best possible outcomes for HSI.
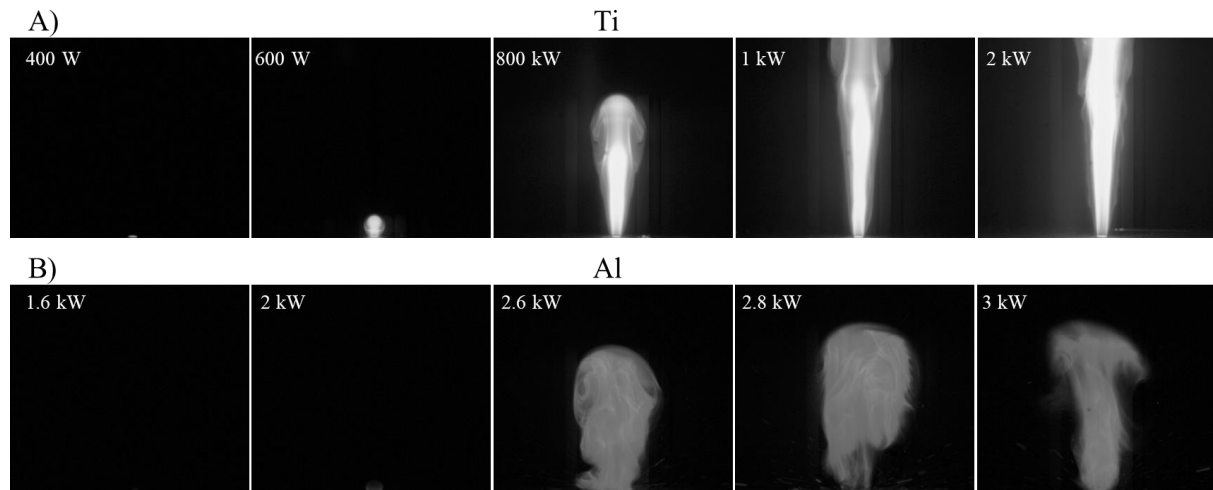
Figure 68. Vapor plume images (at maximum height) for 2 ms pulses on standalone materials for 120 μs exposure time, A) Titanium, B)Aluminum.

The laser welding parameters were chosen to be 2 kW laser power and 2 ms laser pulse duration. The HSI videos which were captured at 6400 fps at 480 x 480 resolution with an exposure time of 120 μs. No additional illumination was used.

First the videos were converted from .cine to .tif format (section 2.3.2.1 p.68). At 6400 fps, every 2 ms pulse every video should constitute a stack of 13 images (Figure 69) with during which the laser pulse was active among several 100s of images, However, it was noted that the time required by the laser to heat the material before the start of the vapor plume jet, and the vapor plume or spatters present after the end of the laser pulse constituted a stack of images that were more than 13 in number (~ 60 frames).
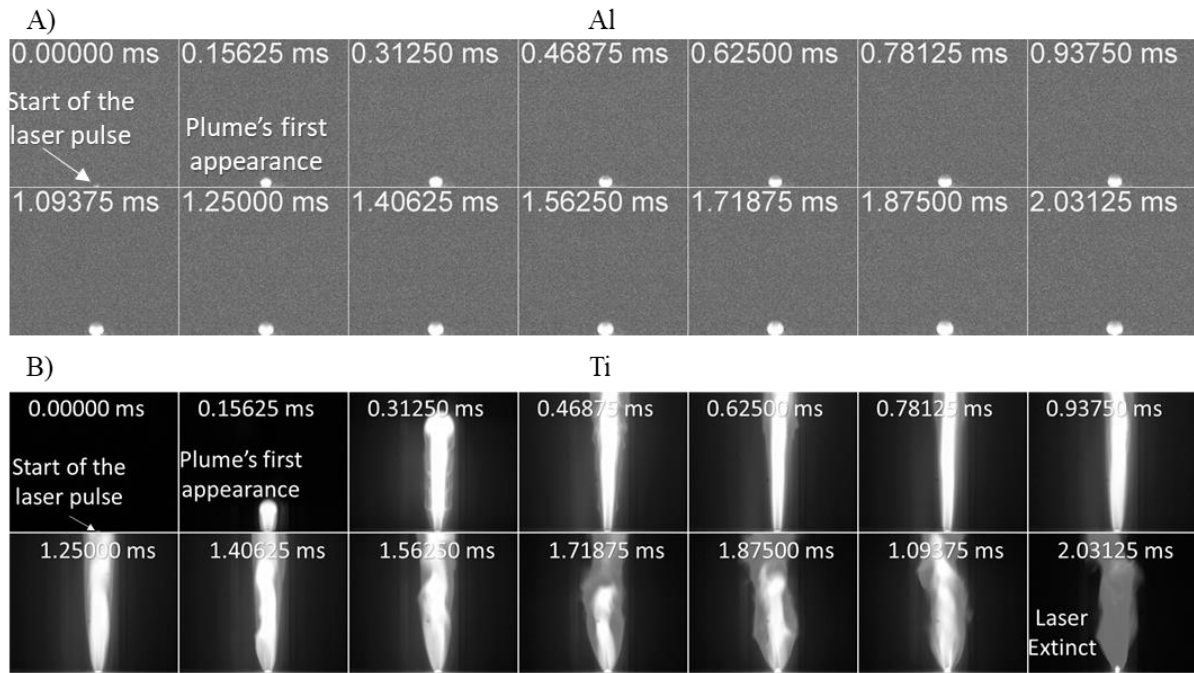
Figure 69. Stack of 13 images of the standalone A) Aluminum (brightness, contrast adjusted) and B) Titanium plume including the start of the pulse. (810 nm, 2 kW, 2 ms).

4.2.1.2.   Image Processing Methodology

Using ImageJ, these stacks were separated and then they were cropped manually for each video to remove the melted zone to allow only the vapor plume to be present in the video. This process had to be done manually because very small changes in the positions of the camera that occurred during manual focusing led to changes in the position of the point of impact of the laser on the metal in the images.

And also, due to the varying plume brightness between the different materials or the laser spot position relative to the joint line, the gray values had to be normalized by equalizing the stack histogram. However, such a normalization method also augmented the background noise, the bleeding effects and other artifacts produced from not imaging in ideal conditions (Figure 70).
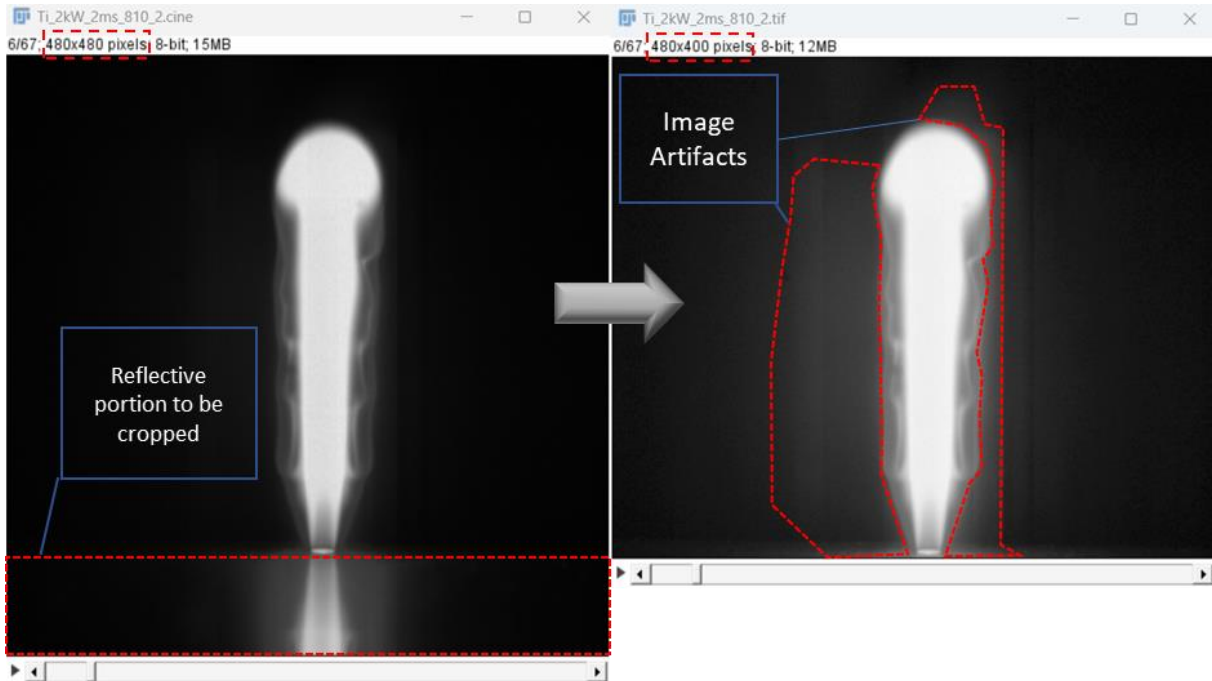
Figure 70. Cropping and normalization of gray values from original image for 810 nm titanium plume.

In order to remove the augmented image artifacts after normalization, thresholding of the stacks with a lower limit of 128 for the gray value was done, 128 being 50% of the maximum gray value 255 for an 8-bit image. As this thresholding step allowed image segmentation into the plume and non-plume zones, the next step was to find an appropriate method to measure the plume characteristics.

The measurement of the plume profile remained a difficult task as it was an irregular and continuously changing shape. However, to quantify the plume profile, it was assumed that the plume can be approximately bounded within the perimeter of an ellipse. And so, with this approximation, the lengths of the major axis, the minor axis and the angle of the major axis of the ellipse with respect to the horizontal corresponded to the height, the width and the angle of the vapor plume. The fitting of this ellipse to the plume profile was done in conjunction with the previous step of the thresholding in ImageJ by first setting the threshold by "Image>>Adjust>>Threshold>>Set" (Figure 71.A) and entering '128' in the "Lower Threshold Level" field (Figure 71.B). This allows setting the minimum threshold to 128 for measurement without modifying the image. Without applying this threshold to the image, the 'Threshold' window was closed to perform the measurement by first setting the measurements to be made by "Analyze>>Set Measurements" (Figure 71.C) and checking the boxes for 'Fit Ellipse' and 'Limit to threshold', and then actually performing the measurements by "Image>>Stacks>>Measure Stack..". This would create a 'Results' window (Figure 71.D) with the lengths of the major and minor axes and the angle of the major axis for each ellipse that was fit on the plume edge limited within 128-255 threshold for every image in the stack. This data is then sometimes pre-processed by setting the scale for the image or later treated in post-processing by converting the number of pixels to millimeters (the values for the Major and Minor axes shown in the 'Results' window Figure 71.D are calculated in pixels' unit length), changing the angle values to be relative to the vertical Figure 71.E, etc.
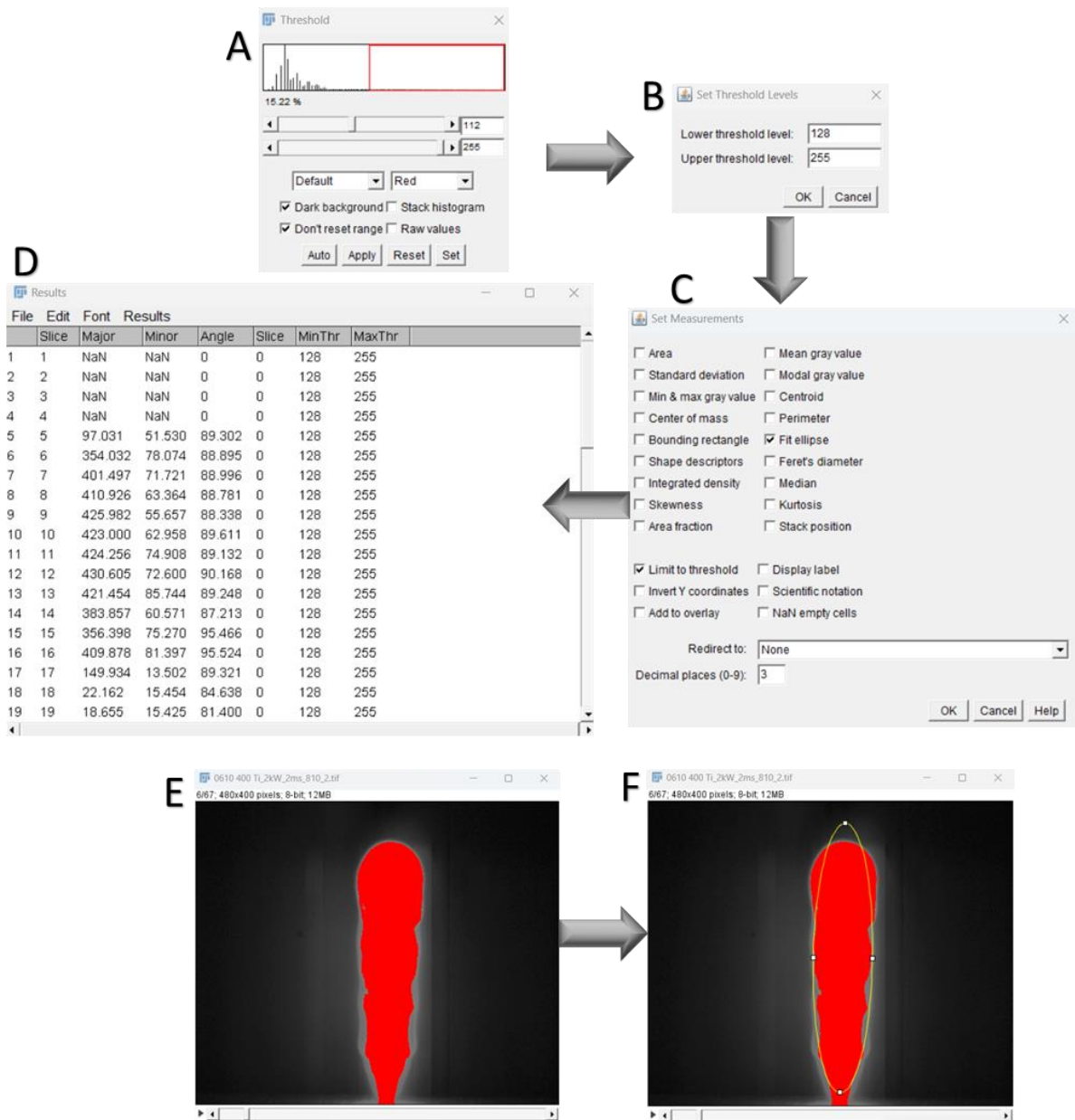
Figure 71. A, B, C, D) Image processing method in ImageJ; E) 128-255 threshold on a plume sample; and F) Fitting Ellipse on the selection.

As it can be noted from Figure 71.F, the dimensions of the ellipse (lengths major and minor axes) only approximately match the dimensions of the plume. The magnitude of this incertitude in the spatial dimensions of the plume was however less than 10 % of the size of the plume.

Another type of uncertainty lies in the calculation of the average of the property from multiple videos. This incertitude (Y-error bars in Figure 75, Figure 76, Figure 77) arising from averaging the height, width and the angle of the plume from several videos (A5754 : 3, T40 : 13, for each laser spot position of A5754/T40 dissimilar plume : 9), is calculated using the half-range formula:

$$Uncertainty\ in\ Y-axis = \frac{Maximum\ value - Minimum\ value}{2} \qquad 57$$

Equally important was the incertitude in the temporal scale because the exact frame in the video at which the laser pulse began was unknown. For the frame rate of 6400 fps, the two

consecutive images n and $n+1$ are separated by the time lapse $(t_{n+1} - t_n)$ of 156 µs. Therefore, the incertitude of ± 78 µs to the interaction time corresponded to each image.

The axial (V_z) and transversal (V_r) velocities of expansion of the plume envelope (Figure 72) were evaluated basing on the average values of height and width according to the expressions:

$$V_z = \frac{H_{n+1} - H_n}{t_{n+1} - t_n} \qquad\qquad 58$$

$$V_r = \frac{W_{n+1} - W_n}{t_{n+1} - t_n} \qquad\qquad 59$$
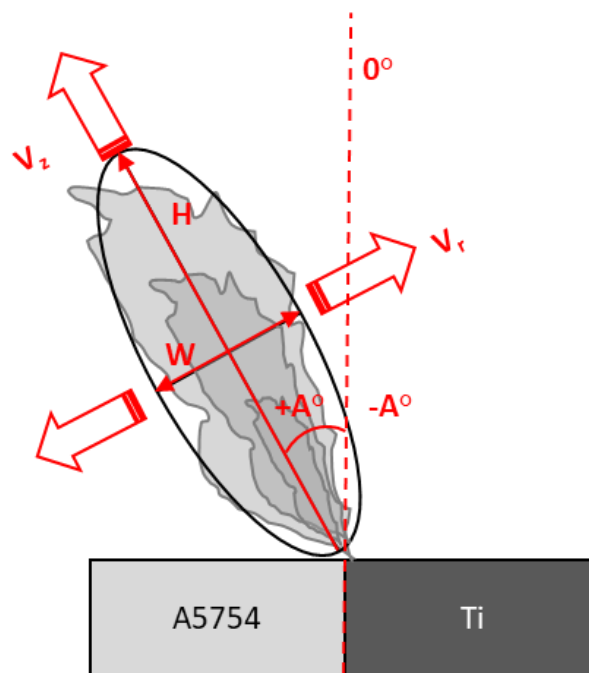
Figure 72. Schematic representation for the axial and transversal velocities of the plume expansion.

4.2.1.3. General observations on plume behavior and morphology

Since the 810 nm optical bandpass filter allowed acquisition of the continuous thermal emission of the vapor plume, originally it led to very dull images for standalone aluminum alloy and to very bright plume images for titanium. This problem was however treated by normalization (section 4.2.1.1, p.100). The experimental results revealed a distinct difference in the behavior of the vapor plumes formed by the standalone materials. Specifically, the aluminum alloy plume adopted a stagnant spherical shape, while the titanium plume took on a mushroom-like form that quickly transformed into an intense vertical jet, with some turbulence emerging towards the end of the pulse (Figure 73).
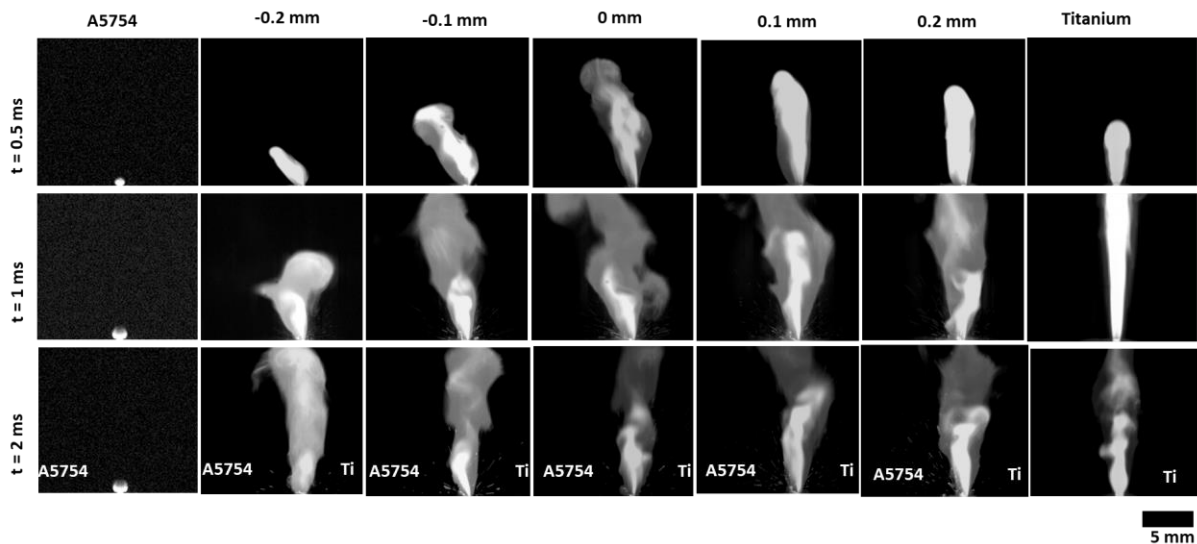
Figure 73. Side by side comparison of the standalone and dissimilar plumes at different instances (810 nm, 2 kW, 2 ms).

The images of the plume with laser pulse centered on the dissimilar joint line (Figure 74) were with an intermediate level of luminosity. These plumes appeared more diffuse and turbulent compared to those of the standalone titanium. And also, a distinct inclination to the aluminum side was noted. Common sense dictates that the dissimilar plume (Figure 73, Figure 74) behavior according to the laser spot position can be attributed to several factor such as, the lower absorption, higher reflectivity, and greater thermal conductivity of aluminum relative to titanium, as well as the difference in their respective vaporization temperatures (Table 2, p.57). It would also seem that the amount of absorbed laser irradiation of the titanium side of the dissimilar joint would make a major contribution to the local heat transfer. While the dissimilar plumes with the laser spot positions moved towards the aluminum side appeared to be more inclined, when the laser spot positions were moved towards titanium from the joint line, they are more vertical in nature. The beam offset on aluminum augmented the plume's inclination and decreased its height, whereas the beam offset on titanium produced plumes that were higher and less inclined.

This clear inclination towards the aluminum side is not only related to the laser spot's position relative to the joint line but also the interaction time, as it can be seen at the 0.5 ms mark of Figure 73, the dissimilar plumes (especially with the laser spot centered on the joint line and moved towards aluminum) appear more inclined, while they are mostly vertical at the 2 ms mark.
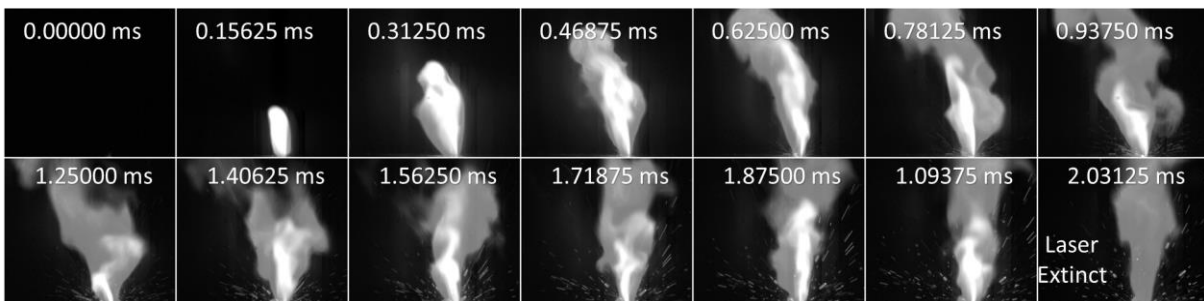
Figure 74. Stack of 13 images of the dissimilar plume (Ω = 0 mm) including the start of the pulse. (810 nm, 2 kW, 2 ms).

106

The "Fit ellipse" tool was an effective means of quantifying the dimensions and orientation of the plumes discussed earlier. Through visual analysis and the data generated by this tool (Figure 75), it was confirmed that the standalone aluminum vapor plume had a spherical shape with a height less than 1 mm throughout the pulse duration. In contrast, the titanium plume quickly expanded to up to 14 mm, occasionally exceeding the field of view. The dissimilar plume displayed intermediate behavior depending on the laser spot position relative to the joint line. As the laser spot shifted from aluminum to titanium, the plume height also increased accordingly. However, when the maximum laser displacement was applied to aluminum, the plume height temporarily decreased after the initiation stage. A similar pattern was observed on pure aluminum, even though on a smaller scale. The momentary decline in plume intensity can be credited to the elimination of the alumina layer, which intensely absorbs the laser radiation until it is replaced by the remarkably reflective liquid aluminum. This substitution can be associated with a temporary reduction in surface temperature. In the case of other beam offsets, the height of the plume remained only slightly lower than that of standalone titanium, emphasizing its significant role in the vaporization process.
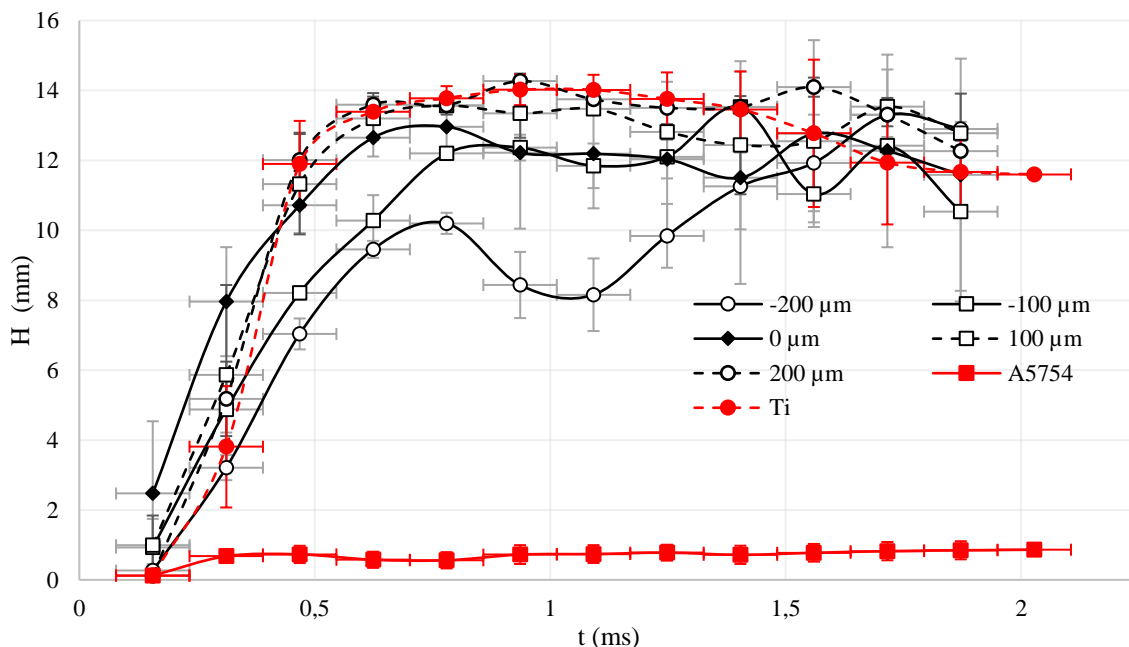
Figure 75. Evolution of the vapor plume height on standalone materials and dissimilar welding with different laser spot positions during a 2 ms, 2 kW laser pulse.

The vapor plume width (Figure 76) surpasses the diameter of the laser spot (600 µm) in all conducted experiments. While standalone aluminum welding results in a plume with a minimum width of below 2 mm, standalone titanium exhibits a maximum width of 3 mm. However, dissimilar joints generate a considerably wider plume (up to 6 mm) for all tested beam offsets. This may be attributed to the presence of two competing jets: a vertical jet and an inclined jet. The widening of the plume could have occurred from the mixing of these two vapor jets, leading to an enhancement in turbulent effects. Moreover, in experiments with laser displacements of 0, -100 µm, and +100 µm, a reduction in width is observed towards the end of the pulse as the competing jets merge into a unidirectional jet.
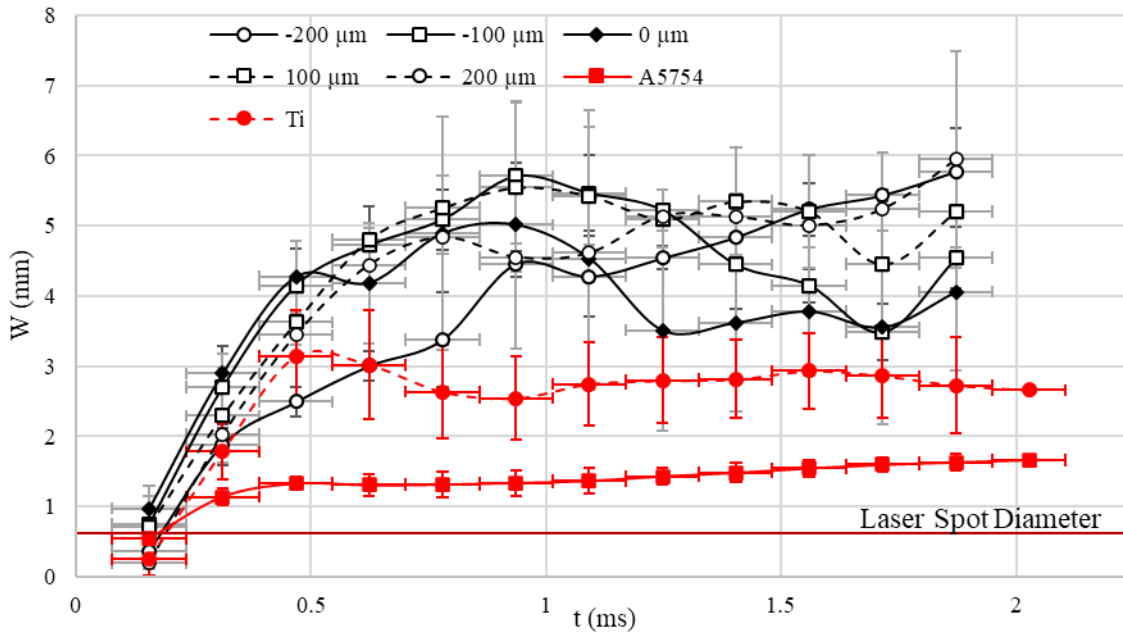
Figure 76. Evolution of the vapor plume width on standalone materials and dissimilar welding with different laser spot positions during a 2 ms, 2 kW laser pulse.

For all the laser spot positions, the average angle of inclination of the vapor plume towards A5754 (Figure 77) peaks between 0.5 and 1 ms. When comparing the plume inclinations during this initiation period between the different laser spot positions, it is observed that the inclination is proportional to the beam offset on A5754. While the laser spot displacement towards Ti ($\Omega = +0.1$ and $+0.2$ mm) produces a plume with $< 15°$ inclination towards A5754, the plume angles for beam offsets on A5754 ($\Omega = -0.1$ and -0.2 mm) were much higher ($> 30°$). When the plume reaches the highest inclination for the respective laser spot positions, a short period of stagnation in the inclination values is observed. After the stagnation period, the plume angle reverts back to vertical.
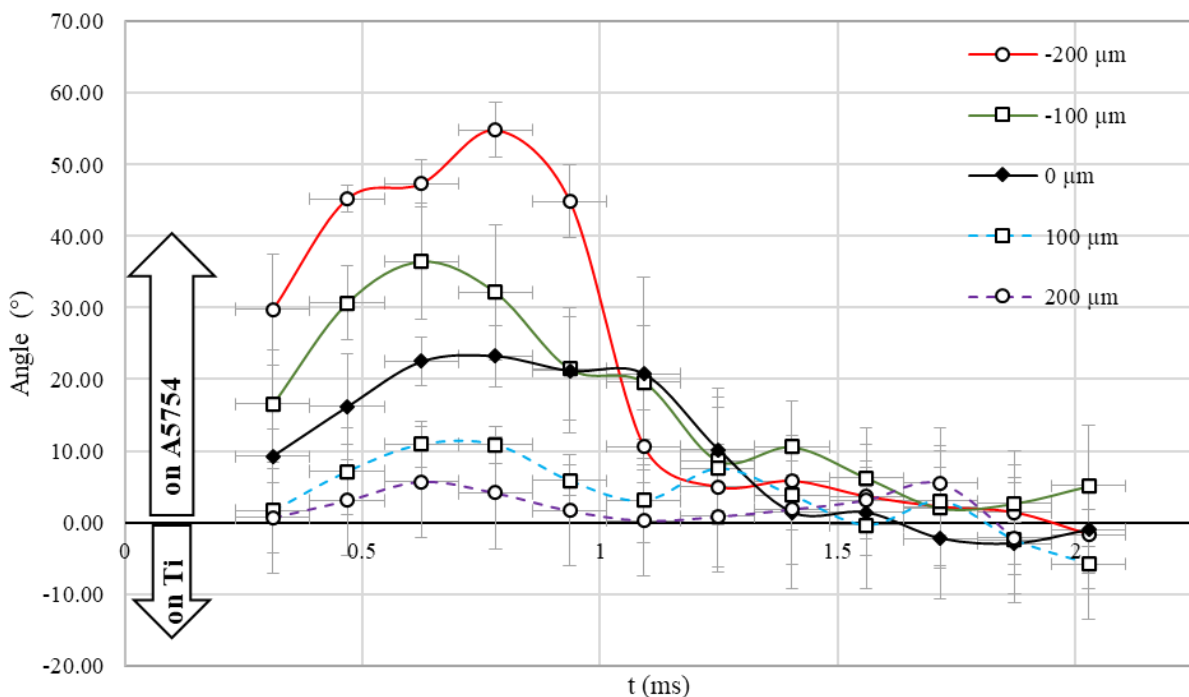
Figure 77. Evolution of the vapor plume inclination angle for dissimilar welding with different laser spot positions during a 2 ms, 2 kW laser pulse.

108

The maximum average inclination of the vapor plume towards the A5754 side (Figure 78) was directly proportional with the amount of laser incident on A5754. The minimum inclination or the inclination towards the T40 side do not exhibit such behavior.
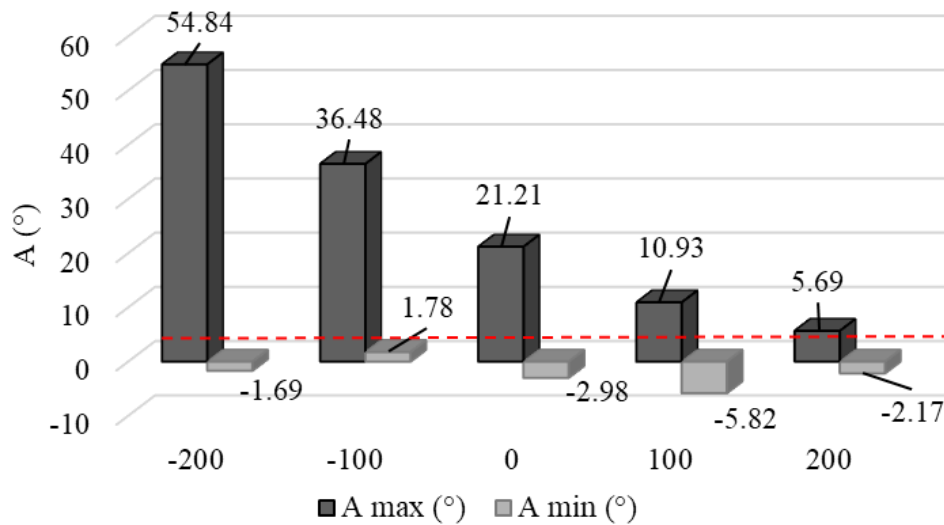
Figure 78. The evolution of maximal and minimal observed inclination angles for the dissimilar joints with different Ω.

During the initiation stage, the average of plume expansion velocities (Figure 79) of pure A5754, T40, and the dissimilar joints exhibit notable differences. Standalone A5754 produces a plume that expands uniformly in both axial and transversal directions at a velocity of approximately 3.5 - 4 m/s. On the other hand, the pure T40 alloy generates a much faster plume with a significant axial expansion velocity of 38 m/s and a transversal velocity of 9 m/s. These differences in plume behavior are due to the differences in the laser absorption coefficients and thermophysical properties of the two materials. Examining the plume velocities in dissimilar joints highlights the increasing influence of the T40 alloy as the laser spot displacement shifts from A5754 towards T40. Such beam offset leads to an upward trend in the axial velocity that approaches the value for pure T40, and also indicates higher temperatures in the interaction zone due to the prominent contribution of the T40 alloy. The transversal velocity shows a different behavior with a low value of 6.8 m/s for the maximum beam offset towards A5754. For the rest of the laser spot positions, the values are approximately 10 m/s which are close to that of T40.
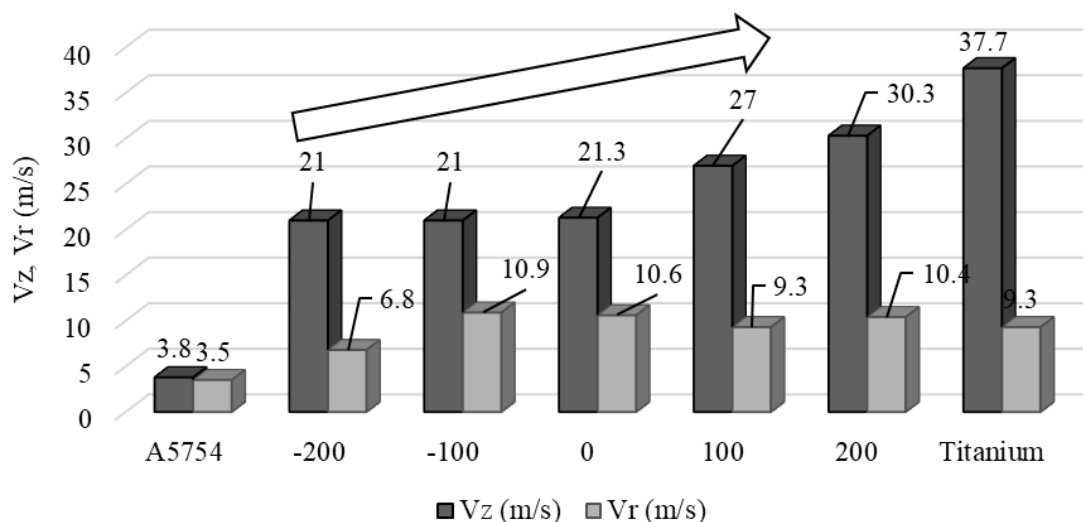
Figure 79. Average plume expansion velocities in the axial and transversal directions during the initiation phase.

4.2.2. Post-mortem investigation

SEM-EDS analysis (Figure 80) showed distinct and characteristic patterns of melt ejection and spattering, with a pronounced preference towards the aluminum side, correlated by the observed plume inclination. Remarkably, for the maximum beam offset on A5754 ($\Omega = -0.2$ mm), the entirety of the melted zone was confined to the aluminum side, while localized ejection of melted titanium was also observed towards the aluminum side within the melted zone.
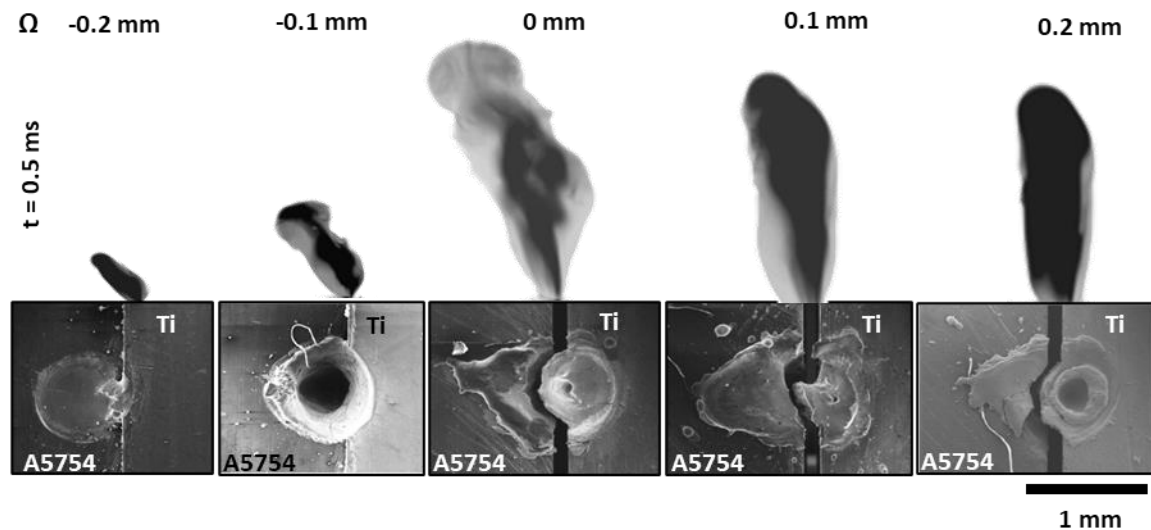
Figure 80. Aspects of the impact zone observed by SEM compared with plume inclination for t = 0.5 ms.

For $\Omega = -0.1$ mm, the observation revealed the emergence of a distinct keyhole formation occurring during rapid solidification of the molten material. Notably, the keyhole exhibited an inclined opening towards the aluminum side, with the right portion of the melted zone enriched in titanium and the left part comprising a mixture of both materials (Figure 81.A). The offsets $\Omega = 0$ and $+0.1$ mm exhibited analogous melt aspects, characterized by elongated ejections of the mixed melted zone towards the aluminum side (Figure 81.B).

A unique formation occurred in the morphology of melted zone when employing the maximal offset on the titanium side ($\Omega = +0.2$ mm). The presence of two discernible solidification fronts could be explained as follows: Initially, ejection of the Ti/Al mixture occurred on the aluminum side similar to the preceding cases. However, there is a second solidification front, a donut-shaped formation of melted titanium region surrounding the keyhole opening. Significantly, this melted titanium region displayed an absence of discernible inclination towards aluminum (Figure 81.C).
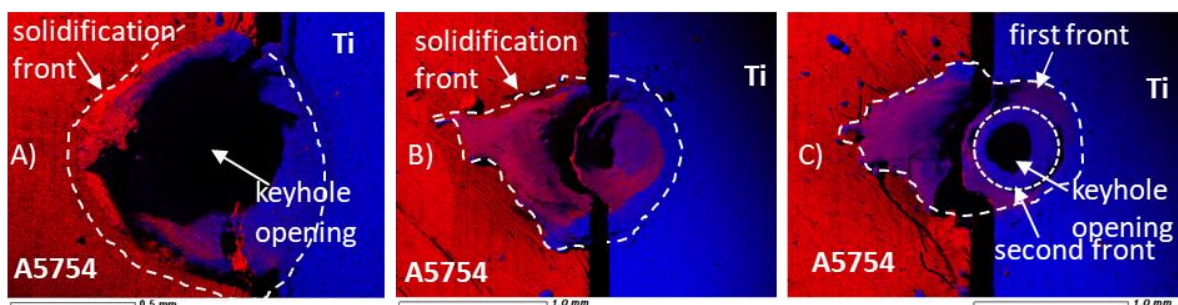
Figure 81. X-mapping of Al (in red) and Ti (in blue) distribution in the melted zones with beam offsets on A5754 of A)-100 μm, B) 0 μm and C) 200 μm

4.2.3. Insights into keyhole dynamics within 2 ms by HSI and post-mortem analysis

4.2.3.1. Conclusions from the preliminary investigations

It was understood from the previously discussed results and conclusions from HSI and post-mortem analysis that the plume inclination can occur not only in continuous welding but also in pulsed welding with pulse times as short as 2 ms.

Standalone aluminum welding produced a small spherical vapor plume with approximately 1 mm diameter, while standalone titanium produced a strong vertical jet that showed no significant inclination. In contrast, the dissimilar plume showed inclinations towards A5754 with angles dependent on the position of the laser spot to the joint line and time period, with inclination increasing when the laser spot moved towards aluminum and decreasing when it moved towards titanium. Furthermore, for all beam offsets, maximum plume inclinations were observed during the first millisecond and declined thereafter.

From temporal analysis, it was observed that in pulsed welding, the inclination of the plume appeared mostly at the beginning of the pulse. Whereas in continuous welding at a high welding speed, the inclination of the plume happened periodically. It is reasonable to assume that this periodicity in continuous welding happens because new parts of the metallic plates become involved in the melted zone with time.

These observations led to the hypothesis that different stages of plume inclination correspond to different stages of keyhole development. In particular, for $\Omega = +0.2$ mm, which corresponds to 5/6 of the beam diameter on the titanium side, the presence of two solidification fronts can be explained in the following manner: at the beginning of the pulse, the plume is slightly inclined. The melted zone is ejected on the A5754 side. Later, the second solidification front which is symmetrical and composed only of Ti corresponds to the formation of the vertical plume jet as the keyhole is drilled deeper on the Ti side. On the other hand, the other beam offsets only show the melted zones with pronounced ejection on the A5754 side.

Based on these observations, it can be deduced that the inclination of the plume and its evolution during the pulse must be due to the transformation of the keyhole profile (Figure 82) based on the following reasons:

- The prominent inclination of the plume towards aluminum was attributed to the preferential evaporation from the titanium surface, which must be more than the evaporation from the more reflective and conductive aluminum side of the joint.
- In addition, the formation of the keyhole must have been initiated on the titanium side, and the emerging curvature of the free surface must have allowed the Ti-rich jet to escape freely (perpendicular to the keyhole wall) to appear inclined towards the opposite aluminum side (Figure 82.a).
- Simultaneously, the impact of this energetic and high-velocity titanium jet impinges on the aluminum surface at the joint line, leading to its liquification and causing the expulsion of a mixed melted spatter onto the surface of the aluminum plate. These events mark the stages of plume initiation and the subsequent stagnation.
- As the molten material continues to receive an amplified amount of laser energy, the keyhole propagates in depth (Figure 82.b). The previously escaping Ti-rich jet that remained unaffected in its original direction during the previous stages cannot escape a deeper keyhole directly from the keyhole wall. So, the vapor plume that escapes the keyhole becomes a mix of the aluminum and titanium vapors which leaves in a vertical manner. This phenomenon is able to explain the third stage of plume evolution : recompensing (p.108).
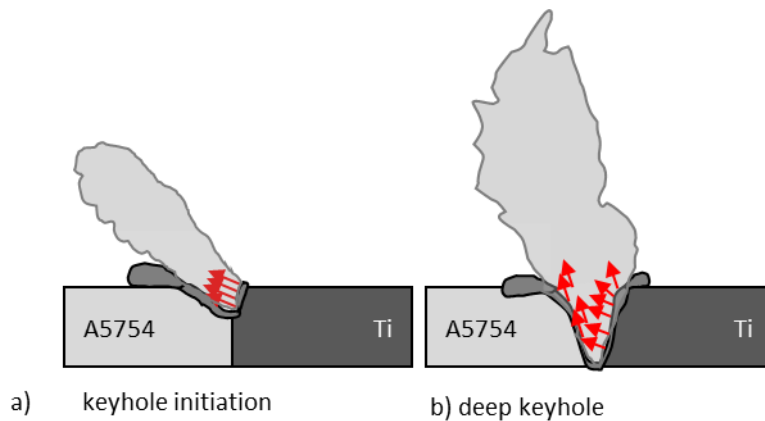
Figure 82. A sketch of plume inclination related to the evolution of the keyhole shape for centered beam position (direction of titanium vapor jets shown with red arrows).

4.2.3.2.   Perspectives and key questions

The variability in the shape, size, and orientation of the vapor plume during welding causes challenges in ensuring repeatability and comparability of experimental results. While averaging the observations from several videos with the same welding and acquisition parameters provided some insights, increasing the sample size would enhance the accuracy of vapor plume behavior studies.

To investigate the welding processes on a smaller time scale, the experimentation shifted from continuous welding to pulsed welding. However, even within a pulse duration as short as 2 ms, the vapor plume was observed to undergo three distinct stages. Based on this observation, it was hypothesized that the three stages of plume behavior correspond to different degrees of keyhole development: During the initiation stage (with the maximum inclination), the Ti side of the relatively flat surface emits a strong vapor jet. During the stagnation stage, the curvature of the free surface appears, leading to no changes in the plume inclination due to lack of keyhole depth. With a deeper keyhole, the plume returns back to the vertical in the recompensing stage. To further verify this hypothesis, it is necessary to conduct studies using longer pulse durations to see if the plume exhibits the same behavior beyond 2 ms or not, and to observe the keyhole in situ.

The wavelength regime of the 810 nm IR bandpass filter used for the vapor plume acquisitions is based on the continuous thermal emissions by the vapors. Therefore, in the numerical models of the vapor plume, the thermal fields should correspond to the plume observed with 810 nm filter (refer annex, p. 238). However, it is unclear whether this wavelength regime fully represents the metallic vapor plume or if additional heat transfer phenomena modify the observations made. Therefore, further investigation by HSI of the vapor plume in other wavelength regimes is needed to verify the accuracy of using the 810 nm filter for vapor plume observations.

4.3. A Comprehensive Study of Vapor Plume Dynamics and Melted Zone Behavior

In the preliminary investigations, the plume behavior and impact zones resulting from the interaction of the 2 ms pulse were thoroughly examined. A single optical filter at 810 nm was utilized to obtain the thermal image of the plume. Specifically, the study elucidated the inclination of different dissimilar plumes concerning corresponding laser spot offsets from the joint line. However, it was necessary to explore the dynamics of the plume beyond the 2 ms mark by extending the pulse duration. Additionally, the implications of employing a different filter to capture atomic emissions, diverging from the conventional focus on thermal emissions, also remained unknown.

This study delves into the phenomenon of plume behavior during Yb:YAG laser pulses on dissimilar titanium/aluminum alloy interfaces in butt configuration, employing a range of methodologies, including HSI, emission spectroscopy, and post-mortem analysis. Two different optical filters were used for HSI. The rationale for using the 810 nm and 394 nm bandpass optical filters was discussed in detail in section 2.3.2.2 (p.70). In addition to the vapor plume observations, post-mortem analysis of the melted zone was conducted. To expand the scope of the study, the pulse time was increased to 6 ms while keeping the laser spot diameter (600 µm), laser power (2 kW), and experimental setup consistent. The impacts were made with 5 different laser spot positions (Ω = -0.2 mm, -0.1mm , 0 mm, +0.1 mm, +0.2 mm) relative to the joint line, as shown in Figure 30 (p.59).

4.3.1. Post-mortem analysis of the dissimilar melted zones from 6 ms pulses

The melted zones were characterized by examining 25 impact zones (5 impacts per laser spot position × 5 laser spot positions) using Jeol JSM-6610 scanning electron microscope (Figure 83). Energy-dispersive X-ray spectroscopy (EDS) to analyze the Al (in red), Mg (in green) and Ti (in blue) distribution. The top view of the melted zones revealed a notable preference for matter ejection from the melted zone on the aluminum side, with depressions left behind primarily on the titanium side after the keyhole closing. With laser spot displacement from titanium towards aluminum, the ejections from the melted zone on the aluminum side became more prominent, which was concurrent with the previously observed evolution of the plume (section 4.2.1.4, p.107). The variations in the melted zones from different impact for the same the laser spot position represented the instabilities in the keyhole and the vapor plume. In all the cases, the melted zone was surrounded by a ring of oxidized magnesium (also seen in section 4.4.4, p.152, discussed in 211).
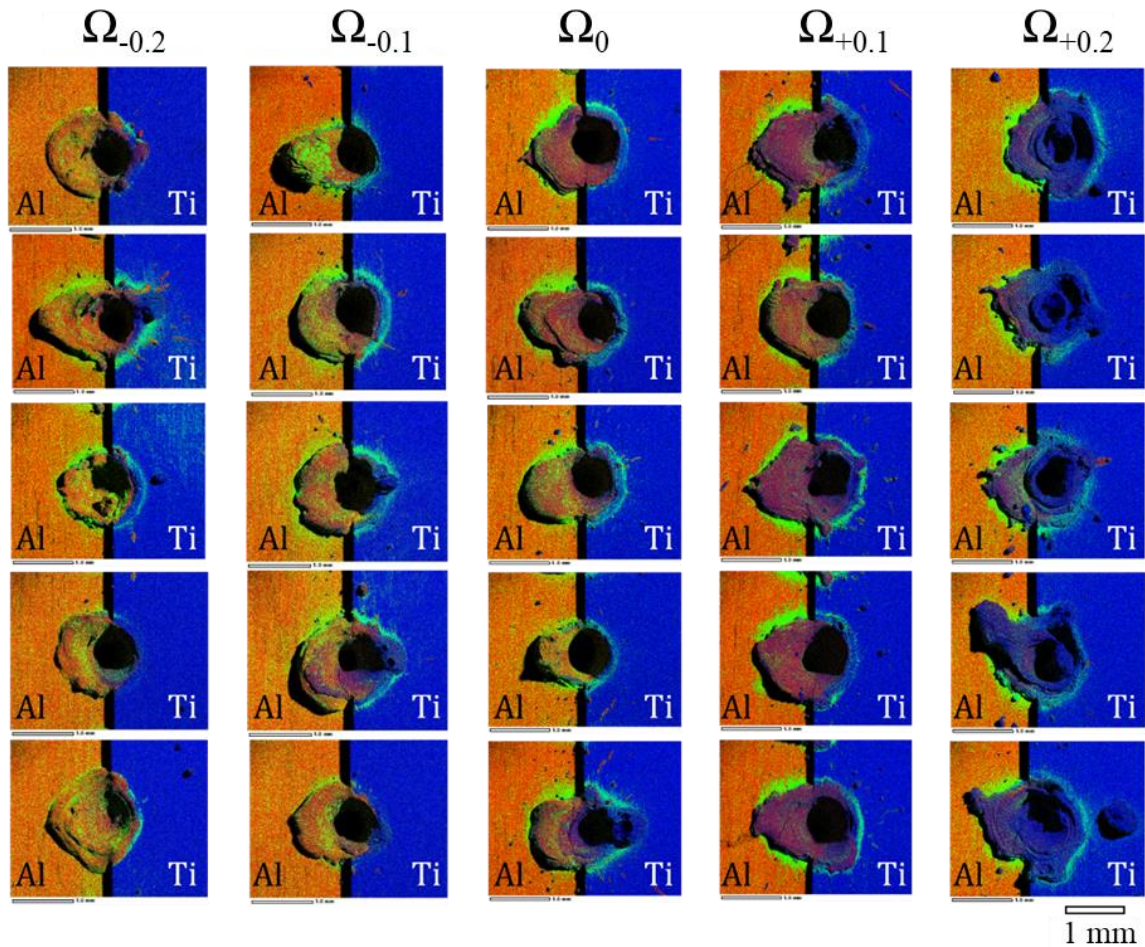
Figure 83. Elemental mapping from EDS analysis of the top view of 25 melted zones.

A small rectangular area (Figure 84. A) measuring approximately 0.3 mm by 0.4 mm was chosen within the melted zone on the aluminum side in the EDS images. This specific region was selected due to the predominant inclination of the vapor towards the aluminum side. Atomic concentrations of the elements within this rectangular selection were determined for all the melted zones. The averages of the atomic concentrations (Figure 84. B) were calculated with confidence intervals from Student's t-Distribution with a standard confidence level of 0.95. While the Al and Ti at.% directly correlating with the laser spot position, it was also noted that due to the lower melting temperature of Al, it remained the predominant element in the melted zone (except for $\Omega_{+0.2}$ where Al and Ti contents in the melted zone are equal).
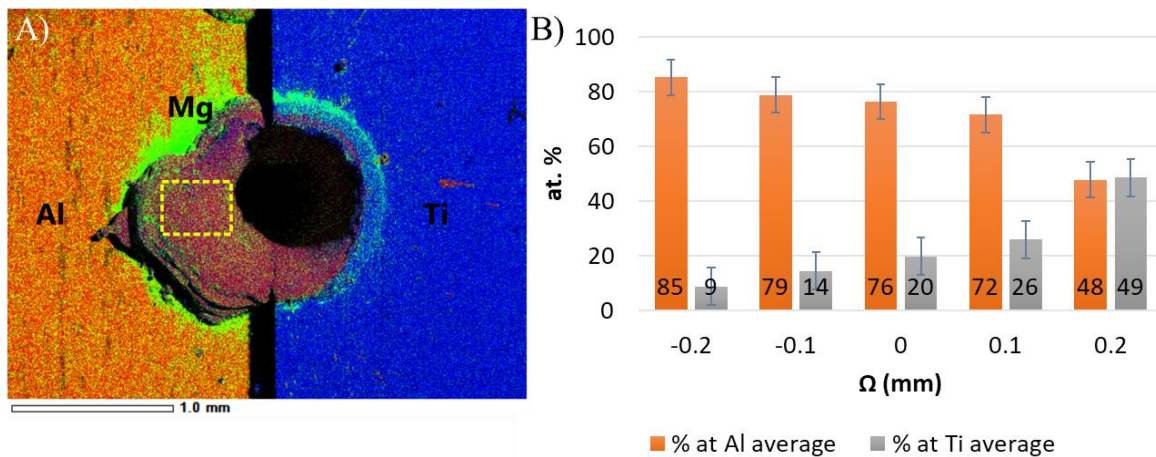
Figure 84. A) Selected rectangular zone for atomic concentration measurements in EDS elemental map of the melted zone and B) Average atomic concentrations of the 25 melted zones.

4.3.2. Vapor plume studies by HSI at 810 nm and 394 nm: *The Conception*

4.3.2.1.   Image Acquisition

The focus of the study was shifted to be on the dissimilar plume captures and the standalone plume studies were not considered. The Phantom v9.1 camera was used in this study. A total of 71 dissimilar welding vapor plume videos were captured, with 31 videos using the 394 nm filter and the remainder using the 810 nm filter. Multiple videos were recorded with the same welding parameters to ensure the accuracy and reliability of the plume behavior data. This was done by repeating the plume captures 5 or 6 times for every changing parameter such as the laser spot position and the wavelength of observation. The number of videos included in this study can be explained as follows: 71 videos were included in this study because there are five laser spot positions, two acquisition wavelengths and six repetitions per video would make 60 videos. However, for confirmation, some of the experiments were repeated a few times more to verify if the observations were the same, leading to the number 71.

The captures for all the welding plume videos were made with a frame rate of 6400 fps, a resolution of 480 x 480 pixels, and an exposure time of 120 µs. The field of view was 15 mm x 15 mm, and the aperture index of the telescopic lens system was set to 11 for all experiments. The lens system had a picture angle of 12.20°, a depth of field of 3 mm, and a reproduction ratio of 1/1.7. To reduce perspective distortions, the inclination of the HSI camera was reduced an angle < 5° with respect to the horizontal plane (previously 13° in section 4.2, p.100).

Despite the various experimental conditions such as laser spot position and optical filters, constant camera parameters were used to ensure data consistency during image processing and statistical analysis. It is essential to consider the potential limitations of this approach as it can lead to losing important information in the images. For instance, if the image suffers from under or overexposure due to a constant exposure time setting without adapting to the brightness of the plume, it can lead to undesirable consequences like a murky or whited-out appearance, making it challenging to discern well-defined edges of the plume. Consequently, relying heavily on thresholding methods to assess plume dimension values may result in inconsistent outcomes. Additionally, various artifacts such as increased noise, loss of shadow and highlight detail, clipping, blooming, and reduced dynamic range can further impact the accuracy and clarity of the image analysis process. While some of these issues can be partially compensated through image processing, the thesis does not specifically address the influence of camera objective and filter's absorption values or the spectral response of the camera's sensor during this process. It is important to acknowledge these potential challenges before further research using HSI in dissimilar welding. By addressing these limitations, the reliability and precision of plume dimensions and other assessments can be augmented and understood better.

4.3.2.2.   Image Processing

At the image processing stage, while the reasoning and most of the steps are similar to what had been done previously for the 2 ms pulses (section 4.2.1.1 p.100), it is prudent to note that the sheer quantity of the number of images that were to be treated have increased by several folds. For a 6 ms pulse recorded 71 times with a frame rate of 6400 fps would yield 17040 (~ 40 x 71 x 6) images.

As the thesis progressed, the image processing methodology had to be updated while maintaining the same format. While writing some algorithms for ImageJ's automation in processing thousands of images saved considerable time, certain portions still had to be handled manually, such as cropping the images. This was because, any time the camera was touched or moved during calibration, it caused a shift in the position of the laser spot in the images by tens of pixels.

1. File Conversion and Stack selection	2. Normalization and Segmentation	3. Cropping reflected parts	4. Data acquisition and interpretation
The file conversions from .cine to .tif were done by batch directly on PCC software. A Macro was written to automatically detect the first presence of the laser illumination and the next 43 images were selected for further processing	The Otsu thresholding method was applied on 2 levels. 1. Global thresholding (Using stack histogram) 2. Local thresholding (Using Image histogram)	No progress in this part and everything had to be done manually since the Phantom V9.1 does not support auto-CSR. (Current Session Reference or Automatic Black Reference)	In addition to Fit-Ellipse, Feret Diameters, Area, Center of Mass, Centroid and Skewness of the images were acquired and charted.

Figure 85. Flowchart of the image processing methodology presented in the order of execution.

Although no updates were required for batch converting the videos, an automatic frame selection method was necessary to facilitate the image processing. Automatically selecting frames containing the vapor plume was made easier with the use of an ImageJ Macro Language detection algorithm, which was written using conditional loops. The algorithm was useful in selecting frames at the beginning and end of the laser pulse. A small rectangular area was selected, and a measurement for either standard deviation or mean was taken. The process would then be repeated on the next image in the stack until the value of the measurement exceeded a particular threshold. Once the program detected a change in the measured variable to satisfy the condition, only the images: the one where the detection was made, and the consecutive 43 images would be conserved (because 6 ms at 6400 fps would need 39 images ± 2 images to avoid any uncertainty). The automatic selection method offered an additional benefit of detecting even the slightest variations in the image properties within the selected area, even if the impact of the laser on the material was not visually discernible.

The stack (corresponding to the duration of the pulse) selection process has been illustrated (Figure 86) for one of the A5754/T40 dissimilar welding plumes acquired with the 810 nm filter. The reduction of the number of images in the stack is noticeable, as it went from 331 to 44 (Figure 86 A, B). Upon examination (with Figure 86 C, D and E corresponding to the 1st, 2nd and 3rd frames), it became apparent that the first appearance of the visually discernible plume in the stack did not correspond to the actual beginning of the laser pulse. Instead, this plume image appears in the third frame after the stack selection process pulse (Figure 86 E). In the Figure 86.C the rectangular area where image measurements were done to detect the beginning of the pulse can be seen. Even though this rectangular region remains empty, using

ImageJ, any minute changes (even though visually indetectable without contrast adjustments) was noted using the previous mentioned algorithm to identify the beginning of the pulse. The first appearance visually distinguishable changes in gray values can only be seen in Figure 86. D. It should be noted that the while no discernable areas of illumination are present, using an algorithm to detect the presence of the variations in the image allows to mark the beginning of the laser pulse (Figure 86.C) while avoiding human error while doing visual analysis. Because the brightness settings of the display, working environment, brightness and contrast settings in the image viewing software can affect appearance of the images.
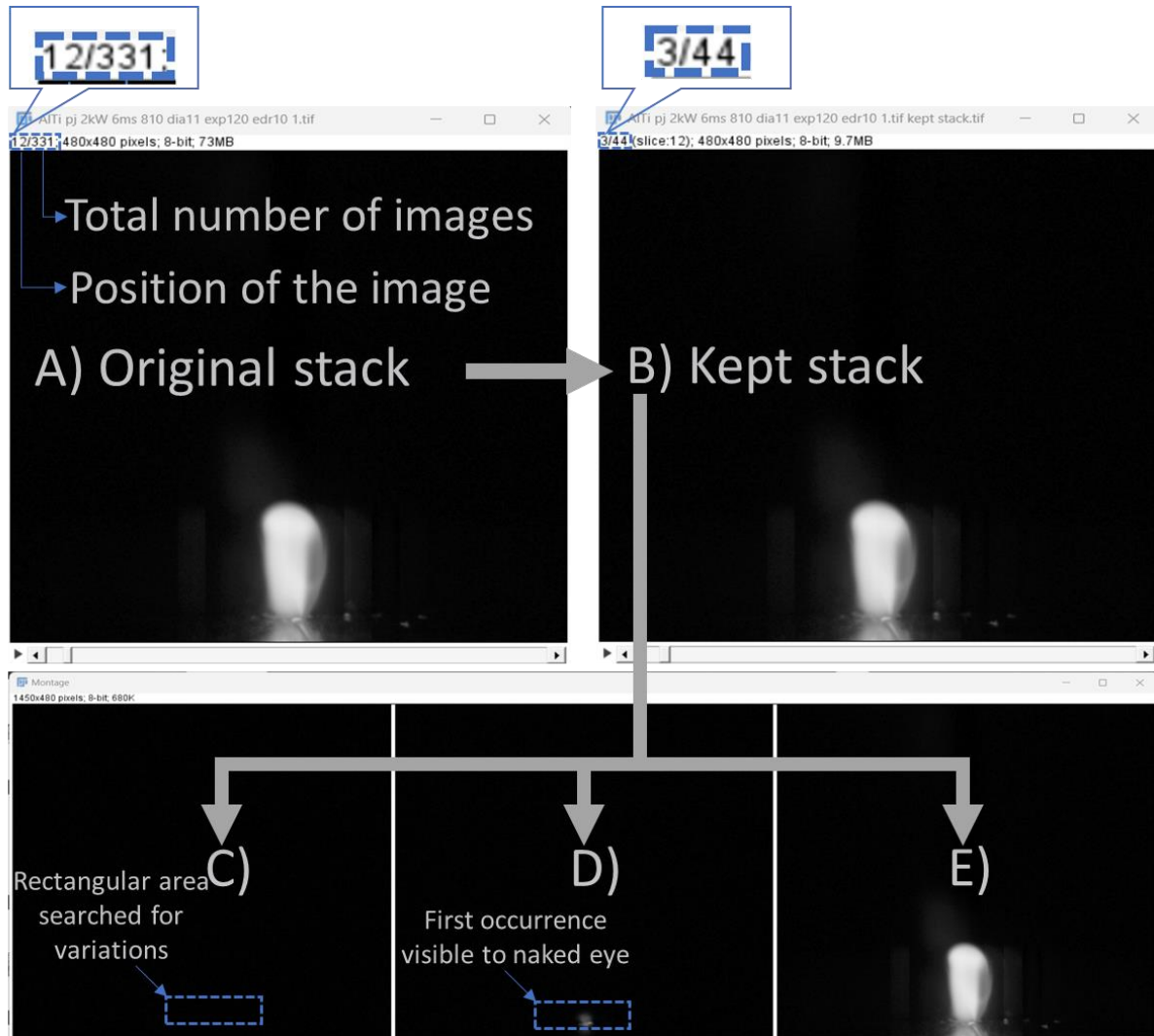
Figure 86. Extraction of images corresponding to the pulse: A, B) Stack editing part in step 1 of image processing, C, D, E) Montage of the first three images in the kept stack.

Due to reasons mentioned previously (section 4.2.1.1, p.100-105), the images had to be normalized before data extraction since the changing welding parameters and wavelength of acquisition (optical filter) can considerably change the image properties. In section 4.2.1.1, the normalization and the subsequent image segmentation was done at a single level (thresholding the image once using any of the methods described in 1.3.2.2, p.38). But due to the widely changing average brightness level of the images with the changing wavelength of capture (section 2.3.2.2, p.70-76), the normalization process which equalized the brightness and contrast was found to be more severe.

This step in image processing is necessary to address the issue of varying brightness levels (results in incorrect measurements during data acquisition) in the untreated images, which is

best illustrated through a colorized image. By applying color to a grayscale image (Figure 87) where the distribution of color is based on the gray level of each pixel (black for lowest, red or yellow with multiple shades of orange for the intermediate values, and white for the highest), the differences can be easily visualized (Menu commands: Image → Look-Up Table → Fire).

The untreated images show a marked difference in color between the 810 nm and 394 nm plumes. While the 810 nm plume (Figure 87.A) appears yellowish-red, the plume observed at 394 nm (Figure 87.C) appears dark red, even though the welding parameters were identical. However, after normalization and equalization, the plumes from 810 nm and 394 nm (Figure 87 B, D) have a similar tone, which eliminates the brightness level distortion issue.
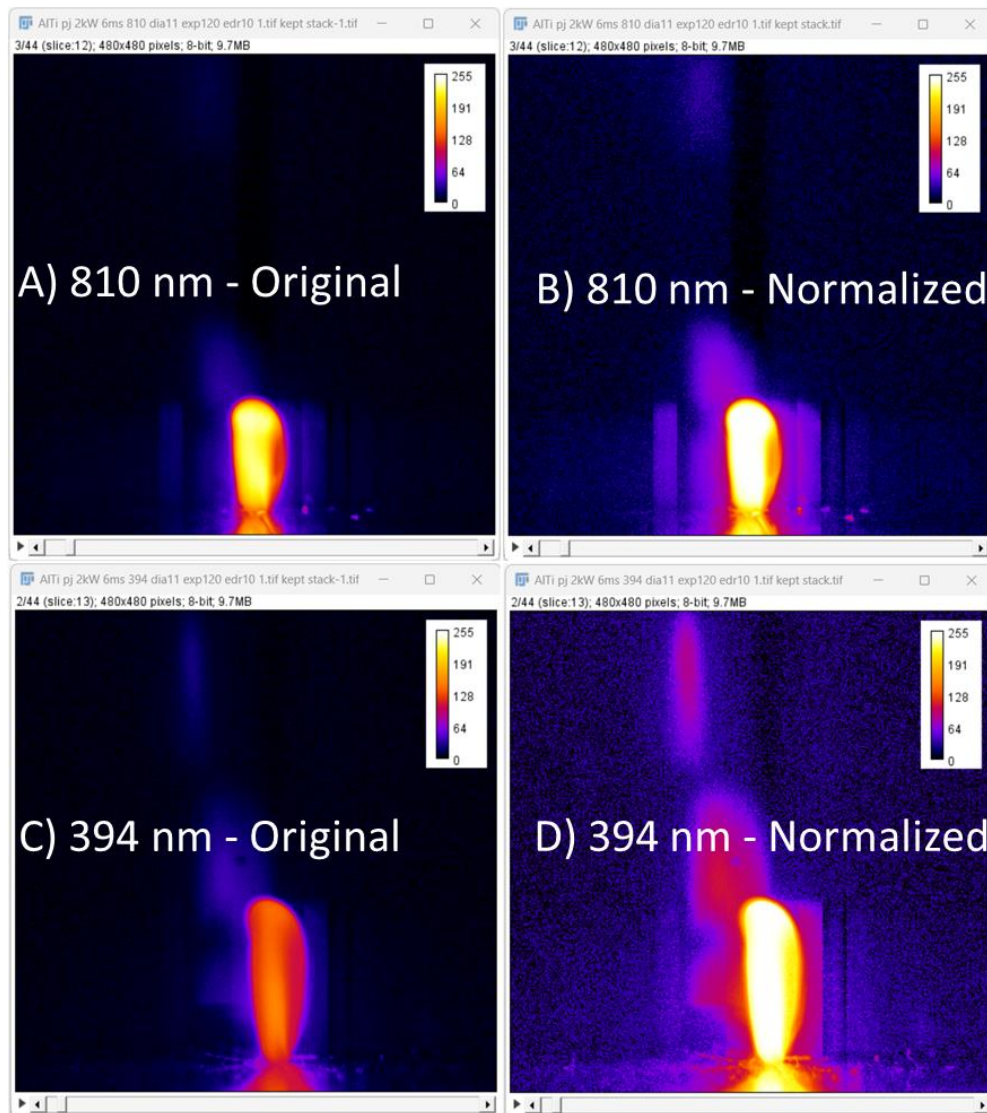
Figure 87. The colorized version of untreated and normalized vapor plumes acquired at 810 nm and 394 nm. (A5754/T40, 2 kW, Ω = 0 mm, time from start of the pulse = 312.5 µs)

This augmented the noise level, spatter regions and other undesirable image artifacts (blooming and bleeding effects) over several folds depending on the brightness of each video (Figure 88). For example, when comparing the amount of background noise that significantly gets augmented to match the selection threshold between the 810 nm and 394 nm plumes of the dissimilar welding (Ω = 0 mm), by examining the number of yellow dots, it is evident that the background noise had substantially increased. These regions of brightness can lead to problems in data acquisitions. A similar effect is also noticeable for the other undesired image artifacts as well.
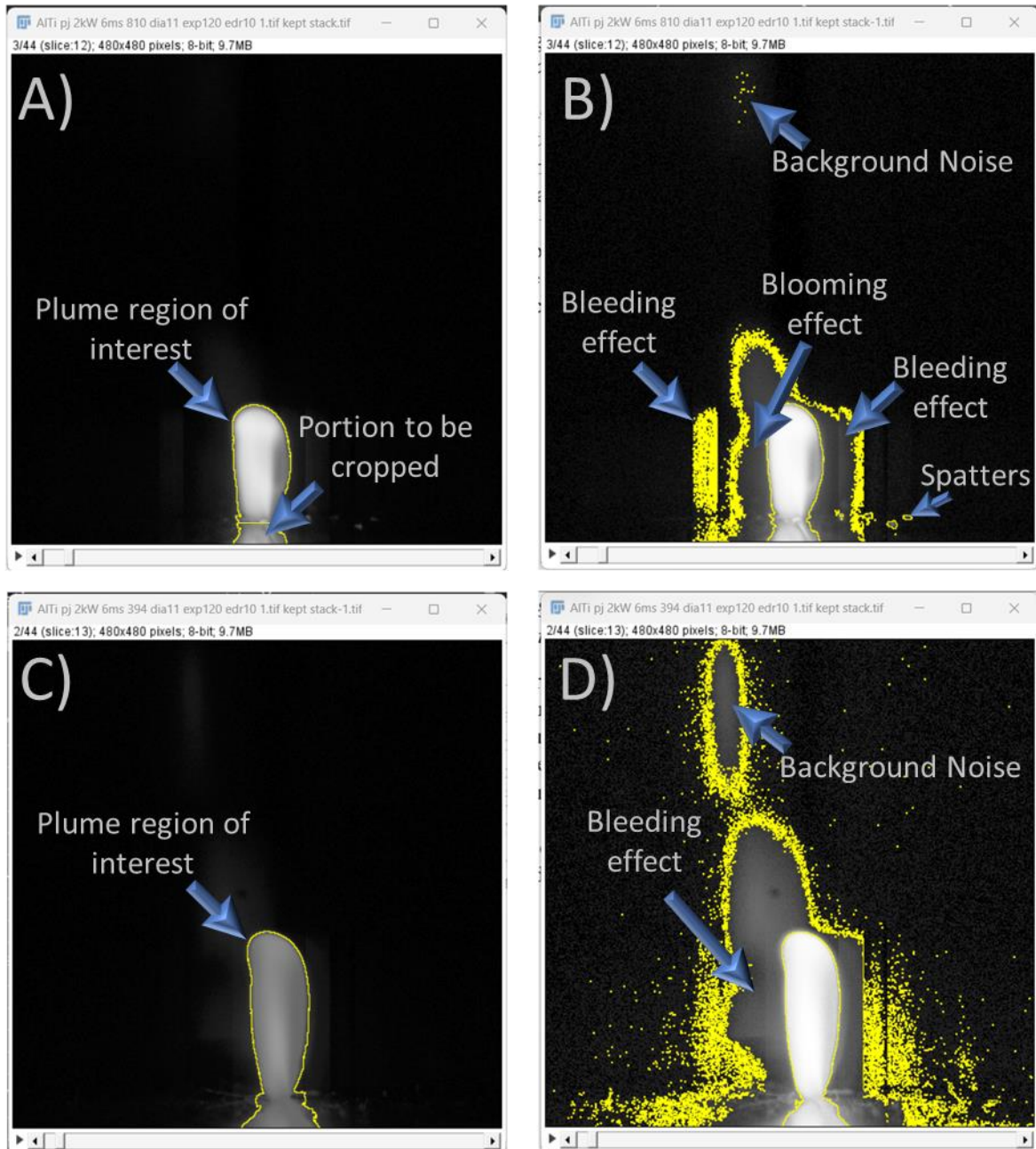
Figure 88. Normalized and equalized plume images before and after processing at A,B) 810 nm and C,D) 394 nm wavelengths.

As the noise and other undesirable image artifacts had increased, a more rigorous method for removing the noise became necessary. However, since the data acquisition in step 4 relied on a threshold value for selection, noise removal was done concurrently to avoid affecting the collected data. However, to better understand the 2-level thresholding method used to remove noise and isolate the plume, illustrations are provided. The cropping of the reflected portions of the plume on the metal surface and limiting the extent of the plume in the images was performed manually, as described in the previous studies (section 4.2.1.1, p.100).

4.3.1.2.1.   The 2-level thresholding method

To eliminate noise and isolate the plume, we applied the Otsu threshold twice. The calculation of the Otsu threshold which uses various statistical tools has already been discussed in detail (section 1.3.2.2 p.38-41). It is important to note that in order to determine the optimal threshold value (maximizing variances between two-classes), the algorithm must iterate through a range

of potential threshold values. If the "Stack histogram" option (Figure 89) is selected, the range of potential values is based on the histogram of the entire stack. If this option is not selected, the range is based on the histogram of the current image.
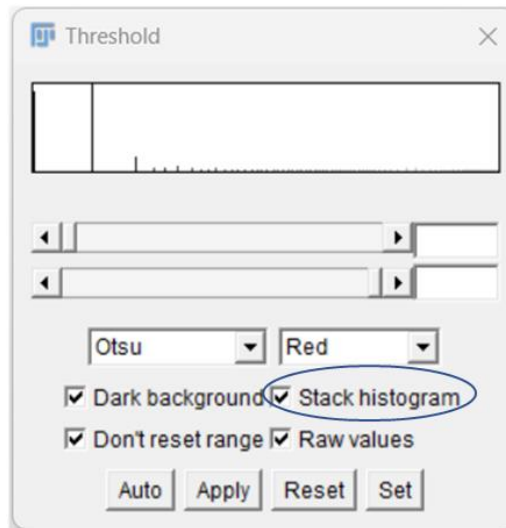
Figure 89. Stack histogram thresholding option to create global and local thresholds.

The consideration of the entire stack's histogram i.e., the histograms of all the images in a video can lead to wider range for the thresholding interval because the brightness level of the plume can vary from one image to another in the stack. This type of thresholding using the stack histogram is referred to as "Global thresholding" in this thesis. However, this was done to remove the outliers caused from the background noise, bleeding effects, blooming effects and the spatter remnants. In addition, this could help in reducing the risk of under-segmenting or over-segmenting the vapor plume. This was the 1st level of thresholding. The second time the thresholding was done, it was done without the "Stack histogram" option which is called "Local thresholding because only the histogram of the image is considered in the search for the optimal threshold value. This was done because the object of interest, the vapor plume was a very bright object moving very rapidly in a dark background. Local thresholding was the better-suited method to isolate the vapor plume because it could help isolate the core the vapor plume from the outer diffuse parts of the plume and regions of brightness produced by motion blur. The flow-chart of the double thresholding in image processing (Figure 90) for ease of understanding and an example of changes produced in the image is provided (Figure 91).
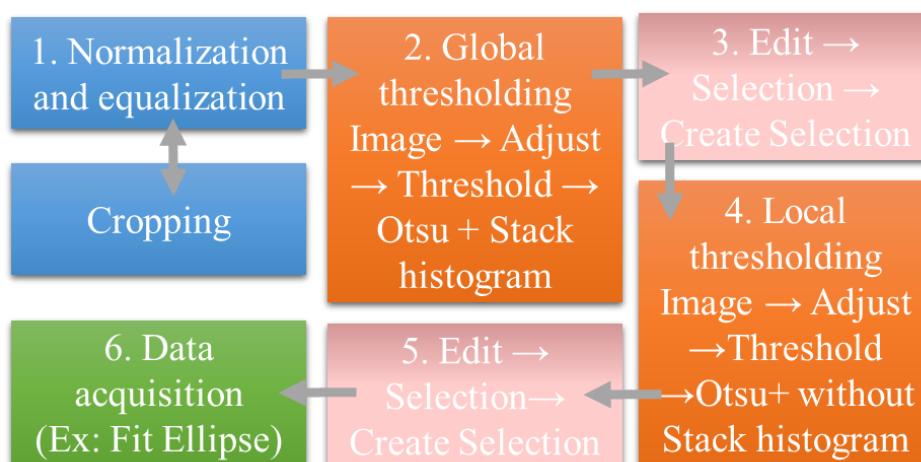
Figure 90. Flowchart guide comprising steps 2 and 3 in vapor plume image processing in ImageJ.
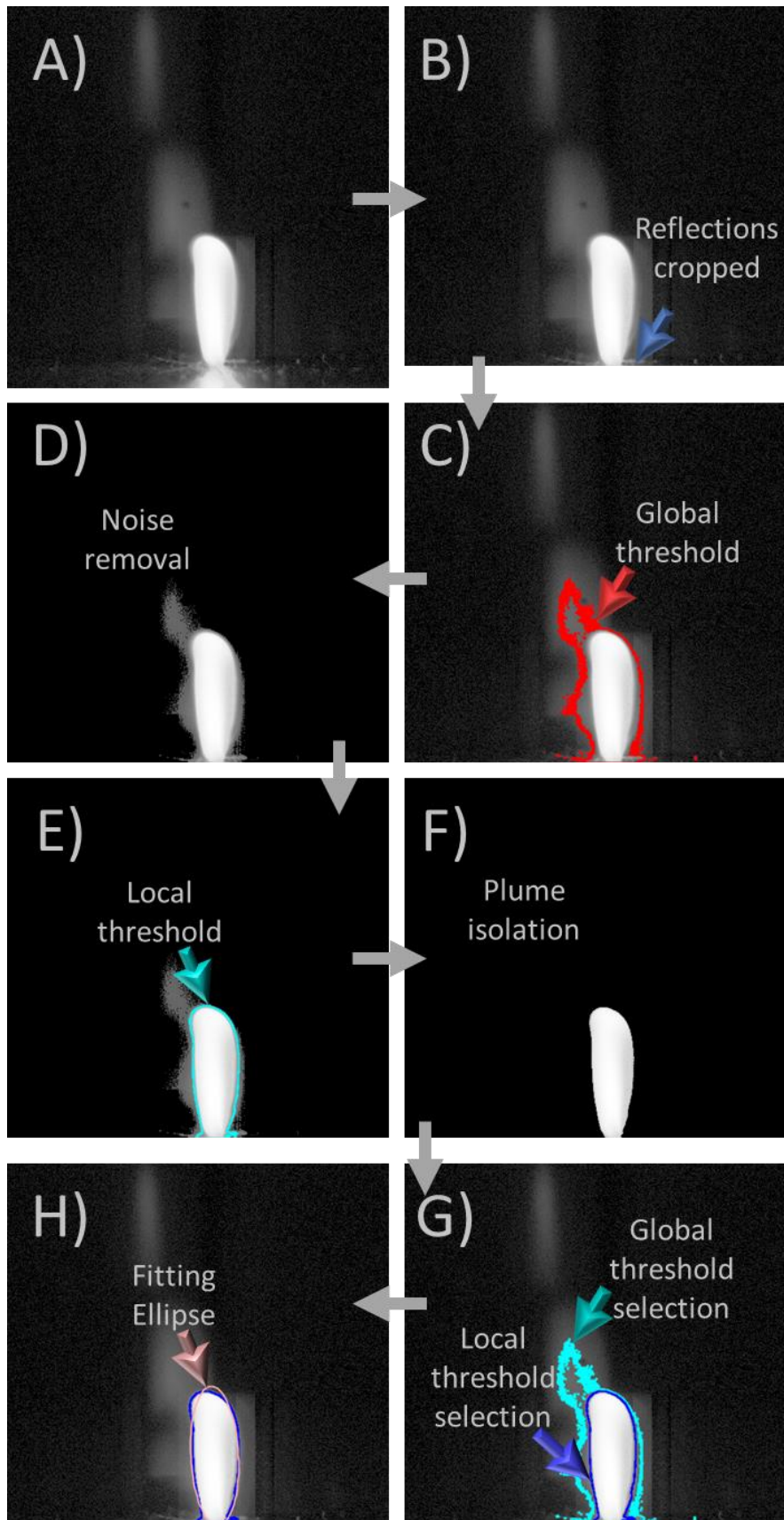
Figure 91. A, B) Normalized image → Cropped normalized image; C, D, E, F) Illustrations on the vapor plume to identify the different stages in the 2-level thresholding method; G) A comprehensive representation of the 2 threshold selections together; H) Application of the fitting ellipse on the ROI. (Initiation stage of the vapor plume of A5754/T40 welding 2 kW, Ω = 0 mm)

121

The data acquisition process is closely related to the image processing work described earlier. Unlike binarization, the non-destructive treatment of the images allowed for the preservation of distribution of intensities within the ROI. While measuring various variables related to the vapor plume are discussed in detail along with the results in (section 4.3.3, p.125), they are briefly introduced here. 3 approaches were taken in the plume characterization. In the first two approaches, distribution of intensity within the plume was not considered.

Approach 1: Considering the plume to be an irregular shape (Area, height, width).

There are several methods which can be used to analyze an image of an object with an irregular shape. In this work, after using the double-thresholding method to find the ROI, calculation of the area of the plume was done from the number of pixels within the ROI.

The "Feret's diameter" (Figure 92), also known as the caliper diameter, is used to ascertain the size and elongation of irregularly shaped or complex objects within an image. There are two different Feret's diameters (to estimate plume height and width). Feret's maximum diameter is defined as the greatest distance between any two points along the object's periphery. To calculate the Feret's maximum diameter, parallel lines are drawn in all directions to encompass the region of interest, and the greatest possible distance between any two of these parallel lines is determined. In contrast, the Feret's minimum diameter is the shortest distance between any two parallel lines (perpendicular to the Feret's maximum diameter) drawn to encompass the region of interest.

The "Bounding Rectangle" is used to calculate the coordinates of the smallest possible rectangle that fully encloses the selected region of interest (Figure 92). The bounding rectangle can serve as complementary information in verifying the plume dimensions. The results produced are the coordinates for the top left corner of the rectangle, the width, and the height of the rectangle. However, the bounding rectangle is always aligned with the horizontal and vertical axes and does not rotate about an angle by default. Therefore, it was not considered for the measurement of plume height and width.
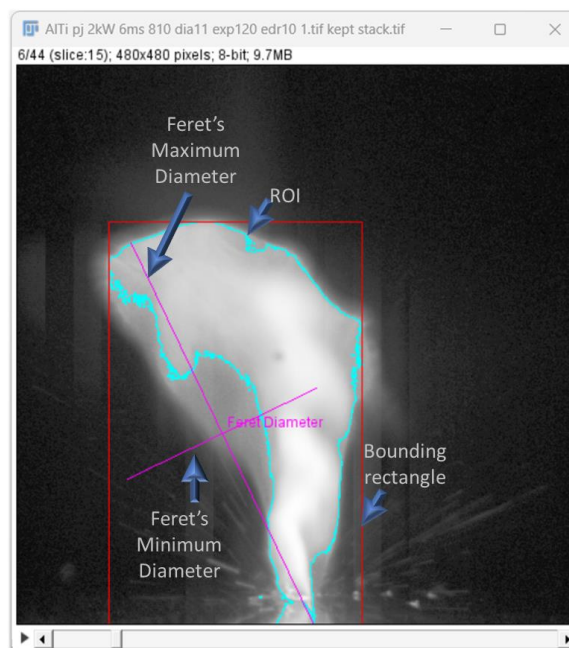
Figure 92. Feret's diameter and the Bounding rectangle for the same example as the previous figure.

Approach 2: Considering the plume to have an approximately regular shape (height, width, circularity).

The "Fit Ellipse" method already used in the preliminary studies (section 4.2.1.2, p.102) was quite useful in obtaining the plume dimensions and orientation.

While the ellipse fitting method plume requires the assumption of the plume to be having an approximately elliptical shape (even though it doesn't at all times), there are other methods to determine the dimensions and orientation of the vapor plume. Because the 'fit ellipse' method is not always successful in finding the dimensions of the vapor plume (Figure 93).

The "Circularity" measure in ImageJ is a way to measure how close the plume is to being perfectly circular. It ranges from 0 (for elongated or irregular shapes) to 1 (for perfect circles). The closer the circularity measure is to 1, the more circular the plume. This measurement in ImageJ is calculated based on the object's perimeter and area. The circularity of the plume in conjunction with the height and width measurements of the plume may indicate instabilities and asymmetricity in the welding process, as it suggests the relative behavior of the height and width of the plume.

[176]
$$Circularity = \frac{4\pi \times Area}{Perimeter^2}$$
60
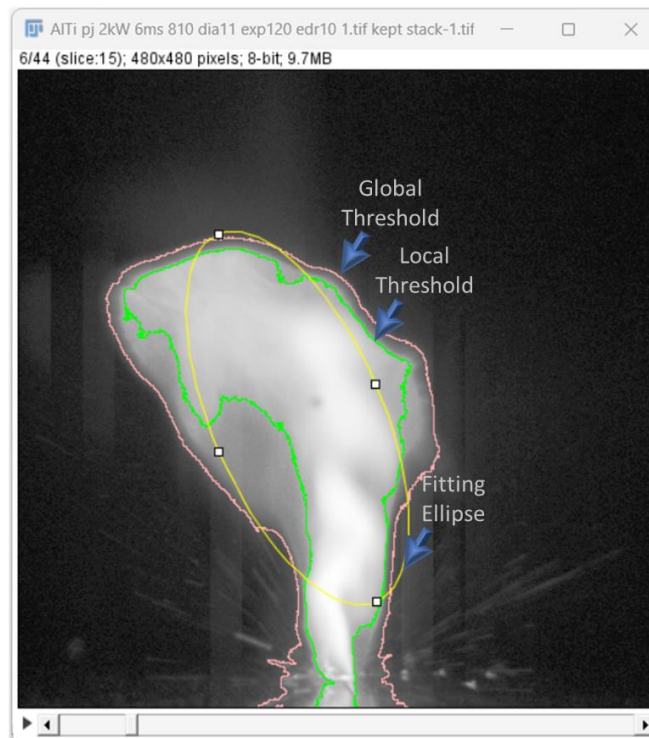
Figure 93. An example where the 'fit ellipse' method is ineffective. (uncropped image)

Approach 3: Considering the plume to be a diffuse cloud-like object.

Even when considering the plume to be cloud-like and without well-defined edges, to avoid perturbation in the measurements, the previously selected ROI from double-thresholding was used.

Another interesting characteristic of 'Fit Ellipse' measurement method was the centroid. The center of the fitting ellipse in ImageJ is the centroid of the image. While the mean represents the overall average grey level in an image, the centroid of the image represents at which point

in the x and y axis the non-zero grey valued pixels in the region of interest find equilibrium. The centroid of a 2-D image is analogous to the center of mass of a 2-dimensional physical object with uniform density. The centroid is absolutely a geometric property in image analysis. Therefore, the measurement of the position of the centroid does not consider the intensity distribution within the ROI.

On the other hand, the center of mass calculated from the average position of all the pixels in the region of interest, weighted by their grey level values takes into account the intensity distribution within the vapor plume. Here, it means that pixels with higher intensity values contribute more to the calculation of the position of the center of mass.

While the centroid depends completely on the ROI, the center of mass takes into account the distribution of pixel intensities within the ROI. This is represented in Figure 94.A and B, where the Figure 94.A has a higher centroid (with the plume sketch showing uniform intensity) compared to Figure 94.B having a relatively lower point for the center of mass because the higher pixel intensities are near the keyhole.

Although normalization and equalization techniques allowed comparison of plumes of different intensities after thresholding, their effects on the pixel intensity distribution could be understood by the skewness of the histograms. As it could be seen from Figure 87 (p.118), the normalized image of the AER is slightly brighter than the TER and certain parts of the AER plume lacks detail compared to the TER. Averaged kurtosis and skewness values were compared to examine variations in the histograms with respect to laser spot position and optical filter. Kurtosis (peakedness of the histogram) indicates the presence or absence of pixel intensities concentrated within a particular range, implying either uniform or non-uniform pixel brightness distribution within the ROI. Skewness indicates the symmetry in the distribution of pixel intensities within the histogram which would indicate the general tendency of the plume ROI to be brighter or darker. Skewness was preferred to study the brightness of the plume rather than the Mean because normalization changes the Mean values. In Figure 94.C and D, the kurtosis value is higher in Figure 94.D because the number of bright pixels were increased. In Figure 94.E and F, Figure 94.F has a higher skewness because the overall plume brightness was increased by brightness/contrast adjustments.
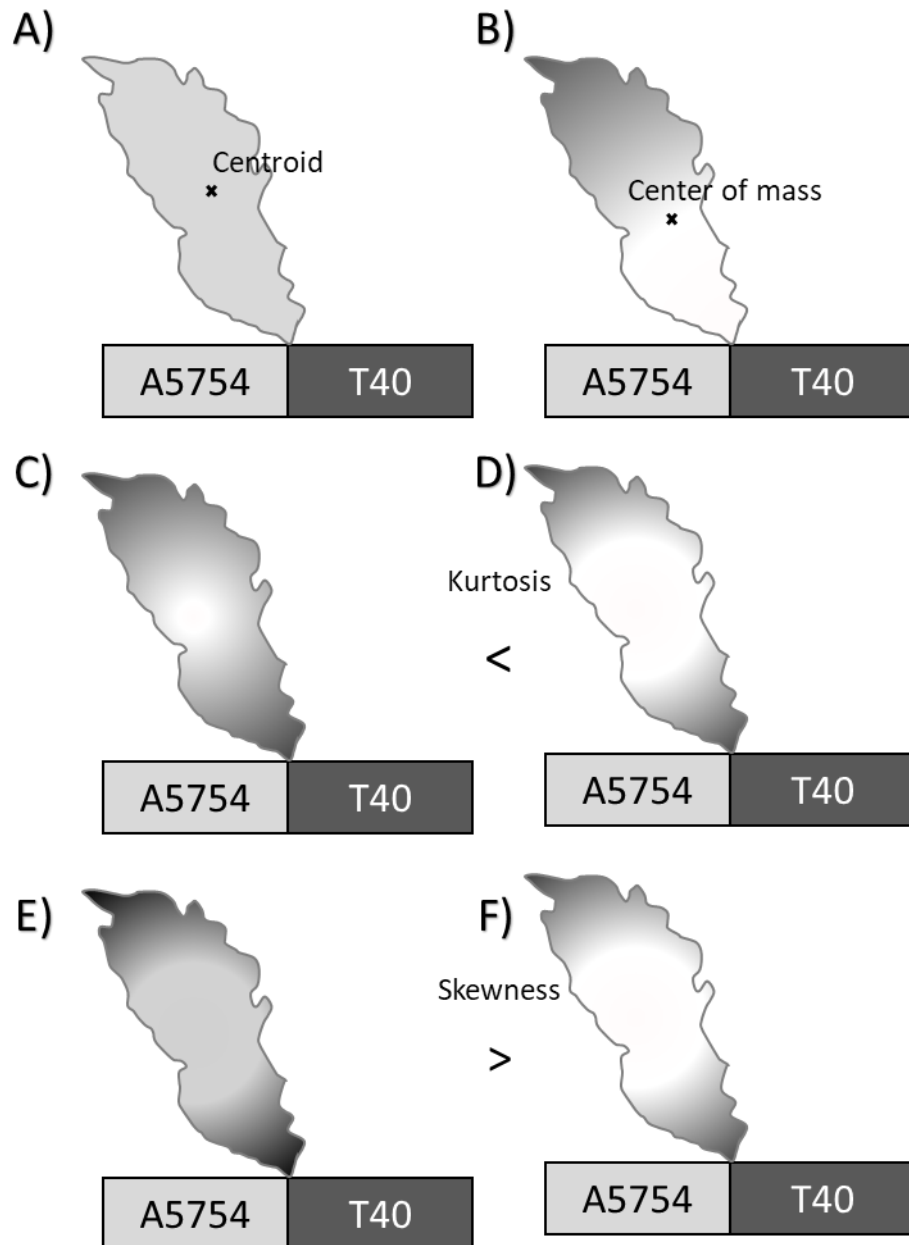
Figure 94. Sketch of centroid, center of mass, kurtosis, and skewness.

Among all the methods describing the plume geometry discussed so far, only the center of mass takes into account the geometry in the distribution of the intensity values. So, in addition, kurtosis and skewness were measured to understand the distribution of the pixel intensity values. Kurtosis measured the "peakedness" or flatness of the histogram relative to normal distribution. In other words, it indicated the presence of high contrast and low contrast zones in the image with high and low values respectively. Skewness on the other hand measured the asymmetry in the distribution in the histogram. A positive skewness value indicated that there were greater number of pixels with lower intensity (relative to the mean) in the ROI and a negative skewness indicated that there were greater number pixels with higher intensity (relative to the mean) in the ROI.

4.3.3. Imaging data analysis, Results, and Consequences

Using the multiple measurement techniques mentioned in the section 4.3.1.2.2, several characteristics of the vapor plume had been measured. These data were exported from ImageJ

and processed in Microsoft Excel using scripts written in VBA (Visual Basic for Applications). The automation of the data processing was necessary due to the sheer quantity of data to be analyzed. Because manually processing 71 individual tables containing more than 17000 rows of data in total could be a daunting task and could lead to misinformation from human errors. And so, even the simple tasks like the conversions (number of pixels → millimeters), rearrangements of the columns (slice number → time), identifying the plume dimensions with respect to the angle (the major axis of the ellipse doesn't correspond to the height of the plume when the plume has a greater width than its height), data consolidation, etc. were done by batch automation.

After all the image processing, it became necessary to develop a methodology to understand the plume characteristics and their correlation with the experimental variables/parameters. This was because the dataset contained over 17,000 records with 11 fields each, including time, area, two Feret's diameters, two ellipse axes, center of mass, centroid, circularity, kurtosis, and skewness. These records were categorized based on experiment variables such as welding parameters, HSI acquisition parameters, physical properties of the materials, spectral properties of the elements in the vapor, etc. Without a proper methodology, understanding this vast dataset would be extremely difficult. It was apparent that analyzing the global spatial behavior of the vapor plume required comparing each individual measured variable separately in relation to the laser spot position and the wavelength of HSI acquisition. This was done by averaging the values of a particular variable among the 5 or 6 videos captured for a laser spot position at a particular wavelength (Figure 95).
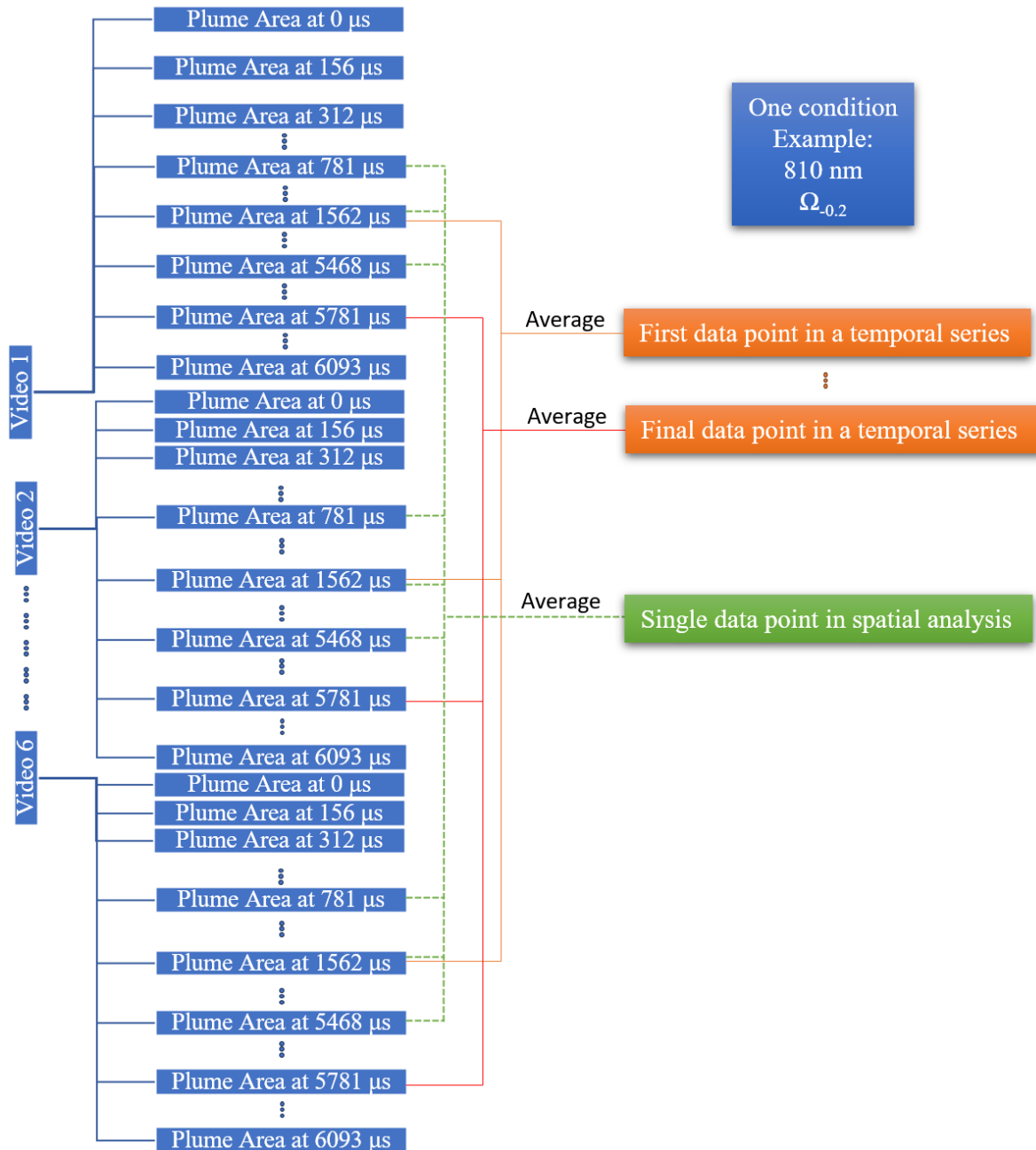
Figure 95. Flowchart representing the averaging of data points for analysis.

4.3.3.1. Temporal analysis of results: plume morphology and orientation

To gain insight into the temporal behavior of the plume, the averages of various measured variables, including area, height, width, and angle, were calculated. These averages were derived from 5 to 6 videos, each corresponding to specific conditions of the optical filter and laser spot position. The laser spot positions considered for the temporal analysis of the plume are $\Omega_{-0.2}$, Ω_0, $\Omega_{+0.2}$. The time periods considered in this analysis are limited from 1.5625 ms to 5.78125 ms. In this section, the presentation of error bars in the charts has been omitted in the interest of clarity and readability. The use of these averages can be justified by the rigorous method used for determining the beginning of the pulse in the images. However, it should be noted that, this introduced ± 78 µs uncertainty on the temporal scale (horizontal axis) as mentioned earlier in the preliminary studies (p. 104) because the laser impact and the camera's first frame of capture were not synchronized.

From studying the average area of the ROI (Figure 96) for the laser spot position $\Omega_{-0.2}$, it is observed that the area of the plume ROI observed at 810 nm (green) is greater than the area of the plume ROI observed at 394 nm (purple). A similar observation can be made when comparing the rest of the plumes observed for the laser spot positions Ω_0 (yellow-810 nm, blue-394 nm), $\Omega_{+0.2}$ (red-810 nm, grey-394 nm). When area of the plume ROI observed at 810 nm was compared between the laser spot positions, the plume for $\Omega_{+0.2}$ (red) had a greater area than Ω_0 (yellow) and $\Omega_{-0.2}$ (green) up to $\approx$ 4ms, after which they had similar values. The convergence of these areas by the descent of the area of the plume for $\Omega_{+0.2}$ (red) and the ascent of the areas of the plume for Ω_0 (yellow) and $\Omega_{-0.2}$ (green), start around 2.5 ms – 3 ms. However, the magnitude of such a difference in the area of the plume observed at 394 nm initially for $\Omega_{+0.2}$ (grey) compared to Ω_0 (blue) and $\Omega_{-0.2}$ (purple) is less. And it is the also noted that the variability of the area of the plume observed at 394 nm within short intervals (< 1 ms) is much higher for Ω_0 (blue) and $\Omega_{-0.2}$ (purple) compared to $\Omega_{+0.2}$ (grey) especially after 3 ms.
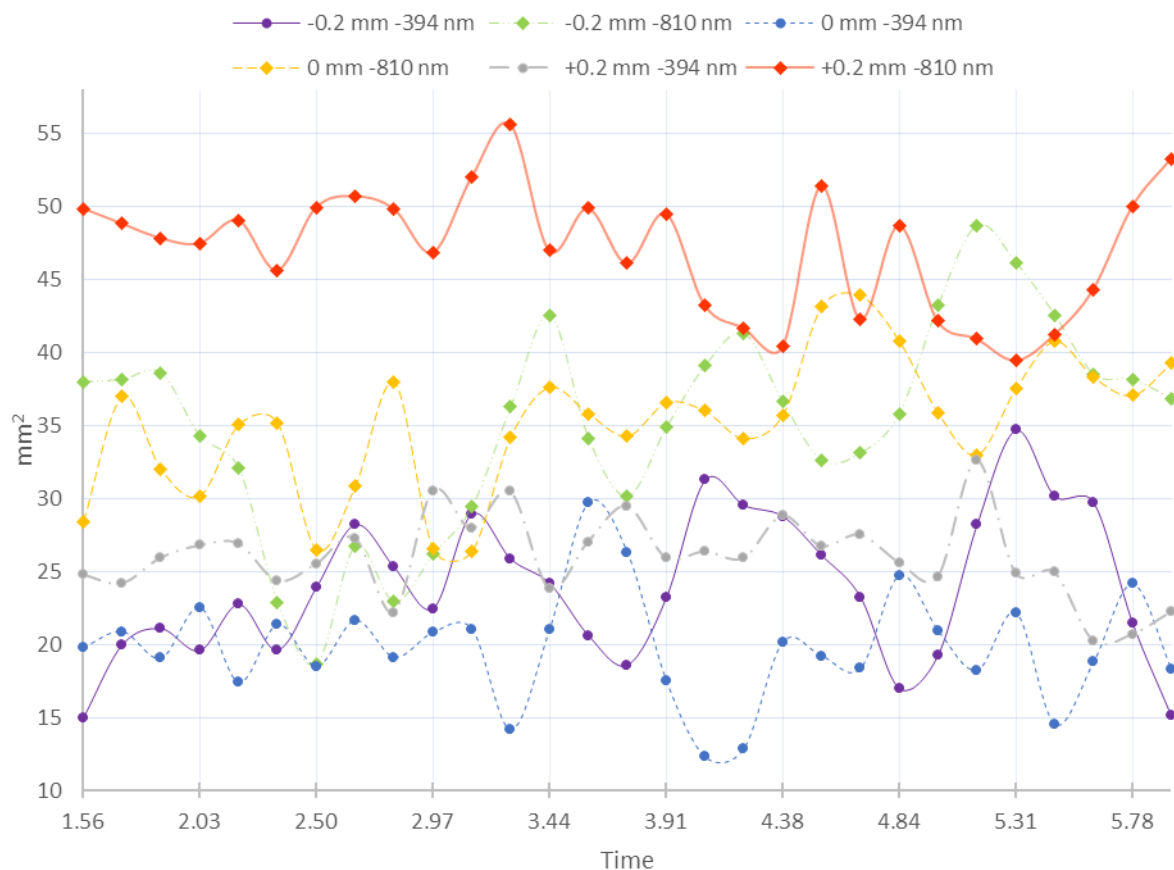
Figure 96. Temporal evolution of the ROI area for the laser spot positions $\Omega_{-0.2}$, Ω_0, and $\Omega_{+0.2}$.

### 4.3.3.1.2.	Plume Dimensions

Although the plume height and width from the Feret diameters measurements produced similar results, for the purpose of continuity with the preliminary studies, only the ellipse height and width of the plume are discussed as a part of the temporal behavior studies.

When comparing the plumes for the different laser spot positions observed (Figure 97) with the two optical filters, it is noted that the plumes observed with the 810 nm filter are taller than the plumes observed with 394 nm filter irrespective of the laser spot position (Figure 97 red, yellow, green > grey, blue, purple). Once again when comparing the plumes observed with the

2 filters for respective laser spot positions, it appears that the plumes observed with the 810 nm filter are taller than the plumes observed with the 394 nm filter for the corresponding the laser spot positions ($\Omega_{+0.2}$: red>grey, Ω_0 : yellow>blue, $\Omega_{-0.2}$: green>purple). The average plume height during the 1.56 ms - 4 ms of the pulse duration is observed to be the highest for the plume observed with the 810 nm filter with the maximum laser spot displacement on T40 ($\Omega_{+0.2}$ - red).
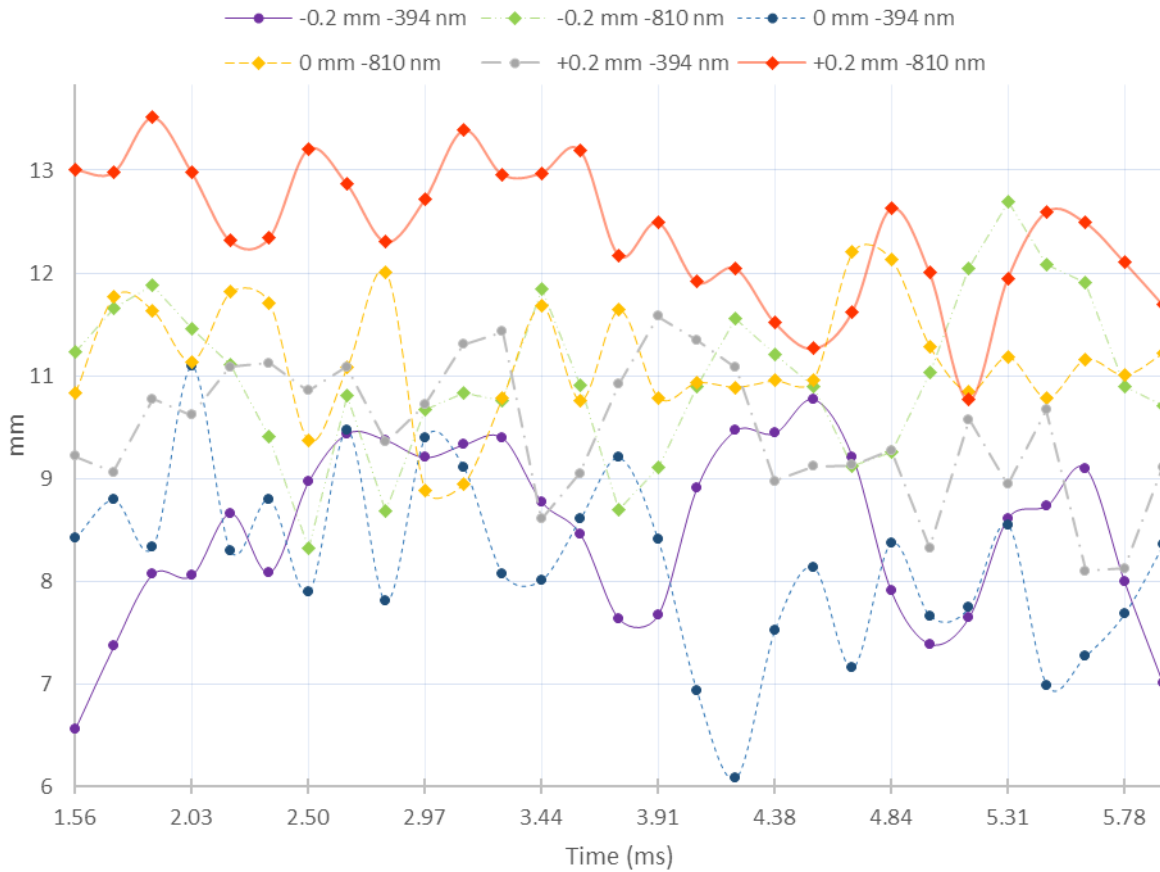
Figure 97. Temporal evolution of the plume height for the laser spot positions $\Omega_{-0.2}$, Ω_0, and $\Omega_{+0.2}$.

The observed width (Figure 98) also shows a similar tendency as the height when comparing the observed plumes with the two filters (810 nm : red, yellow, green > 394 nm : grey, blue, purple) for the corresponding laser spot positions. However, the relative variations (to the average width during 1.56 ms - 3 ms) in the plume width when observed with both the filters after ≈ 3.4 ms is much greater than for all the laser spot positions compared to the plume height. When comparing the plume widths (1.56 ms - 3 ms) for the same filters between different laser spot positions, for $\Omega_{-0.2}$ and $\Omega_{+0.2}$ the difference is much higher (green >> purple, red >> grey) compared to Ω_0 (yellow > blue).
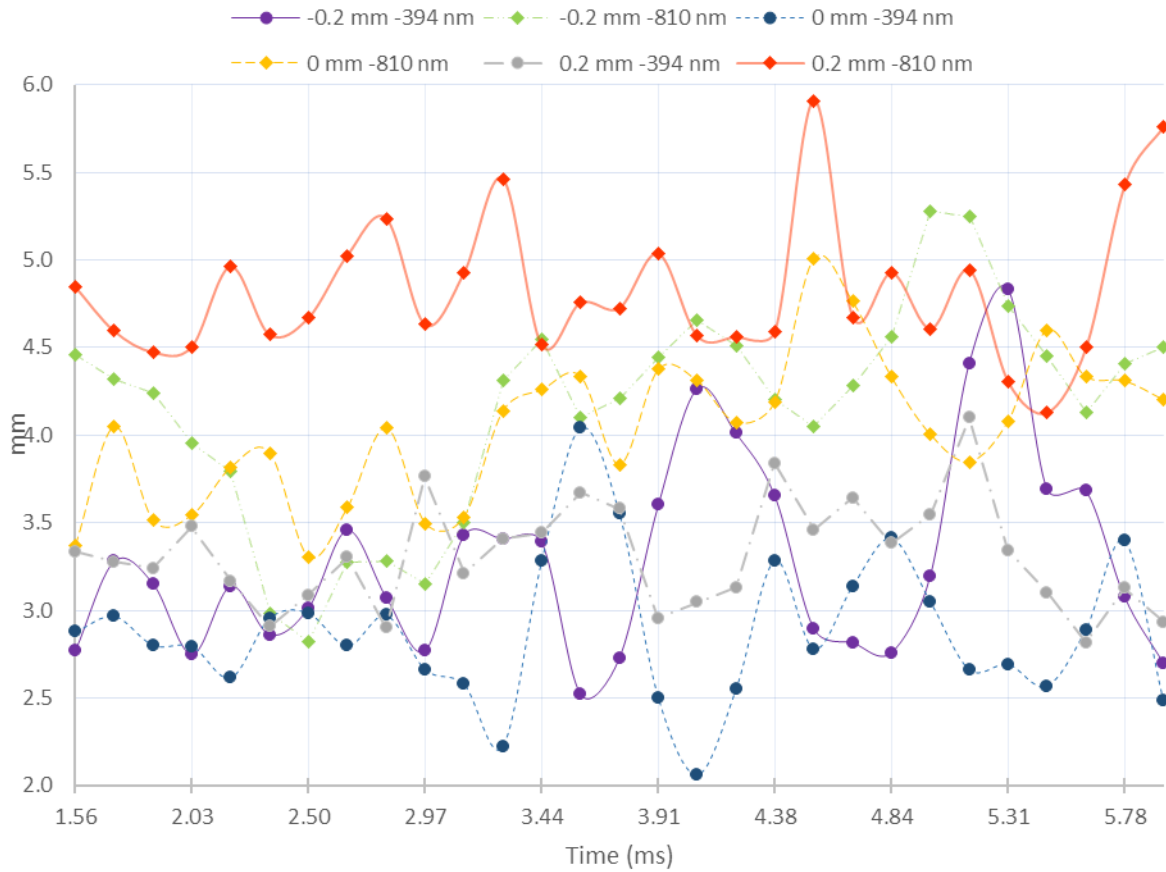
Figure 98. Temporal evolution of the plume width for the laser spot positions $\Omega_{-0.2}$, Ω_0, and $\Omega_{+0.2}$.

4.3.3.1.3.   Plume orientation

The angle of the fitting ellipse was studied to understand the inclination of the dissimilar plume temporally, as it can be observed that the plume does not have perfect symmetry around any axis at all moments (Figure 99). It can be noted while the fitting ellipse doesn't necessarily match the plume ROI (instances where the plume changes angle (3.90 ms), multiple regions of ROI (3.59 ms)), during most of the instances, the plume ROI's angle can be measured by the angle of the fitting ellipse.
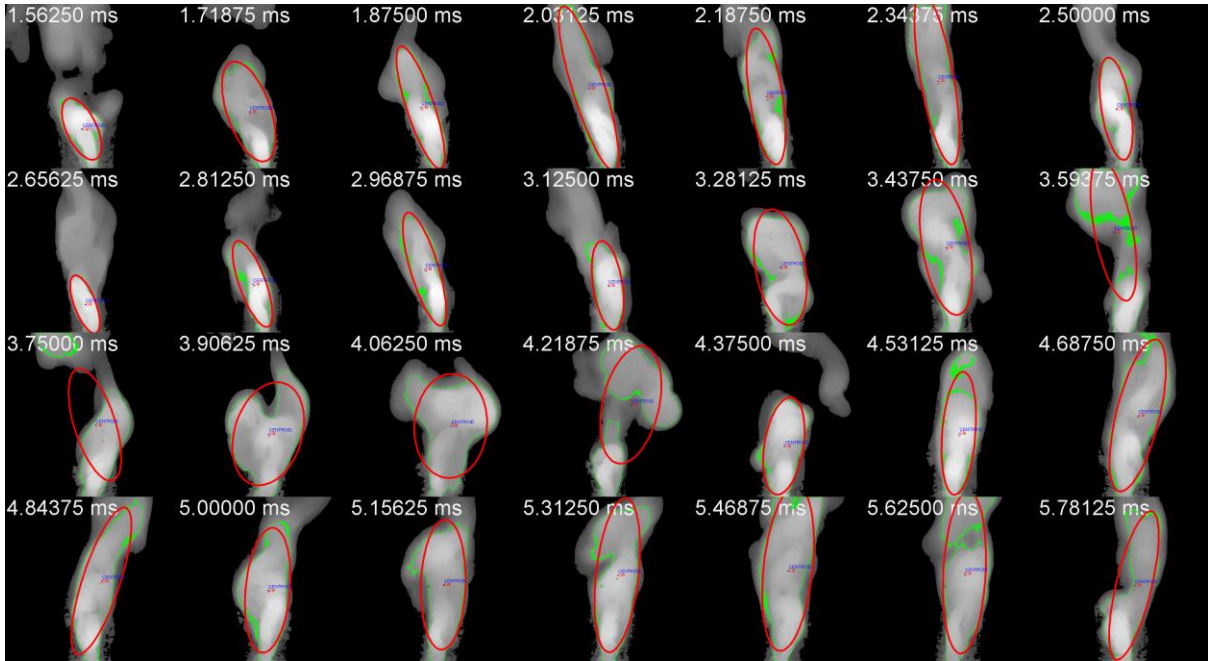
Figure 99. Montage of fitting ellipse on the plume (laser spot position: Ω_0, optical filter: 810 nm).

When comparatively analyzing the angles of inclination (Figure 100) between the plumes observed with 394 nm and 810 nm filters, the plumes observed with the 394 nm filter (grey, blue and purple) exhibit clustering of the angle values with moderate changes around the vertical while the plumes observed with 810 nm (red, yellow and green) display pronounced deviations, with very less frequent near-vertical returns.

When examining the plume inclinations between the 2 filters for the same laser spot position: for $\Omega_{-0.2}$, the plume observed with the 810 nm filter (green) generally had higher inclination and a wider range of inclination than the plume observed with 394 nm filter (purple). While the inclination of the plume observed with 394 nm filter (purple) fluctuated between positive (inclination towards A5754) and negative values (inclination towards T40), the inclination of the plume observed with 810 nm (green) remained predominantly towards A5754. On the contrary, when comparing the inclinations of the plumes observed with the 2 filters for the laser spot position $\Omega_{-0.2}$, the plume observed with the 394 nm filter (blue) generally remained positive with consistent deviation from the vertical, while the plume observed with 810 nm filter (yellow) dynamically fluctuated between positive and negative values.

Similarly, the inclination plume observed with the 810 nm filter had a wider range compared to 394 nm. When comparing the inclinations of the laser spot positions $\Omega_{-0.2}$ (green, purple) and Ω_0 (blue, yellow) with $\Omega_{+0.2}$ (red, grey), the laser spot position $\Omega_{+0.2}$ is almost always vertical while the laser spot positions $\Omega_{-0.2}$, Ω_0 exhibit tendency to incline towards A5754.
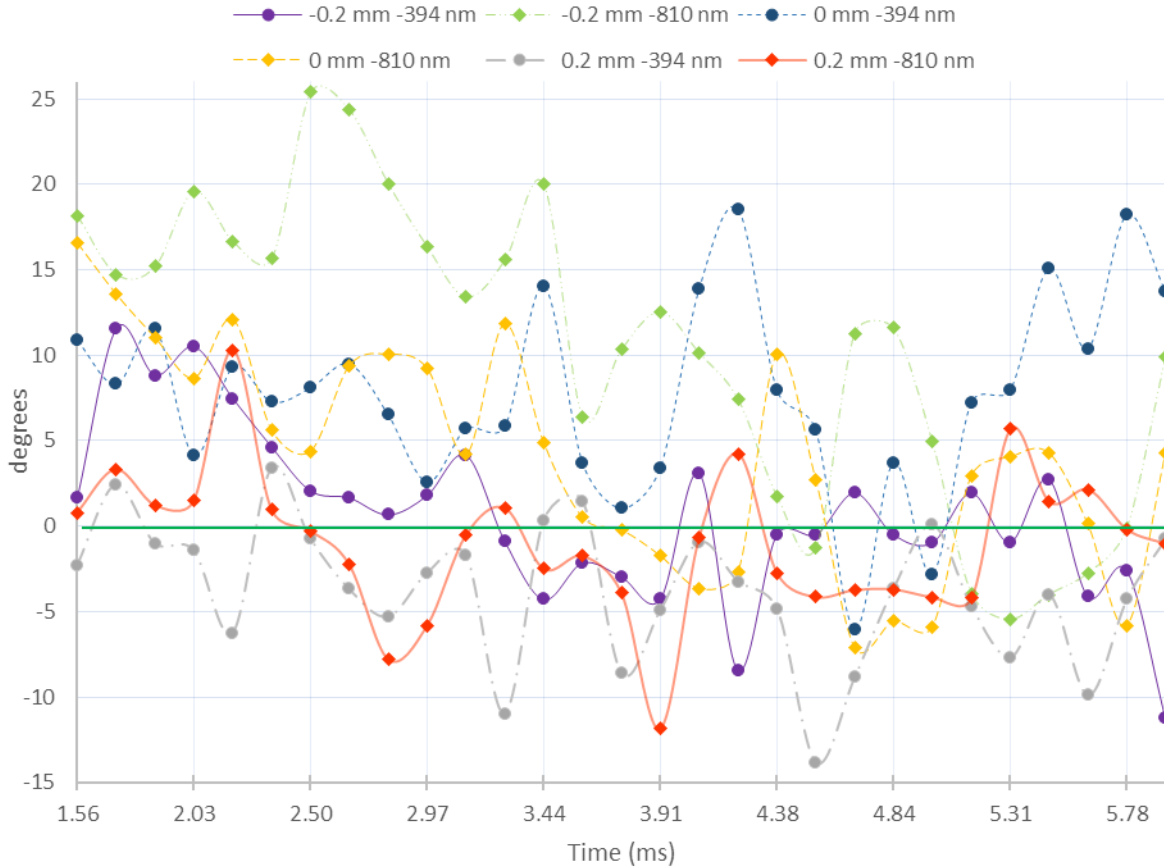
Figure 100. Temporal evolution of the plume inclination for the laser spot positions $\Omega_{-0.2}$, Ω_0, and $\Omega_{+0.2}$.

4.3.3.2. Spatial analysis of the vapor plume characteristics and physical interpretations

Analysis of the spatial characteristics of the plume is done by the calculation of the average properties. It is explained as follows with an example (area of the vapor plume). The average area was calculated for each welding and acquisition condition by averaging the area of the plume calculated for each image over several videos. All the other measured variables discussed in this section were treated in a similar way. This method was better than directly producing an average or a standard deviation image and then applying a threshold as done in Chapter 3 (section 3.1.1). Measuring the properties of the plume in each image separately and then averaging them instead of using the average or standard deviation image directly can be explained by the following reasons:

- The main concern which led to this methodology originated from the observation that any slight movement of the camera relative to the laser spot position can cause an imperfect superposition of the keyholes and the plume, leading to blurry average images and erroneous results.
- When creating average images from 8-bit images, there is a risk of losing critical data due to rounding of significant figures.
- If the measurements were made in each image separately and analyzed, it would be possible to identify temporal regions of high variance, which can then be ignored. This approach allows for a more precise calculation of the plume characteristics and avoids the loss of critical data that can occur when averaging images.

Due to the uncertainties in the start of the pulse and the erratic behavior of the plume, measurements are only taken from a specific interval of time (0.78 ms – 5.47 ms) to ensure accuracy.

The observation of the ROI area allowed for the characterization of the size of the plume (Figure 101). During the analysis of the average area of the vapor plume, two imaginary rectangles (Figure 101) were used to verify and compare the area of the plume. The comparison of the averages of the measured ROI area with the area of the bounding rectangles calculated from the average ellipse axes and average Feret's diameters was done to oversee the behavior and precision of the different measurement techniques employed. The calculated averages of the Feret's maximum diameter, the length of the major axis of the ellipse and the Feret's minimum diameter, the length of the minor axis of the ellipse are discussed in detail in section 4.3.3.1.5 (p.135).

The first rectangle was from the Feret's diameters. The maximum and minimum Feret's diameters were measured and used as the length and width of the rectangle, respectively. The area of this rectangle was calculated by multiplying the length and width values. The second rectangle was constructed from the lengths of the fitting ellipses' axes. The major and minor axis lengths were measured and used as the length and width of the rectangle, respectively. The area of this rectangle was calculated in the same way as the first rectangle.
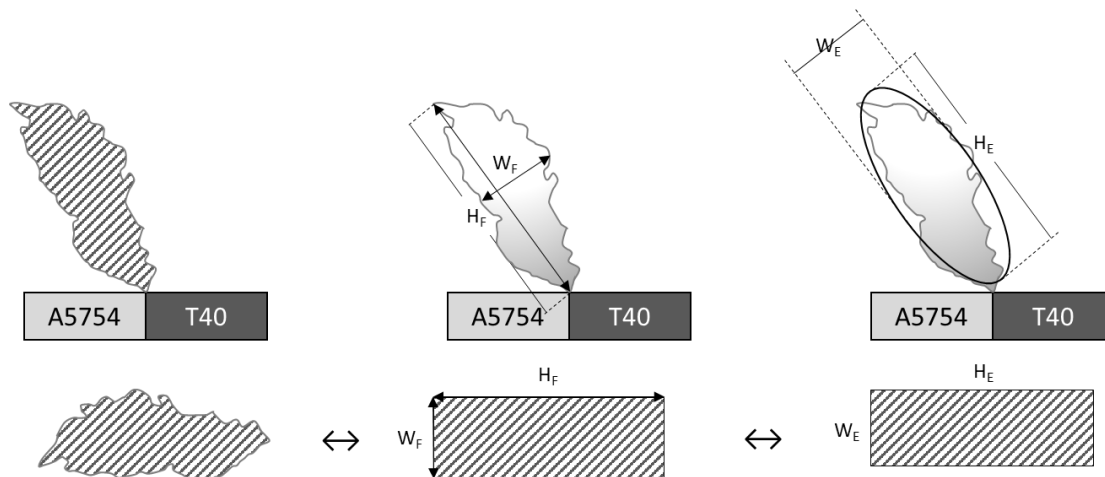
Figure 101. Sketch of the comparison of the plume area to the area of the calculated rectangles from Feret's diameters and Ellipse axes.

The differences in the behavior of the average area between the optical filters for the laser spot position Ω = -0.2 mm, -0.1 mm, 0 mm when analyzed alongside calculated area of the rectangle from the height and width of the plume are presented in the Table 12 (134). The following observations were made from this comparative analysis:

♦ It has been determined that the area of the rectangle is much larger than that of the region of interest (ROI) primarily due to the irregular shape of the ROI. This highlighted the necessity to find better techniques for characterizing the irregular plume shape rather than relying solely on height and width measurements. Therefore, it was understood that alternative techniques must be explored to obtain a more accurate representation of the area of the ROI (especially when dealing with thresholding techniques).

♦ The overestimation in the calculated area of the Feret rectangle is attributed to the significant positive error in Feret's Diameters. When studying elongated particles, a positive error was found to be a common feature of Feret's diameter [291]. As the plume tapers near the keyhole and widens with height, coupled with the varying circularity when the laser spot position is moved towards aluminum, such an error becomes inevitable.

- ♦ Despite the overestimation, it is noteworthy that observed tendencies of the area calculated from the Feret's diameters matches the actual ROI for the optical filter 810 nm with respect to the laser spot position. This observation confirms that Feret's diameter can serve as a complementary measure to Fit Ellipse for the purpose of verification and confirmation.
- ♦ The over-estimation of the calculated area is influenced by both the optical filter and the size of the selection area, whereas the conformity of the ROI to the shape profile is affected only by the optical filter. If the height, width, or area of the plume were to be used for estimating the volume or other properties, such as the plasma, particle distribution, etc., at 810 nm, 394 nm, or any other wavelength regime, it is essential to note that the uncertainties depend on the observation wavelength. Moreover, the error in size and position of the plume should be taken into account for adjusting the uncertainties accordingly.

Table 12. Comparison of the average areas of the ROI and the calculated rectangles.

Optical Filter	394 nm			810 nm		
Laser Spot Position	$\Omega_{-0.2}$	$\Omega_{-0.1}$	Ω_0	$\Omega_{-0.2}$	$\Omega_{-0.1}$	Ω_0
Area_{ROI} (mm^2)	22.9 ↘	20.7 ↘	20.4	34.6 ↗	36.8 ↗	37.2
[1]Area of Rectangle$_{\text{Calculated}}$ (mm^2)						
HEIGHT$_F$ * WIDTH$_F$	38.1 ↘	31.5 ↘	31.2	59.6 ↗	62.5 ↗	62.9
HEIGHT$_E$ * WIDTH$_E$	27.7 ↘	25.2 ↘	24.9	43.4 ↗	46.3 ↘	46.2
HEIGHT$_F$ * WIDTH$_E$	30.8 ↘	27.0 ↘	26.9	49.0 ↗	51.6 ↘	51.3
HEIGHT$_E$ * WIDTH$_F$	30.4 ↘	27.1 ↘	26.9	52.8 ↘	51.6 ↘	51.2

The evolution of the average ROI area of the plume relative to the laser spot displacement for each filter are presented in Figure 102 (with +/- error bar = one standard deviation). The 810 nm filter shows a larger plume surface area compared to the 394 nm filter, likely due to the more intense thermal emission at 810 nm, in addition to the higher sensitivity of the camera sensor leading to an overall increase in registered pixel intensity values.

The observable bright image for a specific spectral region is formed by the superposition of thermal emissivity of the plume's dense core (considered a black body) and atomic and molecular emissions from the less dense outer layers of the plume, according to Planck's law (section 1.4.3.2 p.48, section 2.3.2.2 p.70). The emissivity at 810 nm is much higher than that at 394 nm, particularly at the vaporization temperature of Al. In fact, at the vaporization temperature of Al, the ratio between the emissivity at these two wavelengths is approximately 20 (see Figure 47, p.76).

The lack of atomic or molecular emissions in the 810 nm range means that the observation of the plume at this wavelength can specifically indicate the location of Thermally Excited Regions (TER). The spectral region at 394 nm contains numerous emission lines of both Al I and Ti I, resulting in a strong atomic emission. The image of the plume observed at 394 nm primarily consists of the superposition of atomic emissions, which indicates the location of Atomically Excited Regions (AER). This atomic emission is so intense that it dominates over

---

[1] HEIGHT$_F$ and WIDTH$_F$ are the height and width of the rectangle obtained from the Feret's maximum and minimum diameters, HEIGHT$_E$ and WIDTH$_E$ are the height and width of the rectangle obtained from the Ellipse's major and minor axes.

the thermal emission in this region. This is one reason why the plume area appears smaller in images obtained with the 394 nm filter.

The second reason for the greater 810 nm plume ROI areas compared to the 394 nm, would be the sensitivity of the high speed camera: according to Ametek© (Figure 38 p.68), it is three times higher at 810 nm compared to 394 nm.

While using both the filters, a slight increase in the average plume area was observed while shifting the laser spot on T40. The error bars for the 394 nm filter (i.e., the standard deviations when calculating the average), reduce in size from $\Omega_{-0.2}$ to $\Omega_{+0.2}$ indicating a more regular plume profile with less oscillations when the keyhole lies mainly in T40.
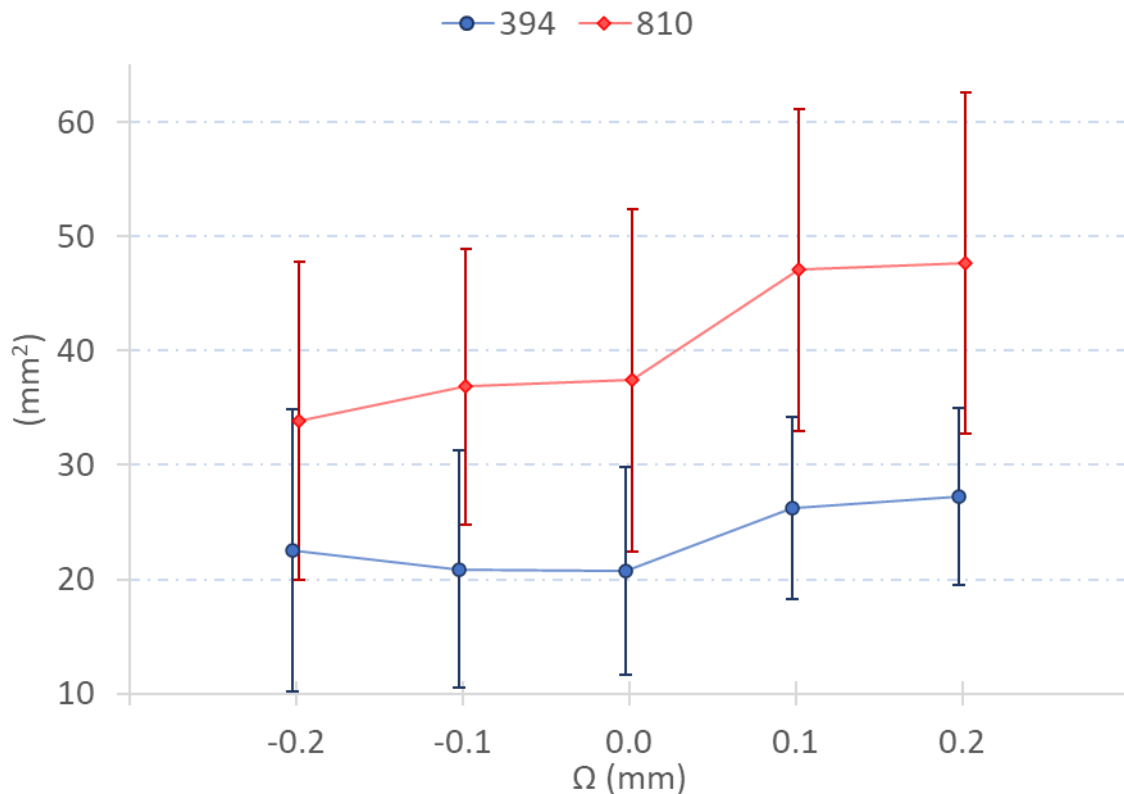
Figure 102. Average area of the plume ROI (error bars = standard deviation).

4.3.3.1.5.   Shape of the Plume

Two methods, the "Feret's diameters" and the "Fit Ellipse" methods were used in this work to measure the height and the width of the vapor plume compared to only the "Fit Ellipse" in the last experimental work (section 4.2 p.100) because it was necessary to validate the plume behavior observed via these methods.

The general behavior of the plume height and width when measured with these methods resemble each other . However, there is about a 10% difference in values measured between the Feret's diameters and the lengths of the ellipse axes. This indicates that the height and the width of the plume measured by these methods can never be exact since the plume has a highly irregular profile. The reasoning why the Feret's diameters are greater than the ellipses' axes can be explained as follows, while the ellipses don't fully encompass the plume profile, the Feret's diameters measure the maximum distances between parallel lines encompassing the plume profile. Nevertheless, even though they differ by a small percentage in their values, the observed tendencies of the average heights and widths of the plumes with laser spot position and optical filter remain the same between both these measurement methods. Also, it has

already been mentioned (section 4.3.2.1.1 p.133) that there is a tendency for the Feret's diameters to overestimate the dimensions of the elongated objects [291].

When the laser spot was moved from the joint line onto T40 ($\Omega_0 \rightarrow \Omega_{+0.2}$), an increase in the height and width vapor plume was observed with the 810 nm filter and 394 nm filters similar to the ROI area. Once again, the height and width of the AER was less than the corresponding height and width of the TER from both the measurement methods due to the reasons mentioned earlier (p.134). The error bars from the standard deviations did not show any significant behavior. However, it can be understood that when the laser spot is offset on T40, higher temperature and more excited atoms in the plume would be present due to greater involvement of Ti in the plume from the increase in laser radiation incident on T40. This leads to the greater height and width for offsets on T40. For the same reasons (decreasing quantity of Ti), the spot offsets on A5754 leads to a small plume in terms of height. However, instabilities generated from increase in Al involvement in the plume leads to a slight increase in width.
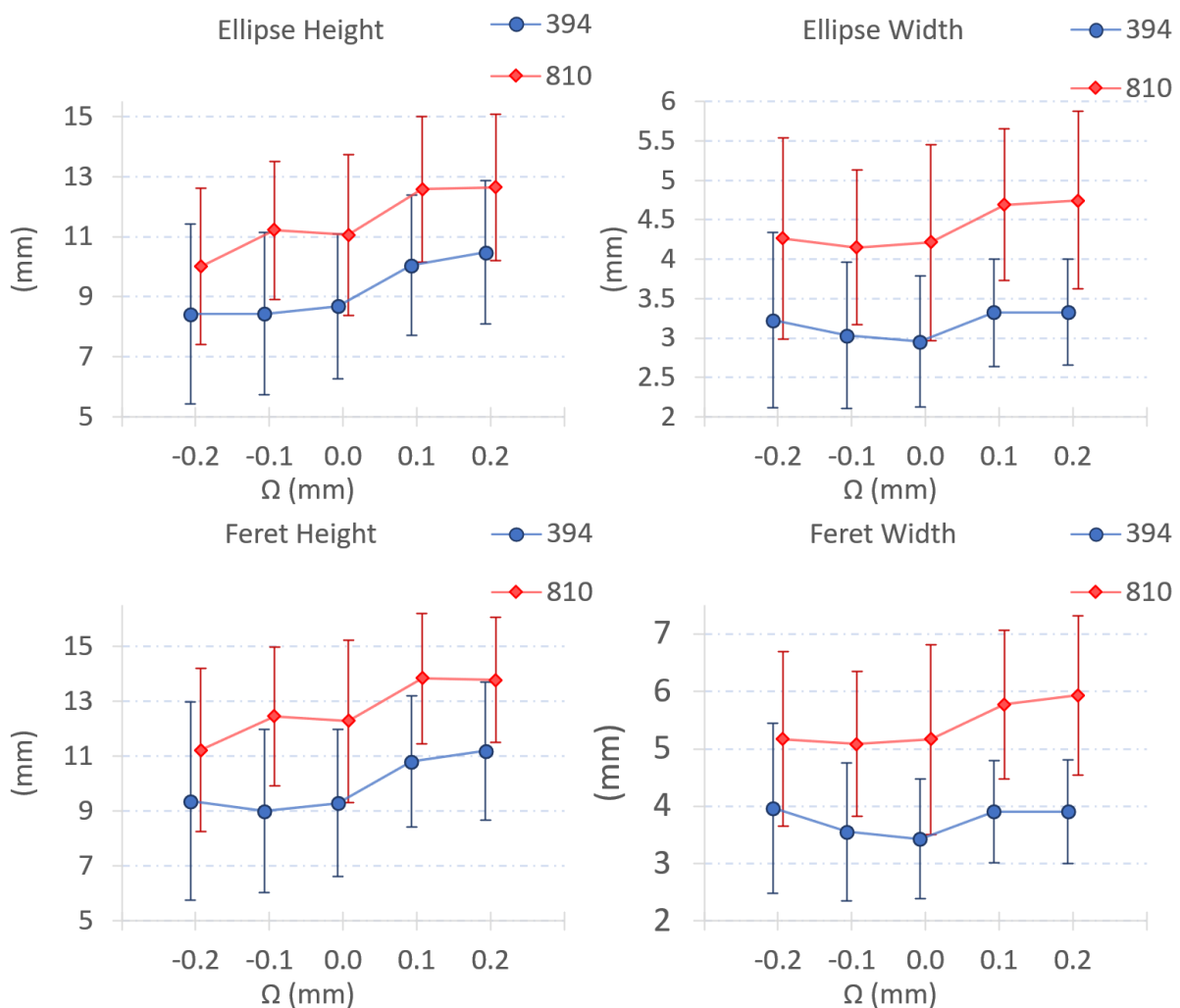
Figure 103. The height and width of the vapor plume measured with fit ellipse and Feret's diameters.

Circularity was considered to be an additional measure in the study of the vapor plume shape (Figure 104). As the circularity value converges towards 1, the object's shape increasingly resembles that of a perfect circle, while lower values signify heightened elongation in the plume shape. Both the AER and TER have a maximum average circularity of $\Omega_{-0.2}$. However, as the laser is displaced from $\Omega_{-0.2}$ to $\Omega_{+0.2}$, the circularity value diminishes indicating that the plume is more elongated which coincides with the higher values of plume height. However, with the measurement of circularity, it can be seen that even though the plume

width values increase as the laser is displaced from $\Omega_{-0.2}$ to $\Omega_{+0.2}$, the plume is more elongated i.e., the ratio of increase in height to width is not the same. This elongation is a direct consequence of the increasing strong Ti jets influencing the shape of the plume.
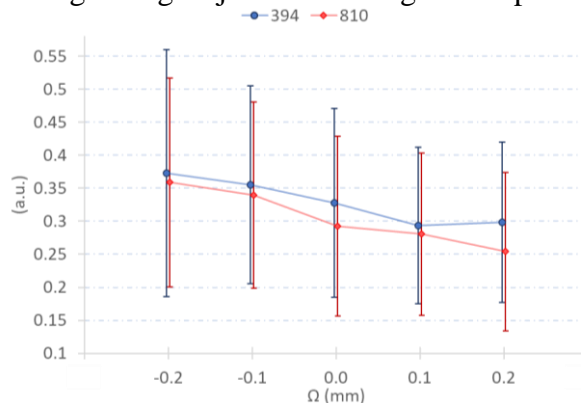
Figure 104. Average circularity of the vapor plume ROI.

4.3.3.1.6.   Plume Inclination

Previous experiments have already discussed the behavior of the plume depending on the angle of inclination (Chapter 3, Section 3.1.3, Chapter 4, Section 4.2.1.4). In order to further understand this behavior, the inclination of the plume was measured again in this experiment. This was done using the angle of the ellipse major axis and Feret's diameter. The Feret's angle and ellipse angle measurements showed similar results (even though their values vary slightly), indicating that the plume orientation behavior remained consistent regardless of the measurement method used. Figure 105 shows a comparison of the average Feret and ellipse angles between the 810 nm and 394 nm filters, where an angle greater than 0° indicates an inclination towards the A5754 side.

While observing the inclination of the TER, when the laser spot is moved from $\Omega_{-0.2}$ to $\Omega_{+0.2}$, the inclination progressively diminishes. However, when observing the AER, the inclination was found not to be dependent on the laser spot position. The differences between the AER and the TER leading to this phenomenon are explained in detail in section 4.3.4 (p.139). It was also noted that the standard deviation (error bars) which could indicate the plume oscillatory behavior progressively reduces when observing the AER while moving the laser from $\Omega_{-0.2}$ to $\Omega_{+0.2}$. It is clear that both the TER and AER are almost completely vertical as the plume is mainly composed of a vertical jet as the laser spot was moved on T40 $\Omega_{+0.1}$, $\Omega_{+0.2}$.
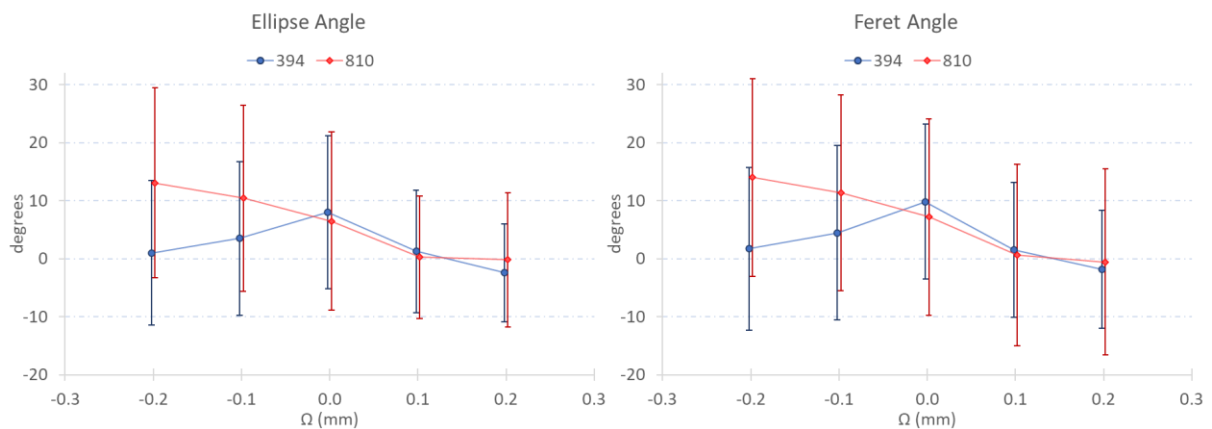
Figure 105. Average angle of the vapor plume from the ellipse and Feret's diameter.

Image moments like centroid and center of mass of the plume were studied to understand the distribution of pixel intensities within the selection ROI. Differences in centroid and center of mass positions are related to brightness distribution in the vapor plume. Y-axis values of these measurements were analyzed to identify the height with the highest vapor plume concentration to aid in identifying the optimum height for spectroscopic acquisitions. The X-axis values were ignored to reduce error caused by camera movements.

The quantification of pixel intensity distribution in laser spot positions on different materials was achieved through image moments such as centroid and center of mass (Figure 106) and these values were termed "Probability Zones" as they represented the most probable locations with maximum intensity for the presence of the plume. Comparing these zones allowed the assessment of TER and AER behavior. Laser spot positions on titanium showed higher probability zones, indicating taller and brighter plumes, with TER exhibiting higher values than AER in certain cases.

The nomenclature "Probability Zones" is attributed to the rationale behind the naming convention explained as follows: Based on common sense and numerical modeling, it is expected that the highest temperature and density within the vapor plume would be situated near the keyhole opening due to the focused laser beam. To study spectroscopy of the plume behavior, it is imperative that the unnecessary signals from the deforming melted surface must be avoided. Moreover, due to the plume's highly oscillatory behavior and irregular shape, precisely localizing the vapor plume to a specific region or volume in space presents challenges. Furthermore, determining temperature or plume composition within this unlocalized space is not ideal. To address this issue, the average of the centroid or center of mass, calculated from multiple selections, proves to be a valuable solution. Despite the plume's non-rigid nature, for a single image (ideally captured with an exposure time less than half the plume's characteristic time period), the centroid or center of mass represents the weighted average position of its constituent parts. Hence, these points aid in localizing the ROI to a much smaller space. Considering the fluctuating orientation and size of the plume, averaging these points enables the determination of the most probable location with maximum intensity for the presence of the plume, thus justifying the term "Probability Zones."

Due to its shape dependency, the centroid tends to have slightly higher Y values compared to the center of mass. This happens because the plume is narrower near the keyhole and becomes slightly wider towards the top while the center of mass is more dependent on the intensity distribution. Additionally, when examining the average images of the plume, it becomes evident that the illuminated regions are primarily located between the probability zone and the opening of the keyhole.

Both the TER and AER of the plume exhibit the tendency to have higher probability zones for laser spot offsets on titanium due to taller and elongated plumes. Similarly, the lower probability zones for the AER are because the atoms with sufficient energy for excited are present at the lower parts of the plume and they lose their energy as they ascend higher. Whereas the TER, which is basically a hot gas propagates much higher while producing thermal emissions.
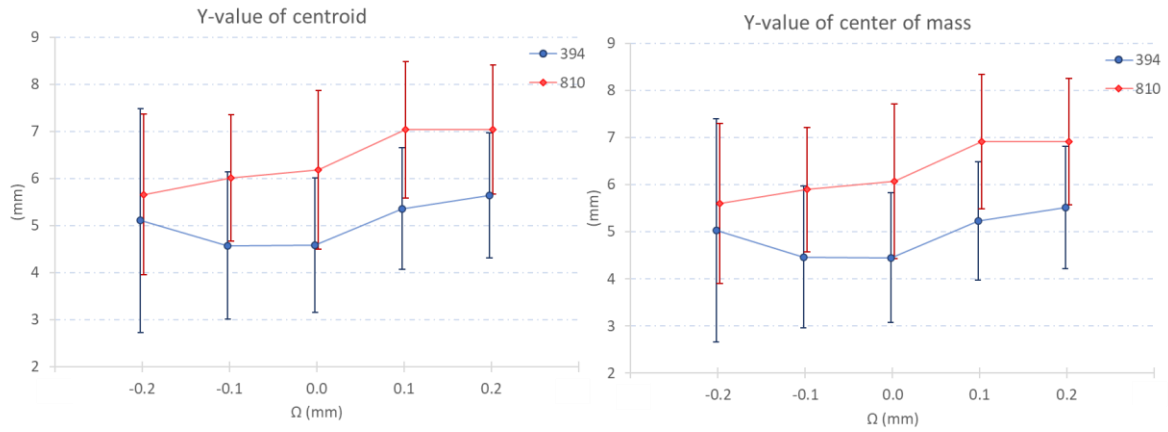
Figure 106. Average Y values of A) Centroid and B) Centroid of the ROI.

The average kurtosis and skewness values of the histograms are presented in Figure 107. While the average kurtosis values did not show any particular trend when comparing different laser spot positions, the kurtosis values of the TER are greater than the AER in general. In other words, the histograms are more peaked with bright pixels than the AER. The average skewness values show a similar difference between the AER and the TER, where the images of the AER have negatively skewed histograms. This is the effect of normalization, where the AER images have been brightened and the TER images have been darkened. When observing the skewness evolution, the maximum laser spot offset on A5754 ($\Omega_{-0.2}$) in particular showed deviation indicating a reduction in general brightness of the plume ROI.
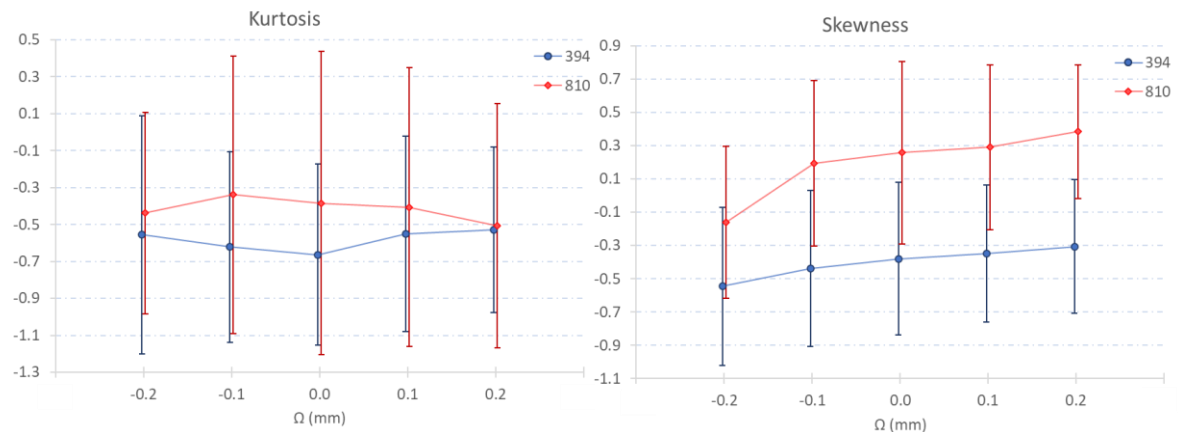
Figure 107. Average values of kurtosis and skewness in the histograms of the ROI.

4.3.4. Unveiling the enigma of the vapor plume: *conclusions and implications*

During the experiments involving continuous welding and the preliminary investigations with pulsed welding (2 ms), the observations made at 810 nm were predominantly attributed to be the vapor plume. This interpretation was valid if we focused solely on the extremely hot region in a gaseous state above the keyhole. However, it is important to note that this viewpoint neglects the fact that the metallic vapor expelled from the keyhole undergoes interactions with the surrounding air, giving rise to more intricate processes. By considering the interaction between the metallic vapor and the surrounding air, we can better understand the complex dynamics and phenomena occurring within the plume because it can significantly influence the behavior, composition, and properties of the plume, leading to variations in its characteristics.

One of the most significant aspects of the interactions between the metallic vapor from the keyhole and air, is from the vaporization of titanium. Because it was concluded from the preliminary investigation in pulsed welding:

"The prominent inclination of the plume towards aluminum was attributed to the preferential evaporation from the titanium surface, which must be more than the evaporation from the more reflective and conductive aluminum side of the joint." (Section 4.2.3.1, p.111)

However, one must note that with the discrepancies in the measurements between the behavior of the thermally excited regions and the atomically excited regions, additional insights about the plume are necessary.

From Section 4.3.3 (p. 125 - 139), the several measurements led to the hypothesis that the plume observed with the 810 nm filter i.e., the TER of the vapor plume, consists of more than just the vaporized metallic material form the keyhole. Because, at the wavelength λ = 810 nm, any material with sufficient temperature can emit thermal radiation (Eqn. 26, p.45). However, from the visual analysis of the vapor plume videos at another wavelength (λ =394 nm), it was understood that the vapor plume behavior has not been the same. This TER region could be influenced by titanium since the vaporization temperature of titanium was higher than that of aluminum, the thermal emission of titanium would be higher than that of aluminum (augmented multiple folds by the higher sensitivity of the camera at 810 nm).

From the spectrometric analysis, it was understood that the atomic emission lines of aluminum and titanium were too close (section 2.3.2.2, p.70), and it was difficult to distinguish them separately. Yet, it was understood that since titanium is more absorbent to the laser wavelength (Table 2, p.57) and also it is easily excitable compared to aluminum (Titanium's first excited energy level 6556 cm^{-1}, Aluminum's first excited level 25347 cm^{-1}), the titanium jets would be brighter than that of the aluminum vapors. Therefore, it would be prudent to discuss the AER's behavior of the vapor plume before discussing the additional (metallic vapor $\leftrightarrow$ air) interactions of the TER.

4.3.4.1.   A discussion on the AER (Atomically Excited Regions) of the vapor plume

Visual analysis of the original videos (before equalization and normalization) of the AER (λ = 394 nm) for the laser spot position $\Omega_{-0.2}$ show that while there is vaporization of both A5754 and T40, the Ti-rich jets are not strong enough to produce an inclined phenomenon. This weakness of the Ti-rich jets is due to the fact that, for this laser spot position only ~ 21% of the total laser power is incident on T40 (Figure 108).
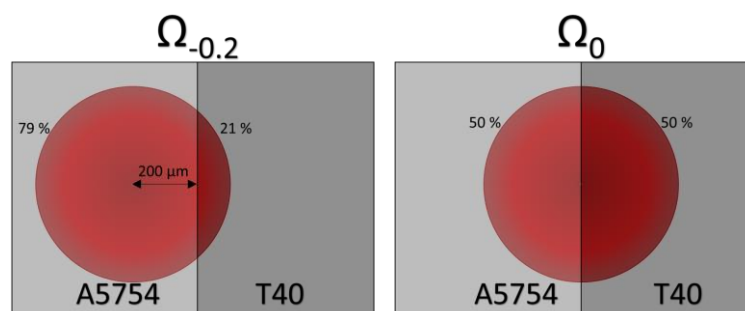
Figure 108. The percentage of area of the laser spot impact shared by A5754 and T40.

With the spectral data indicating that the atomic emissions of aluminum and titanium being very close in the 394 nm wavelength range, this method of visually differentiating isn't very effective. Additionally, with turbulences arising from interactions between the hot metallic vapor and the surrounding air, visual analysis could become more difficult.

However, the AER images for $\Omega_{-0.2}$ are presented here for different instances to better understand the different parts of the plume (Figure 109).

Examination of Figure 109.A reveals that the inclination of the bright region corresponds to the emission of a Ti vapor jet (red) from the keyhole wall. Additionally, a diffuse region of Al atoms (yellow) is present, which may contain minor quantities of Ti.

This observation is corroborated by Figure 109.B, a consecutive image captured over an exposure time of 120 µs. The image demonstrates that the lighter Al atoms are readily influenced by convective or turbulent forces, in contrast to the heavier Ti atoms, which do not exhibit such behavior. It's important to note that other factors such as temperature, density, and vapor pressure can also affect the behavior of the vapor jet and its interaction with convective forces.

The analysis of Figure 109 (C, D, E, F) demonstrates a noteworthy discrepancy in the vaporization rates between aluminum and titanium under examination. Despite the potential for a higher concentration of Ti atoms in comparison to Al atoms, the vaporization rate of Al, characterized by a diameter (of the yellow bounded region) of approximately 2 mm, surpasses that of Ti with a diameter (of the red bounded region) of around 0.2 mm throughout the entire duration of the pulse.

Moreover, convection phenomena are frequently observed, leading to the curvature of Ti jets towards the joint line due to pressure fields at the center of the plume (Figure 109.D). Nevertheless, it is worth noting that the Ti jet exhibits intermittent behavior, and its duration diminishes over time. In contrast, the vaporization rate of Al remains consistently high and is accompanied by significant keyhole instabilities, ultimately resulting in the extinction of both the Ti jet and the vapor plume.

These findings highlight the pronounced differences in the vaporization dynamics of Al and Ti, showcasing the enhanced vaporization of Al during dissimilar welding despite the stronger/brighter jet of Ti.

Figure 109.E exhibits a closed keyhole, presenting a challenge in predicting element concentrations within the cyan polygon solely based on HSI. The visualization indicates the presence of remnants from previously emitted vapors positioned above the keyhole, with no ongoing vapor expulsion. However, the ejection of the vapor plume recommences in Figure 109.F, accompanied by the appearance of a small, tilted Ti vapor jet resembling the initial stages observed in Figure 109.A.When the remnants of the plume fail to remain undiffused within the capture zone, the available illuminated pixels are inadequate for selection of an ROI.

Such an occurrence happened during an extinction event in one of the 394 nm videos in $\Omega_{-0.1}$, wherein the velocity fields in the capture zone facilitated rapid diffusion of the plume remnants. Despite the relatively brief duration of the entire vapor plume's extinction phenomenon, the vaporization of Al, coupled with the frequent extinction of Ti jets, leads to intricate interactions between the plume and the surrounding air. Consequently, predicting the shape, size, and orientation of the plume with 100 % accuracy becomes impossible. However, it becomes very clear that the prominent vaporization of Al caused from the strong initial Ti jets, eventually leads to cooling down, instabilities in the vaporization processes, turbulences in the higher regions and finally the extinction of the vapor plume.
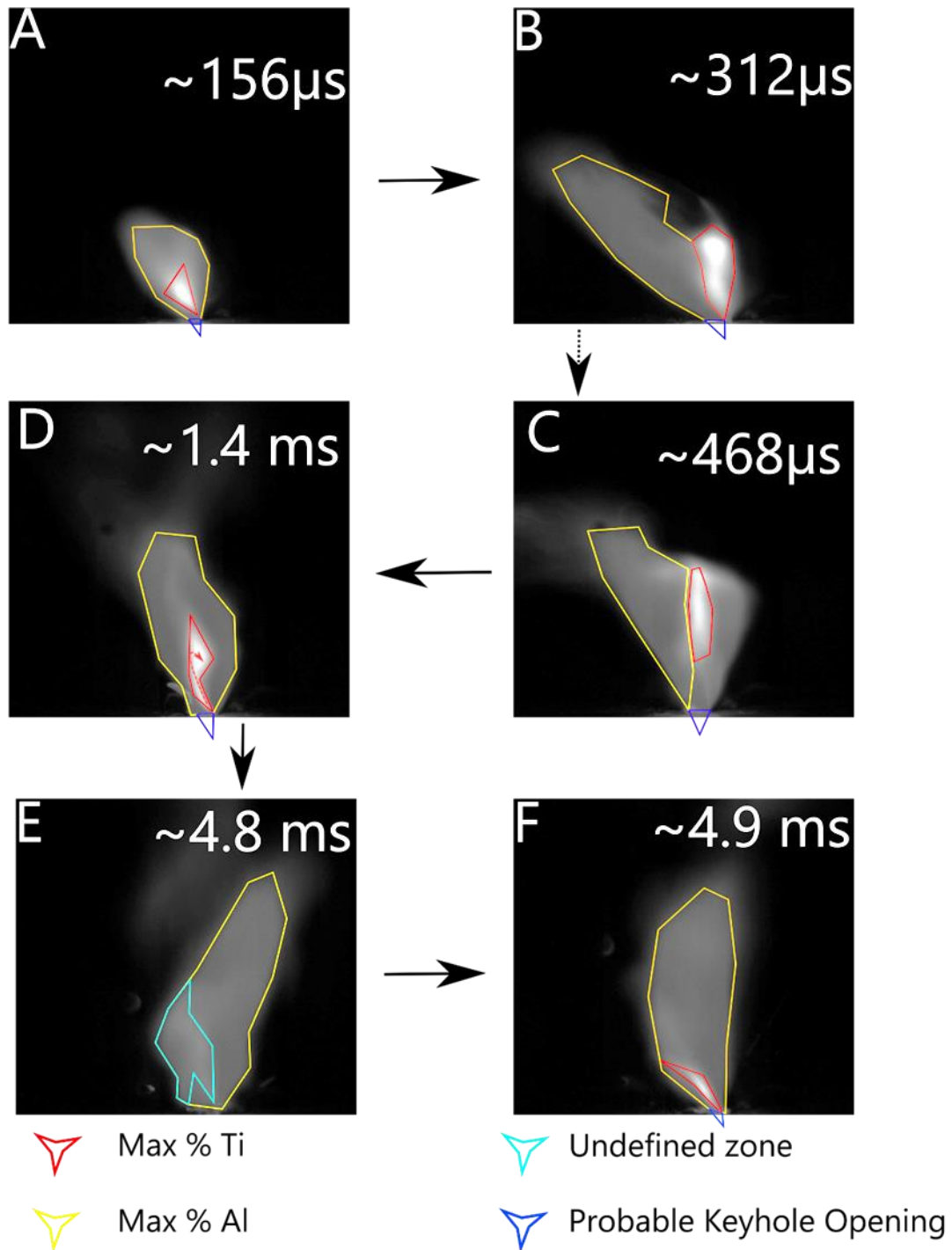
Figure 109. Images of the AER for $\Omega_{-0.2}$ taken at different moments. (Brightness:+40%, Contrast:-20% for better printing)

The analysis of the AER reveals distinct characteristics between the Laser positions of $\Omega_{-0.2}$ and Ω_0. Notably, the Ti jet within the Ω_0 plume exhibits greater height and luminosity, reaching approximately 3-4 times higher than the AER of $\Omega_{-0.2}$ (Figure 110.C). A slight increase in width is also observed, potentially attributed to diffusion under convective velocity fields.

Another significant difference lies in the stability duration of the Ti jet within the plume. The Ω_0 condition maintains a stable Ti jet for approximately 3 ms, while turbulence affects the $\Omega_{-0.2}$ AER at around 1.2 ~ 1.5 ms. This observation correlates with the previous hypothesis that the

Al vaporization leads to the extinction of the plume since $\Omega_{-0.2}$ has majority of the laser incident on A5754, and consequently a higher proportion of Al would be entering into the mix.

The observed variability in strength and stability of the Ti jet among different laser spot positions is of the utmost importance. In the case of Ω_0, the Ti jet possesses sufficient strength and stability to exert influence on the AER's direction. Conversely, the Ti jet in $\Omega_{-0.2}$ is too weak and unstable to induce any discernible changes.

Consequently, the average angle between the TER and AER for Ω_0 displays nearly identical temporal behavior (blue and yellow curves in Figure 100, p.132) with a slight temporal shift. Likewise, the average angles of the AER and TER remain closer for Ω_0 (Figure 105, p.137). In contrast, $\Omega_{-0.2}$ (purple and green curves in Figure 100, p.132) and $\Omega_{-0.1}$ (not presented in this document for continuity) exhibit deviations due to the limited momentum of the Ti jets, which fails to influence the velocity fields. Consequently, the AER inclination of Ω_0 exceeds that of $\Omega_{-0.2}$ (Figure 105, p.137).

These observations (from combining visual analysis with data analysis) bring clarity on the unique characteristics and dynamics of Ti jets in different laser spot positions, underscoring the role of strength, stability, and momentum in shaping the AER behavior.
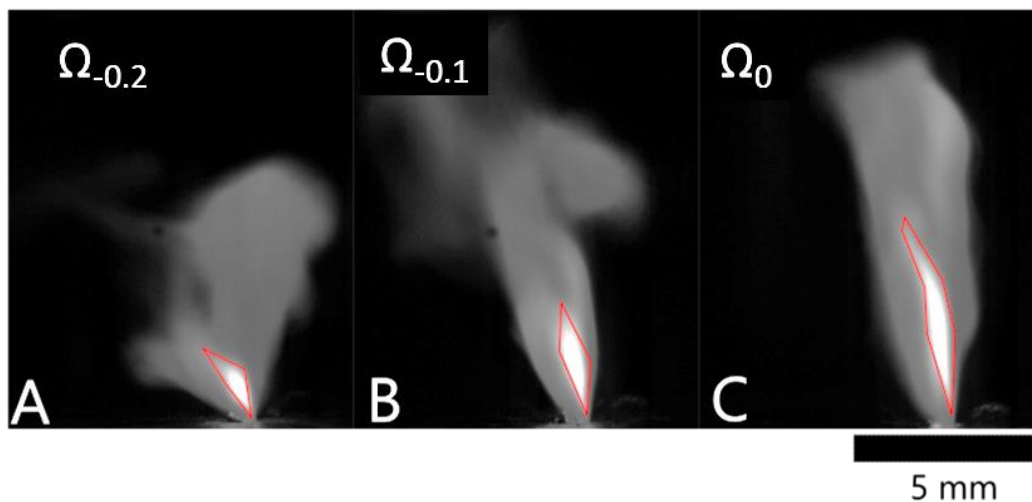
Figure 110. Concentrated Ti jets at time ~625 μs present within the AER for A) Ω-0.2, B) Ω-0.1 and C) Ω0. (Brightness:+40%, Contrast:-20% for better printing)

4.3.4.2. A discussion on the TER (Thermally Excited Regions) of the vapor plume

Despite being relatively less concentrated and having minimal influence on the distribution of Al vapors, the small Ti jets observed in laser spot position $\Omega_{-0.2}$ exhibit thermal effects that should not be overlooked. Figure 111, captured using the 810 nm filter, provides insight into these thermal interactions. Figure 111.A presents the original untreated TER for $\Omega_{-0.2}$, while Figure 111.B, C display the normalized plumes with highlighted ROI in green, fitting ellipses in red, and Feret's diameters in purple. This TER closely corresponds to the AER shown in Figure 110Figure 111.A and was captured at approximately 0.935 ms. The small, concentrated Ti jet from the AER is marked in red on Figure 111.A.

However, notable differences are observed in the region enclosed by the white curves, which appear slightly brighter than the rest of the plume and extends from the Ti jet. Consequently, the surrounding areas become brighter (due to the higher temperature of the Ti vapor), leading to a change in the overall shape and size of the observed plume in the TER compared to the corresponding AER (Figure 111.A). Although the Ti jet for $\Omega_{-0.2}$ did not possess sufficient strength to directly influence the shape and size of the AER (Figure 110.A), its thermal

interactions with the surrounding regions are significant. These thermal effects contribute to higher inclination angle values observed in the TER of $\Omega_{-0.2}$.

These findings emphasize the importance of considering the thermal influence of the weak Ti jet in laser spot position $\Omega_{-0.2}$. Despite its limited impact on the shape and size of the AER, the thermal interactions exert significant effects on the surrounding regions. Such thermal effects should be taken into account when analyzing the dynamics of laser spot positions and their interactions with the surrounding environment.

The properties of titanium such as its higher absorptivity, higher vaporization temperature, and higher emissivity, contribute to the observed phenomenon. Additionally, an intriguing observation is the disparity in the initiation of the laser pulse between $\lambda = 810$ nm and $\lambda = 394$ nm, can explain the temporal shift that arises as an artifact resulting from the discrepant overall emissivity between the two wavelength regions, corresponding to thermal emissions and atomic emissions from the vapor plume.
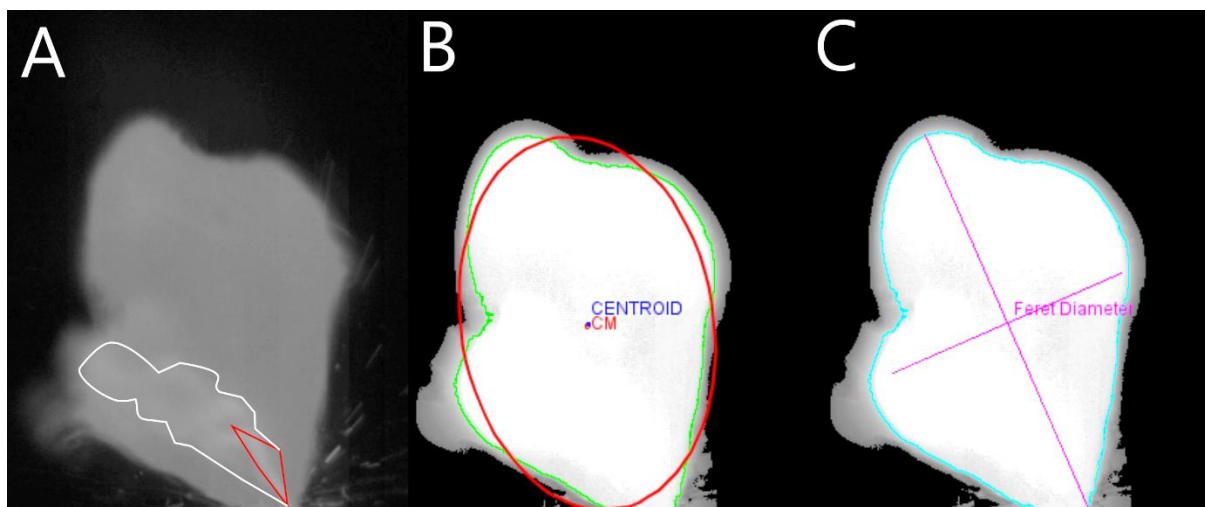
Figure 111. TER for Ω-0.2 at ~0.935 ms A) Untreated image with Ti jet (Red) and high temperature zones (white) B) Normalized with ROI, fitting ellipse, centroid, and center of mass C) Normalized with ROI and Feret's Diameters.(Brightness +20% for better printing)

4.3.4.3. An integrated summary of notable conclusions from HSI

To examine the disparity between the plume observed at 810 nm (TER) and 394 nm (AER), it is essential to visualize the differences between the normalized images. Subtracting the normalized AER (Figure 112.B) from the TER (Figure 112.A) would yield a distinct figure representing the metallic vapor and the surrounding air that were thermally excited but lacked sufficient energy to generate atomic emissions. This resulting (orange line bound bright areas in Figure 112.C) identifies the thermal emissions in the region, which can significantly influence the perception of the vapor plume and potentially introduce inaccuracies in the measurement values. While the figure shown here corresponds to one instant, throughout the duration of the pulse, multiple additional phenomena such as air-metal vapor interactions, turbulences could occur causing more differences between the TER and AER.
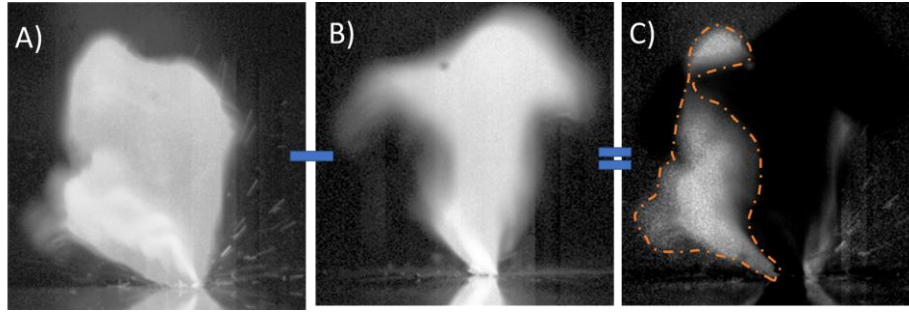
Figure 112. Image operation2 subtracting the difference between the TER and the AER.

To facilitate comprehension of the various analyses, results, and inferences presented in this study, a concise tabulation comparing the relative observations for the two laser spot positions $\Omega_{-0.2}$ and Ω_0 is compiled, accompanied by corresponding explanations.

Table 13. Significant observations and inferences

Property	$\Omega_{-0.2}$	Ω_0	Evidenced by	Inference/Explanation
Atomic % of Ti in vapor	↓	↑	Spectroscopy (section 4.5)	Less incident laser power on Ti
Area of TER	↓	↑	HSI – Area	Depends on % Ti
Area of AER	↑	↓		Higher in $\Omega_{-0.2}$ due to turbulences from Al in vapor
Angle of TER	↑	↓	HSI – Angle	TER surrounds Ti jets even for lesser concentrations and momentum
Angle of AER	↓	↑		Ti jets cannot not dominate the entire AER when weak and unstable in $\Omega_{-0.2}$.
Vertical position of center of mass for TER / High Temperature zones	↓	↑	HSI – Centroid/Center of mass	Depends on the height of the Ti jet.
Vertical position of center of mass for AER / Max concentration zones	↑	↓		Discontinuous plume behavior, unlocalized detached remnants of plume cause higher PZ in $\Omega_{-0.2}$.
Temperature	↓	↑	HSI – Skewness, Spectroscopy (section 4.5)	Depends on Ti % in vapor.

In the case of laser spot position Ω_0, the vapor plume exhibits a relatively stable behavior, influenced by the titanium (Ti) jet originating from the keyhole's wall, which impacts the

---

[2] These images (A and B) were chosen manually by visual analysis to find the TER and AER which closely resemble each other in terms of size, shape and time of occurrence. Imaging using two synchronized cameras would be ideal to make these kinds of operations between the images from different optical filters.

plume's size, shape, and orientation. However, this phenomenon is not observed to the same extent in laser spot position $\Omega_{-0.2}$. In laser spot position $\Omega_{-0.2}$, the Ti jets primarily influence the distribution of thermal energy within the vapor plume and its surrounding air. Spectroscopic analysis reveals lower emission intensity for laser spot position $\Omega_{-0.2}$, attributed to the presence of smaller and less stable Ti jets.

The instabilities observed in laser spot position $\Omega_{-0.2}$ are a consequence of the unstable vaporization of aluminum (Al), characterized by non-directional and unstable behavior. Consequently, both the Ti jets and the entire plume experience frequent extinction events, occurring more frequently in laser spot position $\Omega_{-0.2}$ and rarely in laser spot position $\Omega_{-0.1}$. These repeated extinctions result in enhanced turbulent effects due to convection interactions with the ambient air. As a result, the plume becomes less spatially localized, exhibiting a larger probability zone and a broader ROI in the AER images, as well as increased width in both the TER and AER.

Moreover, the findings indicate that the ellipse angle is more suitable for orientation calculations compared to Feret's angle specifically within the context of laser spot position Ω_0. Notably, both TER and AER have similar orientations in laser spot position Ω_0. The choice between the centroid or center of mass does not yield a significant advantage in orientation determination. Mean values are less useful when image normalization is required. While Feret's diameters may exhibit slightly higher positive errors, they offer greater accuracy in predicting relative variations in plume size compared to the ellipse axes.

These conclusions provide valuable insights into the distinct characteristics and behaviors of vapor plumes for different laser spot positions and the several possibilities in image treatment methodology, contributing to a deeper understanding of the intricate interactions of the laser welding plumes, Ti jets, Al clouds, the surrounding air and most importantly, the differences between a thermal image and an image of the atomic emissions.

4.4. Examination of the keyhole dynamics in pulsed dissimilar welding

In the preceding sections (4.2, 4.3), an exhaustive analysis was performed on the characteristics of the dissimilar vapor plume. This investigation was undertaken due to the intricate relationship between the properties of the laser-induced plume and the behavior of the keyhole, with particular emphasis on the plume's inclination, a parameter intricately linked to the geometry of the keyhole walls [156]. However, the keyhole dynamics were inferred primarily from vapor plume characteristics and post-melt zone observations. Observing the molten surface from the top-view provides an incomplete assessment of the keyhole's geometry. To achieve a lateral view of the keyhole, a practical approach (section 1.2.4, p.32) involves using a combination of a metal plate and optically transparent ceramics like Pyrex glass, which evenly distributes the laser beam's radiation between the metal and glass components [133].

The experimental setup (Figure 113) employed for keyhole observation involved a vertical junction between 3 mm thick plates composed of aluminum alloy A5754 and titanium T40. These metallic plates were secured in place with a 3 mm thick fused quartz plate in front, which extended approximately 2 mm above the metallic plates. To prevent the reflection of the laser beam back into the optics, the laser beam axis was inclined at an angle of 3° from the vertical metal/quartz plane.
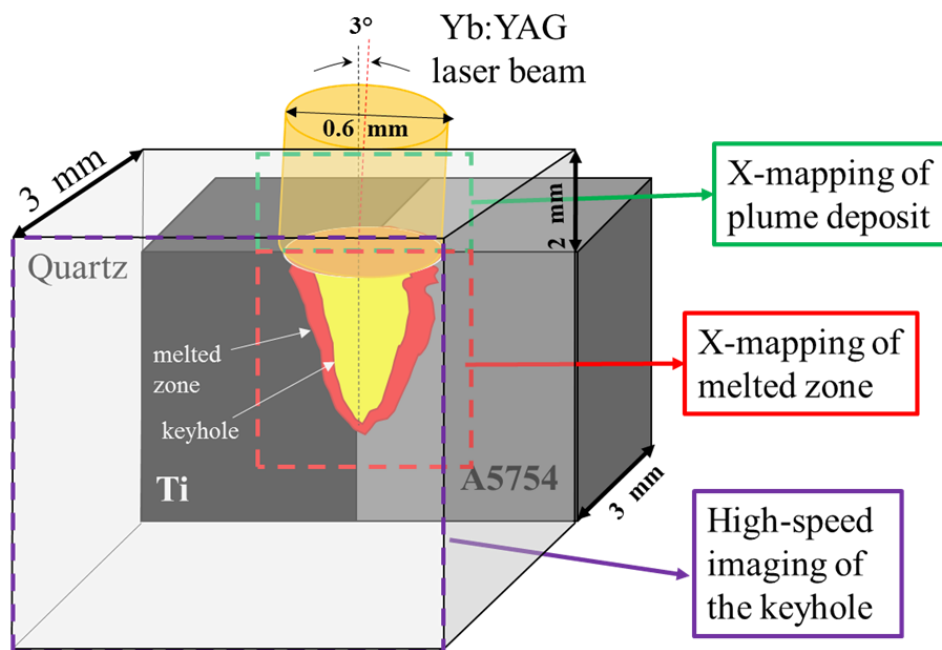
Figure 113. Direct Observation of the Drilled hOle (DODO) experimental setup.

The experimental parameters were selected to align with previous experiments conducted in the butt-configuration (Section 4.3, p.113). Standalone 6 ms laser pulses were made at a consistent power output of 2 kW, with a laser beam diameter of 600 µm operating at a wavelength of 1030 nm. The laser spot was precisely focused on the interface between two metal plates and the quartz plate to evenly distribute half of the spot area on the quartz surface and the other half on the metal side. Five different positions of the laser spot relative to the joint line (Figure 114) were studied. No gas protection was employed.
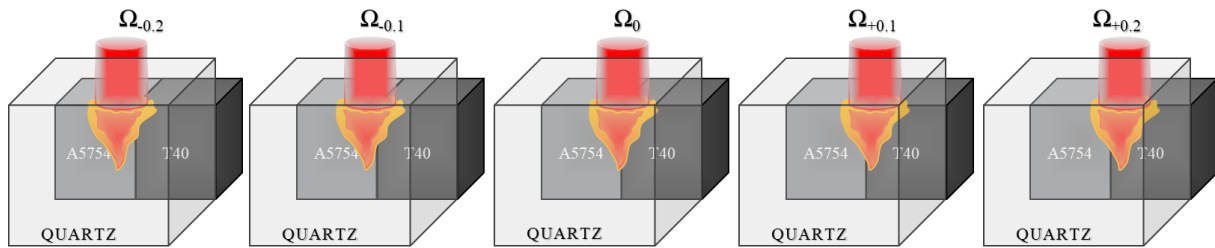
Figure 114. Schematic for the 5 laser spot positions used in the Dodo experiments.

High-speed imaging was conducted to capture a frontal view of the keyhole, which was observed through the quartz plate. The imaging was performed at a frame rate of 6400 fps, with an aperture setting of 11 and an exposure time of 30 µs. The resulting images had a resolution of 480 x 480 pixels and covered a field of view measuring 6.5 mm x 6.5 mm. The 810 ± 3 nm bandpass filter with a full width at half maximum of 10 ± 2 nm, was used in these experiments.

Subsequent to the HSI experiments, a post-mortem examination of the dissimilar metallic joints (highlighted red in Figure 113) and the quartz plates (highlighted green in Figure 113) was conducted employing the JSM-6610 electron microscope. X-maps illustrating the distribution of key elements Al, Ti, and Mg in the melted zones and plume deposits were generated. The average elemental composition of the plume deposits was determined via analysis with an EDX probe.

4.4.1. Validation of the experimental method

Although transparent materials have been employed in studies for keyhole observation, it was essential to validate that the inclusion of quartz in the experiment would not compromise the validity of the results. Quartz was the chosen material owing to its considerably lower thermal diffusivity relative to T40 and A5754 (Table 2 p.57, Table 3 p.60). This selection minimized the potential for substantial modifications in the keyhole dimensions due to localized heat loss effects. Furthermore, quartz's transparency to wavelengths around ~1 µm, with over 95% of the laser radiation directed onto the quartz plate, was not expected to induce significant thermal effects. However, it's important to highlight that the quartz plate's transparency at this wavelength would have prevented the occurrence of some of the multiple reflections within the keyhole, resulting in the lateral dispersion of certain photons. Consequently, prior to interpreting the acquired data, it was crucial to validate the appropriateness of using quartz for keyhole observation [292].

To assess the effect of quartz, a comparative analysis was conducted on the penetrations of the metallic melted zones measured at the joint line (P_{jl}), between the T40/A5754/quartz experiments and the conventional butt-welded A5754/T40 configuration without quartz (Figure 30 p.59). It was observed that the penetrations of the metallic melted zones in the T40/A5754/quartz experiments fell either within or in close proximity to the confidence intervals (evaluated using bilateral Student's t-distribution) associated with the average melted zone penetrations observed in the classical butt-welded configuration (Figure 115). This result validated empirically utilizing fused quartz for keyhole observation in the context of pulsed dissimilar welding in the butt-welding setup.
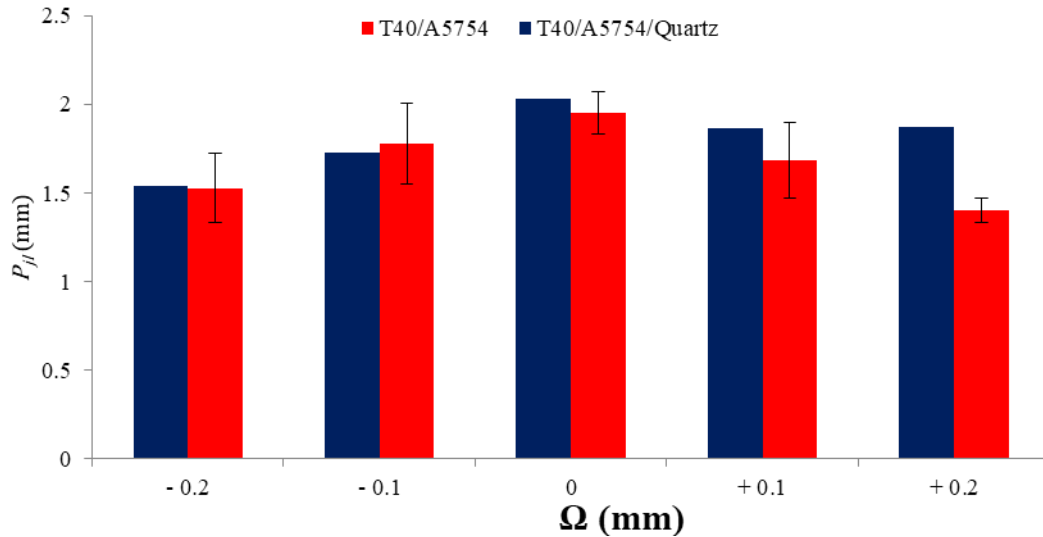
Figure 115. The comparison of melted zone penetrations at T40/AA5754 joint line in T40/AA5754/Quartz and butt-welded T40/AA5754 joints.

4.4.2. Keyhole and Melted zone morphology

The lateral thermal emissions from the keyhole through the quartz medium through the 810 nm bandpass filter using the forementioned welding and acquisition parameters allowed observation of keyhole drilling for the different laser spot positions (Figure 116). It was noted that a relatively higher luminosity was exhibited by the melted zone on the T40 side, while the melted zone with A5754 had a low luminosity, due to the difference in their vaporization temperatures (Table 2 p.57). This observation was consistent with the principles of the Stefan-Boltzmann law, which governs thermal emission phenomena (Eqn.36, p.48). Owing to the elevated vaporization temperature of T40, a bright keyhole with a maximum depth of 1.28 mm was observed in T40, surrounded by the formation of two lateral humps comprised of dull melted material. In contrast, the A5754 alloy, characterized by its high reflectivity and thermal diffusivity, gave rise to a relatively shallow keyhole, measuring only 0.33 mm in depth. This happened only at the end of the pulse after a long period of inactivity (~ 4.5 ms).

In the dissimilar welding of T40 and A5754, with the laser beam centered on the joint line (Ω_0), a significantly greater keyhole penetration of 2.38 mm was achieved, which was almost double the standalone T40 penetration. The keyhole was primarily positioned on the A5754 side, with its root being slightly displaced from the joint line. This behavior of the keyhole can be attributed to the robust synergetic effect that was observed within this dissimilar combination. T40, characterized by a higher absorption coefficient for the Yb:YAG laser and a greater vaporization temperature compared to A5754, facilitated the melting and vaporization of the A5754 side through the heat transfer from the molten titanium and titanium vapor. This is supported by the presence of a well-illuminated surface layer of melted A5754 adjacent to the keyhole wall. Multiple reflections originating from the Ti wall should also contribute to this phenomenon. Therefore, the keyhole develops mainly on A5754 side with the lower vaporization temperature. Nevertheless, the noted displacement of the keyhole root on A5754 by 0.16 mm could also be attributed to the 3° inclination of the welding head, which approaches the theoretical laser beam position at 2.38 mm penetration (calculated by (tan3°)×2.38 mm = 0.12 mm).

The previously observed plume inclination (section 4.3.3.1.6, p.137), especially in instances involving beam offsets on A5754 ($\Omega_{-0.2}$, $\Omega_{-0.1}$), can be directly correlated to the keyhole wall on the T40 side aligning tangentially with the joint line (Figure 116). Conversely, the diminishment in plume inclination with beam displacement ($\Omega_{+0.1}$, $\Omega_{+0.2}$) towards T40

(section 4.3.3.1.6, p.137) is due to the reduced contribution of A5754 in keyhole formation (Figure 116). This behavior can be clearly correlated to the plume evolution toward the characteristic vertical stable jet in the context of standalone titanium welding. This confirmed that plume inclination is initiated by a hot and rapid vapor jet, perpendicular to the surface of the molten T40, which expels the liquefied A5754 material.
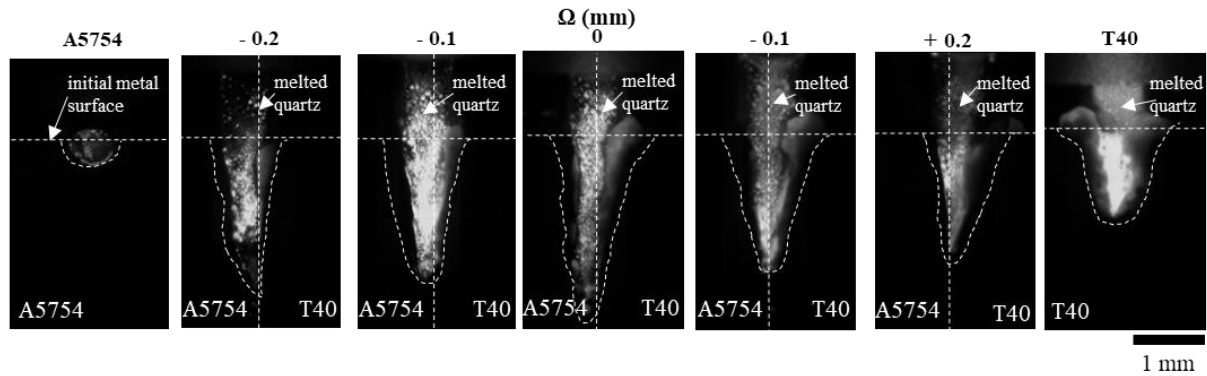
Figure 116. HSI images of the keyhole at the end of the pulse through 810 nm band-pass filter (horizontal lines – surface of metal plates, vertical lines – joint lines, curved lines – limits of the melted zone from SEM observation).

The final depths (P_{max}) of the keyholes were found to be consistent with the penetrations of the melted zones determined from post-mortem analysis (Figure 117). When the beam was offset toward the T40 side ($\Omega_{+0.1}$, $\Omega_{+0.2}$), a notable reduction in keyhole depth was observed. This decrease in keyhole depth was due to the higher energy required for vaporizing the titanium, coupled with a diminished involvement of AA5754. Similarly, when the beam was offset on the A5754 side ($\Omega_{-0.1}$, $\Omega_{-0.2}$), a relatively minor reduction in penetration was observed, due to the continuous synergy between T40 and A5754, even when the keyhole wall on the T40 side was tangent to the joint line. Furthermore, the decrease in penetration compared to the centered beam position can be partly attributed to the shifting of the laser focal point away from a µm-gap between the clamped plates, which facilitates the drilling process.
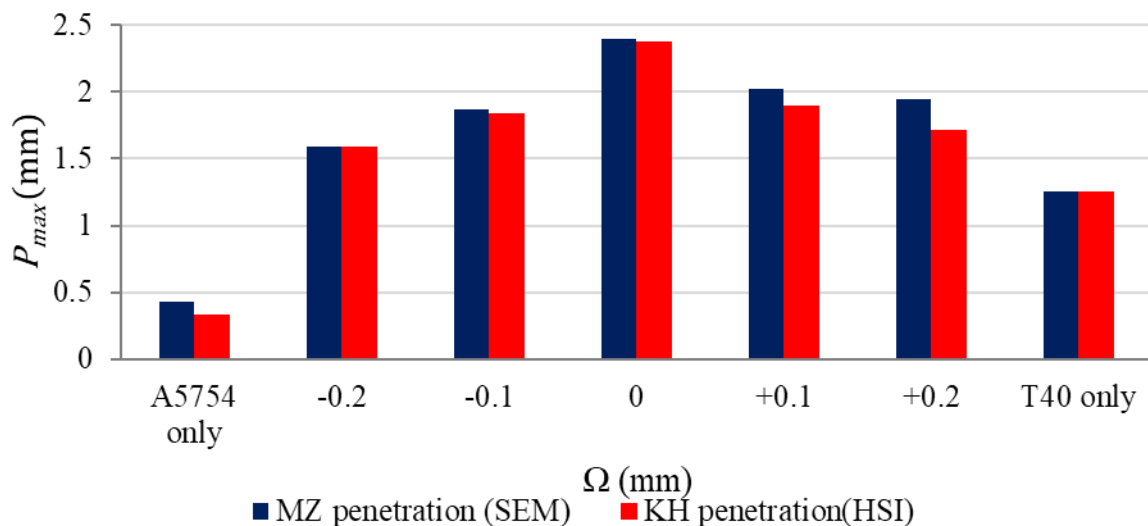
Figure 117. Maximum keyhole and melted zone depths from HSI and SEM observations.

4.4.3. Keyhole dynamics

When studying the temporal evolution of the keyhole depth (P_i) during the pulse duration (Figure 118) the dissimilar joints' drilling dynamics resemble to that of standalone T40. Similar to the results of the keyhole depth, the drilling rate is the highest for laser spot centered on the

joint line (Ω_0) and is proportional to closeness of the laser spot to the joint line. As mentioned earlier, for A5754, there was no keyhole development up to 4.5 ms. Due to the high reflectivity and thermal conductivity of the melted but flat aluminum surface and the energy required to break the native oxide layer, the keyhole drilling starts only after reaching a certain energy threshold.

The instantaneous drilling rates (V_i) were calculated based on the equation:

$$V_i = \frac{P_i - P_{i-1}}{dt} \qquad 61$$

where dt is the time lapse between two images (156 µs) and P_{i-1} and P_i are the keyhole penetrations from two successive frames. The average drilling rates ($\bar{V}$) were calculated for every metal/quartz experiment using the whole set of instantaneous drilling rates:

$$\bar{V} = \frac{\sum_{i=0}^{n} V_i}{n} \qquad 62$$

where n was the total number of the frames with visible keyhole.
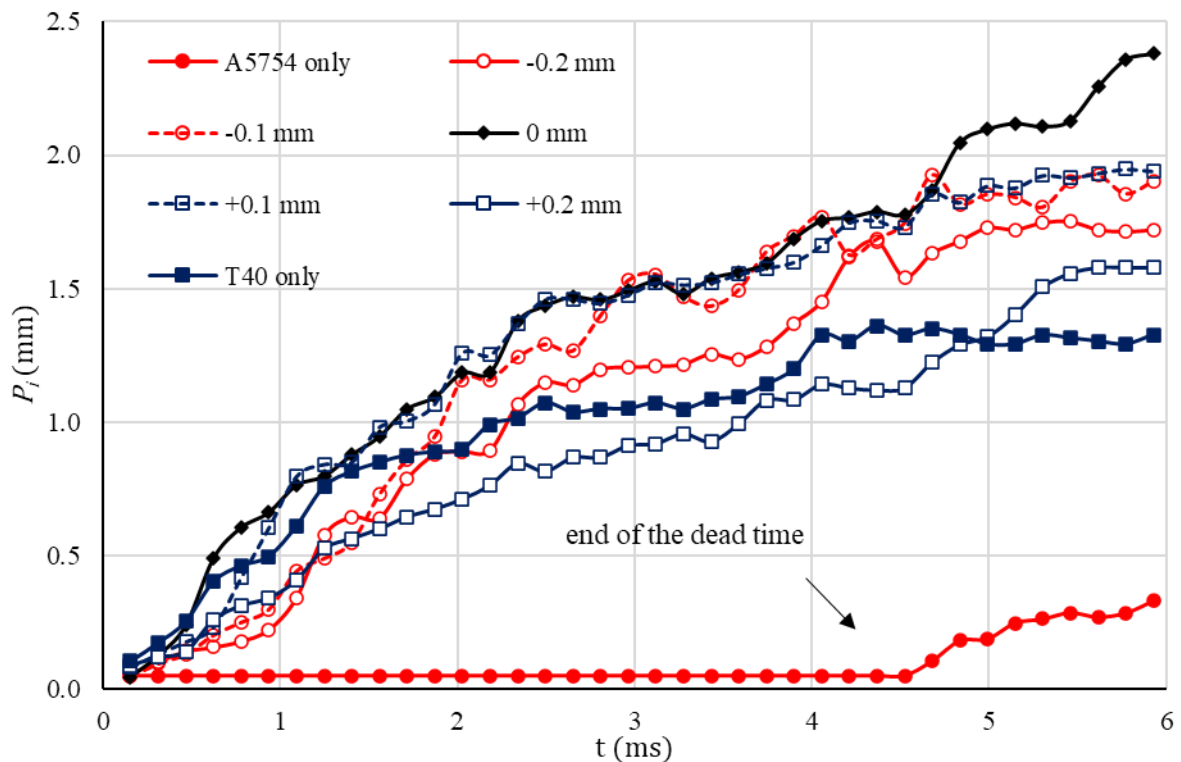
Figure 118. Temporal evolution of the keyhole depth for different laser spot positions and standalone materials.

Table 14. Average keyhole drilling rates for standalone materials and dissimilar welding.

$\bar{V}$	A5754	-0.2mm	-0.1mm	0mm	+0.1mm	+0.2mm	T40
(m/s)	0.21[*]	0.26	0.32	0.4	0.31	0.29	0.19

[*]besides the dead time.

4.4.4. Post-mortem analysis of melted zones

Several common characteristics were observed in the X-maps of the melted zones in the dissimilar joints (Figure 119). The formation of a depression on the surface of the melt partially filled by melted Ti observed in almost all the cases was the result of a evaporative matter loss during the keyhole drilling process. However, proportional to the beam offset towards A5754 the melted material from the A5754 is observed to be forming an expulsion wave. The significant accumulation of magnesium at the top of the melted zones is indicative of substantial evaporation and subsequent oxidation of Mg. And so, the precipitation of MgO particles both within and around the melted zone could be observed (also seen in section 4.3.1, p.113). Evidently, similar accumulation of MgO was also observed in standalone A5754, where the concentration of Mg in the melted zone decreased by ~1.5 at. %. Assessing the depletion of Mg in the dissimilar melted zones is challenging due to the MgO contamination. Furthermore, the presence of remnants of molten quartz in the form of dark regions was frequently found on the hotter T40 side of the melted zone.
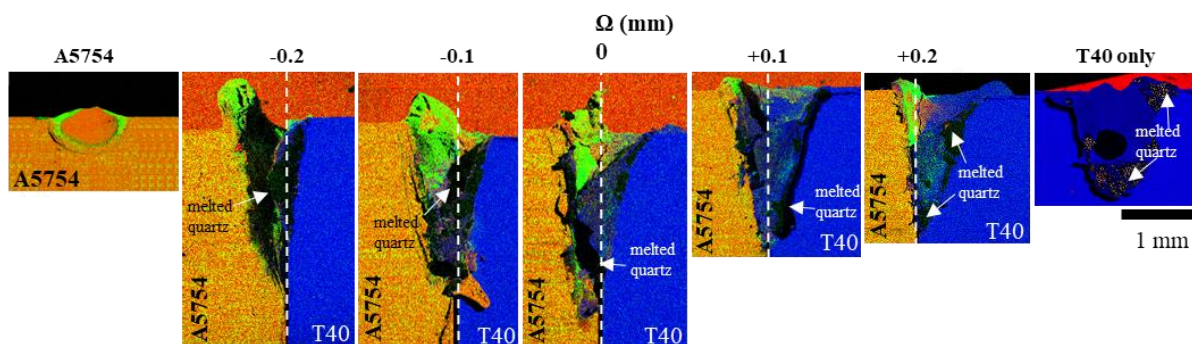
Figure 119. X-mapping of the melted zones on the A5754/T40 interface and standalone materials (Ti-blue, Al-red, Mg-green).

An assessment of geometrical dilutions of the two materials was done by the measurement of melted zone areas on either side of the T40/A5754 joint line (Figure 120). For beam centered on the joint line (Ω_0), approximately two-thirds of the melted zone area was in A5754 corresponding with the observed keyhole offset and the disparity in fusion temperatures between the two metals (Table 2 p.57). Moving the laser spot towards A5754 ($\Omega_{-0.1}$, $\Omega_{-0.2}$) led to corresponding increase in the A5754 melted zone area and moving the laser spot towards T40 ($\Omega_{+0.1}$, $\Omega_{+0.2}$) reduced the contribution of A5754 up to 25 % of the total melted zone area.
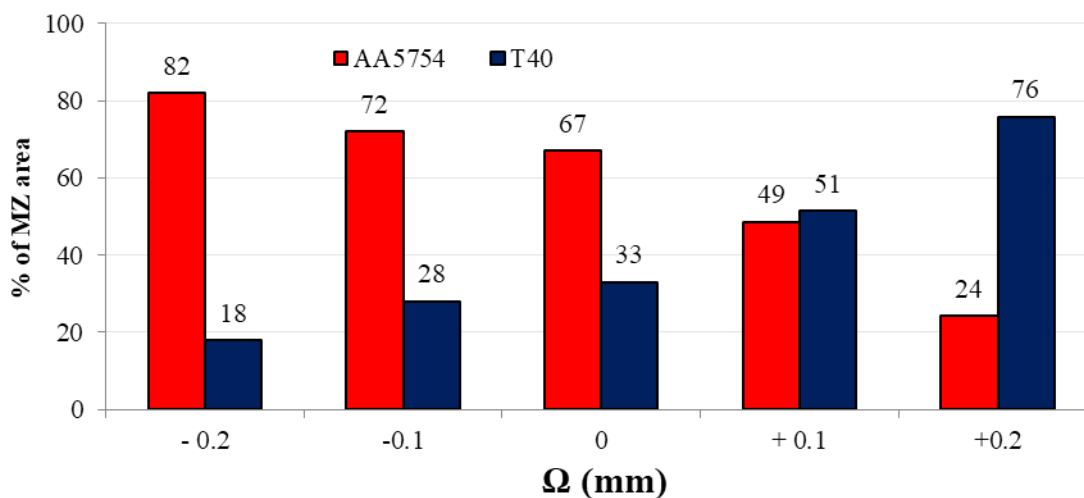
Figure 120. Ratio of melted zone area between A5754 and T40.

4.4.5. Post-mortem analysis of plume deposits

Formation of condensed metal vapor deposits on the quartz plate above the melted zone occurred from the vapor jet leaving the keyhole (Figure 121). From the first glance, it could be noted that all the elements (Ti, Al, Mg) were present for all laser spot positions, and the separate Ti and Al/Mg rich zones were not observed. This represented intense mixing of the respective vapor jets.

The local intensity of an element's X-map relies on its local concentration, and in the context of the plume deposit, this concentration is influenced by three key factors.

- Local temperature, that controls the vaporization intensity for a given element (Eqn. 45, p.53).
- Laser spot position relative to the joint line.
- Local velocity of the vapor jet, influencing the evacuation or accumulation of metallic particles above the keyhole opening.

The accumulation of the metal species on the quartz is also facilitated by local heating and melting of the quartz by its contact with the hot vapor jets (Figure 116). The central portion of the metal deposits is found to have a low concentration of the metal atoms and two large vertical zones rich in metal are present on either side. This phenomenon occurred because the central part of the quart plate located directly above the keyhole encounters the most rapid central parts of the vapor jet, through which the metal atoms were rapidly evacuated. Whereas the two intense lateral zones on the sides encounter less rapid parts of the vapor jets which allow metal atoms and oxide particles to be deposited. Analysis of O content was not done due to quartz composed of SiO_2.
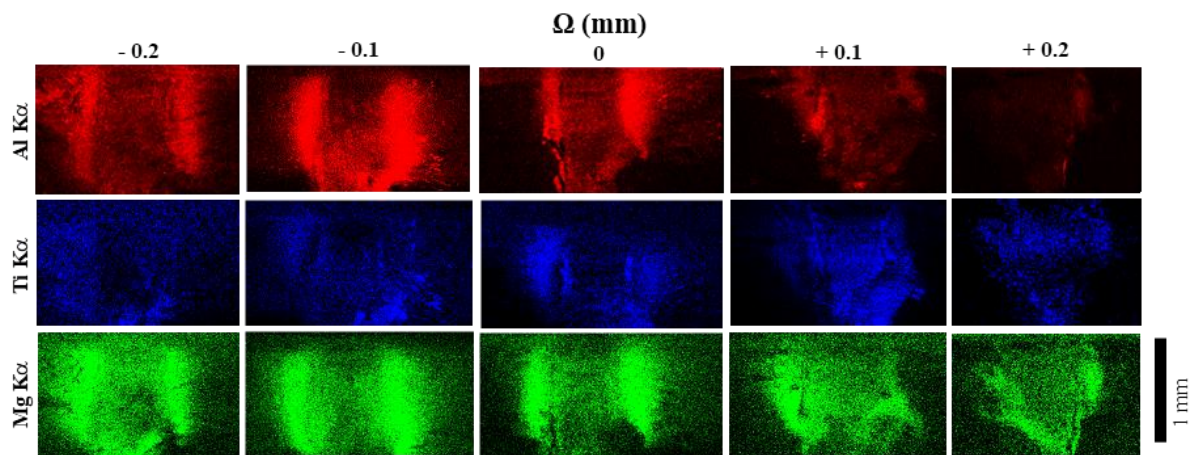
Figure 121. X-mapping of plume deposits on the quartz plate (Al-red, Ti-blue, Mg-green).

The average element content in the plume deposits were analyzed using EDX (Figure 122). These results should be interpreted carefully since, in addition to the metal atoms and oxide particles originating from vapor, spatters from the melted zone present were also present. The experimental ratios of elements in the deposits and the theoretical ratios of vaporization mass fluxes of these elements were compared.

The mass flux of a specific elements vaporizing from the melted multicomponent alloy can be expressed as [293]:

$$\vec{J_\iota} = \varphi_i \frac{(1 - \beta_r)\sqrt{\frac{M_a}{2\pi R T}} P_{sat}}{M_a} \ \vec{n} \qquad 63$$

where φ_i is molar fraction of an element in the alloy, β_r is the recombination coefficient (considered constant), M_a is the molar mass of an element, R – ideal gas constant, T-temperature and P_{sat} – the pressure of saturated vapor of an element calculated from

[293] $$P_{sat} = P_{atm} exp\left[\frac{L_v\, M_a}{R}\left(\frac{1}{T_v} - \frac{1}{T}\right)\right]$$ 64

where L_v is vaporization energy and T_v – its vaporization temperature at normal atmospheric pressure P_{atm}.

If one admits the equality between the ratios between Mg and Al in the deposits and the ratios of their vaporization fluxes, the following observations can be made: It is evident that magnesium with its notably lower vaporization temperature (1364 K) compared to aluminum and titanium, is found in significantly greater quantities within the plume deposit than its initial concentration in the A5754 alloy, which stood at just 2.7 at. %. Using equations (63, 64) and representing A5754 as a binary mixture with $\varphi_{Mg} = 0.0463$ and $\varphi_{Al} = 0.9535$ (based on the EDX analysis of the raw alloy), the Mg/Al ratio of 2.2 in the plume deposit of standalone A5754 suggests the possibility of a vapor temperature reaching 3300 K. It is noteworthy that this temperature surpasses the vaporization temperature of the alloy, which is 2700 K. Similarly, in the case of dissimilar welding ($\Omega_0, \Omega_{+0.1}, \Omega_{+0.2}$), the Mg/Al ratio was $0.5 - 0.55$, which corresponded to a temperature around 4200 K - 4300 K, which was above the vaporization temperature of T40 (3560 K). These temperature levels should be confirmed by measurement of continuous thermal emissions from keyhole walls collected through the quartz plate using equations 68-73 (p.173).
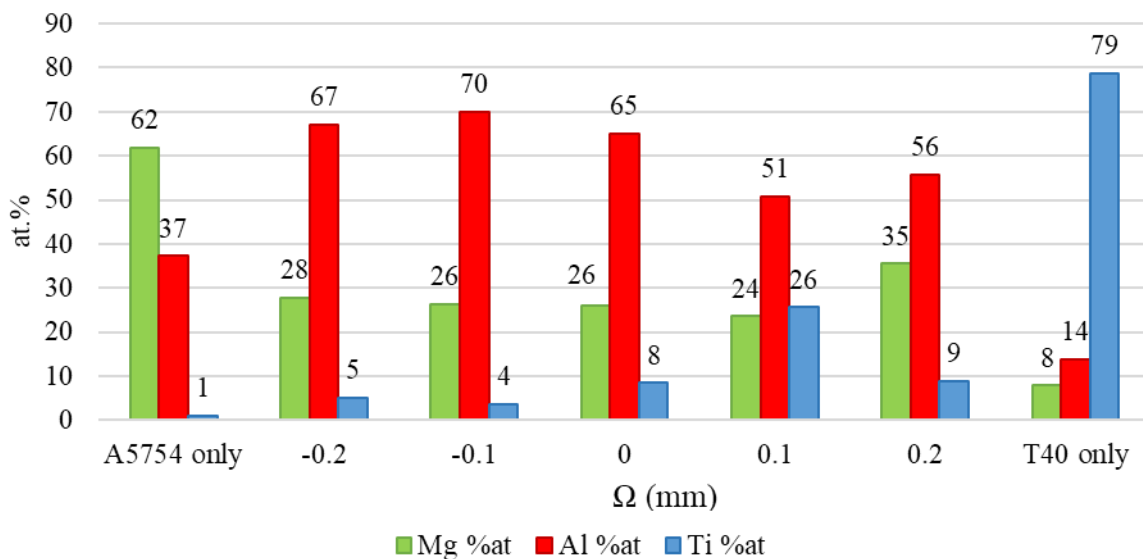
Figure 122. Average composition of the plume deposits on the quartz plate.

4.4.6. Conclusions from keyhole and melted zone observations and plume deposits.

In-situ observation of the keyhole and melted zone in the 6 ms laser pulsed welding of T40/A5754 in butt-configuration was achieved using quartz. In addition, the deposits from the vapor plume on the quartz were also analyzed, compared to previous observations of the plume, and temperature estimations were calculated from the average elemental content in the plume deposits. Using quantitative analysis, it was established that using quartz did not invalidate the keyhole and melted zone experiments.

The keyhole depth and morphology were different between the standalone materials and dissimilar combination. While A5754 struggled to form a keyhole within 6 ms, the keyhole/melted zone in T40 was not as deep as the dissimilar cases. With the laser spot position relative to the joint line affecting keyhole/melted zone depth, maximum synergy (titanium from T40 promoting melting and vaporization of A5754) between A5754 and T40 leading to maximum drilling was noted for the laser beam centered on the joint line.

Critical evaluation about the phenomena depicted and explained with Figure 82 (p.112) had to be done by in-situ keyhole and melted zone observations. It was noted that depending on the laser beam offsets, the keyhole side walls were tangential (aluminum wall for $\Omega_{+0.2}$, titanium wall for $\Omega_{+0.2}$) to the joint line. These observations were consistent with the vapor plume behavior (inclination towards A5754 for $\Omega_{-0.1}$, $\Omega_{-0.2}$). While the order of magnitude of the drilling rates of the keyhole were closer to the keyhole drilling rate in standalone T40, it was also noted that the drilling rate in dissimilar configuration was proportional to the closeness of the laser spot to the joint line.

EDS analysis of the melted zones enabled calculations of the geometrical dilutions (titanium dominant) of the materials in the melted zones. The deposits of Ti-rich zones in the keyhole indicated that the titanium melting and vaporization promotes the melting and vaporization of A5754 on the opposite keyhole wall. It was also observed that magnesium deposits were concentrated near the keyhole opening correlating with previous observations of rings of magnesium in top-view EDS analysis (Figure 83, p.114) of the melted zones.

Post-mortem analysis of the plume deposits on the quartz above the keyhole indicated vaporization of Ti, Al and Mg, and thereby intense mixing of the vapors in the keyhole. Spatial distribution of these elements on the quartz indicated by the local intensities indicated rapid jets of vapor directly above the keyhole opening and slower vapors (allowing precipitation and deposition with cooling) along the sides. Calculations performed to estimate vapor temperatures using at.% in the plume deposits and geometrical dilutions in the A5754 alloy suggested high vapor temperatures beyond the vaporization temperature of A5754. However, such estimations need to be confirmed using emission spectroscopy.

In addition, simultaneous HSI of the plume and the keyhole must be done to confirm the relationship between the keyhole side walls and the vapor plume behavior.

4.5. Emission spectroscopy in pulsed dissimilar welding

4.5.1. Objectives in emission spectroscopy

The objective of this spectroscopic study is to complement the High Speed Imaging study of the T40-A5754 alloy assembly. The aim is to seek additional information that spectroscopy can provide regarding dissimilar welding.

The spectrometer used is a Czerny-Turner monochromator equipped with an ICCD camera. The experimental setup was presented in Chapter 2 (section 2.3.1, p.61). The spectrometric studies without HSI were conducted with laser pulses ranging from 2 to 6 ms in duration. The laser parameters are similar to those used in HSI. Usually, spectrometry and HSI were performed simultaneously (Figure 28, p.58). However, it should be noted that HSI was a study of the entire spatial extent of vapor plume with temporal analysis (from the start to the end of the pulse) at the rate of number of images per second. In contrast, spectrometry was the study that analyzed a spatially localized part (Figure 123) of the vapor plume near the keyhole opening, and temporally comprising the entire lifetime of the vapor plume (i.e., one spectrum per pulse).

In the studies conducted within this thesis, synchronization (between the laser, spectrometer, and the camera) although possible, was not utilized due to technical constraints with the laser system. Consequently, the signal integration time on the spectrometer detector was set to 1 second when using a laser frequency of 1 Hz for spectrometric experiments involving multiple laser pulses.

The advantage of one second acquisition time was to gather a sufficient amount of light to target a specific region within the vapor plume. However, the drawback was the inclusion of ambient background noise (though this noise was minimal compared to the signal). And, for each spectrum (or series of spectra), the background spectrum (corresponding to the ambient noise) was also recorded. Subsequently, during the data processing phase, this background spectrum was subtracted from the total spectrum.
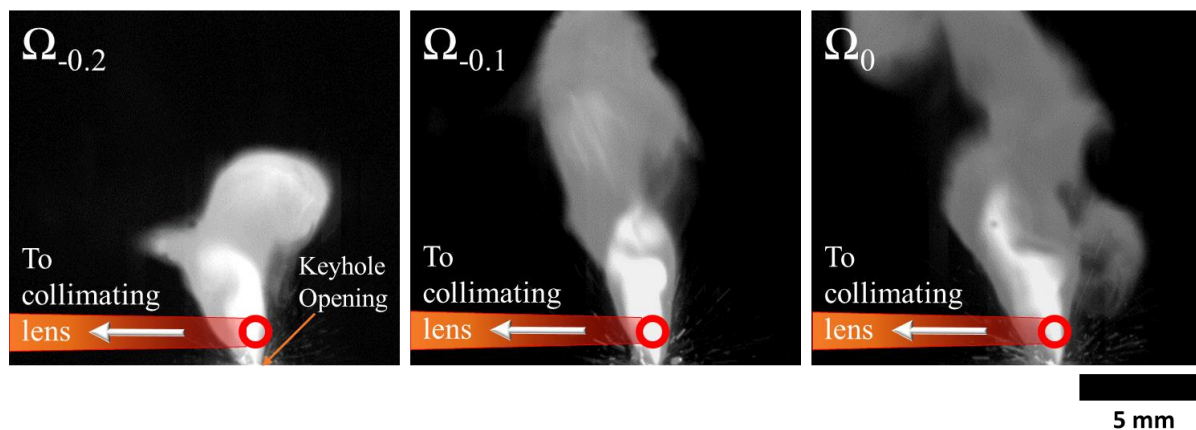
Figure 123. Observation area for spectrometry in the vapor plume (refer Figure 73, p.106).

The focusing setup consisted of two lenses fixed on an optical bench. The collimating lens with a focal length of 400 mm was used to collect the signal emitted by the laser plume. Subsequently, a 100 mm focusing lens was used to inject this signal into the optical fiber. The optical fiber, having a core diameter of 230 µm, resulted in a targeted area of 0.9 mm. Based on HSI analyses, the focal area was placed approximately 0.5~1.5 mm from the surface (as indicated by the red circle in Figure 1 not tangent but a little elevated). This placement was slightly above the crater formed during the interaction to avoid any melted zone entering into

the spectral acquisition zone. Within this region, the vapor could be decisively targeted despite the fluctuations on the surface observed in HSI.

4.5.2. Spectral regions selection for T40-A5754 welding analysis

4.5.2.1. Lowest energy levels

In this study, the assembly of pure Titanium (T40) with an aluminum alloy (A5754) containing 2.6% Mg, 0.5% Mn, and various other impurities was examined.

In previous studies [284]–[286], several titanium lines were observed throughout the spectrometer's observation range (250-650 nm with a 2400 lines/mm grating). However, the aluminum emission lines were not detected. It was evident that the fundamental aluminum lines could have been observed, but there was a risk of auto-absorption (section 1.4.4, p.49). A few lines of manganese (section 3.2.2, p.89) and magnesium [286] were observed.

Therefore, a systematic study was first conducted to identify the lines that could be observed in the case of the T40/A5754 assembly. In welding, the metallic vapor temperature is usually expected to be at the boiling point of the metal. Usually at this temperature, the excitation could only occur up to the first energy levels.

A comparison of the first excited energy levels of titanium, aluminum, and magnesium atoms are presented (Table 15). In the case of titanium and aluminum, the ground level is composed of 2 sub-levels. It can already be noted that the first energy level of titanium (6556 cm^{-1}) is significantly lower than that of aluminum (25347 cm^{-1}) and magnesium (21850 cm^{-1}). A difference, by approximately a factor of 3 is observed. When aluminum or magnesium is excited, a multitude of excited titanium levels are already present, resulting in a very rich spectrum. Considerably more energy is required to excite these atoms.

With the assumption of thermal equilibrium at temperature T, the relative probability P_n can be calculated using the Boltzmann statistics:

$$P_n = \frac{(2J + 1)\ exp(-\ E_s/k_B.T)}{\sum (2J_i + 1)\ exp(-\ E_i/k_B.T)} \qquad 65$$

The calculations were performed at a temperature of 3500 K (close to the boiling point of titanium) and also at 8000 K. Therefore, it was evident that, in order to identify detectable emission lines in the vapor, it is essential to explore transitions involving the least excited levels of aluminum or magnesium.

Table 15.Comparison of the first excited energy levels of titanium, aluminum, and magnesium atoms.

Element	Ground state			First excited level (cm^{-1})		
	E$_i$ (cm^{-1})	P$_n$ (3500 K)	P$_n$ (8000 K)	E$_s$ (cm^{-1})	P$_n$ (3500 K)	P$_n$ (8000 K)
Titanium	3d^{2}4s^2 a ^{3}F 170.132 386.874	22.3 % 29.1 % 34.3 %	9.0 % 12.1 % 15.2 %	3d^3(^{4}F)4s a ^{5}F 6556.83 6598.765 6661.006 6742.756 6842.962	0.905 % 1.482 % 2.023 % 2.515 % 2.950 %	1.669 % 2.760 % 3.822 % 4.842 % 5.812 %
Aluminum	3s^{2}3p ^{2}P° 0.000 112.061	34.364 % 65.635 %	32.30 % 63.30 %	3s^{2}4s ^{2}S 25 347.756	0.0010 %	0.339 %
				3s3p^2 ^{4}P 29 020.41 29 066.96 29 142.78	0.0002 % 0.0004 % 0.0006 %	0.175 % 0.347 % 0.514 %
				3s^{2}3d ^{2}D 32 435.453 32 436.796	0.0001 % 0.0002 %	0.189 % 0.284 %
Magnesium	2p^{6}3s^2 ^{1}S 0.000	99.89 %	82.45 %	3s3p ^{3}P° 21 850.405 21 870.464 21 911.178	0.013 % 0.037 % 0.061 %	1.662 % 4.847 % 8.020 %
				3s3p ^{1}P° 35 051.264	0.0002 %	0.150 %

4.5.2.2. Classification of Al transitions based on upper energy level

The possible transitions of aluminum are given in Table 16. The transitions have been sorted in ascending order of the energy of the upper level and then the lower level (since we are observing atomic emission lines). In this table, the wavelength in air, the energies, and their electronic configurations for both the lower and upper levels of the transitions have been provided.

To gain an understanding of their intensity during experimental research, the theoretical intensities of these emission lines have been calculated, assuming temperatures of 3500 K and 5000 K (in correlation with the findings of this study (section 4.5.3, p.172)).

Considering the grating used in this spectrometer, the observed spectral range was approximately 3.5 nm. In Table 16, the grating position had also been provided, which is linked to the range of observation through an empirical relationship: the grating position is equal to 20 times the wavelength of the 200th pixel of the camera. For example, the grating position (mentioned as "spectral region" from here onwards) 7888 corresponds to the spectral interval [393.5 – 397 nm].

Following this consideration, spectra from A5754 was acquired with laser power ranging from 1 to 3 kW, a pulse duration of 6 ms, and a fiber (and focal spot) diameter of 600 μm. The regions 4740, 5150, 5300, 6160, 7888, and 11100 were studied (Table 16).

Below 250-260 nm, no signal was observed, indicating low temperature.

Table 16. Al (I) observable transitions

Al				Lower level			Upper level				
λ_s Theo (nm)	I_{th} (3500 K)	I_{th} (5000 K)	A_s (s^{-1})	E_i (cm^{-1})	J_i	Conf.	E_s(cm^{-1})	J_s	Conf.	Region	Observation
394.40	181.40	3475.7	5.11E+07	0	0.5	3p 2P	25347	0.5	4s 2S	7888	Observed
396.15	357.30	6846.1	1.01E+08	112.06	1.5	3p 2P	25347	0.5	4s 2S	7888	Observed
308.21	32.42	1418.3	6.27E+07	0	0.5	3p 2P	32435	1.5	3d 2D	6160	Observed
309.28	6.40	280.08	1.24E+07	112.06	1.5	3p 2P	32435	1.5	3d 2D	6160	Observed
309.27	58.36	2553.6	7.55E+07	112.06	1.5	3p 2P	32436	2.5	3d 2D	6160	Observed
265.24	0.48	38.65	1.35E+07	0	0.5	3p 2P	37689	0.5	5s 2S	5300	Not observed
266.03	0.95	76.44	2.65E+07	112.06	1.5	3p 2P	37689	0.5	5s 2S	5300	Not observed
256.79	0.99	92.11	2.20E+07	0	0.5	3p 2P	38929	1.5	4d 2D	5150	Not observed
257.53	0.20	18.22	4.37E+06	112.06	1.5	3p 2P	38929	1.5	4d 2D	5150	Not observed
257.50	1.78	165.98	2.66E+07	112.06	1.5	3p 2P	38933	2.5	4d 2D	5150	Not observed
669.86	0.01	0.91	1.67E+06	25347	0.5	4s 2S	40271	0.5	5p 2P	13400	Not studied
669.60	0.02	1.82	1.67E+06	25347	0.5	4s 2S	40277	1.5	5p 2P	13400	Not studied
237.20	0.03	4.22	4.71E+06	0	0.5	3p 2P	42144	0.5	6s 2S	4740	Not observed
237.83	0.06	8.36	9.34E+06	112.06	1.5	3p 2P	42144	0.5	6s 2S	4740	Not observed
236.70	0.91	124.21	7.09E+07	0	0.5	3p 2P	42233	1.5	5d 2S	4740	Not observed
237.33	0.18	24.58	1.41E+07	112.06	1.5	3p 2P	42233	1.5	5d 2D	4740	Not observed
237.31	1.63	224.03	8.55E+07	112.06	1.5	3p 2P	42237	2.5	5d 2D	4740	Not observed
555.79	0.00	0.11	4.20E+05	25347	0.5	4s 2S	43335	0.5	6p 2P	11100	Not observed
555.70	0.00	0.23	4.19E+05	25347	0.5	4s 2S	43337	1.5	6p 2P	11100	Not observed

Two sets of lines were observed:

- The fundamental lines at 394.40 nm and 396.15 nm were intense, but significant auto-absorption phenomenon was evident (Figure 124. A). These were the transitions reaching the ground state, where the light emitted by the excited atoms was absorbed by the neighboring atoms (at ground state).

- A second, less intense pair of peaks was observed at 308.21 nm and 309.28 nm, with auto-absorption (Figure 124. B). It should be noted that the peak at 309.28 nm was composed of two transitions. However, according to Table 16, the emission line at 309.271 nm was the most intense (by a factor of 10). Thus, the 309.271 line could be effectively utilized.
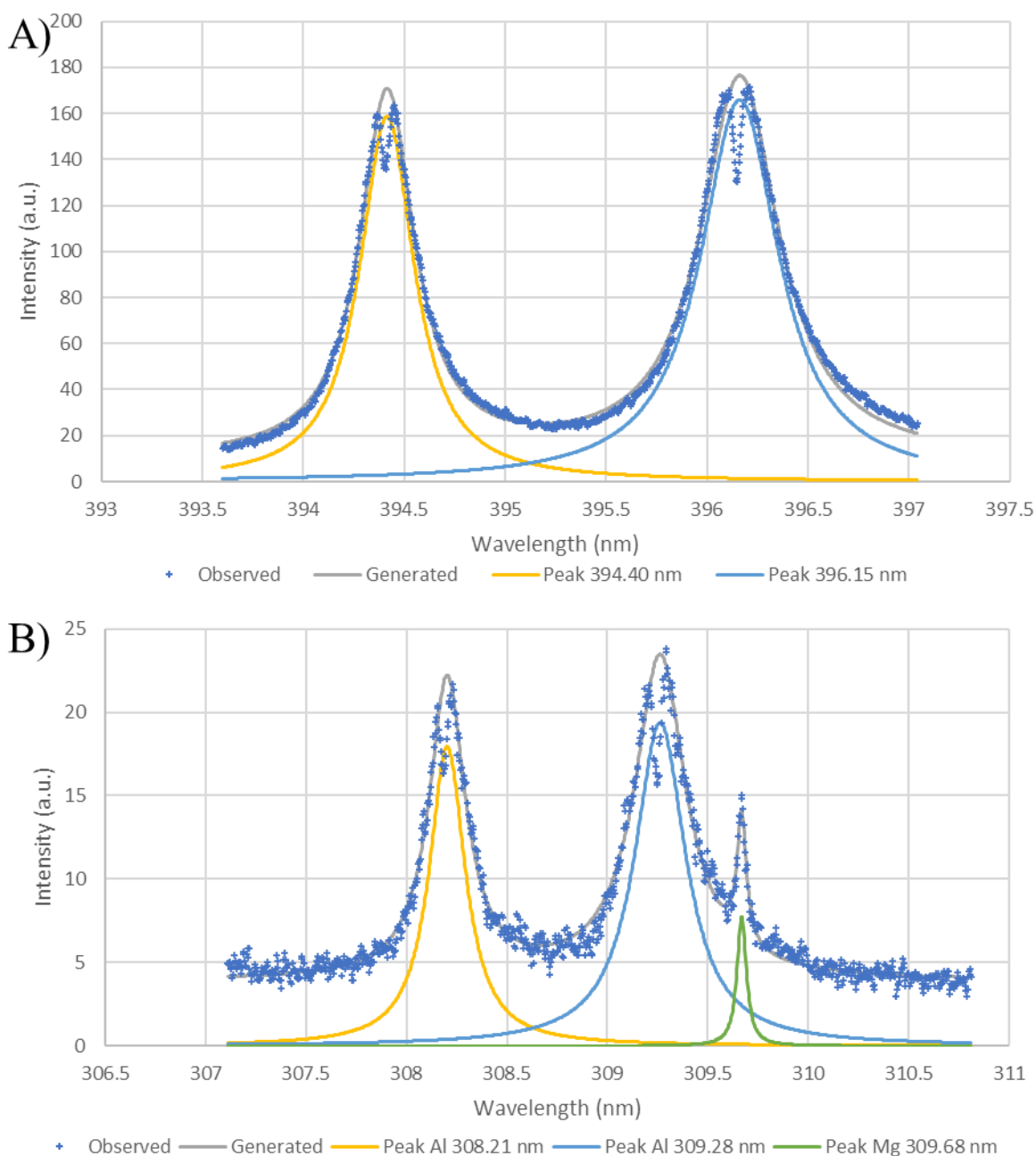
Figure 124. A5754 spectrum in region A) region 7888 and B) 6160 (Generated – calculated from theoretical intensities, Peaks – after fitting observed values with PeakFit).

4.5.2.3. Classification of Mg transitions

Similar to the previous study of aluminum transitions, Table 17 presents the possible transitions of Mg (I). Magnesium is an atom with 2 valence electrons. Spectrally, it has a structure similar to helium, consisting of 2 systems of weakly coupled levels: a system of simple levels (corresponding to spin moment S=0) and a system of triplet levels (S=1). Selection rules (ΔS=0) prohibit transitions between these two systems, except for the fundamental line. Consequently, for the triplet levels corresponding to various possible transitions of the fine structure, the groups of closely spaced lines were difficult to deconvolve.

In Table 17, a list of the studied spectral regions has been presented. Only two spectral regions could be considered for further analysis:

- In the spectral region 7635, three peaks were observed (Figure 125. A). They are, in fact, composed of six magnesium transitions. The first peak was associated with the line at 382.93 nm. The second peak consisted of two lines at 383.23 nm, originating from the same lower level but separated by 0.031 cm^{-1} (with contributions to intensity of 25% and 75%). The third peak contained three lines at 383.83 nm, originating from three neighboring levels (with respective contributions of 1%, 84%, and 15%).

- In the spectral region 10330, three peaks were observed (Figure 125. B) associated with the lines at 516.7321 nm, 517.2684 nm, and 518.3604 nm. These three transitions originated from the same upper level at 41197.403 cm^{-1}.

The peak observed at 309.69 nm in the 6160 region (Figure 124), was also in the region of the aluminum peak. This peak is composed of three transitions, but the intensity of the transition at 309.6891 nm is predominant. Therefore, three small magnesium lines are convoluted within the Al (I) line at 309.271 nm.
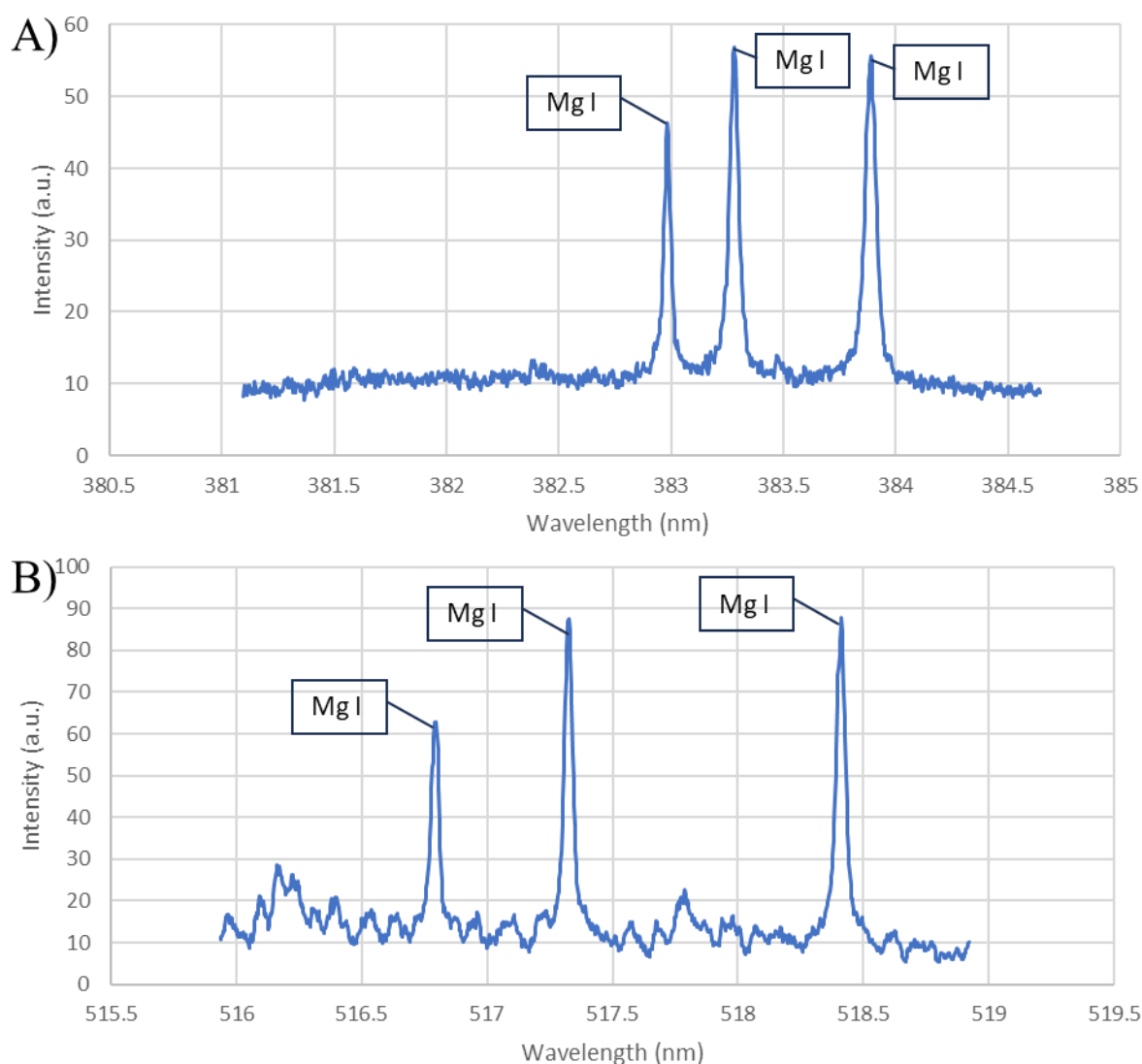
Figure 125. Mg spectrum in A) region 7635, B) region 10330.

Table 17. Mg transitions

Mg				Lower level			Upper level				
λ_s Theo (nm)	I_{th} (3500 K)	I_{th} (5000 K)	A_s (s^{-1})	E_i (cm^{-1})	J_i	Conf.	E_s (cm^{-1})	J_s	Conf.	Region	Observation
285.21	9951	542348	5.09E+08	0	0	3s2 1S	35051	1	s3p 1P	NR	
774.63	0.01	2.77	1.61E+05	35051.264	1	s3p 1P	47957	2	s3d 3D	NR	
202.58	11.28	3142.16	1.18E+08	0	0	3s2 1S	49346	1	s4p 1P	NR	
571.10	0.01	3.82	3.00E+06	35051.264	1	s3p 1P	52556	0	s5s 1S	11420	Weak
552.84	0.13	58.68	1.05E+07	35051.264	1	s3p 1P	53134	2	s4d 1D	11020	Weak
473.00	0.00	0.49	8.94E+05	35051.264	1	s3p 1P	56186	0	s6s 1S	9400	Not observed
470.29	0.05	34.90	1.30E+07	35051.264	1	s3p 1P	56308	2	s5d 1D	9400	Not observed
516.73	**7.35**	807.53	**7.77E+06**	**21850.405**	**0**	**s3p 3P**	**41197**	**1**	**s4s 3S**	**10330**	
517.26	**31.09**	3415.74	**3.29E+07**	**21870.464**	**1**	**s3p 3P**	**41197**	**1**	**s4s 3S**	**10330**	**Observed**
518.36	**51.49**	5656.73	**5.46E+07**	**21911.178**	**2**	**s3p 3P**	**41197**	**1**	**s4s 3S**	**10330**	
382.93	**7.81**	1855.27	**8.90E+07**	**21850.405**	**0**	**s3p 3P**	**47957**	**1**	**s3d 3D**	**7635**	
383.22	**5.85**	1389.34	**6.67E+07**	**21870.464**	**1**	**s3p 3P**	**47957**	**1**	**s3d 3D**	**7635**	
383.23	**17.54**	4165.98	**1.20E+08**	**21870.464**	**1**	**s3p 3P**	**47957**	**2**	**s3d 3D**	**7635**	**Observed**
383.82	**0.39**	92.55	**4.45E+06**	**21911.178**	**2**	**s3p 3P**	**47957**	**1**	**s3d 3D**	**7635**	
383.82	**32.48**	7715.79	**1.59E+08**	**21911.178**	**2**	**s3p 3P**	**47957**	**3**	**s3d 3D**	**7635**	
383.82	**5.84**	1386.49	**4.00E+07**	**21911.178**	**2**	**s3p 3P**	**47957**	**2**	**s3d 3D**	**7635**	
309.10	0.28	133.51	3.00E+07	21850.405	0	s3p 3P	54192	1	s4d 3D	6160	
309.29	0.21	98.74	2.22E+07	21870.464	1	s3p 3P	54192	1	s4d 3D	6160	
309.29	0.42	201.63	2.72E+07	21870.464	1	s3p 3P	54192	2	s4d 3D	6160	In the region of Al peaks
309.68	0.01	6.66	1.50E+06	21911.178	2	s3p 3P	54192	1	s4d 3D	6160	
309.68	0.14	66.48	8.98E+06	21911.178	2	s3p 3P	54192	2	s4d 3D	6160	
309.68	1.14	552.45	5.33E+07	21911.178	2	s3p 3P	54192	3	s4d 3D	6160	

*NR – Not searched

4.5.2.4. Selection of spectral regions for T40/A5754 dissimilar welding investigation

Titanium exhibits multiple emission lines. However, for the temperature estimation study using the Boltzmann method (where we compare the intensity of the line as a function of the energy of the upper transition level), it is essential to select transitions that meet specific criteria: isolated lines (not convolutions of multiple very close lines), non-saturation, minimal background noise interference, absence of auto-absorption, and most importantly, a representative sampling of lines covering a wide range of upper levels. (previously mentioned in section 3.3, p.89)

To determine the relevant spectral regions, previous studies' results [284]–[286] were utilized. An analysis based on ranking upper levels was done, similar to the studies of aluminum and magnesium (section 4.5.2.2, section 4.5.2.3). Consequently, spectral regions were identified.

4.5.2.1.1. Region 7530

Spectra obtained from Titanium T40 during laser pulses at 0.8 kW and 1.6 kW (600mm fiber, 2 ms pulse duration) can be seen in Figure 126. In Table 18, only the observable lines from this spectrum are listed. It contains the lines from both excited Titanium (Ti I) and once-ionized Titanium (Ti II). This indicates that laser interaction with titanium is more efficient. The laser power used is lower (0.8-1.6 kW) than that used for aluminum (3 kW) (section 4.2.1.1, p.101).

Three transitions were selected:

- The line at 377.1651 nm: This is a high-intensity and isolated line (although it is perturbed by neighboring lines at its base, adjusting the line profile with PeakFit enabled accurate intensity determination). This transition is associated with an upper level at 26892.935 cm^{-1}.

- The line at 378.0384 nm is a small line with an easily adjustable profile. This transition is associated with an upper level at 37976.589 cm^{-1}.

- The line at 378.9294 nm is a large line with an easily adjustable profile. This transition is associated with an upper level at 38159.457 cm⁻¹.

The energy difference of the upper level has already provided an initial temperature estimate (section 4.5.3.1, p.173).

Table 18. Observable Ti transitions in the 7530 region (observed lines used for analysis – in blue).

λ_s theoretical (nm)	A_s (s⁻¹)		E_i (cm⁻¹)	J_i	Conf.	E_s(cm⁻¹)	J_s	Conf.
375.9296	9.35E+07	Ti II	4897.65	3.5	(3F)4s a2F	31490.82	3.5	(3F)4p z2F
376.1323	9.89E+07	Ti II	4628.58	2.5	(3F)4s a2F	31207.42	2.5	(3F)4p z2F
376.3077	5.11E+04	Ti I	17215.389	5	(3F)sp z5F	43781.837	5	(4F)4d 5G
376.64419		Ti I	8492.422	1	s2 a3P	35035.137	2	(3P)sp x1D
376.9718	5.30E+06	Ti I	11639.81	3	(4F)4s b3F	38159.457	3	(3P)sp u3D
377.117	1.08E+06	Ti I	19421.58	3	(3F)sp z3F	45931.015	4	s2F)4d 3F
377.1651	**6.02E+06**	**Ti I**	**386.875**	**4**	**s2 a3F**	**26892.935**	**3**	**(1D)sp x3F**
377.4374	7.71E+05	Ti I	20126.06	3	(3F)sp z3D	46612.996	2	s2D)5s 1D
377.7182	4.82E+05	Ti I	21469.487	3	(3F)sp z3G	47936.73	3	s4F)5d h5G
377.8974	2.08E+06	Ti I	8492.421	1	s2 a3P	34947.113	1	(3P)sp y1P
377.9032	1.93E+07	Ti I	19322.984	2	(3F)sp z3F	45777.274	2	s2F)4d 3F
378.0384	**7.51E+06**	**Ti I**	**11531.759**	**2**	**(4F)4s b3F**	**37976.589**	**2**	**(3P)sp u3D**
378.2105	8.90E+05	Ti I	8602.342	2	s2 a3P	35035.138	2	(3P)sp x1D
378.4492	1.73E+07	Ti I	19421.58	3	(3F)sp z3F	45837.7	3	s2F)4d 3F
378.6043	1.38E+08	Ti I	7255.354	2	s2 a1D	33660.659	1	(1D)sp z1P
378.9294	**2.35E+07**	**Ti I**	**11776.811**	**4**	**(4F)4s b3F**	**38159.457**	**3**	**(3P)sp u3D**
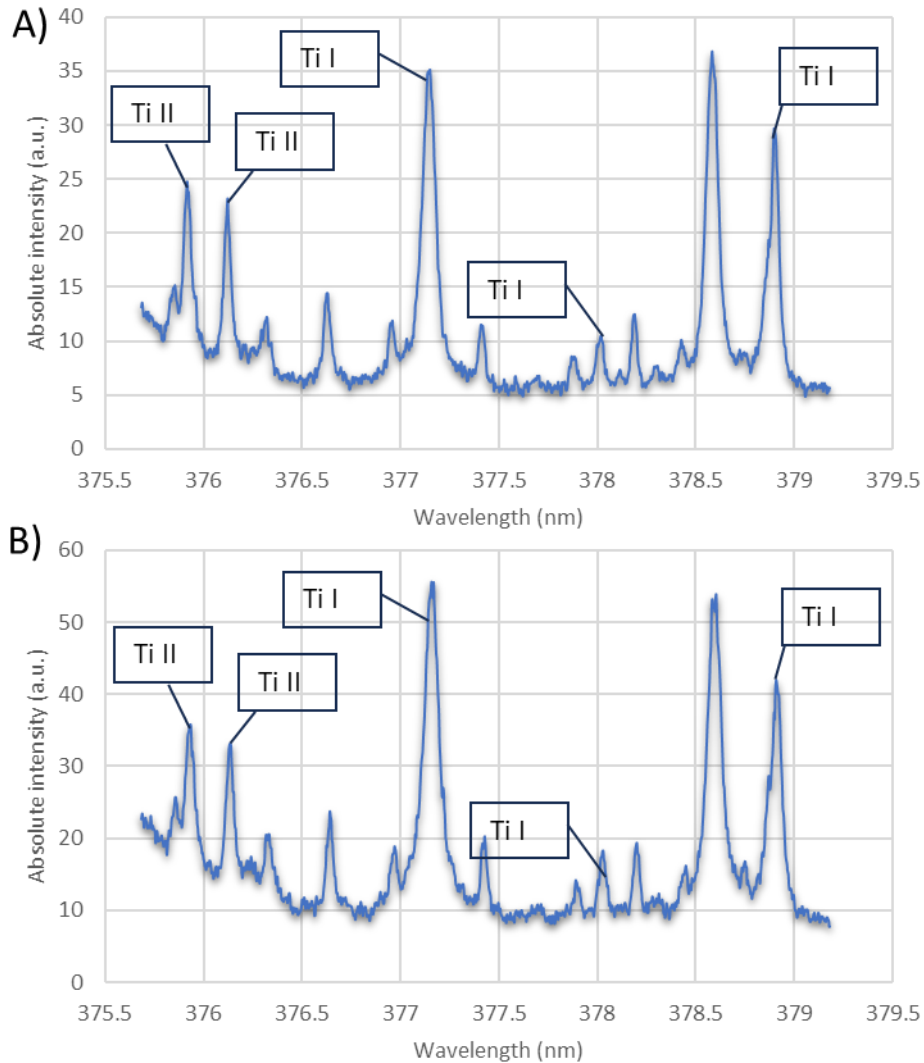
Figure 126. Calibrated spectra in the 7530 region for A) 0.8 kW and B) 1.6 kW laser pulse (2 ms) on T40.

Figure 127 displays spectra obtained from Titanium T40 during laser pulses at 0.8 kW and 1.6 kW in the 7635 region. The spectrum is rich in emission lines.

Table 19 contains the transitions associated with the observable lines in the spectrum.

Among the 8 selected lines, 6 transitions are associated with energy levels around 43000-45000 cm^{-1}, and 2 transitions are associated with levels near 37700 cm^{-1}. It was also possible to use these lines for an initial temperature estimation using only this spectrum. However, there was some dispersion in the data points associated with the levels around 43000-45000 cm^{-1}. Therefore, it was necessary to either associate these lines with those from other spectra or apply a more rigorous selection of usable lines.

164

Table 19. Observable Ti transitions in the 7635 region

λ$_s$ theoretical (nm)	A$_s$ (s^{-1})		E$_i$ (cm^{-1})	J$_i$	Conf.	E$_s$(cm^{-1})	J$_s$	Conf.
381.1399	2.31E+06	Ti I	15108.110	3.0	(2G)4s a3G	41337.747	2.0	s2 4p s3F
381.3269	**3.17E+07**	**Ti I**	**16817.160**	**1.0**	**(3F)sp z5F**	**43033.937**	**1.0**	**s4F)4d g5F**
381.4861	**2.41E+07**	**Ti I**	**16875.121**	**2.0**	**(3F)sp z5F**	**43080.961**	**2.0**	**s4F)4d g5F**
381.7642	**2.74E+07**	**Ti I**	**16961.441**	**3.0**	**(3F)sp z5F**	**43148.187**	**3.0**	**s4F)4d g5F**
381.8199	**3.36E+07**	**Ti I**	**18192.570**	**6.0**	**(2H)4s a3H**	**44375.501**	**5.0**	**s4F)5p t3G**
382.1718	1.86E+07	Ti I	16875.121	2.0	(3F)sp z5F	43033.937	1.0	s4F)4d g5F
382.2023	**3.50E+07**	**Ti I**	**17075.258**	**4.0**	**(3F)sp z5F**	**43231.989**	**4.0**	**s4F)4d g5F**
382.2635	1.11E+06	Ti I	18911.393	2.0	(2P)4s c3P	45063.940	2.0	(4F)5p n3D
382.6969	2.66E+06	Ti I	11531.759	2.0	(4F)4s b3F	37654.689	2.0	a2D)4p u3F
382.7115	2.19E+06	Ti II	39476.800	2.5	(1D)4p y2D	65598.730	3.5	(3F)4d 4D
382.7468	1.82E+07	Ti I	16961.441	3.0	(3F)sp z5F	43080.961	2.0	s4F)4d g5F
382.7635	3.77E+07	Ti I	18037.213	4.0	(2H)4s a3H	44155.594	3.0	s4F)5p t3G
382.8009	3.56E+07	Ti I	18141.264	5.0	(2H)4s a3H	44257.097	4.0	s4F)5p t3G
382.8187	4.61E+07	Ti I	17215.389	5.0	(3F)sp z5F	43330.005	5.0	s4F)4d g5F
382.9721	**2.91E+06**	**Ti I**	**11639.810**	**3.0**	**(4F)4s b3F**	**37743.964**	**3.0**	**a2D)4p u3F**
383.2044	4.97E+06	Ti I	18145.285	2.0	(2P)4s b3P	44233.619	3.0	s4F)5p o3D
383.3184	5.37E+07	Ti I	19322.984	2.0	(3F)sp z3F	45403.557	3.0	s2F)4d 3G
383.3675	1.84E+07	Ti I	19421.580	3.0	(3F)sp z3F	45498.814	4.0	s4F)4d 3G
383.4308	1.48E+07	Ti I	17075.258	4.0	(3F)sp z5F	43148.187	3.0	s4F)4d g5F
383.6768	**4.32E+07**	**Ti I**	**19573.973**	**4.0**	**(3F)sp z3F**	**45630.182**	**5.0**	**s2F)4d 3G**
383.90	1.62E+07	Ti I	12118.394	4.0	s2 a1G	38159.457	3.0	(3P)sp u3D
384.0322	2.22E+07	Ti I	18825.781	1.0	(2P)4s c3P	44857.878	1.0	(4P)4p w3S
384.1621	**3.60E+06**	**Ti I**	**11531.759**	**2.0**	**(4F)4s b3F**	**37555.056**	**3.0**	**(2G)4p v3G**
384.2348	1.04E+07	Ti I	18061.386	1.0	(2P)4s b3P	44079.760	2.0	s4F)5p o3D
384.261	8.90E+06	Ti I	17215.389	5.0	(3F)sp z5F	43231.989	4.0	s4F)4d g5F
384.2864	3.65E+06	Ti I	11639.810	3.0	(4F)4s b3F	37654.689	2.0	a2D)4p u3F
384.3157	2.51E+06	Ti I	15975.630	3.0	(3F)sp z5G	41988.527	3.0	s4F)4d g3F
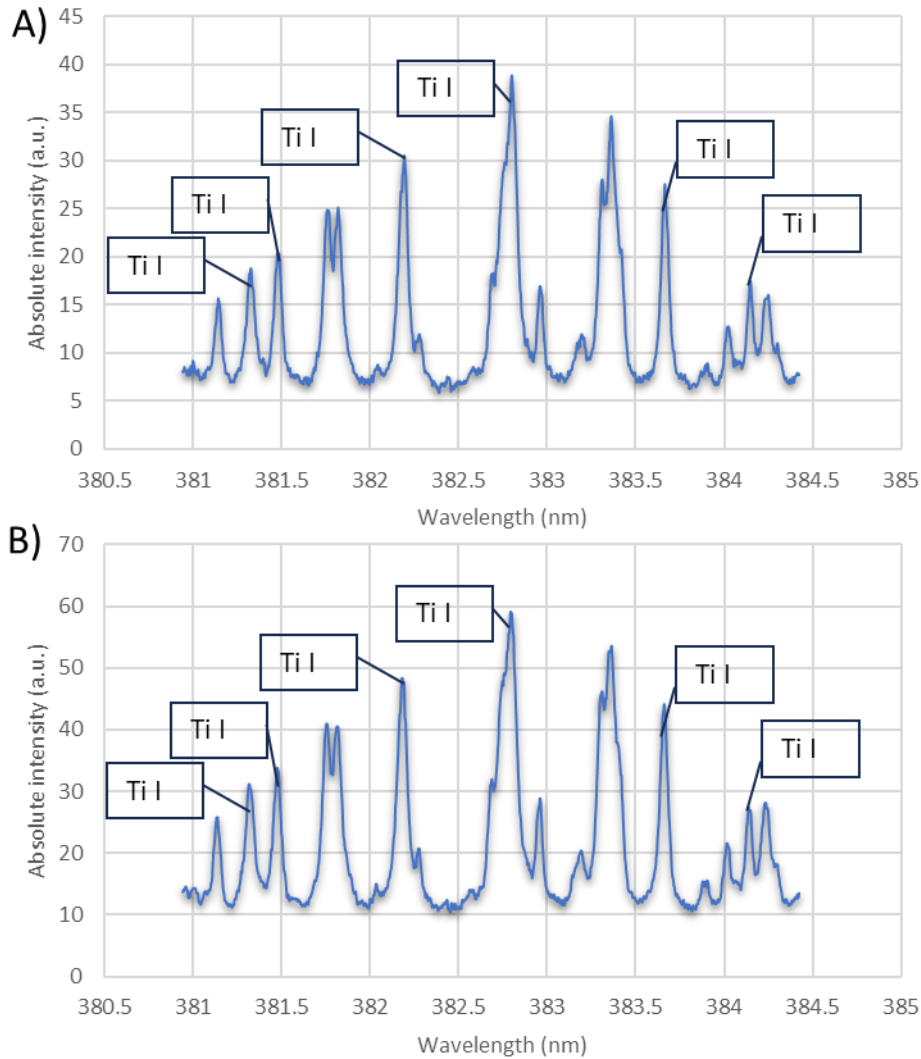
Figure 127. Calibrated spectra in the 7635 region for A) 0.8 kW and B) 1.6 kW laser pulse (2 ms) on T40.

4.5.2.1.3.   Region 7888

The significance of this region lies in the presence of fundamental titanium transitions, providing access to upper levels around 25000 cm^{-1}. However, there was the drawback of potential auto-absorption and closely spaced lines that cannot be deconvolved. It could be observed that the only usable lines (Figure 128 and Table 20) are the two rightmost lines at 396.2851 nm and 396.4269 nm.

This region also corresponded to the region of two fundamental aluminum transitions. Therefore, this region was chosen for HSI with a filter centered at 395 nm, despite the challenge of overlapping titanium emission in the same region.
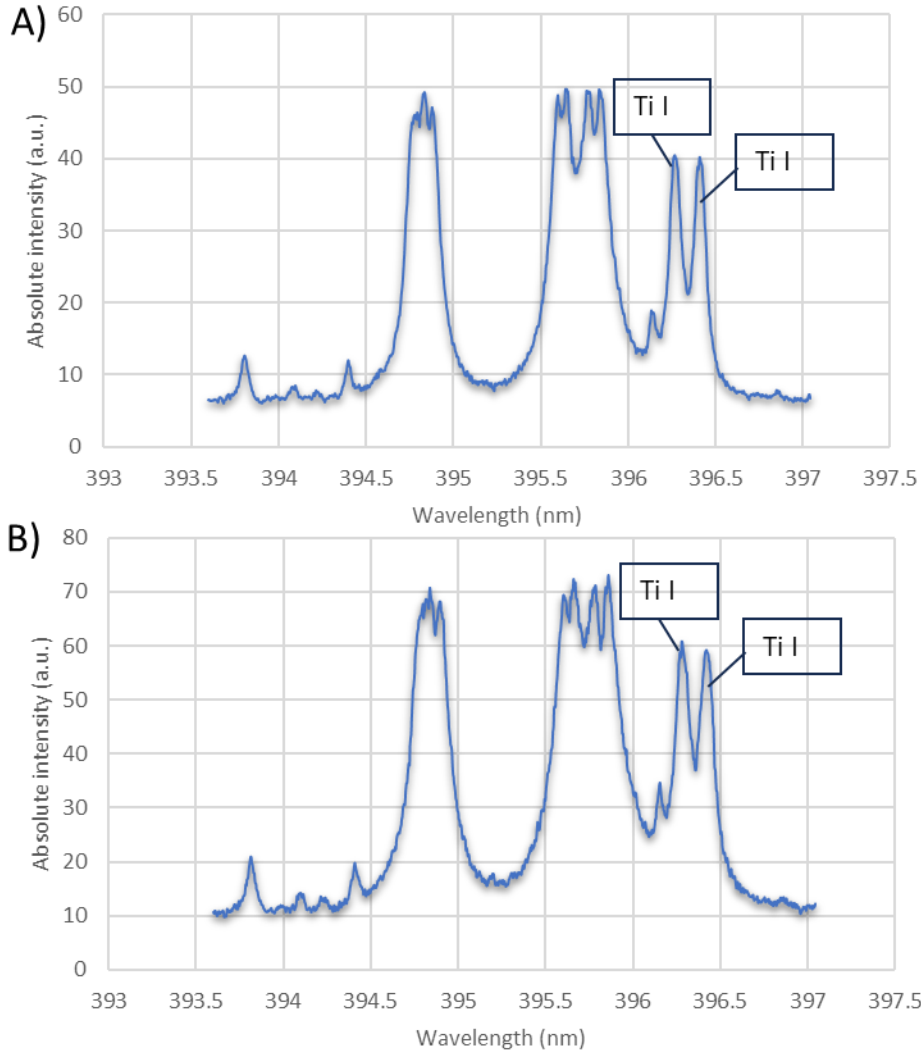
Figure 128. Calibrated spectra in the 7888 region for A) 0.8 kW and B) 1.6 kW laser pulse (2 ms) on T40.

Table 20. Observable Ti transitions in the 7888 region (transitions chosen for analysis in blue).

λ_s theoretical (nm)	A_s (s^{-1})		E_i (cm^{-1})	J_i	Conf.	E_s(cm^{-1})	J_s	Conf.
393.7975	2.394e+07	Ti I	18287.554	4.0	(2G)4s b1G	43674.130	4.0	(2H)4p v1G
394.7768	9.599e+06	Ti I	170.134	3.0	s2 a3F	25493.734	2.0	(1D)sp z3P
394.8670	4.851e+07	Ti I	0.000	2.0	s2 a3F	25317.815	1.0	(4F)4p y3D
394.9125	2.060e+05	Ti I	17215.389	5.0	(3F)sp z5F	42530.289	6.0	s4F)4d e3H
395.6334	3.001e+07	Ti I	170.134	3.0	s2 a3F	25438.906	2.0	(4F)4p y3D
395.8206	4.044e+07	Ti I	386.875	4.0	s2 a3F	25643.699	3.0	(4F)4p y3D
396.2851	**4.128e+06**	**Ti I**	**0.000**	**2.0**	**s2 a3F**	**25227.220**	**3.0**	**(3F)sp y3F**
396.4269	**3.085e+06**	**Ti I**	**170.134**	**3.0**	**s2 a3F**	**25388.331**	**4.0**	**(3F)sp y3F**

4.5.2.1.4.   Region 8006

The line at 399.86 nm is a fundamental line, that is auto-absorbed (green in Table 21). Three relatively isolated lines at 400.2471 nm, 400.3797 nm, and 400.596 nm originate from upper levels around 42,000 cm^{-1} (blue in Table 21 and selected for analysis). The two transitions at

402.1816 nm and 402.6537 nm also provide information about upper levels around 42,000 cm^{-1}.

The line at 402.45 nm stems from the fundamental transition at 402.4572 nm, with the risk of auto-absorption. The presence of a nearby transition at 402.4743 nm (with a similar upper level and A_s as the line at 402.1816 nm) strongly influences the intensity of this line (Figure 129).

Table 21. Observable Ti transitions in the 8006 region (transitions chosen for analysis in blue).

| λ_s theoretical (nm)	A_s (s^{-1})		E_i (cm^{-1})	J_i	Conf.	E_s(cm^{-1})	J_s	Conf.
399.8636	4.07E+07	Ti I	386.875	4	s2 a3F	25388.331	4	(3F)sp y3F
399.8968	2.13E+07	Ti I	17215.389	5	(3F)sp z5F	42214.77	4	s4F)4d e3H
399.9343	2.75E+07	Ti I	16961.441	3	(3F)sp z5F	41958.478	2	s4F)4d e5D
400.2471	4.72E+07	Ti I	17075.258	4	(3F)sp z5F	42052.765	3	s4F)4d e5D
400.3797	4.12E+07	Ti I	17215.389	5	(3F)sp z5F	42184.622	4	s4F)4d e5D
400.596	2.26E+07	Ti I	16961.441	3	(3F)sp z5F	41917.193	4	s4F)4d e5H
400.719	1.79E+07	Ti I	16875.121	2	(3F)sp z5F	41823.209	3	s4F)4d e5H
400.8054	2.96E+07	Ti I	17075.258	4	(3F)sp z5F	42017.973	5	s4F)4d e5H
400.8928	7.03E+06	Ti I	170.134	3	s2 a3F	25107.41	2	(3F)sp y3F
400.9657	1.21E+06	Ti I	170.134	3	s2 a3F	25102.874	2	(3P)sp z5S
401.2791	5.08E+06	Ti I	17075.258	4	(3F)sp z5F	41988.527	3	s4F)4d g3F
401.3249	1.99E+07	Ti I	16961.441	3	(3F)sp z5F	41871.865	2	s4F)4d g3F
401.3583	2.20E+07	Ti I	17215.389	5	(3F)sp z5F	42123.74	6	s4F)4d e5H
401.5373	5.72E+07	Ti I	16817.16	1	(3F)sp z5F	41714.41	2	s4F)4d e5G
401.6273	2.51E+06	Ti I	17215.389	5	(3F)sp z5F	42107.056	4	s4F)4d g3F
401.696	1.01E+07	Ti I	17423.855	2	2D2)4s a3D	42311.265	3	s2 4p q3D
401.7768	4.48E+07	Ti I	16875.121	2	(3F)sp z5F	41757.532	3	s4F)4d e5G
401.7985	1.24E+07	Ti I	20209.443	2	2D2)4s b1D	45090.506	1	t3P
402.1816	4.80E+07	Ti I	16961.441	3	(3F)sp z5F	41818.808	4	s4F)4d e5G
402.4572	6.14E+06	Ti I	386.875	4	s2 a3F	25227.22	3	(3F)sp y3F
402.4743	1.35E+07	Ti I	16875.121	2	(3F)sp z5F	41714.41	2	s4F)4d e5G
402.6537	3.57E+07	Ti I	17075.258	4	(3F)sp z5F	41903.476	5	s4F)4d e5G
402.7153	5.20E+05	Ti I	17369.528	1	2D2)4s a3D	42193.949	1	s4F)5p p3D
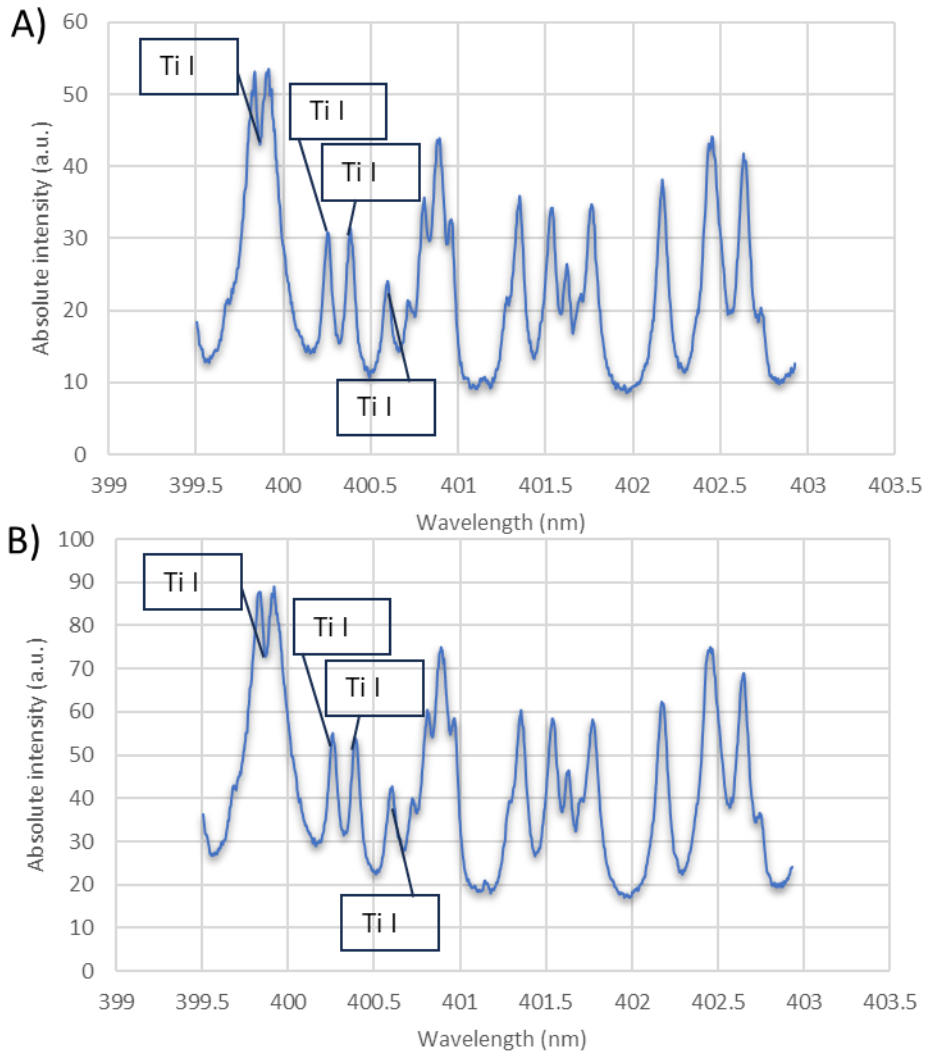
Figure 129. Calibrated spectra in the 8006 region for A) 0.8 kW and B) 1.6 kW laser pulse (2 ms) on T40.

4.5.2.1.5.   Region 9289

The peak at 463.96 nm, influenced by three intense lines at 463.9361 nm, 463.9661 nm, 463.9939 nm, and 464.0418 nm (Table 22), could not be retained. Two intense lines at 464.5188 nm and 465.001 nm, associated with upper levels around 35,500 cm^{-1} have been selected for analysis (Figure 130).

Two fundamental lines can be considered at 465.6469 nm and 466.7585 nm. Their upper level is around 21,500 cm^{-1}. Auto-absorption could be present for these lines. Profile fitting should be done for the 466.8347 nm line while carefully considering the line at 466.7585 nm in proximity.

Table 22. Observable Ti transitions in the 9289 region (transitions chosen for analysis in blue).

λ_s theoretical (nm)	A_s (s⁻¹)		E_i (cm⁻¹)	J_i	Conf.	E_s(cm⁻¹)	J_s	Conf.
463.7828	2.97E+06	Ti I	26772.969	5	(4F)4p y5G	48328.748	4	d2 4p2 j5F
463.7868	2.50E+07	Ti I	18911.393	2	(2P)4s c3P	40466.988	2	s2 4p v3P
463.9361	5.98E+07	Ti I	14028.435	2	(4P)4s a5P	35577.093	2	(4P)4p w5D
463.9661	3.42E+07	Ti I	14105.634	3	(4P)4s a5P	35652.899	3	(4P)4p w5D
463.9939	6.63E+07	Ti I	13981.773	1	(4P)4s a5P	35527.746	1	(4P)4p w5D
464.0418	5.02E+07	Ti I	18825.781	1	(2P)4s c3P	40369.533	0	s2 4p v3P
464.5188	**8.57E+07**	**Ti I**	**13981.773**	**1**	**(4P)4s a5P**	**35503.4**	**0**	**(4P)4p w5D**
465.001	**2.64E+07**	**Ti I**	**14028.435**	**2**	**(4P)4s a5P**	**35527.746**	**1**	**(4P)4p w5D**
465.6469	**1.99E+06**	**Ti I**	**0**	**2**	**s2 a3F**	**21469.487**	**3**	**(3F)sp z3G**
466.7585	**2.18E+06**	**Ti I**	**170.134**	**3**	**s2 a3F**	**21588.494**	**4**	**(3F)sp z3G**
466.8347	6.15E+05	Ti I	8492.421	1	s2 **a3F**	29907.286	2	(4F)4p x5D
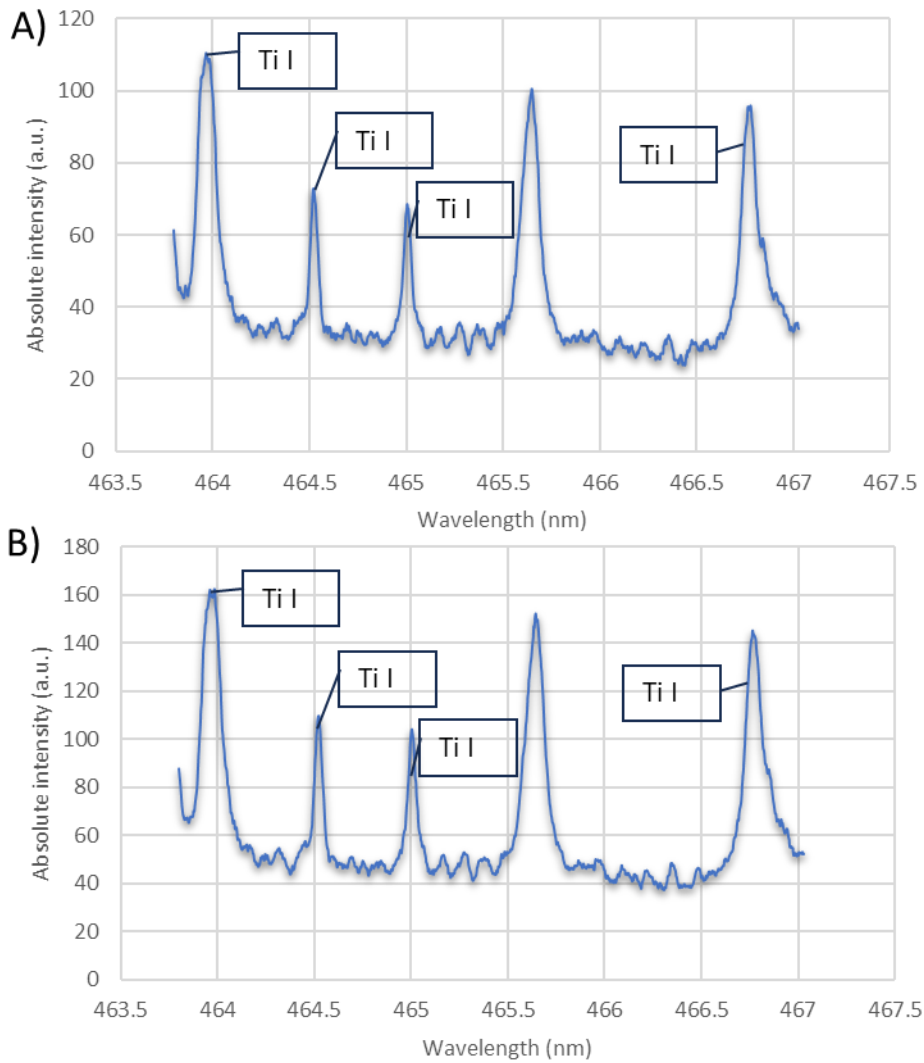
Figure 130. Calibrated spectra in the 9289 region for A) 0.8 kW and B) 1.6 kW laser pulse (2 ms) on T40.

4.5.2.1.6. Emission lines used for temperature estimation

In summary, 22 emission lines were selected (Table 11, Table 23, Table 24) to be used in Boltzmann plot analysis for temperature estimation. These lines correspond to 5 spectral regions (thus requiring intensity calibration using a calibration lamp). The upper energy levels range from 21,469.487 cm^{-1} to 45,630.182 cm^{-1}.

Table 23. Selection of spectral transitions of Titanium for analysis.

λ_s theoretical (nm)	A_s (s^{-1})		Lower level			Upper level		
			E_i (cm^{-1})	J_i	Conf.	E_s (cm^{-1})	J_s	Conf.
Spectral Region 7530								
377.1651	6.02E+06	Ti I	386.875	4	s2 a3F	26892.935	3	(1D)sp x3F
378.0384	7.51E+06	Ti I	11531.759	2	(4F)4s b3F	37976.589	2	(3P)sp u3D
378.9294	2.35E+07	Ti I	11776.811	4	(4F)4s b3F	38159.457	3	(3P)sp u3D
Spectral Region 7635								
381.3269	3.17E+07	Ti I	16817.160	1.0	(3F)sp z5F	43033.937	1.0	s4F)4d g5F
381.4861	2.41E+07	Ti I	16875.121	2.0	(3F)sp z5F	43080.961	2.0	s4F)4d g5F
381.7642	2.74E+07	Ti I	16961.441	3.0	(3F)sp z5F	43148.187	3.0	s4F)4d g5F
381.8199	3.36E+07	Ti I	18192.570	6.0	(2H)4s a3H	44375.501	5.0	s4F)5p t3G
382.2023	3.50E+07	Ti I	17075.258	4.0	(3F)sp z5F	43231.989	4.0	s4F)4d g5F
382.9721	2.91E+06	Ti I	11639.810	3.0	(4F)4s b3F	37743.964	3.0	a2D)4p u3F
383.6768	4.32E+07	Ti I	19573.973	4.0	(3F)sp z3F	45630.182	5.0	s2F)4d 3G
384.1621	3.60E+06	Ti I	11531.759	2.0	(4F)4s b3F	37555.056	3.0	(2G)4p v3G
Spectral Region 7888								
396.2851	4.128e+06	Ti I	0.000	2.0	s2 a3F	25227.220	3.0	(3F)sp y3F
396.4269	3.085e+06	Ti I	170.134	3.0	s2 a3F	25388.331	4.0	(3F)sp y3F
Spectral Region 8006								
400.2471	4.72E+07	Ti I	17075.258	4	(3F)sp z5F	42052.765	3	s4F)4d e5D
400.3797	4.12E+07	Ti I	17215.389	5	(3F)sp z5F	42184.622	4	s4F)4d 5D
400.596	2.26E+07	Ti I	16961.441	3	(3F)sp z5F	41917.193	4	s4F)4d e5H
402.1816	4.80E+07	Ti I	16961.441	3	(3F)sp z5F	41818.808	4	s4F)4d e5G
402.6537	3.57E+07	Ti I	17075.258	4	(3F)sp z5F	41903.476	5	s4F)4d e5G
Spectral Region 9289								
464.5188	8.57E+07	Ti I	13981.773	1	(4P)4s a5P	35503.4	0	(4P)4p 5D
465.001	2.64E+07	Ti I	14028.435	2	(4P)4s a5P	35527.746	1	(4P)4p w5D
465.6469	1.99E+06	Ti I	0	2	s2 a3F	21469.487	3	(3F)sp z3G
466.7585	2.18E+06	Ti I	170.134	3	s2 a3F	21588.494	4	(3F)sp z3G

Table 24. Selection of spectral emission lines from A5754 for analysis.

λ_s theoretical (nm)	A_s (s⁻¹)		Lower level			Upper level		
			E_i (cm⁻¹)	J_i	Conf.	E_s (cm⁻¹)	J_s	Conf.
Spectral Region 6160								
308,2153	**6,27E+07**	**Al I**	**0**	**0,5**	**3p 2P**	**32435,435**	**1,5**	**3d 2D**
309,1064	3,00E+07	Mg I	21850,405	0	s3p 3P	54192,335	1	s4d 3D
309,271	**7,55E+07**	**Al I**	**112,061**	**1,5**	**3p 2P**	**32436,778**	**2,5**	**3d 2D**
309,2839	**1,24E+07**	**Al I**	**112,061**	**1,5**	**3p 2P**	**32435,435**	**1,5**	**3d 2D**
309,2982	2,22E+07	Mg I	21870,464	1	s3p 3P	54192,335	1	s4d 3D
309,2986	2,72E+07	Mg I	21870,464	1	s3p 3P	54192,294	2	s4d 3D
309,6884	**1,50E+06**	**Mg I**	**21911,178**	**2**	**s3p 3P**	**54192,335**	**1**	**s4d 3D**
309,6887	**8,98E+06**	**Mg I**	**21911,178**	**2**	**s3p 3P**	**54192,294**	**2**	**s4d 3D**
309,6891	**5,33E+07**	**Mg I**	**21911,178**	**2**	**s3p 3P**	**54192,256**	**3**	**s4d 3D**
Spectral Region 7635								
382,9355	**8,90E+07**	**Mg I**	**21850,405**	**0**	**s3p 3P**	**47957,058**	**1**	**s3d 3D**
383,2299	6,67E+07	Mg I	21870,464	1	s3p 3P	47957,058	1	s3d 3D
383,2304	1,20E+08	Mg I	21870,464	1	s3p 3P	47957,027	2	s3d3D
383,829	4,45E+06	Mg I	21911,178	2	s3p 3P	47957,058	1	s3d3D
383,8292	1,59E+08	Mg I	21911,178	2	s3p 3P	47957,045	3	s3d3D
383,8295	4,00E+07	Mg I	21911,178	2	s3p 3P	47957,027	2	s3d3D
Spectral Region 7888								
394,4006	**5,11E+07**	**Al I**	**0**	**0,5**	**3p 2P**	**25347,756**	**0,5**	**4s 2S**
396,152	**1,01E+08**	**Al I**	**112,061**	**1,5**	**3p 2P**	**25347,756**	**0,5**	**4s 2S**
Spectral Region 10330								
516,7321	**7,77E+06**	**Mg I**	**21850,405**	**0**	**s3p 3P**	**41197,403**	**1**	**s4s 3S**
517,2684	**3,29E+07**	**Mg I**	**21870,464**	**1**	**s3p 3P**	**41197,403**	**1**	**s4s 3S**
518,3604	**5,46E+07**	**Mg I**	**21911,178**	**2**	**s3p 3P**	**41197,403**	**1**	**s4s 3S**

4.5.3. Temperature estimation for standalone materials T40 and A5754

During the spectral analysis, the presence of two components: atomic emission lines and a continuous background, was consistently observed. Therefore, it would be prudent to consider the vapor exiting the capillary to be a very dense medium at the temperature of the vapor inside the capillary. This vapor would emit thermal radiation following the blackbody curve. However, as the vapor expands into the air, the periphery of the plume would have a lower density. Consequently, the emission of atoms could be observed from this layer with lower density, i.e., an atomic emission spectrum. Because the main objective of using spectroscopy to study dissimilar laser welding was to analyze the light emitted by the core (thermal radiation) and the periphery of the plume (atomic emission) to estimate and compare the two temperatures of these parts of the vapor plume.

Temperature calculated from atomic emissions, based on Boltzmann distribution of energy levels in atoms, refer to the specific wavelengths of light emitted by atoms when they transition from higher energy states to lower energy states. Atomic emissions focus on the discrete spectral lines emitted by atoms in a low-density gas, while thermal emissions consider the continuous spectrum of radiation emitted by objects at a given temperature.

With the assumption of local thermodynamic equilibrium, the determination of the electronic temperature of atoms could be achieved using the Boltzmann plot method. The intensity of an emission line is proportional to the following quantity,

$$I = A_s . N_n . h . \nu = A_s . N_n . \frac{h.c}{\lambda}$$

$$66$$

Where A_s is the Einstein's spontaneous emission coefficient, which is the probability of the transition from the upper level s to the lower level l, ν is the frequency of the light emitted from the transition between the lower and upper states, and λ is the corresponding wavelength.

By taking the logarithm of Eqn.66 and Eqn.28 (p.45) , we obtain:

$$ln\left(\frac{I.\lambda}{g_n . A_s}\right) = -\frac{E_n}{k_B.T} + constant$$

$$67$$

When this logarithmic term is plotted against the energy of the upper level E_n, the slope of $(-1/k_B.T)$ is the atomic excitation temperature.

4.5.3.2.   Thermal radiation

Thermal radiation, modeled by Planck's law, describes the spectral distribution as a function of wavelength (Figure 131. A). Luminance (power emitted per unit area of a blackbody, for a given direction) is a function of wavelength and absolute temperature, expressed by Eqn. 26 (p.45).

Thermal radiation primarily falls in the infrared range. However, the observation range of the atomic emission spectrometer is in the region between ultraviolet and visible light, limited to wavelengths (250 – 580 nm). According to Wien's law, the peak emission of a blackbody shifts towards shorter wavelengths as the absolute temperature increases. If the temperature is around 3000 K, it would result in a peak emission at approximately 950 nm. Therefore, the observed continuous background falls within the rising portion of the blackbody spectrum curve.

$$I_{measured} \approx \frac{2hc^2}{\lambda^5} \frac{1}{e^{\left(hc/\lambda.k_B.T\right)} - 1}$$

$$68$$

Since this work has been done in the range of short wavelengths (Figure 131. B), the value of $\lambda.T$ is small, and the following assumption would be possible:

$$e^{(h.c/\lambda.k_B.T)} >> 1$$

$$69$$

In this case, the intensity could be expressed as,

$$I_{measured} \approx \frac{2hc^2}{\lambda^5} e^{\left(-hc/\lambda.k_B.T\right)}$$

$$70$$

Figure 131 provides a comparison between Planck's law and the approximation is done (represented by dashed lines) for temperatures of 3000 K, and 4000 K. In Figure 131. B the axis is shown on a logarithmic scale. For temperatures in the range of 3000-5000 K, the approximation seems accurate within the observation range (below 0.6 μm).

Taking the natural logarithm of Eqn.70, we have:

$$ln\left(I_{measured}\right) = ln(2hc^2) - 5\ ln(\lambda) - \frac{hc}{\lambda.k_B.T} \qquad 71$$

This radiation law can be linearized. Using Excel, the curve was plotted using,

$$ln\left(I_{measured}\right) + 5\ ln(\lambda) = f\left(\frac{1}{\lambda}\right) \qquad 72$$

For a straight line, the slope of the curve would be,

$$-\frac{hc}{k_B.T} \qquad 73$$

This allowed calculation of the temperature of the vapor generated during the laser pulses.

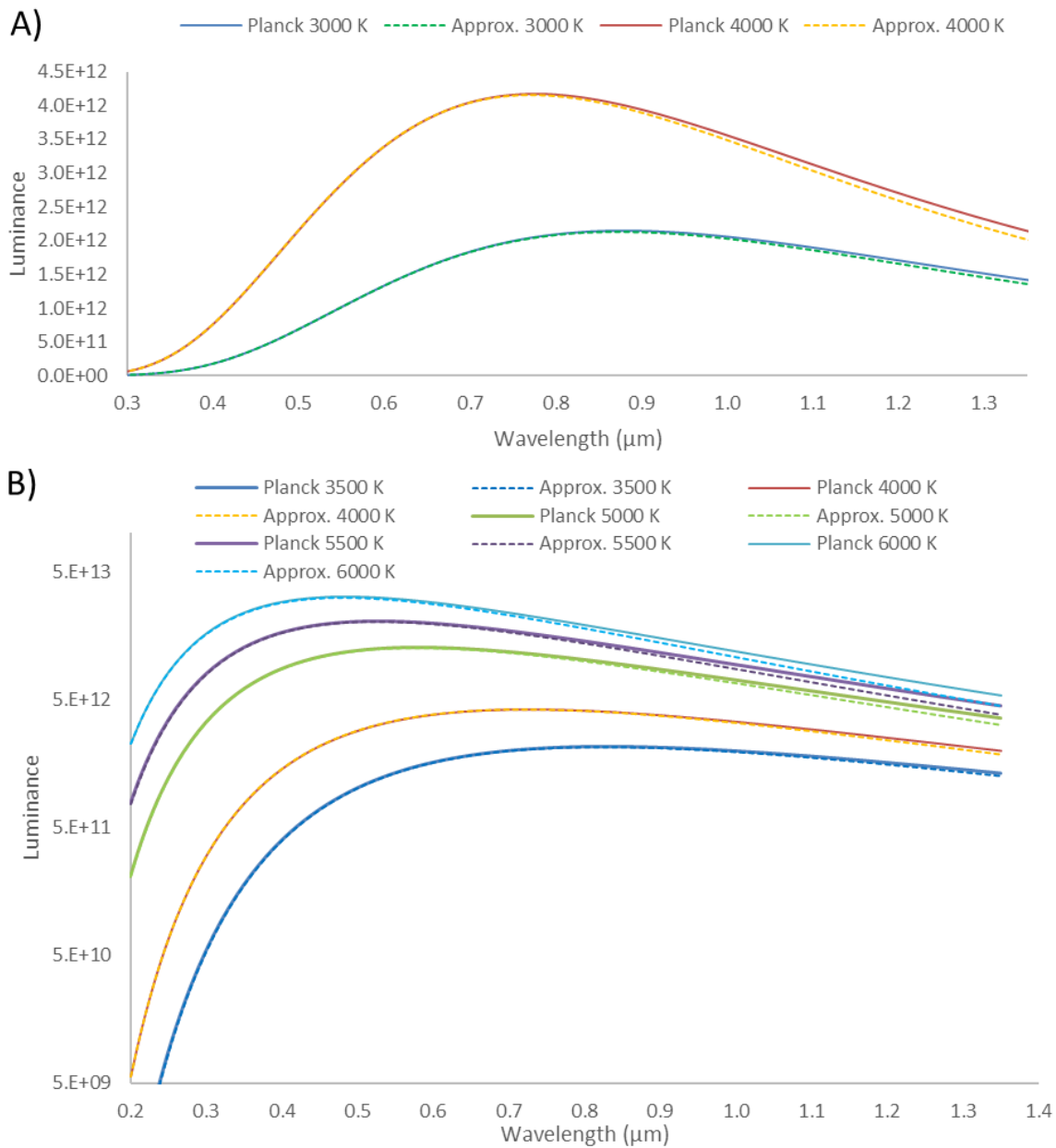*Figure 131. A) Comparison of Planck's law and the approximation used for temperatures 3000 K and 4000 K and B) for temperatures ranging 3500 K to 6000 K with y-axis in logarithmic scale (Approximation in dotted lines).*

From the calibrated spectra, the comparison of spectra obtained in different spectral regions was done using PeakFit. This software is used to identify spectral lines and determine their characteristics, such as wavelength and intensity. While the program suggests lines, it is crucial to validate these choices by considering the study of possible transitions (Table 2-8), while taking into account factors like possible transitions and estimating the order of magnitude of intensity.

The Lorentzian line profile was used. Initially the work was done with a Voigt profile, but since no significant differences were observed, the switch to fitting with a Lorentzian profile was done, because uses two width parameters (from the function of spectrometer and gaussian) instead of one. Figure 21b provides an example of profile fitting.

This process yields a file containing the positions of the lines, their intensities, and a width (not utilized in this study), along with the standard deviation of these three parameters. The software also extracts an intensity level of the continuous background (along with its standard deviation).

In equation (eq.3), uncertainties in λ_s, g_s, A_s, and E_n were neglected and only the estimated standard deviation in intensity during the profile fitting (σ_I) was considered.

From the differential of $ln\left(\frac{I.\lambda_s}{g_s . A_s}\right)$, the standard deviation in the logarithm was obtained.

$$\sigma_{ln} = \frac{\sigma_I}{I} \qquad\qquad 74$$

On the Boltzmann curve, this standard deviation was represented as error bars on the axis.

The determination of the slope was done using a weighted least-squares linear regression method. In other words, the standard deviation σ_{ln} was used to assign each data point with a weight $w = \frac{1}{\sigma_{ln}^2}$, where,

$$\sigma_{ln}^2 = \left(\frac{\sigma_I}{I}\right)^2 \qquad\qquad 75$$

The slope is inversely proportional to temperature:

$$p = -\frac{1}{k_B.T} \qquad\qquad 76$$

Therefore, from the standard deviation σ_p obtained during the linear regression, the standard deviation σ_T in the estimation of atomic temperature was determined using,

$$\left(\frac{\sigma_T}{T}\right)^2 = \left(\frac{\sigma_p}{p}\right)^2 \qquad\qquad 77$$

4.5.3.4.   *Temperature evaluation for titanium*

To compare the evolution of titanium spectra for different laser powers, a series of spectra was recorded for laser impacts on standalone T40 titanium (600 μm - spot diameter). 2 ms were impacted in T40 for powers ranging from 0.6 to 2 kW. Examples of spectra were presented from Figure 126 to Figure 130, recorded in the spectral regions 7530, 7635, 7888, 8006, and 9289. The lines selected for analysis were presented in section 4.5.2.1.6 (Table 23).

Using these transitions, temperatures were estimated. Initially, after calibration of the spectra (to compare different spectral regions), the line profiles were fit. And then, the atomic temperatures were deduced from the slope of the Boltzmann plots based on intensities of the selected lines (Eqn.67, p.173). Furthermore, we estimated the temperature of thermal radiation was estimated from the levels of the continuous background emissions (Eqn.71, p.174).

In Figure 132, the lines obtained for powers ranging from 0.7 kW to 2 kW are presented. For the Boltzmann lines, the energy of the upper level is expressed in eV, which is a more suitable unit for presenting these curves. The 0.7 kW power represented a threshold for which the lines are not usable. Similarly, for 2 kW, the spectra show many saturated lines (in the 7888 and 8006 regions). Therefore, they were ineligible for temperature estimation. The energy domain varied from 3.5 to 5.5 eV.
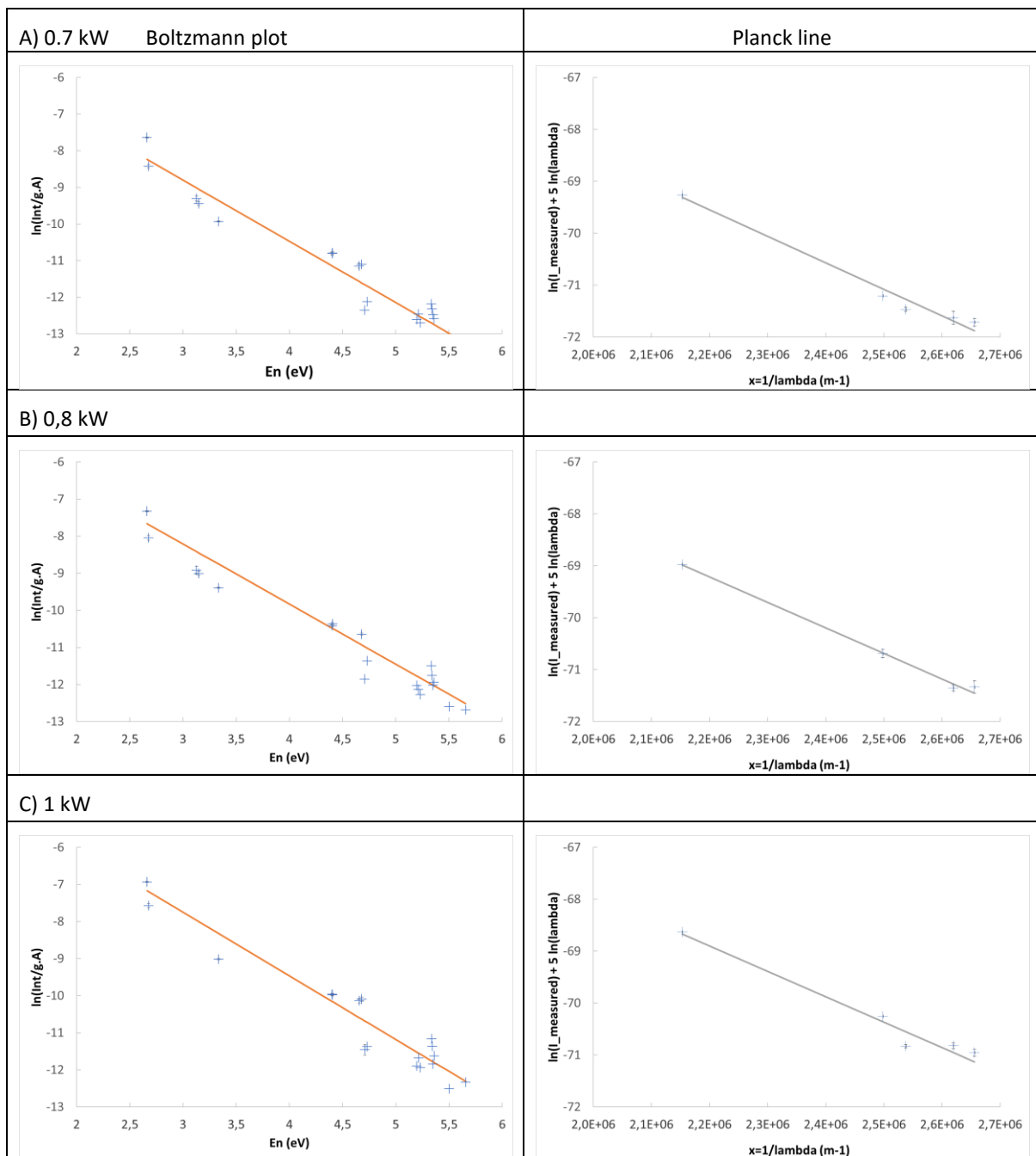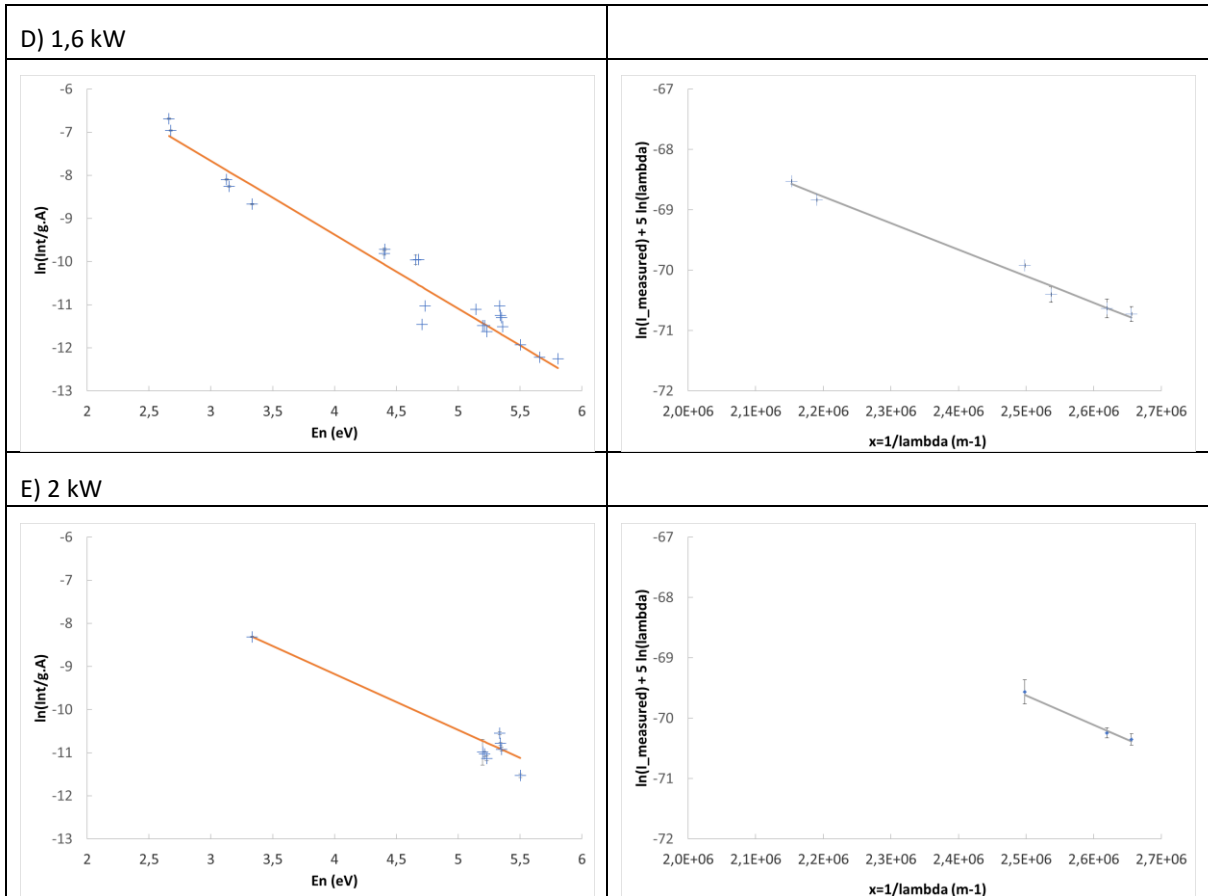
Figure 132. Evolution of Titanium Temperatures as a Function of Power (600 µm fiber, 2 ms pulse duration): Boltzmann and Planck Lines.

The results of temperature estimation obtained from the curves (Figure 132) are presented in Figure 133. The evolution of the two estimated temperatures of the different laser powers show some dispersion of the points. But the trend appears to show that temperatures do not depend on the laser power (in this range which corresponded to a correct welding regime).
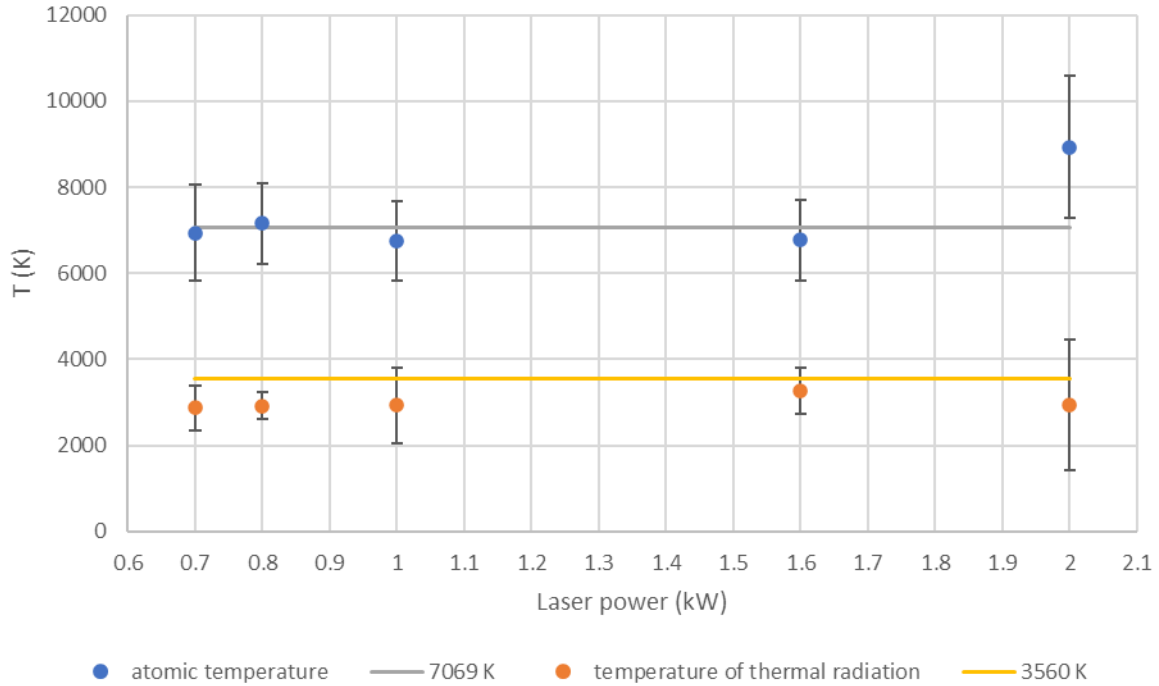
Figure 133. Evolution of Titanium Temperatures as a Function of Power (3σ bar)

The estimation of the continuous background temperature, assumed to be interpreted as the vapor's thermal radiation, led to a value close to the vaporization temperature of titanium (in yellow in Figure 133).

However, a much higher atomic temperature of around 7000 K was observed. This suggested that the atoms have not only been excited by thermal agitation within the ablated vapor but have received an additional energy input. Therefore, it could be hypothesized that there was interaction between the atoms and the laser beam (inverse Bremsstrahlung mechanism usually observed in more energetic cases such as nanosecond laser absorption). It is possible that this absorption occurs when the atoms are still in the capillary, with a high density. However, it is very likely that this phenomenon will disappear as the vapor plume expands into the ambient air. Even if the temperature measurement for the 2 kW appears to be ~9000 K, the uncertainty is much higher. The temperature would be much likely be closer to the average atomic temperature.

4.5.3.5.   Spectrometric analysis of aluminum

Spectral acquisitions were made to study the evolution of aluminum spectra as a function of increasing laser power. In this experiment, 2 ms or 6 ms pulses with 600 µm spot diameter were impacted on A5754. The power varied between 1 to 3 kW (section 4.2, p.100). Spectral recordings are made in the two previously defined regions (7888 and 9400). Figure 134 shows the evolution of spectra in the 7888 region, corresponding to the two most intense lines of aluminum.
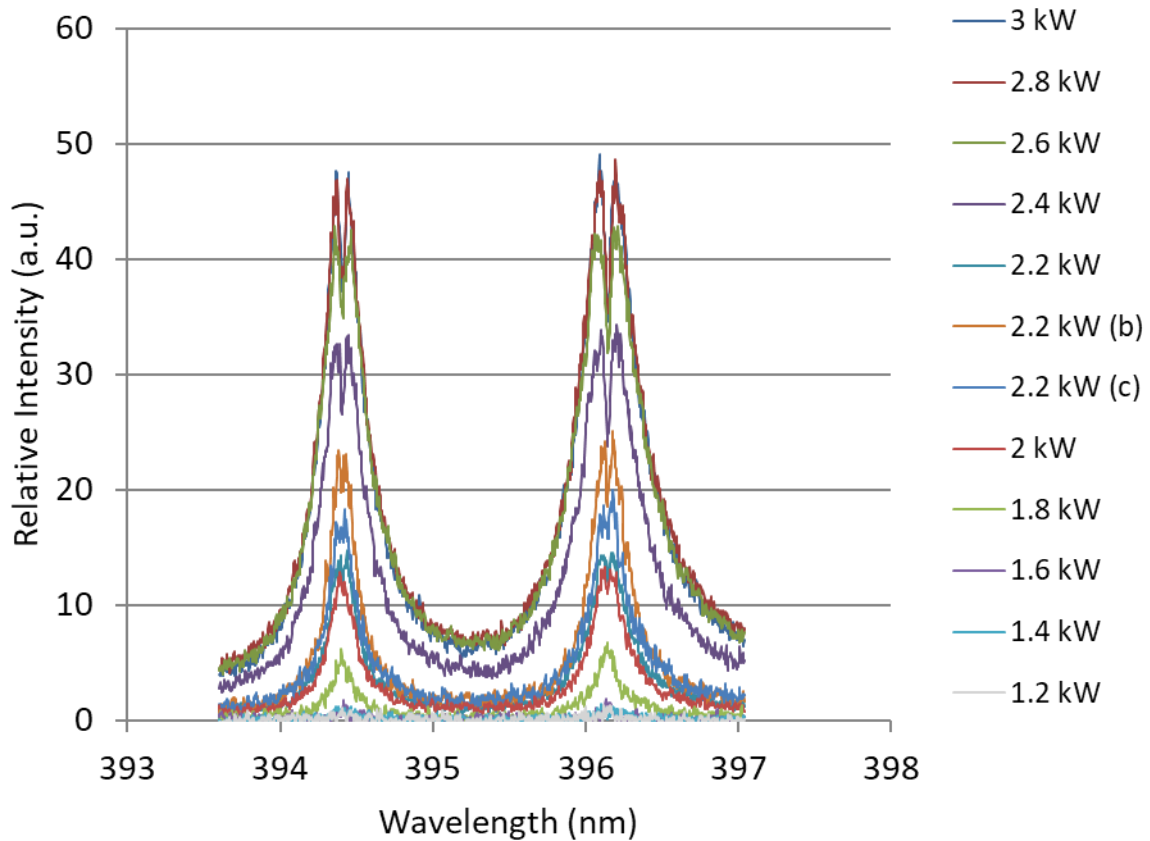
Figure 134. Evolution of the fundamental lines of aluminum (2ms pulse duration) (Multiple fits were tried using different parameters for 2.2 kW are represented with b and c).

The observation threshold for the two fundamental lines of aluminum was at a power of 1.4 kW (2 ms - 2.8 J – 600 μm - 990 J/cm^2 - 0.5 MW/cm^2). These fundamental lines were quickly auto-absorbed: at a power of 2.2 kW, the absorption peak of the atomic emission line could be observed because the emitted light from the excited atoms was absorbed during its path through the less dense peripheral layers of the plume.

From 2.6-2.8 kW, stabilization of the lines' intensity was observed. Because the base of the emission line no longer varied. The peak height (without auto-absorption) probably increases, but this was masked by auto-absorption.

The analysis of the lines was performed using PeakFit. In theory, these lines degraded by auto-absorption would be unusable. However, information was extracted from the foot of the line, the part not degraded by auto-absorption. The principle of this process was, by not taking into account the central part of the line when fitting the line profile, it was possible to obtain a correct fit on a Lorentzian profile (standard deviation given by the software was around 89-99%). An example of fitting is shown in Figure 135. The result of fitting for the two spectral regions was shown in Figure 124.
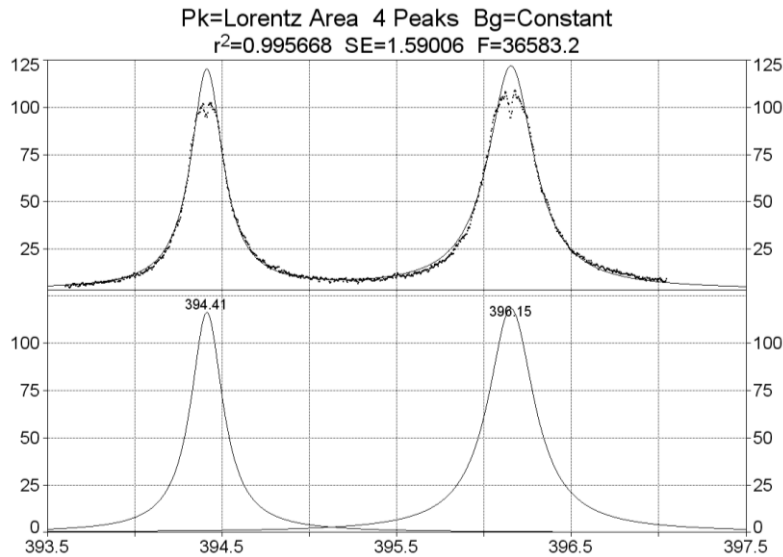
Figure 135. Example of the results for profile adjustments in PeakFit.

From the intensities of 4 Al (I) lines (394.40, 396.15, 308.21, and 309.28 nm), it was possible to make the Boltzmann plot. In Figure 136, the two observed (and calibrated) spectra as well as the Boltzmann line and Planck line are presented.

The result obtained from the continuous background were unusable because the interval between these two regions was small (90 nm), and the spectrum of the 6188 region had too much noise (ideally, having more than 2 points to plot this line would be better).

The Boltzmann lines use 4 points. It was observed that the two points corresponding to the spectrum of the 6188 region were dispersed. This was due to the profile fitting method on degraded lines. The standard deviation in the determination of intensities is likely underestimated. However, there is still coherence in the result obtained.
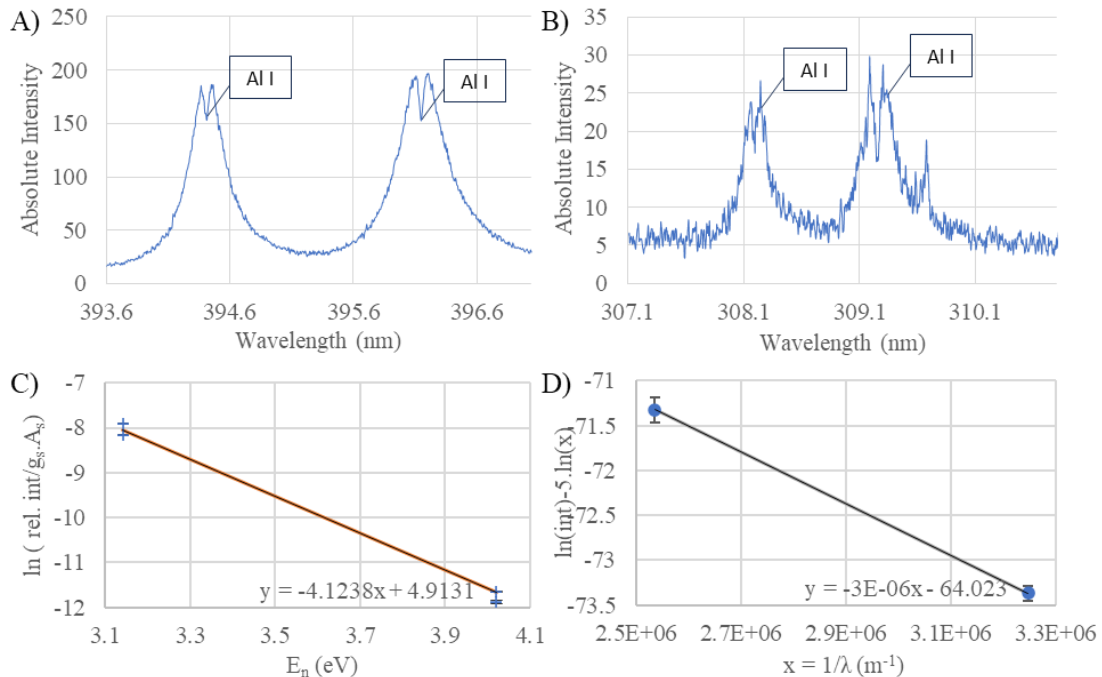
Figure 136. Determination of temperatures (6 ms, 2.8 kW) from spectral regions (calibrated) A) 7888 and B) 6160, and corresponding C) Boltzmann's plot and D) Planck line.

From these estimations of the aluminum atom temperature, temperature evolution as a function of power was obtained (Figure 137). The points are marked with error bars representing the standard deviation of the linear regression. The red line represents the vaporization temperature of aluminum. Despite the liberties taken in the fittings, it was observed that the atomic temperatures obtained are of the same order of magnitude as aluminum's vaporization temperature. The aluminum atoms found to be at the temperature of vaporization, was independent of the laser power (within the studied range). The temperature from the Planck line was ~4700 K, which is incorrect since it is higher than the atomic temperature. Multiple spectra from a wide range of spectral regions at various wavelengths would be needed for an accurate estimation of the macroscopic temperature.

The vapor temperature is constant, but it was observed that the intensity of the lines increases with power. The intensity of a line depends on temperature (equation 3), but it also depends on the amount of emitting material. Therefore, it was concluded that as the laser power increases, the increase in line intensity reflects an increase in the amount of material ejected from the capillary, rather than the temperature.
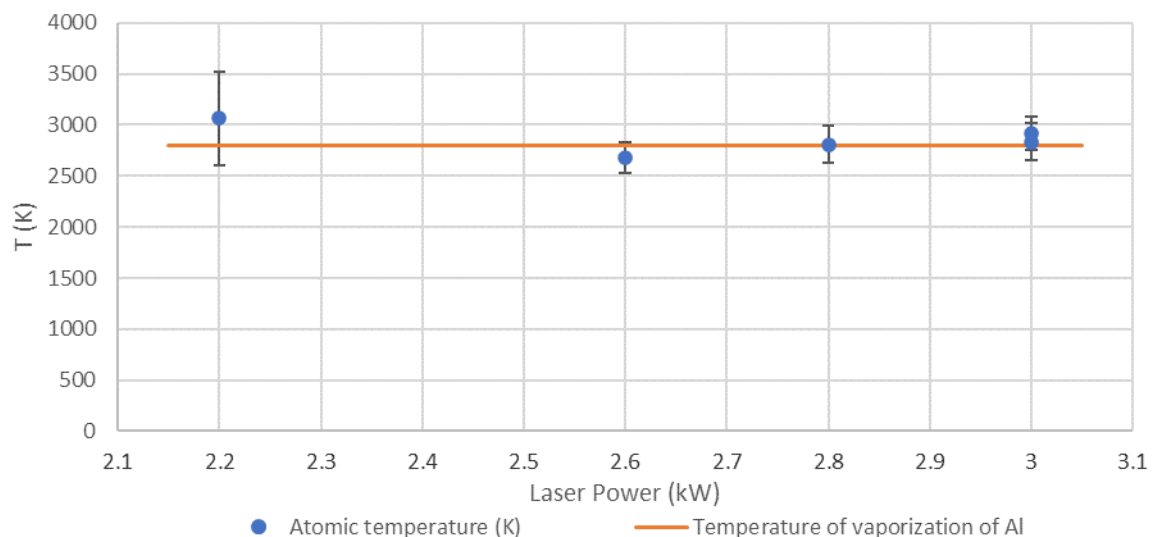
Figure 137. Evolution of atomic temperature of aluminum as a function of laser power.

In Table 25, the results for a laser pulse duration of 2 ms and 6 ms, at a power of 3 kW for 4 different emission lines are compared. The estimated temperature increases slightly, but given the standard deviation, it is not significant. However, when the pulse duration changes from 2 ms to 6 ms (increasing energy by a factor of 3), the intensity increases by a factor of 2. It is evident that by tripling the pulse duration, three times more laser energy was delivered during the interaction.

Table 25. Comparison of emission lines' intensities for different pulse times.

3 kW	Temperature	308.2 nm	309.3 nm	394.4 nm	396.1 nm
2 ms	2803±236 K	4.021	6.449	52.977	77.119
6 ms	2917±168 K	8.879	13.913	99.26	149.3
Ratio of intensities		2.2	2.2	1.9	1.9

According to Eqn.28 (p.45), the intensity of an emission line depends on the temperature (as temperature increases, excited states become more populated) and the amount of ablated material (atoms present in the plume). In continuous laser welding, the increase in the intensity of emission lines only represents an increase in the ablated material (atoms) in the capillary.

Similar conclusions to HSI were obtained from spectroscopy:

- Aluminum is difficult to weld due to its high reflectivity and thermal conductivity and diffusivity. Laser powers of at least 2-3 kW were necessary to achieve penetration (while 1 kW was sufficient to achieve similar results in the case of titanium). For the different laser parameters used on standalone aluminum, the spectroscopic analysis showed that the temperature of the atomic emission lines had the same order of magnitude as the vaporization temperature. Therefore, it was concluded that the vapor's atoms are in equilibrium at the vaporization temperature.

- In the case of titanium, spectroscopic analysis of the continuous background allowed estimation of the temperature to be of the order of the T40's vaporization temperature. The vapor exiting the capillary is a dense and opaque medium at the vaporization temperature. The study of emission lines showed that as the vapor expands into the air, a dense core of vapor emitting thermal radiation, surrounded by atoms at the periphery with lower density generating atomic emissions could be observed. The estimated temperature of the atomic emission lines was in the order of 7000 K. This suggested that the atoms have not only been excited from thermal agitation within the ablated vapor but had also received additional energy. It is generally accepted that in laser welding (with a 1064 nm wavelength source), the vapor plume ejected from the capillary does not absorb the laser beam. Temperature gradients can cause beam defocusing, and the vapor may become slightly opaque near the capillary, but there is no process of inverse Bremsstrahlung. The process of Inverse Bremsstrahlung corresponds to photon absorption during the collision of an electron with an ion. Therefore, the presence of ionized titanium (Ti II) in the spectra of the 7530 region (Figure 126) could be a residue of more significant ionization inside the capillary, with recombination occurring during expansion into the air.

Therefore, the estimated atomic temperature in this study suggests that the atoms from the vapor were excited by the laser beam inside the capillary, where the vapor is very dense with atoms. As a consequence, when modeling the capillary, consideration of laser beam absorption by the vapor inside the capillary is advised.

4.5.4. Spectrometric analysis of dissimilar welding of T40-A5754 butt-joint.

The objective of this work was to study the effect of the laser beam offset relative to the joint plane for laser impacts on T40-A5754 in butt-configuration. The 600 μm spot diameter, a pulse duration of 6 ms and a peak power of 2 kW, the spectral study was initially conducted to estimate atomic temperature using a methodology similar to the previous study conducted with standalone Titanium T40. Subsequently, the influence of the laser beam offset relative to the joint plane on the spectra was investigated.

This analysis was conducted solely based on the titanium lines. When studying the effect of impacts on a single material, successive pulses were impacted on the same plate. Therefore, it was possible to carry out a series of recordings distributed across the plate. Studying impacts at the interface between two materials required aligning the two plates parallel to the XY table's movement and controlling the offset of the beam relative to the path of movement. The series

of tests therefore were localized on a single line, rendering it more challenging to perform a large number of experiments. Additionally, spectral recordings were often performed simultaneously with high-speed imaging tests.

To estimate the temperature evolution (Figure 138), titanium lines from two spectral regions were used: the 7636 region and the 9290 region (Table 23, Table 26). The advantage of these two regions was that they had upper-level energies ranging from 21,500 cm^{-1} (2.66 eV) to 45,600 cm^{-1} (5.65 eV). The transitions used in this study are summarized in Table 26.

The study of the influence of the offset was conducted from $\Omega_{-0.2}$ to $\Omega_{+0.2}$. Two trials were conducted for each condition (Ω) and each spectral region to test repeatability.

Table 26. Ti transitions selected for dissimilar vapor temperature calculation in 7636 and 9290 region.

| λ_s theoretical (nm)	$g_s.A_s$ (s^{-1})	E_i (cm^{-1})	J_i	E_s (cm^{-1})	J_s
381.3269	9.5130E+07	16817.16	1	43033.937	1
381.4861	1.2050E+08	16875.121	2	43080.961	2
382.2023	3.1500E+08	17075.258	4	43231.989	4
383.6768	4.7531E+08	19573.973	4	45630.182	5
384.1621	2.5165E+07	11531.759	2	37555.056	3
464.5188	8.5680E+07	13981.773	1	35503.4	0
465.001	7.9260E+07	14028.435	2	35527.746	1
465.6469	1.3895E+07	0	2	21469.487	3
466.7585	1.9575E+07	170.134	3	21588.494	4
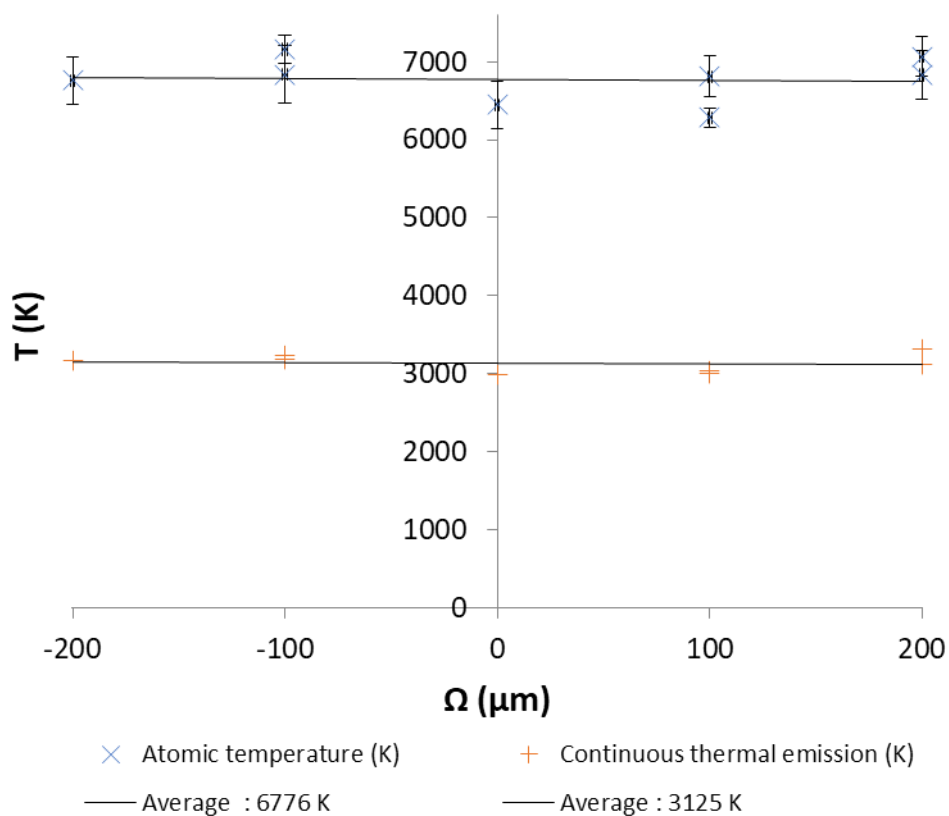
Figure 138. Evolution of temperatures as a function of laser spot position.

From the calibrated spectra (which allowed comparison of spectra from different spectral regions), the intensities of the studied lines were extracted using PeakFit (peak profile fitting). As previously done (section 4.5.3, p.172), the Boltzmann curve was then plotted to estimate atomic temperature. Similarly, based on the continuous background level (thermal radiation), vapor temperature was estimated. The error bars represented the estimated standard deviation during the calculation. This study was conducted for different laser source offsets. Figure 138 showed the evolution of these temperatures as a function of the offset.

Results similar to the results from pulses on standalone materials were observed. The spectra were the superpositions of continuous spectrum and atomic emission spectrum. The continuous spectrum resulted from a dense vapor core emitting thermal radiation with a temperature estimated at 3100 K, in the same order of magnitude as titanium's vaporization temperature. The atomic emission spectrum was the result of emissions from atoms in the periphery of the vapor plume expanding into air. The estimated temperature was around 6800 K, indicating that the atoms from the vapor were excited by the laser beam inside the capillary where the vapor was very dense.

With the radius of the beam being 300 μm, it could be observed that these temperatures seemed to be constant (given the estimated standard deviation) when studying an offset ranging from $\Omega_{-0.2}$ to $\Omega_{+0.2}$. The error bars represented the estimated standard deviation during the calculation. For each position, two trials conducted were consistent, given the estimated standard deviation. However, there was some dispersion due to the fluctuating dynamics of the capillary over time, resulting in temporal fluctuations of the plume (the spectrum was obtained over the plume's lifetime).

4.5.4.2.   Evolution of the spectra with respect to laser spot position

Spectroscopic analysis was conducted with the aim of investigating the effect of the beam offset relative to the joint line. Several spectral regions were examined for this study, and they showed complementary results. Furthermore, 3 pulses were impacted consecutively on the same spot to study the evolution of the spectra as a function of the evolution of the composition of the melting and solidifying zone. During the first pulse, the two materials mixed into the melted zone. And so, in the subsequent pulses, the spectra represented the migration of the two constituents into the melted zone from the first impact.

4.5.4.2.1.   Spectral region 7850: Evolution of Ti emission lines

The effect of beam offset relative to the joint line in the 7850 region was examined. In this region there were a fundamental line of Al (I) and several titanium emission lines (Table 27).

The evolution of spectra as the beam was offset from $\Omega_{-0.2}$ to $\Omega_{+0.3}$ are presented (Figure 139 to Figure 142). Figures labeled (a) show the spectra acquired from the three consecutive laser pulses. This allowed a comparison of the evolution of the continuous emission and the atomic emission lines. Figures labeled (b) show the profile analysis performed using PeakFit by subtracting the continuous thermal emission and extracting the parameters of the various lines.

On each spectrum, the auto-absorbed aluminum line was observed. At $\Omega_{-0.2}$, fundamental transitions yielding Ti (I) lines were observed, confirming the presence of titanium in the molten pool. As the beam was offset towards titanium, the intensity of the observed fundamental Ti (I) lines increased, and subsequently emissions from higher excited states emerged. For the beam offset completely on titanium ($\Omega_{+0.3}$), the Al (I) line at 394.77 nm was still visible. Given the acquisition gain used, this line was saturated along with the titanium line at 394.87 nm. And so, they are not presented in Figure 139.

In Figures (a), the effect of repeated impacts was analyzed. Following the first laser pulse, fusion and mixing of the molten materials occurred. Therefore, the surface for the second and third impacts was already composed of a mixture of materials with different properties (reflectivity, thermophysical properties), which could influence the interaction during the pulse.

- In the case of $\Omega_{-0.2}$, a slight decrease in the intensity of the Ti lines and an increase in the intensity of the aluminum peak were observed. It was possible that the melted zone was enriched in aluminum during the pulse.

- In the case of Ω_0, after the first pulse, a significant decrease in the continuous thermal emission and a decrease in the intensity of the titanium lines were observed. The composition of the material resulting from the mixture and the fusion from the first impact tended to reduce the efficiency of the interaction. Maybe due to the increase in aluminum on the surface or the presence an oxide, beam absorption tended to decrease.

- For $\Omega_{+0.2}$, differences in behavior were observed. The spectra obtained after the 1st and 3rd pulses were similar. It could be supposed that the effect of the first impact modified the composition of the melted zone, making the interaction less efficient during the second pulse.

- For $\Omega_{+0.3}$, the spectra were reproducible. The laser was primarily on titanium during the first impact. However, the presence of the aluminum line indicated that the interaction did indeed result in the melting and vaporization of aluminum, but the aluminum composition in the melted zone was very low.

Table 27. Observable transitions in the 7850 region.

λ_s theoretical (nm)	A_s (s^{-1})	Element	E_i (cm^{-1})	J_i	Conf.	E_s (cm^{-1})	J_s	Conf.
391.8304	1.55E+07	Mg I	34138.88	6.5	(3H)4s a4H	59652.9	5.5	a3F)4p x4G
391.9816	7.35E+06	Ti I	12118.394	4	s2 a1G	37622.573	3	s2 4p x1F
392.1422	2.15E+06	Ti I	0	2	s2 a3F	25493.734	2	(1D)sp z3P
392.4527	7.15E+06	Ti I	170.134	3	s2 a3F	25643.699	3	(4F)4p y3D
392.6318	7.79E+07	Ti I	20795.603	5	(2H)4s a1H	46257.55	4	s2F)5p u1G
392.9245	1.02E+06	Mg I	31124.95	0.5	(6S)sp z4P	56567.93	1.5	(5D)5s i6D
392.9642	9.16E+06	Mg I	34343.9	4.5	(3H)4s a4H	59784.31	3.5	a3F)4p x4G
392.9874	7.52E+06	Ti I	0	2	s2 a3F	25438.906	2	(4F)4p y3D
393.1584	9.25E+05	Ti I	18695.133	4	(3F)sp z5D	44122.976	5	(4F)4d 5F
393.3668	8.15E+06	Mg I	31076.42	1.5	(6S)sp z4P	56490.79	2.5	(5D)5s i6D
393.4233	4.46E+05	Ti I	386.875	4	s2 a3F	25797.594	3	(3P)sp y5D
393.7975	2.39E+07	Ti I	18287.554	4	(2G)4s b1G	43674.13	4	(2H)4p v1G
394.4006	5.11E+07	Al I	0	0.5	3p 2P	25347.756	0.5	4s 2S
394.7768	9.60E+06	Ti I	170.134	3	s2 a3F	25493.734	2	(1D)sp z3P
394.867	4.85E+07	Ti I	0	2	s2 a3F	25317.815	1	(4F)4p y3D
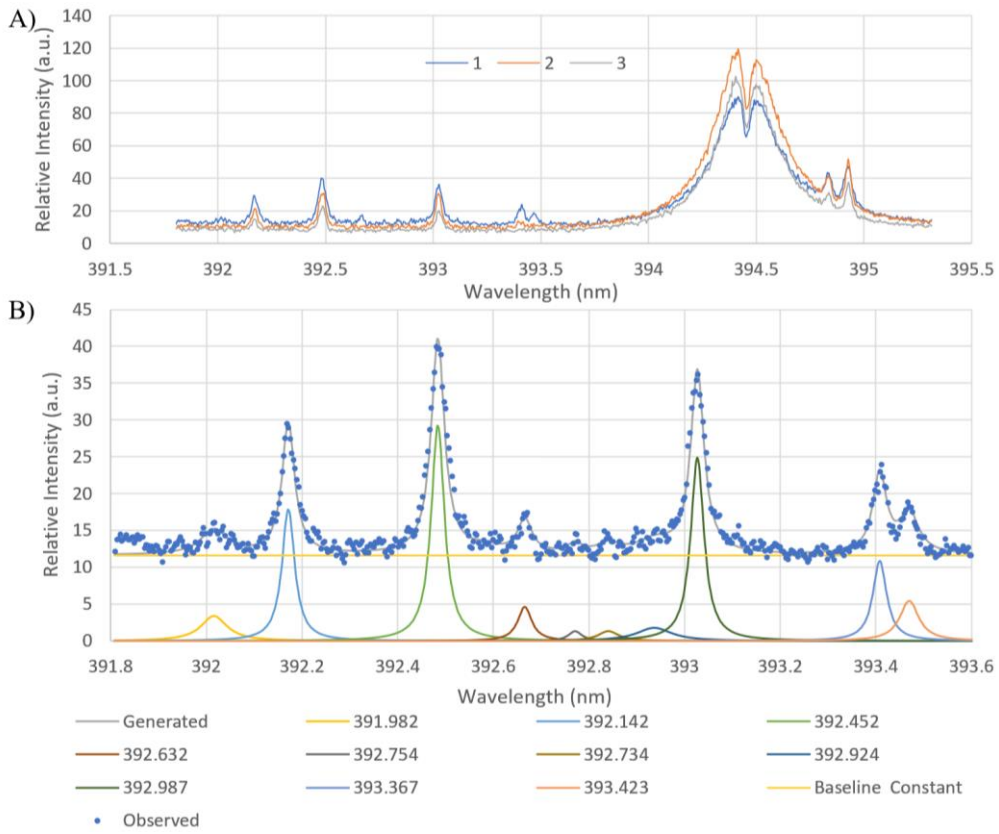
Figure 139. A) 3 impacts at spectral region 7850 - Ω$_{-0.2}$ and corresponding B) Profile analysis. (1,2,3 in legend are the 1st, 2nd and 3rd pulse)

Figure 140. A) Spectral region 7850 - Ω$_0$ and corresponding B) Profile analysis. (1,2,3 in legend are the 1st, 2nd and 3rd pulse)
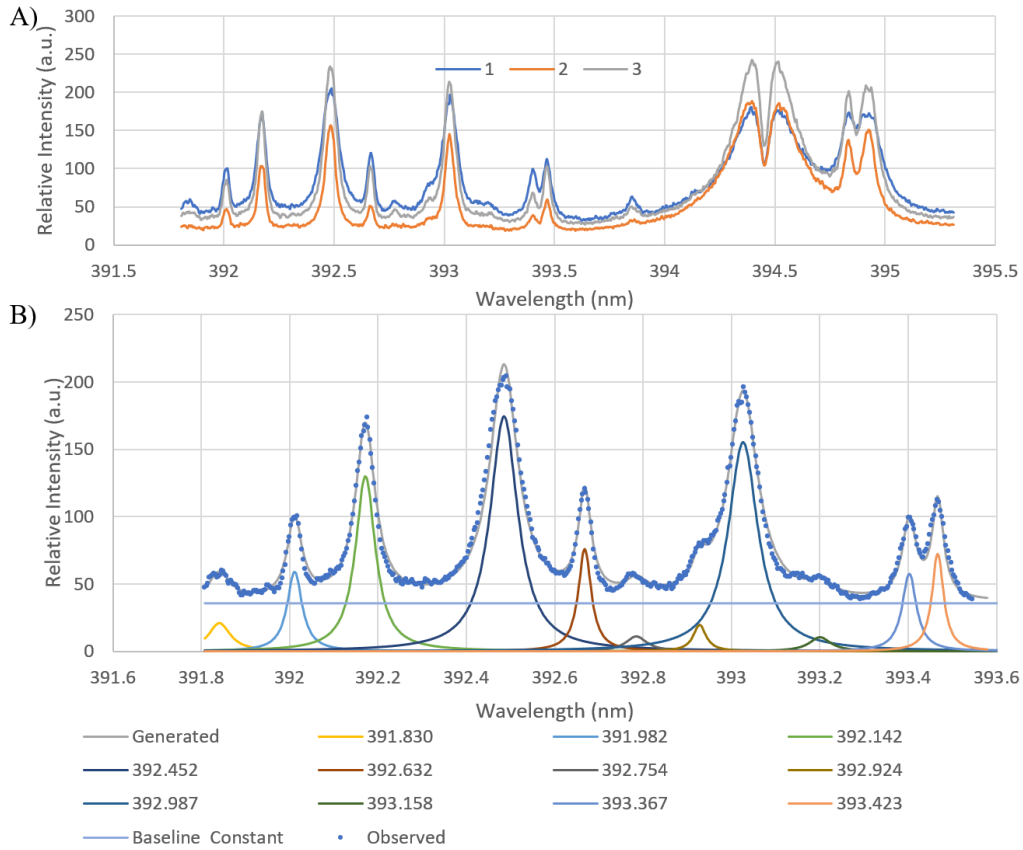
Figure 141. A) Spectral region 7850 - $\Omega_{+0.2}$ and corresponding B) Profile analysis. (1,2,3 in legend are the 1st, 2nd and 3rd pulse)
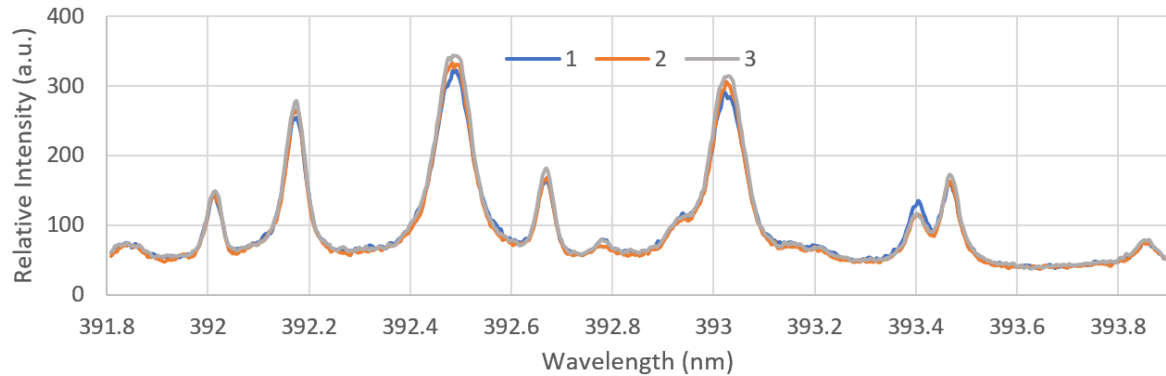
Figure 142. Spectral region 7850 - $\Omega_{+0.3}$. (1,2,3 in legend are the 1st, 2nd and 3rd pulse)

In order to study the evolution of the titanium line intensities (since aluminum is auto-absorbed), fitting of the line profiles located in the left part of the spectra (Figure 139-Figure 141 b) was done.

Figure 143 illustrates the evolution of the titanium line intensities. An increase in the intensity of these titanium lines on all five transitions could be observed. This was found to be in correlation with the population of their upper energy levels ($E_s, g_s. A_s$). The lines at 392.14, 392.45, and 392.98 nm correspond to energy levels around 25500 cm^{-1}, while the lines at 391.98 and 392.63 nm involve higher energy levels of 37622 and 46257 cm^{-1}. Consequently, Boltzmann plots (Figure 144) were generated to estimate the atomic temperature. Similar to the previous study, the temperature estimated was close to 6600 K. Although it appears that the intensity is maximum for the beam centered on the joint line, the precision of the estimation

does not allow for a definitive conclusion, hence the need for the previous study (section 4.5.4.1, p.182) involving more energy levels in the Boltzmann fitting.

An increase in the continuous background level (Figure 145) was observed when the beam was offset from aluminum to titanium. When the shift predominantly occurred on one of the two materials while the continuous background remained relatively stable regardless of the number of pulses. In this case, both the materials melt, while one is predominant, the other element is present in trace amounts. However, in the cases of Ω_0 and $\Omega_{+0.2}$, fluctuations were observed. The dynamics of melting, flow, and subsequent solidification of each of these melted materials appear to play a significant role in the interaction of the subsequent laser pulse.
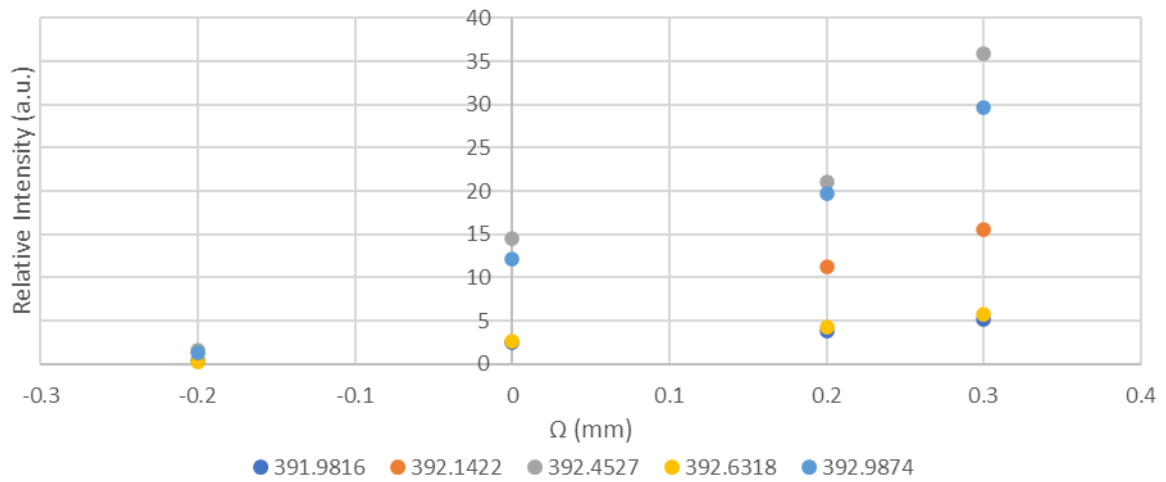
Figure 143. Intensity of emission lines in 7850 spectral region from one laser pulse with respect to Ω.
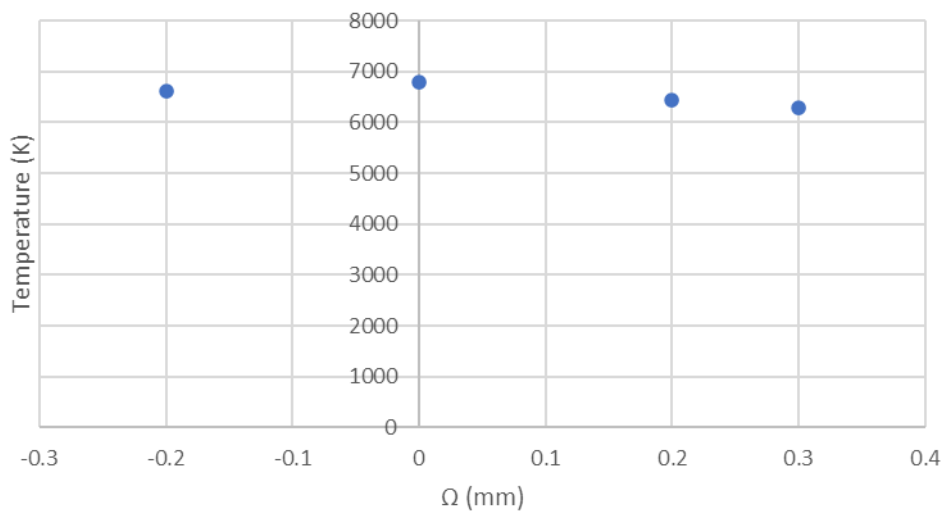
Figure 144. Temperatures in the 7850 spectral region with respect to Ω.
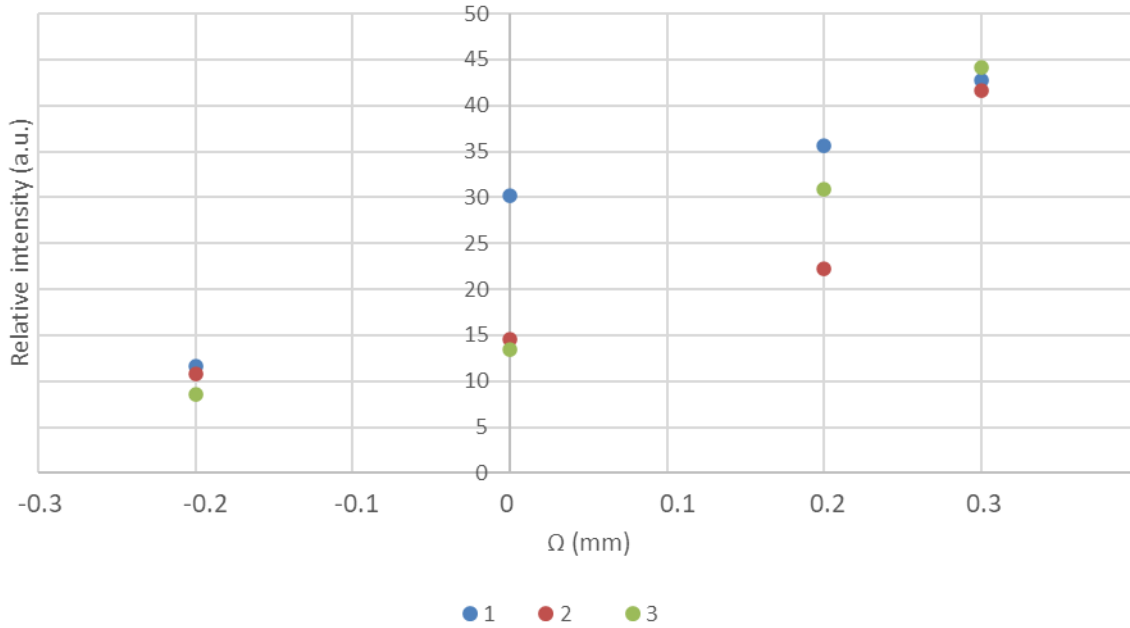
Figure 145. Evolution of continuous thermal radiation with respect to Ω. (1,2,3 in legend are the 1st, 2nd and 3rd pulse)

4.5.4.2.2. Spectral region 7635: Evolution of Ti and Mg emission lines

Region 7635 was characterized by Mg (I) lines present in the aluminum alloy (containing 2.6% Mg) and several Ti (I) lines. The observable lines on these spectra are listed in Table 28.

Table 28. Transitions in the 7635 spectral regions. (Transitions chosen for analysis in bold)

λ_s theoretical (nm)	A_s (s^{-1})	Element	E_i (cm^{-1})	J_i	Conf.	E_s(cm^{-1})	J_s	Conf.
381.3269	**3.17E+07**	**Ti I**	**16817.160**	**1.0**	**(3F)sp z5F**	**43033.937**	**1.0**	**s4F)4d g5F**
381.4861	2.41E+07	Ti I	16875.121	2.0	(3F)sp z5F	43080.961	2.0	s4F)4d g5F
382.6969	2.66E+06	Ti I	11531.759	2.0	(4F)4s b3F	37654.689	2.0	a2D)4p u3F
384.0322	2.22E+07	Ti I	18825.781	1.0	(2P)4s c3P	44857.878	1.0	(4P)4p w3S
384.1621	**3.60E+06**	**Ti I**	**11531.759**	**2.0**	**(4F)4s b3F**	**37555.056**	**3.0**	**(2G)4p v3G**
384.261	8.90E+06	Ti I	17215.389	5.0	(3F)sp z5F	43231.989	4.0	s4F)4d g5F
382.9355	**8.90E+07**	**Mg I**	**21850.405**	**0**	**s3p 3P**	**47957.058**	**1**	**s3d 3D**
383.2299	6.67E+07	Mg I	21870.464	1	s3p 3P	47957.058	1	s3d 3D
383.2304	1.20E+08	Mg I	21870.464	1	s3p 3P	47957.027	2	s3d 3D
383.829	4.45E+06	Mg I	21911.178	2	s3p 3P	47957.058	1	s3d 3D
383.8292	1.59E+08	Mg I	21911.178	2	s3p 3P	47957.045	3	s3d 3D
383.8295	4.00E+07	Mg I	21911.178	2	s3p 3P	47957.027	2	s3d 3D

In Figure 146, Figure 147, Figure 148, the spectra obtained for beam offsets $\Omega_{-0.3}$, Ω_0, and $\Omega_{+0.3}$ are presented. The influence of the number of pulses could also be observed.

- For the beam offset towards aluminum ($\Omega_{-0.3}$), the three magnesium lines from the A5754 alloy were observed. With an increase in the number of pulses, the spectrum remained similar, but the intensities increased slightly.

- When the beam was centered on the joint line (Ω_0), the spectrum obtained after one pulse was a superposition of the titanium and magnesium lines. However, it should be noted that for subsequent pulses, only the magnesium lines were observed, and their intensity decreased with the number of impacts. It could be considered that aluminum localized itself on the surface of the melted zone (aluminum being a lighter element), thus reducing the efficiency of the interaction due to aluminum's specific properties.

- In the case of the beam offset towards titanium ($\Omega_{+0.3}$), the spectra were generally similar (with slight differences related to a less intense continuous background in the case of 2 pulses). The magnesium peaks were less intense than in the case of Ω_0, which was normal since there was less aluminum alloy. However, even if the beam was localized on titanium, the presence of aluminum alloy elements could be observed.
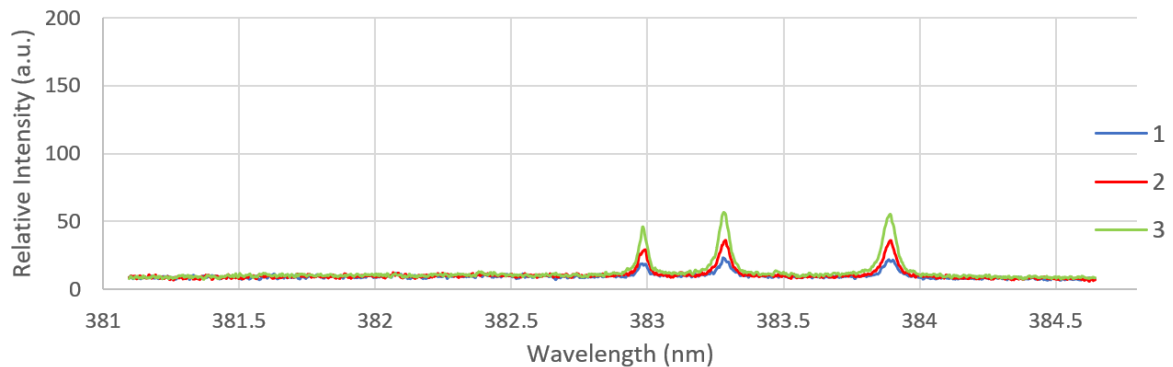
Figure 146. Spectral region 7636 - $\Omega_{-0.3}$ for 3 laser pulses. (1,2,3 in legend are the 1st, 2nd and 3rd pulse)
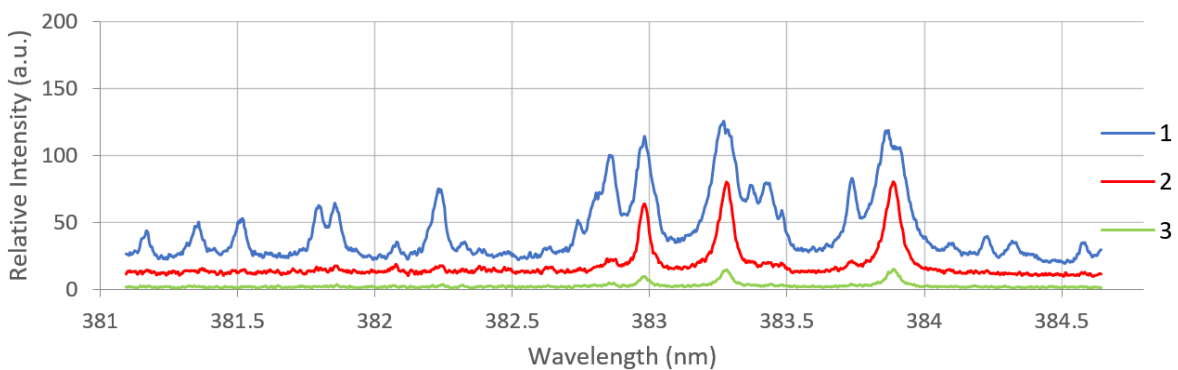
Figure 147. Spectral region 7636 - Ω_0 for 3 laser pulses. (1,2,3 in legend are the 1st, 2nd and 3rd pulse)
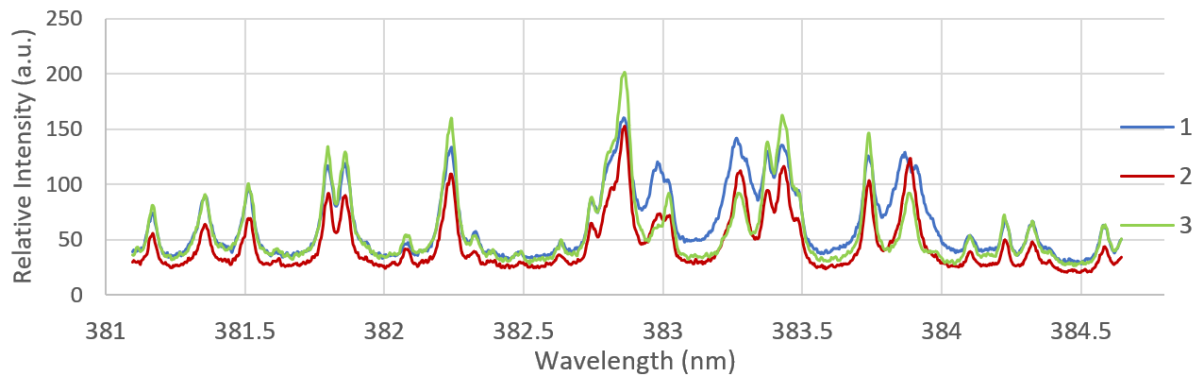
Figure 148. Spectral region 7636 - Ω_{+0.3} for 3 laser pulses. (1,2,3 in legend are the 1st, 2nd and 3rd pulse)

From the fitting of the line profiles, the intensity evolution for the lines marked in bold in Table 28 was investigated.

- For the titanium lines, the intensity was found to be proportional to the beam offset. Figure 149 presents the 381.3269 nm and 384.1621 nm titanium lines. When the beam was offset towards the titanium, the intensities were high and tended to reach a limit.

- For the magnesium lines, there were three peaks, but only the 382.9355 nm peak was an isolated line (Figure 149). The maximum magnesium intensity was observed for an impact centered on the joint line. When the beam was offset towards A5754, the interaction of the laser beam with aluminum became less efficient. As a result, the titanium present in the interaction zone absorbs the laser beam's energy and then transfers energy to the aluminum, causing it to melt and vaporize (as mentioned in section 4.4.6, p.154). When the beam was offset towards T40, there is less aluminum alloy present, leading to a decrease in the intensity of the magnesium lines.

Figure 149 also illustrates the evolution of the continuous thermal background. It exhibits a behavior similar to that of titanium. The laser-matter interaction was directly proportional to the area of titanium exposed to laser radiation, resulting in a greater quantity of vaporized material present in the plume.
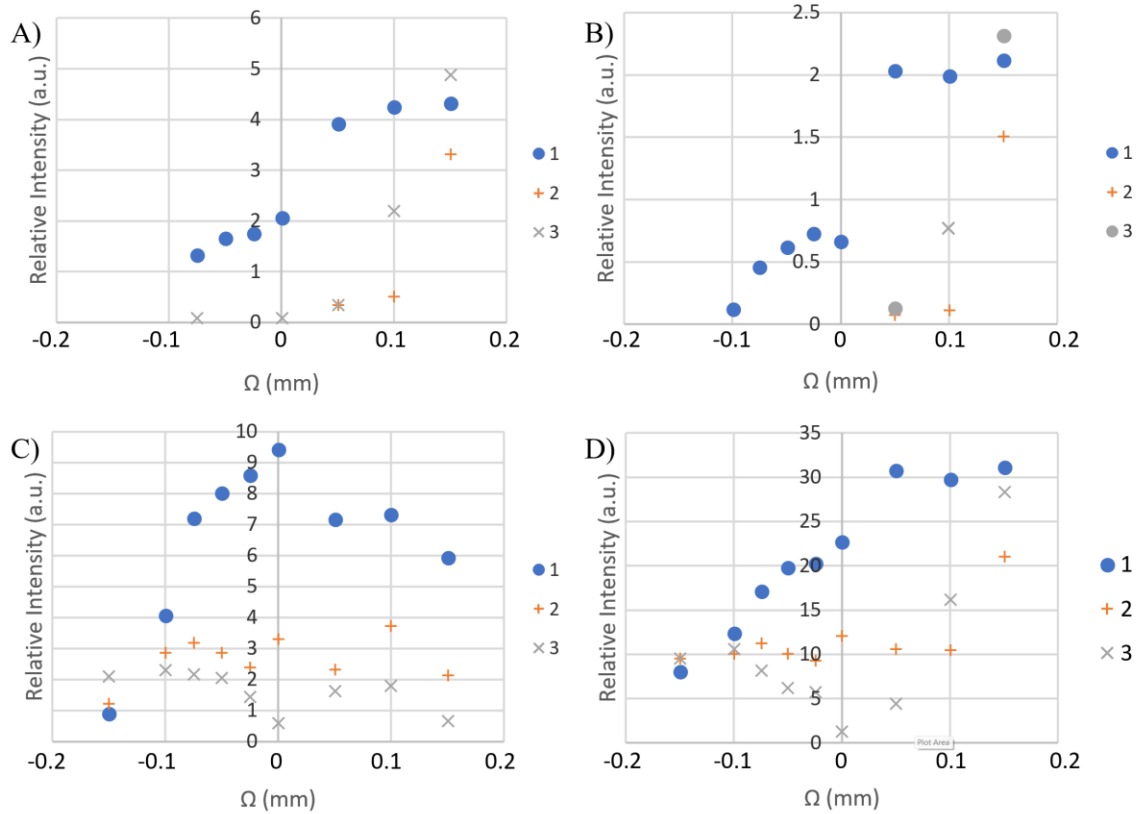
Figure 149. Relative intensities of 3 pulses in the spectral region 7636 of A) Ti (I) 381.327 nm, B) Ti (I) 384.261 nm, C) Mg (I) 382.935 nm and D) continuous thermal emissions with respect to Ω. (1,2,3 in legend are the 1st, 2nd and 3rd pulse)

4.5.4.2.3.   Spectral region 10330: Molecular bands and Mg emission lines

As previously mentioned in section 4.5.2.3 (p.160), (Figure 125. B, p.161), the 10330 region is characterized by three isolated magnesium lines. The characteristics of these lines are summarized in Table 29.

The influence of beam offsets was studied in this spectral region. The acquired spectra are presented in Figure 150. To avoid line saturation, two different gains (G=5 or G=20) were employed while setting parameters of the ICCD detector of the spectrometer. However, saturation of the lines was still observed for $\Omega_{+0.3}$.

Table 29. Molecular bands and Mg transition in 10330 region.

	λ_s theoretical (nm)	A_s (s^{-1})	E_i (cm^{-1})	J_i	Conf.	E_s(cm^{-1})	J_s	Conf.
Mg	516.7321	7.77e+06	21850.405	0	s3p 3P	41197.403	1	s4s 3S
Mg	517.2684	3.29e+07	21870.464	1	s3p 3P	41197.403	1	s4s 3S
Ti	517.3743	3.79e+06	0.000	2	s2 a3F	19322.984	2	(3F)sp z3F
Mg	518.3604	5.46e+07	21911.178	2	s3p 3P	41197.403	1	s4s 3S

For $\Omega_{-0.3}$, three magnesium peaks were observed. However, there was a significant amount of "noise." As the beam was offset towards titanium, the presence of a molecular band was noted. This band corresponded to the molecular spectrum of TiO. Specifically, observe the vibrational bands C$^3\Delta_r$ – X$^3\Delta_r$ with band heads at 516.4 nm and 518.4 nm could be observed.

A titanium line at 517.37 nm was observed, close to the magnesium line at 517.27 nm. This line was not observed at $\Omega_{-0.3}$, and its intensity increased with beam offset towards titanium. However, the molecular bands intensified with beam offsets towards titanium (the rotational bands' intensity increased).

The evolution of the spectra with the number of pulses are presented in Figure 151. Once again, when the laser beam was predominantly on one of the two materials, the spectra were similar. However, when the beam offset was smaller (Ω_0 or $\Omega_{-0.1}$), the impact of the first laser pulse produced a very intense spectrum with a much more significant molecular component.

The presence of these bands complicated the analysis of atomic line profiles. Nevertheless, to evaluate line intensities, it was possible to fit with a decreasing linear background, taking into account the rotational fluctuations on the corresponding band.

Figure 152 displays the evolution of the magnesium's atomic line intensities with beam offsets. In a similar trend, the study of the 7626 band, the magnesium intensity increases as the laser spot approaches the joint line.
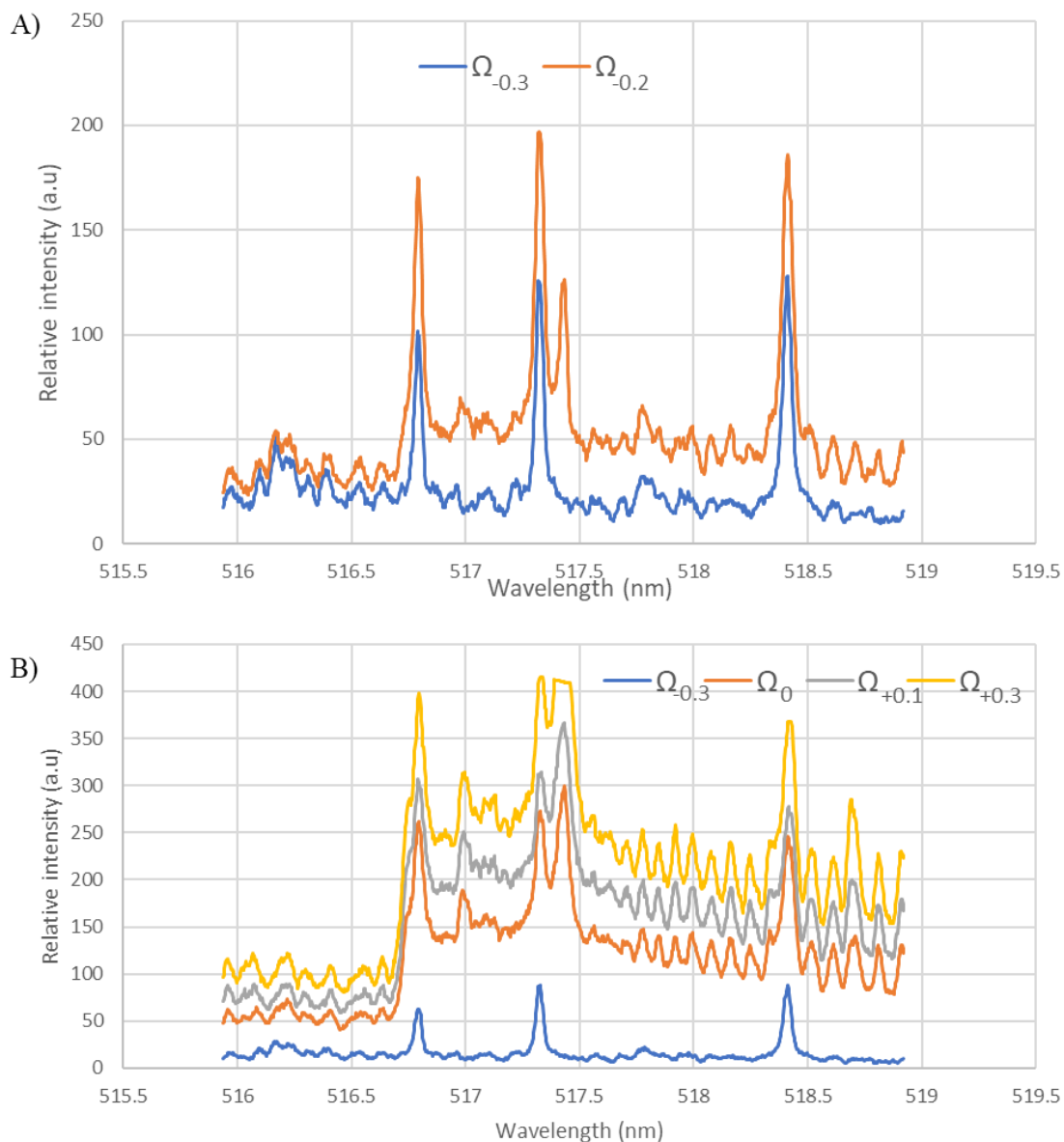
Figure 150. Influence of Ω on emission in spectral region 10330 A) Gain: 20, B) Gain: 5.

Figure 151. Influence of the number of pulses in 10330 spectral region for A) Ω-0.3, Gain: 5 B) Ω0, Gain: 5, C) Ω-0.1, Gain:20, and D) Ω+0.2, Gain: 5. (1,2,3 in legend are the 1st, 2nd and 3rd pulse)

Figure 152. Influence of Ω on Mg (I) lines : A) 516.732 nm, B) 517.268 nm, and C) 518.360 nm. (1,2,3 in legend are the 1st, 2nd and 3rd pulse)

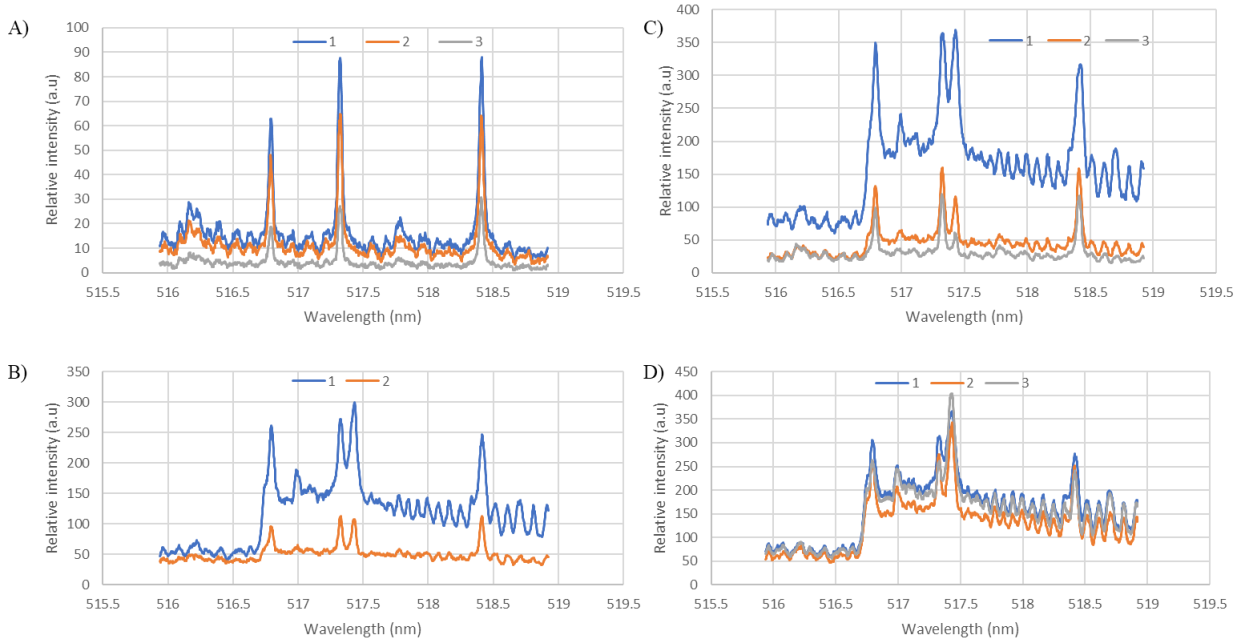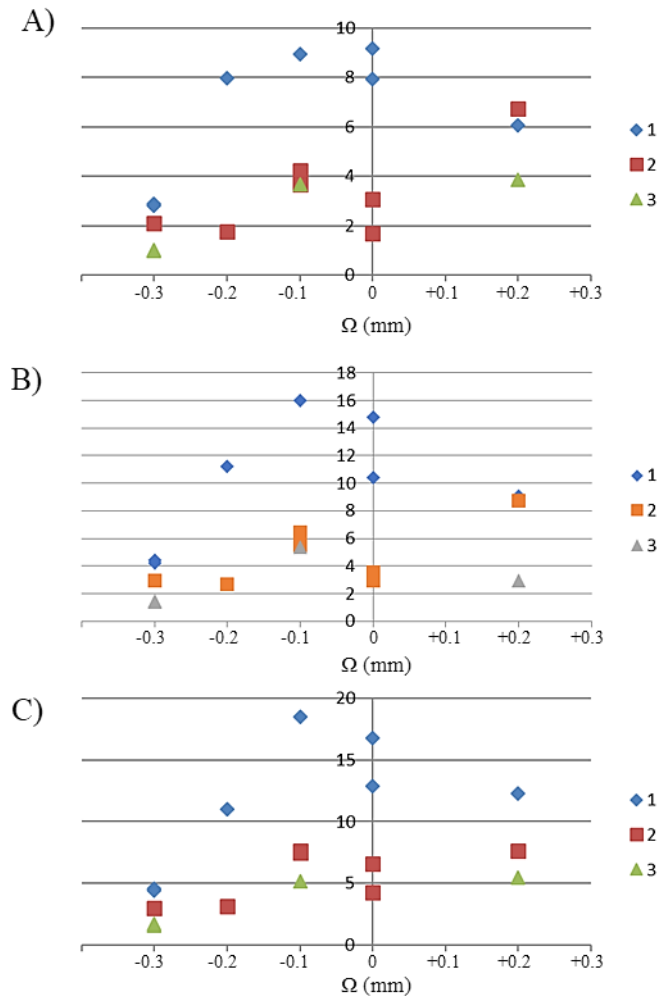Spectrometric analysis was conducted across three distinct spectral regions to discern the presence of titanium and magnesium when pulse welding T40/A5754 alloys. In addition, this examination aimed to investigate the impact of laser beam displacement relative to the joint line on the spectral emissions.

As observed in the preceding study involving standalone materials, the spectra from dissimilar welding exhibited superposition of two components: a continuous spectrum emanating from thermal processes and an atomic emission spectrum. This phenomenon could be elucidated as the coexistence of a dense vapor core emitting thermal radiation and peripheral atoms whose density diminishes as they expand thermally into the surrounding atmosphere, thus generating an atomic emission spectrum. Notably, temperature estimates remained relatively consistent during the examination of beam offsets relative to the joint line. However, this behavior of temperature relies on the presence of titanium within the interaction zone, as titanium predominantly absorbs the incident laser beam. Consequently, alterations in line intensities across the diverse spectra did not signify variations in temperature but rather indicate fluctuations in the quantity of ablated material.

When the laser spot was displaced from aluminum to titanium, a notable increase in the intensities of the fundamental titanium lines was evident. This observation served as proof of the presence of titanium within the molten pool, with line intensities amplifying and the appearance of new titanium lines proportional to the amount of laser incident on T40.

Conversely, the study of magnesium lines within the aluminum alloy revealed a distinct behavior. Notably, the intensity of magnesium lines reached maximum intensity when the laser was centered on the joint line. These magnesium lines were present for all laser spot positions on T40, thereby corroborating the presence of aluminum alloy constituents. In instances of laser beam displacement towards aluminum, the laser-matter interaction with aluminum was found to be inefficient, prompting titanium within the interaction zone to absorb the laser's energy. Subsequently, this energy transfer facilitated the melting and vaporization of aluminum, a conclusion in correlation with HSI observations. However, this dynamic had its limitations, primarily stemming from the diminishing presence of aluminum alloy as titanium predominates, consequently leading to a reduction in the intensity of magnesium lines.

The analysis of the continuous thermal background, corresponding to the thermal radiation emanating from the core of the plume, revealed a notable enhancement in material interaction as the quantity of titanium within the interaction zone increased. This phenomenon was in correlation with an increase in the quantity of vaporized material present in the plume as the laser beam was displaced towards titanium.

In the 10330 region, the presence of the TiO molecular band ($C^3\Delta_r - X^3\Delta_r$) was observed. This molecular band's effect became more pronounced as the beam was offset towards titanium. This observation suggested that the TiO molecule is generated within the plume as a result of the ablation of aluminum atoms and subsequent recombination during the cooling phase.

Furthermore, the influence of overlapping laser impacts was examined. During the first pulse, the surface which consisted of the two materials namely aluminum and titanium was impacted. Subsequent to this initial impact, ensued a process of melting and mixing of the molten materials. The subsequent laser impacts were directed onto a surface that had already undergone mixing, a surface comprising a mixture of materials, each possessing distinct properties, such as reflectivity and thermophysical characteristics. As a consequence, the characteristics of the material at the point of interaction during the successive laser pulses were influenced by the mixing process after the first impact. It was also noted that when the laser

beam predominantly interacted with one of the two materials (maximum beam offsets), this led to the generation of reproducible spectra.

For laser beam displacements corresponding to intermediate positions (ranging from $\Omega_{-0.2}$ to $\Omega_{+0.2}$), commencing with the second laser impact, a significant reduction in the continuous thermal emission and a decrease in the intensity of titanium lines were observed. This occurrence was attributed to the compositional changes within the material resulting from the mixing process and the melting initiated by the initial laser pulse. It could be postulated that aluminum, due to its lower density compared to titanium, migrated towards the surface during the cooling phase. Consequently, in subsequent laser pulses, where aluminum was predominantly located on the surface, the absorption of the laser beam was less efficient.

In conclusion, the dissimilar vapor plume emits two types of emissions: the continuous thermal emissions are primarily from the Al vapor cloud because the estimated macroscopic temperature ~3100 K is lower than the vaporization temperature of the titanium and, the atomic emissions from the excited Al and Ti atoms with a slightly lower atomic temperature calculated for the Ti atoms ~7000 K than the atomic temperature from the welding of standalone titanium. However, this supposition that the continuous thermal emission is mainly from the Al vapor cloud which contains a small quantity of excited Ti atoms, and whether the Al vapor cloud promoted rapid condensation of titanium, could be confirmed by making spectral acquisitions from different parts of plume at various heights.

In summary, the spectral analysis of successive laser pulses provided insights into the fluctuation of composition within the melted zone. These fluctuations were attributed to the dynamic processes of melting, flow, and subsequent solidification of the molten materials. As a result, it is understood that future studies would endeavor to model the distinct flow patterns of the two molten materials and elucidate the intricacies of their mixing within the interaction zone after analyzing the composition of the melted zone after the first pulse.

4.6. Conclusions on vapor plume behavior and melted zone characteristics in pulsed dissimilar welding in butt-configuration

Pulsed welding done on the dissimilar materials of A5754 and T40 yielded several results depending on the parameters utilized. In the preliminary study of the vapor plume, 2 ms pulses with the 810 nm for HSI yielded the following results:

- Aluminum had a threshold for plume initiation where low laser powers did not form any plume, while high laser powers formed a dull and diffuse plume. The minimum required power to form a small spherical plume was at least 2 kW on aluminum for 2 ms pulses. Such a plume was dull and required time to initiate.
- However, titanium plume was initiated for powers as low as 400 W with a bright and rapid jet.
- The inclination of the dissimilar vapor plume happened even at the millisecond scale. And the several stages of plume development based on the plume inclination were noted to also depend on the laser spot position relative to the joint line.
- The melted zones examined in the top-view with SEM-EDS analysis, corresponded to the hypotheses made about the different cases of the dissimilar vapor plume.

However, when the vapor plume was examined with two different optical filters 810 nm and 394 nm, the explanation of the vapor plume needed to be further extended. With an in-depth analysis, the following observations were made:

- The 810 nm plume and the 394 nm plume did not always correspond when the different laser spot positions were tested.
- The thermal emissions of the vapor plume at 810 nm always had a larger envelope than the atomic emissions at 394 nm. It appeared as if the atomic emissions were from the central part of the vapor plume while the thermal emissions were from the outer parts of the plume which was mixed with air due to turbulences.
- The inclination of the 810 nm plume was more dependent on the laser spot position (directly proportional to the displacement towards the A5754 side), in agreement with the preliminary studies. However, the inclinations of the 394 nm plume were more dependent on the strength of the inclined Ti jets. Strong inclined Ti-jets were present for the laser spot centered on the joint line (Ω_0), compared to other beam offsets ($\Omega_{-0.2}$: insufficient Ti vaporization, $\Omega_{+0.2}$: Ti jets were vertical as the keyhole was in T40).
- The atomic concentration measurements on the A5754 side of the melted zone in top-view indicated Al participation in the melting and vaporization for all beam offsets. However, the Ti at.% correlated to the Ti-jets hypothesis about the vapor plume with maximum Ti at.% for $\Omega_{+0.2}$ (49%) and minimum Ti at.% for $\Omega_{-0.2}$ (9%).

From the lateral observations of the keyhole and melted zones with HSI (810 nm) and the examination of the plume deposits on the quartz, the following conclusions were made:

- Maximum penetration depths and maximum penetration rates were observed for the dissimilar keyhole with the beam centered on the joint line.
- A synergy between the two materials existed: titanium which absorbed the laser radiation better, promoted the melting and vaporization of aluminum. And this effect corresponded to the previous plume studies where the inclined Ti was hypothesized to be maximum for Ω_0.
- The analysis of the plume deposits on the quartz indicated the mixing between vaporized Al, Ti and Mg occurred for all beam positions and the vaporization of Mg was particularly favored due to contact with hot Ti liquid and vapor.

An in-depth spectrometric analysis of the vapor plume was done for the standalone and dissimilar materials separately. From the analysis conducted from observations made in several spectral regions, the atomic temperatures and the continuous thermal emissions were studied to make the following conclusions:

- The temperatures calculated from the continuous thermal emissions using Planck law of blackbody radiation were close to the vaporization temperatures of the materials (standalone A5754: unreliable estimation due to lack of points, T40: 3560 K, Dissimilar combination: 3125 K).
- The atomic temperatures were much higher than the macroscopic temperature when titanium was involved (standalone A5754: ~2700 K still close to vaporization temperature, standalone T40: 7069 K, Dissimilar combination: 6500~7000 K).
- The increase in intensities of emissions was found to be proportional to the laser power or duration. The increasing intensities without the associated rise in temperature indicated greater quantity of material vaporized.
- Presence of Al, Mg and Ti lines for all laser spot positions were concurrent with the previous observations made from HSI and post-mortem observations of the keyhole and melted zones.
- From the presence of self-absorbed lines, it was hypothesized that the inner core of the plume was much hotter and denser than the outer periphery where atomic emissions are self-absorbed.

All these results from the different experiments for pulsed welding in butt-configuration could be simplified in the following manner (Figure 153).
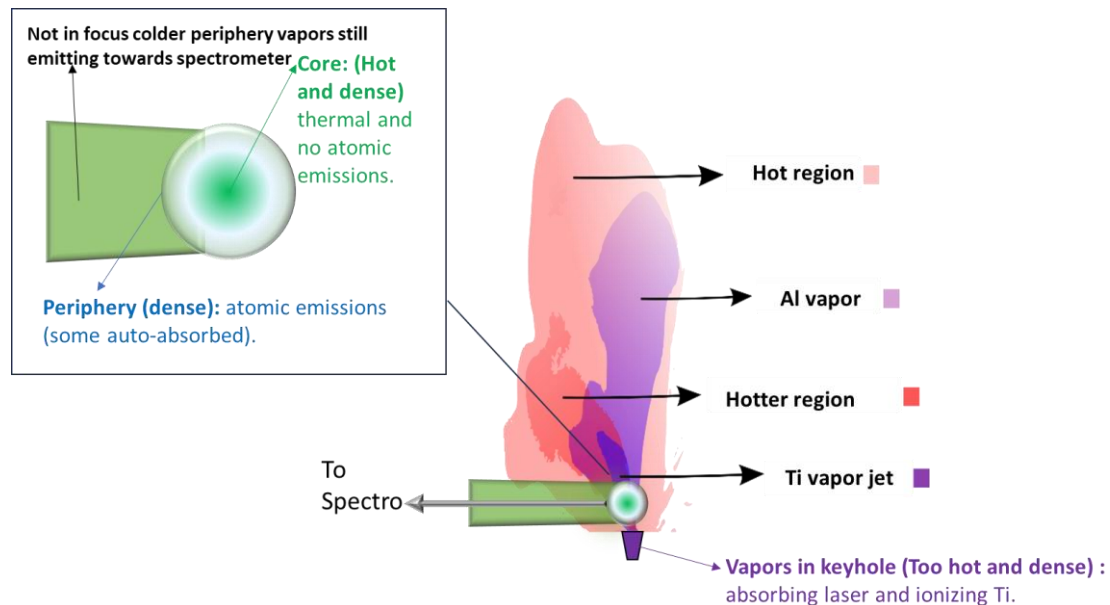
Figure 153. Explaining the vapor plume with HSI and spectrometry combined.

While it is true that the 810 nm plume represents all the hot regions (vaporized metal and heated air) and the 394 nm plume at the center represents the regions of the plume (only vaporized metal with sufficient energy for atomic excitation), spectrometry is rather done over a much smaller region and does not follow the same explanation. While the hottest regions of the vapor plume lie in the path of the Ti-jet directly above the keyhole, there are still temperature gradients within this region. The inner core is hotter and denser than the periphery. However, the vapors in the keyhole are hypothesized to be much hotter and denser (to absorb laser radiation as either a blackbody or inverse Bremsstrahlung) than what has been observed in the vapor plume. However, further research is needed to confirm this hypothesis.

Chapter 5. Dissimilar pulsed welding in overlap configuration

5.1. Introduction

Following all the previous work done to study the vapor plume and the keyhole behavior in continuous and pulsed welding in the butt-configuration (Chapter 2, Chapter 3, Chapter 4), it was deemed necessary to study the overlap welding of the T40-A5754 combination to provide a complete overview of dissimilar welding. While the in-situ (HSI and spectroscopy) and post-mortem (SEM-EDX) techniques remained the same, the experimental setup, equipment and parameters were different (Table 30). Knowing that the amount of information that could be gathered from using millisecond pulses, the overlap welding experiments were only done with laser pulses (i.e., continuous welding was not studied in the overlap configuration). A schematic for the experimental configuration and the dimensions of the melted zone studied post-mortem are given in Figure 154.
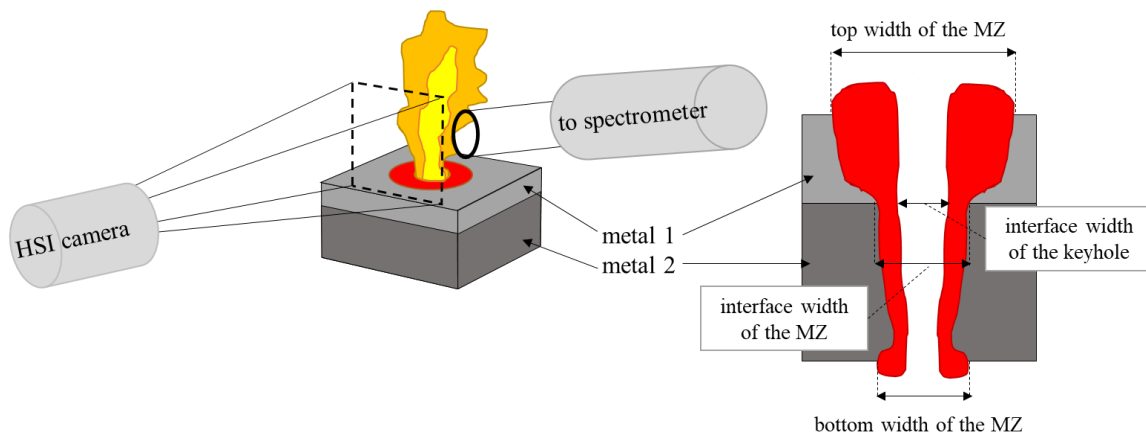
Figure 154. Experimental configuration and controlled dimensions of the melted zones (MZ).

The top and bottom melted zones (at the top and bottom surfaces of the top and bottom plates respectively) and the melted zones at the interface between the two plates were examined by an optical microscope. For every pulse time, the widths of these melted zones were measured to understand the pulse times necessary for the drilling of the top and the bottom plates. It was noted that the melted zones' widths at the interface was equal on both the top plate and the bottom plate, which confirmed efficient clamping of the two plates.

Table 30. Materials and parameters in overlap welding experiments.

Equipment		
Materials	A5754 aluminum alloy T40 commercially pure titanium	Thickness: 1mm A5754 on 2 mm T40 1mm T40 on 2 mm A5754
TRUMPF TRUDISK 6001 Yb:YAG laser (λ = 1030 nm)	Spot diameter	600 μm
	Laser Power	2 kW – T40 on top 4.5 kW – A5754 on top
	Pulse duration	1, 2, 3, …, 14, 15 ms
Phantom V2012	Frame rate	67000 fps
	Resolution	512×512 pixels
	Exposure time	4 μs for A5754 on T40 0.6 μs for T40 on A5754
Nikon AF Micro-Nikkor 200mm f/4D	Aperture index	16
	Working distance	48 cm
	Optical filters	810 ± 3 nm 394 ± 3 nm
Czerny-McPherson type monochromator (model 209)	Focal length	1.33 m
	Acquisition optics	Collimating lens: 40 cm Focusing lens: 10 cm Optical Fiber: 230 μm diameter
	Observation zone diameter	~ 0.9 mm
	Observation zone position	1 mm above keyhole opening
	Grating	2400 lines/mm
	Spectral resolution	0.005 nm
	Integration time	1 s
ICCD Princeton PIMAX-1K-RB camera	Camera Resolution	1024×1024 pixels
	Pixel size	13×13 μm
	Spectral range	195 – 920 nm
	Width of spectral region	3 ~ 4 nm
	Studied spectral regions	381.3 nm – 384.3 nm 394.4 nm – 396.4 nm 463.9 nm – 466.9 nm

5.2. Results from post-mortem observations

In 1 mm A5754 on 2 mm T40 overlap combination, the top A5754 plate was fully pierced by a keyhole in 3-4 ms, while the piercing of the bottom side of T40 plate was reached at 7-8 ms pulse time (Figure 155). This 1 ms uncertainty in the piercing times could be explained by local micro-variations of a gap existing between the plates. The top width of the melted zone increased with the pulse time. However, the growth was not linear probably due to the random ejection of melted material. The diameters of the melted zones, observed after separating the plates, showed linear growth up to the pulse time of 11 ms, followed by stagnation. The bottom width of the melted zone increased up to 13 ms and then stabilized. In some cases, the solidified keyhole was visible after the separation of the plates. During the drilling of the bottom T40 plate, initially the keyhole diameter at the interface approached the value of laser spot diameter (0.6 mm), but it doubled in size when the keyhole reached the bottom surface of the bottom plate (t > 10 ms). Based on these observations, it could be concluded that by the end of the pulse the melted zone reaches a stationary condition, as the excess of energy is lost through the bottom opening of the keyhole.

Figure 155. Measurements of melted zone and solidified keyhole in 1 mm A5754 on 2 mm T40 overlap combination.

The EDS analysis of the melted zones visible at the top surface of A5754 plate indicated the systematic presence of significant amounts of Ti (Figure 156.A) from the pulse time of 4 ms (the time when the keyhole reaches the interface). While the melted zones have rather homogenous distribution of Ti for the 4 ms pulses, they begin to form local inhomogeneities from the ejection of ascending titanium droplets due to convection starting from 5 ms pulses. Finally, bulk ejection of liquid titanium occurs for pulse times > 7 ms. However, the average amount of Ti on the surface of the melted zone did not exceed 20 at.%. The rings of Mg-rich zones observed at the periphery of the melted zones were due to the preferential vaporization of this element from A5754 alloy and its deposition on and around the melted zone in the form of MgO.

The melted zones on the bottom side of T40 plate for pulse times > 7 ms showed a presence of low quantities of the elements from the upper plate (Figure 156.B), which signified the absence of mixing of the materials in the bottom part of the melted zone. The concave and round melted zones surrounded by thin Mg-rich ring were progressively replaced by more irregular shapes with ejection of multiple spatters and bulk liquid, where low amounts of Al ang Mg (~ 1 at. %) were present in the melt and its surroundings. Deposits of Al also occur around the Ti-rich spatters. Considering the vaporization temperatures of the elements (Mg: 1363 K, Al: 2743 K, Ti: 3560 K), Al and Mg evaporate from the liquid titanium and then form the deposits of oxides that cover the melted zone and the neighboring base material T40. Despite the complete drilling of the two plates, low amounts of Al and Mg on the bottom and comparatively high amounts of Ti on the top of the melted zone (Figure 156.A) allow supposing that the mixing processes between the materials primarily occur in the upper part of the melted zone.
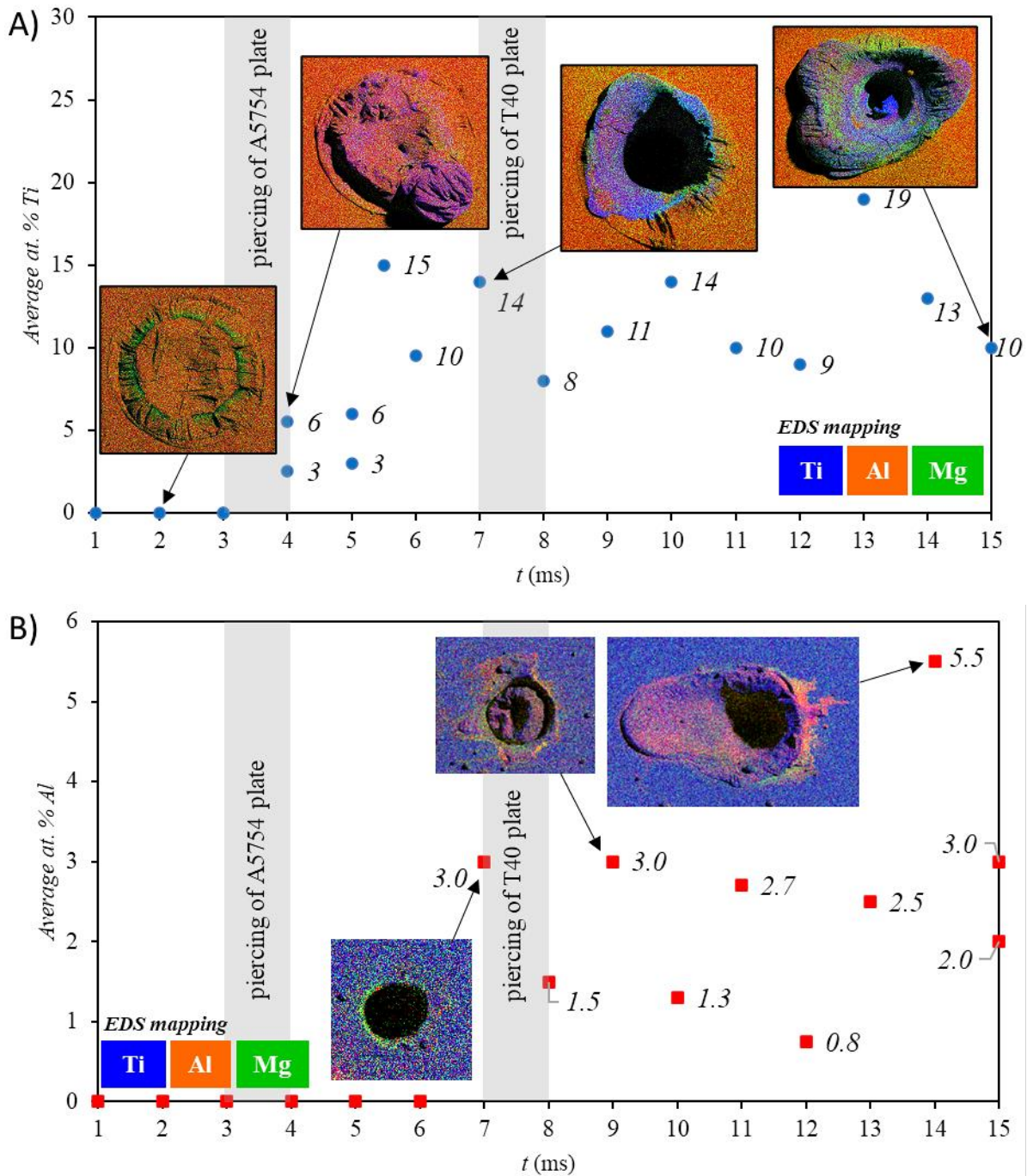
Figure 156. EDS measurements of average concentrations and EDS mappings of A) the top melted zone surfaces and on B) the bottom melted zone surfaces in 1 mm A5754 / 2 mm T40 combination.

In 1 mm T40 on 2 mm A5754 overlap combination (Figure 157), the drilling of the top plate could be done with a pulse time of 5 ms. Unlike the previous case, the piercing time did not fluctuate, possibly due to an easier initiation of the melted zone in A5754 due to contact with liquid titanium having a much higher fusion temperature. The bottom side of A5754 plate was never pierced, which could be explained by lower laser power used for 1 mm T40 on 2 mm A5754 dissimilar combination (2 kW), and the difficulty of drilling A5754 at such laser powers.

The top width of the melted zone showed dispersion after the involvement of bottom A5754 plate in the melted zone (pulse time > 4 ms). The widths of melted zones at the joint interface increased until stabilization at 12 ms. For t<10 ms, these values were close to the diameters of

solidified keyhole, representing a low thickness of the local melted layer. For t>10 ms, the diameters of the solidified keyhole rarely exceeded the size of laser spot, while the interfacial widths of the melted zones were growing along with progressive development of the melted zone in A5754 till stabilization at 12 ms. Thus, it could be concluded that the melted zone also reached a stationary condition before reaching the bottom surface of the A5754 plate.
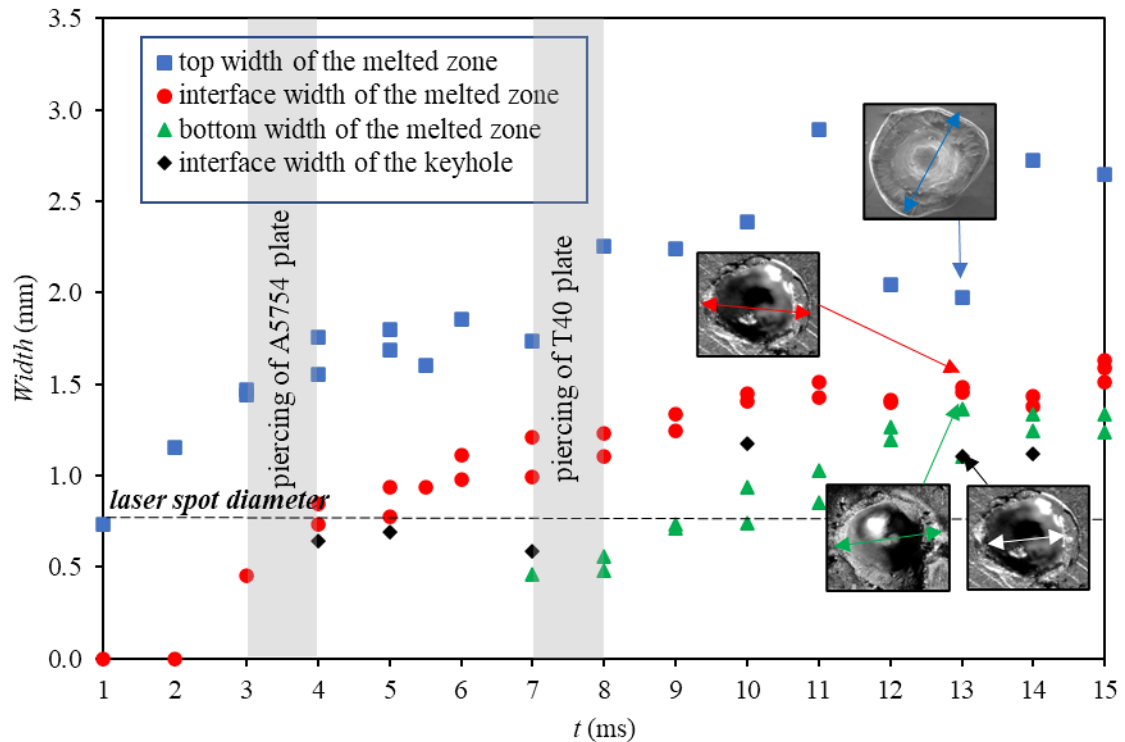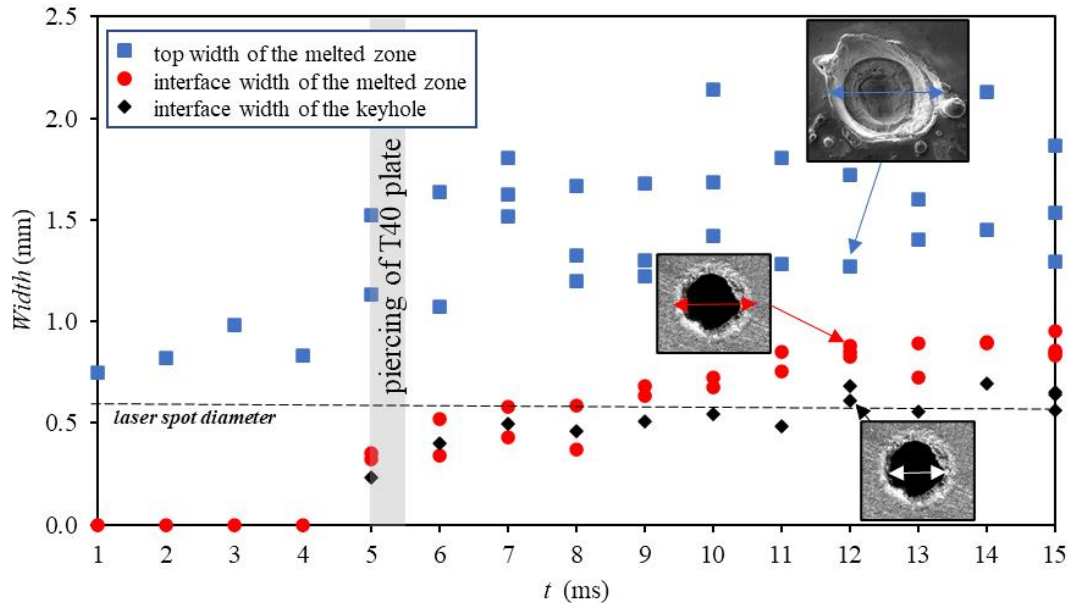

Figure 157. Measurements of melted zone and solidified keyhole in 1 mm T40 on 2 mm A5754 overlap combination.

The EDS analysis of the melted zones visible on the top surface (Figure 158) showed that while the T40 plate on top was drilled in 5 ms, the elements from A5754 alloy appeared on the top of the melted zone only several ms later. Mg (forming rings of MgO) was the first element to leave the keyhole since it has lower vaporization temperature (1363 K) compared to Al (2743 K) which started to appear at the top surface after 7 ms. At pulse time of 8 ms, the first traces of Al appear on the top part of the melted zone and in the surroundings accompanied with oxides deposited as aggregates formed from Al-rich vapor. Finally, only at ~12 ms a bulk ejection of Al-rich liquid from the keyhole takes place.
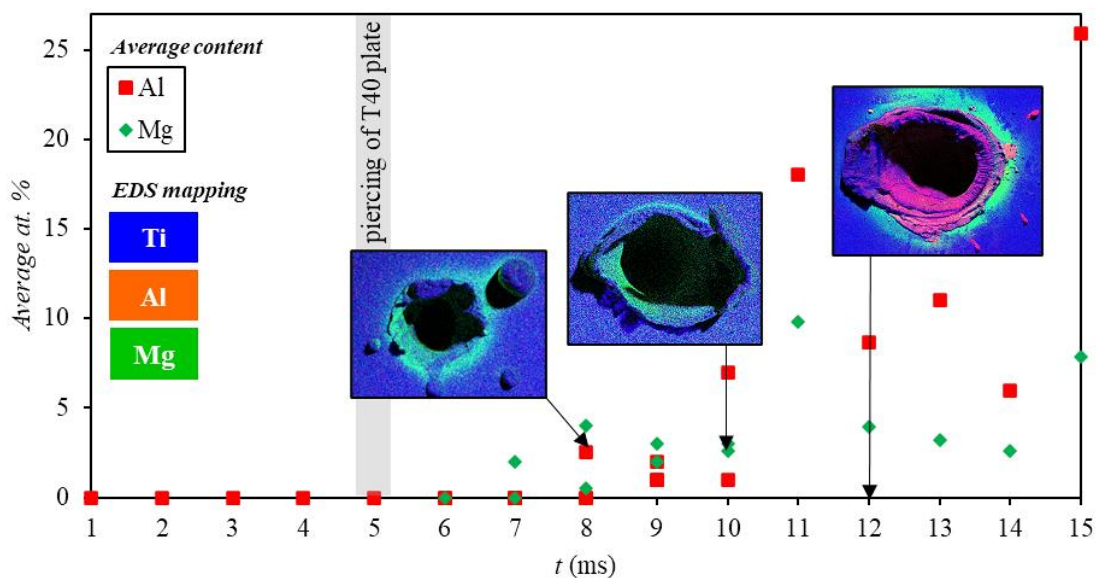
Figure 158. EDS measurements of Al and Mg at. % and EDS mappings of melted zone on top surface of T40 plate in 1mm T40 on 2 mm A5754 overlap configuration.

In conclusion, differences in melted zone and keyhole dynamics alone with transfer of metals during the mixing processes were observed between welding A5754 on T40, and T40 on A5754 overlap combinations. 4.5 kW was necessary for keyhole initiation with the A5754 on top. However, the complete drilling of both the plates combined could be achieved within 7-8 ms. The mixing between the materials was more intense in the top part of the melted zone, as melted titanium ascended the keyhole walls due to convection, while only weak quantities of Al and Mg were found at the bottom surface of the melted zone. For this overlap configuration, the transport of elements that can take place in the liquid phase and vapor phase (with formation of oxide deposits) was quick, i.e., as soon as the A5754 plate was pierced, Ti started appearing in the melted zone in the top surface. Similarly, Al and Mg traces were always found at the bottom part of the melted zone in the bottom plate. Comparatively, the T40 on A5754 configuration did not allow complete drilling for 2 kW laser power, accompanied with slow transport of Al and Mg to the top surface when the keyhole reached the interface between the plates.

5.3. HSI results in overlap welding

The plume characteristics (height, width, inclination, etc.) measured with HSI in the previous chapters (Chapter 3, Chapter 4) were uninformative for overlap welding. Consequently, the image processing methodology utilized to treat the dissimilar plumes in butt-configuration was abandoned and a rather simpler approach was taken. Therefore, the average plume brightness for the different optical filters (810 nm – thermal emissions, 394 nm – atomic emissions) were measured for each image (Figure 159).

Figure 159. Temporal evolution of the average grey values of the plume images of 1mm A5754 on 2 mm T40 in overlap configuration.

For the 1 mm A5754 on 2 mm T40 combination (Figure 159), the plume initiation during the first 1.5 ms corresponded to the elimination of surface oxides followed by keyhole initiation in the top A5754 plate. During the plume initiation, the 810 nm plume (Figure 160) was found to be more diffuse compared to the 394 nm plume which had well defined edges of a mushroom like shape (Figure 160) accompanied with lower maximum brightness reached by the average grey values (Figure 159) during this stage. With A5754 on top, the low temperature of Al

vapors could explain the dull and diffuse plume observation with the 810 nm filter, while the 394 nm filter allowed the atomic emissions of Al and Mg (in the 394.4 nm – 396.4 nm spectral region). The accumulation of melted aluminum on the keyhole walls rapidly led to a drastic decrease in brightness of the plume (between 1.5 and 2.5 ms, Figure 159) due to the partial keyhole collapse followed by the erratic ejection of the melt due to unstable behavior of the keyhole. However, at 3-4 ms the plume brightness for both 810 and 394 nm filters increased again as the keyhole reached the T40 plate which has higher absorptivity (Figure 160. c, d). Periodic bursts (Figure 159) of the plume appeared after reaching the bottom T40 plate due to competing strong Ti vaporization (Figure 160. c, d) and keyhole collapses from instability (Figure 160. e, f). The time period of these plume bursting was estimated to be 0.67 ± 0.58 ms for the 810 nm plume and 0.68 ± 0.38 ms for the 394 nm plume. These Ti-rich burst were tall plumes with a bright core leaving a dull tail when observing thermal radiation (810 nm). The top part of the plume after mixing with air leads to a decrease in temperature causing a dull tail. However, when observing the atomic emission, short and uniformly dull bursts were noted leading to the supposition that there was insufficient quantity of Al and Ti atoms emitting at the top part of the plume. Complete drilling of the second plate (T40 plate at the bottom) did not alter the plume behavior.

Figure 160. 1 mm A5754 on 2 mm T40 vapor plume A,B) plume initiation, C,D,E,F) Plume bursts. (Dashed line: Impact on surface)

With the 1 mm T40 on 2 mm A5754 configuration, the plume initiation (Figure 161) was much quicker with the better absorbing titanium on top. The initial plume formation was a, tall bright, mushroom like shape with small shockwave-like lateral vortices when observed with the 810 nm filter (Figure 162. a). With the 394 nm filter, only a thin plume without any discernible features was observed (Figure 162. b). After the initiation, the plume became diffuse and unstable (Figure 162. c, d), as liquid metal accumulated along the walls of the keyhole. When studying the average grey values, the observed bursts of plume representing oscillations in the keyhole walls (up to 11 ms) had a periodicity of 0.25 ± 0.10 ms when observed with 810 nm filter and 0.29 ± 0.11 ms when observed with 394 nm filter. The overall brightness of the plume progressively decreased with time (Figure 161), which could be related to the decrease of

vaporization intensity with increasing contribution of A5754, accompanied by accumulating keyhole instabilities. The involvement of the A5754 in the melted zone did not produce an immediate effect on the plume. While the titanium plate was already pierced at 5 ms, a sudden change in behavior of the plume occurred only 11.5 ms (Figure 161). With the powerful ejection of spatter (Figure 162. e), the periodic fluctuations slowed down, and the plume was no longer observable with the 810 nm filter. The existence of a "dark" plume (cold plume) could be attributed to the lower temperature at the tip of the keyhole in aluminum that has lower vaporization temperature. On the other hand, little outbursts of atomic emission were seen till the end of the pulse with 394 nm filter, which could be attributed to the presence of Al and Ti in the vapor, emitting in the spectral region of the 394 nm filter. These outbursts had the periodicity of 0.65±0.18 ms when observed with 394 nm filter.
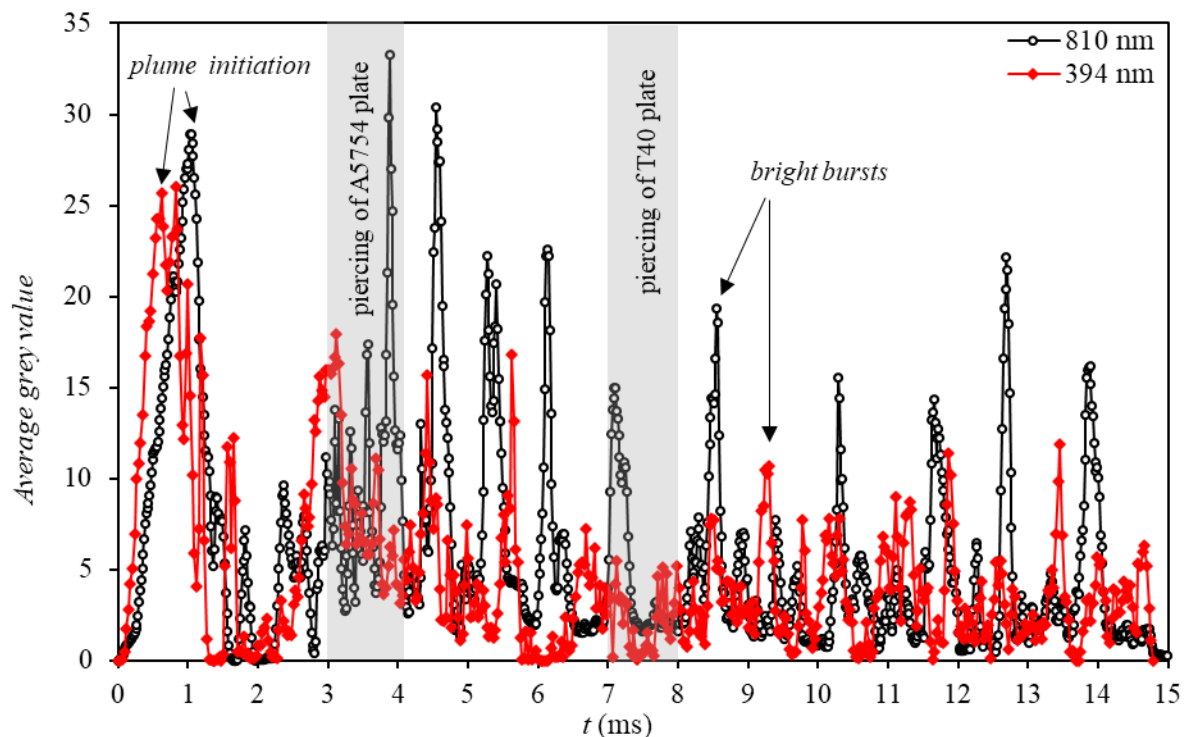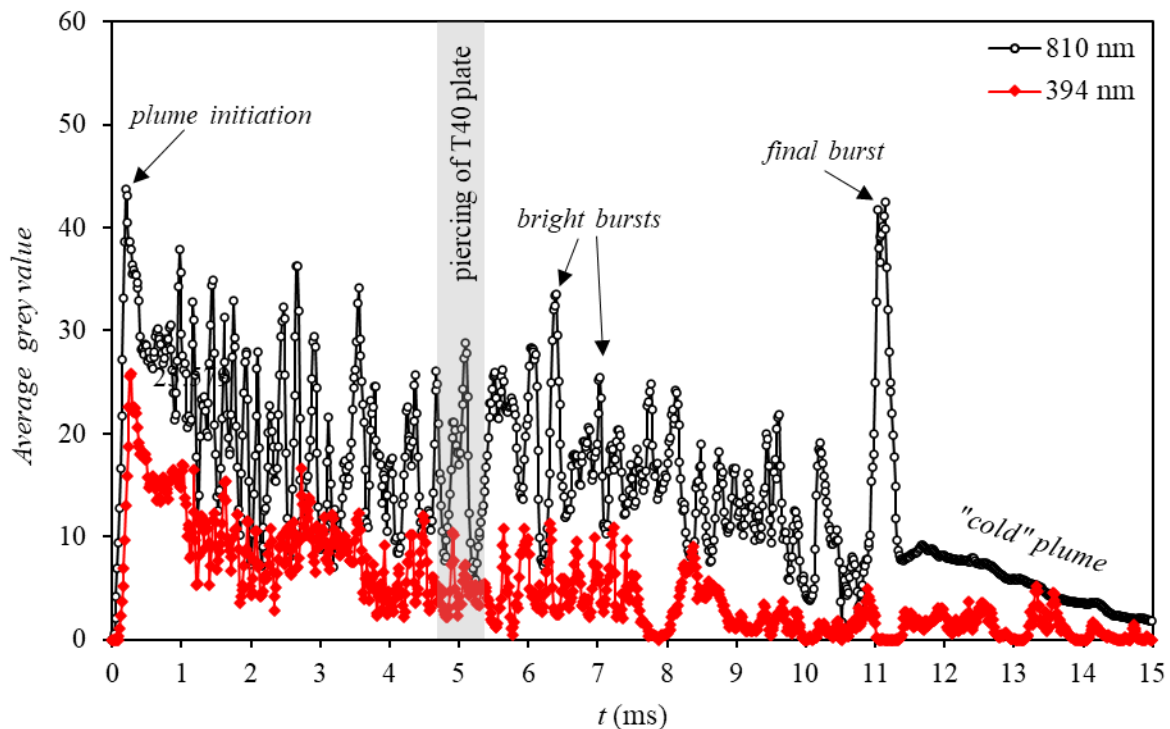

Figure 161. Temporal evolution of the average grey values of the plume images of 1mm T40 on 2 mm A5754 in overlap configuration.

Vapor plume HSI observations in overlap welding were not usable for identification of when the melted zone reached the dissimilar interface or the bottom surface of bottom plate. However, quantitative information about the existing instability in the keyhole walls were obtained by studying the time period of oscillations of the average gray values of the images.
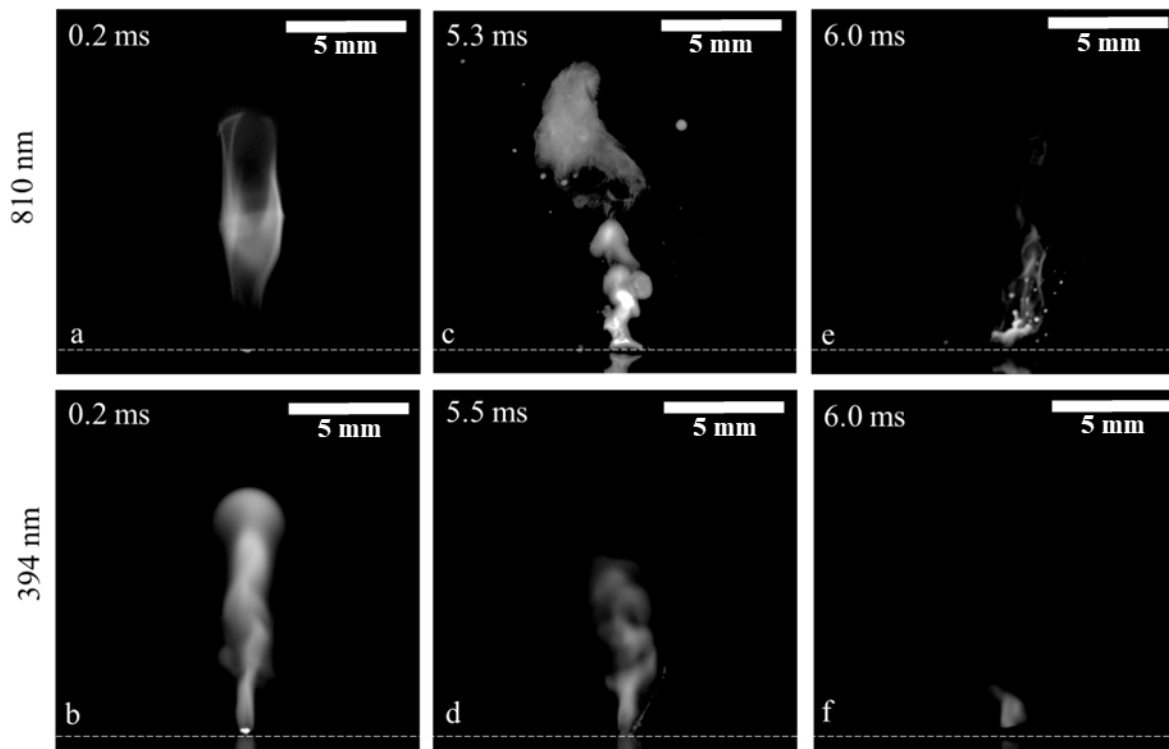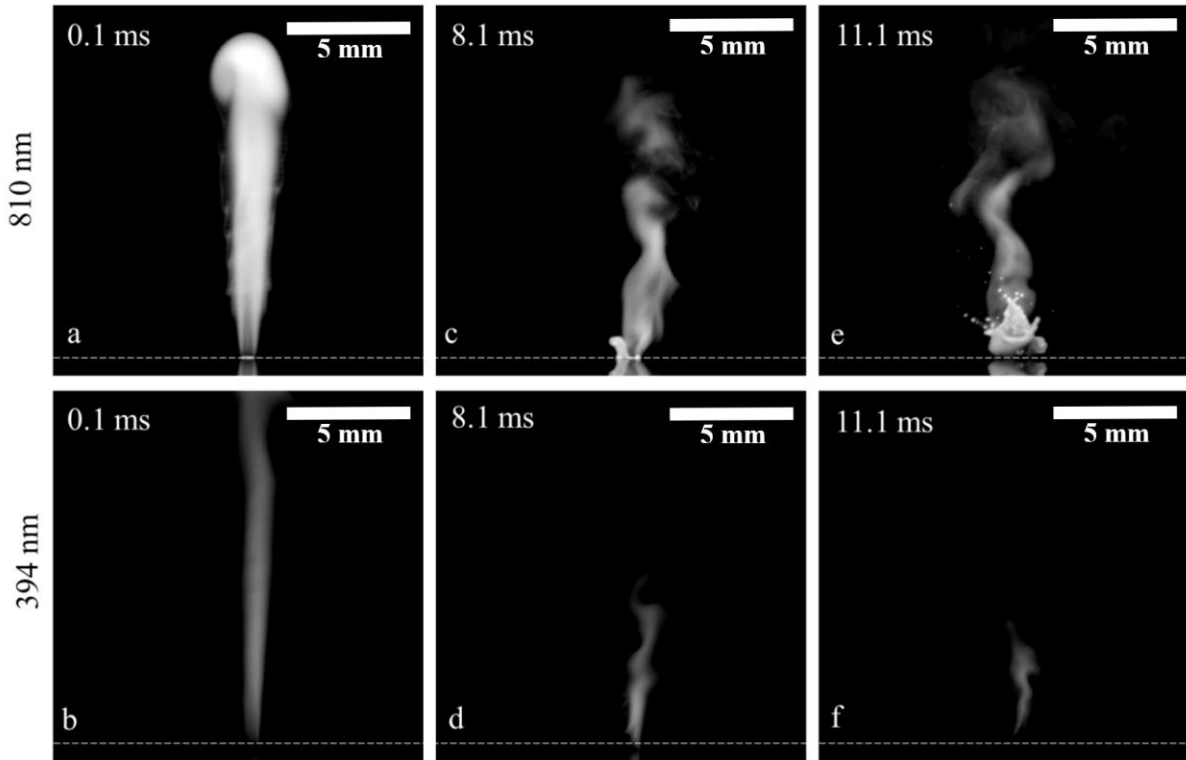
Figure 162. 1 mm T40 on 2 mm A5754 vapor plume A,B) plume initiation, C,D,E,F) Plume bursts. (Dashed line: Impact on surface)

5.4. Emission spectroscopy for overlap welding

Transitions present in the 394.4-396.4 nm spectral region (Table 31) was chosen for analysis. This spectral region corresponded to the 394 ± 3 nm optical filter used in HSI.

Table 31. Aluminum and titanium transitions in 394.9-396.4 nm spectral region.

λ (nm)	Element	A_s (s⁻¹)	Lower energetic level			Upper energetic level		
			E_i (cm⁻¹)	J_i	Configuration	E_u (cm⁻¹)	J_u	E_i (cm⁻¹)
394.4006	**Al I**	**5.105e+07**	**0.000**	**0.5**	**3p 2P**	**25347.756**	**0.5**	**4s 2S**
394.7768	Ti I	9.599e+06	170.134	3.0	s2 a3F	25493.734	2.0	(1D)sp z3P
394.8670	Ti I	4.851e+07	0.000	2.0	s2 a3F	25317.815	1.0	(4F)4p y3D
395.6334	Ti I	3.001e+07	170.134	3.0	s2 a3F	25438.906	2.0	(4F)4p y3D
395.8206	Ti I	4.044e+07	386.875	4.0	s2 a3F	25643.699	3.0	(4F)4p y3D
396.1520	**Al I**	**1.010e+08**	**112.061**	**1.5**	**3p 2P**	**25347.756**	**0.5**	**4s 2S**
396.2851	Ti I	4.128e+06	0.000	2.0	s2 a3F	25227.220	3.0	(3F)sp y3F
396.4269	Ti I	3.085e+06	170.134	3.0	s2 a3F	25388.331	4.0	(3F)sp y3F

For the 1 mm A5754 on 2 mm T40 configuration, the emission spectrum at all pulse times was dominated by two auto-absorbed emission lines of Al (394.40 and 396.15 nm) (Figure 163. a). Using PeakFit, the evolution of cumulated peak intensities with pulse time were analyzed (Figure 163. c). It was noted that during keyhole drilling in both the plates (first A5754 and then T40), the cumulated intensities of these emission lines continuously increased, representing the uninterrupted process of Al evaporation during the drilling of both plates. Shortly after piercing of bottom Ti plate, the intensities of both Al peaks stabilized, indicating that Al-rich vapor was no longer exiting the top opening of the keyhole after a pulse time of 10 ms.

For the 1 mm T40 on 2 mm A5754 configuration, after analyzing the cumulative intensities of the Al emissions (Figure 163. d), it was noted that the Al I peaks of low intensity were already present before the T40 top plate could be completely pierced. This was attributed to Al-containing oxides polluting the surface from the previous laser impacts. For pulse times >6 ms, when the keyhole reached the bottom A5754 plate, the cumulative intensities of the Al peaks increased significantly indicating continuous evaporation of Al in the keyhole. It was noted that after reaching maximum at 12 ms, the intensities of both the Al peaks stagnate, representing a drastic reduction in the flow of the emitting atoms at the keyhole opening. This time corresponded to the darkening cold plume observed with 810 nm filter (Figure 161).

In the study of Ti evaporation in the 393.5-397.5 nm region, it was noted that the Ti emissions relative to Al emissions were much more intense for 1 mm T40 on 2 mm A5754 than 1 mm A5754 on 2 mm T40. When the cumulative Ti peaks' intensities were plotted as a function of pulse time for the 1 mm A5754 on 2 mm Ti configuration, it was noted that the Ti was present in the vapor plume from 4 ms (Figure 163. e). Due to the instabilities in the plume and the probabilistic nature of emissions, these intensities of the Ti emissions were fluctuant. Considering EDS results (Figure 156.b, p.202), it was likely to that after piercing the bottom of titanium plate, most of the Ti vapor exited the keyhole through the bottom opening (spectral acquisitions were not performed at the keyhole's bottom opening).

For the 1 mm T40 on 2 mm A5754 configuration, the intensity of Ti line at 396.40 nm was studied (Figure 163. f). The linear growth of cumulated intensity up to the pulse time of 7 ms indicated continuous involvement of Ti in the vaporization process. However, for greater pulse times, the cumulated intensities stagnated indicating a non-proportional quantity of excited Ti atoms in the plume to the pulse time.
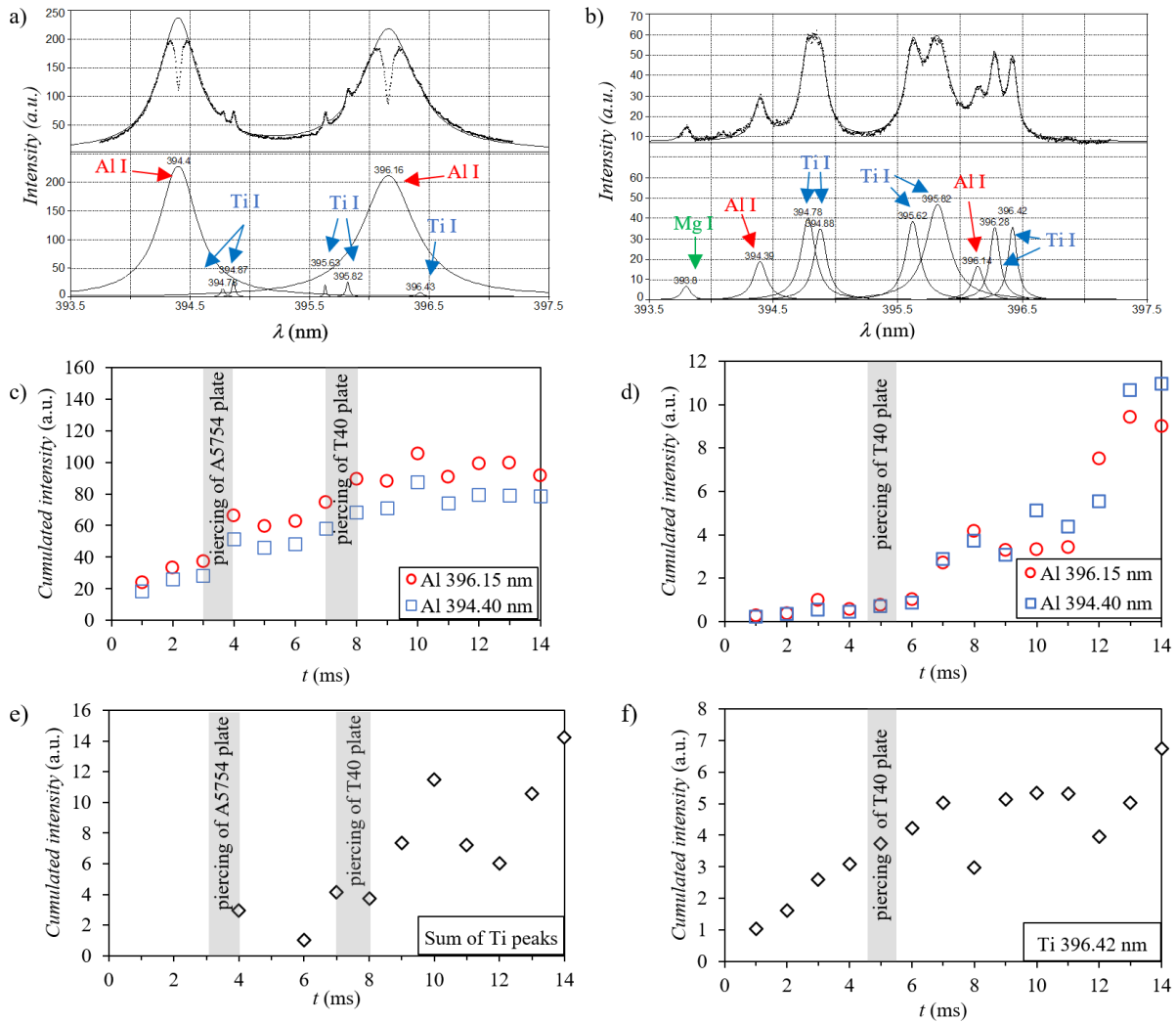
Figure 163. The spectral region of 394±3 nm filter for 1 mm A5754 on 2 mm T40 (on the left) and 1 mm T40 on 2 mm A5754 (on the right) : (a,c) spectra for 14 ms pulse, temporal evolution of cumulated intensities of (b,d) Al I peaks and (e-f)Ti I peaks.

The spectral region of 463.9-466.9 nm (Table 32) was examined to further investigate the involvement of titanium into the evaporation process.

Table 32. Titanium transitions in 463.9-466.9 nm spectral region

λ (nm)	Element	A_s (s^{-1})	Lower energetic level			Upper energetic level		
			E_i (cm^{-1})	J_i	Configuration	E_u (cm^{-1})	J_u	E_i (cm^{-1})
463.9361	Ti I	5.98E+07	14028.435	2	(4P)4s a5P	35577.093	2	(4P)4p w5D
463.9661	Ti I	3.42E+07	14105.634	3	(4P)4s a5P	35652.899	3	(4P)4p w5D
463.9939	Ti I	6.63E+07	13981.773	1	(4P)4s a5P	35527.746	1	(4P)4p w5D
464.5188	Ti I	8.57E+07	13981.773	1	(4P)4s a5P	35503.400	0	(4P)4p w5D
465.0010	Ti I	2.64E+07	14028.435	2	(4P)4s a5P	35527.746	1	(4P)4p w5D
465.6042	Ti I	9.31E+06	14105.634	3	(4P)4s a5P	35577.093	2	(4P)4p w5D
465.6469	Ti I	1.99E+06	0	2	s2 a3F	21469.487	3	(3F)sp z3G
466.7585	Ti I	2.18E+06	170.134	3	s2 a3F	21588.494	4	(3F)sp z3G
466.8347	Ti I	6.15E+05	8492.421	1	s2 a3P	29907.286	2	(4F)4p x5D

For the 1 mm A5754 on 2 mm T40 configuration, the Ti I emission lines were obstructed by molecular spectrum of AlO (Figure 164. a), composed by an intense vibrational transition at 465.00 nm followed by numerous vibrational band sequences [200]. However, after deconvolution, the cumulative intensities of the 464.64 nm and 466.75 nm Ti I lines were plotted for different pulse times (Figure 164. c). Linear growth starting from 4-5 ms was observed for both emission lines, indicating a steady involvement of titanium into the vaporization process, even after complete penetration of the T40 plate.

In 1 mm T40 on 2 mm A5754 configuration, the bands of AlO were barely visible even at high pulse times (Figure 164. b). As the most intense spectral lines of Ti I were auto-absorbed, an emission line of moderate intensity (464.52 nm) was chosen for this study.

Comparison between the spectra of 1 mm T40 on 2 mm A5754 configuration and standalone titanium (Figure 164. d) indicated that for pulse times up to 5 ms (keyhole present only in the T40 plate on top), the cumulated intensities obtained for 1 mm T40 on 2 mm A5754 configuration strictly followed the linear tendency obtained on standalone titanium. However, after 5 ms pulse times, the Ti emissions for the overlap configuration deviated from the linearity and stagnated after 8 ms. It represented that excited Ti I atoms were no longer exiting the keyhole opening as the keyhole tip moves into the A5754 alloy.

Figure 164. Vapor plume spectra in region 463.5-467.5 nm for 15 ms pulse for: a) 1 mm A5754 on 2 mm T40 and b) 1 mm T40 on 2 mm A5754; temporal evolution of cumulated intensities of c) 464.64 nm and 466.75 nm Ti I lines for 1 mm A5754 on 2 mm T40 and d) 464.52 nm Ti I line for 1 mm T40 on 2 mm A5754 configuration compared to standalone titanium.

Transitions in the 381.3-384.3 nm spectral region (Table 33) containing Ti I and Mg I emissions were studied.

For 1 mm A5754 on 2 mm T40, the Mg I lines had high intensities compared to Ti I lines (Figure 165. a). The intensities of the three Mg I lines (382.9355 nm, 383.2299 nm, 383.8292 nm) linearly increased with the pulse time till the keyhole pierced the bottom surface of the T40 plate. This signified that there was steady evaporation of the Mg in the keyhole even if the keyhole tip was in T40.

Table 33. Titanium and magnesium transitions in 381.3-384.3 nm spectral region.

λ (nm)	Element	A_s (s⁻¹)	Lower energetic level			Upper energetic level		
			E_i (cm⁻¹)	J_i	Configuration	E_s (cm⁻¹)	J_s	Configuration
381.3269	Ti I	3.17E+07	16817.16	1	(3F)sp z5F	43033.937	1	s4F)4d g5F
381.4861	Ti I	2.41E+07	16875.121	2	(3F)sp z5F	43080.961	2	s4F)4d g5F
381.7642	Ti I	2.74E+07	16961.441	3	(3F)sp z5F	43148.187	3	s4F)4d g5F
381.8199	Ti I	3.36E+07	18192.57	6	(2H)4s a3H	44375.501	5	s4F)5p t3G
382.1718	Ti I	1.86E+07	16875.121	2	(3F)sp z5F	43033.937	1	s4F)4d g5F
382.2023	Ti I	3.50E+07	17075.258	4	(3F)sp z5F	43231.989	4	s4F)4d g5F
382.6969	Ti I	2.66E+06	11531.759	2	(4F)4s b3F	37654.689	2	a2D)4p u3F
382.7468	Ti I	1.82E+07	16961.441	3	(3F)sp z5F	43080.961	2	s4F)4d g5F
382.7635	Ti I	3.77E+07	18037.213	4	(2H)4s a3H	44155.594	3	s4F)5p t3G
382.8009	Ti I	3.56E+07	18141.264	5	(2H)4s a3H	44257.097	4	s4F)5p t3G
382.8187	Ti I	4.61E+07	17215.389	5	(3F)sp z5F	43330.005	5	s4F)4d g5F
382.9355	**Mg I**	**8.90E+07**	**21850.405**	**0**	**s3p 3P**	**47957.058**	**1**	**s3d 3D**
382.9721	Ti I	2.91E+06	11639.81	3	(4F)4s b3F	37743.964	3	a2D)4p u3F
383.2299	**Mg I**	**6.67E+07**	**21870.464**	**1**	**s3p 3P**	**47957.058**	**1**	**s3d 3D**
383.2304	**Mg I**	**1.20E+08**	**21870.464**	**1**	**s3p 3P**	**47957.027**	**2**	**s3d 3D**
383.3184	Ti I	5.37E+07	19322.984	2	(3F)sp z3F	45403.557	3	s2F)4d 3G
383.3675	Ti I	1.84E+07	19421.58	3	(3F)sp z3F	45498.814	4	s4F)4d 3G
383.3911	Ti I	1.87E+06	11776.811	4	(4F)4s b3F	37852.437	4	a2D)4p u3F
383.4308	Ti I	1.48E+07	17075.258	4	(3F)sp z5F	43148.187	3	s4F)4d g5F
383.6768	Ti I	4.32E+07	19573.973	4	(3F)sp z3F	45630.182	5	s2F)4d 3G
383.8292	**Mg I**	**1.59E+08**	**21911.178**	**2**	**s3p 3P**	**47957.045**	**3**	**s3d 3D**
383.8295	**Mg I**	**4.00E+07**	**21911.178**	**2**	**s3p 3P**	**47957.027**	**2**	**s3d 3D**
383.9000	Ti I	1.62E+07	12118.394	4	s2 a1G	38159.457	3	(3P)sp u3D
384.1621	Ti I	3.60E+06	11531.759	2	(4F)4s b3F	37555.056	3	(2G)4p v3G
384.2610	Ti I	8.90E+06	17215.389	5	(3F)sp z5F	43231.989	4	s4F)4d g5F
384.2864	Ti I	3.65E+06	11639.81	3	(4F)4s b3F	37654.689	2	a2D)4p u3F

After the keyhole tip reached the bottom surface of T40, fluctuations in the emission intensity was noted especially after ~12 ms. The continuous involvement of Mg in the evaporation process during the expansion of the melted zone in A5754 could be associated with convection that brings Mg atoms to surface of the keyhole walls. However, this expansion slowed down with increasing pulse time and consequently, the melted zone progressively depleted in Mg atoms explaining the stagnation of cumulated intensities by the end of the pulse.

For 1 mm T40 on 2 mm A5754, the spectra contained many intense Ti I lines which were superposed with the three Mg lines (Figure 165. b). Due to the pollution of the top surface by oxide aggregates from the neighboring impacts, low intensity peaks of Mg I were observed for the pulse times even when the keyhole did not reach the A5754 plate (Figure 165. d). However, when the keyhole reached the dissimilar interface, the cumulated intensities of Mg increased with arrival of new Mg atoms from bottom A5754 plate. By the end of the pulse, the cumulated intensities reach a plateau, which indicated depletion in Mg of the melted zone situated in A5754.
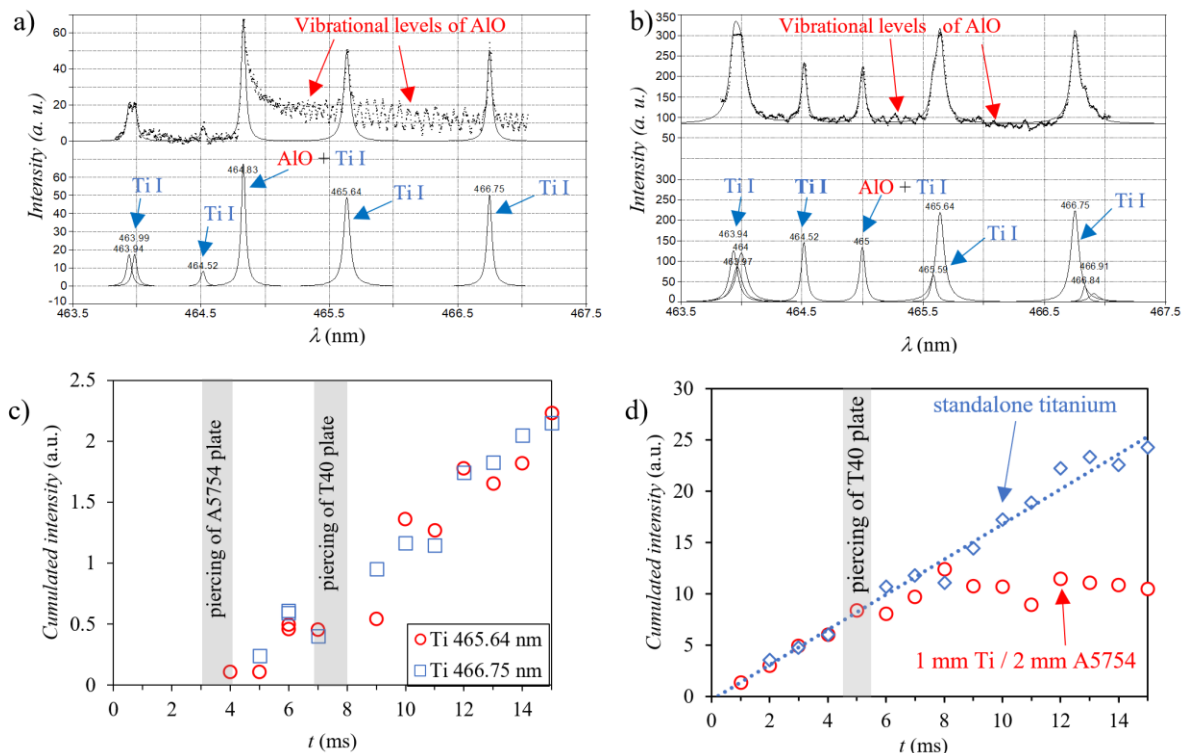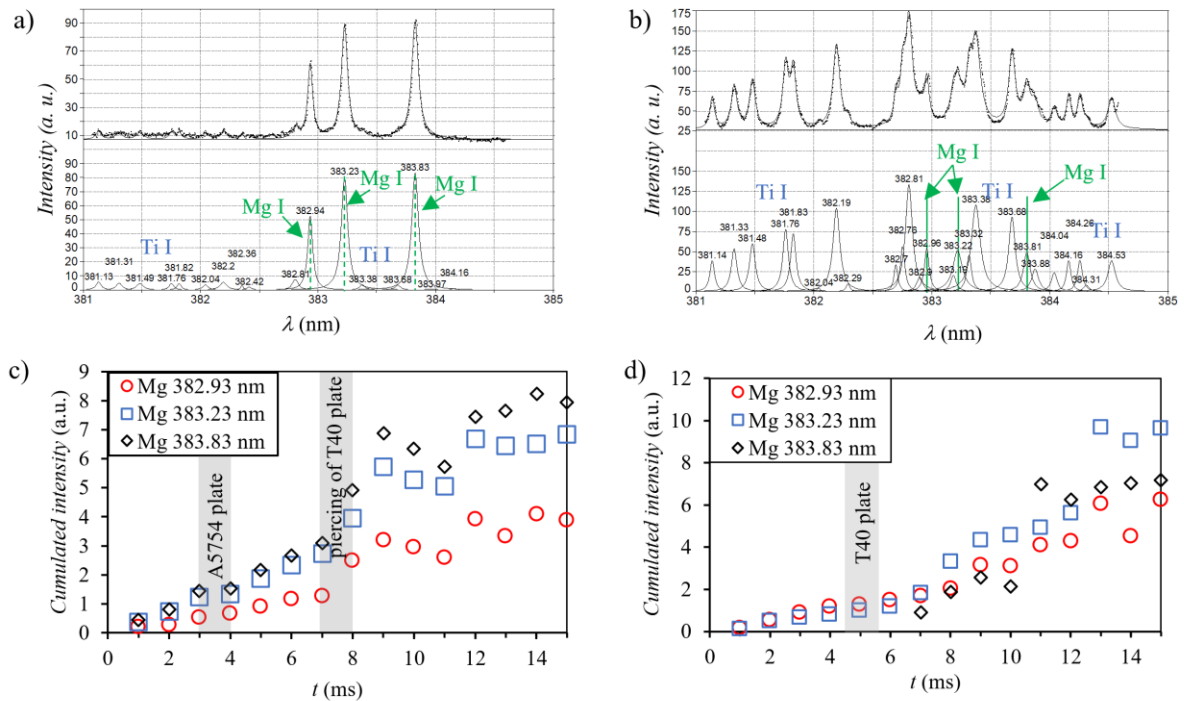
Figure 165. Vapor plume spectra in region 381.5-384.5 nm for a 15 ms pulse for a) 1 mm A5754 on 2 mm T40 and b) 1 mm T40 on 2 mm A5754; c) temporal evolution of cumulated intensity of Mg I peaks for 1 mm A5754 on 2 mm T40 and d) 1 mm T40 on 2 mm A5754.

5.5. A discussion on overlap welding phenomenology

The timelines of events in the evolution of keyhole, melted zones and vapor plume were mapped from the experimental and numerical results (refer Annex 2 for numerical work, p.245) for both the configurations (Figure 166). In both cases, the melted zone and the keyhole reach a stationary condition at the end, characterized by constant dimensions.

In the case of 1 mm A5754 on 2 mm T40 (Figure 166. a), 4.5 kW laser power was sufficient for rapid initiation of the keyhole in A5754 plate. The initial bright burst of the plume was attributed to the instantaneous temporary elevation of temperature on the A5754 surface due to the presence of a native alumina layer being rapidly destroyed by evaporation and convection and replaced by the more reflective liquid aluminum. For pulse times ≥ 1.5 ms, before the involvement of titanium plate, the plume luminosity decreased due to low thermal and atomic emissions from Al-rich vapor.

The keyhole penetration into titanium plate (at t = 4 ms) induced immediate appearance of detectable Ti amounts in the plume and the melted zone, which signified an extremely rapid mixing process. The bursts observed in HSI of the plume at t > 4 ms was attributed to the ejection of Ti-rich jets producing both atomic and thermal emissions. The periodic nature of these bursts of plume was due to the hydrodynamic instabilities on the keyhole walls. Due to the convective flow induced by drops of melted titanium climbing the keyhole walls, their higher temperature than Al-rich melt promote the evaporation of Al and Mg even if the keyhole tip was in the T40 plate at the bottom.

Even when the piercing of T40 plate at the bottom was achieved (at 7~8 ms), the dimensions of the melted zone and the keyhole continued to grow until stabilization around ~10 ms. Simultaneously, the contribution of Al I in the plume decreased as melted titanium was dominant on the keyhole walls. Finally, when the melted zone (and also the plume) became depleted in Mg (t > 12 ms), by the end of the pulse the plume from the top opening of the

keyhole became essentially composed by Ti atoms. The composition and the behavior of the plume on the bottom opening of the keyhole is yet to be studied.

In 1 mm T40 on 2 mm A5754 configuration (Figure 166. b), laser power of 2 kW was insufficient for drilling the keyhole entirely through the A5754 plate. However, the T40 plate at the top was pierced completely at t = 5 ms.

The stagnation of the keyhole tip in A5754 led to a very late appearance of Al atoms on the top of the melted zone (t = 8 ms) and an extremely delayed ejection of bulk aluminum alloy (t = 12 ms). The Mg atoms offered a more rapid response at ~ 7 ms (from EDS analysis) due to their preferential evaporation from the melted A5754 at the bottom of the keyhole. However, both Mg and Al were not suitable for precise spectral determination of the pulse time sufficient for reaching A5754 plate, as they polluted the surroundings of the melted zone over a distance of ~5 mm and consequently contributed to the emission spectra of neighboring impacts, which was never observed for Ti atoms in the A5754 on T40 configuration. The significant growth of cumulated intensities of Al I and Mg I after 6 ms was attributed to the keyhole drilling process, and not to the pollution.

When the keyhole tip established itself in A5754 plate, the plume temperature dropped drastically, which was observed by the stagnation of cumulated intensities of Al I and Mg I peaks (for t > 12 ms) and by very reduced luminosity of the plume in HSI with both the filters. From this instance, the dimensions of the melted zone and the keyhole became almost static. The cumulated intensities of Ti I reached a plateau even before the appearance Al I and Mg I (at t > 7 ms) due to the progressive decrease of the melted zone temperature and due to the displacement of the vaporization zone at the tip of the keyhole into A5754. Thus, it was concluded that both atomic and thermal emissions of the plume diminished for t > 12 ms, as the keyhole tip established itself in A5754 plate, making it impossible to perform any online monitoring for longer pulse times.

Unlike the previous case, the rapid fluctuations of the keyhole walls accompanied by the observable bursts of the plume take place from the very beginning of keyhole formation. The periodicity of these rapid fluctuations was evaluated to be 0.25-0.29 ms. In the "dark" plume at >12 ms, these fluctuations become invisible at 810 nm due to the low plume temperature. However, the periodicity was somewhat visible with 394 nm filter (0.65 ms).
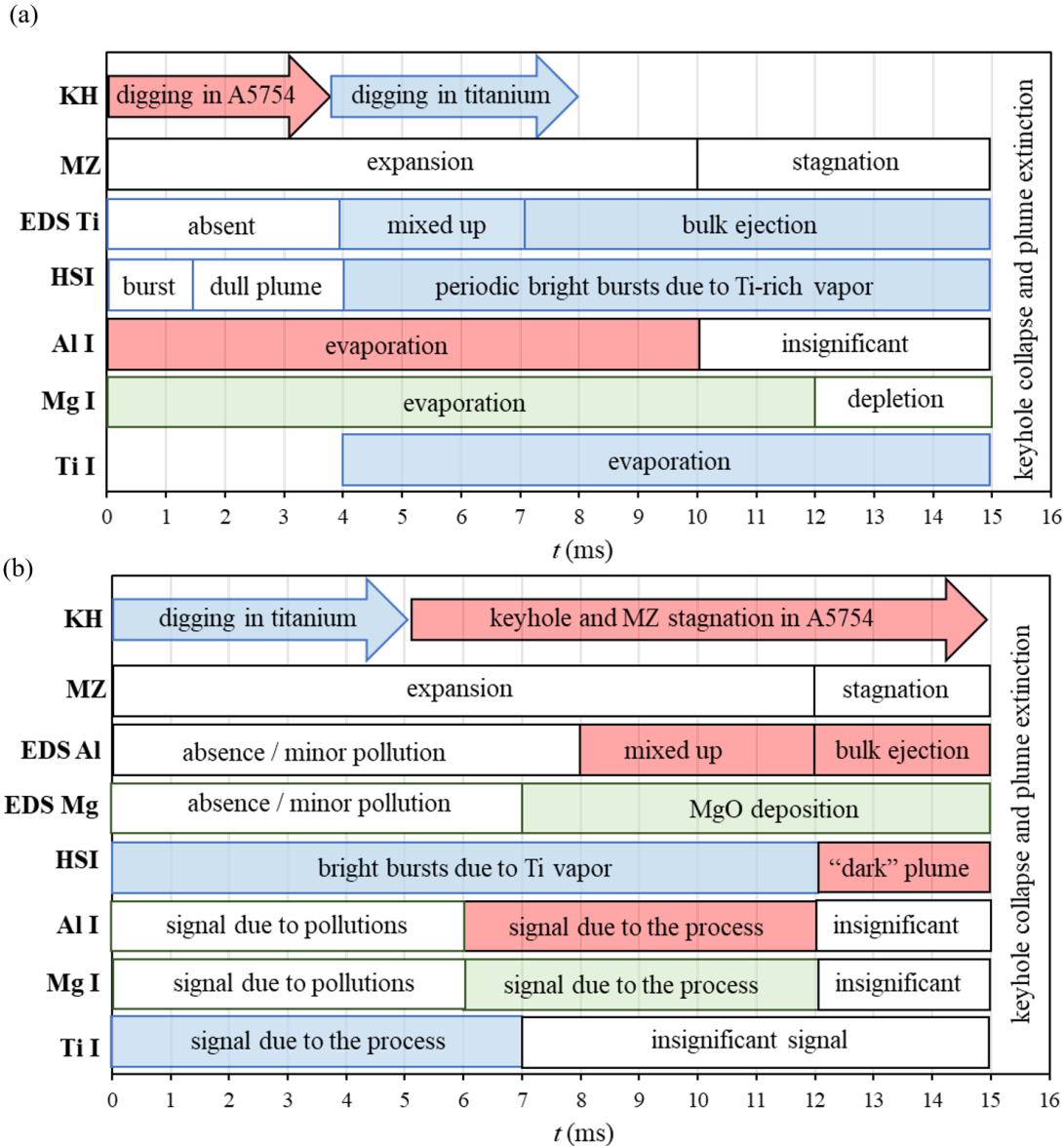
Figure 166. Phenomenological timeline of melted zone and plume evolution in a) 1 mm A5754 on 2 mm T40 and b) 1 mm T40 on 2 mm A5754 overlap welding. (KH - keyhole, MZ - melted zone, EDS - energy dispersive analysis, HSI – High Speed Imaging of the plume, Al I, Mg I and Ti I – atomic emissions of corresponding neutral atoms).

5.6. Conclusions and perspectives from overlap welding

After analyzing both the dissimilar configurations, the advantages and disadvantages of each case were identified. Welding with aluminum on top necessitated a high laser power to commence drilling in the reflective materials. However, this high power rapidly drills through the titanium plate at the bottom. To reduce the mixing of materials which could lead to the formation of undesired intermetallic phases, placing the aluminum on top would be disadvantageous because of lack of control over the mixing processes. From EDS, it was noted that the mixing processes between the two materials occur quickly when the keyhole reached the dissimilar interface. Welding with titanium on top requires less laser power, however, the keyhole could not drill through the bottom aluminum plate even for long pulse durations. However, the advantage of having titanium on top was the prevention of violent mixing of materials due to reduction in the convection dynamics from keyhole stabilization.

HSI results were not very precise indicators of the different phenomenological events in overlap welding. However, fluctuations in the plume were representative of the hydrodynamic instabilities in the keyhole. Simultaneous application of HSI calibrated for the sensitivity at different wavelengths combined with multiple filters on two HSI cameras could yield more accurate results.

Spectrometric analyses were useful in the detection of the involvement of the keyhole with the bottom plate. While the in-situ investigation of Mg lines were hindered by the presence of Ti I lines in the same spectral region, Al I lines at 394.4-394.6 nm were useful in the distinction from titanium emission. On the other hand, it was also noted that Al and Mg impurities from previous neighboring impacts could pollute the surface and thereby yield false results. Analysis of the plume from the bottom opening could enlighten more about conditions within the keyhole in the bottom plate.

Chapter 6. Conclusions and Perspectives

The key objective of the thesis was to *further the understanding of the phenomenology of dissimilar laser welding*. The experimental characterization of the keyhole behavior in dissimilar welding is still very limited. As the composition and the behavior of vapor plume above the keyhole are linked to the keyhole characteristics, the investigation of the vapor plume in the case of dissimilar welding is of particular interest. The high-speed imaging of the vapor plume on standalone materials is frequently used in scientific literature. However, the possibilities of image treatment of plume behavior are not fully explored. Moreover, a precise definition of the vapor plume in laser welding has remained confusing due to the interchangeable use of the term 'plume' in LIBS research, which can refer to either 'plasma plume' or 'vapor plume'. In LIBS, these terms represent ionized plasma and possess very different characteristics from the vapor plume observed in laser welding, where the metallic vapor is usually weakly ionized.

With the objective of understanding the plume and keyhole behavior during laser welding of materials which have an important mismatch in physical properties, two in-situ methods were combined: high-speed imaging (applied to the vapor plume and the keyhole) and emission spectroscopy (which permits evaluation the plume temperature and the nature of the evaporating species). The selected dissimilar couple aluminum alloy A5754/pure titanium T40 was first studied in *butt configuration*, where the *laser beam offset* from the joint line was varied. The developed methodologies were then applied to *overlap configuration*, in which the combinations A5754 on T40 and T40 on A5754 were compared. The groundwork for a comprehensive statement defining the vapor plume in laser welding has been established with this work.

In the first place, the *continuous welding* between A5754 and pure titanium was studied, where the vapor plume was observed from the side and front positions using 810 nm bandpass filter that provides the *thermal image* of the plume. It was noted that the plumes of the standalone materials were very different from each other. The aluminum plume was dull and turbulent without a regular shape which required high exposure times to be observed, while the titanium plume was composed of bright strong jets which was visible even with very low exposures. Therefore, the dissimilar vapor plume with intermediate characteristics had to be observed with intermediate exposure times. Additionally, the dissimilar vapor plume had a peculiar characteristic of inclining away from the vertical towards the aluminum side. To quantify the behavior of *a diffuse cloud-like object* that exhibited rapid variations from one image to the next, initially the stacks of several thousands of images were simplified by making a *standard deviation image*. However, *temporal analysis for average gray levels* from representative plume regions in every image was necessary to understand the periodic nature of different parts of the vapor plume. It was understood that titanium, which absorbed the laser radiation much better than aluminum, periodically formed strong jets causing the vapor plume to be inclined. And the amount of titanium being vaporized along with the amount of titanium exiting in the inclined manner were dependent on the laser spot position relative to the joint line.

In order to investigate the plume initiation process in more detail, further step of the study was conducted with *a standalone laser pulse* of 2 ms. With a reduction in the total number of images to less than 20, the standard deviation images were no longer viable. Also, the dissimilar plumes differed in intensities depending on the amount of titanium being vaporized. This required the images to be *normalized* in order to be comparable to each other. To quantify the *plume morphology and orientation*, the shape of the vapor plume was considered to be approximately an *ellipse*. A *threshold* of grey value was applied to identify the edges of the

vapor plume and an ellipse was fit to those edges. This allowed the measurement of the plume's height, width, angle of inclination, rate of expansion on a temporal scale. However, the following questions remained: What is the most accurate way to apply a threshold to a dissimilar plume that had changes in intensity depending on the materials being vaporized? If the plume has an irregular shape and was not really an ellipse, what other methods could be used to measure its morphology and orientation? Since the plume was a cloud-like object with different intensities at different areas, what measurements could quantify these aspects of the plume? And most importantly, the 810 nm filter only allows the observation of thermal emissions. What would the vapor plume look like when instead of thermal emissions, the atomic emissions were observed?

With emission spectroscopy, 394 nm spectral region was identified to contain the atomic emissions of both aluminum (Al (I): 394.4 and 396.15 nm) and titanium (Ti (I): 394.7, 394.8, 395.8, 396.2, 396.4 nm and more). For this reason, a 394 nm filter was selected for the *observation of atomic emissions* from the plume. In the next step of this work, the plume formed during a standalone laser pulse was observed using both 810 and 394 nm filters, along with emission spectroscopy. Moreover, the pulse duration was extended to 6 ms to observe the established plume, when the keyhole is already produced. Since the vapor plumes exhibited rapid changes which appeared almost random (this may be different if the frame rates are high enough), several repetitions of the same experimental conditions were made to confirm the *repeatability* of the plume properties. To develop on the thresholding method utilized, global thresholding (to account for brightness changes between the images from several videos of same experimental parameter) and local thresholding (to account for brightness differences between different parts of the plume in the same image) were applied to identify the edges of the plume. Since the HSI camera was not synchronized with the laser, the identification of the beginning of the pulse had always been a question mark. And so, a new method of identifying the variations in the grey values in a small region around the keyhole was done using an automated algorithm to avoid human errors from visually determining the start of the pulse. The measurement methods were further extended by studying the area of the plume, measuring the Feret's diameters (because it did not necessitate the approximation that the plume resembles an ellipse), and other parameters (such as center of mass, skewness and kurtosis) which were dependent on the intensity distribution within the plume. With multiple videos for every beam offset from the joint line, using averages, the temporal behavior and the spatial behavior obtained from the thermal mappings (810 nm) and atomic emission mappings (394 nm) of the plume were characterized. With this comparative analysis, it was observed that the thermal mapping of the plume does not coincide with its atomic emission mapping. Because the thermally excited plume could consist of heated air, oxidized vapors, etc. in addition to the metallic vapor exiting the keyhole. However, at the 394 nm region, only the excited aluminum and titanium atoms would be visible. To identify the parts of the plume containing titanium emissions only, another wavelength region should be utilized. However, this method could not be used to study the isolated aluminum emissions from a dissimilar plume because titanium emissions are always present in the regions of the fundamental emissions of aluminum. To perfectly identify the difference between the thermal mapping and atomic emission mapping of the plume, simultaneous imaging of the plume must be done using both the filters by using two HSI cameras side by side (calibrated for wavelength sensitivity).

In order to link the observed plume behavior with keyhole behavior, a separate study of *keyhole imaging* with 810 nm filter with identical operational conditions, was performed using a fused quartz plate transparent to laser radiation. A strong synergetic effect between titanium and aluminum was observed, where the titanium with a high absorption coefficient, acted as the main vector of heat accumulation, consequently inducing the melting and vaporization of the

opposite aluminum side by its strong vapor jets. Consequently, the keyhole became more prominent on aluminum side. Moreover, reflective and conductive aluminum induced keyhole instabilities and strong spattering, observable in both continuous and pulsed welding. The keyhole curvatures on the titanium side correlated well with the previously observed inclinations of plume. In both continuous and pulsed welding, the keyhole and the vapor plume were stable for beam offsets on the titanium side, while increased plume inclinations and temperature drop were observed for beam offsets on the aluminum side.

Emission spectroscopy of the plume was done over several spectral regions to estimate the plume temperature and to identify the composition of the vapor plume. For all the laser spot positions studied, the vaporization of both the materials was observed. However, the changes in the emission intensities of different materials with respect to the laser spot positions correlated well with the HSI analyses of the plume and post-mortem characterization results of the melted zones. *Two different kinds of temperatures* could be obtained from the emission spectra: the *macroscopic temperature* that is explained by the kinetic motion of the atoms and molecules (evaluated based on continuous thermal emission) and the *electronic temperature* explained by the excitation in atoms' individual electronic states (based on Boltzmann plot method). For standalone A5754, the electronic temperature was ~2700 K, which is close to the vaporization temperature of aluminum at normal pressure, while the macroscopic temperature could not be evaluated with enough precision. The standalone titanium welding produced a macroscopic temperature of ~3560 K (equal to its vaporization temperature at normal pressure) and an electronic temperature up to ~7000 K. This indicated that *the plume does not have a homogenous temperature*: while some part of Ti present in the plume remains relatively "cold", some atoms gained sufficient energy for excitation of their electronic states. In the case of the dissimilar welding plume, the macroscopic temperature was ~3100 K, which is less than the vaporization temperature of Ti. Consequently, this temperature can only reflect the state of Al vapor that exceeded the vaporization temperature of aluminum. On another hand, the electronic temperature of Ti atoms was slightly below 7000 K. Compared to standalone materials, it can be concluded that Ti vapor is cooled down by the involvement of aluminum into laser/matter interaction, while Al vapor on the contrary is heated up. A particularly high levels of electronic temperatures reached by Ti atoms in the plume allow hypothesizing that the temperature inside the keyhole could be even higher and thus could produce ionization. Additional spectral regions should be studied in search of Ti II and Al II, however, it is possible that recombination of the ionized species occurs as they quit the keyhole. The presence of self-absorbed lines of aluminum and titanium were indicative of a cooler periphery and a hotter and denser core of the plume. The electronic temperatures for continuous welding and pulsed welding, calculated from Ti (I) lines were essentially the same (~9000 K for standalone Ti and ~7000 K for dissimilar welding) for 2 kW laser power. For all the experiments, the spectral acquisition zone was directly above the keyhole opening. The increase in emission intensities in relation to pulse times without any augmentation of temperature represented an increase in the amount of matter vaporized. Acquisitions from different heights and other positions away from the vertical axis need to be tested to further characterize the plume. Synchronization between the HSI and spectrometer could be done if the spectrometer ICCD had a higher frame rate. Synchronization between the laser and the spectrometer would lead to better temporal analysis of the vapor plume's emissions at the millisecond scale.

The developed methodologies of HSI and emission spectroscopy were applied to *the overlap welding* configurations with 1 mm thick A5754 on top of 2 mm T40; and 1 mm T40 on top of 2 mm A5754. In these experiments, the plume dynamics reflected the periodic fluctuations of the keyhole walls occurring at high pulse times. This part of work was performed with a newer HSI camera having 10 times higher frame rate (67000 fps compared to 6400 fps for the older

model). It could be said that, using higher frame rates to study the butt-configuration dissimilar plume would yield a better analysis and reveal similar periodic pulsations as overlap welding. The two configurations tested in overlap welding (aluminum on top and titanium on top) necessitated the use of different laser powers and produced distinct keyhole and plume behaviors. The previously observed synergy between the titanium and aluminum was exhibited differently. When titanium was placed on aluminum, the vaporization and the keyhole digging suddenly slowed down as the keyhole tip entered the bottom aluminum plate. When aluminum plate was placed on the top, higher laser powers were needed for the keyhole initiation, which promoted rapid keyhole digging in the bottom titanium plate. Whilst the keyhole drilling process was not viewed directly but only evaluated basing on numerical model, the suppositions about the keyhole behavior should be confirmed by experimental observation through a fused quartz plate, just like in the case of butt-welding. The results of emission spectroscopy were found in the detection of the involvement of bottom material into the melted zone. However, they were affected by plume fluctuations and by the pollution of the top plate by volatile elements.

The high-speed imaging data and image treatment methodologies during this thesis could serve as another advancement in further investigation of the dissimilar vapor plumes. Especially, the influence of the wavelength of observation on the vapor plume characteristics is crucial if the plume behavior is to be used for in-situ control methods. Distribution of elements within the different parts of the vapor plume needs to be identified and analyzed for further correlation with the keyhole behavior. Simultaneous observation of the keyhole using quartz, and the vapor plume, could provide a final confirmation on the hypotheses made relating the keyhole walls to the vapor plume inclinations. Using at least three synchronized HSI cameras, a 3D image of the dissimilar plume could be created. During this thesis, the data filtering and treatment consumed most of the time. With the rapidly growing advent of artificial intelligence in data treatment, HSI and spectrometric analyses of the vapor plume, especially with synchronization between the different instruments for welding and observation, could form an important part in the automation of dissimilar welding.

The conducted works on plume characterization by high-speed imaging and emission spectroscopy prepare a field for the novel in-situ control methodologies and accumulate the data necessary for further development of numerical modeling of vapor plume behavior.

References

[1] A. Mathieu, S. Pontevicci, J. Viala, E. Cicala, S. Matteï, and D. Grevey, "Laser brazing of a steel/aluminium assembly with hot filler wire (88% Al, 12% Si)," *Mater. Sci. Eng. A*, vol. 435–436, pp. 19–28, Nov. 2006, doi: 10.1016/j.msea.2006.07.099.

[2] A. Mathieu, S. Matteï, A. Deschamps, B. Martin, and D. Grevey, "Temperature control in laser brazing of a steel/aluminium assembly using thermographic measurements," *NDT E Int.*, vol. 39, no. 4, pp. 272–276, Jun. 2006, doi: 10.1016/j.ndteint.2005.08.005.

[3] S. Matteï, D. Grevey, A. Mathieu, and L. Kirchner, "Using infrared thermography in order to compare laser and hybrid (laser+MIG) welding processes," *Opt. Laser Technol.*, vol. 41, no. 6, pp. 665–670, Sep. 2009, doi: 10.1016/j.optlastec.2009.02.005.

[4] N. Pierron, P. Sallamand, J.-M. Jouvard, E. Cicala, and S. Matteï, "Determination of an empirical law of aluminium and magnesium alloys absorption coefficient during Nd : YAG laser interaction," *J. Phys. Appl. Phys.*, vol. 40, no. 7, pp. 2096–2101, Apr. 2007, doi: 10.1088/0022-3727/40/7/035.

[5] E. Cicală, A. Soveja, P. Sallamand, D. Grevey, and J. M. Jouvard, "The application of the random balance method in laser machining of metals," *J. Mater. Process. Technol.*, vol. 196, no. 1–3, pp. 393–401, Jan. 2008, doi: 10.1016/j.jmatprotec.2007.05.049.

[6] Y. Li, M. Založnik, J. Zollinger, L. Dembinski, and A. Mathieu, "Effects of the powder, laser parameters and surface conditions on the molten pool formation in the selective laser melting of IN718," *J. Mater. Process. Technol.*, vol. 289, p. 116930, Mar. 2021, doi: 10.1016/j.jmatprotec.2020.116930.

[7] A. Mannucci *et al.*, "Use of pure vanadium and niobium/copper inserts for laser welding of titanium to stainless steel," *J. Adv. Join. Process.*, vol. 1, p. 100022, Mar. 2020, doi: 10.1016/j.jajp.2020.100022.

[8] L. Lavisse *et al.*, "Pulsed laser growth and characterization of thin films on titanium substrates," *Appl. Surf. Sci.*, vol. 253, no. 19, pp. 8226–8230, Jul. 2007, doi: 10.1016/j.apsusc.2007.02.136.

[9] M. Cirisan, J. M. Jouvard, L. Lavisse, L. Hallo, and R. Oltra, "Laser plasma plume structure and dynamics in the ambient air: The early stage of expansion," *J. Appl. Phys.*, vol. 109, no. 10, p. 103301, May 2011, doi: 10.1063/1.3581076.

[10] G. D. Förster *et al.*, "Oxidation-Induced Surface Roughening of Aluminum Nanoparticles Formed in an Ablation Plume," *Phys. Rev. Lett.*, vol. 115, no. 24, p. 246101, Dec. 2015, doi: 10.1103/PhysRevLett.115.246101.

[11] M. Girault *et al.*, "Modelling nanoparticles formation in the plasma plume induced by nanosecond pulsed lasers," *Appl. Surf. Sci.*, vol. 258, no. 23, pp. 9461–9465, Sep. 2012, doi: 10.1016/j.apsusc.2012.04.117.

[12] L. Lavisse *et al.*, "*In-situ* small-angle x-ray scattering study of nanoparticles in the plasma plume induced by pulsed laser irradiation of metallic targets," *Appl. Phys. Lett.*, vol. 100, no. 16, p. 164103, Apr. 2012, doi: 10.1063/1.4703930.

[13] L. Lavisse *et al.*, "Evolution of the composition of nanoparticles formed by the nanosecond Nd:YAG laser irradiation of an aluminium target in N2–O2 gas mixtures," *Appl. Phys. A*, vol. 123, no. 11, p. 692, Nov. 2017, doi: 10.1007/s00339-017-1283-9.

[14] I. Shupyk *et al.*, "Study of surface layers and ejected powder formed by oxidation of titanium substrates with a pulsed Nd:YAG laser beam," *Appl. Surf. Sci.*, vol. 255, no. 10, pp. 5574–5578, Mar. 2009, doi: 10.1016/j.apsusc.2008.08.108.

[15]   F. Torrent *et al.*, "Wavelength influence on nitrogen insertion into titanium by nanosecond pulsed laser irradiation in air," *Appl. Surf. Sci.*, vol. 278, pp. 245–249, Aug. 2013, doi: 10.1016/j.apsusc.2012.11.110.

[16]   I. Tomashchuk, P. Sallamand, J. M. Jouvard, and D. Grevey, "The simulation of morphology of dissimilar copper–steel electron beam welds using level set method," *Comput. Mater. Sci.*, vol. 48, no. 4, pp. 827–836, Jun. 2010, doi: 10.1016/j.commatsci.2010.03.042.

[17]   I. Tomashchuk, P. Sallamand, and J. M. Jouvard, "Multiphysical modeling of dissimilar welding via interlayer," *J. Mater. Process. Technol.*, vol. 211, no. 11, pp. 1796–1803, Nov. 2011, doi: 10.1016/j.jmatprotec.2011.06.004.

[18]   I. Tomashchuk, P. Sallamand, and J. M. Jouvard, "The modeling of dissimilar welding of immiscible materials by using a phase field method," *Appl. Math. Comput.*, vol. 219, no. 13, pp. 7103–7114, Mar. 2013, doi: 10.1016/j.amc.2012.01.039.

[19]   I. Bendaoud *et al.*, "The numerical simulation of heat transfer during a hybrid laser–MIG welding using equivalent heat source approach," *Opt. Laser Technol.*, vol. 56, pp. 334–342, Mar. 2014, doi: 10.1016/j.optlastec.2013.09.007.

[20]   A. Métais, S. Matteï, I. Tomashchuk, and S. Gaied, "Modelling of Transport Phenomena in Laser Welding of Steels," p. 7, 2015.

[21]   A. Métais, S. Matteï, I. Tomashchuk, and S. Gaied, "Multiphysical Modeling of Transport Phenomena During Laser Welding of Dissimilar Steels," *Phys. Procedia*, vol. 83, pp. 1387–1396, 2016, doi: 10.1016/j.phpro.2016.08.145.

[22]   A. Mannucci *et al.*, "Numerical simulation of residual stresses in laser welding: application to Ti6Al4V/316L steel assembly with vanadium insert," p. 11, 2019.

[23]   I. Tomashchuk, I. Bendaoud, J.-M. Jouvard, and P. Sallamand, "The numerical challenges in multiphysical modeling of laser welding with arbitrary Lagrangian-Eulerian method," *COMSOL Conf.*, p. 8, 2018.

[24]   I. Tomashchuk, I. Bendaoud, P. Sallamand, E. Cicala, S. Lafaye, and M. Almuneau, "Multiphysical modelling of keyhole formation during dissimilar laser welding," p. 7, 2016.

[25]   A. Mathieu, I. Tkachenko, J. Jouvard, and I. Tomashchuk, "Tandem laser-gas metal arc welding joining of 20 mm thick super duplex stainless steel: An experimental and numerical study," *Proc. Inst. Mech. Eng. Part J. Mater. Des. Appl.*, vol. 234, no. 5, pp. 697–710, May 2020, doi: 10.1177/1464420720904113.

[26]   A. Z. Kechiche, O. Aubreton, A. Mathieu, A. Mannucci, and C. Stolz, "Polarimetric imaging method for surface quality evaluation of a liquid metal pool obtained during welding," *Opt. Eng.*, vol. 59, no. 10, Oct. 2020, doi: 10.1117/1.OE.59.10.100501.

[27]   I. Lertrusdachakul, A. Mathieu, and O. Aubreton, "Vision-based control of wire extension in GMA welding," *Int. J. Adv. Manuf. Technol.*, vol. 78, no. 5–8, pp. 1201–1210, May 2015, doi: 10.1007/s00170-014-6290-9.

[28]   Z. Sun and JC. Ion, "Laser welding of dissimilar metal combinations," *Springer*, vol. 30, no. 17, pp. 4205–4214, 1995, doi: https://doi.org/10.1007/BF00361499.

[29]   G. Casalino, M. Mortello, and P. Peyre, "Yb–YAG laser offset welding of AA5754 and T40 butt joint," *J. Mater. Process. Technol.*, vol. 223, pp. 139–149, Sep. 2015, doi: 10.1016/j.jmatprotec.2015.04.003.

[30]   Y. Chen, S. Chen, and L. Li, "Effects of heat input on microstructure and mechanical property of Al/Ti joints by rectangular spot laser welding-brazing method," *Int. J. Adv. Manuf. Technol.*, vol. 44, no. 3–4, pp. 265–272, Sep. 2009, doi: 10.1007/s00170-008-1837-2.

[31]   B. Majumdar, R. Galun, A. Weisheit, and B. L. Mordike, "Formation of a crack-free joint between Ti alloyand Al alloy by using a high-power CO2 laser," p. 10.

[32] F. Möller, M. Grden, C. Thomy, and F. Vollertsen, "Combined Laser Beam Welding and Brazing Process for Aluminium Titanium Hybrid Structures," *Phys. Procedia*, vol. 12, pp. 215–223, 2011, doi: 10.1016/j.phpro.2011.03.028.

[33] Z. Song, K. Nakata, A. Wu, and J. Liao, "Interfacial microstructure and mechanical property of Ti6Al4V/A6061 dissimilar joint by direct laser brazing without filler metal and groove," *Mater. Sci. Eng. A*, vol. 560, pp. 111–120, Jan. 2013, doi: 10.1016/j.msea.2012.09.044.

[34] W. V. Vaidya *et al.*, "Structure-property investigations on a laser beam welded dissimilar joint of aluminium AA6056 and titanium Ti6Al4V for aeronautical applications Part I: Local gradients in microstructure, hardness and strength," *Mater. Werkst.*, vol. 40, no. 8, pp. 623–633, Aug. 2009, doi: 10.1002/mawe.200900366.

[35] W. V. Vaidya *et al.*, "Improving interfacial properties of a laser beam welded dissimilar joint of aluminium AA6056 and titanium Ti6Al4V for aeronautical applications," *J. Mater. Sci.*, vol. 45, no. 22, pp. 6242–6254, Nov. 2010, doi: 10.1007/s10853-010-4719-6.

[36] M. J. Torkamany, F. Malek Ghaini, R. Poursalehi, and A. F. H. Kaplan, "Combination of laser keyhole and conduction welding: Dissimilar laser welding of niobium and Ti-6Al-4V," *Opt. Lasers Eng.*, vol. 79, pp. 9–15, Apr. 2016, doi: 10.1016/j.optlaseng.2015.11.001.

[37] D. Grevey *et al.*, "Microstructural and micro-electrochemical study of a tantalum–titanium weld interface," *Mater. Des.*, vol. 87, pp. 974–985, Dec. 2015, doi: 10.1016/j.matdes.2015.08.074.

[38] G. Phanikumar, P. Dutta, and K. Chattopadhyay, "Continuous welding of Cu–Ni dissimilar couple using CO_2 laser," *Sci. Technol. Weld. Join.*, vol. 10, no. 2, pp. 158–166, Apr. 2005, doi: 10.1179/174329305X36043.

[39] Y. Cai, H. Heng, F. Li, and M. Wang, "The influences of welding parameters on the metal vapor plume in fiber laser welding based on 3D reconstruction," *Opt. Laser Technol.*, vol. 107, pp. 1–7, Nov. 2018, doi: 10.1016/j.optlastec.2018.05.016.

[40] X. Chen *et al.*, "Sub-microsecond vapor plume dynamics under different keyhole penetration regimes in deep penetration laser welding," *J. Phys. Appl. Phys.*, vol. 50, no. 20, p. 205601, May 2017, doi: 10.1088/1361-6463/aa69b7.

[41] D. F. Farson and K. R. Kim, "Generation of optical and acoustic emissions in laser weld plumes," *J. Appl. Phys.*, vol. 85, no. 3, pp. 1329–1336, Feb. 1999, doi: 10.1063/1.369263.

[42] M. Gao, C. Chen, M. Hu, L. Guo, Z. Wang, and X. Zeng, "Characteristics of plasma plume in fiber laser welding of aluminum alloy," *Appl. Surf. Sci.*, vol. 326, pp. 181–186, Jan. 2015, doi: 10.1016/j.apsusc.2014.11.136.

[43] J. Greses, P. A. Hilton, C. Y. Barlow, and W. M. Steen, "Plume attenuation under high power Nd:yttritium–aluminum–garnet laser welding," *J. Laser Appl.*, vol. 16, no. 1, pp. 9–15, Feb. 2004, doi: 10.2351/1.1642636.

[44] J. Li *et al.*, "Analysis of vapor plume and keyhole dynamics in laser welding stainless steel with beam oscillation," *Infrared Phys. Technol.*, vol. 113, p. 103536, Mar. 2021, doi: 10.1016/j.infrared.2020.103536.

[45] S. Pang, X. Chen, W. Li, X. Shao, and S. Gong, "Efficient multiple time scale method for modeling compressible vapor plume dynamics inside transient keyhole during fiber laser welding," *Opt. Laser Technol.*, vol. 77, pp. 203–214, Mar. 2016, doi: 10.1016/j.optlastec.2015.09.024.

[46] S. Pang, X. Chen, X. Shao, S. Gong, and J. Xiao, "Dynamics of vapor plume in transient keyhole during laser welding of stainless steel: Local evaporation, plume swing and gas entrapment into porosity," *Opt. Lasers Eng.*, vol. 82, pp. 28–40, Jul. 2016, doi: 10.1016/j.optlaseng.2016.01.019.

[47] S. Pang, X. Chen, J. Zhou, X. Shao, and C. Wang, "3D transient multiphase model for keyhole, vapor plume, and weld pool dynamics in laser welding including the ambient pressure effect," *Opt. Lasers Eng.*, vol. 74, pp. 47–58, Nov. 2015, doi: 10.1016/j.optlaseng.2015.05.003.

[48] S. Pang, X. Shao, W. Li, X. Chen, and S. Gong, "Dynamic characteristics and mechanisms of compressible metallic vapor plume behaviors in transient keyhole during deep penetration fiber laser welding," *Appl. Phys. A*, vol. 122, no. 7, p. 702, Jul. 2016, doi: 10.1007/s00339-016-0230-5.

[49] P. Y. Shcheglov, A. V. Gumenyuk, I. B. Gornushkin, M. Rethmeier, and V. N. Petrovskiy, "Vapor–plasma plume investigation during high-power fiber laser welding," *Laser Phys.*, vol. 23, no. 1, p. 016001, Jan. 2013, doi: 10.1088/1054-660X/23/1/016001.

[50] P. Yu. Shcheglov, S. A. Uspenskiy, A. V. Gumenyuk, V. N. Petrovskiy, M. Rethmeier, and V. M. Yermachenko, "Plume attenuation of laser radiation during high power fiber laser welding," *Laser Phys. Lett.*, vol. 8, no. 6, pp. 475–480, Jun. 2011, doi: 10.1002/lapl.201110010.

[51] Z. Szymanski, J. Kurzyna, and W. Kalita, "The spectroscopy of the plasma plume induced during laser welding of stainless steel and titanium," *J. Phys. Appl. Phys.*, vol. 30, no. 22, pp. 3153–3162, Nov. 1997, doi: 10.1088/0022-3727/30/22/014.

[52] M. J. Zhang, G. Y. Chen, Y. Zhou, S. C. Li, and H. Deng, "Observation of spatter formation mechanisms in high-power fiber laser welding of thick plate," *Appl. Surf. Sci.*, vol. 280, pp. 868–875, Sep. 2013, doi: 10.1016/j.apsusc.2013.05.081.

[53] S.-J. Lee, S. Katayama, J.-D. Kim, and J. Suh, "The Effect of Plume Generated on the Microstructural Behavior of the Weld Mixed Zone in High-Speed Laser Dissimilar Welding," *Metals*, vol. 11, no. 10, p. 1556, Sep. 2021, doi: 10.3390/met11101556.

[54] D. A. Rusak, B. C. Castle, B. W. Smith, and J. D. Winefordner, "Recent trends and the future of laser-induced plasma spectroscopy," *TrAC Trends Anal. Chem.*, vol. 17, no. 8–9, pp. 453–461, Aug. 1998, doi: 10.1016/S0165-9936(98)00058-2.

[55] Y. A. Mayi *et al.*, "Laser-induced plume investigated by finite element modelling and scaling of particle entrainment in laser powder bed fusion," *J. Phys. Appl. Phys.*, vol. 53, no. 7, p. 075306, Feb. 2020, doi: 10.1088/1361-6463/ab5900.

[56] A. Al-Sayyad, P. Lama, J. Bardon, P. Hirchenhahn, L. Houssiau, and P. Plapper, "Laser joining of titanium alloy to polyamide: influence of process parameters on the joint strength and quality," *Int. J. Adv. Manuf. Technol.*, vol. 107, no. 5–6, pp. 2917–2925, Mar. 2020, doi: 10.1007/s00170-020-05123-1.

[57] S. T. Auwal, S. Ramesh, F. Yusof, and S. M. Manladan, "A review on laser beam welding of titanium alloys," *Int. J. Adv. Manuf. Technol.*, vol. 97, no. 1–4, pp. 1071–1098, Jul. 2018, doi: 10.1007/s00170-018-2030-x.

[58] M. Chludzinski, R. E. dos Santos, C. Churiaque, M. Ortega-Iguña, and J. M. Sánchez-Amaya, "Pulsed Laser Welding Applied to Metallic Materials—A Material Approach," *Metals*, vol. 11, no. 4, p. 640, Apr. 2021, doi: 10.3390/met11040640.

[59] M. Boley, F. Abt, R. Weber, and T. Graf, "X-Ray and Optical Videography for 3D Measurement of Capillary and Melt Pool Geometry in Laser Welding," *Phys. Procedia*, vol. 41, pp. 488–495, 2013, doi: 10.1016/j.phpro.2013.03.105.

[60] M. Vasilev *et al.*, "Non-contact in-process ultrasonic screening of thin fusion welded joints," *J. Manuf. Process.*, vol. 64, pp. 445–454, Apr. 2021, doi: 10.1016/j.jmapro.2021.01.033.

[61] A. Zösch, M. Seidel, and Imq Ingenieurbetrieb Für Materialprüfung Qualitätssicherung, "Non destructive testing of laser-welded lap seams by eddy current technique," *Citeseer*, p. 8, 2006.

[62] P. Kah, B. Mvola, J. Martikainen, and R. Suoranta, "Real Time Non-Destructive Testing Methods of Welding," *Adv. Mater. Res.*, vol. 933, pp. 109–116, May 2014, doi: 10.4028/www.scientific.net/AMR.933.109.

[63] I. J. Spalding, "Laser systems development," *Phys. Bull.*, vol. 22, no. 7, pp. 401–402, Jul. 1971, doi: 10.1088/0031-9112/22/7/013.

[64]   J. Alexis, J. D. Beguin, P. Cerra, and Y. Balcaen, "Yb: YAG Laser Welding of Aeronautical Alloys," *Mater. Sci. Forum*, vol. 941, pp. 1099–1104, Dec. 2018, doi: 10.4028/www.scientific.net/MSF.941.1099.

[65]   J. M. Sánchez-Amaya, T. Delgado, L. González-Rovira, and F. J. Botana, "Laser welding of aluminium alloys 5083 and 6082 under conduction regime," *Appl. Surf. Sci.*, vol. 255, no. 23, pp. 9512–9521, Sep. 2009, doi: 10.1016/j.apsusc.2009.07.081.

[66]   C. Magnus, "Feasibility study of metal to polymer hybrid joining," Laboratory of Welding Technology, Department of Mechanical Engineering, Lappeenranta University Of Technology, 2012.

[67]   J. Coroado *et al.*, "Fundamental understanding of the interaction of continuous wave laser with aluminium," *Int. J. Adv. Manuf. Technol.*, vol. 93, no. 9–12, pp. 3165–3174, Dec. 2017, doi: 10.1007/s00170-017-0702-6.

[68]   J. Hou, R. Li, C. Xu, T. Li, and Z. Shi, "A comparative study on microstructure and properties of pulsed laser welding and continuous laser welding of Al-25Si-4Cu-Mg high silicon aluminum alloy," *J. Manuf. Process.*, vol. 68, pp. 657–667, Aug. 2021, doi: 10.1016/j.jmapro.2021.05.064.

[69]   P. M. Sakate, S. Mullick, and M. Gopinath, "An investigation on physical phenomena of water-jet assisted underwater wet laser welding technique under continuous and pulsed mode operation," *Optik*, vol. 242, p. 167272, Sep. 2021, doi: 10.1016/j.ijleo.2021.167272.

[70]   X. Han, X. Tang, T. Wang, C. Shao, F. Lu, and H. Cui, "Role of ambient pressure in keyhole dynamics based on beam transmission path method for laser welding on Al alloy," *Int. J. Adv. Manuf. Technol.*, vol. 99, no. 5–8, pp. 1639–1651, Nov. 2018, doi: 10.1007/s00170-018-2592-7.

[71]   V. Dimatteo, A. Ascari, and A. Fortunato, "Continuous laser welding with spatial beam oscillation of dissimilar thin sheet materials (Al-Cu and Cu-Al): Process optimization and characterization," *J. Manuf. Process.*, vol. 44, pp. 158–165, Aug. 2019, doi: 10.1016/j.jmapro.2019.06.002.

[72]   Z. Lei, Y. Chen, H. Zhou, X. Wang, J. Liu, and P. Xia, "Melt flow and grain refining in laser oscillating welding of β-21S titanium alloy," *Opt. Laser Technol.*, vol. 145, p. 107496, Jan. 2022, doi: 10.1016/j.optlastec.2021.107496.

[73]   M. M. Quazi *et al.*, "Current research and development status of dissimilar materials laser welding of titanium and its alloys," *Opt. Laser Technol.*, vol. 126, p. 106090, Jun. 2020, doi: 10.1016/j.optlastec.2020.106090.

[74]   Y. Tzeng, "Parametric analysis of the pulsed Nd:YAG laser seam-welding process," *J. Mater. Process. Technol.*, vol. 102, no. 1–3, pp. 40–47, May 2000, doi: 10.1016/S0924-0136(00)00447-7.

[75]   X.-L. Gao, J. Liu, L.-J. Zhang, and J.-X. Zhang, "Effect of the overlapping factor on the microstructure and mechanical properties of pulsed Nd:YAG laser welded Ti6Al4V sheets," *Mater. Charact.*, vol. 93, pp. 136–149, Jul. 2014, doi: 10.1016/j.matchar.2014.04.005.

[76]   H.-C. Chen, G. Bi, B. Y. Lee, and C. K. Cheng, "Laser welding of CP Ti to stainless steel with different temporal pulse shapes," *J. Mater. Process. Technol.*, vol. 231, pp. 58–65, May 2016, doi: 10.1016/j.jmatprotec.2015.12.016.

[77]   F. Brueckner *et al.*, "Enhanced manufacturing possibilities using multi-materials in laser metal deposition," *J. Laser Appl.*, vol. 30, no. 3, p. 032308, Aug. 2018, doi: 10.2351/1.5040639.

[78]   M. S. Dresselhaus, *SOLID STATE PHYSICS PART II*. 2001.

[79]   F. Wooten and S. P. Davis, "Optical Properties of Solids," *Am. J. Phys.*, vol. 41, no. 7, pp. 939–940, Jul. 1973, doi: 10.1119/1.1987434.

[80] X. Jin, L. Li, and Y. Zhang, "A study on fresnel absorption and reflections in the keyhole in deep penetration laser welding," *J. Phys. Appl. Phys.*, vol. 35, no. 18, pp. 2304–2310, Sep. 2002, doi: 10.1088/0022-3727/35/18/312.

[81] A. M. Prokhorov, V. I. Konov, I. Ursu, and I. N. Mihăilescu, *Laser Heating of Metals*. CRC Press, 2018.

[82] M. Volterrani, A. Minelli, M. Gaetani, N. Grossi, S. Magni, and L. Caturegli, "Reflectance, absorbance and transmittance spectra of bermudagrass and manilagrass turfgrass canopies," *PLOS ONE*, vol. 12, no. 11, p. e0188080, Nov. 2017, doi: 10.1371/journal.pone.0188080.

[83] C. Niu, T. Zhu, and Y. Lv, "Influence of Surface Morphology on Absorptivity of Light-Absorbing Materials," *Int. J. Photoenergy*, vol. 2019, pp. 1–9, Sep. 2019, doi: 10.1155/2019/1476217.

[84] C. Bertrand, O. Laplanche, J. P. Rocca, Y. Le Petitcorps, and S. Nammour, "Effect of the combination of different welding parameters on melting characteristics of grade 1 titanium with a pulsed Nd–Yag laser," *Lasers Med. Sci.*, vol. 22, no. 4, pp. 237–244, Nov. 2007, doi: 10.1007/s10103-006-0438-2.

[85] A. Kumar and M. C. Gupta, "Surface preparation of Ti–3Al–2.5V alloy tubes for welding using a fiber laser," *Opt. Lasers Eng.*, vol. 47, no. 11, pp. 1259–1265, Nov. 2009, doi: 10.1016/j.optlaseng.2009.05.011.

[86] C. Sainte-Catherine, M. Jeandin, D. Kechemair, J.-P. Ricaud, and L. Sabatier, "STUDY OF DYNAMIC ABSORPTIVITY AT 10.6 µm (CO_2) AND 1.06 µm (Nd-YAG) WAVELENGTHS AS A FUNCTION OF TEMPERATURE," *J. Phys. IV*, vol. 01, no. C7, pp. C7-151-C7-157, Dec. 1991, doi: 10.1051/jp4:1991741.

[87] T. R. Allen, T. G. Fleming, T. J. H. Krause, and J. M. Fraser, "Simultaneous high-speed keyhole depth and absorptance measurements in laser spot welding of dissimilar metals," *Procedia CIRP*, vol. 111, pp. 5–9, 2022, doi: 10.1016/j.procir.2022.08.041.

[88] V. M. Fomin, A. G. Malikov, A. M. Orishich, and V. B. Shulyat'ev, "Energy conditions of gas laser cutting of thick steel sheets," *J. Appl. Mech. Tech. Phys.*, vol. 52, no. 3, pp. 340–346, May 2011, doi: 10.1134/S0021894411030023.

[89] A. Mahrle, M. Lütke, and E. Beyer, "Fibre laser cutting: Beam absorption characteristics and gas-free remote cutting," *Proc. Inst. Mech. Eng. Part C J. Mech. Eng. Sci.*, vol. 224, no. 5, pp. 1007–1018, May 2010, doi: 10.1243/09544062JMES1747.

[90] T. R. Allen, W. Huang, J. R. Tanner, W. Tan, J. M. Fraser, and B. J. Simonds, "Energy-Coupling Mechanisms Revealed through Simultaneous Keyhole Depth and Absorptance Measurements during Laser-Metal Processing," *Phys. Rev. Appl.*, vol. 13, no. 6, p. 064070, Jun. 2020, doi: 10.1103/PhysRevApplied.13.064070.

[91] G. Nordet *et al.*, "Absorptivity measurements during laser powder bed fusion of pure copper with a 1 kW cw green laser," *Opt. Laser Technol.*, vol. 147, p. 107612, Mar. 2022, doi: 10.1016/j.optlastec.2021.107612.

[92] R. Indhu, V. Vivek, L. Sarathkumar, A. Bharatish, and S. Soundarapandian, "Overview of Laser Absorptivity Measurement Techniques for Material Processing," *Lasers Manuf. Mater. Process.*, vol. 5, no. 4, pp. 458–481, Dec. 2018, doi: 10.1007/s40516-018-0075-1.

[93] W. Jones and N. H. March, *Theoretical solid state physics. 2: Non-equilibrium and disorder*, 1. publ. New York: Dover, 1985.

[94] G. C. Rodrigues, H. Vanhove, and J. R. Duflou, "Direct Diode Lasers for Industrial Laser Cutting: A Performance Comparison with Conventional Fiber and CO2 Technologies," *Phys. Procedia*, vol. 56, pp. 901–908, 2014, doi: 10.1016/j.phpro.2014.08.109.

[95] R. Fabbro, S. Slimani, F. Coste, and F. Briand, "Analysis of the various melt pool hydrodynamic regimes observed during cw Nd-YAG deep penetration laser welding," in *International*

Congress on Applications of Lasers & Electro-Optics, Orlando, Florida, USA: Laser Institute of America, 2007, p. 802. doi: 10.2351/1.5061093.

[96] C. Zhang, Y. Yu, C. Chen, X. Zeng, and M. Gao, "Suppressing porosity of a laser keyhole welded Al-6Mg alloy via beam oscillation," *J. Mater. Process. Technol.*, vol. 278, p. 116382, Apr. 2020, doi: 10.1016/j.jmatprotec.2019.116382.

[97] R. Fabbro, K. Hirano, and S. Pang, "Analysis of the physical processes occurring during deep penetration laser welding under reduced pressure," *J. Laser Appl.*, vol. 28, no. 2, p. 022427, May 2016, doi: 10.2351/1.4944002.

[98] L. I. Kuznetsov, "Recoil momentum at a solid surface during developed laser ablation," *Quantum Electron.*, vol. 23, no. 12, pp. 1035–1038, Dec. 1993, doi: 10.1070/QE1993v023n12ABEH003279.

[99] R. Fabbro, S. Slimani, F. Coste, F. Briand, B. Dlubak, and G. Loisel, "Analysis of basic processes inside the keyhole during deep penetration Nd-YAG cw laser welding," in *International Congress on Applications of Lasers & Electro-Optics*, Scottsdale, Arizona, USA: Laser Institute of America, 2006, p. 101. doi: 10.2351/1.5060748.

[100] R. Pordzik and P. Woizeschke, "An Experimental Approach for the Direct Measurement of Temperatures in the Vicinity of the Keyhole Front Wall during Deep-Penetration Laser Welding," *Appl. Sci.*, vol. 10, no. 11, p. 3951, Jun. 2020, doi: 10.3390/app10113951.

[101] Y. Sone, *Kinetic Theory and Fluid Dynamics*. in Modeling and Simulation in Science, Engineering and Technology. Boston, MA: Birkhäuser Boston, 2002. doi: 10.1007/978-1-4612-0061-1.

[102] I. Krivtsun, S. Sukhorukov, V. Sidorets, and O. Kovalev, "modelling of the processes of evaporation of metal and gas dynamics of metal vapour inside a keyhole in laser welding," *Paton Weld. J*, vol. 10, pp. 16–21, 2008.

[103] J. Zhou and H. L. Tsai, "Welding heat transfer," in *Processes and Mechanisms of Welding Residual Stress and Distortion*, Elsevier, 2005, pp. 32–98. doi: 10.1533/9781845690939.1.32.

[104] C. Kägeler and M. Schmidt, "Frequency-based analysis of weld pool dynamics and keyhole oscillations at laser beam welding of galvanized steel sheets," *Phys. Procedia*, vol. 5, pp. 447–453, 2010, doi: 10.1016/j.phpro.2010.08.072.

[105] S. Li, G. Chen, S. Katayama, and Y. Zhang, "Relationship between spatter formation and dynamic molten pool during high-power deep-penetration laser welding," *Appl. Surf. Sci.*, vol. 303, pp. 481–488, Jun. 2014, doi: 10.1016/j.apsusc.2014.03.030.

[106] S. M. Robertson, A. F. H. Kaplan, and J. Frostevarg, "Material ejection attempts during laser keyhole welding," *J. Manuf. Process.*, vol. 67, pp. 91–100, Jul. 2021, doi: 10.1016/j.jmapro.2021.04.052.

[107] A. F. H. Kaplan and J. Powell, "Spatter in laser welding," *J. Laser Appl.*, vol. 23, no. 3, p. 032005, Aug. 2011, doi: 10.2351/1.3597830.

[108] I. Tomashchuk, "Assemblage hétérogène cuivre-inox et TA6V-inox par les faisceaux de haute énergie: compréhension et modélisation des phénomènes physico-chimiques," Theses, Université de Bourgogne, 2010. [Online]. Available: https://tel.archives-ouvertes.fr/tel-00651486

[109] S. Kou, *Welding metallurgy*, 2. ed. Hoboken, NJ: Wiley-Interscience, 2003.

[110] J. M. Jouvard, K. Girard, and O. Perret, "Keyhole formation and power deposition in Nd:YAG laser spot welding," *J. Phys. Appl. Phys.*, vol. 34, no. 18, pp. 2894–2901, Sep. 2001, doi: 10.1088/0022-3727/34/18/324.

[111] R. Cunningham *et al.*, "Keyhole threshold and morphology in laser melting revealed by ultrahigh-speed x-ray imaging," *Science*, vol. 363, no. 6429, pp. 849–852, Feb. 2019, doi: 10.1126/science.aav4687.

[112] M. Miyagi and J. Wang, "Keyhole dynamics and morphology visualized by in-situ X-ray imaging in laser melting of austenitic stainless steel," *J. Mater. Process. Technol.*, vol. 282, p. 116673, Aug. 2020, doi: 10.1016/j.jmatprotec.2020.116673.

[113] K. Schricker *et al.*, "Characterization of keyhole dynamics in laser welding of copper by means of high-speed synchrotron X-ray imaging," *Procedia CIRP*, vol. 111, pp. 501–506, 2022, doi: 10.1016/j.procir.2022.08.079.

[114] M. Miyagi, H. Wang, R. Yoshida, Y. Kawahito, H. Kawakami, and T. Shoubu, "Effect of alloy element on weld pool dynamics in laser welding of aluminum alloys," *Sci. Rep.*, vol. 8, no. 1, p. 12944, Dec. 2018, doi: 10.1038/s41598-018-31350-4.

[115] P. J. L. Webster *et al.*, "Fully-automatic laser welding and micro-sculpting with universal in situ inline coherent imaging," vol. 39, no. 21, pp. 6217–6220, 2014.

[116] M. Boley, F. Fetzer, R. Weber, and T. Graf, "Statistical evaluation method to determine the laser welding depth by optical coherence tomography," *Opt. Lasers Eng.*, vol. 119, pp. 56–64, Aug. 2019, doi: 10.1016/j.optlaseng.2019.03.014.

[117] M. Werner *et al.*, "Influence of the incident angle on the OCT measurement during remote laser beam welding," *Procedia CIRP*, vol. 111, pp. 513–517, 2022, doi: 10.1016/j.procir.2022.08.081.

[118] T. R. Allen, B. J. Simonds, J. R. Tanner, and J. M. Fraser, "Simultaneous in operando monitoring of keyhole depth and absorptance in laser processing of AISI 316 stainless steel at 200 kHz," *Procedia CIRP*, vol. 94, pp. 419–424, 2020, doi: 10.1016/j.procir.2020.09.157.

[119] M. Kogel Hollacher, "Laser welding using optical coherence tomography," *Laser User*, vol. 92, pp. 26–27, 2019.

[120] M. Kos, E. Arko, H. Kosler, and M. Jezeršek, "Remote-laser welding system with in-line adaptive 3D seam tracking and power control," *Procedia CIRP*, vol. 81, pp. 1189–1194, 2019, doi: 10.1016/j.procir.2019.03.290.

[121] T. Purtonen, A. Kalliosaari, and A. Salminen, "Monitoring and Adaptive Control of Laser Processes," *Phys. Procedia*, vol. 56, pp. 1218–1231, 2014, doi: 10.1016/j.phpro.2014.08.038.

[122] S. W. Kercel, R. A. Kisner, M. B. Klein, G. D. Bacher, and B. F. Pouet, "In-process detection of weld defects using laser-based ultrasound," presented at the Photonics East '99, A. Wang, Ed., Boston, MA, Dec. 1999, pp. 81–92. doi: 10.1117/12.372829.

[123] S. Lee, S. Ahn, and C. Park, "Analysis of Acoustic Emission Signals During Laser Spot Welding of SS304 Stainless Steel," *J. Mater. Eng. Perform.*, vol. 23, no. 3, pp. 700–707, Mar. 2014, doi: 10.1007/s11665-013-0791-9.

[124] D. Farson, A. Ali, and Y. Sang, "Relationship of optical and acoustic emissions to laser weld penetration," *Weld. J.*, vol. 77, no. 4, p. 142, 1998.

[125] J. Hoffman, Z. Szymanski, J. Jakubowski, and A. Kolasa, "Analysis of acoustic and optical signals used as a basis for controlling laser-welding processes," *Weld. Int.*, vol. 16, no. 1, pp. 18–25, Jan. 2002, doi: 10.1080/09507110209549484.

[126] F. Bardin *et al.*, "Closed-loop power and focus control of laser welding for full-penetration monitoring," *Appl. Opt.*, vol. 44, no. 1, p. 13, Jan. 2005, doi: 10.1364/AO.44.000013.

[127] J. Günther, "Machine intelligence for adaptable closed loop and open loop production engineering systems," *Tech. Univ. Munchen*, 2018.

[128] A. Molino *et al.*, "FPGA implementation of time–frequency analysis algorithms for laser welding monitoring," *Microprocess. Microsyst.*, vol. 33, no. 3, pp. 179–190, May 2009, doi: 10.1016/j.micpro.2008.11.001.

[129] M. Wagner *et al.*, "Digitalized laser beam welding for inline quality assurance through the use of multiple sensors and machine learning," *Procedia CIRP*, vol. 111, pp. 518–521, 2022, doi: 10.1016/j.procir.2022.08.082.

[130] S. Kang, M. Kang, Y. H. Jang, and C. Kim, "Deep learning-based penetration depth prediction in Al/Cu laser welding using spectrometer signal and CCD image," *J. Laser Appl.*, vol. 34, no. 4, p. 042035, Nov. 2022, doi: 10.2351/7.0000767.

[131] I. Eriksson, "New high-speed photography technique for observation of fluid flow in laser welding," *Opt. Eng.*, vol. 49, no. 10, p. 100503, Oct. 2010, doi: 10.1117/1.3502567.

[132] M. Luo and Y. C. Shin, "Estimation of keyhole geometry and prediction of welding defects during laser welding based on a vision system and a radial basis function neural network," *Int. J. Adv. Manuf. Technol.*, vol. 81, no. 1–4, pp. 263–276, Oct. 2015, doi: 10.1007/s00170-015-7079-1.

[133] S. Li, G. Chen, M. Zhang, Y. Zhou, and Y. Zhang, "Dynamic keyhole profile during high-power deep-penetration laser welding," *J. Mater. Process. Technol.*, vol. 214, no. 3, pp. 565–570, Mar. 2014, doi: 10.1016/j.jmatprotec.2013.10.019.

[134] I. Tomashchuk, M. Mostafa, T. Caudwell, P. Sallamand, and M. Duband, "Behavior of laser induced keyhole during dissimilar welding of metals," *Lasers Manuf. Conf. 2017*, pp. 26–29, 2017.

[135] M. Seibold, K. Schricker, and J. P. Bergmann, "Systematic adjustment of the joining time in pulsed laser beam welding of aluminum-copper joints by means of a closed-loop control," *J. Adv. Join. Process.*, vol. 5, p. 100104, Jun. 2022, doi: 10.1016/j.jajp.2022.100104.

[136] Y. Arata, H. Maruo, I. Miyamoto, and S. Takeuchi, "Dynamic behavior of laser welding and cutting," in *Proceedings of the 7th Intl. Conf. on Electron and Ion Beam Sci and Tech*, 1976, pp. 111–128.

[137] Y. Zhang, G. Chen, H. Wei, and J. Zhang, "A novel 'sandwich' method for observation of the keyhole in deep penetration laser welding," *Opt. Lasers Eng.*, vol. 46, no. 2, pp. 133–139, Feb. 2008, doi: 10.1016/j.optlaseng.2007.08.010.

[138] M. J. Torkamany, F. Malek Ghaini, and R. Poursalehi, "An insight to the mechanism of weld penetration in dissimilar pulsed laser welding of niobium and Ti–6Al–4V," *Opt. Laser Technol.*, vol. 79, pp. 100–107, May 2016, doi: 10.1016/j.optlastec.2015.11.005.

[139] Q. Nguyen, A. Azadkhou, M. Akbari, A. Panjehpour, and A. Karimipour, "Experimental investigation of temperature field and fusion zone microstructure in dissimilar pulsed laser welding of austenitic stainless steel and copper," *J. Manuf. Process.*, vol. 56, pp. 206–215, Aug. 2020, doi: 10.1016/j.jmapro.2020.03.037.

[140] I. Tomashchuk, M. Mostafa, P. Sallamand, and M. Duband, "Modeling of the keyhole asymmetry in dissimilar laser welding," presented at the COMSOL Conference, 2020.

[141] J. Zhou, H.-L. Tsai, and P.-C. Wang, "Transport Phenomena and Keyhole Dynamics during Pulsed Laser Welding," *J. Heat Transf.*, vol. 128, no. 7, pp. 680–690, Jul. 2006, doi: 10.1115/1.2194043.

[142] J. Mazumder and A. Kar, *Theory and Application of Laser Chemical Vapor Deposition*. Boston, MA: Springer US, 1995. doi: 10.1007/978-1-4899-1430-9.

[143] D. Bäuerle, *Laser Processing and Chemistry*. Berlin, Heidelberg: Springer Berlin Heidelberg, 2011. doi: 10.1007/978-3-642-17613-5.

[144] Y. Peng, W. Chen, C. Wang, G. Bao, and Z. Tian, "Controlling the plasma of deep penetration laser welding to increase power efficiency," *J. Phys. Appl. Phys.*, vol. 34, no. 21, pp. 3145–3149, Nov. 2001, doi: 10.1088/0022-3727/34/21/307.

[145] W. Qiu, L. Yang, S. Zhao, R. Yang, and T. Liu, "A study on plasma plume fluctuation characteristic during A304 stainless steel laser welding," *J. Manuf. Process.*, vol. 33, pp. 1–9, Jun. 2018, doi: 10.1016/j.jmapro.2018.04.001.

[146] S. A. Uspenskiy, P. Yu. Shcheglov, V. N. Petrovskiy, A. V. Gumenyuk, and M. Rethmeier, "Spectral diagnostics of a vapor-plasma plume produced during welding with a high-power ytterbium fiber laser," *Opt. Spectrosc.*, vol. 115, no. 1, pp. 140–146, Jul. 2013, doi: 10.1134/S0030400X13070205.

[147] J. D. Kim, Y. H. Kim, and J. S. Oh, "Diagnostics of Laser-Induced Plasma in Welding of Aluminum Alloy," *Key Eng. Mater.*, vol. 261–263, pp. 1671–1676, Apr. 2004, doi: 10.4028/www.scientific.net/KEM.261-263.1671.

[148] J. D. Kim, J. S. Oh, M. H. Lee, and Y. S. Kim, "Spectroscopic Analysis of Plasma Induced in Laser Welding of Aluminum Alloys," *Mater. Sci. Forum*, vol. 449–452, pp. 429–432, Mar. 2004, doi: 10.4028/www.scientific.net/MSF.449-452.429.

[149] S. J. Hill, Ed., *Inductively coupled plasma spectrometry and its applications*, 2nd ed. in Analytical chemistry. Oxford ; Ames, Iowa: Blackwell Pub, 2007.

[150] G. J. Pendley, "High speed imaging technology: yesterday, today, and tomorrow," presented at the 25th international Congress on High-Speed photography and Photonics, C. Cavailler, G. P. Haddleton, and M. Hugenschmidt, Eds., Beaune, Finland, Jul. 2003, p. 110. doi: 10.1117/12.516992.

[151] M. Vollmer and K.-P. Möllmann, "High speed and slow motion: the technology of modern high speed cameras," *Phys. Educ.*, vol. 46, no. 2, pp. 191–202, Mar. 2011, doi: 10.1088/0031-9120/46/2/007.

[152] B. Carnathan, "Sony Alpha 7 III Specifications," The-Digital-Picture.com. Accessed: Apr. 03, 2022. [Online]. Available: https://www.the-digital-picture.com/Reviews/Camera-Specifications.aspx?Camera=1194

[153] Vision Research, "Phantom® v2012 DATASHEET." AMETEK ® MATERIALS ANALYSIS DIVISION.

[154] J. Manin, S. A. Skeen, and L. M. Pickett, "Performance comparison of state-of-the-art high-speed video cameras for scientific applications," *Opt. Eng.*, vol. 57, no. 12, p. 1, Dec. 2018, doi: 10.1117/1.OE.57.12.124105.

[155] J. Xie, "Dual beam laser welding," *Welding Journal*, p. 223/S-230/S, Oct. 2002.

[156] R. Fabbro, S. Slimani, I. Doudet, F. Coste, and F. Briand, "Experimental study of the dynamical coupling between the induced vapour plume and the melt pool for Nd–Yag CW laser welding," *J. Phys. Appl. Phys.*, vol. 39, no. 2, pp. 394–400, Jan. 2006, doi: 10.1088/0022-3727/39/2/023.

[157] I. Eriksson, J. Powell, and A. F. H. Kaplan, "Signal overlap in the monitoring of laser welding," *Meas. Sci. Technol.*, vol. 21, no. 10, p. 105705, Oct. 2010, doi: 10.1088/0957-0233/21/10/105705.

[158] T. Wang, J. Chen, X. Gao, and W. Li, "Quality Monitoring for Laser Welding Based on High-Speed Photography and Support Vector Machine," *Appl. Sci.*, vol. 7, no. 3, p. 299, Mar. 2017, doi: 10.3390/app7030299.

[159] H. Zheng, H. Li, L. Lang, S. Gong, and Y. Ge, "Effects of scan speed on vapor plume behavior and spatter generation in laser powder bed fusion additive manufacturing," *J. Manuf. Process.*, vol. 36, pp. 60–67, Dec. 2018, doi: 10.1016/j.jmapro.2018.09.011.

[160] S. Mihai, D. Chioibasu, M. A. Mahmood, L. Duta, M. Leparoux, and A. C. Popescu, "Real-Time Defects Analyses Using High-Speed Imaging during Aluminum Magnesium Alloy Laser Welding," *Metals*, vol. 11, no. 11, p. 1877, Nov. 2021, doi: 10.3390/met11111877.

[161] Y. Kawahito, N. Matsumoto, M. Mizutani, and S. Katayama, "Characterisation of plasma induced during high power fibre laser welding of stainless steel," *Sci. Technol. Weld. Join.*, vol. 13, no. 8, pp. 744–748, Nov. 2008, doi: 10.1179/136217108X329313.

[162] C. Brock, F. Tenner, F. Klämpfl, R. Hohenstein, and M. Schmidt, "Detection of Weld Defects by High Speed Imaging of the Vapor Plume," *Phys. Procedia*, vol. 41, pp. 539–543, 2013, doi: 10.1016/j.phpro.2013.03.113.

[163] Y. Huang, X. Hua, F. Li, C. Shen, G. Mou, and B. Tang, "Spatter feature analysis in laser welding based on motion tracking method," *J. Manuf. Process.*, vol. 55, pp. 220–229, Jul. 2020, doi: 10.1016/j.jmapro.2020.04.016.

[164] C.-H. Kim and D.-C. Ahn, "Coaxial monitoring of keyhole during Yb:YAG laser welding," *Opt. Laser Technol.*, vol. 44, no. 6, pp. 1874–1880, Sep. 2012, doi: 10.1016/j.optlastec.2012.02.025.

[165] M. Seibold, H. Friedmann, K. Schricker, and J. P. Bergmann, "Process control by real-time pulse shaping in laser beam welding of different material combinations," *Procedia CIRP*, vol. 94, pp. 769–774, 2020, doi: 10.1016/j.procir.2020.09.137.

[166] L. Nicolosi, F. Abt, A. Blug, A. Heider, R. Tetzlaff, and H. Höfler, "A novel spatter detection algorithm based on typical cellular neural network operations for laser beam welding processes," *Meas. Sci. Technol.*, vol. 23, no. 1, p. 015401, Jan. 2012, doi: 10.1088/0957-0233/23/1/015401.

[167] B. Xue, B. Chang, and D. Du, "Monitoring of high-speed laser welding process based on vapor plume," *Opt. Laser Technol.*, vol. 147, p. 107649, Mar. 2022, doi: 10.1016/j.optlastec.2021.107649.

[168] J. Sheng, Y. Cai, F. Li, and X. Hua, "Online detection method of weld penetration based on molten pool morphology and metallic vapor radiation for fiber laser welding," *Int. J. Adv. Manuf. Technol.*, vol. 92, no. 1–4, pp. 231–245, Sep. 2017, doi: 10.1007/s00170-017-0129-0.

[169] P. Zhao, R. Lu, J. Wu, and Y. Zhang, "Monitoring method of weld penetration in laser keyhole welding irradiated by laser auxiliary illuminant," *J. Laser Appl.*, vol. 32, no. 2, p. 022037, May 2020, doi: 10.2351/7.0000104.

[170] J. Xu, Y. Rong, Y. Huang, P. Wang, and C. Wang, "Keyhole-induced porosity formation during laser welding," *J. Mater. Process. Technol.*, vol. 252, pp. 720–727, Feb. 2018, doi: 10.1016/j.jmatprotec.2017.10.038.

[171] J. Volpp and D. Freimann, "Indirect measurement of keyhole pressure oscillations during laser deep penetration welding," in *International Congress on Applications of Lasers & Electro-Optics*, Miami, Florida, USA: Laser Institute of America, 2013, pp. 334–340. doi: 10.2351/1.5062896.

[172] J. Zou, X. Han, Y. Zhao, Q. Wu, and R. Xiao, "Investigation on plume formation during fiber laser keyhole welding based on in-situ measurement of particles in plume," *J. Manuf. Process.*, vol. 65, pp. 153–160, May 2021, doi: 10.1016/j.jmapro.2021.03.030.

[173] J. Wang, C. Wang, D. Liu, X. Hu, Y. Yu, and X. Meng, "Study on periodical oscillation of plasma/vapor induced in high power fibre laser penetration welding," in *Pacific International Conference on Applications of Lasers and Optics*, Wuhan, People's Republic of China: Laser Institute of America, 2010, p. 402. doi: 10.2351/1.5057196.

[174] J. P. Fugal, R. A. Shaw, E. W. Saw, and A. V. Sergeyev, "Airborne digital holographic system for cloud particle measurements," *Appl. Opt.*, vol. 43, no. 32, p. 5987, Nov. 2004, doi: 10.1364/AO.43.005987.

[175] G. T. Shrivakshan, "A Comparison of various Edge Detection Techniques used in Image Processing," vol. 9, no. 5, p. 8, 2012.

[176] C. A. Schneider, W. S. Rasband, and K. W. Eliceiri, "NIH Image to ImageJ: 25 years of image analysis," *Nat. Methods*, pp. 671–675, Jun. 2012, doi: https://doi.org/10.1038/nmeth.2089.

[177] L. Nichele, V. Persichetti, M. Lucidi, and G. Cincotti, "Quantitative evaluation of ImageJ thresholding algorithms for microbial cell counting," *OSA Contin.*, vol. 3, no. 6, p. 1417, Jun. 2020, doi: 10.1364/OSAC.393971.

[178] Y. Gao, P. Zhong, X. Tang, H. Hu, and P. Xu, "Feature Extraction of Laser Welding Pool Image and Application in Welding Quality Identification," *IEEE Access*, vol. 9, pp. 120193–120202, 2021, doi: 10.1109/ACCESS.2021.3108462.

[179] G. Q. Liu and X. D. Gao, "Investigation of Image Characteristics of Plume and Spatters during High-Power Disk Laser Welding," *Adv. Mater. Res.*, vol. 709, pp. 301–304, Jun. 2013, doi: 10.4028/www.scientific.net/AMR.709.301.

[180] Y. Zhang, F. Li, Z. Liang, Y. Ying, Q. Lin, and H. Wei, "Correlation analysis of penetration based on keyhole and plasma plume in laser welding," *J. Mater. Process. Technol.*, vol. 256, pp. 1–12, Jun. 2018, doi: 10.1016/j.jmatprotec.2018.01.032.

[181] R. Zheng, P. Zhang, A. Duan, and P. Xiao, "Measurement of laser welding pool geometry using a closed convex active contour model," *Meas. Sci. Technol.*, vol. 25, no. 3, p. 035603, Mar. 2014, doi: 10.1088/0957-0233/25/3/035603.

[182] J. Yousefi, "Image Binarization using Otsu Thresholding Algorithm," 2015, doi: 10.13140/RG.2.1.4758.9284.

[183] X. Xu, S. Xu, L. Jin, and E. Song, "Characteristic analysis of Otsu threshold and its applications," *Pattern Recognit. Lett.*, vol. 32, no. 7, pp. 956–961, May 2011, doi: 10.1016/j.patrec.2011.01.021.

[184] M. Cheriet, J. N. Said, and C. Y. Suen, "A recursive thresholding technique for image segmentation," *IEEE Trans. Image Process.*, vol. 7, no. 6, pp. 918–921, Jun. 1998, doi: 10.1109/83.679444.

[185] J. Gong, L. Li, and W. Chen, "Fast recursive algorithms for two-dimensional thresholding," *Pattern Recognit.*, vol. 31, no. 3, pp. 295–300, Mar. 1998, doi: 10.1016/S0031-3203(97)00043-5.

[186] D.-Y. Huang and C.-H. Wang, "Optimal multi-level thresholding using a two-stage Otsu optimization approach," *Pattern Recognit. Lett.*, vol. 30, no. 3, pp. 275–284, Feb. 2009, doi: 10.1016/j.patrec.2008.10.003.

[187] J. Chen, T. Wang, X. Gao, and L. Wei, "Real-time monitoring of high-power disk laser welding based on support vector machine," *Comput. Ind.*, vol. 94, pp. 75–81, Jan. 2018, doi: 10.1016/j.compind.2017.10.003.

[188] T. Donnelly, G. O'Connell, and J. G. Lunney, "Metal Nanoparticle Film Deposition by Femtosecond Laser Ablation at Atmospheric Pressure," *Nanomaterials*, vol. 10, no. 11, p. 2118, Oct. 2020, doi: 10.3390/nano10112118.

[189] A. Mohanta, M. Leistner, and M. Leparoux, "Effect of plume dynamics on surface contamination during interaction of millisecond infrared fiber laser with titanium," *Opt. Lasers Eng.*, vol. 153, p. 106996, Jun. 2022, doi: 10.1016/j.optlaseng.2022.106996.

[190] D. Ye, K. Zhu, J. Y. H. Fuh, Y. Zhang, and H. G. Soon, "The investigation of plume and spatter signatures on melted states in selective laser melting," *Opt. Laser Technol.*, vol. 111, pp. 395–406, Apr. 2019, doi: 10.1016/j.optlastec.2018.10.019.

[191] P. Shcheglov, "Study of Vapour-Plasma Plume during High Power Fiber Laser Beam Influence on Metals," *Bundesanst. Für Mater. -Prüf. BAM*, p. 125, 2012.

[192] R. S. Adrain and J. Watson, "Laser microspectral analysis: a review of principles and applications," *J. Phys. Appl. Phys.*, vol. 17, no. 10, pp. 1915–1940, Oct. 1984, doi: 10.1088/0022-3727/17/10/004.

[193] P. Drude, "Zur Elektronentheorie der Metalle," *Ann. Phys.*, vol. 306, no. 3, pp. 566–613, 1900, doi: 10.1002/andp.19003060312.

[194] R. Siegel and J. R. Howell, *THERMAL RADIATION HEAT TRANSFER Volume III Radiation Transfer With Absorbing, Emitting, and Scattering Media*, vol. 3. 1971.

[195] H.-J. Kunze, *Introduction to Plasma Spectroscopy*, vol. 56. in Springer Series on Atomic, Optical, and Plasma Physics, vol. 56. Berlin, Heidelberg: Springer Berlin Heidelberg, 2009. doi: 10.1007/978-3-642-02233-3.

[196] G. Cristoforetti *et al.*, "Local Thermodynamic Equilibrium in Laser-Induced Breakdown Spectroscopy: Beyond the McWhirter criterion," *Spectrochim. Acta Part B At. Spectrosc.*, vol. 65, no. 1, pp. 86–95, Jan. 2010, doi: 10.1016/j.sab.2009.11.005.

[197] A. Mendys, M. Kański, A. Farah-Sougueh, S. Pellerin, B. Pokrzywka, and K. Dzierżęga, "Investigation of the local thermodynamic equilibrium of laser-induced aluminum plasma by Thomson scattering technique," *Spectrochim. Acta Part B At. Spectrosc.*, vol. 96, pp. 61–68, Jun. 2014, doi: 10.1016/j.sab.2014.03.009.

[198] H. R. Griem, *Principles of plasma spectroscopy*, 1. paperback ed. in Cambridge monographs on plasma physics, no. 2. Cambridge: Cambridge University Press, 2005.

[199] A. Farah Sougueh, "Spectroscopie optique d'émission et spectroscopie laser pour le diagnostic des plasmas induits par laser.pdf," Theses, Université de Orléans, 2015. [Online]. Available: https://tel.archives-ouvertes.fr/tel-01371913

[200] A. Kramida and Y. Ralchenko, "NIST Atomic Spectra Database, NIST Standard Reference Database 78." National Institute of Standards and Technology, 1999. doi: 10.18434/T4W30F.

[201] K. S. Krane, *Modern physics*, 3rd ed. Hoboken, NJ: Wiley, 2012.

[202] H. Aroeste and W. C. Benton, "Emissivity of Hydrogen Atoms at High Temperatures," *J. Appl. Phys.*, vol. 27, no. 2, pp. 117–121, Feb. 1956, doi: 10.1063/1.1722319.

[203] A. Mohanta, B. Lanfant, and M. Leparoux, "In-situ optical emission spectroscopic investigation of direct laser melting process during fabrication of Ti-6Al-4V parts," p. 6, 2019.

[204] C. Aragón and J. A. Aguilera, "Characterization of laser induced plasmas by optical emission spectroscopy: A review of experiments and methods," *Spectrochim. Acta Part B At. Spectrosc.*, vol. 63, no. 9, pp. 893–916, Sep. 2008, doi: 10.1016/j.sab.2008.05.010.

[205] N. Konjević, M. Ivković, and S. Jovićević, "Spectroscopic diagnostics of laser-induced plasmas," *Spectrochim. Acta Part B At. Spectrosc.*, vol. 65, no. 8, pp. 593–602, Aug. 2010, doi: 10.1016/j.sab.2010.03.009.

[206] J.-M. Li *et al.*, "Self-absorption reduction in laser-induced breakdown spectroscopy using laser-stimulated absorption," *Opt. Lett.*, vol. 40, no. 22, p. 5224, Nov. 2015, doi: 10.1364/OL.40.005224.

[207] A. G. Paleocrassas and J. F. Tu, "Inherent instability investigation for low speed laser welding of aluminum using a single-mode fiber laser," *J. Mater. Process. Technol.*, vol. 210, no. 10, pp. 1411–1418, Jul. 2010, doi: 10.1016/j.jmatprotec.2010.04.002.

[208] J. A. Goldak and M. Akhlaghi, *Computational welding mechanics*. New York: Springer, 2005.

[209] O. Desmaison, "Modélisation numérique d'un procédé de soudage hybride arc / laser en approche level set : application au soudage multi-passes de tôles d'acier de forte épaisseur," Ecole Nationale Supérieure des Mines de Paris, 2013. [Online]. Available: https://www.theses.fr/2013ENMP0079

[210] M. von Allmen and A. Blatter, *Laser-Beam Interactions with Materials: Physical Principles and Applications*, vol. 2. in Springer Series in Materials Science, vol. 2. Berlin, Heidelberg: Springer Berlin Heidelberg, 1995. doi: 10.1007/978-3-642-57813-7.

[211] A. Kaplan, "A model of deep penetration laser welding based on calculation of the keyhole profile," *J. Phys. Appl. Phys.*, vol. 27, no. 9, pp. 1805–1814, Sep. 1994, doi: 10.1088/0022-3727/27/9/002.

[212] P. Sahoo, T. Debroy, and M. J. McNallan, "Surface tension of binary metal—surface active solute systems under conditions relevant to welding metallurgy," *Metall. Trans. B*, vol. 19, no. 3, pp. 483–491, Jun. 1988, doi: 10.1007/BF02657748.

[213] W.-I. Cho, S.-J. Na, C. Thomy, and F. Vollertsen, "Numerical simulation of molten pool dynamics in high power disk laser welding," *J. Mater. Process. Technol.*, vol. 212, no. 1, pp. 262–275, Jan. 2012, doi: 10.1016/j.jmatprotec.2011.09.011.

[214] Y. T. Cho, W. I. Cho, and S. J. Na, "Numerical analysis of hybrid plasma generated by Nd:YAG laser and gas tungsten arc," *Opt. Laser Technol.*, vol. 43, no. 3, pp. 711–720, Apr. 2011, doi: 10.1016/j.optlastec.2010.09.013.

[215] J.-H. Cho and S.-J. Na, "Implementation of real-time multiple reflection and Fresnel absorption of laser beam in keyhole," *J. Phys. Appl. Phys.*, vol. 39, no. 24, pp. 5372–5378, Dec. 2006, doi: 10.1088/0022-3727/39/24/039.

[216] M. Courtois, M. Carin, P. L. Masson, S. Gaied, and M. Balabane, "A new approach to compute multi-reflections of laser beam in a keyhole for heat transfer and fluid flow modelling in laser welding," *J. Phys. Appl. Phys.*, vol. 46, no. 50, p. 505305, Dec. 2013, doi: 10.1088/0022-3727/46/50/505305.

[217] J.-H. Cho and S. J. Na, "Three-Dimensional-Analysis-of-Molten-Pool-in-GMA-Laser-Hybrid-Welding.pdf," *Weld J*, vol. 2, no. 88, pp. 35–43.

[218] M. Dal and R. Fabbro, "[INVITED] An overview of the state of art in laser welding simulation," *Opt. Laser Technol.*, vol. 78, pp. 2–14, Apr. 2016, doi: 10.1016/j.optlastec.2015.09.015.

[219] R. Fabbro and K. Chouf, "Keyhole modeling during laser welding," *J. Appl. Phys.*, vol. 87, no. 9, pp. 4075–4083, May 2000, doi: 10.1063/1.373033.

[220] R. Fabbro and K. Chouf, "Dynamical description of the keyhole in deep penetration laser welding," *J. Laser Appl.*, vol. 12, no. 4, pp. 142–148, Aug. 2000, doi: 10.2351/1.521924.

[221] X. He, "Finite Element Analysis of Laser Welding: A State of Art Review," *Mater. Manuf. Process.*, vol. 27, no. 12, pp. 1354–1365, Dec. 2012, doi: 10.1080/10426914.2012.709345.

[222] B. Fotovvati, S. F. Wayne, G. Lewis, and E. Asadi, "A Review on Melt-Pool Characteristics in Laser Welding of Metals," *Adv. Mater. Sci. Eng.*, vol. 2018, pp. 1–18, 2018, doi: 10.1155/2018/4920718.

[223] "Ansys® Fluent." Ansys Inc, 2022.

[224] "FLOW-3D® Version 12.0." Flow Science, Inc., Santa Fe, NM, 2019. [Online]. Available: https://www.flow3d.com/

[225] C. Multiphysics, "Introduction to COMSOL multiphysics extregistered." COMSOL Multiphysics, Burlington, MA, 2022.

[226] "ABAQUS UNIFIED FEA." in SIMULIA. Dassault Systemes Simulia Corp, United States, 2022.

[227] K. A. Bunting and G. Cornfield, "Toward a General Theory of Cutting: A Relationship Between the Incident Power Density and the Cut Speed," *J. Heat Transf.*, vol. 97, no. 1, pp. 116–122, Feb. 1975, doi: 10.1115/1.3450258.

[228] W. M. Steen and J. Mazumder, *Laser Material Processing*. London: Springer London, 2010. doi: 10.1007/978-1-84996-062-5.

[229] J. Dowden, M. Davis, and P. Kapadia, "The flow of heat and the motion of the weld pool in penetration welding with a laser," *J. Appl. Phys.*, vol. 57, no. 9, pp. 4474–4479, May 1985, doi: 10.1063/1.334571.

[230] A. A. Vedenov and E. B. Levchenko, "Maximum depth of penetration of a laser beam in an absorbing medium," *Sov. J. Quantum Electron.*, vol. 13, no. 10, pp. 1406–1407, Oct. 1983, doi: 10.1070/QE1983v013n10ABEH004930.

[231] Z. Li, G. Yu, X. He, C. Tian, S. Li, and H. Li, "Probing thermocapillary convection and multisolute dilution in laser welding of dissimilar miscible metals," *Int. J. Therm. Sci.*, vol. 172, p. 107242, Feb. 2022, doi: 10.1016/j.ijthermalsci.2021.107242.

[232] E. dos S. Magalhães, L. E. dos S. Paes, M. Pereira, C. A. da Silveira, A. de S. P. Pereira, and S. M. M. Lima e Silva, "A thermal analysis in laser welding using inverse problems," *Int. Commun. Heat Mass Transf.*, vol. 92, pp. 112–119, Mar. 2018, doi: 10.1016/j.icheatmasstransfer.2018.02.014.

[233] T. Kik, "Computational Techniques in Numerical Simulations of Arc and Laser Welding Processes," *Materials*, vol. 13, no. 3, p. 608, Jan. 2020, doi: 10.3390/ma13030608.

[234] S. I. Anisimov, "VAPORIZATION OF METAL ABSORBING LASER RADIATION," in *World Scientific Series in 20th Century Physics*, vol. 11, WORLD SCIENTIFIC, 1996, pp. 14–15. doi: 10.1142/9789814317344_0002.

[235] V. Semak and A. Matsunawa, "The role of recoil pressure in energy balance during laser materials processing," *J. Phys. Appl. Phys.*, vol. 30, no. 18, pp. 2541–2552, Sep. 1997, doi: 10.1088/0022-3727/30/18/008.

[236] S. Pang, K. Hirano, R. Fabbro, and T. Jiang, "Explanation of penetration depth variation during laser welding under variable ambient pressure," *J. Laser Appl.*, vol. 27, no. 2, p. 022007, May 2015, doi: 10.2351/1.4913455.

[237] M. Courtois, M. Carin, P. Le Masson, S. Gaied, and M. Balabane, "A complete model of keyhole and melt pool dynamics to analyze instabilities and collapse during laser welding," *J. Laser Appl.*, vol. 26, no. 4, p. 042001, Nov. 2014, doi: 10.2351/1.4886835.

[238] C. Bonacina, G. Comini, A. Fasano, and M. Primicerio, "Numerical solution of phase-change problems," *Int. J. Heat Mass Transf.*, vol. 16, no. 10, pp. 1825–1832, Oct. 1973, doi: 10.1016/0017-9310(73)90202-0.

[239] Y. Hu, X. He, G. Yu, Z. Ge, C. Zheng, and W. Ning, "Heat and mass transfer in laser dissimilar welding of stainless steel and nickel," *Appl. Surf. Sci.*, vol. 258, no. 15, pp. 5914–5922, May 2012, doi: 10.1016/j.apsusc.2012.02.143.

[240] S. Mukherjee, S. Chakraborty, R. Galun, Y. Estrin, and I. Manna, "Transport phenomena in conduction mode laser beam welding of Fe–Al dissimilar couple with Ta diffusion barrier," *Int. J. Heat Mass Transf.*, vol. 53, no. 23–24, pp. 5274–5282, Nov. 2010, doi: 10.1016/j.ijheatmasstransfer.2010.07.032.

[241] I. Tomashchuk, M. Mostafa, P. Sallamand, and M. Duband, "The modeling of keyhole digging during ablative laser beam interaction iwth aluminum/magnesium joint," presented at the COMSOL Conference, 2020.

[242] V. Garcia Navas, J. Leunda, J. Lambarri, and C. Sanz, "Optimization of Laser Keyhole Welding Strategies of Dissimilar Metals by FEM Simulation," *Metall. Mater. Trans. A*, vol. 46, no. 7, pp. 3140–3156, Jul. 2015, doi: 10.1007/s11661-015-2906-4.

[243] V. B. Shaibu, S. K. Sahoo, and A. Kumar, "Computational Modeling of Dissimilar Metal CO2 Laser Welding: Applied to Copper and 304 Stainless Steel," *Procedia Eng.*, vol. 127, pp. 208–214, 2015, doi: 10.1016/j.proeng.2015.11.330.

[244] M. R. N. Esfahani, J. Coupland, and S. Marimuthu, "Numerical simulation of alloy composition in dissimilar laser welding," *J. Mater. Process. Technol.*, vol. 224, pp. 135–142, Oct. 2015, doi: 10.1016/j.jmatprotec.2015.05.005.

[245] S. Borrmann, A. Asad, L. Halbauer, A. Buchwalder, H. Biermann, and R. Schwarze, "Numerical Simulation of the Particle Displacement during Electron Beam Welding of a Dissimilar Weld Joint with TRIP-Matrix-Composite," *Adv. Eng. Mater.*, vol. 21, no. 5, p. 1800741, May 2019, doi: 10.1002/adem.201800741.

[246] J. Wu, H. Zhang, Y. Feng, and B. Luo, "3D Multiphysical Modelling of Fluid Dynamics and Mass Transfer in Laser Welding of Dissimilar Materials," *Metals*, vol. 8, no. 6, p. 443, Jun. 2018, doi: 10.3390/met8060443.

[247] A. Mannucci, R. Bolot, I. Tomashchuk, A. Mathieu, E. Cicala, and S. Lafaye, "On the mechanisms involved in the tensile strength of a dissimilar Ti6Al4V/316L laser welded assembly," *Metall. Res. Technol.*, vol. 118, no. 6, p. 608, 2021, doi: 10.1051/metal/2021082.

[248] A. Evdokimov, N. Doynov, R. Ossenbrink, A. Obrosov, S. Weiß, and V. Michailov, "Thermomechanical laser welding simulation of dissimilar steel-aluminum overlap joints," *Int. J. Mech. Sci.*, vol. 190, p. 106019, Jan. 2021, doi: 10.1016/j.ijmecsci.2020.106019.

[249] W. Huang, H. Wang, T. Rinker, and W. Tan, "Investigation of metal mixing in laser keyhole welding of dissimilar metals," *Mater. Des.*, vol. 195, p. 109056, Oct. 2020, doi: 10.1016/j.matdes.2020.109056.

[250] M. Aghaee Attar, M. Ghoreishi, and Z. Malekshahi Beiranvand, "Prediction of weld geometry, temperature contour and strain distribution in disk laser welding of dissimilar joining between copper & 304 stainless steel," *Optik*, vol. 219, p. 165288, Oct. 2020, doi: 10.1016/j.ijleo.2020.165288.

[251] A. H. Faraji, C. Maletta, G. Barbieri, F. Cognini, and L. Bruno, "Numerical modeling of fluid flow, heat, and mass transfer for similar and dissimilar laser welding of Ti-6Al-4V and Inconel 718," *Int. J. Adv. Manuf. Technol.*, vol. 114, no. 3–4, pp. 899–914, May 2021, doi: 10.1007/s00170-021-06868-z.

[252] G. Chianese, S. Jabar, P. Franciosa, D. Ceglarek, and S. Patalano, "A multi-physics CFD study on the part-to-part gap during remote laser welding of copper-to-steel battery tab connectors with beam wobbling," *Procedia CIRP*, vol. 111, pp. 484–489, 2022, doi: 10.1016/j.procir.2022.08.075.

[253] W.-I. Cho, S.-J. Na, M.-H. Cho, and J.-S. Lee, "Numerical study of alloying element distribution in CO2 laser–GMA hybrid welding," *Comput. Mater. Sci.*, vol. 49, no. 4, pp. 792–800, Oct. 2010, doi: 10.1016/j.commatsci.2010.06.025.

[254] N. Chakraborty, "The effects of turbulence on molten pool transport during melting and solidification processes in continuous conduction mode laser welding of copper–nickel dissimilar couple," *Appl. Therm. Eng.*, vol. 29, no. 17–18, pp. 3618–3631, Dec. 2009, doi: 10.1016/j.applthermaleng.2009.06.018.

[255] N. Chakraborty and S. Chakraborty, "Modelling of turbulent molten pool convection in laser welding of a copper–nickel dissimilar couple," *Int. J. Heat Mass Transf.*, vol. 50, no. 9–10, pp. 1805–1822, May 2007, doi: 10.1016/j.ijheatmasstransfer.2006.10.030.

[256] G. Phanikumar, K. Chattopadhyay, and P. Dutta, "Modelling of transport phenomena in laser welding of dissimilar metals," *Int. J. Numer. Methods Heat Fluid Flow*, vol. 11, no. 2, pp. 156–174, Mar. 2001, doi: 10.1108/09615530110381575.

[257] P. S. Wei and F. K. Chung, "Unsteady marangoni flow in a molten pool when welding dissimilar metals," *Metall. Mater. Trans. B*, vol. 31, no. 6, pp. 1387–1403, Dec. 2000, doi: 10.1007/s11663-000-0024-0.

[258] R. Liang and Y. Luo, "A study on keyhole evolution and weld ripple formation in dissimilar welding under pulsed laser," *Sci. Technol. Weld. Join.*, vol. 22, no. 7, pp. 587–594, Oct. 2017, doi: 10.1080/13621718.2016.1278318.

[259] A. Otto and M. Schmidt, "Towards a universal numerical simulation model for laser material processing," *Phys. Procedia*, vol. 5, pp. 35–46, 2010, doi: 10.1016/j.phpro.2010.08.120.

[260] H.-X. Wang and X. Chen, "Three-dimensional modelling of the laser-induced plasma plume characteristics in laser welding," *J. Phys. Appl. Phys.*, vol. 36, no. 6, pp. 628–639, Mar. 2003, doi: 10.1088/0022-3727/36/6/304.

[261] J. F. Ready, *Effects of high-power laser radiation*. New York: Academic Press, 1971.

[262] J. Hoffman and Z. Szymanski, "Absorption of the laser beam during welding with co2 laser.pdf," *Opt. Appl.*, vol. 32, no. 1–2, pp. 129–145, 2002.

[263] C. J. Knight, "Theoretical Modeling of Rapid Surface Vaporization with Back Pressure," *AIAA J.*, vol. 17, no. 5, pp. 519–523, May 1979, doi: 10.2514/3.61164.

[264] Y. A. Mayi *et al.*, "Two-Phase Flow Modelling of Metal Vaporisation under Static Laser Shot using a Double Domain ALE Method – A Feasibility Study," presented at the COMSOL Conference, Lausanne, France, 2018, p. 7.

[265] A. A. Samokhin, *Effect of laser radiation on absorbing condensed matter*. in Proceedings of the Institute of General Physics / Academy of the Sciences of the USSR, no. 13. Commack, NY: Nova Science Publ, 1990.

[266] "EST ACIERS INDUSTRIE S.A.S." [Online]. Available: serv-com@estaciers.com

[267] C. Nüsser, I. Wehrmann, and E. Willenborg, "Influence of Intensity Distribution and Pulse Duration on Laser Micro Polishing," *Phys. Procedia*, vol. 12, pp. 462–471, 2011, doi: 10.1016/j.phpro.2011.03.057.

[268] M. Schneider, L. Berthe, M. Muller, and R. Fabbro, "A fast method for morphological analysis of laser drilling holes," *J. Laser Appl.*, vol. 22, no. 4, pp. 127–131, Nov. 2010, doi: 10.2351/1.3508232.

[269] "GVB Solutions in glass." [Online]. Available: https://g-v-b.de/quarzglas-2/

[270] "McPherson, Inc. - Model 789A-3 Stepper Drive Scan Controller." Accessed: Dec. 13, 2022. [Online]. Available: https://people.physics.anu.edu.au/~jnh112/mcpherson/spectrometers/model789a3.htm

[271] "Model 209 PDF Data Sheet." McPherson, Inc. [Online]. Available: https://mcphersoninc.com/dwg/209dwg.png

[272] "ICCD PI-MAX: 1K." ©SK Advanced Solutions. Accessed: Dec. 13, 2022. [Online]. Available: http://www.sk-advanced.com/shop_product/iccd-cameras/pi-max:-1k

[273] "ST-133 Controller Manual." ©Copyright Roper Scientific, Inc., 2004. [Online]. Available: http://www.pi-j.jp/pdf/manual/ST-133_ControllerManual.pdf

[274] ©2000 Marconi Applied Technologies Limited, "A1A-CCD47-10 Backthinned Compact Pack Issue 1." Great Shefford Observatory. Accessed: Dec. 13, 2022. [Online]. Available: https://birtwhistle.org.uk/4710aibc1.pdf

[275] "WinSpec32_UserManual2.6.pdf." ©Copyright 2001-2012 Princeton Instruments, a division of Roper Scientific, Inc. [Online]. Available: http://www.pi-j.jp/pdf/manual/WinSpec32_UserManual2.6.pdf

[276] M. Linkert *et al.*, "Metadata matters: access to image data in the real world," *J. Cell Biol.*, vol. 189, no. 5, pp. 777–782, May 2010, doi: 10.1083/jcb.201004104.

[277] "PeakFit, Systat software." Inpixon HQ, : 2479 E. Bayshore Rd, Suite 195 Palo Alto, CA 94303, 2003 1999. [Online]. Available: https://systatsoftware.com/peakfit/

[278] "Phantom v9.1 Datasheet." PHANTOM® Vision Research, Oct. 08, 2007. [Online]. Available: https://www.adept.net.au/cameras/visionresearch/pdf/PhantomV91.pdf

[279] "Phantom v9.1 Response Curve.png." PHANTOM® Vision Research, Jan. 16, 2023. [Online]. Available: http://service.phantomhighspeed.com/Documentation/Support%20By%20Model%20Pages/Phantom%20V9.1/PHANTOM_V9.1_spectral_and_color_response_rev_7.pdf

[280] "Phantom v2012 Response curve." PHANTOM® Vision Research. [Online]. Available: https://www.phantomhighspeed.com/-/media/project/ameteksxa/visionresearch/documents/speccurve/uhs/vxx12spec.pdf?download=1

[281] "Cine File Importer Plugin." [Online]. Available: https://imagej.nih.gov/ij/plugins/cine-reader/index.html

[282] "Phantom Camera Control." PHANTOM® Vision Research. [Online]. Available: https://www.phantomhighspeed.com/resourcesandsupport/phantomresources/pccsoftware

[283] "Coating Curve - Bandpass Interference Filter." Edmund Optics ®. [Online]. Available: https://www.edmundoptics.com/document/download/358477, https://www.edmundoptics.com/document/download/377764

[284] M. Girault, "Etude d'un plasma généré lors d'un traitement de surface métallique par ablation laser dans l'air : caractérisations du rayonnement et des nanoparticules induits," Thèse de doctorat en Physique, UNIVERSITE DE BOURGOGNE, Dijon, France, 2015. [Online]. Available: https://www.theses.fr/2015DIJOS028

[285] F. N'GOMESSE, "Analyse de plasma par spectrométrie d'émission atomique: Application à l'ablation d'argent et au soudage de matériaux dissemblables par laser," Université d'Orléans, Masters internship report, 2017.

[286] A. SADALLAH, "Caractérisation physique par spectrométrie d'émission atomique des vapeurs/plasmas générées lors du soudage laser des matériaux dissemblables," Université Nancy, Masters internship report, 2018.

[287] I. Tomashchuk, A. Chabot, P. Cottet, M. Duband, P. Sallamand, and A. Mannucci, "Liquid zone and spatter behavior during continuous laser welding of titanium," 2019.

[288] D. D. Nogare, "An Intoduction To Biological Image Processing in ImageJ, Part 3: Stacks and Stack Projections," An Introduction To Biological Image Processing In ImageJ. [Online]. Available: https://medium.com/@damiandn/an-intoduction-to-biological-image-processing-in-imagej-part-3-stacks-and-stack-projections-942aa789420f

[289] J.-D. Kim and A. Matsunawa, "Plasma analysis in laser welding of aluminum alloys," *Int. Inst. Weld.*, pp. 1–9, 1996.

[290] R. L. Kurucz and B. Bell, "1995 Atomic Line Data." in Kurucz CD-ROM No. 23. Cambridge, Mass.: Smithsonian Astrophysical Observatory. [Online]. Available: https://www.cfa.harvard.edu/amp/ampdata/kurucz23/sekur.html

[291] W. H. Walton, "Feret's Statistical Diameter as a Measure of Particle Size," *Nature*, vol. 162, no. 4113, pp. 329–330, Aug. 1948, doi: 10.1038/162329b0.

[292] S. Guo, J. Zou, J. Xu, Q. Wu, and R. Xiao, "Multi-stage keyhole evolution in fiber laser welding: An experimental study and theoretical analysis," *Results Phys.*, vol. 31, p. 104943, Dec. 2021, doi: 10.1016/j.rinp.2021.104943.

[293] M. R. Kumar, I. Tomashchuk, J. M. Jouvard, and M. Duband, "A first approximation to the modeling of vapor plume evolution in laser welding," *COMSOL Conf. Eur.*, vol. 14, 2020.

Annex 1

Numerical modelling – Al vapor plume
A first approximation to the modeling of vapor plume evolution in laser welding

M. Raja Kumar, I.Tomashchuk*, J.-M. Jouvard, M. Duband
Laboratoire Interdisciplinaire Carnot de Bourgogne, UMR CNRS 6303 - Université de Bourgogne – Franche Comté, 12 rue de la Fonderie – 71200 Le Creusot, France
* iryna.tomashchuk@u-bourgogne.fr

Abstract : A quantification of spatial and temporal evolution of laser-induced plume would enhance the comprehension of results from high speed imaging and optimization of emission spectroscopy acquisition parameters. What temperature and concentrations of the evaporating species are sufficient for obtaining an emission spectrum? Which part of the plume should be targeted? How long does the plume persist after the extinction of the laser? To answer these questions, a first approximation to the multiphysical modeling of the vapor plume during a millisecond scale Yb:YAG laser pulse on the metallic material was attempted. A time-dependent 2D axisymmetric model comprising strongly coupled heat transfer, fluid flow, diffusion and moving mesh problems is proposed. In the metal domain, the heat transfer involving the evaporative energy loss is coupled with a non-isothermal flow represented by incompressible Navier-Stokes equation, which takes into account recoil pressure, surface tension, Marangoni effect and gravity. In the gas domain, the non-isothermal flow represented by compressible Navier-Stokes equation is strongly coupled with diffusion equation, which is based on the flux of evaporating metal atoms and Fuller approximation of diffusion coefficient. The proposed model was applied to the case of aluminum and compared with the experimental results of high-speed imaging and post-mortem analysis of the impact zone.

Keywords: laser welding, vapor plume, multiphysics.

1. Introduction

The analysis of vapor plume produced during a high power laser-metal interaction allows better comprehension of keyhole dynamics and can give a hint about the characteristics of metallic vapor inside the keyhole. The main methods of plume analysis nowadays are high speed imaging [1], Schlieren imaging [2] and emissive spectroscopy [3]. The use of high-speed imaging in combination with different VIS and IR filters allows obtaining the bright image of the plume induced mainly by the continuous emission of the hot vapor on a chosen wavelength, while Schlieren imaging represents the existing gradient of density. The emissive spectroscopy of laser-induced plume allows identifying the species that form the vapor, estimating the vapor temperature through Boltzmann plot method etc [3]. However, there is no experimental method capable to capture a velocity field inside the plume that should not be confused with the propagation velocity of plume envelope, which can be easily calculated using above-mentioned imagining techniques. Moreover, the concentration of evaporated species and their dilution in the ambient gas is quite complicated to evaluate experimentally.

The emission spectroscopy analysis of "classical" (not nano or pico-second) laser welding of aluminum met with many difficulties [4]: the absence of emission lines besides the fundamental transitions at 394.4 and 396.1 nm, low intensity of the continuous emission and the fluctuations of the signal. The

numerical modeling of the laser-induced plume would provide the necessary information about the influence of welding parameters on the plume temperature and the concentration of the evaporating species, to identify the energy densities sufficient for the acquisition of a good quality emission spectrum. Moreover, the comprehension of species dilution in the plume would help with would help with optimization of signal acquisition parameters from the different parts of the plume. The information about the extinction of the plume at the end of interaction would also be helpful in the interpretation of time-dependent spectra intensity.

The recent progress around the numerical modeling of laser–induced vapor jets was closely related with the need to comprehend the loss of metallic powder in SLM and LMD techniques. The first COMSOL Multiphysics model of laser-induced vapor jet was proposed by Eppes et al [5] and was based on the fixed mesh and phase transitions created by temperature-dependent properties. The further works on the plume propagation with COMSOL Multiphysics were based on two concurrent methods: level set [6] and ALE [7]. The level set method allows taking into account the complex fluctuations of metal/gas interface, like the formation of spatter or volume defects in the melted zone. However, it implies the solving of the common incompressible Navier-Stokes equation for both metal and gas domains. ALE method does not model the discontinuities of metal/gas interface, but it allows separating the incompressible fluid flow in the metal domain from the vapor expansion problem in gas domain, where compressible flow is necessary for the realistic representation of plume behavior. Mayi et al. [7] described such ALE-based numerical scheme that involves two separate Navier-Stokes equations coupled with heat transfer, where the propagation of metal atoms in the plume was evaluated using the atomic fraction as the solved variable in Fick equation. The resulting plume had a mushroom structure with a characteristic Rayleigh-Taylor instability, and the maximal gas velocity next to the metal/gas interface exceeded 100 m/s. In view of typical velocities of the vapor jet and the formation of lateral vortexes, the laminar flow formulation represents a first approximation to the description of plume behavior. The existing turbulence-based models deal only with vapor domain, without considering the free surface deformation. Arshed et al [8] proposed a k-ε turbulence model for the description of laser-induced jet that showed a good correspondence between calculated and experimental heights of the plume. Bidare at al. [2] described the plume behavior using RANS SST turbulence model in COMSOL Multiphysics.

The present study is dedicated to the multiphysical modeling of the vapor plume evolution during a millisecond Yb:YAG laser pulse on the metal surface. The proposed 2D axisymmetric time-dependent model uses the deformed geometry approach for the description of metal/gas interface and solves separate Navier-Stokes equations for metal and gas domains, strongly coupled with the respective heat transfer equations. As the turbulence effects were not taken into

account, the proposed model represents a first approximation to the auto-consistent description of the plume. The main novelty of this work is the calculation of molar concentration of metal atoms in the plume using Fuller approximation of diffusion coefficient of metal atoms in the ambient atmosphere. The proposed model was applied to the case of aluminum and compared with experimental results of high speed imaging and post-mortem analysis of the impact zone.

2. Governing equations

The complete description of plume propagation during the laser impact demands the coupled solving of heat transfer, fluid flow and mass transfer problems in the gas phase, which comprises both air and evaporating metal atoms. As the evaporation process occurring in the melted zone acts as the motor of plume formation, the heat transfer and fluid flow problems should be accurately solved for the metal domain as well. Consequently, the problem of plume propagation is strongly multiphysical and needs several couplings between the different kinds of physics. The scheme of the proposed multiphysical couplings is provided on the Figure 1. A strong coupling is established between heat transfer and fluid flow in the metal, to provide the temperature of melted zone surface. The output vaporization flux controls the temperature of metal/gas interface, necessary for resolving the thermal field in the gas domain. The second strong coupling is established between heat transfer, fluid flow and the diffusive transport of metal atoms in the air, as the local physical properties must depend on the fraction of metal atoms in the plume. The position of free surface between gas domain and metal domain is calculated based on the velocity fields of both liquid metal and plume jet. The governing equations and main boundary conditions for each physics are described in the following sub-chapters. For the reduction of calculation time, a 2D axisymmetric formulation was used.
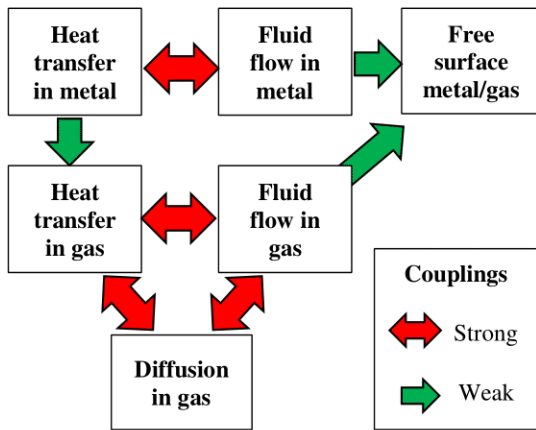

Figure 1. The scheme of multiphysical couplings.

2.1. Heat transfer in the metal

Heat transfer equation for the metal was solved in time-dependent form

$$\rho_m \, C_{p\,m}^{eq} \frac{\partial T_m}{\partial t} + \rho_m \, C_{p\,m}^{eq} \overrightarrow{U_m} \cdot \overrightarrow{\nabla} T_m = \overrightarrow{\nabla} \cdot \left(k_m \overrightarrow{\nabla} T_m \right) \qquad (1)$$

with ρ_m - density of metal (kg/m^3), $C_{p\,m}^{eq}$ – equivalent heat capacity of the metal (J/(kg·K)), k_m – thermal conductivity of the metal (W/(m·K)), T_m – solved metal temperature (K) and t – time (s).

The energy supply from a standalone laser pulse was introduced as surface Gaussian heat source applied to metal/gas interface:

$$q_m^{laser} = \frac{2\,a\,P_l}{\pi \, R_l^2} exp^{-2\frac{r^2}{R_l^2}} \cdot \left(t \geq t_{imp} \right) \qquad (2)$$

with a – absorption coefficient of laser radiation, P_l – laser power (W), R_l – laser spot radius (m) and t_{imp} – the duration of laser pulse (ms).

The heat loss through evaporation was represented by surface vaporization heat flux applied to metal/gas interface [9]:

$$q_m^{vap} = -(1 - \beta_r) L_m^{vap} \sqrt{\frac{M_m}{2\pi R T_m}} P_{sat} \qquad (3)$$

where β_r – the recombination coefficient, L_m^{vap} – latent heat of vaporization (J/kg), M_m – molar mass of the metal (kg/mol), R – ideal gas constant (J/(mol·K)) and P_{sat} – pressure of saturated metal vapor (Pa).

For the lateral walls of the metal domain, an ambient temperature was applied.

2.2. Fluid flow in the metal

The metal domain was considered as an incompressible Newtonian liquid having T-dependent dynamic viscosity μ_m (Pa·s). The time-dependent laminar flow is governed by Navier-Stokes equation:

$$\rho_m \frac{\partial \overrightarrow{U_m}}{\partial t} + \rho_m (\overrightarrow{U_m} \cdot \overrightarrow{\nabla}) \overrightarrow{U_m} = \overrightarrow{\nabla} \cdot \left\{ p_m \, [I] + \mu_m \left[\nabla \overrightarrow{U_m} + \right. \right.$$
$$\left. \left. + \left(\nabla \overrightarrow{U_m} \right)^T \right] \right\} + \vec{F}_D + \rho_m \vec{g}$$
$$\rho_m \overrightarrow{\nabla} \cdot \overrightarrow{U_m} = 0 \qquad (4)$$

where p_m is the relative pressure (Pa) and $\overrightarrow{U_m}$ is the velocity field in the metal domain

$$\overrightarrow{U_m} = \begin{cases} u_m \\ w_m \end{cases} \qquad (5)$$

To inhibit the convection in the solid part of the domain, Darcy damping force was applied [10]:

$$\vec{F}_D = K_{ip} \overrightarrow{U_m} \qquad (6)$$

where K_{ip} is an isotropic permeability defined as:

$$K_{ip} = \frac{-C(1 - f_l)^2}{(f_l^3 + b)} \qquad (7)$$

with constants $C = 1 \cdot 10^6$, $b = 1 \cdot 10^{-3}$ and f_l - numerical fraction of liquid that turns to 1 when the temperature becomes equal to the melting point T_f (K) :

$$f_l = flc2hs\left(T_m - (T_f - dT), dT \right) \qquad (8)$$

At the metal/gas interface, the recoil pressure [11] was applied:

$$P_r = \left(\frac{1 + \beta_r}{2} \right) P_{sat} \qquad (9)$$

where the pressure of saturated vapor is given as :

$$P_{sat} = P_0 exp^{\left[\frac{L_m^{vap} M_m}{R} \left(\frac{1}{T_m^{vap}} - \frac{1}{T_m} \right) \right]} \qquad (10)$$

The surface tension σ (N/m) was given as :

$$\sigma = \sigma_f + \gamma_m T_m \qquad (11)$$

where σ_f (N/m) is the surface tension at fusion temperature and γ_m is a temperature coefficient of surface tension (N/(m·K)).

Surface tension is taken into consideration through Laplace equation [12] :

$$p_m \vec{n} = -\sigma \frac{\partial \vec{t}}{\partial s} \qquad (12)$$

where $\vec{t}$ is the tangent vector to the free surface s.

Finally, a thermocapilary convection is taken into account:

$$\left\{-p_m[I] + \mu_m \left[\nabla \overrightarrow{U_m} + \left(\nabla \overrightarrow{U_m}\right)^T\right]\right\} \vec{n} = \gamma_m \overrightarrow{V_t} T_m \qquad (13)$$

Non-slip condition is applied to the lateral and bottom boundaries.

2.3. Material properties of in the metal domain

The physical properties of the metal are introduced as Heaviside functions of temperature, with T-dependent expressions for solid (A_m^s) and liquid (A_m^l) state:

$$A_m = A_m^s + (A_m^l - A_m^s) f_l, \qquad (14)$$

where $A_m = a, \rho_m, C_{p}^{eq}{}_m, k_m, \mu_m, \sigma, \gamma_m$.

The latent heat of fusion of L_m^f (J/kg) is taken into account by means of equivalent enthalpy approach [13]:

$$C_p^{eq}{}_m = C_{p_m}^s + \left(C_{p_m}^l - C_{p_m}^s\right) f_l + + L_m^f \frac{exp\frac{\left(T-T_f\right)^2}{dT^2}}{\sqrt{\pi \, dT^2}}. \qquad (15)$$

2.4. Heat transfer in the gas phase

Heat transfer equation for the gas phase is solved in time-dependent form:

$$\rho_g \, C_{p_g} \frac{\partial T_g}{\partial t} + \rho_g \, C_{p_g} \overrightarrow{U_g} \cdot \overrightarrow{\nabla} T_g = \overrightarrow{\nabla} \cdot \left(k_g \overrightarrow{\nabla} T_g\right) \qquad (16)$$

with ρ_g - density of gas phase (kg/m³) given by the ideal gas law (equation 25) , C_{p_g} – equivalent heat capacity of the gas at constant pressure (J/(kg·K)), k_g – thermal conductivity of the gas (W/(m·K)), T_g – solved temperature of the gas (K) and t – time (s).

The general inward heat flux at metal/gas interface is given as:

$$q_g^{vap} = -q_m^{vap} \qquad (17)$$

Outflow condition is applied to the top and lateral boundaries.

2.5. Fluid flow in the gas phase

In the gas domain, a compressible laminar flow is described by Navier-Stokes equation in time-dependent form:

$$\rho_g \frac{\partial \overrightarrow{U_g}}{\partial t} + \rho_g (\overrightarrow{U_g} \cdot \overrightarrow{\nabla}) \overrightarrow{U_g} = \overrightarrow{\nabla} \{p_g \, [I] + [K]\} + \rho_g \vec{g}$$

$$\frac{\partial \rho_g}{\partial t} + \overrightarrow{\nabla} \cdot \left(\rho_g \overrightarrow{U_g}\right) = 0$$

$$[K] = \mu_g \left[\nabla \overrightarrow{U_g} + \left(\nabla \overrightarrow{U_g}\right)^T\right] - \frac{2}{3} \mu_g (\vec{\nabla} \cdot \overrightarrow{U_g})[I] \qquad (18)$$

where μ_g is the dynamic viscosity of the gas phase and $\overrightarrow{U_g}$ is the velocity field in the gas domain:

$$\overrightarrow{U_g} = \begin{cases} u_g \\ w_g \end{cases} \qquad (19)$$

The recoil pressure is applied on the metal/gas interface:

$$P_r = \left(\frac{1+\beta}{2}\right) P_{sat} \qquad (20)$$

Open boundary condition with zero viscous stress is applied to top and lateral boundaries.

2.6. Diffusion problem in the plume

For calculating the concentration field of metal atoms c_m (mol/m³) during the evaporation process, Fick equation is solved in the gas domain

$$\frac{\partial c_m}{\partial t} + \overrightarrow{\nabla} \cdot \overrightarrow{J_m} + \overrightarrow{U_g} \cdot \overrightarrow{\nabla} c_m = 0$$

$$\overrightarrow{J_m} = -D_m \overrightarrow{\nabla} c_m \qquad (21)$$

where the diffusion coefficient of metal atom in the gas phase D_m (m²/s) is estimated using Fuller approximation of Chapman-Enskog equation [14]:

$$D_m = \frac{1 \cdot 10^{-3} T_g^{1.75} \cdot \left(\frac{1}{M_m} + \frac{1}{M_{air}}\right)^{0.5}}{p_g [(\Sigma V_m)^{1/3} + (\Sigma V_{air})^{1/3}]^2} \qquad (22)$$

where M_m and M_{air} are the molar mass of metal and air respectively (g/mol), p_g – absolute gas pressure (atm), ΣV_m and ΣV_{air} are the diffusion volumes of metal atom and air.

The general inward flux of metal atoms is applied to the metal/gas interface:

$$\overrightarrow{J_v} = \frac{(1-\beta_r)\sqrt{\frac{M_m}{2\pi R T_m}} P_{sat}}{M_m} \vec{n} \qquad (23)$$

The outflow condition is applied to the top and lateral boundaries.

The solved molar concentration of the metal allows to express the local molar fraction of metal atoms in the gas phase φ_m as follows:

$$\varphi_m = c_m \frac{R T_g}{p_g} \qquad (24)$$

2.7. Material properties of the gas domain

The gas phase is represented as a mixture between the air and the metal atoms. The density of this mixture is given by ideal gas law

$$\rho_g = \frac{PM}{R T_g} \qquad (25)$$

where M is the molar mass of the mixture that depends on local fraction of metal atoms:

$$M = M_m \varphi_m + M_{air}(1 - \varphi_m) \qquad (26)$$

All other properties of gas phase ($A_g = C_{p_g}, k_g, \mu_g$) are also represented as functions of local fraction of metal atoms:

$$A_g = A_g^m \varphi_m + A_g^{air}(1 - \varphi_m) \qquad (27)$$

2.8. Moving mesh

The displacement of metal/gas interface is given by the normal velocity $\overrightarrow{V_n}$ formulated as:

$$\overrightarrow{V_n} = f_l(\overrightarrow{V_l} + \overrightarrow{V_g}) \qquad (28)$$

where $\overrightarrow{V_l}$ is the superposition of the velocity fields of the melted metal and the gas given as

$$\overrightarrow{V_l} = \frac{\rho_m(u_m \overrightarrow{n_r} + w_m \overrightarrow{n_z}) - \rho_g(u_g \overrightarrow{n_r} + w_g \overrightarrow{n_z})}{\rho_m - \rho_g} \qquad (29)$$

and $\overrightarrow{V_g}$ is the velocity of the vaporization front

$$\overrightarrow{V_g} = \frac{(1-\beta_r)\sqrt{\frac{M_m}{2\pi R T_m}} P_{sat}}{\rho_m} \vec{n} \qquad (30)$$

3. Use of COMSOL Multiphysics® Software

The model is created in a 2D axi-symmetric form and comprises a rectangular metal domain of 1x2.5 mm² and a gas domain of 11x2.5 mm² (Figure 2). The rectangular mesh of 0.06

mm is applied to both domains. Additionally, a 0.01 mm mesh size is applied to the metal/gas interface and a 0.03 mm mesh size - to the external boundaries and symmetry axis.

Two separate modules of heat transfer in fluids are used : Metal Heat Transfer (calculated variable T_m) and Gas Heat Transfer (calculated variable T_g). Laminar flow with incompressible formulation is solved for the metal domain (calculated variables $\overrightarrow{U_m}$ and p_m), with surface tension and thermocapillary effects programmed in a weak form. Compressible Laminar flow is solved for the gas domain (calculated variables $\overrightarrow{U_g}$ and p_g). The Non-Isothermal flow Multiphysics is used for sharing the density of the gas phase defined in the Gas Heat Transfer module with Compressible Laminar flow module. The transport of evaporating metal atoms is calculated with Transport of Diluted Species module. In order to account for the loss of matter through evaporation, the *Deformed Geometry* module with Yeoh smoothing was used to describe the motion of metal/gas interface. The progressive stiffening of the meshes (S) in function of local vertical displacement (*material.dZ*) was introduced in order to lower the risk of excessive mesh deformation and inversion:

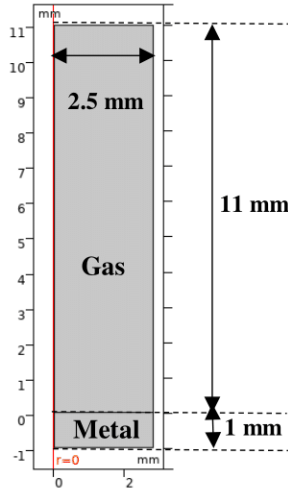$$S = s_{const}.flc2hs(abs(material.dZ)-2e-5, 1e-5) \qquad (31)$$

Figure 2. Model geometry.

Due to the high complexity of this multiphysical model, the intricacies are managed by profuse application of consistent and inconsistent numerical stabilization coefficients. However, the influence of inconsistent stabilization on the quality of obtained solution has been verified.

The calculation was performed over the time (4 ms) twice superior to the pulse duration (2 ms), to include the process of plume extinction and melt solidification. A time step of 1 µs was applied for better convergence. The user controlled relative tolerance was fixed to 0.05. A time-dependent solver MUMPS using full coupling with Automatic Highly nonlinear Newton method was used. The model was solved on the workstation with Intel ® Xeon ® CPU E5-2699v4 (2 processors, 2.2 GHz, 44 cores) and 256 Gb RAM. The longest calculation took ~ 5 h.

4. Experiment

The experiments were performed using a Yb:YAG laser (λ =1030 nm) TruDisk 6001 (Trumpf) at a focal distance of 200 mm, focused spot diameter of 0.6 mm and pulse duration of 2 ms. Laser beam of 3 kW power was focused at the top surface of A5754 aluminum alloy plate. No gas protection of the melted zone was used. The dimensions of the melted zone were evaluated post-mortem using a scanning electronic microscope JSM-6610LA (Jeol), equipped with an EDS analyzer.

The plume development was observed with a high speed camera Phantom V9.1 using 810 nm filter that allows highlighting the zones with continuous thermal emission. The resolution of the image was of 480x480 px, which corresponded to the dimension of the filmed zone of about 15x15 mm². Framerate of 6420 pps and exposure time of 120 µs were used.

5. Results and discussion

5.1. Validation of the model

In the first place, the laser impact on the surface of A5754 plate after a 2 ms long pulse was compared with the calculated melted zone (Figure 3). The measured radius of the impact (480 µm) was close to the calculated radius (410 µm). A ~15 % relative error can be explained by a large numerical mushy zone necessary for the optimal numerical convergence of the model. The irregular ejection of metal droplets out of the impact zone was not reflected by the model.
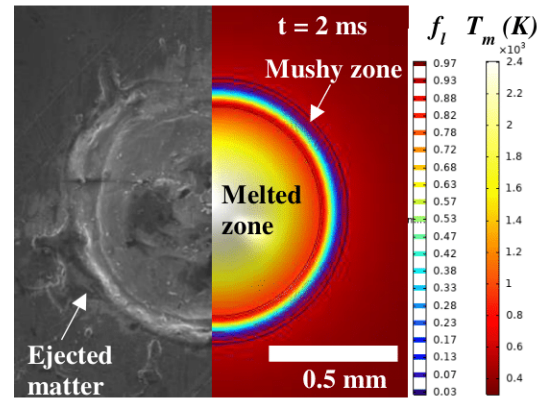

Figure 3. Experimental validation of the impact size.

Taking into consideration a sharp temperature gradient between the plume and the ambient air, the profile of calculated high-temperature zone was assimilated to the experimentally observable envelope of the plume. The plume size was characterized by the height (H_p) and the radius (R_p) of a cylinder limiting its envelope (Figure 4a). The comparison between experimentally observed plume envelope and the calculated thermal field (Figure 4a) showed a good correspondence for the pulse times << 1 ms, when the plume has a pronounced mushroom shape. However, at bigger times (Figure 4b-c), the calculated height of the plume was increasing more rapidly than experimentally observed (Figure 5a), while the experimentally observed maximal radius of the plume progressively became wider than the calculated one (Figure 5b). The average velocities of vertical plume expansion were estimated to 6.4 m/s for HSI observations and to 7.7 m/s for the model. The H_p/R_p ratio rapidly stabilized at ~3 for the experimentally observed plume and continued to grow continuously up to ~4.5 for the numerical result. The overestimation of plume height by the model can be attributed to the omission of turbulence and other convection phenomena such as the gas flow protecting the welding head lens, the air currents in the welding hall etc.
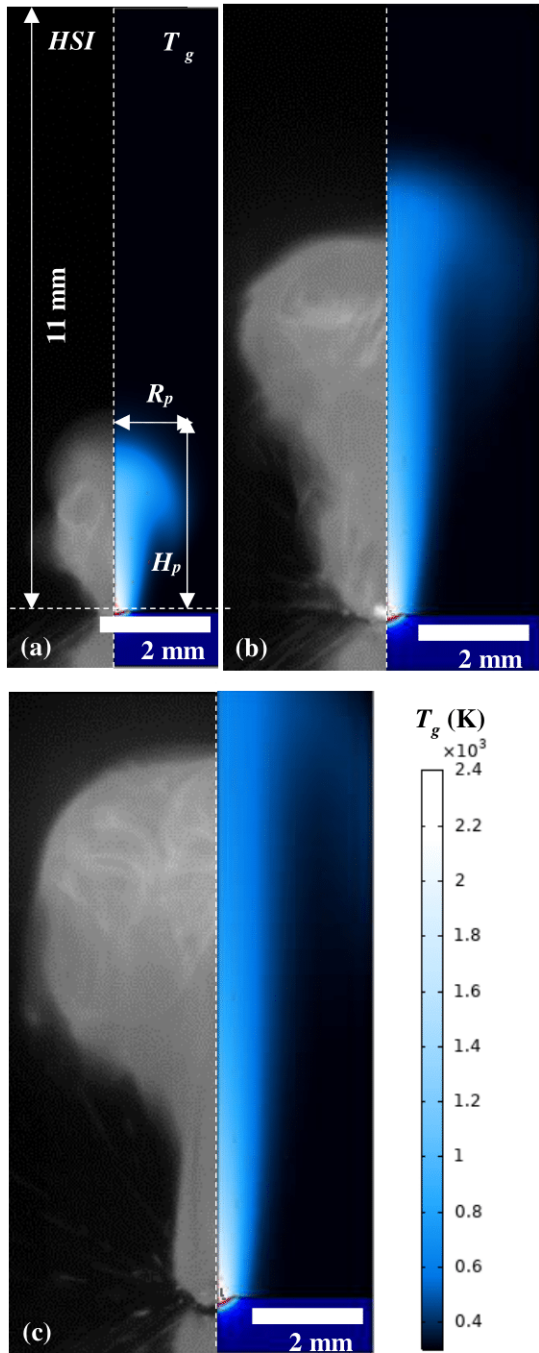
Figure 4. The comparison between the experimentally observed plume (on the left) and the calculated thermal field (on the right) at pulse times of (a) 468 μs, (b) 936 μs and (c) 1404 μs.

5.2. The behavior of the melt and the vapor plume

To represent the global evolution of the melted zone during and after the 2 ms long pulse, the maximal surface temperatures ($T_m\ max$) and the fraction of liquid metal (f_l) were plotted against time (Figure 6). The first elements of the liquid metal (having $f_l = 1$) appeared at 25 μs after the start of the pulse, which is reflected by to the sharp increase of surface temperature. In the considered operational conditions, the melt temperature rapidly reaches 2300 K ($t = 0.7$ ms), which is still below the vaporization temperature of aluminum, and remains constant until the end of the pulse, due to the circular convection in the melt.
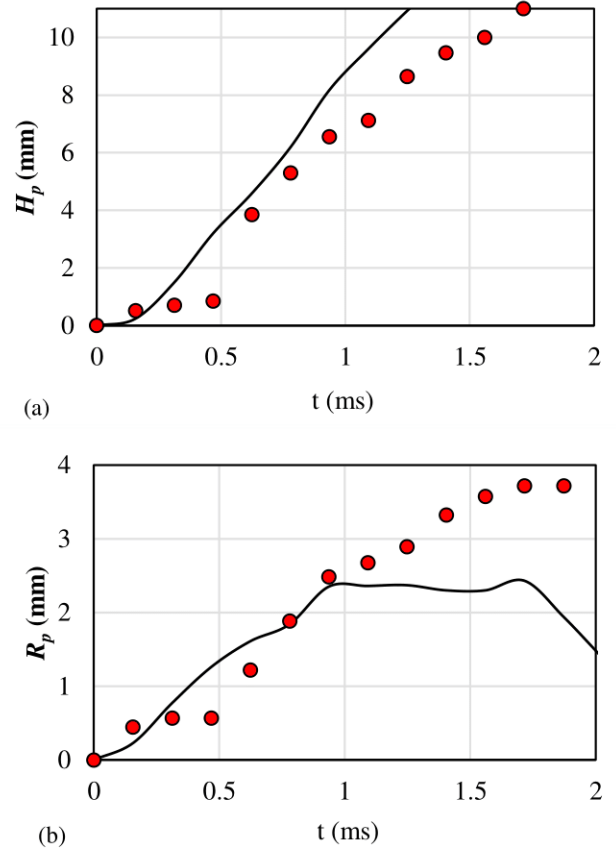

Figure 5. The comparison between the experimentally observed (dots) and calculated dimensions of the plume (line): (a) plume height; (b) maximal plume radius.

The extinction of the laser is followed by a sharp cooling of the metal surface down to 1300 K ($t = 2.2$ ms). However, the solidification of the melted zone is completed only 1 ms after the extinction of the laser. At 2 ms after the end of the pulse, the metallic domain returns to the ambient temperature. In the chosen operational conditions, some vaporization of aluminum from the melted zone can still take place: the maximal relative pressure (at 2300 K) at the metal/gas interface reached 8700 Pa.
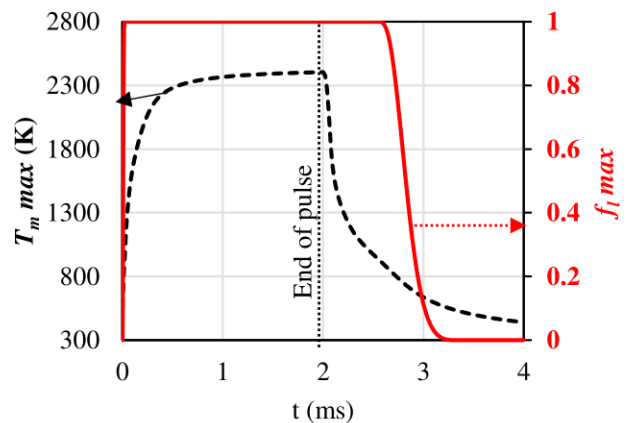

Figure 6. The evolution of maximal temperature and fluid fraction in the melted zone.
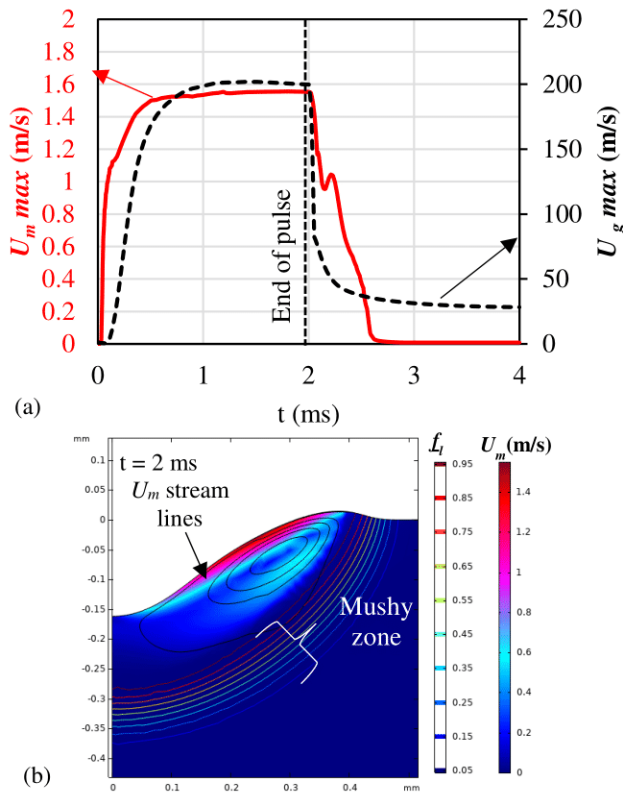
242

Figure 7. The evolution of maximal velocity field in the melted zone and in the gas phase (a); the velocity field and the fraction of liquid in the melted zone at the end of the pulse (b).

The maximal velocities calculated in liquid and in gas phases were growing up to t = 0.7 ms along with increasing temperature, and then remained constant till the end of the pulse (Figure 7a). The circular convection movements in the melted zone, produced by the recoil pressure and thermocapilary effect, resulted in the maximal velocity of 1.6 m/s in the proximity of the metal/gas surface. At the end of the pulse, the melted zone had an important depression in the center and some liquid matter was displaced toward the borders (Figure 7b). The parasite velocity field in solidified metal was successfully suppressed. The velocity of the gas above the melted zone reached 200 m/s or 0.83 Mach. It is clear that the further increase of laser power (>3 kW) would soon induce the surface temperatures close to the vaporization temperature and produce a supersonic flow of the gas above metal/gas interface, at least for the light metals such as aluminum. After the extinction of the pulse, the velocity of the gas sharply decreased down to the residual values of 25 m/s that correspond to the evacuation of hot air from the cooling metal plate. The maximal velocity field in the metal decreases more progressively, with little fluctuations related to the liquid collapse, and became insignificant 0.5 ms after the end of the pulse.

Besides the lateral vortex, the velocity field of the plume was developing mainly in the vertical direction with a rapid deceleration along z axis (Figure 8). During the pulse, the associated cloud of atoms expanded progressively in a form of a cone. The most concentrated part of the plume was situated next to the metal/gas interface, which justifies the positioning of the spectral acquisition system immediately above the metal surface.
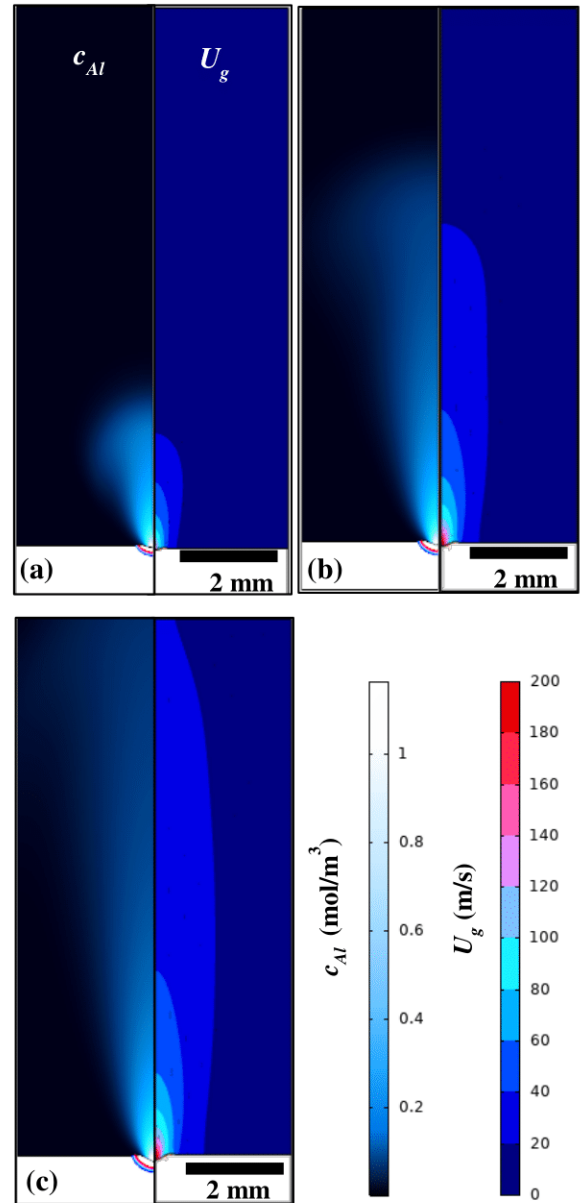

Figure 8. The calculated concentration of Al atoms in the gas phase (on the left) and gas velocity field (on the right) at pulse times of (a) 468 μs, (b) 936 μs and (c) 1404 μs.

The maximal concentration of Al atoms above the metal/gas interface in the considered operational conditions did not exceed 1.5 mol/m^3, which corresponds to ~20% of Al atoms in the most concentrated part of the plume (Figure 9). Such a low molar fraction is determined by the difficulty to bring the aluminum surface to the vaporization temperature, because of its high thermal diffusivity and low absorptivity of laser radiation (considered as 0.15 in this study). Such behavior is consistent with the difficulties to acquire Al emission lines in the similar operational conditions [4]. The rapid dilution of the plume is aggravated by the lower density of Al vapor compared to the density of the surrounding hot air. After the extinction of the laser, the concentration of Al in the gas phase sharply drops below 0.1 mol/m^3 and reaches zero at 0.5 ms after the end of the pulse.
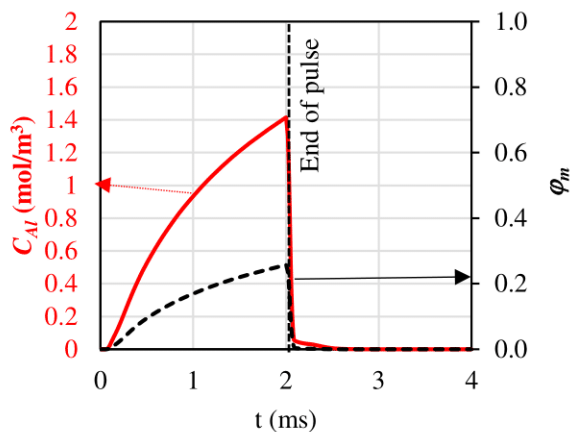
Figure 9. The evolution of maximal Al concentration in the plume (a) and corresponding maximal molar fraction of Al atoms in the air (b).

6. Conclusions

The comparison between calculated thermal field and HSI imaging of the laser-induced plume showed that the proposed multiphysical model allows reproducing the global dynamics of plume propagation during the laser impact on the aluminum alloy surface. The model demonstrated a good correspondence between calculated and experimental dimensions of the impact zone. However, the velocities of plume propagation were overestimated for the times of the pulse > 1 ms, which may be attributed to the existence of turbulent convection and some other possible velocity fields present in the work environment. These effects can be incorporated into the model upon further development.

The maximal gas velocity in the plume neared the sonic speed above the metal/gas interface, but rapidly decreased along the vertical axis. The concentration of Al atoms in the plume was also rapidly decreasing along the vertical axis, which signifies the necessity to target the plume in the immediate proximity of the melt, to increase the chance of obtaining an exploitable emission spectrum. High velocities of the jet produced a sudden drop of Al concentration in the plume after the extinction of the laser.

The present model will be confronted with the results of emission spectroscopy measurements performed in different experimental conditions, to relate the temperature and concentrations of the evaporating species with presence or absence of the chosen excitation lines.

7. References

[1] R. Fabbro, S. Slimani, I. Doudet, F. Coste, F. Briand, Experimental study of the dynamical coupling between the induced vapour plume and the melt pool for Nd–Yag CW laser welding. *Journal of Physics D: Applied Physics,* **39**, 394-400 (2006).

[2] P. Bidare, I. Bitharas, R.M. Ward, M.M. Attallah, A.J. Moore, Fluid and particle dynamics in laser powder bed fusion, *Acta Materialia*, **142**, 107-120 (2018).

[3] C. Aragon, J.A. Aguilera, Characterization of laser induced plasmas by optical emission spectroscopy : A review of experiments and methods. *Spectrochimica Acta B*, **63**, 893-916 (2008).

[4] M. Raja Kumar, J.M. Jouvard, I. Tomashchuk, P. Sallamand, Vapor plume and melted zone behavior during dissimilar laser welding of titanium to aluminum alloy. *Proceedings of the Institution of Mechanical Engineers, Part L: Journal of Materials: Design and Applications*, **234:5**, 681–696 (2020).

[5] T.A. Eppes, I. Milanovic, H. Patrolla, Early Stage Melt Ejection in Percussion Laser Drilling, *Proceedings of Comsol Conference Boston 2012*, October 3-5, 2012, Newton, MA, USA.

[6] S. Sharma, H. Ramkumar, A Pragmatic Multiphysics Numerical Model for Melt Hydrodynamics in Selective Laser Melting, *Proceedings of Comsol Conference Bangalore 2018*, Aug 9-10, 2018, Bangalore, India.

[7] Y. A. Mayi, M. Dal, P. Peyre, M. Bellet, C. Metton, C. Moriconi, R. Fabbro, Two-Phase Flow Modeling of Metal Vaporisation under Static Laser Shot Using a Double ALE Method, *Proceedings of Comsol Conference Lausanne 2018*, October 22-24, 2018, Lausanne, Swissland.

[8] G.M. Arshed, S. Z. Shuja, B.S. Yilbas, M.O. Budair, Numerical investigation of a transient free jet resembling a laser-produced vapor jet. *International Journal of Heat and Mass Transfer*, **47**, 1037-1052 (2004).

[9] C. J. Knight, Theoretical modeling of rapid surface vaporization with back pressure, *American Institute of Aeronautics and Astronautics Journal*, **17:5**, 19–523 (1979).

[10] M. Courtois, M. Carin, P. Le Masson, S. Gaied, M. Balabane. A complete model of keyhole and melt pool dynamics to analyze instabilities and collapse during laser welding. *Journal of Laser Applications*, **26:4**, 042001 (2014).

[11] R. Fabbro, K. Chouf, Dynamical description of the keyhole in deep penetration laser welding, *Journal of Laser Applications*, **12:4**, 142-148 (2000).

[12] E. Guyon, J.P. Hulmin, L. Petit, *Hydrodynamique Physique*, Edition du CNRS (1994).

[13] C. Bonacina, G. Comini, A. Fassano, M. Primicerio, Numerical solutions of phase change problems, *International Journal of Heat Mass Transfer*, **16**, 1825-1832 (1973).

[14] E. N. Fuller, P. D. Schettler, J. C. Giddings, New method for prediction of binary gas-phase diffusion coefficients, *Industrial & Engineering Chemistry,* **58:5**, 18-27 (1966).

8. Acknowledgements

Annex 2

Numerical modelling – overlap welding.

List of abbreviations

Symbol	Significance	Unit
α	thermal diffusivity	$\text{m}^2 \cdot \text{s}^{-1}$
β	empirical attenuation plume attenuation coefficient	m^{-1}
β_r	recombination rate	-
γ	thermal coefficient of surface tension	$\text{N} \cdot \text{m}^{-1} \cdot \text{K}^{-1}$
λ	wavelength	m
μ	local equivalent dynamic viscosity	Pa·s
μ_l	local dynamic viscosity in melted metal	Pa·s
μ_s	artificial value of unmelted material viscosity	Pa·s
ρ	local density	$\text{kg} \cdot \text{m}^{-3}$
σ	local surface tension	$\text{N} \cdot \text{m}^{-1}$
σ_m	surface tension at melting temperature	$\text{N} \cdot \text{m}^{-1}$
φ	Heaviside function dividing the calculation domain into Ti and A5754 parts	
a	laser absorption coefficient	-
a_0	laser absorption coefficient on a flat polished surface	-
a_{KH}	laser absorption coefficient in the keyhole	-
a_{att}	attenuated laser absorption coefficient in a keyhole	-
Al I	label of emission peaks of neutral Al	
$A_{u \rightarrow l}$	Einstein coefficient	s^{-1}
C_p^{eq}	local equivalent heat capacity at constant pressure	$\text{J} \cdot \text{kg}^{-1} \cdot \text{K}^{-1}$
dz	semi-interval of smoothing in *flc2hs* functions of z	m
$|dZ_{max}|$	absolute maximal displacement of the top boundary (or keyhole depth)	m
E_l	energy of lower electron level	cm^{-1}
E_u	energy of upper electron level	cm^{-1}
F	mesh deformation gradient	-
$\vec{F}_D$	Darcy damping force	N
f_l	local fraction of liquid	-
flc2hs	a smoothed Heaviside function with a continuous second derivative without overshoot (in Comsol Multiphysics)	-
g	gravity constant	$\text{m} \cdot \text{s}^{-2}$
h	heat transfer coefficient	$\text{W} \cdot \text{m}^{-2} \cdot \text{K}^{-1}$
J	Jacobian determinant of mesh deformation gradient	-
J_l	angular momentum corresponding to lower electron level	
J_u	angular momentum corresponding to upper electron level	
I	identity matrix in 3D space	-
$I_1(E_{iso})$	isochoric Green–Lagrange strain of the mesh	-
k	local thermal conductivity	$\text{W} \cdot \text{m}^{-1} \cdot \text{K}^{-1}$
K	isotropic permeability	-
L_f	latent heat of fusion	$\text{J} \cdot \text{kg}^{-1}$
L_{vap}	evaporation energy	$\text{J} \cdot \text{kg}^{-1}$
M	molar mass	$\text{kg} \cdot \text{mol}^{-1}$
M_i	indexing of metal plates numbered as $i = 1$ or 2	-
Mg I	label of emission peaks of neutral Mg	
n	space dimension	-
$\vec{n}$	normal vector with cartesian components $\vec{n_x}, \vec{n_y}, \vec{n_z}$	-
q_{conv}	heat outflow due to convection	$\text{W} \cdot \text{m}^{-2}$
q_{laser}	heat inflow due to laser radiation	$\text{W} \cdot \text{m}^{-2}$
q_{vap}	heat outflow through vaporization	$\text{W} \cdot \text{m}^{-2}$
p	relative pressure	Pa
P_0	ambient pressure	Pa
P_l	laser power	W
P_r	recoil pressure	Pa
P_{sat}	local pressure of saturated vapor	Pa
R	ideal gas constant	$\text{J} \cdot \text{mol}^{-1} \cdot \text{K}^{-1}$
R_l	laser beam radius	m

t	time	s
$\vec{t}$	tangent vector to the free surface s	
t_{imp}	laser pulse duration	s
T	absolute temperature	K
dT	semi-interval of smoothing in *flc2hs* functions of temperature	K
T_{amb}	ambient temperature	K
T_m	melting temperature	K
T_{th}	threshold temperature of intense vaporization	K
T_{vap}	vaporization temperature	K
Ti I	label of emission peaks of neutral Ti	
Ti II	label of emission peaks of Ti$^+$ ion	
$\vec{V_l}$	velocity of the liquid on the free surface	m·s^{-1}
$\vec{V_n}$	normal velocity of the free surface	m·s^{-1}
$\vec{V_v}$	normal velocity of vaporization front	m·s^{-1}
$\vec{U}$	velocity field with cartesian components u, v, w	m·s^{-1}
$\varnothing$	laser spot diameter	μm

1. Introduction

Numerical modelling is a powerful tool for understanding and prediction of keyhole and melted zone behavior in dissimilar welding. However, only few publications were dedicated to the numerical modelling of overlap welding between dissimilar metals or alloys. They are based on strong coupling between heat transfer, incompressible Newtonian fluid flow with free surface and diffusive mass transfer and aim to represent the keyhole dynamics and mass transfer between two melted materials. Wu et al. [1] developed a 3D model of melted zone dynamics resulting in reduced mixing between the materials during continuous laser welding of 0.8 mm thick stainless steel/titanium sandwich combination using FLUENT software. Huang et al. [2] used FLOW 3D for the modelling of continuous welding of overlapped foils of 0.2 mm thick aluminum and 0.5 mm thick copper, where the intense mixing between the materials was validated by comparison with experimental X-maps. Recently, Chianese et al. [3] developed a FLOW-3D model of overlap welding between thin (0.3 mm) foils of copper and stainless steel, that reproduced complex melted zone shapes and mixing patterns created by wobbling beam and affected by eventual gap between the plates. The numerical modeling of pulsed welding in overlap configuration between several mm thick dissimilar plates has not yet been reported.

A 3D numerical model of keyhole evolution during laser beam pulse on the metallic surface of standalone metal plates and their overlapped configurations was developed basing on strong coupling between heat transfer, incompressible fluid flow and free surface displacement managed by ALE method. It contains a number of important upgrades compared to the previously proposed model of keyhole evolution during dissimilar welding in butt configuration [4]. The model was implemented in COMSOL Multiphysics 6.1 software. The validation of the model was initially performed by comparison with laser pulses on standalone materials. It was further employed to comprehend and quantify the keyhole and melted zone evolution in the overlapped configurations.

1.1.1. Governing equations

1.1.1.1. Heat transfer

Heat transfer equation containing a convective term was solved in time-dependent form:

$$\rho\, C_p^{eq} \frac{\partial T}{\partial t} + \rho\, C_p^{eq} \vec{U} \cdot \vec{\nabla} T = \vec{\nabla} \cdot \left(k\, \vec{\nabla} T \right) \tag{1}$$

The standalone laser pulse of a given duration t_{imp} was represented by a Gaussian heat source applied to the top boundary of the calculation domain:

$$q_{laser} = \frac{2\, a\, P_l}{\pi\, R_l^2} exp^{-2\frac{(x^2+y^2)}{R_l^2}} \cdot \left(t \geq t_{imp} \right) \tag{2}$$

The heat outflow due to vaporization from the metal M_i was applied to the top boundary of the calculation domain [5]:

$$q_{vap\,Mi} = -(1 - \beta_r)\sqrt{\frac{M_{Mi}}{2\pi RT}} L_{vap\,Mi} P_{sat\,Mi} \qquad (3)$$

where β_r – the recombination rate specified in equation 40.

The heat outflow due to the convective interaction with environment was applied to the top and the bottom boundaries of the calculation domain:

$$q_{conv} = h(T_{amb} - T) \qquad (4)$$

Thermal insulation is applied to the lateral walls of the calculation domain.

1.1.1.2. Fluid flow

The melted metal was considered as an incompressible Newtonian liquid with temperature-dependent dynamic viscosity μ (Pa·s) that undergoes time-dependent laminar flow governed by Navier-Stokes equation:

$$\rho\,\frac{\partial \vec{U}}{\partial t} + \rho\,(\vec{U}\cdot\vec{\nabla})\vec{U} = \vec{\nabla}\cdot\left\{-p\,[I] + \mu\left[\nabla\vec{U} + +(\nabla\vec{U})^T\right]\right\} + \vec{F}_D + \rho\,\vec{g} \qquad (5)$$

To suppress the velocity field in the solid metal, Darcy damping force was applied to the domain [6]:

$$\vec{F}_D = K\vec{U} \qquad (6)$$

where $\vec{U}$ is the velocity field in the liquid metal

$$\vec{U} = \begin{cases} u \\ v \\ w \end{cases} \qquad (7)$$

and K is an isotropic permeability formulated as:

$$K = \frac{-C(1-f_{l\,Mi})^2}{(f_{l\,Mi}^3 + b)} \qquad (8)$$

with C = 1·10⁶, b = 1·10⁻³ and f_l – numerical liquid fraction programmed by smoothed Heaviside function* that reaches 1 as the local temperature becomes equal to the fusion temperature T_m of metal <u>M_i</u>:

$$f_{l\,Mi} = flc2hs\big(T - (T_{m\,Mi} - dT), dT\big) \qquad (9)$$

The width of the associated temperature interval dT is much higher than the typical difference between solidus and liquidus temperatures of metallic alloys and is adjusted to enable an accurate spatial smoothing of the solved variables with regard to the mesh size (see equation 36).

At the top surface of the domain, the recoil pressure created for the metal M_i [7] was applied

$$P_{r\,Mi} = \left(\frac{1+\beta_r}{2}\right) P_{sat\,Mi} \qquad (10)$$

with pressure of saturated vapor of metal M_i given as:

$$P_{sat\,Mi} = P_0\,exp\left[\frac{L_{vap\,Mi}\cdot M_{Mi}}{R}\left(\frac{1}{T_{vap\,Mi}} - \frac{1}{T}\right)\right] \qquad (11)$$

The surface tension of liquid metal Mi was defined as a function of temperature

$$\sigma_{Mi} = \sigma_{m\,Mi} + \gamma\cdot T \qquad (12)$$

Surface tension between the liquid metal and the ambience was taken into consideration through Laplace equation [8]:

$$p\cdot\vec{n} = -\sigma\frac{\partial\vec{t}}{\partial s} \qquad (13)$$

Finally, a thermocapillary (or Marangoni) convection applied to the top surface:

$$\left\{-p[I] + \mu\left[\nabla\vec{U} + (\nabla\vec{U})^T\right]\right\}\vec{n} = \gamma\overrightarrow{V_t}T. \qquad (14)$$

---

* Smoothed Heaviside function of x with a continuous second derivative without overshoot $flc2hs(x - x_{threshold}, dx)$ varies from 0 when $x < x_{threshold} - dx$ to 1 when $x > x_{threshold} + dx$ within a smoothing interval equal to $2dx$.

1.1.1.3. Moving mesh

The free mesh displacement was solved with ALE method using hyperelastic smoothing. The normal velocity of top surface $\overrightarrow{V_n}$ was formulated as:

$$\overrightarrow{V_n} = \overrightarrow{V_l} + \overrightarrow{V_v} \tag{15}$$

where $\overrightarrow{V_l}$ is the velocity field of the melted metal on the free surface

$$\overrightarrow{V_l} = u\,\overrightarrow{n_x} + v\,\overrightarrow{n_y} + w\,\overrightarrow{n_z} \tag{16}$$

and $\overrightarrow{V_v}$ is the velocity of the ablative vaporization front that for metal M_i can be formulated as:

$$\overrightarrow{V_v}_{Mi} = \frac{(1-\beta_r)P_{sat\,Mi}\sqrt{\frac{M_{Mi}}{2\pi RT}}}{\rho}\,\vec{n} \tag{17}$$

To deal with excessive deformation of the meshes created by the displacement of the free surface during the keyhole formation, the remeshing technique integrated in COMSOL Multiphysics 6.1 was applied. The remeshing of the geometry occurs when the square root of the nonnegative first invariant of the isochoric Green–Lagrange strain of the mesh attains the empirically defined condition:

$$\sqrt{I_1(E_{iso})} > 0.7 \tag{18}$$

(the default remeshing criterion being $\sqrt{I_1(E_{iso})} > 2$ [9])
The mesh strain was calculated as:

$$I_1(E_{iso}) = tr\,\frac{1}{2}\left(\frac{F^T F}{J^{2/n}} - I\right) \tag{19}$$

where F is the mesh deformation gradient, J its Jacobian determinant, and n=3 is the space dimension.

1.1.1.4. Materials properties

The shift in physical properties across the joint line was programmed using smoothed Heaviside-based function φ that horizontally divides the calculation domain in two parts that correspond to the top metal plate of thickness h_{top} and the bottom plate in another metal (with z axis that points upwards):

$$\varphi = flc2hs\left(-h_{top} - z, dz\right) \tag{20}$$
$$a = a_{M1} + (a_{M2} - a_{M1}) \cdot \varphi \tag{21}$$
$$\rho = \rho_{M1} + (\rho_{M2} - \rho_{M1}) \cdot \varphi \tag{22}$$
$$C_p^{eq} = C_p^{eq}{}_{M1} + \left(C_p^{eq}{}_{M2} - C_p^{eq}{}_{M1}\right) \cdot \varphi \tag{23}$$
$$k = k_{M1} + (k_{M2} - k_{M1}) \cdot \varphi \tag{24}$$
$$\mu = \mu_{M1} + (\mu_{M2} - \mu_{M1}) \cdot \varphi \tag{25}$$
$$\sigma = \sigma_{M1} + (\sigma_{M2} - \sigma_{M1}) \cdot \varphi \tag{26}$$
$$\gamma = \gamma_{M1} + \left(\gamma_{M2} - \gamma_{M1}\right) \cdot \varphi \tag{27}$$

This transitional approach is necessary to go beyond the numerical limitation of ALE method disabling the keyhole tip to cross the explicitly defined boundary between two overlapped domains. The semi-width of transition zone $dz = 1 \cdot 10^{-4}\,m$ is needed for reaching the numerical convergence with a given mesh size. The mixing process between the materials is not yet taken in consideration.

The following material-dependent variables were also solved considering the transition between the materials given by the function φ:

$$f_l = f_{l\,M1} + \left(f_{l\,M2} - f_{l\,M1}\right) \cdot \varphi \tag{28}$$
$$P_r = P_{r\,M1} + \left(P_{r\,M2} - P_{r\,M1}\right) \cdot \varphi \tag{29}$$
$$q_{vap} = q_{vap\,M1} + \left(q_{vap\,M2} - q_{vap\,M1}\right) \cdot \varphi \tag{30}$$
$$\overrightarrow{V_v} = \overrightarrow{V_v}_{M1} + \left(\overrightarrow{V_v}_{M2} - \overrightarrow{V_v}_{M1}\right) \cdot \varphi \tag{31}$$

For an individual material Mi, the physical properties such as k_{Mi} and ρ_{Mi} were introduced as Heaviside functions of temperature, with separate T-depend expressions for solid (s) and liquid (l) state:

$$k_{Mi} = k_s + (k_l - k_s)\,flc2hs(T - T_m, dT) \tag{32}$$
$$\rho_{Mi} = \rho_s + (\rho_l - \rho_s)\,flc2hs(T - T_m, dT) \tag{33}$$

The latent heat of fusion of individual material L_f was taken in account by means of equivalent enthalpy approach [11]:

$$C_{p\,Mi}^{eq} = C_p^s + \left(C_p^l - C_p^s\right) flc2hs(T - T_m, dT) + L_f \frac{exp^{-\frac{(T-T_m)^2}{dT^2}}}{\sqrt{\pi\, dT^2}} \tag{34}$$

It was found that the combination of Darcy damping force with equivalent viscosity approach provides better numerical convergence. For this reason, the mean value $\mu_s = 100$ Pa·s was considered for the solid material, and the viscosity of liquid phase was applied for the temperatures $\geq T_m$:

$$\mu_{Mi} = \mu_s + \left(\mu_{l_{Mi}} - \mu_s\right) \cdot f_{l_{Mi}} \tag{35}$$

During the preliminary calculations, it was noticed, that using the same smoothing semi-interval dT in the Heaviside functions for titanium and aluminum was causing convergence problems. The temperature interval sufficient for good spatial transition of the physical properties in aluminum, was too thin for titanium, and it led to the calculation failure. Because of a much lower thermal conductivity compared to aluminum, in titanium, the isotherms limiting the transition interval are much closer than in aluminum. Consequently, a much wider temperature interval ($dT_{Ti} \approx 2 \cdot dT_{Al}$) is needed for accurate spatial resolution of properties change in titanium. To address this problem, separate values of transition semi-intervals were used:

$$dT = dT_{M1} + (dT_{M2} - dT_{M1}) \cdot \varphi \tag{36}$$

The evolution of metal absorption coefficient a_{Mi} is programmed to represent the transition between the flat surface and the keyhole. Before the creation of the keyhole, the absorption coefficient of a polished flat surface $a_{0\,Mi}$ can be evaluated for Yb:YAG laser radiation based on the thermal conductivity of the metal [10,11]:

$$a_{0\,Mi} = 0.365 \sqrt{\frac{2.45 \cdot 10^{-8}\, T}{\lambda\, k_{Mi}}}, \tag{37}$$

which gives 0.25 for titanium and 0.17 for aluminum.

When the maximal depth of the deformed top boundary exceeds the diameter of the laser spot ($|dZ_{max}| \geq 2R_l$), the absorption coefficient in the keyhole increases due to multiple reflections. For this condition, the values of absorption coefficients $a_{KH\,Mi}$ commonly found in the literature for the considered materials are used (0.4 for titanium and 0.3 for aluminum).

As this simulation deals with a rather long pulse time, for several mm deep keyholes, the digging process slows down progressively due to the establishment of thermal equilibrium with the environment. But this thermal damping effect cannot completely explain the observed decrease of keyhole drilling rate. However, it is known that the laser radiation reaching the keyhole walls can be attenuated due to several causes:

- the presence of ionized metallic vapor in the keyhole favorizes the inverse bremsstrahlung absorption [12, 13, 16, 17];
- the formation of nanoaggregates during the plume expansion in the air induces an additional absorption and scattering [14,15];
- the undulations of keyhole walls and the emission of micrometric spatter droplets create some local shielding effect.

This global attenuation effect was integrated to the local absorption coefficient in the keyhole (which means, when the condition $|dZ_{max}| \geq 2R_l$ is true) by using a common exponential attenuation expression, where z<0 and $\beta = 800$ m^{-1} is an empirically adjusted attenuation coefficient:

$$a_{att\,Mi} = a_{KH\,Mi} \cdot e^{\beta z} \tag{38}$$

The same value of attenuation coefficient β was used for both metals, as the vapors mix in the keyhole during the dissimilar welding.

The maximal attenuation coefficients attributed to the inverse bremsstrahlung absorption cited in the literature for ~1 µm laser wavelengths were only 100 cm^{-1} for Ti-6Al-4V [16], 5-25 m^{-1} for aluminum [17] and up to 300 m^{-1} for steel [12]. The contribution of nanoaggregates, on another hand, can be estimated to 3-7 m^{-1} according to [14]. In the present case, both mechanisms are possible. In the additionally studied spectral region 375.93-378.92 nm, some Ti II emission lines were observed on standalone titanium even for low laser power and pulse durations (Annex: Table 5 and Figure A1). As the plume emissions are collected above the keyhole opening, it can be supposed that in the keyhole itself the ionization of Ti is more important and thus capable to produce a pronounced inverse bremsstrahlung absorption. Moreover, as no gas protection was used for the observation of the undisturbed plume, the formation of oxide nanoaggregates also takes place and contributes to beam scattering at high pulse times.

The main limitation in the experimental estimation of a global attenuation coefficient resides in the difficulty to conduct the measurement directly in the keyhole: in fact, only the expanding and thus the less dense part of the plume is studied, while the most dense and hot vapor residing in the keyhole remains inaccessible for measurement. On the other hand, the global absorption coefficients that are experimentally available, for example, through integrated sphere measurements [18], are based on the measurements of the residual laser radiation quitting the keyhole and do not provide the information about the actual quantity of radiation that could reach the bottom of the keyhole. It is likely that the attenuation coefficients inside the keyhole are much more important than the above cited values obtained from the attenuation of a lateral laser beam crossing the expanding plume. Further investigation on beam attenuation coefficients is needed. The indirect experimental validation of the employed β value based on keyhole penetrations is described in section 3.4.3.

The transition between the absorption coefficient for the flat surface and for the keyhole is managed by smoothed Heaviside function:

$$a_{Mi} = a_{0\,Mi} + (a_{att\,Mi} - a_{0\,Mi}) \cdot flc2hs\left(\frac{|dZ_{max}|}{2R_l} - 1, 0.5\right) \tag{39}$$

The resulting evolution of the local absorption coefficient of the keyhole walls is illustrated in Figure 1: for both dissimilar configurations, the constant value of absorption coefficient on the flat surface, grows with the initiation of the keyhole, and then decreases drastically due to the attenuation of the beam inside the keyhole, which leads to the keyhole stagnation by the end of the 15 ms pulse.

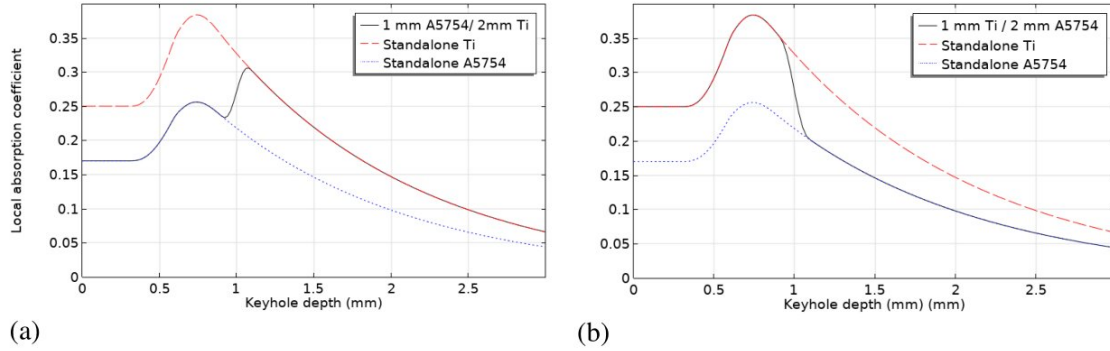(a)   (b)

Figure 1. The variation of local absorption coefficient with keyhole depth in the dissimilar combinations: (a) 1 mm A5754 / 2mm Ti and (b) 1 mm Ti / 2 mm A5754.

Finally, as the two considered metals have quite different vaporization temperatures, their respective recombination rates β_r can differ a lot during the evolution of the keyhole. For using different β_r value for each of the metals, the smoothed Heaviside function was used:

$$\beta_r = \beta_{r\,M1} + \left(\beta_{r\,M2} - \beta_{r\,M1}\right) \cdot \varphi \tag{40}$$

For an individual metal, the evolution of $\beta_{r\,Mi}$ within the range from 1 to 0.2 [19] is programmed as a smoothed Heaviside function inside the interval starting by the vaporization temperature of the metal T_{vap} and ending by the threshold temperature of intense vaporization T_{th}:

$$\beta_{r\,Mi} = 1 + (0.2 - 1)\, flc2hs\left(T - \frac{T_{th\,Mi} + T_{vap\,Mi}}{2}, \frac{T_{th\,Mi} - T_{vap\,Mi}}{2}\right) \tag{41}$$

As proposed by Pang et al. [20], when T_{th} was evaluated using the saturated vapor pressure curve of the metal: the values of 4500 and 6100 K were obtained in this manner for aluminum and titanium respectively.

1.1.2. Numerical implementation in Comsol Multiphysics 6.1

The symmetry along xz plane was considered to save the calculation time and resources. The calculation domain was given the thickness (z) of 3 mm, width (x) of 3 mm and depth (y) of 1.5 mm (Figure 2a). After each remeshing, the calculation goes on in the new automatically created geometry.

For the modeling of the most profound keyhole, 27 remeshings were needed. Due to the formalism of ALE method, when the deformed top boundary touches the bottom boundary, the calculation fails, as the mesh cannot be pierced. The remeshing method based on distortion criterion (equations 18-19) showed very good numerical stability and allowed reaching some quite impressive deformations of the top boundary, otherwise impossible (Figure 2b).

The calculation domain was meshed with tetrahedral elements with a maximal size of 120 µm. The semi-circular zone at the top boundary having a radius of 1.2 mm and roughly corresponding to the location of the melted zone and the keyhole, was meshed with the elements having a maximal size of 40 µm. In this way, the laser spot having 600 µm in diameter has about 15 elements at width on a flat surface. The use of small enough meshes for the top boundary and for the whole domain is needed in order to avoid losing the keyhole tip when remeshing highly-deformed geometries. In this calculation, the beam spot covers 5 volume elements, which seems to be enough to avoid this numerical artefact.
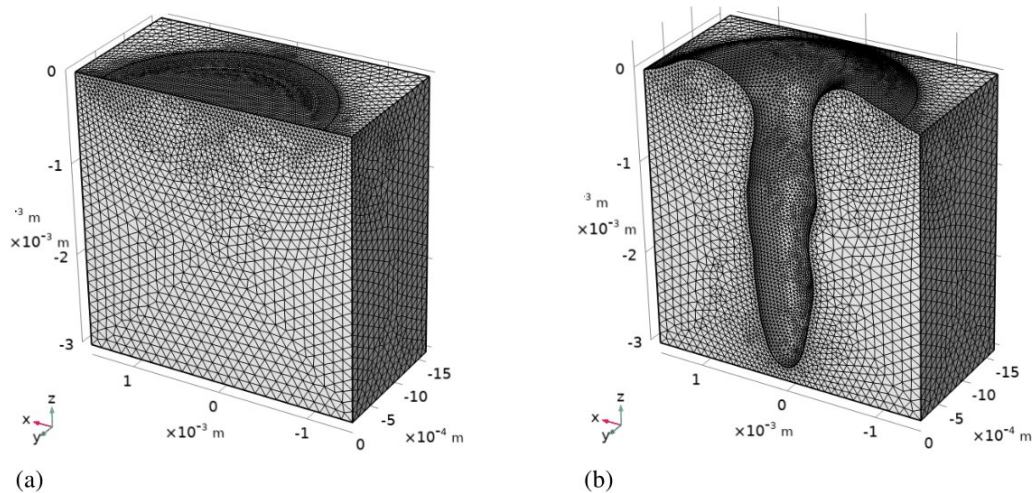

(a) (b)

Figure 2. Initial mesh (a) and the last remeshing (b).

In order to enhance the convergence of the model, the numerical stabilization methods based on artificial diffusion approach (such as consistent stabilization and isotropic diffusion) were activated for the solving of heat transfer and Navier-Stokes equations. Moving boundary smoothing option was activated in ALE method to avoid local roughness of the free surface due to local numerical instabilities.

The strong coupling between Heat transfer in fluids, Laminar Navier-Stokes and Moving Mesh modules was solved using direct solver PARDISO with constant Newton damping factor and Anderson acceleration. The model was solved up to output time of 18 ms with time step of 0.01 ms using the work station Intel ® Xeon ® CPU E5-2699v4 (2 processors, 2.2 GHz, 44 cores) and 256 Gb RAM. The longest calculation took about 3 days.

1.1.3.   Validation on mono-material cases

Before moving to the dissimilar overlap configurations, the model was validated on the standalone materials (by imposing h_{top} >> plate thickness) in different operational conditions. In the first place, the keyhole digging in titanium was compared to the experimental data obtained from 1.5 kW Yb:YAG laser pulses of duration from 2 to 12 ms on the butt-joint between two titanium plates (the spot diameter was 560 µm). The resulting variations of the depth and the width of the melted zone were compared to the calculation results (Figure 3). A quite good correspondence was observed for both parameters. In particular, the deceleration of keyhole digging starts to become visible after the melted zone penetration exceeds 1.2 mm (Figure 3a). Without the application of beam attenuation coefficient β, the penetration continues to increase in a linear manner and progressively deviates from the experimental values.
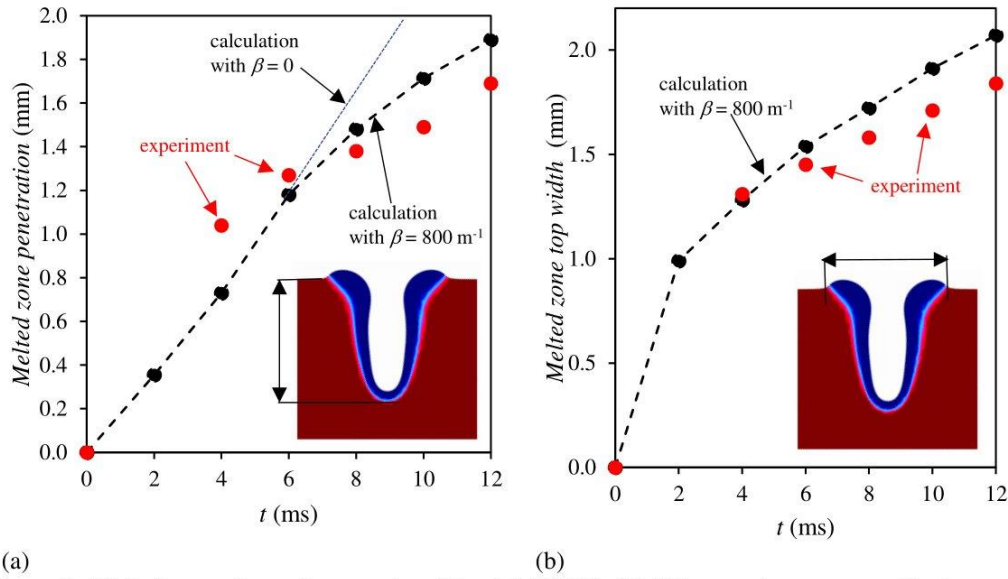
251

Figure 3. Melted zone dimensions produced by 1.5 kW Yb:YAG laser pulses on pure titanium : comparison between calculated and experimental penetrations (a) and top widths (b). Colored insert: equivalent viscosity map with liquid metal in blue and solid metal in red.

For standalone A5754, two operational conditions were tested, as this aluminum alloy exhibits a threshold character of keyhole initiation: 1.5 kW and 2.5 kW laser powers were used and the laser pulses of duration at A5754/A5754 butt-joint varied from 2 to 12 ms (the spot diameter was 560 μm). Good correspondence between calculated and experimental results was observed for both laser powers tested (Figure 4). The 1.5 kW laser power resulted in a conduction regime, where the energy density was not sufficient for keyhole initiation (in other words, the curvature of the melted zone was not enough to increase the local absorption coefficient), while 2.5 kW allowed to produce a several mm deep keyhole (Figure 4a). The attenuation of local absorption coefficient sensibly slowed down the keyhole drilling in this more energetic condition for penetrations > 1.5 mm, while for 1.5 kW laser power the stagnation of melted zone penetration corresponds to the inability to initiate the keyhole due to two reasons: insufficient absorbed energy and high thermal diffusivity impeding the efficient increase of surface temperature.
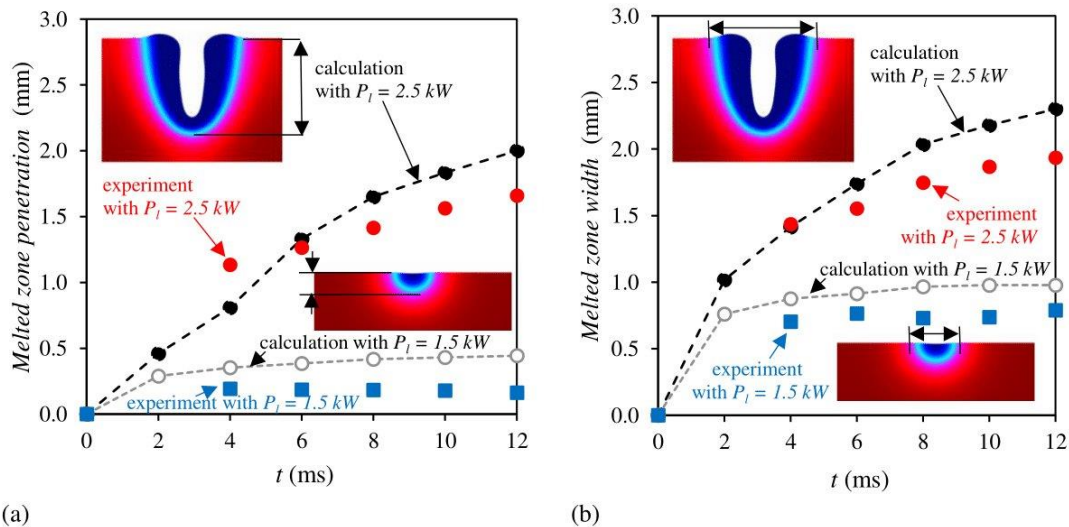

Figure 4. Melted zone dimensions produced by 1.5 and 2.5 kW Yb:YAG laser pulses on A5754 alloy : comparison between calculated and experimental penetrations (a) and top widths (b). Colored insert: equivalent viscosity map with liquid metal in blue and solid metal in red.

These encouraging results validated the hypotheses used in the model and permitted to move to the second part of the work: representing the keyhole and melted zone evolution in the overlapped dissimilar configurations.

1.1.4. Study of the overlapped configurations

The comparison with experiment for the overlap configuration was done basing on the measurements performed on the top plate and after the separation of the plates (Figure 5): width of the melted zone at the surface of the top plate, width of the broken melted zone after the separation of the plates (called interface melted zone width) and the width of the solidified keyhole that is often visible after the separation of the plates due to the keyhole trapping phenomenon. In 1 mm A5754 / 2 mm Ti overlap combination, the model stopped as the keyhole tip touched the bottom of the calculation domain (at ~10 ms), while in 1 mm Ti / 2 mm A5754 keyhole did not reach the bottom of the calculation domain, and the laser pulse of 15 ms was fully represented.

The melted zone development in 1 mm A5754 / 2 mm Ti combination (4.5 kW pulses) is composed of the following stages (illustrated at Figure 5): keyhole creation at A5754 alloy placed on the top, piercing of the joint interface (~2.4 ms) with keyhole progression in the bottom titanium plate, keyhole digging at the titanium plate and finally the end of the calculation due to the collision between top and bottom boundaries of the domain (10.3 ms). The characteristic times are close enough to the experimental values for the full penetration of the top plate (3-4 ms) and the bottom plate (7-8 ms). It can be noticed that the widths of the melted zones in top and bottom materials are very different: with A5754 alloy on top, the melted zone was wide and finally touched the lateral boundaries of the domain, the thickness of liquid layer in underlying titanium remained rather thin. This behavior is determined by the mismatch in fusion temperatures and thermal diffusivities. On the other hand, the keyhole did not show any visible asymmetry, despite the existing offset in vaporization temperatures. With time, the keyhole walls develop periodic ascending waves that propagate asymmetrically, which can explain the experimentally observed fluctuations of the plume.
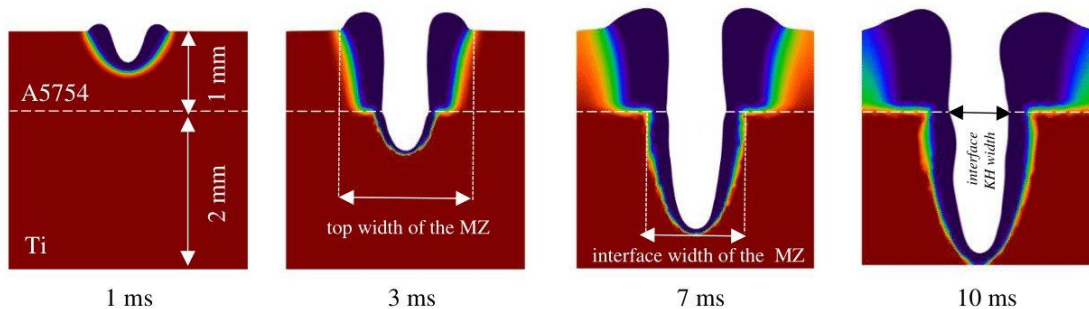

Figure 5. Melted zone evolution in 1 mm A5754 / 2 mm Ti overlap combination. Color map of equivalent viscosity: liquid metal in blue, solid metal in red. The indicated dimensions of the melted zone (MZ) and the keyhole (KH) were used for comparison with experiment.

The comparison of controlled dimensions (Figure 6) showed that the top width of the melted zone on A5754 plate was correctly estimated for pulse times < 4 ms, but then became a little overestimated, probably due to the small size of the calculation domain compared to the experimental plates. On the other hand, very good correspondence was found in melted zone widths at the interface between the plates. For some pulses (t > 3 ms), the keyhole opening at the interface between the plates could be experimentally observed. It was found to be close to the calculated size of the keyhole. Both calculated and observed keyhole widths tend to reach the value of spot diameter (600 µm).
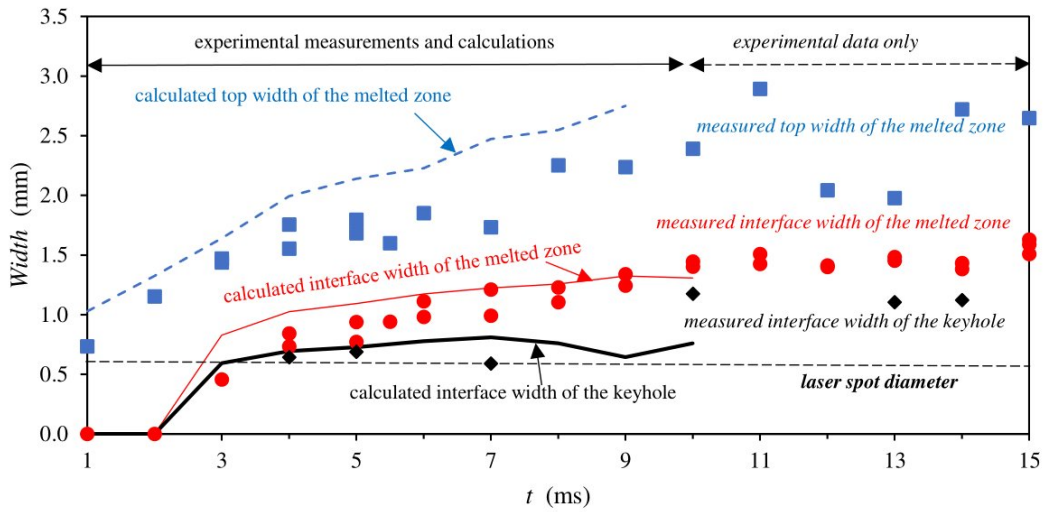
Figure 6. Measured and calculated melted zone and keyhole dimensions produced by 4.5 kW Yb:YAG laser pulses on 1 mm A5754 / 2 mm Ti overlap combination.

The melted zone development in 1 mm Ti / 2 mm A5754 combination (2 kW pulses) is composed of the following stages (illustrated at Figure 7) : keyhole evolution in top titanium plate, the penetration of the keyhole into underlying A5754 plate (at ~4.2 ms, which is close to the experimentally observed 5 ms) and the keyhole stagnation in A5754 till the end of the 15 ms pulse, characterized by asymmetrical undulations of keyhole walls. The width of the keyhole doesn't seem to be affected by the material change.
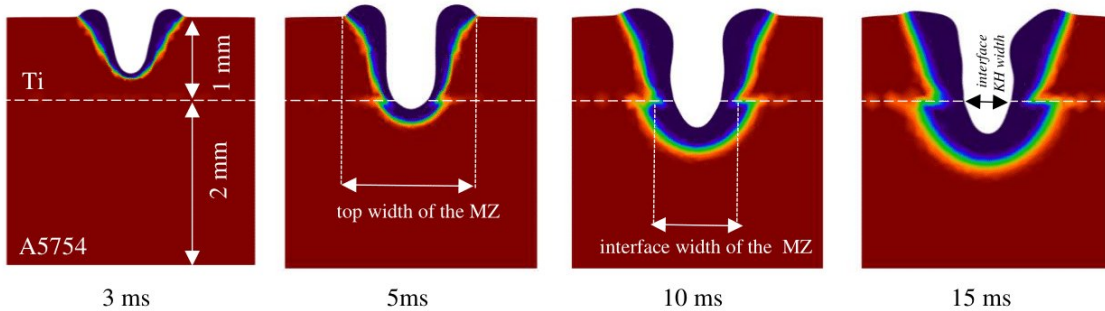

Figure 7. Melted zone evolution in 1 mm Ti / 2 mm A5754 overlap combination. Color map of equivalent viscosity: liquid metal in blue, solid metal in red. The indicated dimensions of the melted zone (MZ) and the keyhole (KH) were used for comparison with experiment.

The top width of the melted zone in the titanium plate was a little overestimated compared to a rather dispersed experimental data reflecting the irregular ejection of the melted matter (Figure 8). The melted zone width at the interface between the plates as a little overestimated, while the keyhole size is well-described and approaching the laser spot diameter.
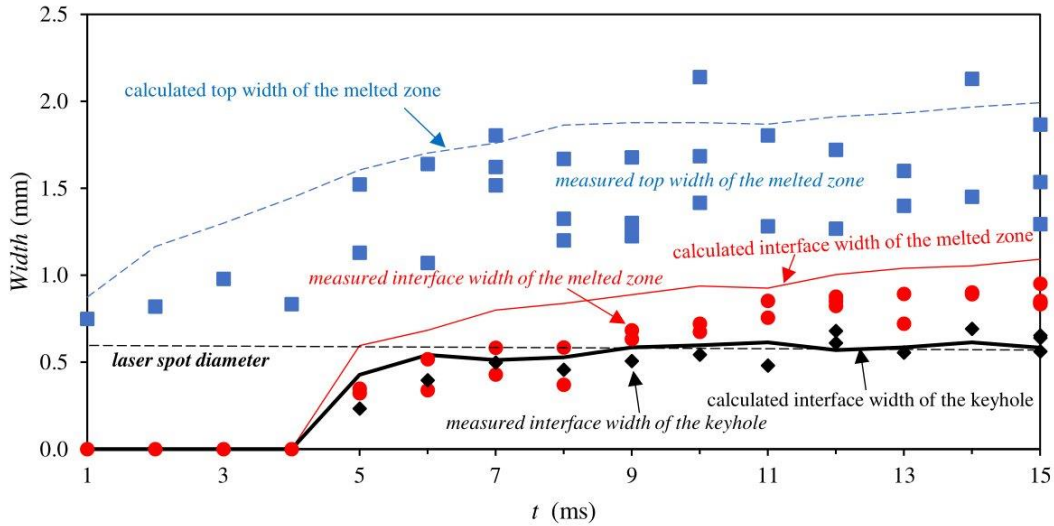
Figure 8. Measured and calculated melted zone and keyhole dimensions produced by 2 kW Yb:YAG laser pulses on 1 mm Ti / 2 mm A5754 overlap combination.

The keyhole penetration is not easily accessible for measurement in overlap welding, thus the numerical modelling of this parameter is of particular interest. The position of keyhole tip was controlled through the measurement of minimal value of z coordinate on the top boundary that undergoes deformation (z_{min} on Figure 9), as the z axis points upwards. Each curve of keyhole evolution presents three main segments that correspond to the keyhole initiation and keyhole progression in the top material followed by keyhole progression in the bottom material. The keyhole drilling velocities at these different stages were evaluated as the slopes of the linear functions fitted to the respective segments. In 1 mm A5754 / 2 mm Ti welded with 4.5 kW laser pulse, the velocity of keyhole initiation can be estimated as 0.41 m/s, the keyhole progression in the top A5754 occurs with drilling rate of 0.57 m/s, and, finally, the drilling rate in titanium equals 0.16 m/s. This deceleration is due to two reasons: higher vaporization temperature of titanium compared to A5754 and progressive shielding of keyhole bottom by the metallic vapor. The calculation stops as the keyhole reaches the bottom boundary of calculation domain.
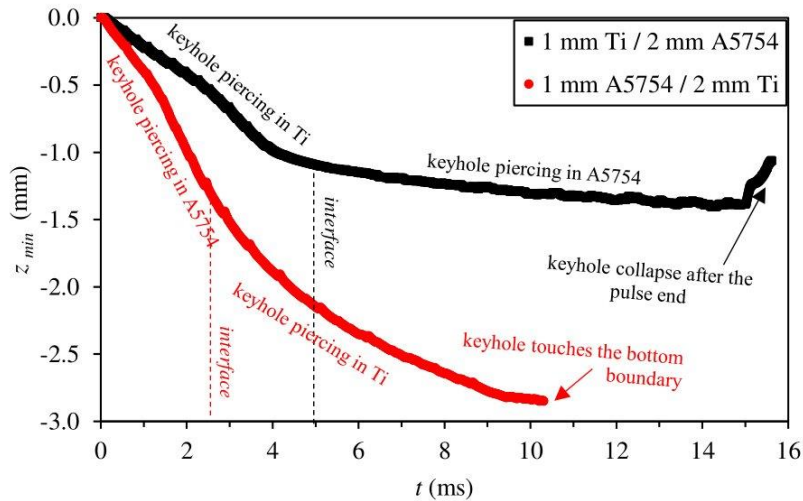

Figure 9. Temporal evolution of keyhole tip z-coordinate.

In 1 mm Ti / 2 mm A5754 configuration, welded with only 2 kW laser power (sufficient to produce the keyhole in titanium), the keyhole initiation in titanium occurs with rate of 0.2 m/s and keyhole progression in the top titanium plate at 0.30 m/s. However, the applied laser power is not sufficient to maintain the keyhole digging in A5754, despite its position in the bottom of the keyhole: the drilling

rate was of only 0.03 m/s till the end of the pulse (which correspond to the penetration of only 0.24 mm in bottom A5754 plate). For comparison, the calculated keyhole depth after 15 ms of 2 kW pulse on a flat A5754 surface resulted in keyhole penetration of 0.22 mm. The closeness of these penetration values allows supposing that the used laser power is not sufficient for deep keyhole drilling in A5754 even when it is situated at the bottom of the already existing keyhole. After the end of the pulse, the beginning of keyhole collapse is visible, with liquid flowing back into the keyhole and decreasing z_{min} value.

The maximal temperatures attained in the calculation domain varied in a different manner for the two considered overlap configurations (Figure 10). For the case 1 mm A5754 / 2 mm Ti, during the piercing in A5754 the maximal keyhole temperature fluctuated around 2600 K, which is about 100 K lower than $T_{vap\ Al}$, despite a high applied laser power of 4.5 kW. While entering the Ti plate at 4.2 ms, the maximal keyhole temperature suddenly rose up to ~3750 K, which exceeds by 100 K $T_{vap\ Ti}$, but then progressively dropped down to ~3300 K due to the growing beam attenuation by the plume. The temperature of keyhole remained very non-uniform: the keyhole top part remained much colder (T ~2000 K) as it is situated in a less absorptive and more conductive A5754. However, further taking into consideration of materials mixing would modify the obtained temperature distribution. For the case 1 mm Ti / 2 mm A5754, the keyhole initiated in titanium plate had a maximal temperature around 3500 K. With the involvement of underlying A5754 alloy after 4.5 ms, the temperature in the top part of the keyhole situated in Ti diminished down to ~3150 K in 1 ms and remained around this value till the end of the pulse, while the keyhole bottom stagnating in A5754 had a temperature of only ~2100 K. This cooling effect in titanium part of the keyhole can be attributed the domination of ascending convection movement from colder aluminum into hotter titanium.
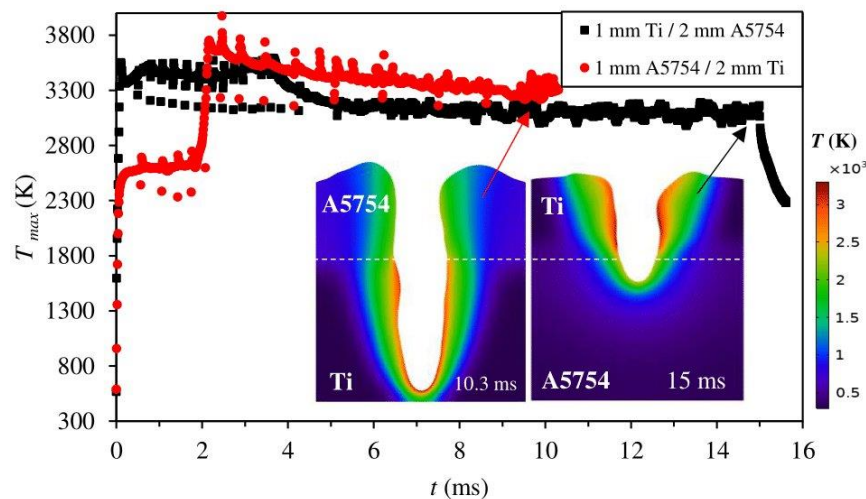

Figure 10. Temporal evolution of maximal temperature in the calculated domain and the illustration of thermal fields at given pulse times.

The amplitude of simulated velocity fields in the melted zones was rather moderate (Figure 11a) as it did not exceed 5 m/s. The case 1 mm A5754 / 2 mm Ti showed the maximal velocity of 3.5 m/s during the keyhole initiation in A5754, due to a high laser power, but after 4 ms the maximal velocity of the liquid metal fluctuated around 1 m/s. The case 1 mm Ti / 2 mm A5754, performed with lesser laser power (2 kW), resulted in a less intense velocity field amplitude ~ 1 m/s. After the extinction of the laser, the sudden rise of liquid velocity reflects the process of keyhole collapse.

The average melt velocity on the keyhole walls (Figure 11b) is of particular interest as it is related to the time necessary for the bottom material to reach the surface of the melted zone. During the keyhole evolution in top plates, the average velocity increases progressively to reach a fluctuating plateau at the pulse times corresponding to the drilling of the bottom plates. The realism of the calculated velocity field on the keyhole walls can be verified by a simple estimation of time needed to ascend the keyhole wall of 1 mm height, which corresponds to the thickness of a top plate. For 1 mm A5754 / 2 mm Ti, the experimental observation witnesses the ejection of bulk melted titanium starting from 7 ms pulse time, while the piercing of the top A5754 plate happens at minimum 3 ms. Consequently, the liquid titanium

takes about 4 ms to reach the top surface of the melted zone, which corresponds to the average velocity of 0.25 m/s, while the model provides the velocity interval of 0.26-0.12 m/s. On the other hand, according to experimental observations, in 1 mm Ti / 2 mm A5754 configuration, the bulk melted aluminum reaches the melted zone surface at pulse time of 12 ms, while the joint interface is reached by the melted zone at 5 ms. Consequently, melted aluminum takes 7 ms to reach the top surface of the melted zone, which corresponds to the average velocity of 0.14 m/s, while the model gives 0.2-0.1 m/s. These results allow concluding that the model provides an adequate amplitude of velocity field and correctly reacts to the variation of laser power, as the velocities are more intense for the 1 mm A5754 / 2 mm Ti configuration welded with 4.5 kW (0.26-0.12 m/s) compared to 1 mm Ti / 2 mm A5754 configuration welded with 2 kW (0.2-0.1 m/s).
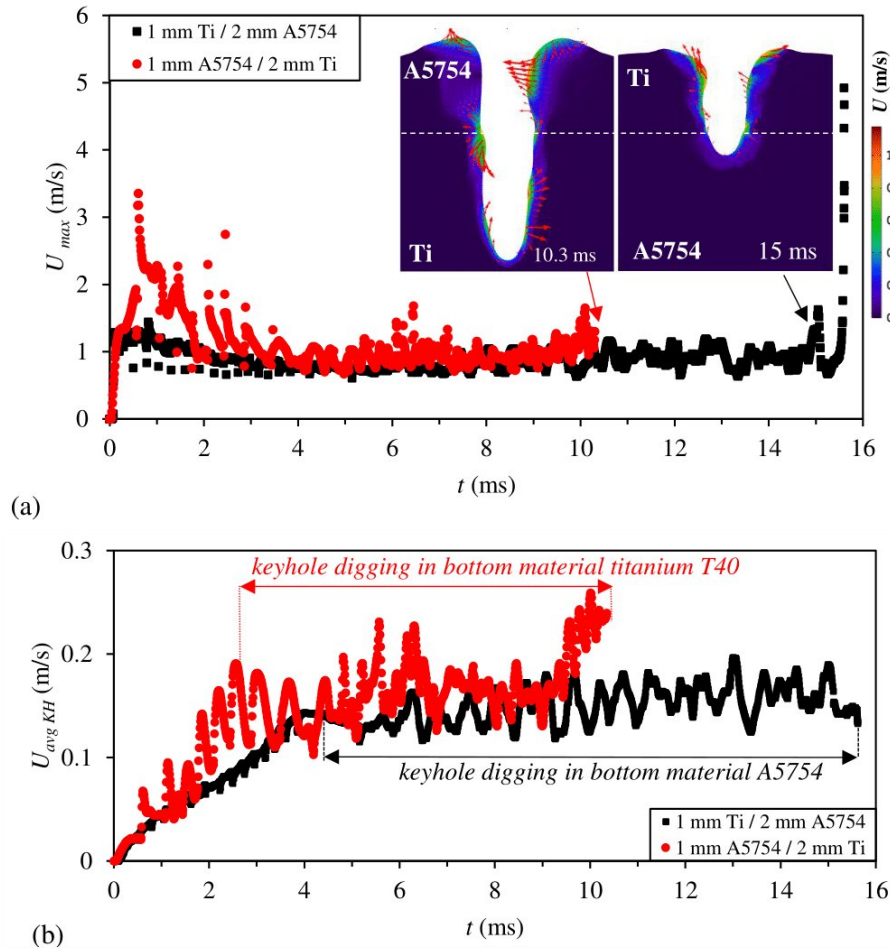

(a)

(b)

Figure 11. Temporal evolution of maximal velocity field in the calculated domain along with illustration of velocity field morphologies at given pulse times (a); temporal evolution of average velocity on keyhole walls (b).

It is interesting to note that the velocity fields in the melted zones progressively develop important instabilities (Figure 11a: color inserts) that create the asymmetrical ascending waves along the keyhole walls. The frequency of this waves was monitored through the fluctuation of x-coordinate of the keyhole wall situated in a symmetry plane xz at depth of $z = -0.5$ mm from the top plate surface (Figure 12).

In case of 1 mm A5754 / 2 mm Ti combination, the first fluctuations of very weak amplitude begin between 2 and 3 ms, as the bottom plate is reached by the keyhole, however, they gain in amplitude only after 5 ms. The periodicity of these fluctuations was of 0.43±0.12 ms. On the other hand, in 1 mm Ti / 2 mm A5754 combination, the quick and pronounced fluctuations begin at ~ 6 ms, after the melting of A5754 plate begins, and then they slow down and gain in amplitude after 9 ms, as the keyhole tip progressively moves in A5754. The periodicities of quick and slow fluctuations were of 0.29±0.09 ms and 0.47±0.09 ms respectively.

It can be supposed that these fluctuations are related to the increase of liquid layer thickness (producing local gravitational instability) rather than to the simple increase of keyhole depth, as the keyhole depth is quite different in these two considered cases. However, such pronounced fluctuations were not observed in the calculations for standalone materials (Figure 12), which may signify a specific synergetic effect from the association of titanium and aluminum in overlapped configuration.
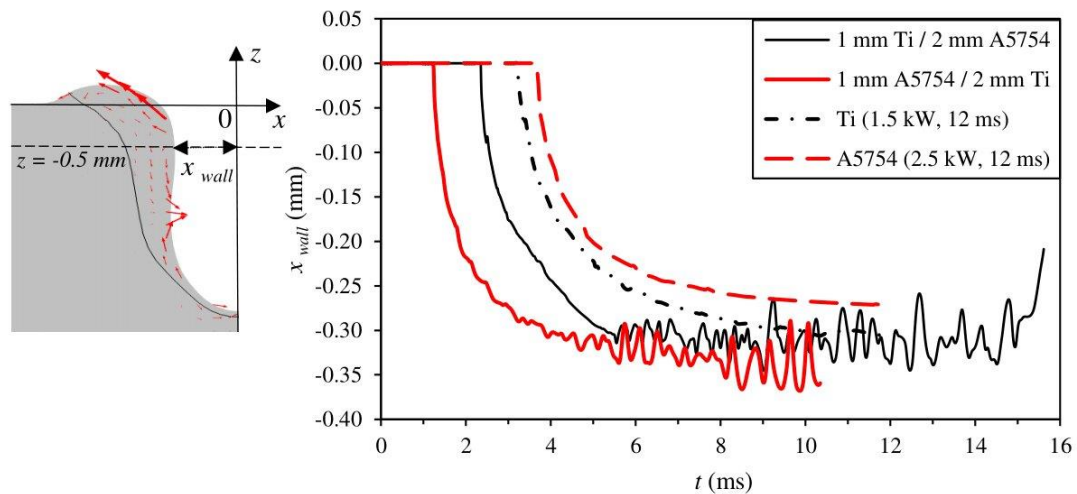

Figure 12. Temporal evolution of *x*-coordinate of the left keyhole wall on the symmetry plane *xz* at depth *z* = -0.5 mm in overlapped configurations and in standalone materials.

1.2. Discussion

1.2.1.1. Phenomenological timelines

The obtained experimental and numerical results allowed to elaborate the timelines resuming the main findings on the evolution of the melted zone and the plume for two considered dissimilar configurations. In both cases, the melted zone and the keyhole reach a stationary condition, characterized by constant dimensions.

In case of 1 mm A5754 / 2 mm Ti, the numerical model slightly overestimates the frequency of hydrodynamic instabilities (calculated periodicity of 0.43 ms instead of observed 0.67-0.68 ms), but probably underestimates their amplitude, as the luminosity of the plume varies to a high extent. This can be related to the lack of precision in the representation of local temperature fluctuations of keyhole walls and local variations of surface tension in ambient atmosphere. Due to the ascendant convective flow, the drops of melted titanium having a higher temperature than Al-rich melt promote the evaporation of Al and Mg even as the keyhole drills the underlying titanium plate. The ejection of bulk melted titanium is delayed (to *t* = 7 ms) by a moderate liquid velocity field on the keyhole walls.

The stagnation of the keyhole tip in A5754 alloy was correctly reproduced by the model. Unlike the previous case, the rapid fluctuations of the keyhole walls traduced by the observable bursts of the plume take place from the very beginning of keyhole formation, while the model shows these only starting from *t* = 5 ms. The periodicity of these rapid fluctuations is however well evaluated by the model (0.29 ms) compared to the experimental observations (0.25-0.29 ms).

1.2.1.2. Critical evaluation and perspectives

The first question that arises after analyzing both dissimilar configurations is which material should be on top. Placing aluminum alloy on the top signifies the necessity to use a higher laser power, that is sufficient to drill the keyhole in this reflective material. However, this very power produces a rapid keyhole drilling in underlying titanium. Taking into account the need to reduce the mixing between the materials during their dissimilar joining by fusion in order to reduce the formation of intermetallic phase, placing aluminum on the top makes it delicate to control the dilution process. According to EDS analysis, the mixing between the materials occurs rapidly after reaching the dissimilar interface. On the

other hand, placing titanium on the top and using laser power sufficient for drilling titanium but too weak for drilling of highly conductive and reflective aluminum, offers a comfortable set of pulse times when the bottom material is already melted, but the keyhole is stagnating and the violent mixing does not take place.

High-speed imaging of the plume showed moderate sensibility to the different events taking place in the keyhole, mainly because of the important fluctuations of the plume. As it was demonstrated through numerical modeling (*section 1.1.4*), such fluctuations originate from the instabilities of keyhole walls. This kind of monitoring would be more informative with a more stable keyhole, created by the superposition of two different laser spots [21] or a combination of a ring spot with Gaussian spot [22] etc. Nevertheless, the monitoring of plume luminosity at 810 nm for detecting the time when the keyhole tip becomes established in lower aluminum plate would be interesting to explore, basing on approach using photodiodes proposed by Seibold et al.

The quality of results in emission spectroscopy also suffers from plume instability, as the emission peaks of the minor elements present in the plume are not detected systematically, and the cumulated intensities of all peaks present some random variations. Another problem consists in the redeposition of volatile elements (Al, Mg and their oxides) around the melted zone and their further involvement in the plume of the next impact. However, analyzing the obtained spectra is a powerful tool for understanding the whole process.

Concerning the spectral monitoring based on atomic emissions, the Al involvement in the melted zone in Ti/A5754 combination can be monitored directly using main Al I line at 394.40 nm, that is unobstructed by Ti I emissions, while the online monitoring of Mg I in the studied 381.3-384.3 nm region is not possible due to the superposition with numerous intense Ti I lines and the necessity to perform deconvolution. Moreover, it is important do either get rid of Al and Mg impurities on the plate surface during the process or apply a threshold to reject the neglectable contributions. The detection of the involvement of bottom titanium plate into the process is possible using 465.64 and 466.75 nm Ti I lines, however, the contribution of molecular AlO bands should be eliminated through deconvolution.

2. Conclusions

The numerical modelling contributed significantly for the better understanding and quantification of melted zone and keyhole development. The performed validation demonstrated that the proposed approach allows a globally correct representation of the heat transfer and fluid flow dynamics. However, it should be completed by the mixing aspect between the materials, such as level set [23] or diffusion of species supported by convection [1]. The aspect of laser beam shielding by condensed metallic vapor inside the keyhole and by undulating keyhole walls should be more researched upon, both experimentally and numerically.

A multiphysical finite element model was proposed to represent the keyhole progression into the dissimilar joint. A hypothesis about the strong shielding of laser beam by a dense and ionized metallic vapor existing inside the keyhole allowed approaching experimentally observed weld penetrations, however, it demands an additional experimental investigation. Moreover, the accumulating instabilities of the keyhole walls were found to be in agreement with the observed fluctuations of the vapor plume.

3. References

[1] J. Wu, H. Zhang, Y. Feng, B. Luo, 3D Multiphysical Modelling of Fluid Dynamics and Mass Transfer in Laser Welding of Dissimilar Materials. *Metals 8*, 443 (2018). https://doi.org/10.3390/met8060443

[2] W. Huang, H. Wang, T. Rinker, W.Tan, Investigation of metal mixing in laser keyhole welding of dissimilar metals. Materials & Design 195, 109056 (2020). https://doi.org/10.1016/j.matdes.2020.109056.

[3] G. Chianese, S. Jabar, P. Franciosa, D. Ceglarek, S. Patalano, A multi-physics CFD study on the part-to-part gap during remote laser welding of copper-to-steel battery tab connectors with beam wobbling. Procedia CIRP 111, 484-489 (2022). https://doi.org/10.1016/j.procir.2022.08.075.

[4] I. Tomashchuk, J.-M. Jouvard, P. Sallamand, M. Duband, Modeling of the keyhole asymmetry in dissimilar laser welding, in: Comsol Conference Europe 14-16 October 2020, Virtual Edition. https://www.comsol.fr/paper/modeling-of-the-keyhole-asymmetry-in-dissimilar-laser-welding-94091

[5] C. J. Knight, Theoretical modeling of rapid surface vaporization with back pressure. American Institute of Aeronautics and Astronautics Journal 17 (5), 19–523 (1979). https://doi.org/10.2514/3.61164

[6] M. Courtois, M. Carin, P. Le Masson, S. Gaied, M. Balabane, A complete model of keyhole and melt pool dynamics to analyze instabilities and collapse during laser welding. Journal of Laser Applications 26 (4), 042001 (2014). https://doi.org/10.2351/1.4886835

[7] R. Fabbro, K. Chouf, Dynamical description of the keyhole in deep penetration laser welding, Journal of Laser Applications 12 (4), 142-148 (2000). https://doi.org/10.2351/1.521924

[8] E. Guyon, J.P. Hulmin, L. Petit, Hydrodynamique Physique, Edition du CNRS (1994).

[9] COMSOL Multiphysics 6.1 integrated help.

[10] R. Indhu, V. Vivek, L. Sarathkumar, A. Bharatish, S. Soundarapandian, Overview of laser absorptivity measurement techniques for material processing, Lasers in Manufacturing and Materials Processing 5, 458–481 (2018). https://doi.org/10.1007/s40516-018-0075-1

[11] I. Tomashchuk, J.-M. Jouvard, M. Duband, In-situ study of keyhole behavior during a laser pulse applied to the dissimilar metal joint. Metallurgical Research & Technology 120, 412 (2023). https://doi.org/10.1051/metal/2023043

[12] J. F. Ready, Effects of high-power laser radiation. New York: Academic Press (1971).

[13] D. Coviello, A. D'Angola, D. Sorgente, Numerical Study on the Influence of the Plasma Properties on the Keyhole Geometry in Laser Beam Welding, Frontiers in Physics 9, 754672 (2022). https://doi.org/10.3389/fphy.2021.754672

[14] J. Greses, P. Hilton, C. Barlow, W. Steen, Plume attenuation under high power Nd:YAG laser welding. In : Proceedings of ICALEO 2002, Scottsdale, Arizona (USA), paper 808. https://doi.org/10.2351/1.5065740

[15] P. Y. Shcheglov, S.A. Uspenskiy, A Gumenyuk, V.N. Petrovskiy, M. Rethmeier, V.M. Yermachenko, Plume attenuation of laser radiation during high power fiber laser welding. Laser Physics Letters 8, 475 – 480 (2011). https://doi.org/10.1002/lapl.201110010

[16] R. Rai, J. W. Elmer, T.A. Palmer, T. Debroy, Heat transfer and fluid flow during keyhole mode laser welding of tantalum, Ti–6Al–4V, 304L stainless steel and vanadium. Journal of Physics D: Applied Physics 40, 5753 (2007). http://dx.doi.org/10.1088/0022-3727/40/18/037

[17] N. Shaikh, S. Hafeez, B. Rashid, M. A. Baig, Spectroscopic studies of laser induced aluminum plasma using fundamental, second and third harmonics of a Nd:YAG laser. European Physics Journal D 44, 371–379 (2007) https://doi.org/10.1140/epjd/e2007-00188-3

[18] N. Pierron, P. Sallamand, S. Matteï, Study of magnesium and aluminum alloys absorption coefficient during Nd:YAG laser interaction. Applied Surface Science 253 (6) 2007, 3208-3214. https://doi.org/10.1016/j.apsusc.2006.07.035

[19] A. A. Samokhin, Effect of laser radiation on absorbing condensed matter, Nova Science Publishers, 1990.

[20] S. Pang, X. Chen, J. Zhou, X. Shao, C. Wang , 3D transient multiphase model for keyhole, vapor plume, and weld pool dynamics in laser welding including the ambient pressure effect. Optics and Lasers in Engineering 74, 47-58 (2015). https://doi.org/10.1016/j.optlaseng.2015.05.003

[21] F. Nagel, L. Brömme, J. P. Bergmann, Description of the influence of two laser intensities on the spatter formation on laser welding of steel. Procedia CIRP 74, 2018, 475-480. https://doi.org/10.1016/j.procir.2018.08.147

[22] E. Punzel, F. Hugger, T. Dinkelbach, A. Bürger, Influence of power distribution on weld seam quality and geometry in laser beam welding of aluminum alloys. Procedia CIRP 94, 2020, 601-604. https://doi.org/10.1016/j.procir.2020.09.086

[23] I. Tomashchuk, P. Sallamand, J.M. Jouvard, D. Grevey, The simulation of morphology of dissimilar copper-steel electron beam welds using level set method. Computational Materials Science 48 (4), 827-836 (2010). https://doi.org/10.1016/j.commatsci.2010.03.042